Construction of Covalent Organic Frameworks as Platforms for Molecular Heterogeneous Catalysis in Defined Geometries

Sebastian Thomas Emmerling

aus
München, Deutschland

2022

Erklärung

Diese Dissertation wurde im Sinne von § 7 der Promotionsordnung vom 28. November 2011 von Frau Professor Dr. Bettina V. Lotsch betreut.

Eidesstattliche Versicherung

Diese Dissertation wurde eigenständig und ohne unerlaubte Hilfe erarbeitet.

München, 12.09.2022

…………………………………..

(Sebastian Thomas Emmerling)

Dissertation eingereicht am: 14.09.2022

1. Gutachterin: Prof. Dr. Bettina Lotsch

2. Gutachter: Prof. Dr. Konstantin Karaghiosoff

Mündliche Prüfung am: 17.10.2022

„The mystery of life isn't a problem to solve, but a reality to experience."

Frank Herbert, *Dune*

Abstract

Given the overwhelming negative impact that humanity has had on the planet's ecosystem and climate over the last century, triggered by industrialization and a rapidly growing population, a rethink of how we provide necessary and luxurious consumer goods is imperative. A shift to greener production alternatives that continue to provide us with vital chemical products and enable environmentally friendly prosperity is urgently needed. One way to improve production efficiency and reduce unnecessary waste of energy and resources is to take a cue from nature itself. By emulating principles found in nature that have stood the test of time for millions of years, we could evolve our production methods toward similar, highly efficient processes and reduce our impact on the environment. One of these principles is found in highly specialized and productive enzymes - confining reactions in a defined local environment that allows a high degree of control over reactions, such as selectivity, stabilization of intermediates, or spatial approximation of substrates.

In this thesis, the influence of confinement on molecular heterogeneous catalytic reactions in pores of covalent organic frameworks (COFs) is investigated. As a new class of framework materials consisting of two- or three-dimensional covalently extended crystalline networks composed of light elements, COFs are suitable substrates for this investigation due to their intrinsic porosity, chemical flexibility, and defined structures. They provide a large surface area in the well-defined pores for heterogenized, defined molecular catalysts, and knowledge of the atomistic structure of the material allows conclusions to be drawn about the local environment and its influence on the reaction.

The pore sizes relevant for the observation of confinement effects are expected to be maximized between 4 and 6 nm in diameter, which is larger than the pore sizes of up to 3 to 4 nm prevalent in most COFs. To this end, an isoreticular series of large pore 2D COFs with hexagonal pore structure was developed. The challenging development of COFs with large pores is realized in a comprehensive study of the effects of noncovalent interlayer interactions on large-pore COF systems. The strength of the noncovalent interlayer interactions is modulated by incorporating different numbers of methoxy groups into the building blocks that make up the framework, and the pore size is varied by increasing the length of the building blocks. By varying building block length and interlayer interactions, a matrix of six COFs was created, and correlations between these features were found. Increasing the pore size/building block lengths leads to AB stacking structures where the layers are displaced from each other, leading to a pore size decrease. Increasing the noncovalent bonds between the layers, acting as "anchors", prevents the layers from shifting against each other, resulting in a nearly eclipsed structure. By adjusting the interactions between the layers, different stacking modes can be achieved, enabling modified stacking polytypes and thus effective pore sizes as large as 5.8 nm. In addition, a strong correlation between stacking energy

and enhanced structural stability at elevated temperatures was observed, as well as a novel thermally induced phase transition of stacking modes in COFs. These results shed light on viable design strategies for improved structural control and stability in large pore size COFs.

Based on these design principles, a highly porous and crystalline large pore size COF was developed and selected as a catalytic support to study confinement effects in α,ω-diene ring closure metathesis reactions. By modifying the pore wall with a Ru-Grubbs-Hoveyda type catalyst, the selectivity of macro(mono)cyclization (MMC) over oligomerization (O) in the α,ω-diene ring closure reaction was tested with four substrates of different sizes and polarities. A dependence of selectivity on substrate size was observed, indicating diffusion limitations due to pore confinement, which resulted in an increase in the MMC:O ratio for the heterogeneous COF catalyst system (MMC:O = 1.35) by up to 51% compared to the homogeneous catalyst (MMC:O = 0.90).

In addition, fundamental aspects of green and scalable COF formation by mechanosynthesis were investigated, which are currently poorly understood. By combining *in situ* X-ray powder diffraction and Raman spectroscopy to elucidate the underlying reaction mechanism of liquid-assisted mechanochemical synthesis of imine COFs, two important intermediate solvates were observed, providing the first direct experimental evidence for the role of liquid additives in framework formation. A solid scandium triflate catalyst was used for the first time in the mechanochemical formation, affecting the reaction kinetics and mechanism and leading to more crystalline and porous COFs that were on par with the solvothermal products. This work represents a significant advance in the mechanistic understanding and improving product quality of mechanochemical COF formation and validated it as a green route for sustainable COF synthesis.

Finally, the adsorption of nitric oxide on COFs was investigated for the first time as a potential new application of COFs for separation and storage of hazardous gases. On four different COF linkages - imine, amine, imide and thiazole - the scaffold integrity, gas adsorption capacity and selectivity of NO, according to the ideal adsorption solution theory (IAST), were tested. With ^{15}N enrichment at the crucial linkages of all four COFs for improved sensitivity of solid-state nuclear magnetic resonance spectroscopy, different physical and chemical interactions of NO with the materials were investigated. The reaction and deamination of unreacted terminal amine groups during NO exposure was detected, suggesting a novel passivation strategy for the outer surface of COFs. In addition, the reaction of amine-linked COF with NO formed a novel NONOate linkage that showed controlled release of bound NO under physiological conditions, making this material or linkage type a potential candidate for drug delivery and biomedical applications.

Table of Contents

1. Introduction to Biomimetic Catalysis under Confinement

According to most current theories, life on Earth began rather simply more than 3 billion years ago with a probiotic synthesis of small and robust molecules that then assembled into more complex, self-replicating entities.[1–4] These early molecules must have been strongly defined by their ability to withstand harsh conditions during this Earth period, rather than the high specialization, diversity and complexity now associated with cell biology.[5–7] This high specialization of biomolecules, like DNA, RNA, proteins and enzymes, is the product of natural selection – the molecular evolution.[8,9] There the concepts of the Darwinian theory for the transmutation of species by a change in heritable characteristics over successive generations and the outcomes – adaptation, coevolution, cooperation, speciation, and extinction - can be applied on a molecular level.[10,11] Over millions of years, these processes resulted in the refined enzymes we can see in cell biology today, which act as examples for chemist in catalysis in terms of efficiency and specialization. Sophisticated substrate confinement at well-defined active sites allows for exceptional shape selectivity and often even selection of a particular enantiomer (Figure 1.1).[12,13] Considering that catalysts are used in an estimated 80% of all reactions in the chemical and pharmaceutical industries, their undeniable importance for industrial purposes becomes clear as well.[14–16] High selectivity is essential for the utility and economy of these processes. It is only logical that researchers look to the sophisticated catalysts in nature and their concepts to achieve a similar level of specialization and efficiency for further improvements in artificial catalysis.[17] While the growing field of biocatalysis is already taking advantage of confinement, the field of artificial homogeneous and heterogeneous catalysis can further leverage and apply successful confinement concepts to catalysis in a biomimetic approach (enzyme mimetics) to further improve its reaction selectivity and efficiency. The following chapter will look at the general principles of confinement and how researchers have utilized them so far in various fields of catalysis.
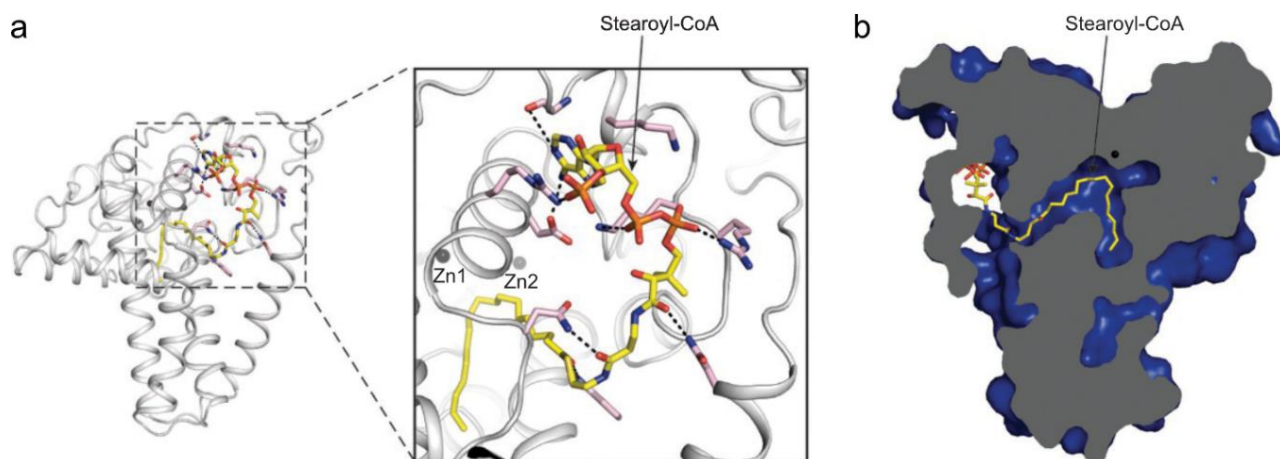
Figure 1.1. (a) Substrate stearoyl-CoA–binding site in hSCD1 structure showing the confinement of stearoyl-CoA at the well-defined binding site. This substrate shape selectivity and predefined orientation translates into the high enantiomer selectivity of the desaturation product of the stearoyl moiety. (b) Cross-sections of the hSCD1 surface area (blue) showing a tunnel-like pocket for the acyl tail of stearoyl-CoA. Taken and adapted with permission from Ref. [13]. Copyright 2015 Springer Nature.

1.1. Principles of Confinement in Catalysis

In catalysis, confinement is usually understood as the presence of a chemically and geometrically well-defined space around the active catalyst center, which influences and changes the reaction outcome.[18] This surrounding space is also referred to as the second coordination sphere. The second coordination sphere can alter and improve the key parameters of catalysis - activity, selectivity and stability - in several ways: (i) It can favor the proximity, local concentration and pre-organization of substrates to the active site, thereby increasing the reaction rate.[19] (ii) The geometric aspects of the confined space can act selectively toward substrate size and shape or isolate substrates to single or few molecules around the catalytic center preventing undesired polymerization side reactions (Figure 1.2).[20–22] (iii) Pre-organization of the substrate into high-energy conformations and strong binding of transition state intermediates can lower activation barriers and increase reactivity or force and enhance stereo- or enantioselectivity.[13,23] (iv) Confinement can also alter fundamental properties of molecules such as excitation energies, enlargement of the HOMO-LUMO gap, or molecular electrostatic potentials.[17,24,25] (v) Finally, surface adsorption can be affected, and structure, dynamics, and dielectric constants of liquids/solvents under confinement are altered, changing the conditions for solubilized substrates.[26–28] This wide range of effects induced by confinement opens up nearly limitless possibilities for chemists to use in developing more efficient homogeneous or heterogeneous catalyst systems. However, little is known about the interplay of these effects, making it a major challenge to fully predict and engineer them to achieve specific properties. The recent and increasing focus on confinement effects, particularly in homogeneous catalysis, will certainly help to understand the underlying relationships and enable rational design of catalyst systems in the future.
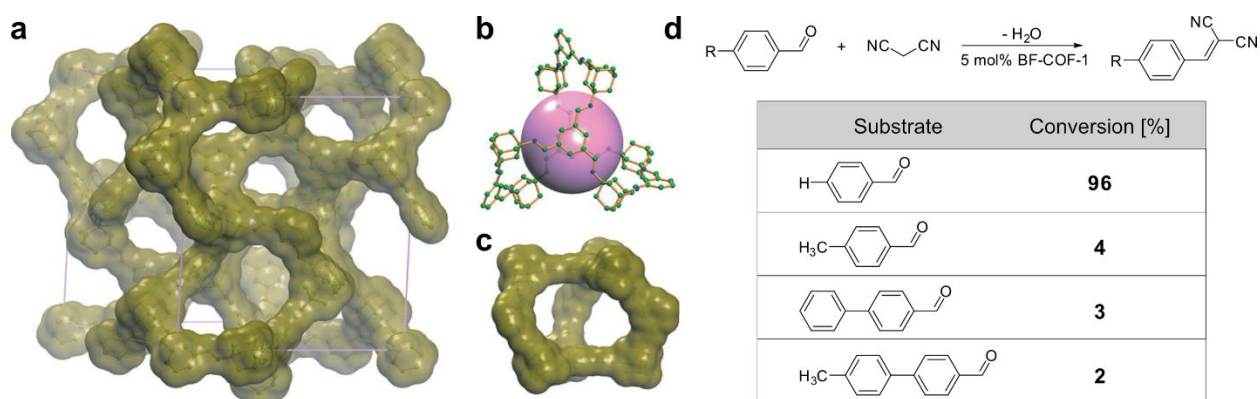
Figure 1.2. Example for a catalyst BF-COF-1 utilizing confinement to impose size-selectivity. (**a**) Structure of BF-COF-1 with atom surfaces in olive green. (**b**) Depiction of a microporous cavity (pink sphere, 7.8 Å diameter). (**c**) Display of pore openings with a diameter of 7.8 x 11.3 Å^2. (d) Knoevenagel condensation reaction catalysed by BF-COF-1 showing selectivity in substrate size. Taken and adapted with permission from Ref. [20]. Copyright 20014 John Wiley and Sons.

1.2. Confinement in Homogeneous Catalysis

Small Molecule Systems

Examples of reactions and catalysts using confinement effects in small molecule systems are still rare, and there remain unresolved questions about the precise definition of confinement and second-coordination sphere effects in some of these systems.[17] Nevertheless, early examples may involve the use of bulky groups that affect the reaction outcome by occupying and confining the reaction space.[29,30] Maruoka *et al.* reported a molecular recognition approach for an *exo*selective Diels-Alder reaction using a sterically demanding Lewis acid (Figure 1.3).[31] These Diels-Alder cycloadditions usually exhibit strongly favored *endo*-selectivity due to secondary orbital interactions during the *endo* transition state.[32,33] By using the Al(ATPH)$_3$ Lewis acid they developed instead of the commonly used AlMe$_3$ to activate the carbonyl, they were able to abolish the *endo* preference in favor of the *exo*-diastereomer product. Complexation with the sterically bulkier Lewis acid creates an effective carbonyl pocket that ultimately favors the *exo*-transition state, leading to the observed selectivity.

While this size-selective reactivity due to complexation mimics the geometric aspects and influences on the transition state energies found in confined spaces, the Lewis acid usually acts as a reagent and cannot be classified as catalyst. The shown reaction is a rare exception where the Lewis acid also acts as a catalyst for the transformation.
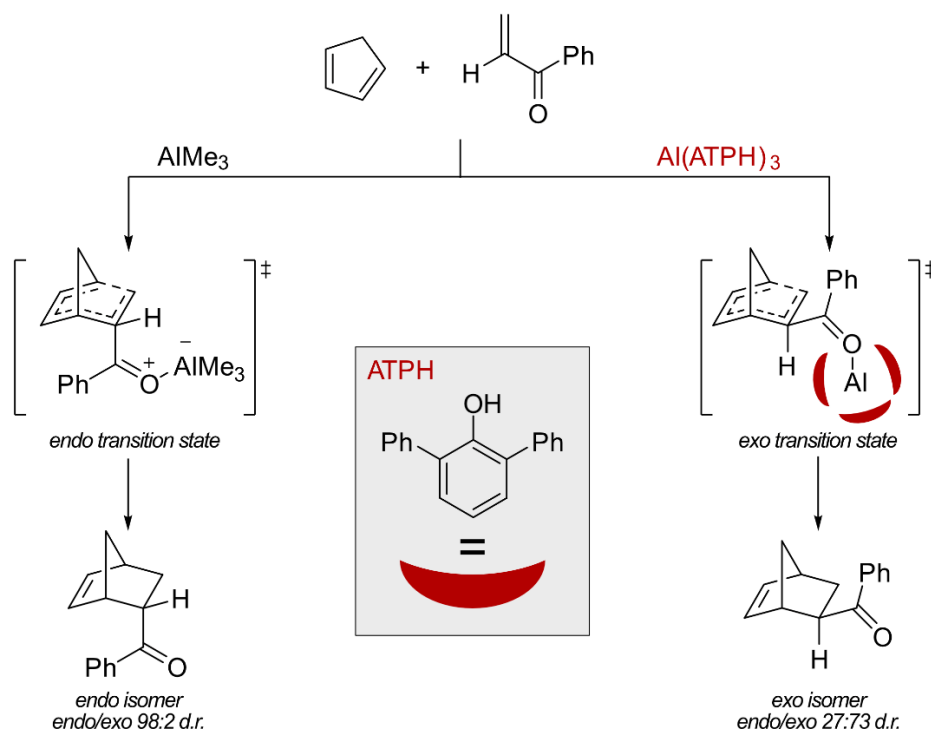
Figure 1.3. Coordination of bulky organoaluminium Lewis acids shields the carbonyl moity and leads to a size-selective control of the diastereoisomeric reaction towards the *exo* product.[31]
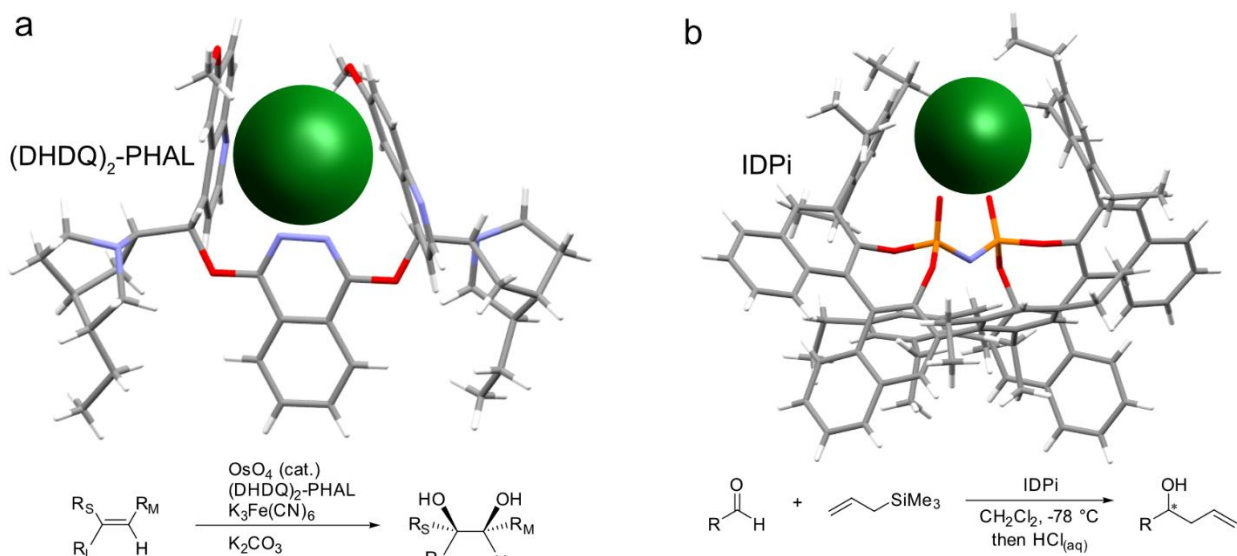
Figure 1.4. Comparison of crystal structure of (a) (DHDQ)2-PHAL and (b) IDPi and the corresponding reaction they catalyse below. Green balls clarify the active site pockets enclosed and influenced by a second ligand sphere.[34,35]

Alkaloid-based catalyst systems for the asymmetric dihydroxylation of olefins (Figure 1.4, a),[34,36,37] or imidodiphosphate (IDP) based systems acting as constrained chiral Brønsted and Lewis acids (Figure 1.4, b), better fit the concept of confined catalysis.[35,38,39] In both cases, the active catalyst sites are located in well-defined cavities enclosed by a second ligand sphere, allowing stereoinduction in these asymmetric transformations. The crystal structure of the alkaloid-based ligand shows an Angstrom-scale pocket with well-defined binding sites for the OsO4 catalyst that can accommodate olefin substrates for highly selective dihydroxylation. Corey *et al.* demonstrated this selectivity on retinyl acetate (vitamin A) in an enzyme-like reaction with an exclusive reaction at the 13,14-olefinic bond with high enantioselectivity (40:1).[37] They attribute the high enantioselectivity to extensive π-contacts of the polyene chain of retinyl acetate with the catalytic binding pocket and a favorable contact between the acetate end group and the phthalazine moiety. Reaction with other olefin units of retinyl acetate is prevented by steric constraints of the bulky cyclohexyl group with the catalyst.

The IDP-based system, developed as recently as 2012,[38] uses the same enzyme-like steric shielding of the reaction site. The high modularity of the IDP catalyst and its very general use as Brønsted and Lewis acids lead to a broader range of asymmetric reactions than the alkaloid-based catalyst systems, e.g., in spiroacetalization, Diels-Alder reactions, Mukai-Yama-Michael reactions, or Nazarov cyclizations.[17,39–42] In 2018, Schreyer *et al.* used confinement provided by IDPi not only for stereoinduction but also for substrate isolation and size selectivity in single aldolizations of acetaldehyde enolates.[43] The Mukaiyama aldol reaction of a simple triethylsilyl (TES) enolate of acetaldehyde usually leads to uncontrolled polymerization, as the originally formed product contains a new reactive site. A classic approach to prevent continuous polymerization is reagent control with a less reactive tris(trimethylsilyl)silyl enolate of acetaldehyde without additional enantioselectivity control. By confining the aldol reaction to the shielded active site of

IDPi, Schreyer *et al.* were able to obtain the enantioselective aldol reaction product and prevent subsequent oligomerization due to steric hindrance of the newly formed product to a second reaction. As rare as small molecule systems utilizing confinement effects currently are, they display an enormous potential for further research and the recent rising interest in them is well justified.

Supramolecular Systems and Cages
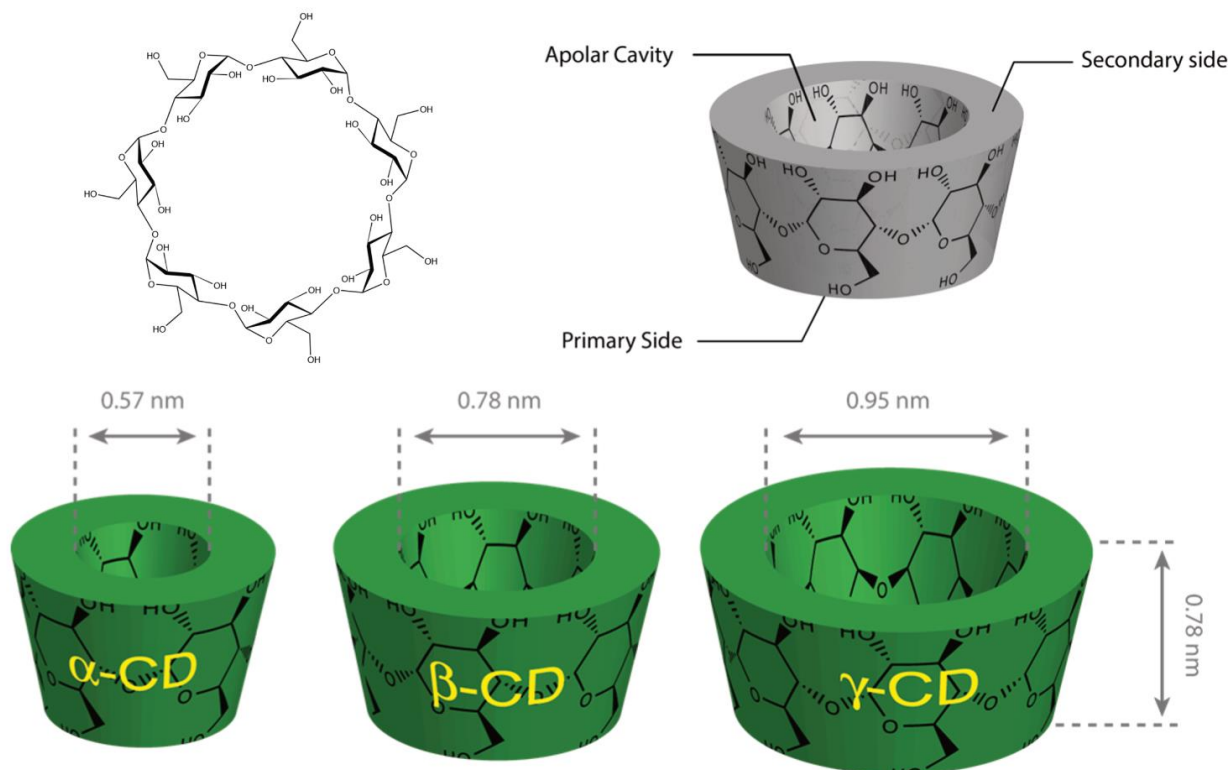
Figure 1.5. Chemical structure of β-cyclodextrin (top left) and functional structure (top right). Geometric dimensions of different cyclodextrins and cavity opening diameters.[44] Taken and adapted with permission from Ref. [52]. Copyright 2009 Elsevier.

Supramolecular systems have been one of the most promising candidates for biomimetic chemistry since the term was introduced in 1972.[45,46] Although much simpler than proteins, the self-assembly of small molecules into larger complex structures can already be reminiscent of enzyme assembly.[47] These supramolecular systems were among the first to be explored for biomimetic catalysis and can be considered as archetypes of artificial enzymes mimicking their natural counterparts in many aspects regarding substrate confinement and secondary ligand sphere. The wide range of available systems consisting of cyclodextrins (CDs), cucurbit[n]urils (CBs), calix[n]arenes, and various self-assembled cages and capsules, combined with their chemical variability, allows for a wide range of reactions.[18,48,49]

Cyclodextrins are cyclic oligosaccharides composed of either 6 (α-cyclodextrin), 7 (β-cyclodextrin), or 8 (γ-cyclodextrin) α-D-glucopyranoside monomers and were first described in 1942 (
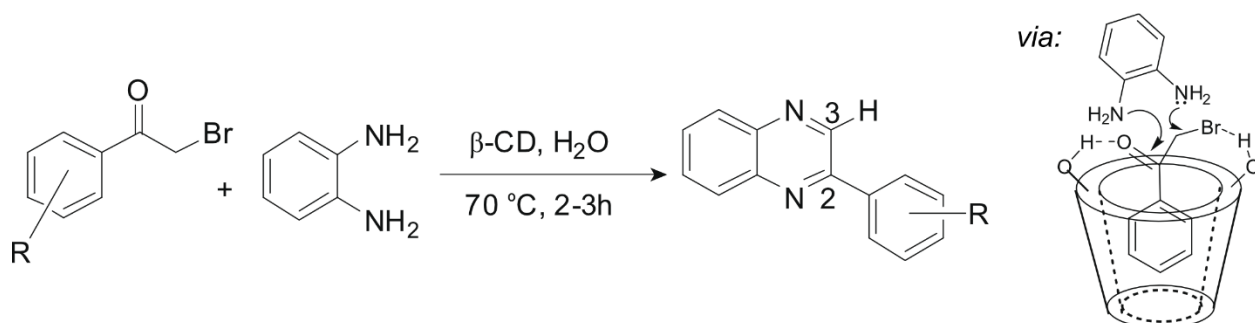
Figure 1.6. The biomimetic synthesis of quinoxalines in water by Madhav et al. and their proposed mechanistic pathway. Taken and adapted with permission from Ref. [52]. Copyright 2009 Elsevier.

Figure 1.5).[44] Their structure forms a slightly V-shaped hydrophobic cavity with hydroxyl groups on the rim, making them water soluble. The ability of these cavities to encapsulate a substrate was first described in 1969 by Breslow and Campbell, who demonstrated regioselectivity in the chlorination of anisole partially shielded by an α-cyclodextrin pocket.[50] The shape selectivity and role of the hydroxyl groups of CDs in substrate alignment and activation are well illustrated by the quinoxaline synthesis in water by Madhav *et al.* (Figure 1.6).[51] The proposed mechanistic pathway for this reaction shows the confined substrate with its nonpolar aromatic phenyl group in the pocket, while favorable hydrogen bonds are formed between the ketone and bromine functions with the hydroxyl groups at the outer edge. These hydrogen bonds hold the substrate in place while activating the ketone and C-Br bonds, leading to a nucleophilic attack on o-phenylenedia-mine and eventually resulting in the formation of quinoxaline. CDs have also been successfully used as cytochrome P-450 mimics with a metal cofactor for the oxidation of cis-stilbene or steroid substrates, and their use in the synthesis of optically active amino acids has been reported.[52–54]

Closely related to CDs in form and water solubility are calix[n]arene and cucurbit[n]urile (CBs). These classes of molecular containers to accommodate substrate molecules are products of the polymerization of electron-rich aromatic compounds with an aldehyde, usually formaldehyde, and the copolymerization of glyoxal, formaldehyde, and urea, respectively.[18] These tunable systems have been studied for the Wacker oxidation of linear alkenes involving Pd^{2+} metal ions as catalyt-ically active sites, asymmetric aldol reactions, chemoselective photoreactions of azoalkanes us-ing entrapped metal ions, or chiral nanoreactors, among others.[55–58] As with CDs, these systems lend themselves well to illustrative studies of the importance of the cavity in catalysis.[18,59]

In addition to these supramolecular systems built by (co)polymerization, self-assembled cages and capsules have gained interest as systems utilizing confinement in catalysis and have been the subject of several reviews.[60–63] The relatively simple fabrication of self-assembled hosts that provide a (non-hydrophobic) cavity has several advantages. The assembly from simple molecular components, like aldehydes and Resorcin, reduces the synthetic effort while allowing wide chem-ical variability and larger internal cavities than macrocyclic hosts. Control over the extent of the internal cavity can help tune secondary interactions to stabilize transition states and exclude sol-vents and other unwanted molecules during the reaction.[64] The dynamics of self-assembly can
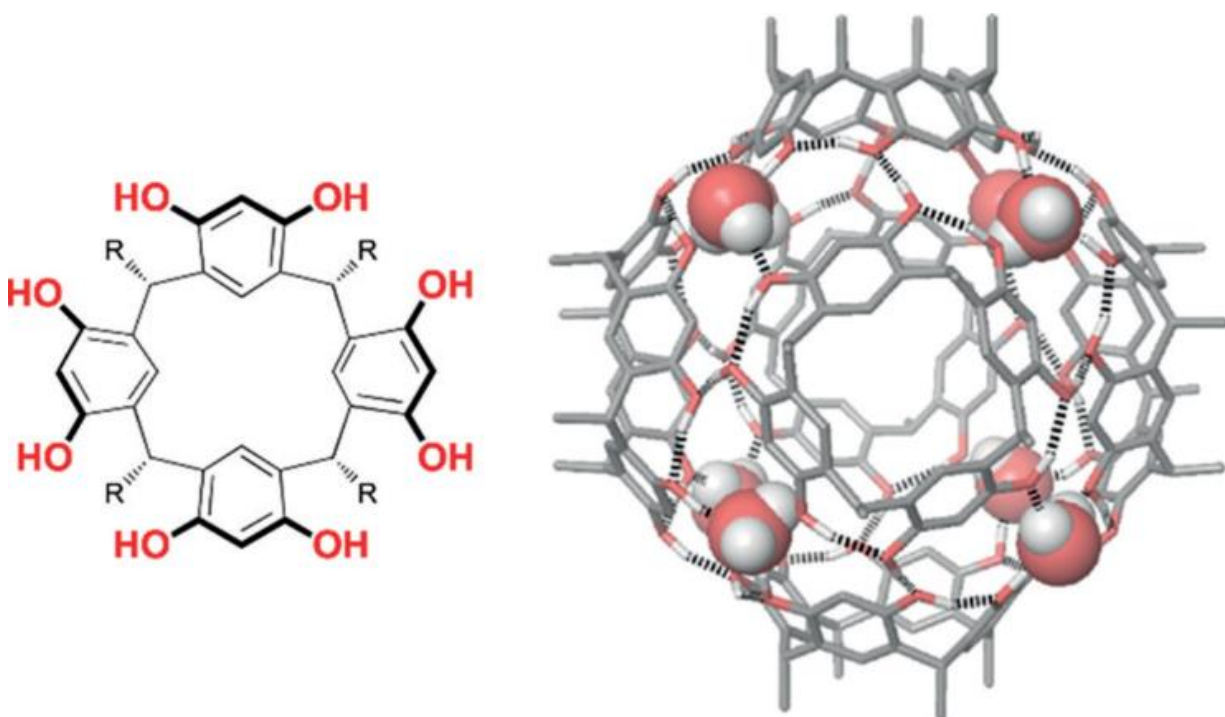
Figure 1.7. Structure of C-undecylresorcin[4]arene (left) and a model of the hexameric capsule (right). Taken and adapted with permission from from Ref. [72]. Copyright 2018 John Wiley and Sons.

further enhance catalytic turnover. The self-assembly of these systems is driven by either metal-ligand interactions or hydrogen bonding. Examples of these capsules and cages include the well-studied hexameric Atwood capsule (Figure 1.7) first reported in 1997, and the Fujita nanocages (Figure 1.8).[65–67]

Encapsulation of substrates or reagents in these capsules and the resulting conformational control increases reaction rates and selectivity in reactions. Giust *et al.* reported increased substrate selectivity in amide synthesis reactions between carboxylic acids and primary amines when confined in the nano-environment.[68] Encapsulation of the required cationic carbodiimide coupling agent in the self-assembling capsule strongly favored condensation of smaller substrates in competitive coupling pairs compared to unconfined reaction conditions. The limited reaction space in the nanoreactors resulted in preferential co-encapsulation of the smaller substrates, leading to size selectivity.

The inclusion in the capsule can strengthen and amplify halogen bonding. These intermolecular forces are usually very short-lived and are overwhelmed by solvent effects. By isolating substrates in cages and thus eliminating interfering solvent interactions, Sarwar *et al.* were able to amplify and then observe these interactions.[69] In 2020, La Manna *et al.* were able to take advantage of these amplified intermolecular forces and demonstrate the activation of neutral substrates in Michael reactions in these nanoconfined spaces. This occurred through an interplay between halogen bonding of an iodine-containing co-catalyst inside the cage and hydrogen bonding with bridg-
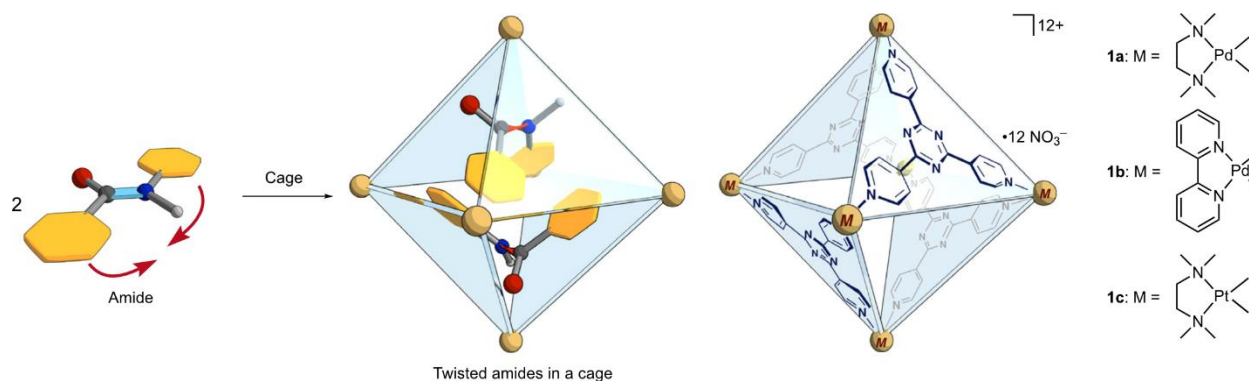
Figure 1.8. Representation of twisted, capsuated amides in coordiantion cage (left). Representation of octahedral coordination cage with six Pd-capped metal corners. Taken and adapted with permission from Ref. [68]. Copyright 2020 Springer Nature.

ing water molecules of the capsule.[70,71] Solvent exclusion also plays an important role in reactions based on the stabilization of a cationic intermediate and a transition state that can be readily chemically quenched by solvent interaction.[60,72,73] The confinement of these fragile intermediates during reaction in cavities leads to higher yields in (sesqui-)terpene cyclization cascades by protecting the cationic intermediates and opens new avenues in natural product synthesis such as presilphiperfolan-1β-ol by supramolecular catalysis.[74–76]

Another important function of cage confinement is in the control of substrate conformation during catalysis. Takezawa *et al.* reported the increased hydrolytic reactivity of amides under basic conditions due to the twisting of the amide bond in the confined cavities of a molecular cage (Figure 1.8).[67] Compared to the unconfined amides, they found a remarkable increase in the rate of hydrolysis. Moreover, they can relate the different torsion angles that distort and perturb the conjugation of the amide group to the different confinement geometry and rate increase. In one case, co-encapsulated planar phenanthrene was able to enhance the distortion of the amide bond and further increase the rate. The authors compare this novel non-covalent manipulation leading to stress-induced hydrolysis to a proposed mechanism of biological peptide cleavage under certain conditions, but one that has not yet been experimentally demonstrated.

The unique cavities provided by small molecules or self-assembling supramolecular compounds can be exploited to provide steric constraints, shape and size selectivity, protect and stabilize intermediates, confer unusual conformations to substrates, or promote stereochemical reaction outcomes. Through careful design and control of covalent, non-covalent, and second ligand sphere interactions, confinement effects can be used to steer the reaction in a different direction than in the bulk. This review of the history and recent developments in homogeneous confined catalysis demonstrate the enormous potential of a confinement strategy for further developments.

1.3. Confinement in Heterogeneous Catalysis

Zeolite and Silicates
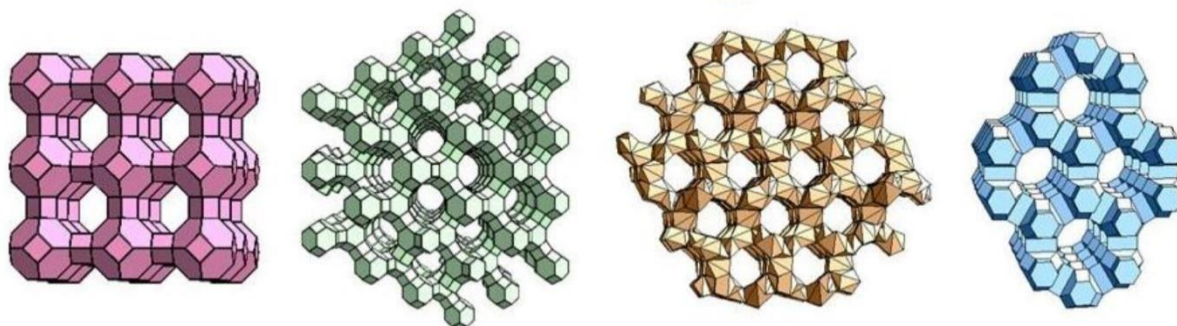
Figure 1.9. Representative zeolite frameworks: zeolite A; zeolite Y; zeolite L; ZSM-5 (silicalite) (left to right). Taken and adapted with permission from Ref. [78]. Copyright 2012 MDPI.

Heterogeneous (porous) catalysis systems contrast strongly from homogeneous ones with their reactivity and selectivity determined by diffusion, adsorption phenomena, and rigid geometrical constraints.[18,77,78] It can be considered the fundamental base for industrial and technical large-scale processes.[16,79,80] Easier application and innovative process management including flow setups, gas-solid reactions, and catalyst removal and re-use as well as their high productivity, space-time yields, and activity are benefits for industrial applications.

Zeolites, a class of crystalline, microporous (alumino)silicates with well-defined cavities and pores in molecular dimensions are applied in more than hundred industrial applications (Figure 1.9).[81,82] With a highly tunable chemical composition, chemical robustness, and high surface areas they emerged as environmentally friendly catalyst alternatives.[83] They could replace toxic reactant and cost intensive catalysts while lowering byproduct formation and energy costs. Their pores of molecular dimension, which can even strongly influence the molecular orbitals of confined substrates, and Lewis acidity is ideal for use in size and shape selective catalysis.[84] The selective alkylation of toluene with methanol towards para-xylene is one of the first descriptions of shape selectivity in catalysis.[85] Confined in the cylindrical microporous zeolite cavities of P-modified ZSM-5, inducing steric hindrance for the ortho- and meta-alkylation, the thermodynamic distribution of this reaction outcome can be altered.[22,86] Another example of shape-selectivity is the formation of lactide formation from lactic acids by Sels *et al.* Using the reaction confinement in a highly Brønsted acidic H-Beta zeolite the unwanted oligomerization during the catalytic process could be suppressed due so size restrains (Figure 1.10).[87] Despite their broad success in industrial application, being robust and tunable, the utility of the catalyst is hard to predict, and the microporous nature limits the zeolite utility towards small molecule transformations.

For reactions with larger substrates, other silica-based catalyst platforms like amorphous, mesoporous silicas (MS), like SBA-15 with cylindrical pore shape, can be utilized.[88,89] Composition, surface area, pore structure and diameter of these platforms can be controlled during synthesis
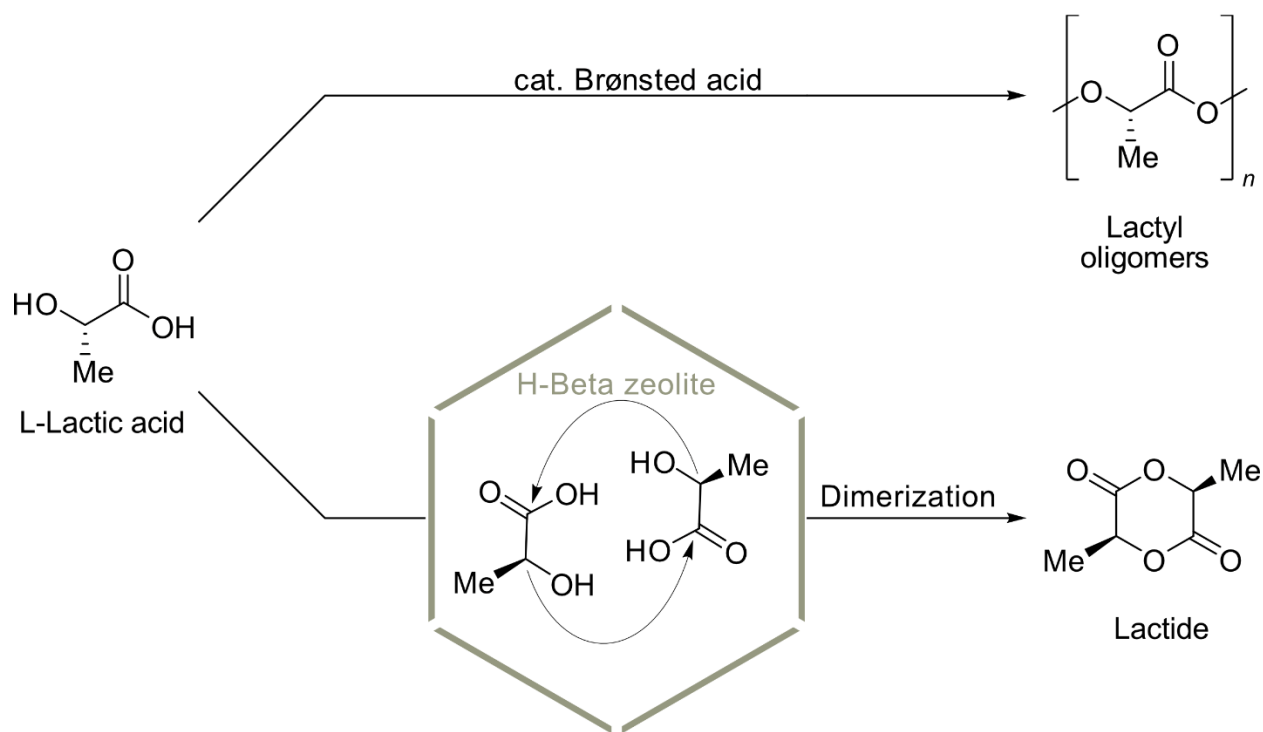
Figure 1.10. Oligomerization (n = 11-14) of L-lactide acid with conventionell Brønsted acid (e.g. H_2SO_4) and shape-selective dimerization utilizing H-beta zeolite confinement.[87]

and they allow a sophisticated surface crafting.[90] Pore wall polarity can be altered or attachment points for molecular catalysts including widening their range of applications to molecular hetero-geneous catalysis.[91,92]

Li *et al.* reported a highly selective semihydrogenation of phenylacetylene with Pd-Zn alloy nano-particles encapsulated into mesoporous silica (MS).[93] To obtain this selective catalyst, Pd-NPs were first encapsulated in ZIF-8 before the resulting Pd-NPs@ZIF-8 were coated with a layer of ordered mesoporous silica (Figure 1.11). The composite was annealed in reducing atmosphere to obtain Pd-Zn@MS, a unique nano-hollow structure encapsulated with Pd-Zn alloy nanoparticle. The high selectivity for styrene of 92% at a conversion rate of 95% is due to the high selectivity of the entrapped nanoparticles and the steric hindrance effect for the molecular size of the reac-tant.

Taking advantage of the larger mesopores of SAB-15, Ziegler *et al.* demonstrated a biomimetic approach for selective olefin metathesis macrocyclization of larger α,ω-diene substrates.[94] By pore size-selective functionalization of the Hoveyda-Grubbs catalyst in the inner pore surface, and careful tuning of the pore diameter, a correlation between the macro(mono)cyclization (MMC)/oligomerization (O) ratio and the substrate to pore size ratio was successfully established. By bringing the substrates close to the catalyst during the reaction while reducing the random encounters with other substrates, oligomerization was effectively reduced. The optimization steps on the catalyst initially increased the MMC/O ratio from 0.55 to 1.49. Additional fine-tuning of the
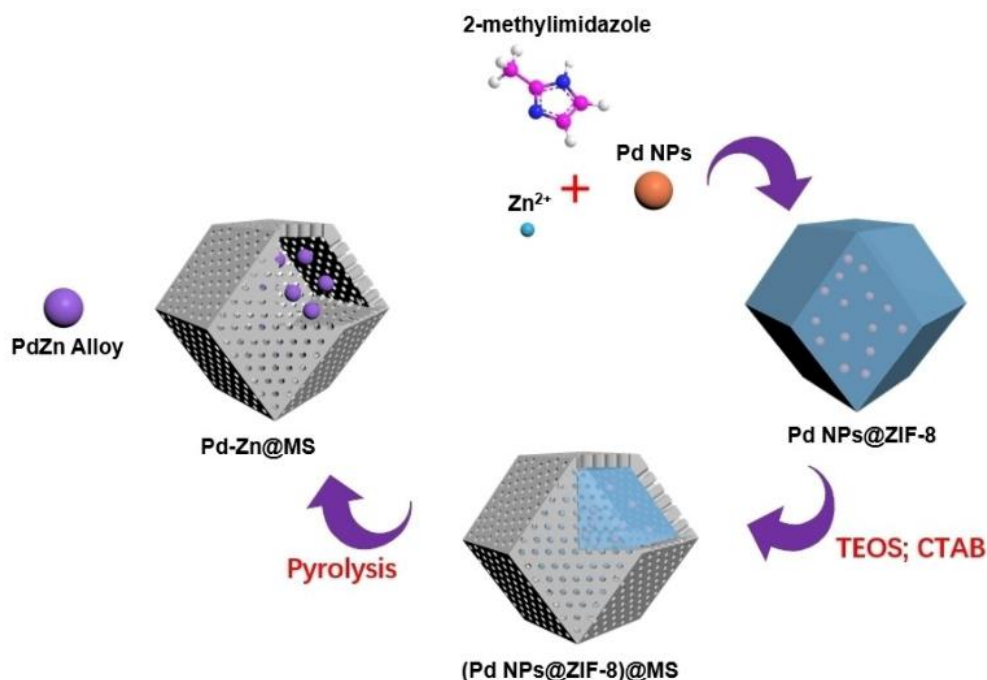
Figure 1.11. Synthesis process of Pd-Zn@MS. Taken and adapted with permission from Ref. [94]. Copyright 2020 Wiley-VCH GmbH.

pore size and reversal of the polarity of the inner pore surface by modification with dimethoxydimethylsilane increased the ratio even further to 2.2. This selective placement of the catalyst in the inner surface and the well-matched pore size allowed the reaction to have better selectivity over MMC compared to homogeneous catalysis, even at elevated concentrations. Following these results, Ziegler *et al.* were able to further perform olefin ring closure metathesis under spatial confinement under continuous flow conditions.[95] These studies could shed additional light on the persistent confinement effects and pathways of olefin metathesis and link ring chain equilibria to residence time and flow rate.

Silica-based materials are highly useful due to their relative ease of fabrication and high robustness to withstand harsh conditions sometimes required in industrial processes. Between zeolites and mesoporous silica, a wide range of pore sizes and structures are available, and surface processing allows fine-tuning of surface properties, pore sizes, and incorporation of nanoparticles and molecular catalysts. However, the prediction of pore structures and surface properties, in addition to continued advances, is still a challenge, and catalytic properties without post-modification are limited.[96]

Metal-Organic Frameworks (MOFs)

Metal-organic frameworks (MOFs), a relative new type of porous materials, are hybrid materials composed of inorganic metal nodes and organic linker molecules, forming networks with well-defined topologies and characterized by crystalline character, high porosity, high specific surface area, low density, and modular pore geometries, diameters, and openings.[97,98] The almost infinite

variety of structures resulting from the combination of different linkers and metal nodes, and the possibility of incorporating functionalities into both structural parts, can be strategically exploited to develop multifunctional catalysts or support materials.[99,100] The fine-tuning and modulation of host-guest chemistry in MOFs lead to a wide range of applications in confined catalysis, and the versatility of MOFs has made them one of the most studied solid catalysts.[101] They have emerged as promising candidates for size-selective catalysts affecting the selectivity of reactants, products, or transition states, with properties very similar to those of zeolites, while extending the substrate range due to their different pore sizes from ultramicro- to mesoporous. Additional dynamic features that enable guest-responsive systems further distinguish them from silica based materials.[102]

Acid catalysis using cavities of MOFs for size selectivity was demonstrated by Roberts *et al.*[103] The urea derivative-based NU-601 MOF developed in this work was used as an effective hydrogen-bond catalyst. While urea usually loses its catalytic competence due to self-recognition and aggregation, they succeeded in spatially isolating it while it remained accessible in the porous MOF environment. A 98% alkylation conversion of N-methylindole with (E)-1-nitropropene in the presence of NU-601 compared to a 65% conversion with a homogeneous diphenylurea catalyst highlights the effectiveness of this catalyst strategy (Figure 1.12). Size selectivity was observed for larger substrates where only a negligible amount of product was formed once their size exceeded the pore size of NU-601. The study of reaction rates for the heterogeneous and homogeneous catalyst systems with different substrate sizes also indicates that catalysis occurs mainly within the MOF pores.
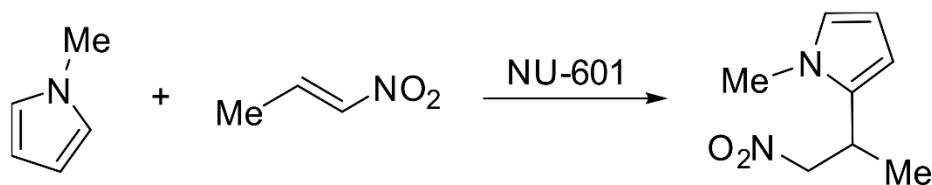
Figure 1.12. NU-601 as a solidcatalyst for alkylation of N-methylindole with (E)-1-nitropropeneusing.

Zhou *et al.* demonstrated the enhancement of orthoformate hydrolysis in basic solutions by acid catalysis in confined channels of MOFs.[104] They reported the enzyme-mimicking KLASCC-1-MOF with protonated pyridyl groups at open sites protruding into the channels (Figure 1.13). As an acid catalyst for the hydrolysis of triethyl orthoformate, they achieved a substrate conversion of 97% and a selectivity of the resulting formate anion of 98%, while maintaining the framework structure. Compared to MOF analogues without a pyridyl group in the channels or pyridine molecules as homogeneous catalysts, a critical role of reaction confinement in the channels and its ability to regulate reactivity and size selectivity was found. The X-ray diffraction pattern of KLASCC-1 with encapsulated substrates confirmed the existence and important influence of channel confinement. By using a well-designed MOF confinement, Zhou *et al.* successfully achieved acidic hydrolysis in basic media with high selectivity and activity.
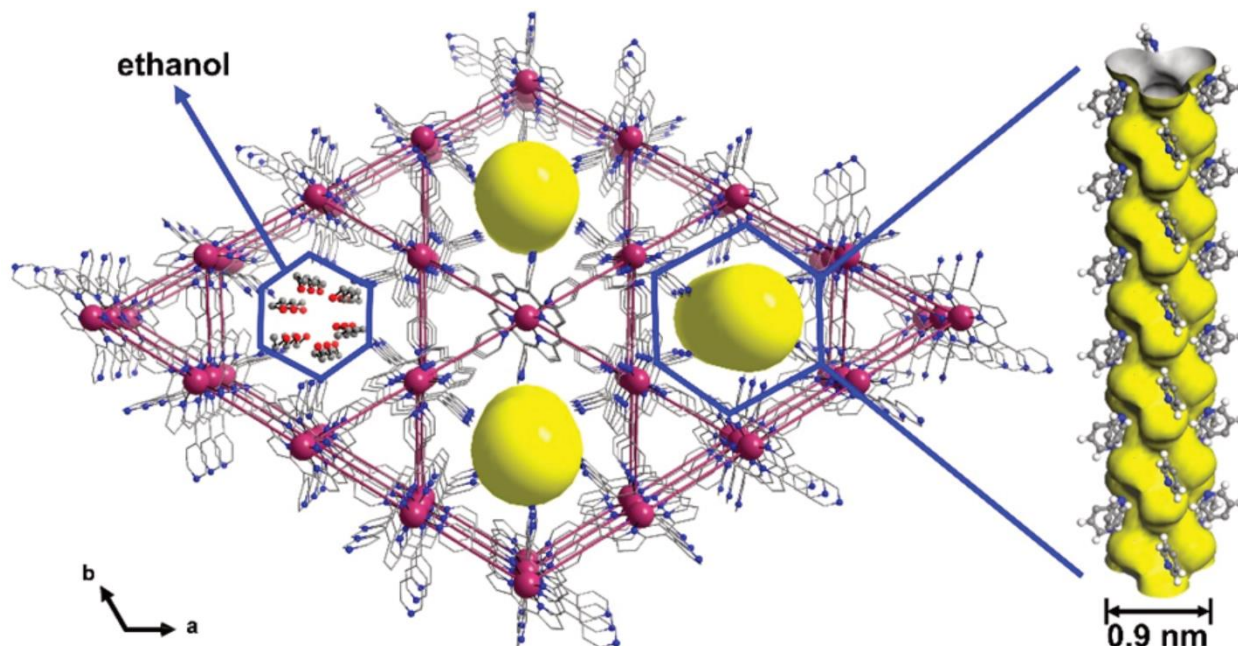
Figure 1.13. 3D framework structures of KLASCC-1 displaying solvent residue and channels (yellow). Pop-out desplays channels and inside-channel pyridyl groups. Taken and adapted with permission from Ref. [105]. Copyright 2020 American Chemical Society.

Instead of incorporating catalytic functionalities into the organic linker moiety as in the previous examples, the encapsulation of metal nanoparticles (NP) into MOF pores provides stabilization of the NP and induces confinement effects in these catalytic reactions. Encapsulation of Pt-NP in UiO-66 led to substrate size selectivity in the reduction of olefins in the liquid phase.[105] Increasing the molecular size of olefins reduced the catalytic rate for hydrogenation in the case of Pt@UiO-66, while in contrast, Pt@CNT (carbon nanotubes) showed no significant discrimination. The slower diffusion of the substrates to the catalytically active NPs encapsulated by the MOF decreased the reaction rate and the reaction fails for sufficiently large olefins exceeding the diameter of the pore opening.

A particularly interesting case of confinement effect was demonstrated by Kutzschner *et al.* who showed a reversal of diastereoselectivity in aldol reactions for catalytically active proline after immobilization on UiO-67 and UiO-68 (Figure 1.14).[106] A Boc-protected proline was introduced into the scaffold by functionalizing the dicarboxylate linkers used for the zirconium-based MOF, followed by in situ deprotection during MOF formation. Boc removal was performed without racemization, and an enantiopure, proline-functionalized MOF was obtained. High yields of up to 97% were obtained for the aldol addition, while reverse stereoselectivity was observed compared to the homogeneous proline catalyst and a dependence of the reaction rate on the pore size was observed, indicating size-selective effects. Initially, the reason for the reverse stereoselectivity was not fully understood, and the authors attributed it to either the interactions of the pore wall with the substrate, the additional Lewis acidity of the Zr^{4+} contained in the MOF clusters, or the

interactions with neighboring proline groups accumulated in the pores. A later study by the same group using a molecular Zr_6 cluster model compound revealed that these Zr_6 clusters were responsible for the reverse diastereoselectivity.[107] Higher enantioselectivities for the solid-state catalyst could be achieved when the remaining acidic sites in the MOF clusters were masked, which improved the overall efficiency of the system. This example demonstrates the intricate interplay between the organic linkers and the metal nodes in terms of selectivity and reactivity and highlights the tunability of MOF frameworks for catalytic challenges given their wide structural and chemical diversity.
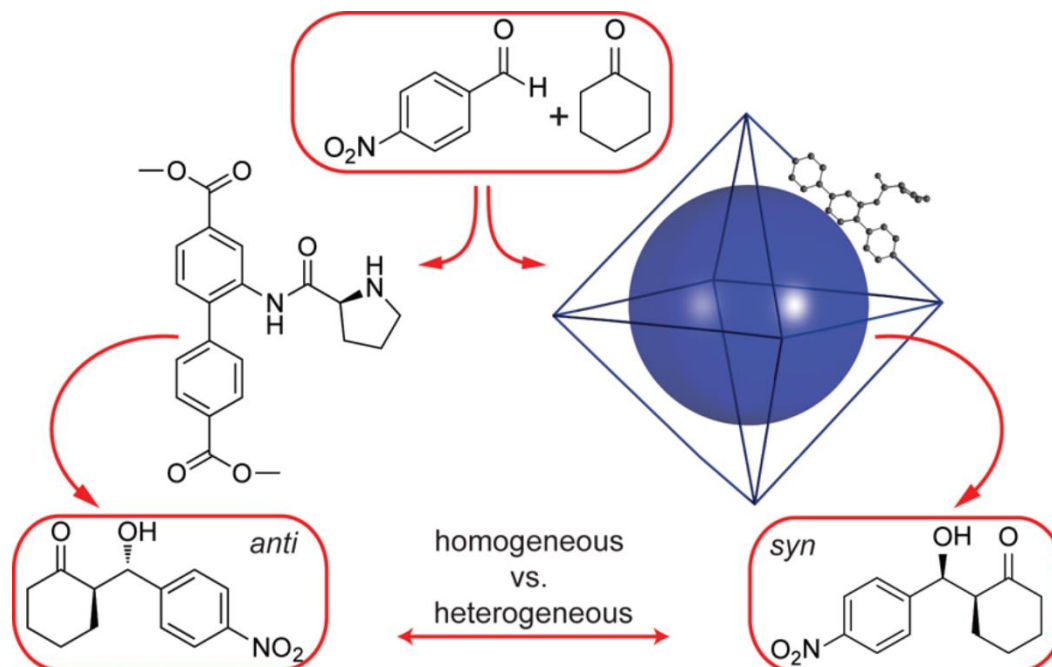
Figure 1.14. Reversed diastereoselectivity in aldol addition reactions catalysed by proline functionalized UiO-67 and UiO-68 type MOFs. Taken and adapted with permission from Ref. [107]. Copyright 2016 American Chemical Society.

Covalent Organic Frameworks (COFs)

COFs are the newest class of materials under discussion. They are closely related to MOFs, but differ in the connectivity of the building blocks. While MOFs are built by coordination chemistry in which metal nodes are connected by organic building blocks, COFs are entirely organic and are built by the formation of covalent bonds between building blocks.[108] Structures and topologies can be rationally designed by the direction and multiplicity of covalent bonds. Due to the induced long-range ordering of the building blocks, they exhibit permanent porosity, low density, and crystallinity.[109,110] While the potential applications of COFs are broad, examples of using pore confinement to alter reaction outcomes are still exceptional.[111]
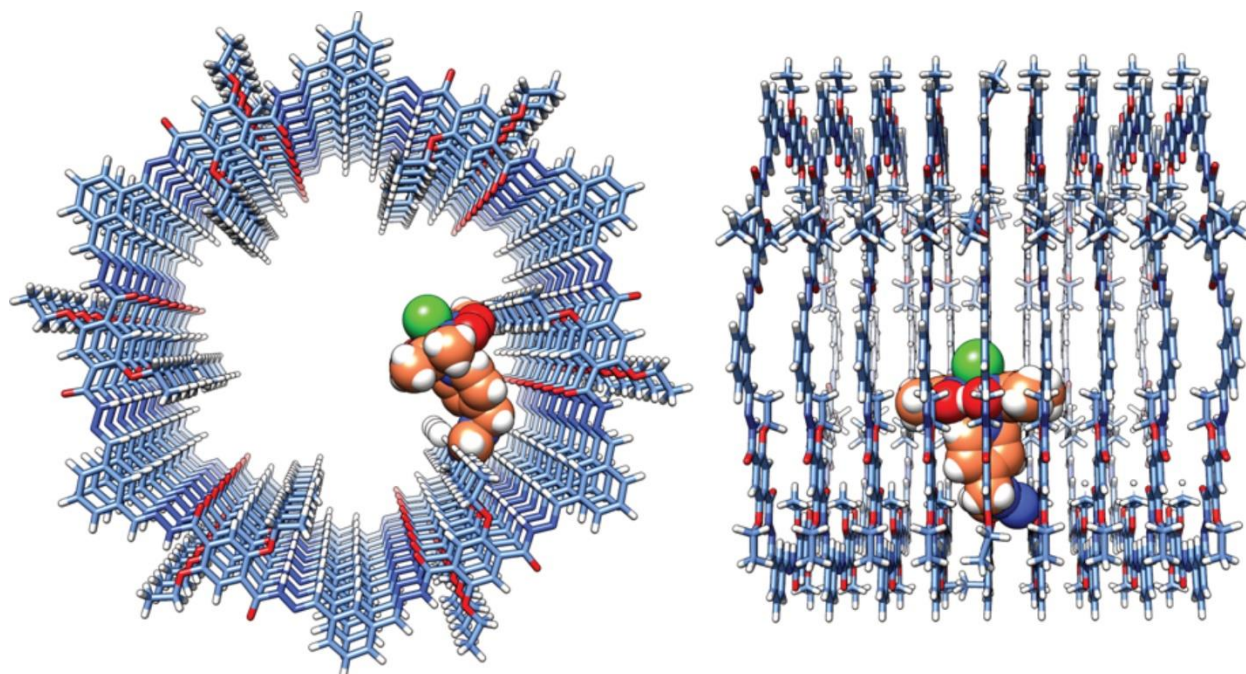
Figure 1.15. MD-simulated structural model of cobaloxime-COF-42 hybride displaying the possible arrangement of the cocatalyst inside the pore, which directed local confinement and interactions with the pore wall and led to improved catalytic efficency in photocatalytic hydrogen evolution. Taken and adapted with permission from Ref. [114]. Copyright 2019 American Chemical Society.

Fang *et al.* reported the microporous 3D imines BF-COF-1 and BF-COF-2 for Knoevenagel condensation reactions (Figure 1.2).[112] With a microporous cavity of 7.8 Å in diameter, the solid-state catalyst exhibited fine-tuned and high size selectivity when using substrates of different sizes. In the Knoevenagel condensation of aldehydes with malononitrile by BF-COF-1 and BF-COF-2, only the smallest benzaldehyde substrate was converted in the yield of 96% and 98%, respectively. The somewhat larger 4-methylbenzaldehyde was already converted only in traces. The catalyst could be recovered by simple filtration and was reused without loss of activity.

Gottschling *et al.* reported a covalent cobaloxime-COF hybrid for enhanced photocatalytic hydrogen evolution[113] Covalently immobilized cobaloxime on a hydrazone-based COF-42 showed 110% improved activity and turnover number compared to simple physisorbed systems. This improvement is attributed to local confinement of the catalyst due to interactions between the COF backbone and the cobaloxime (Figure 1.15).

The examples of homo- and heterogeneous biomimetic catalysis using confinement selected above represent only a small portion of the research that has focused on this topic in recent years. They are intended to highlight the various strategies and systems that have been developed to improve the key parameters of catalysis - activity, selectivity and stability - for the different areas of catalysis. These successful applications demonstrate the feasibility of the challenging concept of artificially mimicking biological enzymes and their impressive catalytic activities. The relatively low use of COFs for this purpose compared to other systems is certainly in part due to the fact

that they are relatively new and have only recently been discovered, but also the unique challenges presented by this new type of material. Achieving crystalline, stable, and functional COFs is the biggest challenge in COF research, also referred to as the "COF trilemma",[114] and continues to pose design, synthesis, and application problems for COF researchers. In addition, a finely tunable pore size from the micro to the larger mesoporous range would be particularly welcome for a material to be used for its pore confinement effects, but is still very difficult to achieve in COFs. For some materials, such as zeolites, this can quickly become an application limitation, while others, such as MOFs and SBA-15, can overcome this problem and significantly expand their range of applications.[115] Despite the (unresolved) challenges facing COFs as a platform for biomimetic catalysis using confinement, their chemical and structural variability, crystallinity, and porosity make them promising candidates for future research. The focus of this work, the development and construction of COF platforms to study and exploit confinement effects in catalysis, will explore and investigate strategies to overcome the "COF trilemma", expand the achievable pore size range, and find suitable model reactions. To understand the nature of the challenges and problems, the following chapter will delve into the principles of COF design, their properties, and applications.

1.4. Bibliography

[1]   J. Trefil, H. J. Morowitz, E. Smith, *Am. Sci.* **2009**, *97*, 206–213.
[2]   S. I. Walker, N. Packard, G. D. Cody, *Philos. Trans. R. Soc. A Math. Phys. Eng. Sci.* **2017**, *375*, 20160337.
[3]   K. A. Dill, L. Agozzino, *Open Biol.* **2021**, *11*, rsob.200324.
[4]   M. Levy, S. L. Miller, K. Brinton, J. L. Bada, *Icarus* **2000**, *145*, 609–613.
[5]   B. K. D. Pearce, R. E. Pudritz, D. A. Semenov, T. K. Henning, *Proc. Natl. Acad. Sci. U. S. A.* **2017**, *114*, 11327–11332.
[6]   W. Martin, J. Baross, D. Kelley, M. J. Russell, *Nat. Rev. Microbiol.* **2008**, *6*, 805–814.
[7]   W. Martin, M. J. Russell, *Philos. Trans. R. Soc. B Biol. Sci.* **2007**, *362*, 1887–1925.
[8]   M. R. Dietrich, *J. Hist. Biol. 1998 311* **1998**, *31*, 85–111.
[9]   J. B. Hagen, *J. Hist. Biol. 1999 322* **1999**, *32*, 321–341.
[10]   A. P. Hendry, M. T. Kinnison, *Genet. 2001 1121* **2001**, *112*, 1–8.
[11]   J. C. Fay, C.-I. Wu, *Annu. Rev. Genomics Hum. Genet.* **2003**, *4*, 213–235.
[12]   C. M. Paton, J. M. Ntambi, *Am. J. Physiol. - Endocrinol. Metab.* **2009**, *297*, 28–37.
[13]   H. Wang, M. G. Klein, H. Zou, W. Lane, G. Snell, I. Levin, K. Li, B.-C. Sang, *Nat. Struct. Mol. Biol.* **2015**, *22*, 581–585.
[14]   G. Rothenberg, *Catalysis: Concepts and Green Applications*, Wiley, **2008**.
[15]   F. H. Ribeiro, *J. Am. Chem. Soc.* **2000**, *122*, 1563–1564.
[16]   R. Schlögl, *Angew. Chemie Int. Ed.* **2015**, *54*, 3465–3520.
[17]   B. Mitschke, M. Turberg, B. List, *Chem* **2020**, *6*, 2515–2532.
[18]   V. Mouarrawis, R. Plessius, J. I. van der Vlugt, J. N. H. Reek, *Front. Chem.* **2018**, *6*, 623.
[19]   L. Yang, L. Zhao, Z. Zhou, C. He, H. Sun, C. Duan, *Dalt. Trans.* **2017**, *46*, 4086–4092.
[20]   Q. Fang, S. Gu, J. Zheng, Z. Zhuang, S. Qiu, Y. Yan, *Angew. Chemie - Int. Ed.* **2014**, *53*, 2878–2882.
[21]   M. Garcia-Viloca, J. Gao, M. Karplus, D. G. Truhlar, *Science* **2004**, *303*, 186–195.
[22]   W. W. Kaeding, C. Chu, L. B. Young, B. Weinstein, S. A. Butter, *J. Catal.* **1981**, *67*, 159–174.
[23]   D. L. Pompliano, A. Peyman, J. R. Knowles, *Biochemistry* **1990**, *29*, 3186–3194.
[24]   A. Borgoo, D. J. Tozer, P. Geerlings, F. De Proft, *Phys. Chem. Chem. Phys.* **2008**, *10*, 1406–1410.
[25]   A. Borgoo, D. J. Tozer, P. Geerlings, F. De Proft, *Phys. Chem. Chem. Phys.* **2009**, *11*, 2862–2868.
[26]   W. H. Thompson, *J. Chem. Phys.* **2018**, *149*, 170901.
[27]   H. Weiss, H. W. Cheng, J. Mars, H. Li, C. Merola, F. U. Renner, V. Honkimäki, M. Valtiner, M. Mezger, *Langmuir* **2019**, *35*, 16679–16692.
[28]   A. Schlaich, E. W. Knapp, R. R. Netz, *Phys. Rev. Lett.* **2016**, *117*, 048001.
[29]   K. Maruoka, T. Itoh, M. Sakurai, K. Nonoshita, H. Yamamoto, *J. Am. Chem. Soc.* **1988**, *110*, 3588–3597.
[30]   K. Maruoka, T. Itoh, H. Yamamoto, *J. Am. Chem. Soc.* **1985**, *107*, 4573–4576.
[31]   K. Maruoka, H. Imoto, H. Yamamoto, *J. Am. Chem. Soc.* **1994**, *116*, 12115–12116.
[32]   R. Hoffmann, R. B. Woodward, *J. Am. Chem. Soc.* **1965**, *87*, 4388–4389.
[33]   D. M. Birney, K. N. Houk, *J. Am. Chem. Soc.* **1990**, *112*, 4127–4133.
[34]   W. Amberg, Y. L. Bennani, R. K. Chadha, G. A. Crispino, W. D. Davis, J. Hartung, K. S. Jeong, Y. Ogino, T. Shibata, K. B. Sharpless, *J. Org. Chem.* **1993**, *58*, 844–849.
[35]   P. S. J. Kaib, L. Schreyer, S. Lee, R. Properzi, B. List, *Angew. Chemie - Int. Ed.* **2016**, *55*, 13200–13203.
[36]   E. J. Corey, M. C. Noe, S. Sarshar, *Tetrahedron Lett.* **1994**, *35*, 2861–2864.
[37]   E. J. Corey, M. C. Noe, A. Guzman-Perez, *Tetrahedron Lett.* **1995**, *36*, 4171–4174.
[38]   I. Čorić, B. List, *Nature* **2012**, *483*, 315–319.
[39]   N. Tsuji, J. L. Kennemur, T. Buyck, S. Lee, S. Prévost, P. S. J. Kaib, D. Bykov, C. Farès, B. List, *Science* **2018**, *359*, 1501–1505.
[40]   J. Ouyang, J. L. Kennemur, C. K. De, C. Farès, B. List, *J. Am. Chem. Soc.* **2019**, *141*, 3414–3418.
[41]   M. B. Boxer, H. Yamamoto, *J. Am. Chem. Soc.* **2006**, *128*, 48–49.
[42]   T. Gatzenmeier, P. S. J. Kaib, J. B. Lingnau, R. Goddard, B. List, *Angew. Chemie - Int. Ed.* **2018**, *57*, 2464–2468.
[43]   L. Schreyer, P. S. J. Kaib, V. N. Wakchaure, C. Obradors, R. Properzi, S. Lee, B. List, *Science* **2018**,

362, 216–219.

[44] G. Crini, *Chem. Rev.* **2014**, *114*, 10940–10975.

[45] R. Breslow, *Chem. Soc. Rev.* **1972**, *1*, 553–580.

[46] R. Breslow, *Breslow, R. Proc. XVIII Solvay Conf. Chem-istry·* **1995**, *28*, 7816.

[47] L. Marchetti, M. Levine, *ACS Catal.* **2011**, *1*, 1090–1118.

[48] R. Breslow, L. E. Overman, *J. Am. Chem. Soc.* **1970**, *92*, 1075–1077.

[49] F. Hapiot, A. Ponchel, S. Tilloy, E. Monflier, *Comptes Rendus Chim.* **2011**, *14*, 149–166.

[50] R. Breslow, P. Campbell, *J. Am. Chem. Soc.* **1969**, *91*, 3085.

[51] B. Madhav, S. Narayana Murthy, V. Prakash Reddy, K. Rama Rao, Y. V.D. Nageswar, *Tetrahedron Lett.* **2009**, *50*, 6025–6028.

[52] N. Hessenauer-Ilicheva, A. Franke, D. Meyer, W. D. Woggon, R. Van Eldik, *J. Am. Chem. Soc.* **2007**, *129*, 12473–12479.

[53] R. Breslow, J. Yang, J. Yan, *Tetrahedron* **2002**, *58*, 653–659.

[54] R. Breslow, J. Chmielewski, D. Foley, B. Johnson, N. Kumabe, M. Varney, R. Mehra, *Tetrahedron* **1988**, *44*, 5515–5524.

[55] A. L. Maksimov, T. S. Buchneva, E. A. Karakhanov, *J. Mol. Catal. A Chem.* **2004**, *217*, 59–67.

[56] E. Demircan, S. Eymur, *Tetrahedron: Asymmetry* **2014**, *25*, 443–448.

[57] L. Zheng, S. ilvia Sonzini, M. Ambarwati, E. Rosta, O. A. Scherman, A. Herrmann, L. Zheng, M. Ambarwati, D. Herrmann, S. Sonzini, D. Rosta, *Angew. Chemie Int. Ed.* **2015**, *54*, 13007–13011.

[58] A. L. Koner, C. Márquez, M. H. Dickman, W. M. Nau, *Angew. Chemie Int. Ed.* **2011**, *50*, 545–548.

[59] R. Cacciapaglia, A. Casnati, L. Mandolini, D. N. Reinhoudt, R. Salvio, A. Sartori, R. Ungaro, *J. Am. Chem. Soc.* **2006**, *128*, 12322–12330.

[60] C. Gaeta, P. La Manna, M. De Rosa, A. Soriente, C. Talotta, P. Neri, *ChemCatChem* **2021**, *13*, 1638–1658.

[61] S. H. A. M. Leenders, R. Gramage-Doria, B. De Bruin, J. N. H. Reek, *Chem. Soc. Rev.* **2015**, *44*, 433–448.

[62] M. M. Conn, J. Rebek, *Chem. Rev.* **1997**, *97*, 1647–1668.

[63] D. M. Vriezema, M. C. Aragonès, J. A. A. W. Elemans, J. J. L. M. Cornelissen, A. E. Rowan, R. J. M. Nolte, *Chem. Rev.* **2005**, *105*, 1445–1489.

[64] M. Yamanaka, A. Shivanyuk, J. Rebek, *J. Am. Chem. Soc.* **2004**, *126*, 2939–2943.

[65] L. R. MacGillivray, J. L. Atwood, *Nat. 1997 3896650* **1997**, *389*, 469–472.

[66] T. Kusukawa, M. Fujita, *Angew. Chemie Int. Ed.* **1998**, *37*, 3142–3144.

[67] H. Takezawa, K. Shitozawa, M. Fujita, *Nat. Chem. 2020 126* **2020**, *12*, 574–578.

[68] S. Giust, G. La Sorella, L. Sperni, G. Strukul, A. Scarso, *Chem. Commun.* **2015**, *51*, 1658–1661.

[69] M. G. Sarwar, D. Ajami, G. Theodorakopoulos, I. D. Petsalakis, J. Rebek, *J. Am. Chem. Soc.* **2013**, *135*, 13672–13675.

[70] P. La Manna, M. De Rosa, C. Talotta, A. Rescifina, G. Floresta, A. Soriente, C. Gaeta, P. Neri, *Angew. Chemie Int. Ed.* **2020**, *59*, 811–818.

[71] P. La Manna, C. Talotta, G. Floresta, M. De Rosa, A. Soriente, A. Rescifina, C. Gaeta, P. Neri, *Angew. Chemie Int. Ed.* **2018**, *57*, 5423–5428.

[72] D. W. Christianson, *Chem. Rev.* **2006**, *106*, 3412–3442.

[73] J. Degenhardt, T. G. Köllner, J. Gershenzon, *Phytochemistry* **2009**, *70*, 1621–1637.

[74] Q. Zhang, K. Tiefenbacher, *Nat. Chem. 2015 73* **2015**, *7*, 197–202.

[75] Q. Zhang, J. Rinkel, B. Goldfuss, J. S. Dickschat, K. Tiefenbacher, *Nat. Catal. 2018 18* **2018**, *1*, 609–615.

[76] L. D. Syntrivanis, I. Némethová, D. Schmid, S. Levi, A. Prescimone, F. Bissegger, D. T. Major, K. Tiefenbacher, *J. Am. Chem. Soc.* **2020**, *142*, 5894–5900.

[77] R. A. Van Santen, *J. Mol. Catal. A Chem.* **1997**, *115*, 405–419.

[78] A. J. Medford, A. Vojvodic, J. S. Hummelshøj, J. Voss, F. Abild-Pedersen, F. Studt, T. Bligaard, A. Nilsson, J. K. Nørskov, *J. Catal.* **2015**, *328*, 36–42.

[79] J. M. Thomas, *ChemSusChem* **2014**, *7*, 1801–1832.

[80] K. Reuter, D. Frenkel, M. Scheffler, *Phys. Rev. Lett.* **2004**, *93*, 116105.

[81] Y. Zheng, X. Li, P. K. Dutta, *Sensors 2012, Vol. 12, Pages 5170-5194* **2012**, *12*, 5170–5194.

[82] J. Čejka, A. Corma, S. Zones, *Zeolites and Catalysis*, Wiley, **2010**.

[83] M. Dusselier, M. E. Davis, *Chem. Rev.* **2018**, *118*, 5265–5329.

[84] F. Márquez, H. García, E. Palomares, L. Fernández, A. Corma, *J. Am. Chem. Soc.* **2000**, *122*, 6520–

6521.

[85] P. B. Weisz, *Pure Appl. Chem.* **1980**, *52*, 2091–2103.

[86] T. Yashima, K. Yamazaki, H. Ahmad, M. Katsuta, N. Hara, *J. Catal.* **1970**, *17*, 151–156.

[87] M. Dusselier, P. Van Wouwe, A. Dewaele, P. A. Jacobs, B. F. Sels, *Science* **2015**, *349*, 78–80.

[88] R. Huirache-Acuña, R. Nava, C. Peza-Ledesma, J. Lara-Romero, G. Alonso-Núez, B. Pawelec, E. Rivera-Muñoz, *Materials* **2013**, *6*, 4139–4167.

[89] B. N. Mahato, T. Krithiga, *Can. J. Chem.* **2022**, *100*, 9–17.

[90] P. Verma, Y. Kuwahara, K. Mori, R. Raja, H. Yamashita, *Nanoscale* **2020**, *12*, 11333–11363.

[91] V. Chaudhary, Sweta, *Chinese J. Chem. Eng.* **2018**, *26*, 1300–1306.

[92] A. Chołuj, W. Nogaś, M. Patrzałek, P. Krzesiński, M. J. Chmielewski, A. Kajetanowicz, K. Grela, *Catalysts* **2020**, *10*, 438.

[93] Z. Li, M. Hu, B. Liu, J. Liu, P. Wang, J. Yao, X. Zhang, M. He, W. Song, *ChemCatChem* **2021**, *13*, 868–873.

[94] F. Ziegler, J. Teske, I. Elser, M. Dyballa, W. Frey, H. Kraus, N. Hansen, J. Rybka, U. Tallarek, M. R. Buchmeiser, *J. Am. Chem. Soc.* **2019**, *141*, 19014–19022.

[95] F. Ziegler, T. Roider, M. Pyschik, C. P. Haas, D. Wang, U. Tallarek, M. R. Buchmeiser, *ChemCatChem* **2021**, *13*, 2234–2241.

[96] J. R. Bruckner, J. Bauhof, J. Gebhardt, A.-K. Beurer, Y. Traa, F. Giesselmann, *J. Phys. Chem. B* **2021**, *125*, 3207.

[97] K. Hemmer, M. Cokoja, R. A. Fischer, *ChemCatChem* **2021**, *13*, 1683–1691.

[98] D. Kim, X. Liu, M. S. Lah, *Inorg. Chem. Front.* **2015**, *2*, 336–360.

[99] S. M. J. Rogge, A. Bavykina, J. Hajek, H. Garcia, A. I. Olivos-Suarez, A. Sepúlveda-Escribano, A. Vimont, G. Clet, P. Bazin, F. Kapteijn, M. Daturi, E. V. Ramos-Fernandez, F. X. I. Llabrés Xamena, V. Van Speybroeck, J. Gascon, *Chem. Soc. Rev.* **2017**, *46*, 3134–3184.

[100] A. Dhakshinamoorthy, Z. Li, H. Garcia, *Chem. Soc. Rev.* **2018**, *47*, 8134–8172.

[101] A. Dhakshinamoorthy, A. M. Asiri, H. Garcia, *ChemCatChem* **2020**, *12*, 4732–4753.

[102] E. Y. Lee, S. Y. Jang, M. P. Suh, *J. Am. Chem. Soc.* **2005**, *127*, 6374–6381.

[103] J. M. Roberts, B. M. Fini, A. A. Sarjeant, O. K. Farha, J. T. Hupp, K. A. Scheidt, *J. Am. Chem. Soc.* **2012**, *134*, 3334–3337.

[104] G. Zhou, B. Wang, R. Cao, *J. Am. Chem. Soc.* **2020**, *142*, 14848–14853.

[105] W. Zhang, G. Lu, C. Cui, Y. Liu, S. Li, W. Yan, C. Xing, Y. Robin Chi, Y. Yang, F. Huo, F. W. Huo, W. N. Zhang, G. Lu, C. L. Cui, Y. Y. Liu, S. Z. Li, W. J. Yan, Y. H. Yang, C. Xing, Y. G. R Chi, *Adv. Mater.* **2014**, *26*, 4056–4060.

[106] C. Kutzscher, G. Nickerl, I. Senkovska, V. Bon, S. Kaskel, *Chem. Mater.* **2016**, *28*, 2573–2580.

[107] K. D. Nguyen, C. Kutzscher, S. Ehrling, I. Senkovska, V. Bon, M. de Oliveira, T. Gutmann, G. Buntkowsky, S. Kaskel, *J. Catal.* **2019**, *377*, 41–50.

[108] M. S. Lohse, T. Bein, *Adv. Funct. Mater.* **2018**, *28*, 1705553.

[109] O. M. Yaghi, *ACS Cent. Sci.* **2019**, *5*, 1295–1300.

[110] C. S. Diercks, O. M. Yaghi, *Science* **2017**, *355*, 923.

[111] S. Y. Ding, W. Wang, *Chem. Soc. Rev.* **2012**, *42*, 548–568.

[112] Q. Fang, S. Gu, J. Zheng, Z. Zhuang, S. Qiu, Y. Yan, *Angew. Chemie Int. Ed.* **2014**, *53*, 2878–2882.

[113] K. Gottschling, G. Savasci, H. Vignolo-González, S. Schmidt, P. Mauker, T. Banerjee, P. Rovó, C. Ochsenfeld, B. V. Lotsch, *J. Am. Chem. Soc.* **2020**, *142*, 12146–12156.

[114] F. Haase, B. V. Lotsch, *Chem. Soc. Rev.* **2020**, *49*, 8469–8500.

[115] H. Deng, S. Grunder, K. E. Cordova, C. Valente, H. Furukawa, M. Hmadeh, F. Gándara, A. C. Whalley, Z. Liu, S. Asahina, H. Kazumori, M. O'Keeffe, O. Terasaki, J. F. Stoddart, O. M. Yaghi, *Science* **2012**, *336*, 1018–1023.

2. Covalent Organic Frameworks

Covalent organic frameworks (COFs) were introduced to the field of porous materials in 2005 by Yaghi *et al.* when they discovered COF-1 and COF-5 through the condensation of phenyldiboronic acids and hexahydroxytriphenylene, leading to the formation of these new materials (Figure 2.1).[1] Unlike the closely related MOFs, which were discovered earlier but share the key features of crystallinity and high structural porosity, they are composed entirely of light elements and are linked by covalent bonds rather than coordination chemistry.[2–4] To achieve this characteristic high long-range order of the framework, certain design principles have been applied: (i) A reversible bond-forming reaction that allows healing of defect sites and rearrangement of originally wrongly formed connections. (ii) Rigid building blocks that dictate the final structure and network topology. (iii) Aromatic compounds as building blocks that preferentially undergo π-π stacking to form three-dimensional structures from two-dimensional layers, as is the case with the most 2D COFs.[5,6] These design principles are still used today, but also continue to challenge chemists to extend them or overcome some of the limitations associated with them.[7] Similar to MOFs, which have a wide range of applications, COFs are predominantly studied for their great potential for various applications.[8] High intrinsic surface areas - ideal for catalysis, gas storage and separation - a known structure that allows a breakdown of structure-property relationships, high chemical modularity - adaptable to the application at hand - as well as optical and electrochemical activity make COFs one of the most promising materials of the early 21st century.[9–11]
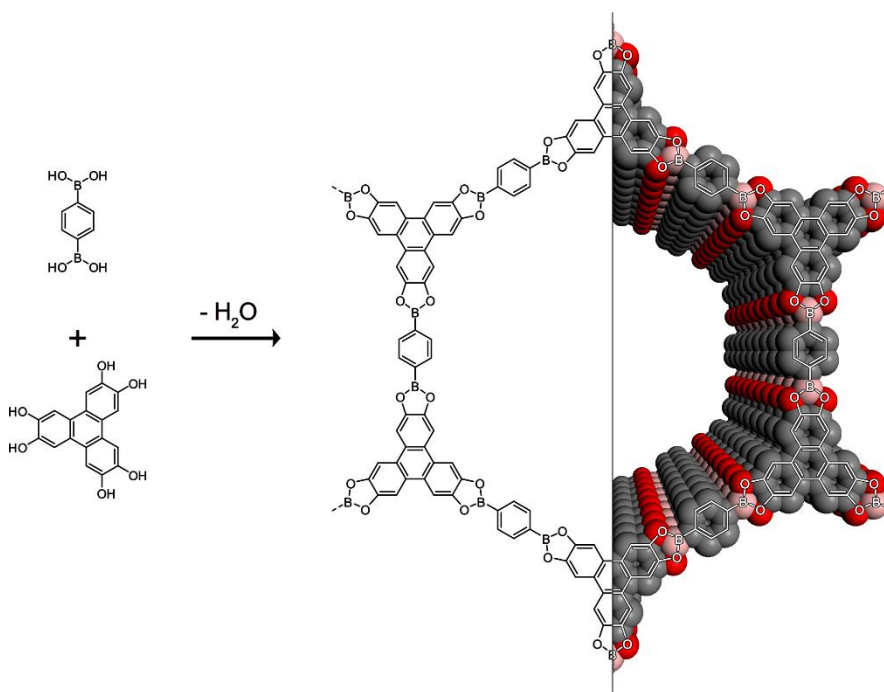
Figure 2.1. Synthesis of COF-5 by condensation of phenyldiboronic acid and hexahydroxytriphenylene.[1] Right side: perspective view of a pore formed by stacking layers.

2.1. Principles and Design
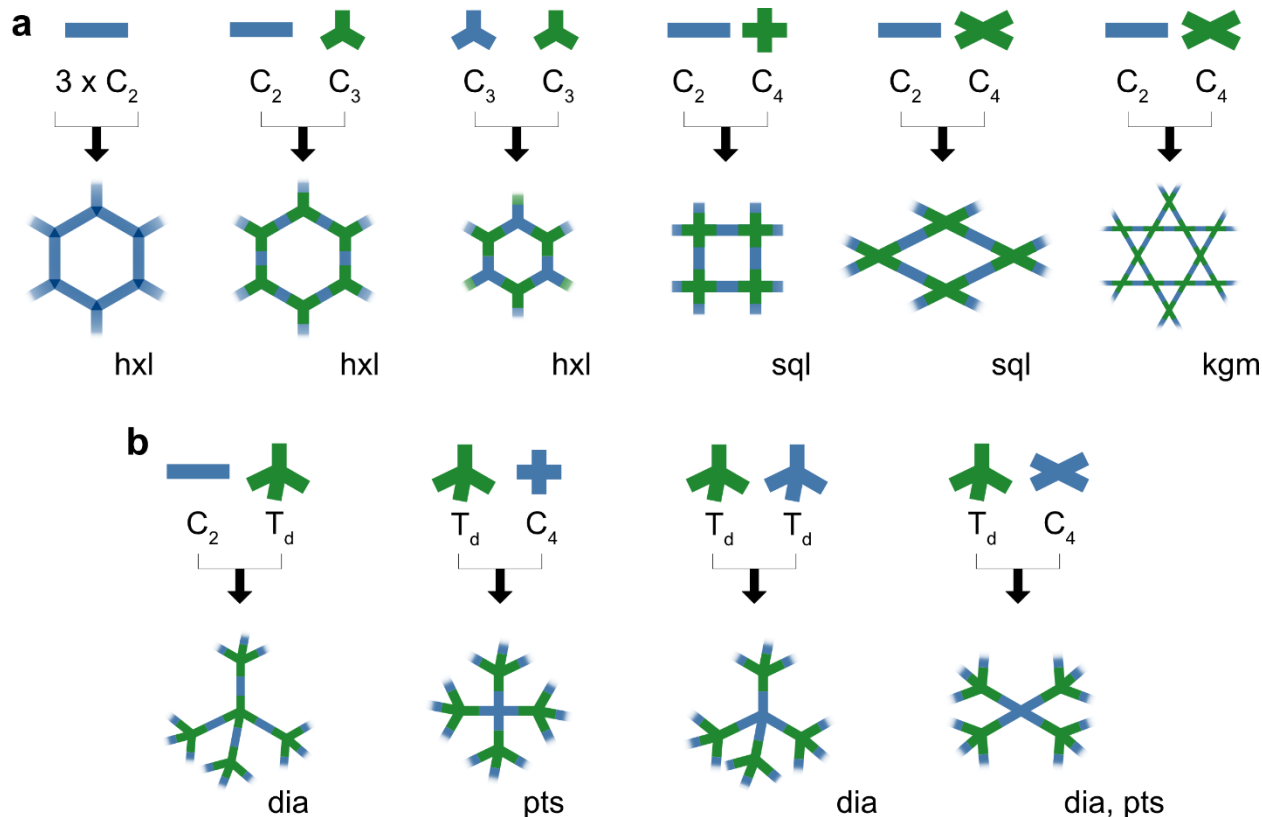
Figure 2.2. Most common topologies available in the design of 2D and 3D COFs.

Reticular chemistry is the rational design and controlled formation of extended structures with well-defined geometry and intrinsic porosity by linking molecular building blocks *via* strong bonds (e.g., coordinative, covalent) and represents a recent development in organic chemistry and materials science toward new materials.[12] According to the principles of reticular chemistry, the choice of the geometry of the molecular building block determines the final geometry and structure of the resulting scaffold, the strength and nature of the bonds determine the stiffness, thermal and chemical stability, and the high order enables crystallinity and ensures structure determination by X-ray or electron diffraction techniques.[12] COFs represent an important part of reticular chemistry, and compared to hybrid MOFs, their construction is based solely on organic chemistry. The reticular assembly of COFs in predetermined structures based on repeating subunits not only introduces crystallinity and porosity into the frameworks or enables a variety of characterization methods and potential applications, but also enables the design of targeted materials with spatial precision at the atomic level.[11]

Since the structure of the resulting COFs is dictated by the distinct geometry of the rigid building blocks with defined symmetry and functional moieties, they can extend in two- (2D) or three-dimensional (3D) structures with different topologies, point group symmetries, pore sizes, and
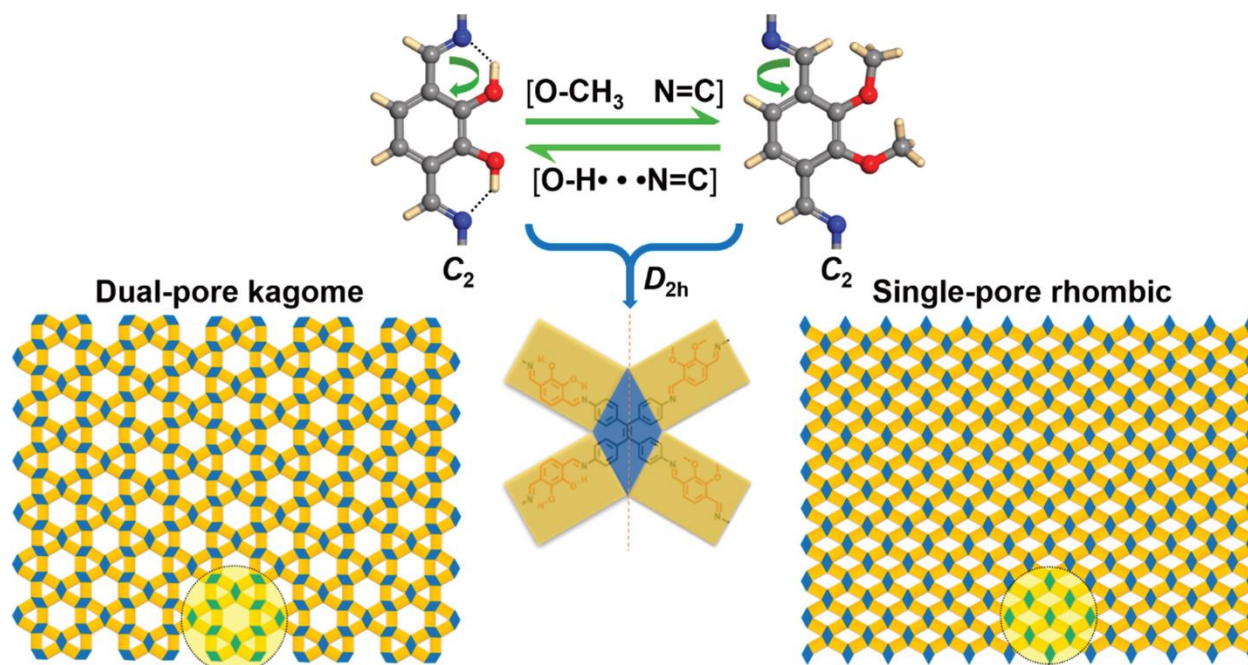
Figure 2.3. Topology diagrams of TPE-COF-OH and TPE-COF-OMe COF. Condensation of C_4 TPE-NH$_2$ and C_2 2,3-DHTA or 2,3-DMTA leading to *kgm* or *sql* topology determined by the imine configuration influenced by intermolecular hydrogen bonding. Taken and adapted with permission from Ref. [14]. Copyright 2020 American Chemical Society.

shapes. It should be noted that 2D COFs form two-dimensional network topologies through co-valent bonding, but rarely occur as single isolated sheets, instead coming together in layered structures of multiple sheets held together by non-covalent π-π interactions.[13] This sheet stack-ing creates a quasi three-dimensional structure, which in turn forms the extended pores for these materials. The formal symmetry and functionality of the molecular building blocks is usually de-noted by simplified molecular point group symmetry abbreviations, which may differ from the ac-tual symmetry of the molecules and correspond to their role in reticular framework formation, e.g., 1,4-benzenedicarboxaldehyde (terephthalaldehyde) and 2-methyl-1,4-benzenedicarboxaldehyde are both described as C_2 building blocks, taking into account only the bifunctionality of the alde-hydes and their linear arrangement. Considering this simplification, the design concept for COFs of different topologies consisting of building blocks with distinct geometry can be illustrated with a block model (Figure 2.2).[11] For example, a bifunctional C_2 monomer will condense with a tri-functional C_3 monomer to form a 2D hexagonal *hcb* structure (honeycomb), as will the combina-tion of two different C_3 and C_3 monomers.[5] The combination of a C_2 monomer with a T_d monomer that extends in three dimensions will lead to the formation of 3D COFs in a *dia*-structure type (diamond).[14] As shown in the diagram, this topology determination based on the geometry and functionality of the monomers allows for the rational design of frameworks or a desired topology can be deconstructed into its basic geometric units, and with finding representative molecular monomers for these units, they can then crosslinked to form the desired network.
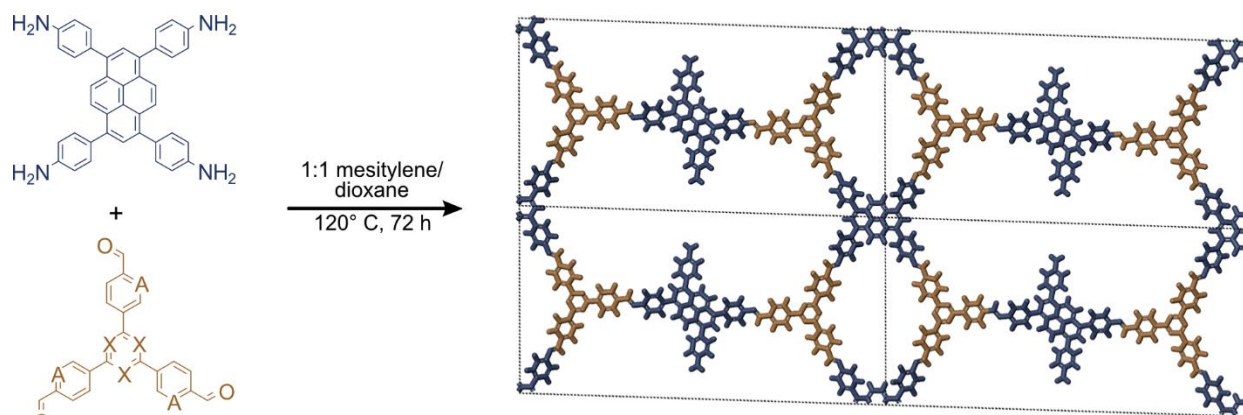
Figure 2.4. Synthesis and structure of PT- and PY-COFs and illustration of the structure model with *bex* toplogy visualizing the uncondesed amine-functionalities oriented towards the pore. Taken and adapted with permission from Ref. [16]. Copyright 2019 Springer Nature.

Rare examples, limiting the predictability of structure types exist, especially for *sql* and *kgm* type COFs, both of which are composed of C_2 and C_4 monomers. Peng *et al.* showed that intramolecular hydrogen bonding can be used to regulate the topology of 2D imine COFs (Figure 2.3).[15] By changing the substituents of an otherwise identical C_2 molecular linker, topology-selective synthesis between a *sql* and *kgm* structure type was achieved. The authors found that the intramolecular hydrogen bonding of the hydroxyl groups affected the conformation of the imine bonds in the scaffold, which was reflected in the altered topology. Li *et al.* reported a solvent-dependent polymorphism of 2D imine COFs.[16] For COFs prepared from A_2B_2-type tetraphenylbenzene monomers (p- and m-TetPB), a change in reaction solvent resulted in either *sql* or *kgm* structure types. For (o-TetPB), only the *sql* structure type was observed. The authors conclude that the growth process is dominated by the geometry of the monomers and the solvent effects determine the perturbation of the chain growth pattern.

Another case for COFs where the structures are hard to predict are substochiometric COF designs. With this design strategy, one obtains a framework that is not fully condensed, thus extending the design rules for COFs. Banerjee *et al.* showed that the combination of C_3 and C_4 linkers leads to a *bex* net topology with periodic, non-condensed functionalities of the C_4 monomer (Figure 2.4).[17] This introduces additional functionalities on the COF pore surface without the need to redesign the monomers. A COF with the same network topology was also obtained by replacing half of the C_4 monomers with C_2 units.

Predictable rational design and retrosynthesis of structures is one of the greatest advantages of reticulated chemistry. Combined with the spatial precision at the atomic level and the high variability of the different building blocks and their possible functionalization, the targeted design of materials with desired properties is possible.
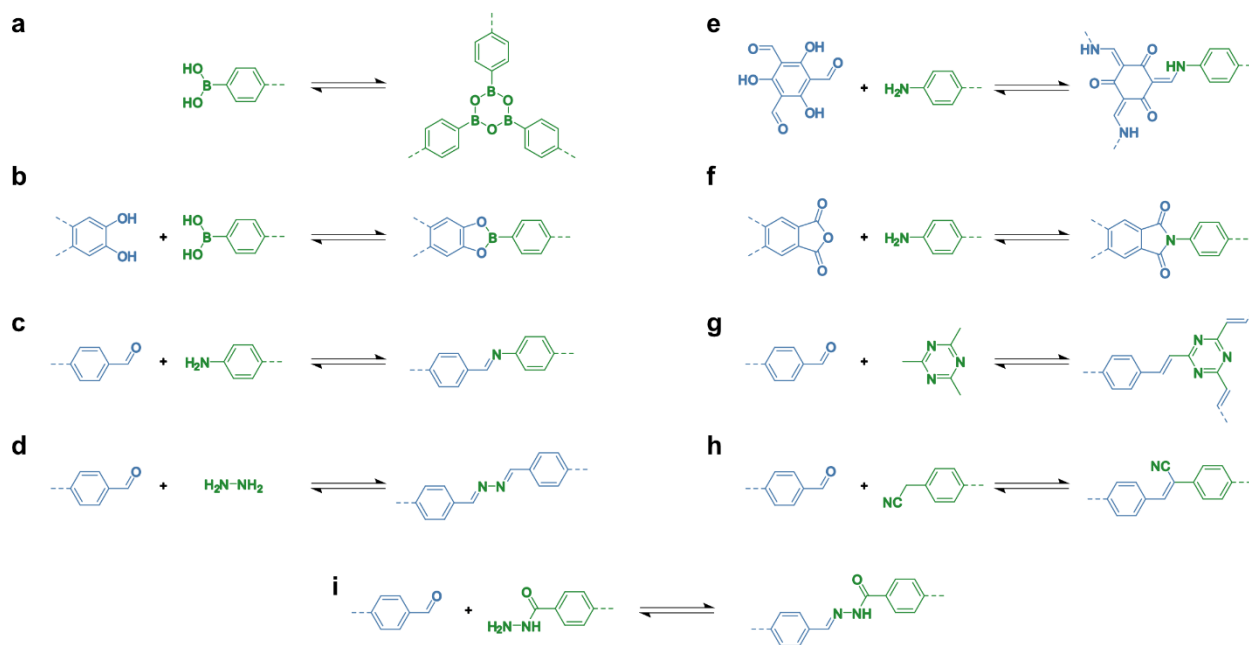
Figure 2.5. Common chemical bond forming reactions used in the formation of COFs. (a) Boroxine, (b) boronic ester, (c) imine, (d) azine, (e) β-ketoenamine, (f) imide, (g, h) olefin, (i) hydrazone linkages.

In addition to the choice of building block geometry, the successful formation of COFs also depends on the type of covalent bond used in their formation. As with monomers, a wide range of different chemical bonds have been investigated for the preparation of COFs.[5] These include boronic ester,[1,18] imine,[19] hydrazone,[20,21] imide,[22,23] olefin,[24] and β-ketoenamine[25] which are of great interest (Figure 2.5). One of the most important common features of COF linkages is the reversible covalent bond formation.[3] This is crucial for crystallinity and a well-ordered structure in COF formation, as it allows for error correction after the initial bond formation reaction. By breaking and reforming the bonds between the building blocks, erroneous linkages between the building blocks can be corrected and larger, more crystalline domains are obtained.[26] The reversibility of bond formation often correlates with crystallinity, but also with the stability of the final framework or with harsh reaction conditions during synthesis. Less reversible bonds such as imide, hydrazone, or olefin bonds often require higher temperatures or longer reaction times to form crystalline materials.[24,27] The most common linkage used today is the imine bond, which was first reported in 2009, four years after the first report on boronic ester-linked COF-1 and COF-5, published by Uribe-Romo *et al.*[19] The excellent control over the reversibility of the reaction, the good stability of the scaffold, and the wide commercial availability or ease of synthesis of the building blocks, either as amines or aldehydes, favor the widespread use for COF chemistry.[5]

Stable, crystalline, and functional COFs are required for applications in the laboratory and beyond. One of the major challenges in COF chemistry is the interplay between the reversibility of the reaction required to achieve crystallinity and the stability of the final scaffold, which decreases when more reversible bond forming reactions are used, and the difficulty of harsh reaction conditions required for more stable bonds, which often prevent the incorporation of functionality into

The COF Trilemma
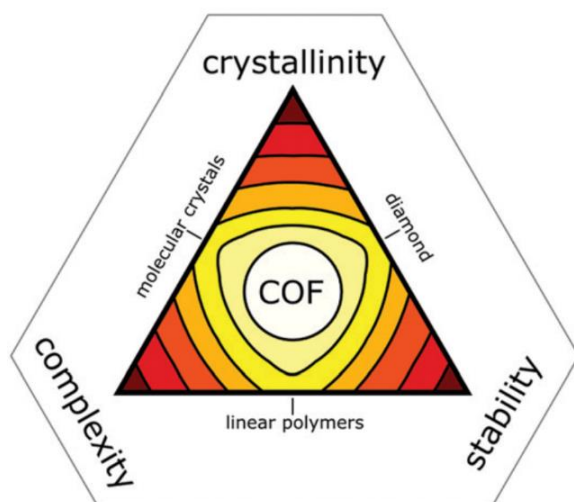
Figure 2.6. The COF trilemma of combining complexity, crystallinity, and stability. Taken and adapted with permission from Ref. [7]. Copyright 2020 The Royal Society of Chemistry.

the monomers. This problem, also referred to as the "COF trilemma" (Figure 2.6) of combining complexity, crystallinity, and stability for COF formation often leaves researchers wondering which properties should take precedence, or they end up with materials of lower quality than desired.[7] A variety of approaches can be taken to overcome this challenge. From pre-orientation of monomers,[28] slow addition of building blocks or seeding growth of reaction mixtures,[29] addition of modulators that slow initial bond formation,[30] to adjusting stacking interactions between COF layers.[13,31] In addition, new synthesis strategies and methods can be developed to obtain COFs formed from less reversible bond formation reactions with better crystallinity, or formed with milder reaction conditions.[32,33] Post-synthetic bond conversion to lock the structure with irreversible bonds,[34] or post-synthetic introduction of functionalities that would be too fragile under harsh COF formation reaction conditions are also approaches to solve this challenge.[7,35]

2.2. State of the Art COF Formation and Synthesis

Solvothermal synthesis

Solvothermal synthesis, the initial method for the preparation of COF-1 and COF-5, is still the most commonly approach to prepare COFs today:[1,6,10] In a typical procedure, the building block mixtures and catalyst are placed in a pressure-tight reaction vessel of sufficient size, dissolved in a solvent, and heated for several days after sealing. The conditions of this method are highly variable and range from 70-150 °C in temperature, 3-7 days of reaction time, and with carefully selected solvent mixtures in sealed Pyrex tubes, autoclaves, or quartz ampoules. Reactions are often performed under vacuum after several freeze-pump-thaw cycles. After the reaction has cooled back to room temperature, the precipitate is collected by filtration or centrifugation, washed thoroughly with appropriate solvents, or subjected to Soxhlet extraction to remove oligomers or remaining monomers. The washed material is then dried and activated *in vacuo* at up to 120 °C or, in the case of more sensitive scaffolds, activated by a supercritical CO_2 drying process.[36,37]

Although the type of solvents and their ratio in the reaction mixtures are crucial for the production of crystalline and porous materials, their role is not yet fully understood. However, sufficient solubility of the linker is required. Therefore, to obtain crystalline COFs of sufficient quality, different combinations of solvent mixture, catalyst, temperature, and reaction time have to be screened. In addition, upscaling of reactions is sometimes limited to a few milligrams of material and/or requires rescreening of reaction conditions. Despite this drawback, most COFs are still prepared in this way because the material obtained is of high quality and has often a Brunauer–Emmett–Teller surface area (S_{BET}) greater than 1500 m^2 g^{-1}.[38,39]

Ambient conditions

To circumvent the harsh and experimentally adverse solvothermal conditions, several methods for COF production under ambient conditions were investigated. Peng *et al.* performed batch synthesis of several COFs at room temperature by dissolving the building blocks with the acetic acid catalyst in the solvent mixture and leaving it undisturbed for three days before collecting the precipitated COF powder.[33] This simple procedure was able to provide COFs with excellent S_{BET} values of up to 1722 m^2 g^{-1} in the case of N3-COF. In 2017, Matsumoto *et al.* presented scandium triflate as a novel catalyst for the rapid formation of imine COF at room temperature.[40] They demonstrated that this catalyst was able to form their model system TAPB-PDA COF in only 20 min at room temperature, compared to the conventional solvothermal synthesis requiring acetic acid, 70 °C and 72 h, while almost doubling the obtained specific surface area of the COF. Zhang *et al.* reported a room-temperature synthesis of COF-LZU1 in a CO_2/water solvent by dissolving CO_2 in water.[41] They could not only provide an environmentally friendly synthesis method for COF-LZU1, but also enable the formation of a new nanobar morphology. Zhu *et al.* reported the formation of imine COFs at ambient temperature using metal nitrates as catalysts.[42] They were

able to identify the cheap and abundant $Fe(NO_3)_3 \cdot 9H_2O$ as the most efficient catalyst to obtain well crystalline and porous products, even in the presence of oxygen.

COF formation under ambient conditions represents a useful and simple alternative to classical solvothermal synthesis, especially in view of possible scaling to industrial scale in regard to its lower energy consumption. However, the lower solubility at room temperature limits the scope of the building blocks or even requires larger amounts of potentially toxic solvents than a solvothermal approach.

Mechanochemistry

In recent years, mechanochemistry has re-emerged as a simple, solvent-free, and environmentally friendly room-temperature synthesis method in many fields.[43–45] It was adopted to COF chemistry by Biswal *et al.* as a viable synthesis method using a pestle and mortar or a ball mill with liquid-assisted grinding (LAG) technique.[25,46,47] They report a rapid and almost solvent-free reaction yielding porous and crystalline materials. The mechanochemical approach was also used in an organic terra cotta process for COFs using solid p-toluenesulfonic acid as a catalyst, which allowed the formation of COFs into various macroscopic shapes.[28] Wang *et al.* successfully synthesized TpAzo-COF *via* the mechanochemical synthesis and observed the formation of layered structures not obtained with the solvothermal route.[48] Mechanochemistry can also be used in top-down approaches for the exfoliation of COFs.[49]

The mechanochemical route for the production of COFs offers numerous advantages in economic and environmental terms and circumvents the problems of solubility of the building blocks. However, this method of synthesis usually results in materials of lower quality compared to solvothermal processes, which rarely has a specific surface area greater than 300 m^2 g^{-1}, limiting its widespread use in practice.[25,50]

Ionothermal synthesis

The use of a molten salt as a solvent and catalyst for COFs was first introduced by Kuhn *et al.* in the formation of triazine-based covalent frameworks (CTFs) by the trimerization of nitriles in a $ZnCl_2$ melt at 400 °C.[51] These CTFs showed crystallinity and high porosity. However, the harsh conditions of this method limit the scope for linkages or building blocks due to possible undesirable decomposition and side reactions. Maschita *et al.* demonstrated that the ionothermal method can also be used to synthesize imide-linked COFs with $ZnCl_2$ at lower temperatures or with eutectic salt mixtures.[27] Similar to the mechanochemical route, this strategy does not require solubility of the building blocks, and allow for shortening the reaction time and producing new COF systems that cannot be obtained through solvothermal reactions. By using ionic liquids, Guan *et al.* were able to extend the scope of ionothermal reactions to room-temperature for the preparation of imine COFs.[52] Recently, it was also shown that cheaper deep eutectic solvents can be used for COF formation.[53]

Other methods

In recent years, various other strategies for COF formation have been developed and reported. Yang *et al.* demonstrated the first successful COF formation by sonochemical synthesis of COF-1 and COF-5 based on boronic esters.[54] Recently, sonochemistry was also discovered as a rapid and ecological alternative for imine-based COF formation in water.[55] Microwave-assisted synthesis has also been investigated and successfully used for COF production. With shorter reaction times and better control over temperature and pressure than classical solvothermal synthesis, cleaner and higher quality materials can be obtained.[56,57] Kim *et al.* reported a rare light-promoted synthesis of hcc-COF from 1,2,4,5-benzenetetramine and hexaketocyclohexane in an efficient reversible dynamic imine condensation reaction.[58] They were able to obtain a uniform and crystalline product with an extended π-conjugated structure along the lateral direction to improve the electrical properties of COFs.

2.3. Post-Synthetic Modifications and Functionalization of COFs

Post-synthetic linkage modifications

The stability and variability of COFs also allows for interesting and useful post-modifications after the original framework has been formed. These modifications can be useful to introduce or add new functionalities to the COF, change the pore surface properties, or improve the chemical stability of the scaffolds. Due to the high intrinsic porosity, which allows reagents privileged access to the bonds or building blocks in question, the subsequent modification of COFs is one of the interesting advantages compared to non-porous polymeric materials.[5,11] While many of the COF linkages are remarkably stable under mild conditions for catalysis or other applications, their intrinsic property of being formed from reversible bond formation reactions always implies that the bonds holding the scaffold together can be broken under harsher conditions. The trade-off between highly reversible bond formation for high crystallinity and the resulting lower chemical stability is a core problem in COF design and part of the COF trilemma.[7] One approach to solving this problem is to convert the originally reversible bonds into chemically irreversible bonds.

In 2016, Waller *et al.* reported one of the first examples of this approach, namely the direct chemical conversion of imine linkages to amide linkages by oxidation (Figure 2.7).[59] Using sodium chlorite as a reagent, they were able to completely convert the imines to 2D COFs while maintaining the crystallinity and porosity of the scaffold. The transformed scaffold was found to be stable for 24 hours to treatment with 12 M aqueous HCL and 1 M aqueous NaOH, conditions that degraded the original imine scaffold.

The same group also showed a different approach for the conversion of imine to oxazole and thiazole bonds in COFs.[60] In contrast to direct oxidation to amides, this conversion was based
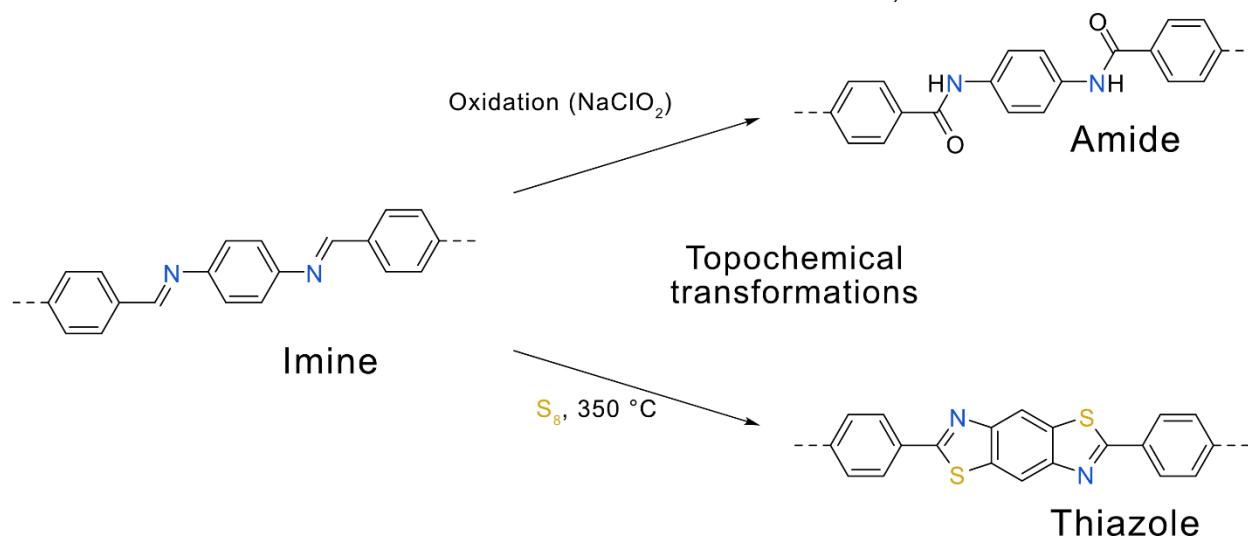
Figure 2.7 Direct topochemical conversions of imine bonds to amide (upper pathway) or thiazole (lower pathway). [34,59] The resulting bonds are chemically much more stable than the original imine bond, which is susceptible to hydrolysis.
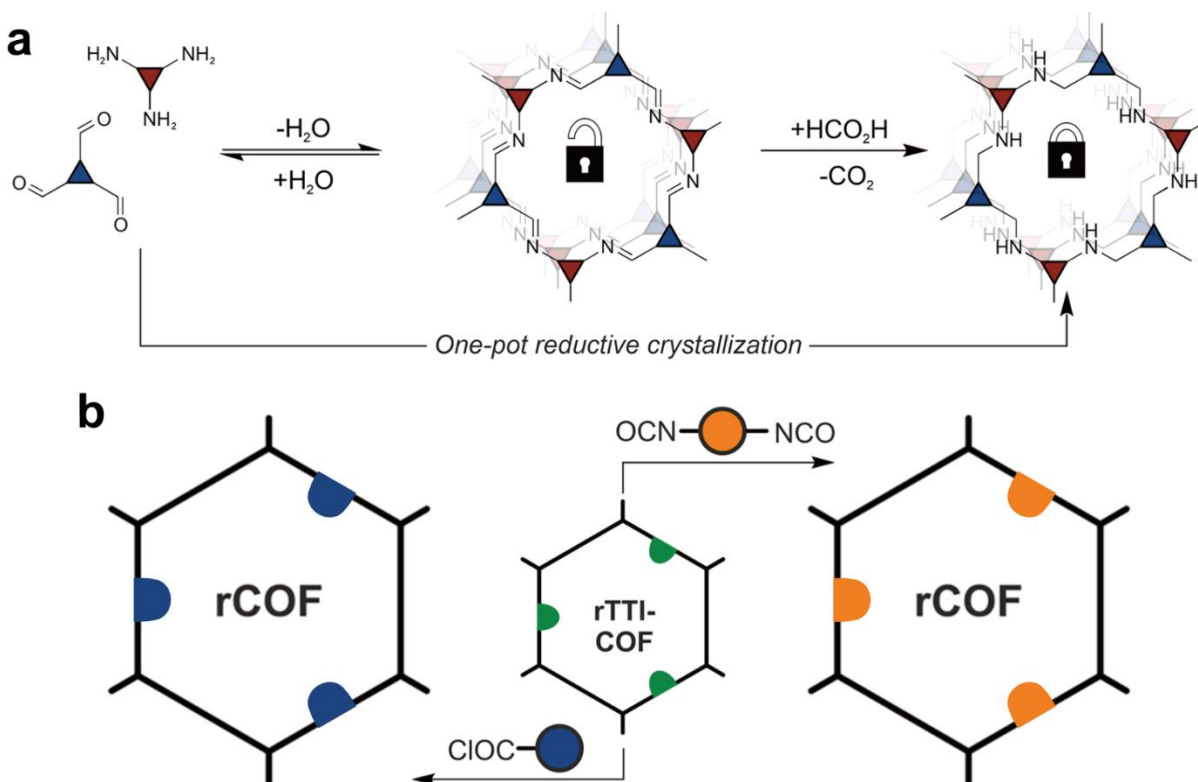
Figure 2.8. (a) Synthesis pathway to amine-linked COFs by a two-step process of imine condensation followed by reduction by formic acid or reductive one-pot crystallization in which formic acid acts as acid catalyst and reducing agent. (b) Post-synthetic functionalization of the pore wall at secondary amine bonds by immobilization of acyl chlorides (left) or isocyanates (right). Taken and adapted with permission from Ref. [63]. Copyright 2021 American Chemical Society.

on the substitution of the original C_2 aldehyde linker by a hydroxy- or thiol-functionalized mono-mer. After linker exchange, intralayer cyclization and oxidation lead to the oxazole or thiazole linkages. The resulting material is isostructural to the original COF and also exhibits significantly increased chemical stability.

Direct conversion of imine to thiazole linkage without linker exchange was simultaneously demon-strated by Haase *et al.* in a topochemical conversion of the scaffold at 350 °C using elemental sulfur (Figure 2.7).[34] A recent one-pot synthesis of thiazole-linked COFs was carried out in a multicomponent reaction with the addition of sulfur during the initial COF formation.[61] The one-pot reaction resulted in a material with higher crystallinity and porosity compared to a two-step approach.

Li *et al.* developed a transformation by aza-Diels-Alder cycloaddition reaction of phenylacetylene derivatives with the imines to form a stable, porous, and fully aromatic framework.[62] The newly formed quinoline-bonded COF retained its crystallinity and acquired improved chemical stability. The newly protruding phenyl groups bearing tunable functional groups can be used to modify the properties of the inner pore surface and shape its features.
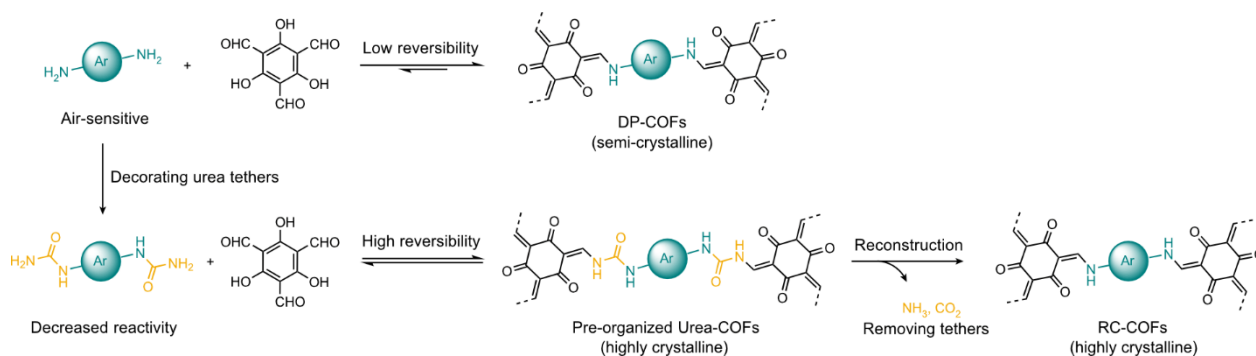
Figure 2.9. Direct reaction pathway to β-ketoenamine-linked COFs with low reversibility, leading to low crystallinity (upper pathway). One-pot multi-step reconstruction pathway through urea tether, where urea COFs are first formed in a highly reversible reaction, followed by reconstruction by removal of the tether (lower pathway). Taken and adapted with permission from Ref. [64]. Copyright 2022 Springer Nature.

In 2021, Grunenberg *et al.* reported the direct conversion of imines to secondary amine linkages by a mild Leuckart-Wallach reduction with formic acid or ammonium formate (Figure 2.8, a).[63] The secondary amine linkages were also obtained in a one-pot reaction during the initial COF formation, with formic acid serving as both acid catalyst and reducing agent. The reduced COFs were obtained with high crystallinity and porosity. As in the aza-Diels-Alder cycloaddition reaction, the newly formed amines also introduced additional functions into the framework. In addition to the intrinsic basicity of the secondary amines, they can also be used as reactive sites for post-synthetic functionalization by serving as attachment points for acyl chlorides or isocyanates (Figure 2.8, b). This could provide access to tailored, more stable covalent organic scaffolds.

The most recent addition to post-synthetic modifications to increase the stability of COFs is the reconstruction of urea COF into very stable β-keteneamine-linked COFs in a multi-step one-pot reaction (Figure 2.9).[64] The high reversibility in the formation of urea-based COFs leads to highly porous and crystalline preorganized materials in the first step. In a subsequent step, hydrolysis of the urea bond combined with the formation of β-ketoenamines on the resulting free functional groups leads to *in situ* polymerization to reconstructed COFs. Thus, the scaffold is reconstructed by a formal loss of carbon dioxide, ammonia, and water. The original structural information, high crystallinity, and porosity of urea-linked COFs are retained and exceed the quality of the same COFs formed by direct β-ketoenamine formation.

Post synthetic pore wall modifications

Another general strategy for post-synthetic functionalization of COF is the modification of the building blocks that form the pore walls. While post-synthetic modification of the linkages is primarily aimed at increasing stability, modification at the pore wall is aimed at implementing additional functionality. The rationale for this strategy is concern about stability or disruption of the desired functionality during COF formation, or a library-like diversification of functionalities that relies on the creation of a simple COF and saves the synthesis of several different building blocks.[65] However, while bond modification is limited to the chemistry that exists around it, pore

X%N$_3$-COF-5 X = 5, 25, 50, 75, or 100%N$_3$-COF-5   X%RTrz-COF-5
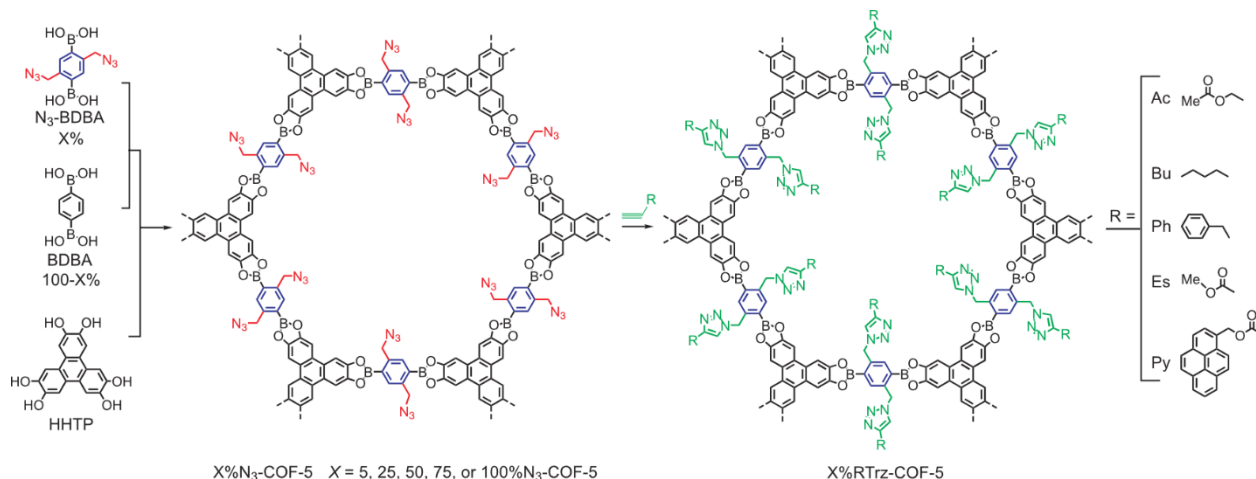
Figure 2.10. Nagais *et al.* reported a general strategy for the surface engineering of COFs. Initially an azide bearing building block is added, substituting a certain percentage of non-functionalized building block. The pore wall mounted azides are then used as anchors for various alkyne organic molecules *via* click chemistry, attaching the novel groups on the COF pore wall and tailoring its properties. Taken and adapted with permission from Ref. [67]. Copyright 2011 Springer Nature.

wall modification can utilize more broader, versatile chemistry. Because the functionalization processes are heterogeneous reactions and the separation of unwanted byproducts is challenging, high yield and clean reaction are necessary.[66]

For post-synthetic modification of the pore wall, simple functional groups are introduced into the scaffold, which can then be reacted with coupling agents to form covalent bonds between the pore wall and the functional moieties. These side groups may include azide - coupling with alkyne *via* click chemistry -, hydroxyl - coupling with alkyl halides, acyl chlorides or anhydrides, to form the corresponding ethers or esters -, or amine - coupling with acyl chlorides or anhydrides to form amides.

Nagai *et al.* demonstrated functionalization of the pore surface of COFs by click chemistry.[67] Using building blocks containing azide units, they were able to form COFs with different densities of azides on the pore walls depending on the ratio of azide/non-azide building blocks used, serving as anchoring units. They were able to perform successfully and quantitatively click reactions on these azides attached to the pore wall with different alkynes. Their protocol was compatible with various organic functionalities and allowed tailoring of the COF surface to specific properties. A dependence on the density of azides was observed for the retention of crystallinity and porosity. However, at a low density of azides, there was no change in COF quality after the click reaction. To evaluate the effects of functionalization of the pore walls, the gas sorption selectivity of CO$_2$ versus N$_2$ was measured, and up to 16-fold higher selectivity of the functionalized material was observed compared to the untreated material.

In 2016, Dong *et al.* reported on the immobilization of ionic liquids on COFs.[68] They processed the hydroxy-containing COF surface by a Williamson ether reaction with (2-bromoethyl)tri-ethylammonium bromide to immobilize the ionic liquid. The subsequent modification significantly increased the affinity of the framework for CO_2, resulting in a high adsorption capacity of 164.6 mg g^{-1} at 273 K and 1 bar, while making it an effective heterogeneous catalyst for the conversion of CO_2 to formamide under ambient conditions. The surface-treated catalyst afforded the formylation product of amines and CO_2 - enabled by a reducing agent $PhSiH_3$ - in excellent yields of 88% or more.

Ji *et al.* successfully prepared an amine-functionalized imine-COF.[69] This functionality, which would easily interfere with imine-COF formation, is initially introduced as an azide group. The decision to reduce the azide group instead of using it for click chemistry resulted in an amine functionalized COF with no loss of crystallinity and only minor loss of specific surface area, even with maximized azide coverage on the surface. The COFs modified with amine were found to be efficient in removing GenX and other perfluorinated alkyl substances from water. For 12 of 13 PFASs, a COF with a lower amine loading of 28% successfully removed more than 90% of the contaminants. The higher removal efficiency at slightly reduced amine loading is attributed by the authors to a synergistic combination of the polar amine group and the hydrophobic pore surface.

Pachfule *et al.* demonstrate post-synthetic COF modification by ionic immobilization of gold [Au(0)] nanoparticles (NPs).[70] Using a solution infiltration method, they first loaded TpPa-1 COF with $HAuCl_4 \cdot 3H_2O$ before reducing it with $NaBH_4$ to form catalytically active gold NPs. These NPs were found to be well distributed in the ordered porous COF support architecture, which exhibited high stability in aqueous and common organic solvents. The Au(0)@TpPa-1 composite showed high activity as a catalyst for nitrophenol reduction reactions, superior to reduction with $HAuCl_4 \cdot 3H_2O$ as catalyst.

Post-synthetic modification and functionalization of COFs is a powerful tool to expand the application range of COFs. Bond conversion for robust, stable frameworks can improve their resistance to harsher catalytic reaction conditions and ensure catalyst recovering and recycling. Post-synthetic modification of the pore wall is also ideal for further specializing COFs for specific applications and introducing more sensitive functionalities into the scaffold.

2.4. Application of COFs

Gas capture and storage

The high specific surface area, the adaptability of the pores and the low density make COFs promising materials for the capture, storage and separation of gases. Gases relevant to climate, energy and industrial policy, such as carbon dioxide, methane, hydrogen, ammonia or sulfur dioxide, are generally the focus of this research, and COF systems are being developed for these specific gases.[71]

CO_2, which is released by fossil fuel consumption and the major greenhouse gas, is an urgent and important focus for gas storage research in COFs as well as for other porous materials such as porous carbons, silica, and MOFs.[21,72] To obtain information on the general affinity of COFs for CO_2 and their suitability for CO_2 adsorption, measurements are performed between 273 K and 313 K up to 1 bar to determine the heat of adsorption and the amount of CO_2 adsorbed.[73] To investigate their storage capacity, measurements are made at room temperature up to 60 bar.[71]

Even the first synthesized COFs, COF-1 and COF-5, showed promising CO_2 uptake of 230 mg g^{-1} and 870 mg g^{-1} at 298 K and 55 bar, respectively. Later synthesized boron-based COF-102 and COF-103 achieved excellent CO_2 uptakes of 1200 mg g^{-1} and 1190 mg g^{-1} at 298 K and 55 bar, respectively.[74] The variable configurations for COFs also inspired others who used design principles for better CO_2 adsorption properties by fabricating polar, nitrogen-rich, or ionic scaffolds. Li *et al.* reported an azine-linked framework, COF-JLU2 (Figure 2.11), in which CO_2 adsorption is enhanced by polar β-ketoenamine groups.[75] Despite the rather moderate S_{BET} of 415 m^2 g^{-1}, CO_2 uptake of 217 mg g^{-1} was achieved at 273 K and 1 bar. El-Mahdy *et al.* demonstrated a strategic design of triphenylamine- and triphenyltriazine-based 2D COFs for enhanced CO_2 uptake.[76] They were able to relate planarity and higher nitrogen content in the backbone in a series of six isoreticular COFs to enhanced interaction with CO_2 and thus improved gas uptake. Their most efficient system was optimized to 92.38 mg g^{-1} CO_2 uptake at 273 K and 1 bar. Hung *et al.* demonstrated efficient functionalization of the pore wall for enhanced CO_2 affinity in H2P-COF.[72] In a ring-opening reaction of succinic anhydride with hydroxyl groups present in the original COF, the pore wall was functionalized with carboxylic acid moieties to induce dipolar interaction with CO_2. This post-modification improved CO_2 uptake by more than 300% and significantly increased the selectivity of CO_2 over N_2 in gas separation. In 2017, the same group reported an ionic PyTTA-BFBIm-iCOF with the cationic linker 5,6-bis(4-formylbenzyl)-1,3-dimethyl-benzimidazolium bromide.[77] The cationic benzimidazolium sites protruding into the COF pore channels greatly altered the CO_2 affinity compared to the neutral analog. They found a promising uptake of 93 mg g^{-1} at
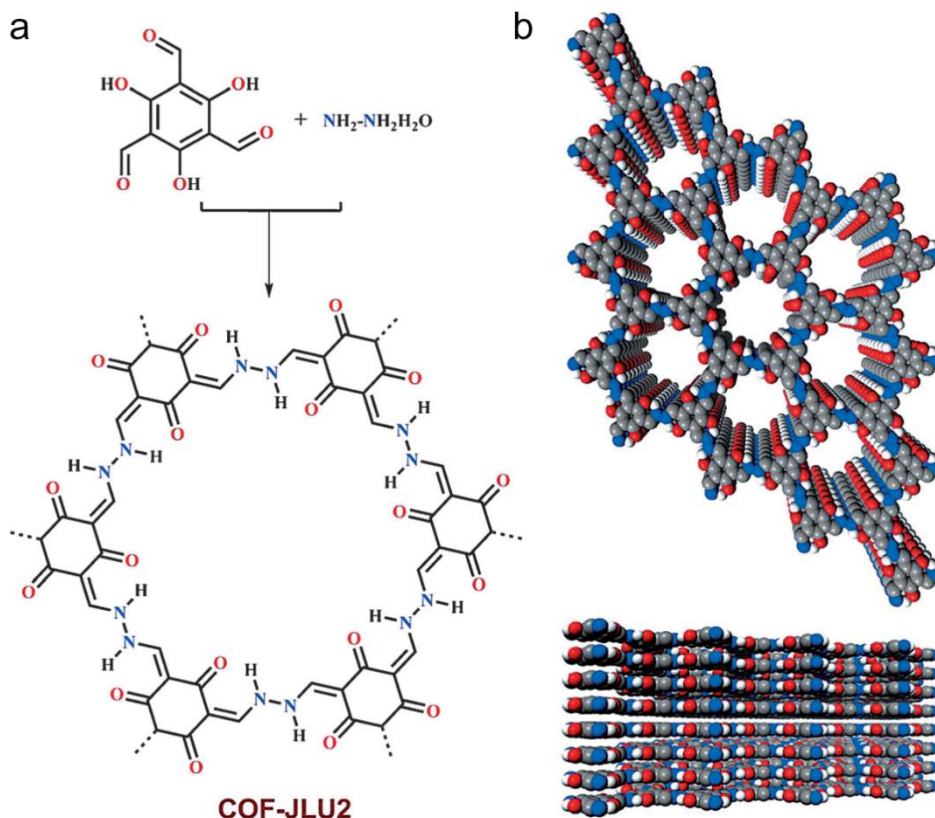
Figure 2.11. (a) Synthesis of COF-JLU2. (b) Structural model showing the AA stacking of COF-JLU2. The high density of polar bonds on the backbone increases CO_2 affinity and uptake. Taken and adapted with permission from Ref. [75]. Copyright 2015 John Wiley and Sons.

298 K and 177 mg g^{-1} at 273 K and 1 bar for their ionic system and demonstrated that the construction of the ionic interface of COFs provides a new avenue in the development of CO_2-affine storage materials.

COFs are also being investigated as promising materials for hydrogen storage. Despite its high potential as a clean energy source, safe storage and transport of the highly reactive gas remains one of the major challenges.[78] COF-102 and COF-103 were found to be excellent materials for hydrogen storage, with uptake of 72.4 mg g^{-1} and 70.5 mg g^{-1} at 298 K and 35 bar, respectively.[74] Similar to CO_2 adsorption, 3D COF structures were found to be superior to their 2D counterparts for gas storage. This effect and the general exceptional storage properties of COFs for hydrogen have been investigated in theoretical studies.[79] Xia *et al.* investigated the influence of different functionalization of COF-320 on hydrogen adsorption properties. Substitution of the H atoms of the benzenes contained in the COF by various moieties, e.g., hydroxyl, amine, methyl, or cyano, showed that these could improve the storage capacity between 27.6 and 35.2%.

As with hydrogen, the adsorption of methane is also a difficult case. Due to the low polarity of these gases, high adsorption depends exclusively on large surfaces and pore volumes. The successful design principles for CO_2 with nitrogen-rich, polar or ionic backbones and pore walls are not suitable for significantly improving adsorption as for the other gases.[6]
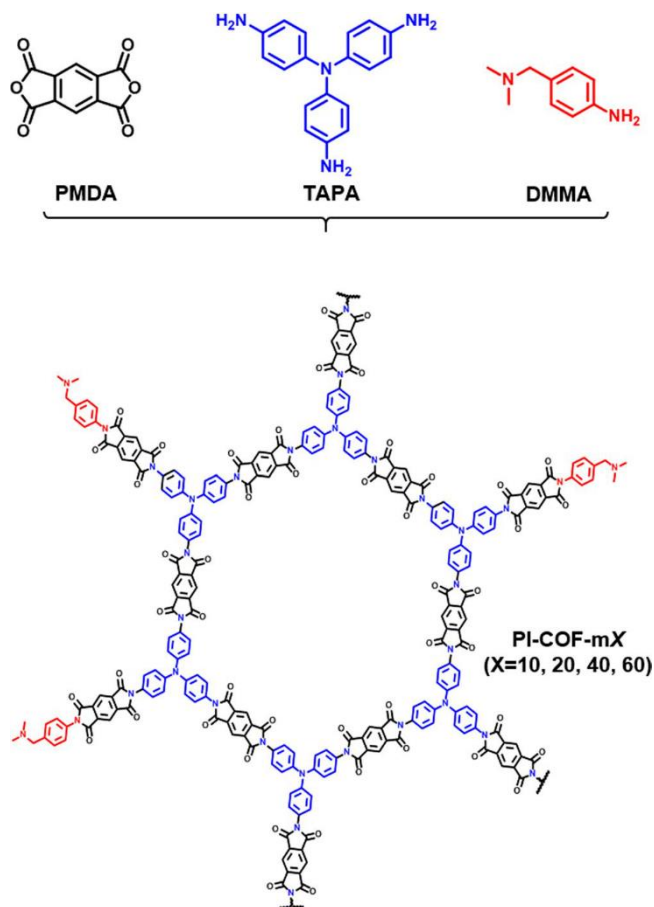
Figure 2.12. Synthesis of PI-COF-mX with the modulator DMMA to introduce secondary amine structures for enhanced SO_2 uptake. Taken and adapted with permission from Ref. [82]. Copyright 2017 Springer Nature.

Studies on other gases, especially ammonia or sulfur dioxide, are still quite rare. Boronate ester-linked COFs were found to be efficient for ammonia adsorption due to the strong Lewis acidity of the boron components. Doonan *et al.* demonstrated exceptional ammonia uptake in COF-10 of up to 255.5 mg g^{-1}, which significantly outperformed zeolite 13X (153.3 mg g^{-1}), a state-of-the-art material for ammonia storage.[80] The adsorbed ammonia can be released under vacuum or by heating, which allows repeating of the adsorption/desorption cycles of the COF without damaging it. Using pore wall engineering with amine, carbonyl, and carboxyl groups and combined metal ion integration, Yang *et al.* were able to achieve excellent ammonia absorption capacities of 243.5 mg g^{-1} at 298 K.[81] This approach demonstrates that successful pore engineering can significantly alter ammonia uptake. By modulating the imide-linked PI-COF with a secondary amine (Figure 2.12), Lee *et al.* were able to functionalize the COF for efficient SO_2 capture with high stability and reversibility.[82] With the optimized modulator amount, they recorded SO_2 uptake of 410 mg g^{-1}.

Heterogeneous catalysis

Catalysis in heterogeneous systems occurs at the interface between different phases.[83] The efficiency and productivity in heterogeneous catalysis strongly correlates with the interfacial area and the active sites that contribute to catalysis. The high specific surface area of COFs makes them promising materials for heterogeneous catalysts, optimizing the available surface interface and catalytic sites with respect to liquid or gas phase substrates.[84] Thanks to their high chemical stability and versatility in terms of design and functions, these materials can be used to overcome various catalytic challenges.

One of the first examples of COFs as heterogeneous catalysts was reported by Ding *et al.* in the construction of a Pd/COF-LZU1 composite for the Suzuki-Miyaura coupling reaction.[85] By post-treatment of COF-LZU1 with Pd(II) acetate, the palladium coordinates to the imine bonds between

Figure 2.13. Formation of COF-LZU1 and Pd/COF-LZU1 by post-treatment with $Pd(OAc)_2$ and coordination to imines between adjacent layers. Taken and adapted with permission from Ref. [85]. Copyright 2011 American Chemical Society.

two layers and the catalyst is incorporated into the framework (Figure 2.13). This delicate incorporation of Pd(II) was detected by spectroscopic analysis. The final catalyst is characterized by high stability and recyclability, a broad range of reactants, and excellent yields in Suzuki-Miyaura coupling reactions. The authors attribute the enhanced activity of Pd/COF-LZU1 to its unique structure. The 3.7 Å spacing, corresponding to the layer spacings, of the capped imine nitrogen corresponds to an ideal condition for strong coordination of palladium.

Another example of the coordination of metal species in COFs to create functional catalysts is the bimetallic docking of a rhodium and palladium species to bipyridine-containing BPy-COF.[86] In two postsynthetic steps, a Rh(COD)Cl complex can first be formed on the bipyridine sites in the COF backbone, followed by the immobilization of $Pd(OAc)_2$ between two imine nitrogen atoms of the adjacent layer, similar as shown by Ding *et al.*. This bimetallic catalyst system shows remarkable activity in a one-pot cascade reaction of phenylboronic acid and benzaldehyde to benzophenone *via* a diphenylmethanol intermediate in good yields of 90%.
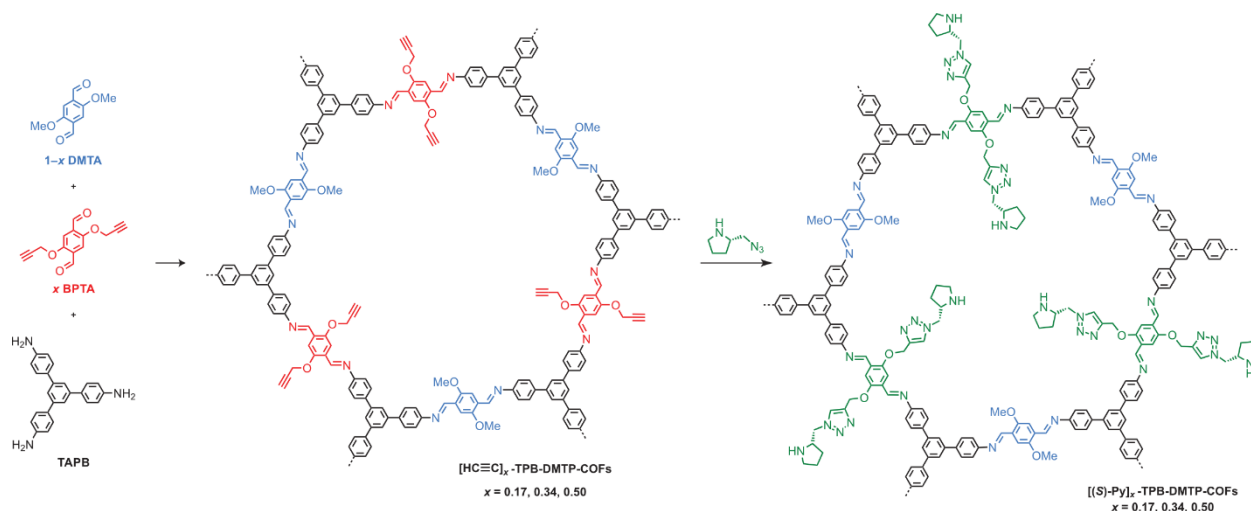
Figure 2.14. Synthesis of alkyne-functionalized TPB-DMTP-COF. Synthesis of chiral COFs ([(S)-Py]x-TPB-DMTP-COFs, x = 0.17, 0.34, and 0.50) by channel-wall engineering via click reaction. Taken and adapted with permission from Ref. [89]. Copyright 2015 Springer Nature.

Li *et al.* developed a metal-free heterogeneous COF catalyst with dual linkages for bifunctional cascade catalysis.[87] In the first example of a 3D COF with dual linkages, boronic acid esters and imines, they implemented both acidic and basic sites in the framework to create a bifunctional catalyst for one-pot cascade reactions. High activity was demonstrated in the cascade of acid-catalyzed hydrolysis of an acetal, followed by base-catalyzed Michael addition of the resulting benzaldehyde with acetylacetone in high yields of 92% or more.

Xu *et al.* demonstrated the construction of a metal-free chiral covalent organic framework as a heterogeneous organocatalyst from chiral building blocks.[88] Based on a chiral pyrrolidine moiety, they were able to implement the chiral information directly into the COF backbone, resulting in materials with high crystallinity and S_{BET}. The organocatalytically active pyrrolidine moiety in the COF was successfully used in asymmetric aldol reactions, leading to high yields and enantiomeric ratios.

COFs can also be used for chiral organocatalytic platforms by pore wall engineering. Xu *et al.* reported the successful immobilization of chiral proline organocatalysts by click chemistry.[89] By partially replacing a methoxy-functionalized linker in the known TPB-DMTP-COF with an alkyne-containing linker, they are able to immobilize an azide-functionalized proline on their pore walls in a post-synthetic step (Figure 2.14). The resulting metal-free organocatalytic COF shows high activity, enantioselectivity, as well as recyclability in enantioselective Michael reactions with enantiomeric excess (ee) ratios of 90% and more.

Sun *et al.* employed sophisticated control of the pore environment in COFs to improve the performance and stability of the enzymes infiltrated into the scaffold to create heterogeneous COF-enzyme composites (Figure 2.15).[90] The practical application of enzymes in organic synthesis is often limited and hindered by their poor long-term stability and recyclability. By incorporating the enzyme lipase PS into the pores of various COFs, higher stability and robustness of the enzyme
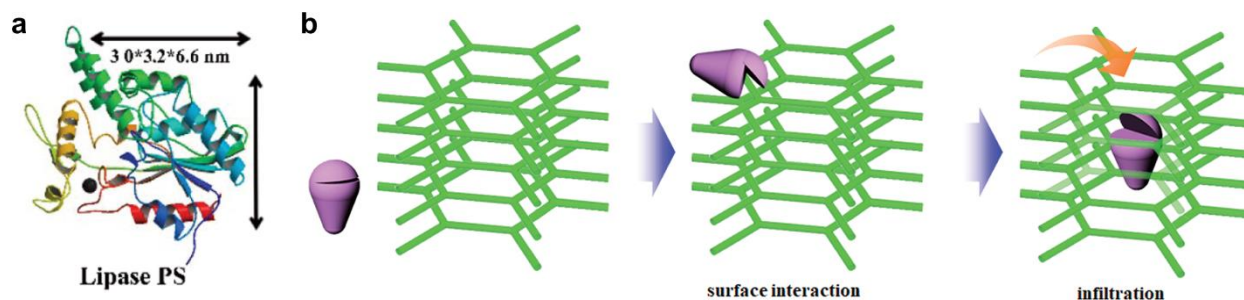
Figure 2.15. (a) Model of lipase PS. (b) Schematic representation of the translocation of the enzyme into the pore channels. Taken and adapted with permission from Ref. [90]. Copyright 2018 American Chemical Society.

as well as significantly higher activity of the biocomposite could be achieved compared to the free enzyme in activity tests. The high modularity and pore adaptability of the COFs also made it possible to control the orientation and accommodation of the enzyme in the pore channels.

Sensing

Due to their aromatic nature and delocalization of conjugated π-electrons in their layer, many COFs exhibit photoluminescence properties whose application in chemical sensing has been widely explored.[11,91] Their fluorescence or quenching of this property by adsorption or coordination of guest molecules can be targeted using the wide range of design options for COF. Great attention is paid to the detection of chemical pollutants in the aqueous phase, e.g., selective detection of dyes, metals, organic compounds, or biomolecules.[92–96]

Peng *et al.* reported the preparation of ultrathin COF nanosheets and their application for selective DNA detection.[97] An imine-linked TPA-COF was formed by choosing two unusual flexible building blocks. The flexibility leading to weakened interlayer interactions enabled exfoliation into thin 2D-COF nanosheets. These nanosheets were successfully used as a novel sensing platform for DNA, utilizing fluorescence quenching when DNA adsorbed on the sheets.

Moreover, COFs are receiving increased attention as electrochemical sensors due to their numerous intriguing properties.[91] Although there are still many unsolved problems, such as poor electrical conductivity, lack of a general synthesis strategy for films, and immobilization methods, they have emerged as promising candidates in the field.

Biosensors were demonstrated by Xu *et al.* using DHTA-TTA-COF, taking advantage of the multiple redox active states of this COF.[98] Their electrochemical studies showed that their COF-based ratiometric electrochemical sensor could determine H_2O_2 concentrations from 5.66 µM to 400 µM, as well as pH values between 11.0 and 3.0. The redox-active COF could additionally be loaded with glucose oxidase in its pores, allowing the detection of glucose in a range of 1.26 µM to 6.0 mM.

Another example of COFs as electrochemical sensors is DAAQ-TFP COF, which was used by Liang *et al.* for the simultaneous detection and removal of hydrazine.[94] By incorporating anthraquinone units as electroactive sites, an effective response to hydrazine concentrations in the ppb range and a linear detection range between 0.5 and 1223 μM were achieved. At the same time, a maximum removal capacity of up to 1108 mg g^{-1} hydrazine was measured.

Photocatalysts and photosensitizers

Due to their extended conjugate π-electron delocalization, ability to incorporate organic chromophores, and semiconducting properties, COFs have emerged as potential materials for energy conversion applications.

In 2014, Stegbauer *et al.* reported the first COF for photocatalytic hydrogen production.[20] The hydrazone-linked and triazine-containing network showed continuous hydrogen production from water under visible light irradiation (1970 μmol g^{-1} h^{-1}) after doping with nanoparticulate Pt as co-catalyst.

The important role of triazine, its influence on the electronic properties and structure of COFs leading to increased activity for hydrogen evolution, was investigated by Vyas *et al.*[99] In a series of water- and photostable 2D azine-linked COFs with different numbers of nitrogen at the junctions, it was shown that the steric variations and electronic properties of the building blocks are transferred to the final network (Figure 2.16). A reduced dihedral angle in the building blocks due to nitrogen incorporation leads to a more planar 2D COF structure and better electron delocalization in the COF layer. In addition, the nitrogen content in the COFs alters the HOMO-LUMO level and thus the band gap. The combined effects of structure and electronic properties result in a gradual increase in hydrogen evolution activity under visible light irradiation with increasing nitrogen content.

Wang *et al.* reported a sulfone-containing COF for photochemical hydrogen evolution.[100] The COF proved to be stable under long-term irradiation in the visible region and produced hydrogen
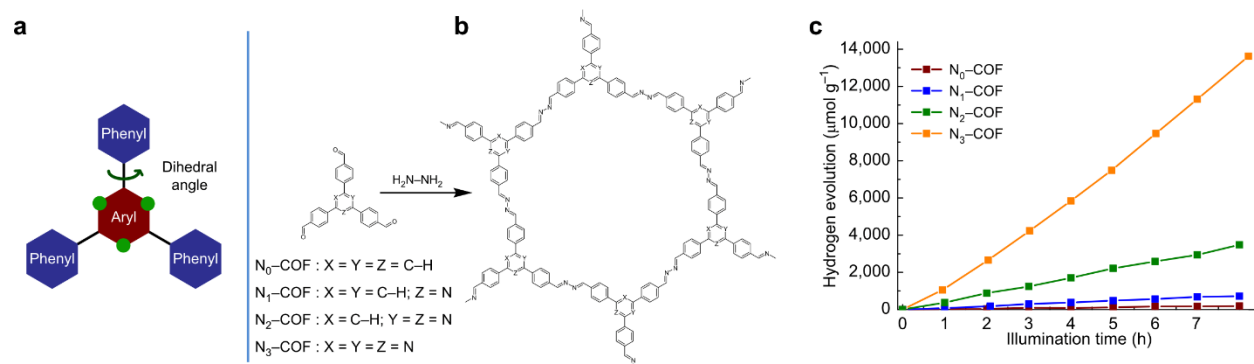
Figure 2.16. (a) The nitrogen atoms at the green dots decrease the dihedral angle between the central aryl group and the peripheral phenyls compared to C-H. (b) This increased planarity of the building block is translated into a planer 2D COF sheet that enhances the delocalization of conjugated π-electrons. (c) The electronic and structural properties of the nitrogen-enriched network lead to enhanced photocatalytic activity and hydrogen production. Taken and adapted with permission from Ref. [99]. Copyright 2015 Springer Nature.

with the rate of up to 16.3 mmol g^{-1} h^{-1} under the optimal condition. The authors attributed the excellent production rate and stability to the high quantum efficiency of the sulfone COF, its strong absorption of visible light, and its wettable, hydrophilic mesopores. The higher productivity compared to the amorphous or semi-crystalline counterpart showed the importance of the crystallinity of the framework.

Besides water splitting, photochemical reduction of CO_2 is becoming more and more relevant. Yang *et al.* reported a 2D COF with an incorporated Re-complex as an intrinsic photocatalyst for CO_2 reduction to CO under visible light irradiation.[101] The COF showed high selectivity of 98% and better activity than the homogeneous Re-complex analog. Using this system, they were able to further investigate and decipher the key intermediates during the reduction and determine the rate-limiting steps, demonstrating the usefulness of these scaffolds for studying reaction processes.

In 2019, Zhong *et al.* reported a COF for photocatalytic CO_2 reduction bearing individual Ni sites.[102] They used the chelation of bipyridine units in TPBpy-COF to immobilize the individual Ni sites and demonstrated synergistic effects in the coordination and stabilization of the individual metal sites, as well as in the activation and conversion of CO_2 to CO under visible light.

2.5. Bibliography

[1]   A. P. Côté, A. I. Benin, N. W. Ockwig, M. O'Keeffe, A. J. Matzger, O. M. Yaghi, *Science* **2005**, *310*, 1166–70.

[2]   C. S. Diercks, O. M. Yaghi, *Science* **2017**, *355*, 923.

[3]   S. Y. Ding, W. Wang, *Chem. Soc. Rev.* **2012**, *42*, 548–568.

[4]   H. C. Zhou, J. R. Long, O. M. Yaghi, *Chem. Rev.* **2012**, *112*, 673–674.

[5]   M. S. Lohse, T. Bein, *Adv. Funct. Mater.* **2018**, *28*, 1705553.

[6]   K. Geng, T. He, R. Liu, S. Dalapati, K. T. Tan, Z. Li, S. Tao, Y. Gong, Q. Jiang, D. Jiang, *Chem. Rev.* **2020**, *120*, 8814–8933.

[7]   F. Haase, B. V. Lotsch, *Chem. Soc. Rev.* **2020**, *49*, 8469–8500.

[8]   R. Freund, O. Zaremba, G. Arnauts, R. Ameloot, G. Skorupskii, M. Dincă, A. Bavykina, J. Gascon, A. Ejsmont, J. Goscianska, M. Kalmutzki, U. Lächelt, E. Ploetz, C. S. Diercks, S. Wuttke, *Angew. Chemie Int. Ed.* **2021**, *60*, 23975–24001.

[9]   S. Chen, B. Yuan, G. Liu, D. Zhang, *Front. Chem.* **2020**, *8*, 1082.

[10]   H. R. Abuzeid, A. F. M. EL-Mahdy, S. W. Kuo, *Giant* **2021**, *6*, 100054.

[11]   T. F. Machado, M. E. S. Serra, D. Murtinho, A. J. M. Valente, M. Naushad, *Polym. 2021, Vol. 13, Page 970* **2021**, *13*, 970.

[12]   O. M. Yaghi, *ACS Cent. Sci.* **2019**, *5*, 1295–1300.

[13]   F. Auras, L. Ascherl, A. H. Hakimioun, J. T. Margraf, F. C. Hanusch, S. Reuter, D. Bessinger, M. Döblinger, C. Hettstedt, K. Karaghiosoff, S. Herbert, P. Knochel, T. Clark, T. Bein, *J. Am. Chem. Soc.* **2016**, *138*, 16703–16710.

[14]   Y. B. Zhang, J. Su, H. Furukawa, Y. Yun, F. Gándara, A. Duong, X. Zou, O. M. Yaghi, *J. Am. Chem. Soc.* **2013**, *135*, 16336–16339.

[15]   Y. Peng, L. Li, C. Zhu, B. Chen, M. Zhao, Z. Zhang, Z. Lai, X. Zhang, C. Tan, Y. Han, Y. Zhu, H. Zhang, *J. Am. Chem. Soc.* **2020**, *142*, 13162–13169.

[16]   Y. Li, L. Inshuo Guo, Y. Ongkang Lv, Z. Zhao, Y. Anhang Ma, W. Chen, G. Xing, D. Jiang, L. Chen, *Angew. Chemie* **2021**, *133*, 5423–5429.

[17]   T. Banerjee, F. Haase, S. Trenker, B. P. Biswal, G. Savasci, V. Duppel, I. Moudrakovski, C. Ochsenfeld, B. V. Lotsch, *Nat. Commun. 2019 101* **2019**, *10*, 1–10.

[18]   S. Wan, J. Guo, J. Kim, H. Ihee, D. Jiang, *Angew. Chemie Int. Ed.* **2008**, *47*, 8826–8830.

[19]   F. J. Uribe-Romo, J. R. Hunt, H. Furukawa, C. Klöck, M. O'Keeffe, O. M. Yaghi, *J. Am. Chem. Soc.* **2009**, *131*, 4570–4571.

[20]   L. Stegbauer, K. Schwinghammer, B. V. Lotsch, *Chem. Sci.* **2014**, *5*, 2789–2793.

[21]   K. Gottschling, L. Stegbauer, G. Savasci, N. A. Prisco, Z. J. Berkson, C. Ochsenfeld, B. F. Chmelka, B. V. Lotsch, *Chem. Mater.* **2019**, *31*, 1946–1955.

[22]   Q. Fang, Z. Zhuang, S. Gu, R. B. Kaspar, J. Zheng, J. Wang, S. Qiu, Y. Yan, *Nat. Commun.* **2014**, *5*, 4503.

[23]   X. Zhu, S. An, Y. Liu, J. Hu, H. Liu, C. Tian, S. Dai, X. Yang, H. Wang, C. W. Abney, S. Dai, *AIChE J.* **2017**, *63*, 3470–3478.

[24]   H. Lyu, C. S. Diercks, C. Zhu, O. M. Yaghi, *J. Am. Chem. Soc.* **2019**, *141*, 6848–6852.

[25]   G. Das, D. Balaji Shinde, S. Kandambeth, B. P. Biswal, R. Banerjee, *Chem. Commun.* **2014**, *50*, 12615–12618.

[26]   R. L. Li, N. C. Flanders, A. M. Evans, W. Ji, I. Castano, L. X. Chen, N. C. Gianneschi, W. R. Dichtel, *Chem. Sci.* **2019**, *10*, 3796–3801.

[27]   J. Maschita, T. Banerjee, G. Savasci, F. Haase, C. Ochsenfeld, B. V. Lotsch, *Angew. Chemie Int. Ed.* **2020**, *59*, 15750–15758.

[28]   S. Karak, S. Kandambeth, B. P. Biswal, H. S. Sasmal, S. Kumar, P. Pachfule, R. Banerjee, *J. Am. Chem. Soc.* **2017**, *139*, 1856–1862.

[29]   A. M. Evans, L. R. Parent, N. C. Flanders, R. P. Bisbey, E. Vitaku, M. S. Kirschner, R. D. Schaller, L. X. Chen, N. C. Gianneschi, W. R. Dichtel, *Science* **2018**, *361*, 52–57.

[30]   T. Ma, E. A. Kapustin, S. X. Yin, L. Liang, Z. Zhou, J. Niu, L.-H. Li, Y. Wang, J. Su, J. Li, X. Wang, W. D. Wang, W. Wang, J. Sun, O. M. Yaghi, *Science* **2018**, *361*, 48–52.

[31]   F. Haase, K. Gottschling, L. Stegbauer, L. S. Germann, R. Gutzler, V. Duppel, V. S. Vyas, K. Kern, R. E. Dinnebier, B. V. Lotsch, *Mater. Chem. Front.* **2017**, *1*, 1354–1361.

[32]   C. H. Feriante, S. Jhulki, A. M. Evans, R. R. Dasari, K. Slicker, W. R. Dichtel, S. R. Marder, *Adv. Mater.* **2020**, *32*, 1905776.

[33]   Y. Peng, W. K. Wong, Z. Hu, Y. Cheng, D. Yuan, S. A. Khan, D. Zhao, *Chem. Mater.* **2016**, *28*, 5095–5101.

[34]   F. Haase, E. Troschke, G. Savasci, T. Banerjee, V. Duppel, S. Dörfler, M. M. J. Grundei, A. M. Burow, C. Ochsenfeld, S. Kaskel, B. V. Lotsch, *Nat. Commun.* **2018**, *9*, 1–10.

[35]   H. Xu, X. Chen, J. Gao, J. Lin, M. Addicoat, S. Irle, D. Jiang, *Chem. Commun.* **2014**, *50*, 1292–1294.

[36]   T. Sick, J. M. Rotter, S. Reuter, S. Kandambeth, N. N. Bach, M. Döblinger, J. Merz, T. Clark, T. B. Marder, T. Bein, D. D. Medina, *J. Am. Chem. Soc.* **2019**, *141*, 12570–12581.

[37]   C. Feriante, A. M. Evans, S. Jhulki, I. Castano, M. J. Strauss, S. Barlow, W. R. Dichtel, S. R. Marder, *J. Am. Chem. Soc.* **2020**, *142*, 18637–18644.

[38]   M. Calik, T. Sick, M. Dogru, M. Döblinger, S. Datz, H. Budde, A. Hartschuh, F. Auras, T. Bein, *J. Am. Chem. Soc.* **2016**, *138*, 1234–1239.

[39]   J. Ozdemir, I. Mosleh, M. Abolhassani, L. F. Greenlee, R. R. Beitle, M. H. Beyzavi, *Front. Energy Res.* **2019**, *7*, 77.

[40]   M. Matsumoto, R. R. Dasari, W. Ji, C. H. Feriante, T. C. Parker, S. R. Marder, W. R. Dichtel, *J. Am. Chem. Soc.* **2017**, *139*, 4999–5002.

[41]   F. Zhang, J. Zhang, B. Zhang, X. Tan, D. Shao, J. Shi, D. Tan, L. Liu, J. Feng, B. Han, G. Yang, L. Zheng, J. Zhang, *ChemSusChem* **2018**, *11*, 3576–3580.

[42]   D. Zhu, Z. Zhang, L. B. Alemany, Y. Li, N. Nnorom, M. Barnes, S. Khalil, M. M. Rahman, P. M. Ajayan, R. Verduzco, *Chem. Mater.* **2021**, *33*, 3394–3400.

[43]   T. Friić, *J. Mater. Chem.* **2010**, *20*, 7599–7605.

[44]   P. Baláž, M. Achimovicová, M. Baláž, P. Billik, C. Z. Zara, J. M. Criado, F. Delogu, E. Dutková, E. Gaffet, F. J. Gotor, R. Kumar, I. Mitov, T. Rojac, M. Senna, A. Streletskii, W. C. Krystyna, *Chem. Soc. Rev.* **2013**, *42*, 7571–7637.

[45]   D. Hasa, W. Jones, *Adv. Drug Deliv. Rev.* **2017**, *117*, 147–161.

[46]   B. P. Biswal, S. Chandra, S. Kandambeth, B. Lukose, T. Heine, R. Banerjee, *J. Am. Chem. Soc.* **2013**, *135*, 5328–5331.

[47]   D. B. Shinde, H. B. Aiyappa, M. Bhadra, B. P. Biswal, P. Wadge, S. Kandambeth, B. Garai, T. Kundu, S. Kurungot, R. Banerjee, *J. Mater. Chem. A* **2016**, *4*, 2682–2690.

[48]   X. Wang, R. Ma, L. Hao, Q. Wu, C. Wang, Z. Wang, *J. Chromatogr. A* **2018**, *1551*, 1–9.

[49]   Y. Tao, W. Ji, X. Ding, B. H. Han, *J. Mater. Chem. A* **2021**, *9*, 7336–7365.

[50]   B. P. Biswal, S. Chandra, S. Kandambeth, B. Lukose, T. Heine, R. Banerjee, *J. Am. Chem. Soc.* **2013**, *135*, 5328–5331.

[51]   P. Kuhn, M. Antonietti, A. Thomas, *Angew. Chemie Int. Ed.* **2008**, *47*, 3450–3453.

[52]   X. Guan, Y. Ma, H. Li, Y. Yusran, M. Xue, Q. Fang, Y. Yan, V. Valtchev, S. Qiu, *J. Am. Chem. Soc.* **2018**, *140*, 4494–4498.

[53]   J. Qiu, P. Guan, Y. Zhao, Z. Li, H. Wang, J. Wang, *Green Chem.* **2020**, *22*, 7537–7542.

[54]   S. T. Yang, J. Kim, H. Y. Cho, S. Kim, W. S. Ahn, *RSC Adv.* **2012**, *2*, 10179–10181.

[55]   W. Zhao, P. Yan, H. Yang, M. Bahri, A. M. James, H. Chen, L. Liu, B. Li, Z. Pang, R. Clowes, N. D. Browning, J. W. Ward, Y. Wu, A. I. Cooper, *Nat. Synth. 2022 11* **2022**, *1*, 87–95.

[56]   L. K. Ritchie, A. Trewin, A. Reguera-Galan, T. Hasell, A. I. Cooper, *Microporous Mesoporous Mater.* **2010**, *132*, 132–136.

[57]   M. B. Gawande, S. N. Shelke, R. Zboril, R. S. Varma, *Acc. Chem. Res.* **2014**, *47*, 1338–1348.

[58]   S. Kim, H. C. Choi, *Commun. Chem. 2019 21* **2019**, *2*, 1–8.

[59]   P. J. Waller, S. J. Lyle, T. M. Osborn Popp, C. S. Diercks, J. A. Reimer, O. M. Yaghi, *J. Am. Chem. Soc.* **2016**, *138*, 15519–15522.

[60]   P. J. Waller, Y. S. Alfaraj, C. S. Diercks, N. N. Jarenwattananon, O. M. Yaghi, *J. Am. Chem. Soc.* **2018**, *140*, 9099–9103.

[61]   K. Wang, Z. Jia, Y. Bai, X. Wang, S. E. Hodgkiss, L. Chen, S. Y. Chong, X. Wang, H. Yang, Y. Xu, F. Feng, J. W. Ward, A. I. Cooper, *J. Am. Chem. Soc.* **2020**, *142*, 11131–11138.

[62]   X. Li, C. Zhang, S. Cai, X. Lei, V. Altoe, F. Hong, J. J. Urban, J. Ciston, E. M. Chan, Y. Liu, *Nat. Commun.* **2018**, *9*, 2998.

[63]   L. Grunenberg, G. Savasci, M. W. Terban, V. Duppel, I. Moudrakovski, M. Etter, R. E. Dinnebier, C. Ochsenfeld, B. V. Lotsch, *J. Am. Chem. Soc.* **2021**, *143*, 3430–3438.

[64] W. Zhang, L. Chen, S. Dai, C. Zhao, C. Ma, L. Wei, M. Zhu, S. Y. Chong, H. Yang, L. Liu, Y. Bai, M. Yu, Y. Xu, X.-W. Zhu, Q. Zhu, S. An, R. S. Sprick, M. A. Little, X. Wu, S. Jiang, Y. Wu, Y.-B. Zhang, H. Tian, W.-H. Zhu, A. I. Cooper, *Nature* **2022**, *604*, 72–79.

[65] Y. Yusran, X. Guan, H. Li, Q. Fang, S. Qiu, *Natl. Sci. Rev.* **2020**, *7*, 170–190.

[66] S. J. Lyle, P. J. Waller, O. M. Yaghi, *Trends Chem.* **2019**, *1*, 172–184.

[67] A. Nagai, Z. Guo, X. Feng, S. Jin, X. Chen, X. Ding, D. Jiang, *Nat. Commun.* **2011**, *2*, 536.

[68] B. Dong, L. Wang, S. Zhao, R. Ge, X. Song, Y. Wang, Y. Gao, *Chem. Commun.* **2016**, *52*, 7082–7085.

[69] W. Ji, L. Xiao, Y. Ling, C. Ching, M. Matsumoto, R. P. Bisbey, D. E. Helbling, W. R. Dichtel, *J. Am. Chem. Soc.* **2018**, *140*, 12677–12681.

[70] P. Pachfule, S. Kandambeth, D. Díaz Díaz, R. Banerjee, *Chem. Commun.* **2014**, *50*, 3169–3172.

[71] H. Furukawa, O. M. Yaghi, *J. Am. Chem. Soc.* **2009**, *131*, 8875–8883.

[72] N. Huang, X. Chen, R. Krishna, D. Jiang, N. Huang, X. Chen, D. Jiang, R. Krishna, *Angew. Chemie Int. Ed.* **2015**, *54*, 2986–2990.

[73] L. Wang, L. Wang, J. Zhao, T. Yan, *J. Appl. Phys.* **2012**, *111*, 112628.

[74] H. Furukawa, O. M. Yaghi, *J. Am. Chem. Soc.* **2009**, *131*, 8875–8883.

[75] Z. Li, Y. Zhi, X. Feng, X. Ding, Y. Zou, X. Liu, Y. Mu, *Chem. – A Eur. J.* **2015**, *21*, 12079–12084.

[76] A. F. M. El-Mahdy, C. H. Kuo, A. Alshehri, C. Young, Y. Yamauchi, J. Kim, S. W. Kuo, *J. Mater. Chem. A* **2018**, *6*, 19532–19541.

[77] N. Huang, P. Wang, M. A. Addicoat, T. Heine, D. Jiang, *Angew. Chemie Int. Ed.* **2017**, *56*, 4982–4986.

[78] F. Xu, S. Yang, X. Chen, Q. Liu, H. Li, H. Wang, B. Wei, D. Jiang, *Chem. Sci.* **2019**, *10*, 6001–6006.

[79] S. H. Sang, H. Furukawa, O. M. Yaghi, W. A. Goddard, *J. Am. Chem. Soc.* **2008**, *130*, 11580–11581.

[80] C. J. Doonan, D. J. Tranchemontagne, T. G. Glover, J. R. Hunt, O. M. Yaghi, *Nat. Chem. 2010 23* **2010**, *2*, 235–238.

[81] Y. Yang, M. Faheem, L. Wang, Q. Meng, H. Sha, N. Yang, Y. Yuan, G. Zhu, *ACS Cent. Sci.* **2018**, *4*, 748–754.

[82] G. Y. Lee, J. Lee, H. T. Vo, S. Kim, H. Lee, T. Park, *Sci. Reports 2017 71* **2017**, *7*, 1–10.

[83] R. . Sheldon, R. . Downing, *Appl. Catal. A Gen.* **1999**, *189*, 163–183.

[84] D. Ma, Y. Wang, A. Liu, S. Li, C. Lu, C. Chen, *Catal. 2018, Vol. 8, Page 404* **2018**, *8*, 404.

[85] S.-Y. Ding, J. Gao, Q. Wang, Y. Zhang, W.-G. Song, C.-Y. Su, W. Wang, *J. Am. Chem. Soc.* **2011**, *133*, 19816–19822.

[86] W. Leng, Y. Peng, J. Zhang, H. Lu, X. Feng, R. Ge, B. Dong, B. Wang, X. Hu, Y. Gao, *Chem. – A Eur. J.* **2016**, *22*, 9087–9091.

[87] H. Li, Q. Pan, Y. Ma, X. Guan, M. Xue, Q. Fang, Y. Yan, V. Valtchev, S. Qiu, *J. Am. Chem. Soc.* **2016**, *138*, 14783–14788.

[88] H. Sen Xu, S. Y. Ding, W. K. An, H. Wu, W. Wang, *J. Am. Chem. Soc.* **2016**, *138*, 11489–11492.

[89] H. Xu, J. Gao, D. Jiang, *Nat. Chem. 2015 711* **2015**, *7*, 905–912.

[90] Q. Sun, C.-W. Fu, B. Aguila, J. Perman, S. Wang, H.-Y. Huang, F.-S. Xiao, S. Ma, *J. Am. Chem. Soc.* **2018**, *140*, 984–992.

[91] S. Chen, B. Yuan, G. Liu, D. Zhang, *Front. Chem.* **2020**, *8*, 1082.

[92] P. Albacete, A. López-Moreno, S. Mena-Hernando, A. E. Platero-Prats, E. M. Pérez, F. Zamora, *Chem. Commun.* **2019**, *55*, 1382–1385.

[93] Q. Gao, X. Li, G. H. Ning, K. Leng, B. Tian, C. Liu, W. Tang, H. Sen Xu, K. P. Loh, *Chem. Commun.* **2018**, *54*, 2349–2352.

[94] C. Liang, H. Lin, Q. Wang, E. Shi, S. Zhou, F. Zhang, F. Qu, G. Zhu, *J. Hazard. Mater.* **2020**, *381*, 120983.

[95] J. Dong, X. Li, S. B. Peh, Y. Di Yuan, Y. Wang, D. Ji, S. Peng, G. Liu, S. Ying, D. Yuan, J. Jiang, S. Ramakrishna, D. Zhao, *Chem. Mater.* **2019**, *31*, 146–160.

[96] W. R. Cui, C. R. Zhang, W. Jiang, R. P. Liang, J. D. Qiu, *ACS Appl. Nano Mater.* **2019**, *2*, 5342–5349.

[97] Y. Peng, Y. Huang, Y. Zhu, B. Chen, L. Wang, Z. Lai, Z. Zhang, M. Zhao, C. Tan, N. Yang, F. Shao, Y. Han, H. Zhang, *J. Am. Chem. Soc.* **2017**, *139*, 8698–8704.

[98] M. Xu, L. Wang, Y. Xie, Y. Song, L. Wang, *Sensors Actuators B Chem.* **2019**, *281*, 1009–1015.

[99] V. S. Vyas, F. Haase, L. Stegbauer, G. Savasci, F. Podjaski, C. Ochsenfeld, B. V. Lotsch, *Nat.*

Commun. **2015**, *6*, 8508.

[100] X. Wang, L. Chen, S. Y. Chong, M. A. Little, Y. Wu, W. H. Zhu, R. Clowes, Y. Yan, M. A. Zwijnenburg, R. S. Sprick, A. I. Cooper, *Nat. Chem.* **2018**, *10*, 1180–1189.

[101] S. Yang, W. Hu, X. Zhang, P. He, B. Pattengale, C. Liu, M. Cendejas, I. Hermans, X. Zhang, J. Zhang, J. Huang, *J. Am. Chem. Soc.* **2018**, *140*, 14614–14618.

[102] W. Zhong, R. Sa, L. Li, Y. He, L. Li, J. Bi, Z. Zhuang, Y. Yu, Z. Zou, *J. Am. Chem. Soc.* **2019**, *141*, 7615–7621.

3. Research Objective

Thanks to their large specific surface area and tunability, COFs have been successfully used as heterogeneous catalysts and supports, as shown by the numerous publications on this promising application. However, despite the large variety of COFs for heterogeneous catalysis, there are no studies on the specific influence of COF pore confinement effect on thermal catalysis with immobilized single-site molecular catalysts. The fabrication and development of a suitable isoreticular COF platform that meets the numerous requirements remains a major challenge. Combining (i) high crystallinity and (ii) porosity with precisely tunable pores that are beyond the "comfortable" COF pore size of 2-4 nm, while providing (iii) accessible anchoring sites for catalyst immobilization and (iv) sufficient stability for reaction conditions, presents a platform design challenge that involves a multitude of issues. In addition, an appropriate thermal catalysis and a catalyst to study pore confinement effects must be employed. Furthermore, new strategies to overcome the current scaling limitations of classical synthesis need to be considered to provide adequate amounts of material for academic purposes up to industrial scales, as well as novel post-synthesis modification techniques to further diversify such a platform. The scope of the thesis is to develop an isoreticular COF platform to investigate pore confinement effects and explore alternative synthesis routes for COFs as well as post-modification strategies.

First, an isoreticular series of COFs with large and tunable pore sizes is developed to serve as a basic framework for the study of molecular heterogeneous catalysis under COF pore confinement (Chapter 4). Based on phenylphenanthridine-aldehyde C2 building blocks, this series should be modifiable by its protruding phenyl group to provide further points of attachment for the molecular catalysts. In combination with C3-amine building blocks of different sizes, the desired isoreticular series of 2D-imine COFs with hexagonal pores can be generated. To obtain this series, the influence of interlayer interactions on stacking and thermal stability in large 2D COFs is investigated to derive pore size trend with increasing building block length and develop a general design tool for rarely studied large-pore COFs.

Once the COF backbone is designed, the next step is to introduce anchoring sites on the COF pore wall for a suitable molecular catalyst to test the effect of confinement on α,ω-diene ring closure metathesis reactions (Chapter 5). Modification of the phenylphenanthridine building block with hydroxyl groups allows the attachment of the trimethoxy(alkyl)silane modified catalyst via a mild silylation reaction and provides a molecularly precise heterogeneous metathesis catalyst. In this biomimetic approach, the reaction should lead to an increase in the desired selectivity of macro(mono)cyclization (MMC) over oligomerization (O) by spatially confining a Grubbs-Hoveyda type catalyst and shifting the ring chain equilibrium during catalysis. The study of substrates of different sizes and their MMC/O selectivity provides important insights into the confinement effect and interactions between scaffold, catalyst, and reactant.

In addition, the mechanosynthesis through liquid-assisted grinding (LAG) is explored for COF synthesis, which enables an environmentally friendly process and scalable COF products. The fundamentals of the synthesis are investigated to understand the mechanism of crystallite formation (Chapter 6). While successful formation of COFs during milling has been demonstrated to date, little is known about the reaction mechanism involved. By investigating the chemical and structural formation of COFs using *in situ* XRPD and Raman monitoring, important insights into the mechanism can be gained to further improve the previously lacking quality of mechanosynthesized COFs, expand the scope to novel COF systems, and pave the way for controlled scaling of the reaction.

Finally, the adsorption of nitric oxide on covalent organic frameworks is investigated as a novel and alternative application (Chapter 7). COFs are often investigated for gas storage and separation applications due to their high specific surface area. While current research focuses on hydrogen or carbon dioxide, they are rarely considered for more chemically reactive gas species such as ammonia or sulfur dioxide, and there are no literature reports on the adsorption of nitrogen oxides on COFs. We investigate the effect of nitric oxide and its adsorption behavior on different scaffolds with different linkages. Targeted ^{15}N isotope enrichment for enhanced NMR sensitivity at the most sensitive sites of the materials is used to decipher the reactions involved.
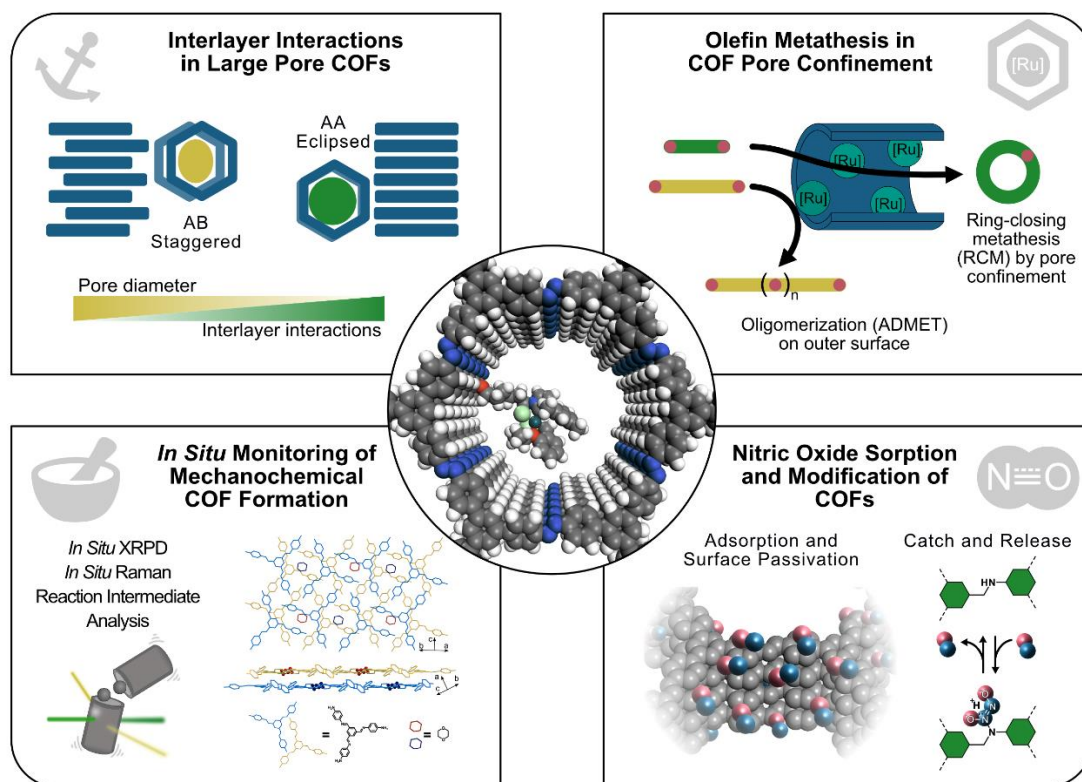
Figure 3.1. Development of a COF platform to study molecular heterogeneous catalysis under confinement. The goal is addressed by studying isoreticular large pore scaffolds (top, left) and confined olefin metathesis using this scaffolds (top, right). Furthermore, green mechanosynthesis of COFs is investigated (bottom, left) and alternative applications and further modifications of the scaffolds are explored (bottom, right).

4. Interlayer Interactions as Design Tool for Large-Pore COFs

The work in this chapter was published, reproduced, and adapted from:

Supporting information can be found in Chapter 9.1.

Abstract

Covalent organic frameworks (COFs) with a pore size beyond 5 nm are still rarely seen in this emerging field. Besides obvious complications like the elaborated synthesis of large linkers with sufficient solubility, more subtle challenges regarding large-pore COF synthesis, including pore occlusion and collapse, prevail. Here we present two isoreticular series of large-pore imine COFs with pore sizes up to 5.8 nm and correlate the interlayer interactions with the structure and thermal behavior of the COFs. By adjusting interlayer interactions through the incorporation of methoxy groups acting as pore-directing "anchors", different stacking modes can be accessed, resulting in modified stacking polytypes and, hence, effective pore sizes. A strong correlation between stacking energy towards highly ordered, nearly-eclipsed structures, higher structural integrity during thermal stress, and a novel, thermally induced phase transition of stacking modes in COFs was found, which
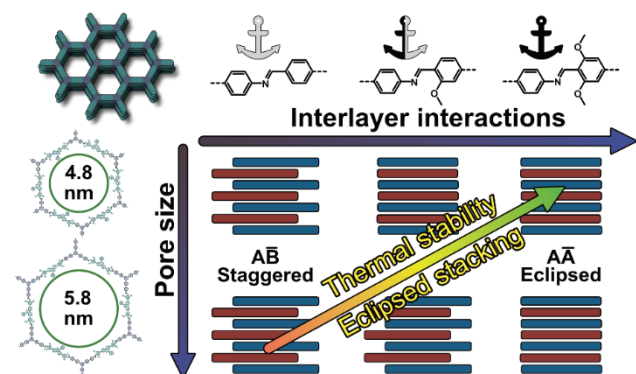
Figure 4.1. Table of content figure for the influence of interlayer interactions in large-pore COFs on thermal stability and stacking mode.

sheds light on viable design strategies for increased structural control and stability in large-pore COFs.

4.1. Introduction

Covalent organic frameworks (COFs) are highly stable, permanently porous and crystalline materials assembled from organic building blocks to form defined periodic networks.[1] Due to their structural and chemical diversity, COFs have been attracting great interest for various applications such as catalysis,[2–5] gas separation and storage,[6–8] water harvesting,[9,10] energy storage,[11–13] and chemical sensing.[14–16] To design and optimize COFs for applications, materials with high crystallinity and accessible surface areas, as well as chemical and thermal stability are targeted.[17] In particular, well-defined structures with accessible docking sites and large pore sizes become increasingly important to tailor COFs for distinct applications. While micro- and small mesoporous COFs are widespread today, large-pore COFs with pore diameters exceeding 5 nm are still rare.[18–23] With a large open pore structure, such COFs could host bulky guest molecules such as biomolecules,[24–26] or allow sufficient diffusion of substrates and products in heterogeneous catalysis, making them ideal candidates to further widen the scope of applications for COFs.

In 2014, Fang *et al.*[20] designed the first polyimide-based COF with a pore size exceeding 5.0 nm, which could absorb the large dye molecule rhodamine B in its channels. Recently Zhao *et al.*[23] synthesized an ester-linked COF spanning 10 phenylene units at one edge. While the polyimide COF crystallizes - as all other examples known to date - in a slipped configuration, slightly reducing the apparent pore size, the ester-linked COF showed a significantly smaller pore size in dry conditions than anticipated. However, low crystallinity due to the high flexibility of the structure precluded a definite structure analysis. Controlling the synthesis and structure of large-pore COFs to maximize their pore size seems to impose unique problems compared to COFs with smaller pores. Besides synthetic challenges like reduced linker solubility with increasing length, the observed effect of layer slipping and potential pore collapse upon removal of guests[27] have to be considered. For mesoporous systems like COFs, large interfacial energies are expected due to their high surface areas, leading to a natural tendency to minimize their free energy by the closure of the energetically unfavorable pores.[28,29] For COFs this tendency could be a lateral slipping of the layers to decrease pore size and surface area, or ultimately a pore collapse, while both are counterbalanced by the strong interlayer stacking interactions and rigid linkers, keeping the porous structure intact. The so far generally observed slipping of layers within large-pore COFs may be the result of an imbalance between increasing pore aperture and relatively larger free volume, while the same "wall-thickness" and therefore similar interlayer interactions are maintained. The
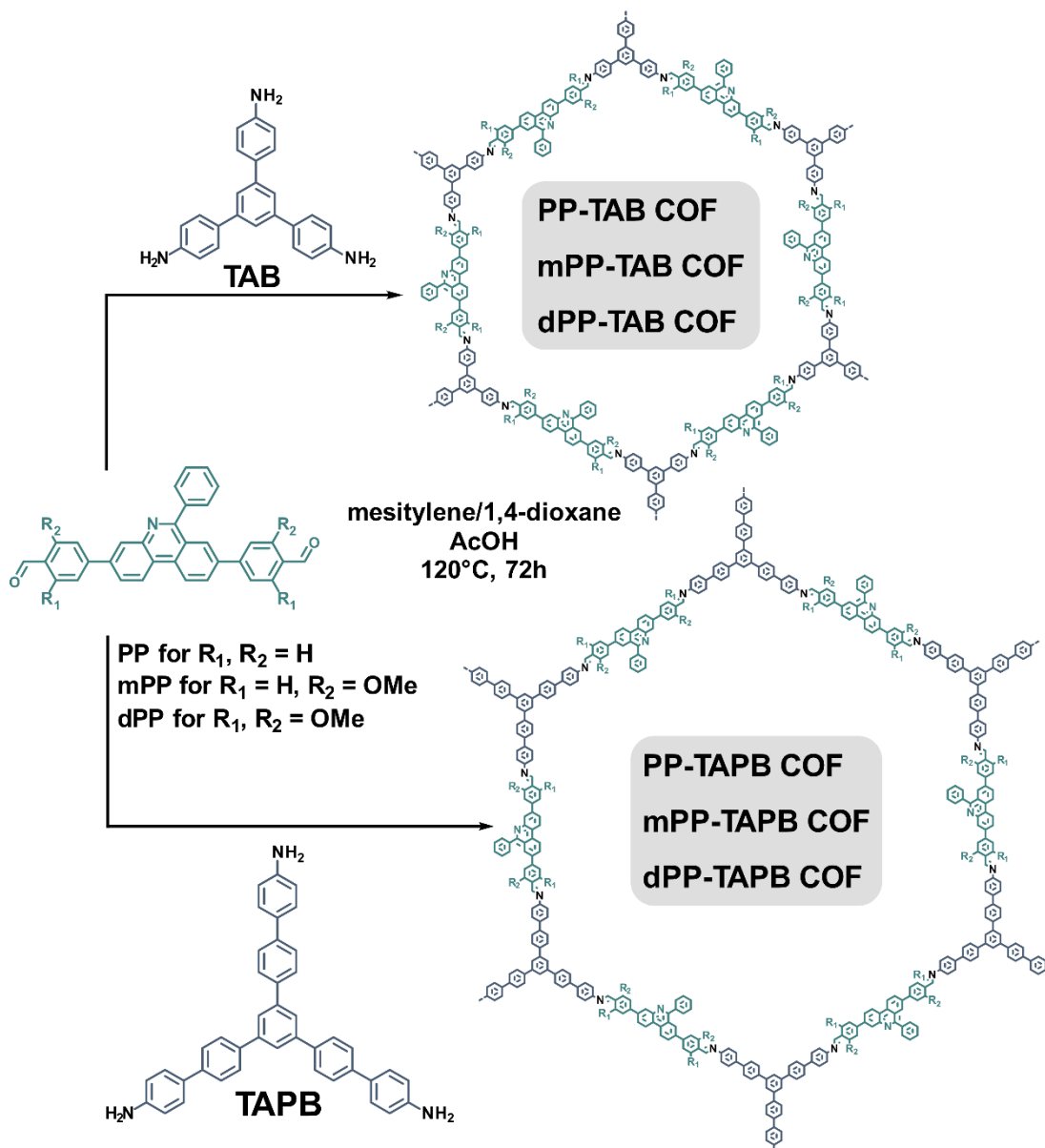
Scheme 4.1. Synthesis of PP-TAB, mPP-TAB, dPP-TAB, PP-TAPB, mPP-TAPB, and dPP-TAPB COFs to obtain a set of six isoreticular COFs with varying pore sizes and interlayer interactions.

total free energy of the system may then become unfavorable and the system is forced to minimize its free energy by pore collapse or layer slipping instead of maintaining nearly eclipsed structures. We thus hypothesize that increasing the interlayer interactions might help to anchor the layers in nearly eclipsed stacking modes and prevent slipping or even pore collapse. Considering these observations, an in-depth understanding of the factors affecting pore structure and structural stability is necessary to successfully obtain large-pore COFs without sacrificing crystallinity and porosity.

In recent years a great deal of attention has been devoted to the task to increase crystallinity and surface area of COFs, e.g., by modulating reversibility during the formation process, or facilitating

beneficial stacking interactions, both of which can be instrumental in the design of large-pore COFs.[30–32] In addition, an increasing repertoire of new linkages or post-modification of linkages was developed to extend the portfolio of synthetic tools to create chemically stable networks that withstand harsh chemical conditions.[23,33–36] However, in terms of thermal stability Evans *et al.*[37,38] recently showed that TGA analysis is not sufficient to assess thermal stability of the frameworks. They found that the structural integrity and crystallinity of the networks could be compromised by buckling of the layers under thermal stress at significantly lower temperatures than the TGA measurements suggest. Given the high flexibility of larger COF structures,[23] thermal stress can have an even bigger impact on their structural integrity.

Herein, we reveal the structure-directing influence of interlayer interactions in two isoreticular series of 2D large-pore COFs. We pay specific attention to the effect of interlayer interactions on structure and pore size and investigate the structural integrity of large-pore COFs under thermal stress. Methoxy groups are introduced into the COF structures in meta position to the imine bond to alter and modulate the interlayer interactions by reducing the inherent dipole moment of the imine linkage[39] and by adding favorable interlayer hydrogen bonding.[40] By varying the amount of methoxy functionalization and the pore size, a series of six isoreticular, hexagonal COFs with a maximum pore size of 5.8 nm are prepared. Recursive X-ray powder diffraction (XRPD) simulations and refinements, sorption analysis and density functional theory (DFT) calculations show that increasing the pore size leads to a tendency towards staggered layer arrangements, which can be reverted into eclipsed arrangements by increasing the stacking interaction and anchoring the layers in nearly eclipsed stacking. *In situ* XRPD and correlating *ex situ* sorption analysis establish a close connection between interlayer interactions and thermal stability and reveal a novel thermally induced phase transition from eclipsed to staggered conformation at temperatures as low as 120 °C. Our observations demonstrate that modulating interlayer interactions is a viable tool to influence COF stacking and maximize thermal stability and pore sizes in large pore COF systems.

4.2. Results and Discussion

Synthesis and Structural Analysis of Phenylphenanthridine COFs

To study the influence of interlayer interactions on the structure, crystallinity, porosity and thermal stability of large-pore COFs, we selected three phenylphenanthridine based building blocks, 4,4'-(6-phenylphenanthridine-3,8-diyl)dibenzaldehyde (PP), 4,4'-(6-phenylphenanthridine-3,8-diyl)bis(2-methoxybenz-aldehyde) (mPP) and 4,4'-(6-phenylphenanthridine-3,8-diyl)bis(2,6-di-methoxybenzaldeyde) (dPP), in combination with 5'-(4-aminophenyl)-[1,1':3',1''-terphenyl]-4,4''-diamine (TAB) or 1,3,5-tris[4-amino(1,1-biphenyl-4-yl)]benzene (TAPB). By the combination of these building blocks, six isoreticular COFs, PP-TAB, mPP-TAB, dPP-TAB, PP-TAPB, mPP-TAPB, and dPP-TAPB, with varying amounts of methoxy groups - zero to two regarding each
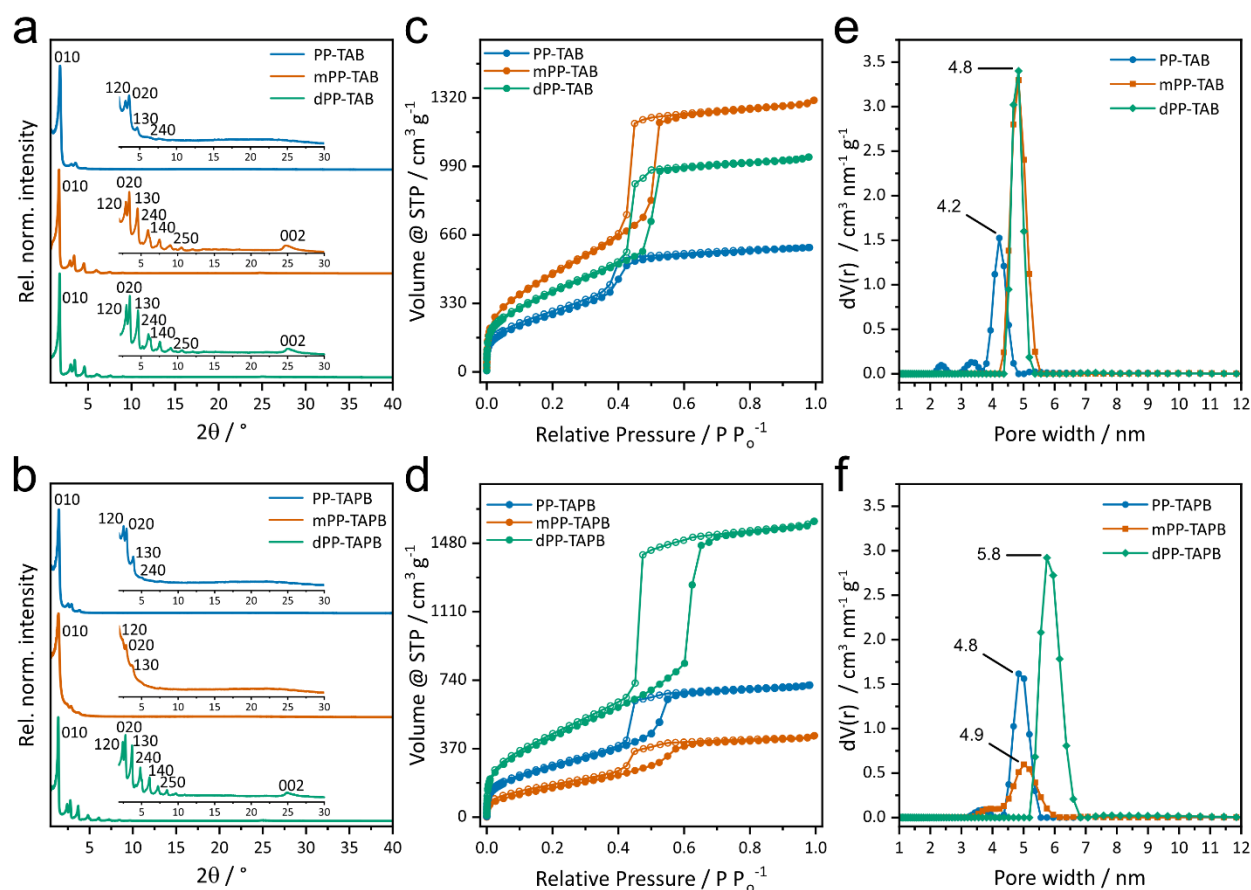
Figure 4.2. XRPD patterns (Cu-K$_{\alpha 1}$) (a, b), nitrogen sorption isotherms at 77 K (c, d) and calculated pore size distributions (e, f) of PP-TAB, mPP-TAB, dPP-TAB, PP-TAPB, mPP-TAPB, and dPP-TAPB COF.

imine bond - and differing pore sizes were obtained (Scheme 4.1). The descriptors "m" and "d" denote mono- and di-methoxy-functionalized linear linkers.

The successful conversion of the building blocks into imine-linked COFs was established by Fourier transform infrared analysis (FT-IR), ^{13}C cross-polarization magic angle spinning (CP-MAS) NMR spectroscopy, nitrogen sorption analysis at 77 K and XRPD. FT-IR reveals the full consumption of starting materials by the disappearance of typical amine and aldehyde stretching bands at around 3300 cm^{-1} and 1670 cm^{-1}, respectively. Further, the appearance of a new imine-stretching band around 1620 cm^{-1} confirms the successful formation of imine-linkages for all six COFs (Figure S9.1.1-6). ^{13}C CP-MAS NMR spectra show the typical imine signal at around 160 ppm and reveal that no residual aldehydes are left for all six COFs (Figure S9.1.33). The signals of PP-TAB, PP-TAPB, and mPP-TAPB display significant broadening and overlapping, indicating higher disorder, compared to the spectra of mPP-TAB, dPP-TAB, and dPP-TAPB, which show sharper and more defined signals.
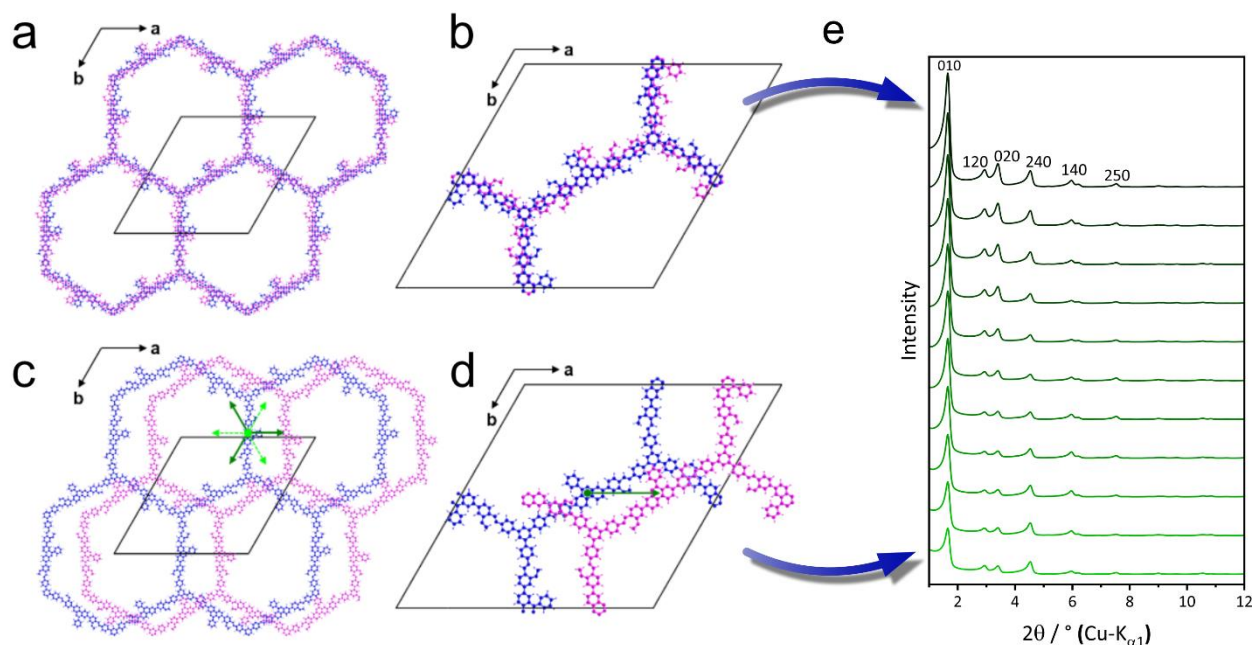
Figure 4.3. Possible stacking orders in mPP-TAB, (a) overview and (b) detailed view of a nearly eclipsed stacking of A-(magenta) and Ā-type stacked layers, (c) overview and (d) detailed view of a staggered stacking of A- (magenta) and B̄-type stacked layers. The possible stacking vectors for a staggered stacking are indicated by green and light green arrows. The constitution of the Ā-type layer is identical to the A-type layer, but the Ā-type layer is flipped vertically by 180° around the 110 vector axis. (e) Corresponding simulated XRPD patterns of mPP-TAB on moving from an eclipsed (top) to a staggered (bottom) conformation. Note the decreasing intensity of the reflections

Structure Analysis

XRPD measurements show that all six COFs of the series are highly crystalline (Figure 4.2, a and b). However, it is noteworthy that mPP-TAB and dPP-TAB of the smaller isoreticular series as well as dPP-TAPB of the larger isoreticular series display a seemingly higher crystallinity, supported by the large number of reflections in the XRPD patterns of up to 13, which is unusual for COFs. In comparison, the other COFs show less reflections, and especially in the case of mPP-TAPB, substantial peak broadening is observed. In addition, a distinct 00l stacking reflection is absent for the latter ones. These noticeable differences in the apparent crystallinity in the isoreticular series can be attributed to inherent differences in stacking order between these COFs. The stacking orders can generally be described as an alternating AĀ-type stacking, where the A- (Figure 4.3, a, b, blue) and Ā-type layers (Figure 4.3, a, b, magenta) exhibit identical constitution but the Ā-type layer is flipped vertically by 180° around the 110 vector axis with respect to the A-type layer (Figure 4.3, b). These layers can either occupy an almost eclipsed AĀ-type stacking, with a slight random stacking disorder,[41] or a staggered AB̄-type stacking, where layer B̄ is shifted by a certain stacking vector, indicated by green and light green arrows in Figure 4.3 c and d.

To gain further insights into the different effects of structure and stacking for this isoreticular set of COFs, we performed systematic DIFFaX like simulations of the XRPD patterns[42,43] for mPP-TAB as an exemplary COF, using different stacking and faulting scenarios (Figure 4.3, e and

S9.1.13). This simulation shows the transition of a nearly eclipsed A$\overline{\text{A}}$-type structure into an ordered, staggered A$\overline{\text{B}}$-type stacking as the most likely scenario. The shift within the ab-plane by applying the stacking vector was incrementally increased to 12 Å. This leads to a decrease of the peak intensities of the 010, $\overline{1}$20, 020 and $\overline{1}$30 reflections, as observed in the measured pattern with low apparent crystallinity. To evaluate this proposed structure model, we performed Rietveld refinements on the collected powder patterns. The layers were modelled as flat layers without any torsions as including this would have led to an overextension of the parameter space. Symmetry adapted spherical harmonics were applied to the peak widths in order to compensate the peak broadening caused by intra- and interlayer disorder. The refinement of the XRPD patterns collected for mPP-TAB, dPP-TAB, and dPP-TAPB (Figure S9.1.9, S9.1.11, and S9.1.12, respectively) with the nearly eclipsed A$\overline{\text{A}}$-type stacked model led to a good fit of the measured XRPD pattern and to a satisfying agreement factor (R_{wp} = 4.58 %, 3.83 %, and 3.73 %, respectively). For PP-TAB, PP-TAPB, and mPP-TAPB (Figure S9.1.7, S9.1.8, and S9.1.10, respectively), which exhibit a staggered A$\overline{\text{B}}$-type stacking, a 12 layer-supercell had to be used for refinement to ensure a satisfying fit (R_{wp} = 1.44 %, 2.23 %, and 2.56 %, respectively). Within the refined supercell all layers show a staggered arrangement with a stacking vector of around 12 Å. The results, summarized in Table 4.1, also show reduced a and b lattice parameters of the COFs in staggered stacking compared to the isoreticular, eclipsed COFs, which indicates additional distortion by layer buckling and twisting, introduced by the additional degrees of freedom in the staggered arrangement.

Table 4.1. Comparison of crystal structure features and pore size distribution of investigated COFs.

COF	a and b / Å	stacking type	layer buckling	S_{BET} / $m^2 g^{-1}$	pore size / nm
PP-TAB	56.62(9)	staggered A$\overline{\text{B}}$	yes	1063	4.2
mPP-TAB	58.83(4)	nearly eclipsed A$\overline{\text{A}}$	no	1823	4.8
dPP-TAB	58.49(7)	nearly eclipsed A$\overline{\text{A}}$	no	1467	4.8
PP-TAPB	69.29(6)	staggered A$\overline{\text{B}}$	yes	1032	4.8
mPP-TAPB	69.97(4)	staggered A$\overline{\text{B}}$	yes	631	4.9
dPP-TAPB	73.17(6)	nearly eclipsed A$\overline{\text{A}}$	no	1670	5.8

All patterns were refined in P1 symmetry, due to stacking faults present. Lattice parameters were constrained to pseudo hexagonal values, a = b, α = β = 90 ° and γ = 120 °C.

Scanning electron microscopy (SEM) and transmission electron microscopy (TEM) imaging was performed for all samples to gain further insights into the morphology of the COF particles (Figure S9.1.56-67). SEM images shows a cauliflower-like morphology for A$\overline{\text{B}}$-type stacked PP-TAB, PP-TAPB, and mPP-TAPB due to intergrown, curved sheets forming smooth spheres. A$\overline{\text{A}}$-Type stacked mPP-TAB, dPP-TAB, and dPP-TAPB show a comparatively rugged morphology exposing crystal facets, which points to the growth of ordered, plate-like crystallites. TEM images show

high crystallinity for all samples, with domain sizes ranging from 20 to 300 nm. The domains seem to be generally larger for A$\overline{A}$-type stacked mPP-TAB, dPP-TAB, and dPP-TAPB COFs. This can be rationalized by their increased stacking interactions favoring larger domains.

Computational Structure Investigations

To gain additional insights into the structural arrangement of the nearly eclipsed COFs, we performed a computational study to acquire an in-depth understanding of the stacking of phenylphenanthridine units, the role of the methoxy groups, and the imine configurations. We first analyzed the interaction of two isolated molecular building units. We performed DFT calculations using TURBOMOLE[44] on the PBE-D3/def2-TZVPP-level[45–47] and geometry optimizations using the DL-find[48] interfaced via CHEMSHELL[49] for the combination of molecules as well as for their isolated counterparts (details see ESI S10). In a second step, we investigated different arrangements of building units by constructing cut-out blocks of the COF structure to model single pore walls (Figure 4.4, a). All our solid-state density functional calculations were performed using the quick step (QS) gaussian and plane waves (GPW) approach as implemented in CP2K[50] with periodic boundary conditions, the PBE-D3[46,47] functional with GTH-pseudopotentials[51] and a TZV2P-GTH[52] basis set. For the structures that we identified as the most promising, we then performed a complete unit-cell treatment, leading to an optimal arrangement of these large-pore COFs (Figure 4.4, c).

To investigate the stacking behavior of the phenylphenanthridine units, all four possible stacking variants (Scheme S5) were initially optimized on a non-periodic molecular level (Table S9.1.4). Further optimization in a periodic combination of blocks modeled the restricted in-plane movement of a multilayer COF pore wall. The results of the non-periodic model and the comparison of relative energies of isolated components of the COF pore wall simulation (Table S9.1.9) find the s10 variant to be the optimal stacking configuration of the phenylphenanthridine units. Assuming a rotation of the protruding phenyl groups, parallel-displaced or T-stacked configurations (Figure 4.4, b), which are both commonly found as stacking motifs in proteins,[53,54] are possible and, due to their similar energies, likely to coexist in the structure. For judging the influence of methoxy groups on the imine linkage stacking and orientation, we again initially optimized a non-periodic model to gain insight into the overall properties stemming from the components. The in-vacuo analysis suggests the alternating arrangement of imine linkers as most probable (Table S9.1.5, Figure S9.1.46).

To gain insight in the underlying electrostatic interactions, molecular electrostatic potential maps were calculated for all isolated components. These maps explain the alternating arrangement by the possibility to arrange differently charged areas in a more favorable manner to minimize repulsion (Figure S9.1.48). We could also observe that the difference in interaction energy between the two orientations is reduced by added methoxy groups. Furthermore, we performed calculations with periodic combinations of blocks to model a multilayer COF pore wall. The interaction

Parallel displaced   T-shape
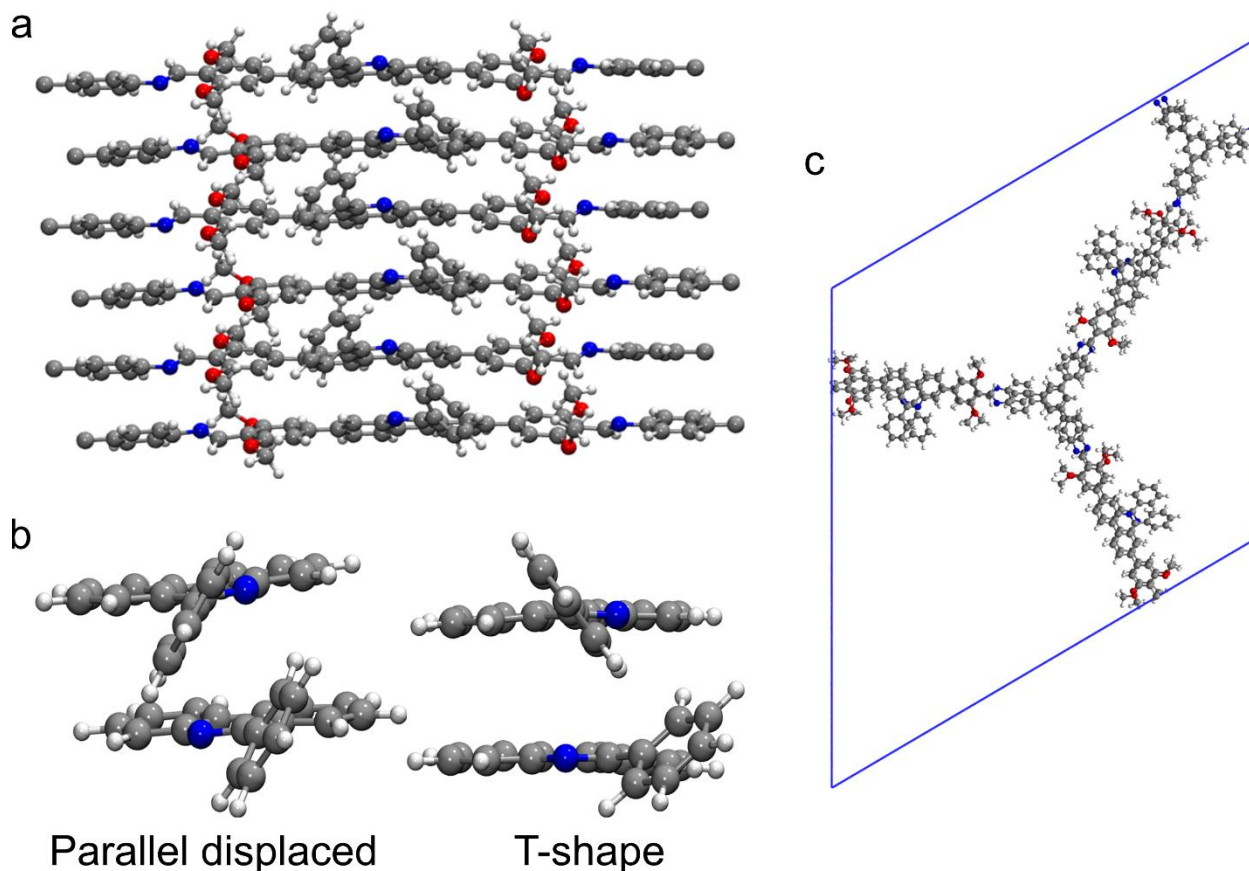
Figure 4.4. (a) Exemplary periodic combinations of blocks modeling a multilayer dPP-TAB COF pore wall. (b) Parallel-displaced and T-shape stacking arrangement of phenylphenanthridine units. (c) Final unit cell of dPP-TAB after geometry optimization with GPW-DFT.

energies show, in analogy to the isolated model, alternatingly oriented imine groups to be energetically favorable as they minimize repulsion between the layers (Figure S9.1.49). However, for the periodic case that restricts the molecules in their in-plane movement, the difference between alternating and parallel orientations is smaller (ΔE = -12.7 kcal/mol) and becomes even smaller when methoxy groups are added to the linking site (ΔE = -1.13 kcal/mol). This structural effect results from the reduction of the inherent dipole moment of the imine linker by the adjacent methoxy groups,[39] which "softens" the repulsion between the imine groups, especially in a parallel orientation. This is seen in both models and in the periodic simulation of multilayer COF pore walls, taking different phenylphenanthridine orientations into account (Figure S9.1.50 and Table S9.1.6-8). Furthermore, we observed that structures with the phenylphenanthridine oriented on different sides become significantly less favorable when methoxy groups are added (Table S9.1.7), which is not observed in the methoxy-free case (lowest ΔE = 13.01 kcal/mol). As a result, the number of possible orientations can be expected to be halved in the methoxy case, which indicates an increase in structural order. In building blocks with only one methoxy group we found that same-side, parallel-oriented methoxy groups, as those shown in Figure S9.1.51, are always energetically favorable compared to alternatingly oriented ones (Table S9.1.8). We conclude that

the methoxy groups add stability due to their steric interactions with each other, which is in most cases also indicated by their apparent out-of-plane orientation (Figure S9.1.49).

This behavior was further studied by a complete unit cell treatment of the dPP-TAB COF. Taking into account the influence of the dispersion interactions, we performed cell optimizations of the whole unit cell for methoxy groups ordered in parallel and antiparallel arrangements (Table S9.1.10-12). It was observed that systematic out-of-plane orientations of the methoxy groups are energetically favorable for every utilized method but even more so the systematic parallel arrangement of the groups (Table S9.1.14 and Figure S9.1.53). With these results on the configuration the complete unit cell of eclipsed stacked dPP-TAB and PP-TAB with parallel and alternating imine linkers, as well as s10 and s11 phenylphenanthridine units, was optimized using the periodic GFN-xTB implementation in CP2K for a broad analysis as well as GPW-DFT calculations for the most probable structures (Table S9.1.13).

For dPP-TAB, the obtained values for the lattice parameters ($a = b = 58.198$ Å, $c = 7.25$ Å for alternating imines and s10, unit cell displayed in Figure 4.4, c) are in good agreement with the ones refined from the powder patterns. Calculating PP-TAB as a nearly eclipsed structure results in strikingly similar values for lattice parameters as dPP-TAB (Table S9.1.13). These differ by almost 2 Å to the smaller lattice parameters found experimentally, probably due to a lack of buckling of the structure in the DFT calculations. However, if the eclipsed stacking is abandoned by shifting layers towards the actually staggered $A\bar{B}$-stacking, increased buckling is observed (Figure S9.1.55), and the lattice parameters a and b are reduced to 56.709 Å, matching the values found experimentally.

Porosity Investigations

The porosity and Brunauer–Emmett–Teller surface area (S_{BET}) of the COFs were characterized by measuring nitrogen sorption isotherms at 77 K to further confirm our structural models via their pore sizes. S_{BET} of all the COFs was determined in a suitable pressure region ($P/P_0 = 0.1$-0.3) and pore size distributions (PSDs) were calculated from the adsorption branch by quenched solid density functional theory (QSDFT) based on the carbon model for cylindrical pores and are summarized in Table 4.1.[55,56] All isoreticular COFs are porous with typical type IV isotherms[57] and show, except for PP-TAB, a distinct hysteresis (Figure 4.2, c and d). The calculated S_{BET} for the COFs show a spread ranging from moderately porous (631 m^2 g^{-1} for mPP-TAPB) to highly porous (1823 m^2 g^{-1} for mPP-TAB). The COFs crystallizing in a staggered conformation show overall significantly lower S_{BET} values compared to the nearly eclipsed staggered COFs. This can be rationalized by an increase in porosity by both well-defined layer stacking[32] and a decrease in effective pore size through the staggered arrangement.

a

b
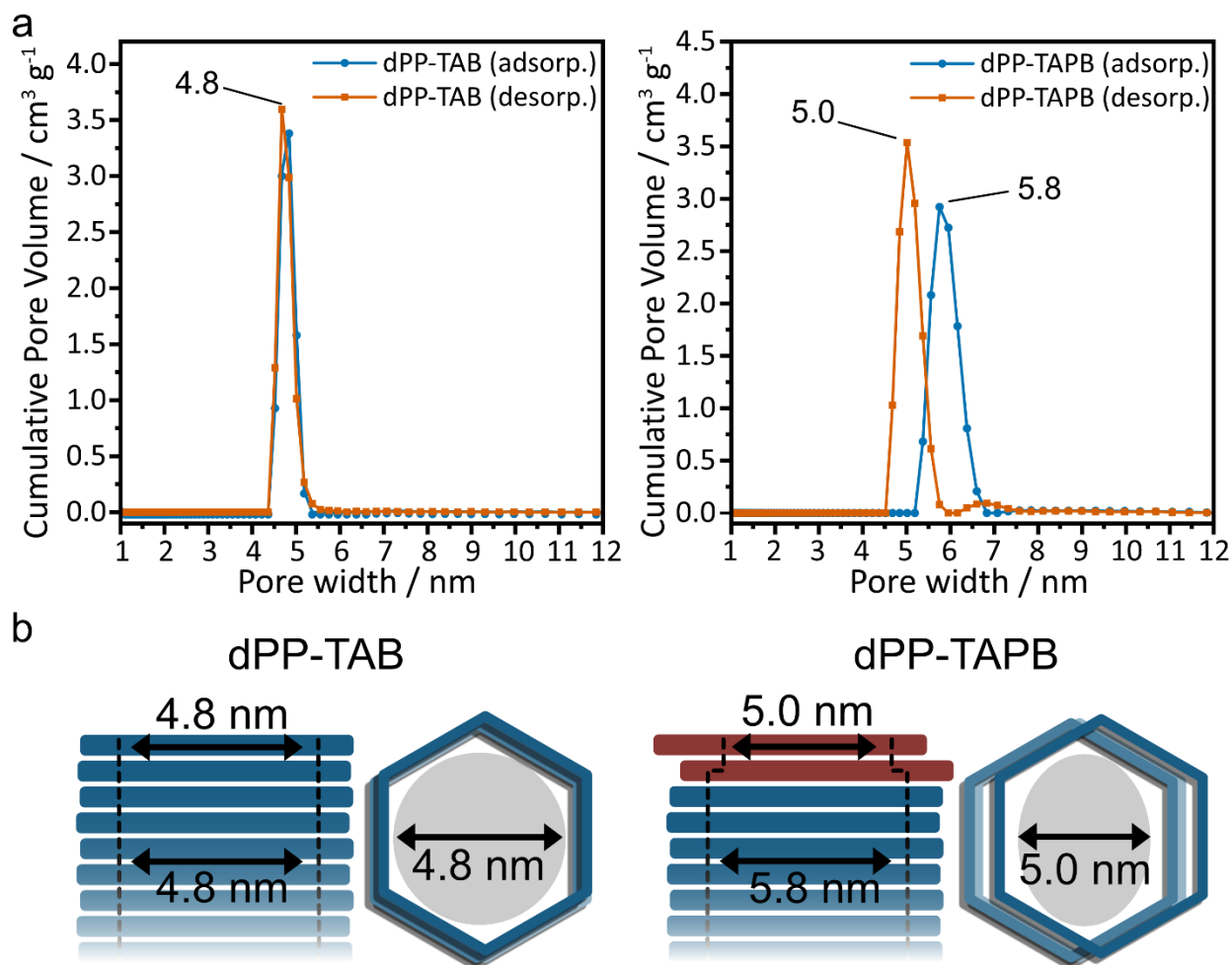
Figure 4.5. (a) Calculated PSDs of dPP-TAB (left) and dPP-TAPB (right) for the adsorption and desorption branches, calculated with quenched solid density functional theory (QSDFT) based on the carbon model for cylindrical pores.[55,56] (b) Schematic representation of neck-less open pore system of dPP-TAB (left) and occurrence of pore neck by an offset of the outer layers for dPP-TAPB.

Calculated PSDs show a pore size of 4.8 nm for methoxy-containing mPP-TAB and dPP-TAB of the smaller set of isoreticular COFs (Figure 4.2, e). This finding is in good agreement with our structure model assuming a nearly eclipsed $A\overline{A}$-type stacking. However, the remaining, methoxy-free COF of this set, PP-TAB, shows a smaller pore size of 4.2 nm, corresponding to a reduced pore size, in line with our structure model of a staggered $A\overline{B}$-type stacking. In the series of larger isoreticular COFs, dPP-TAPB shows a large pore size of 5.8 nm, while for PP-TAPB and mPP-TAPB a smaller pore size of 4.8 nm and 4.9 nm is found, respectively (Figure 4.2, f). Also in this series, the observed pore sizes correspond well with our structure models of a nearly eclipsed $A\overline{A}$-type stacking for dPP-TAPB and a staggered $A\overline{B}$-type stacking for PP-TAPB and mPP-TAPB.

For that, we crosschecked the obtained experimental results and our interpretation by using an additional geometric pore analysis. Here we determined the pore diameter by calculating the biggest sphere able to fit through the spanned pore arrangement, by constructing a pore system

using the experimentally obtained structures for both COF systems using the PP- and dPP-COFs, respectively (details see ESI S9). The obtained results summarized in Table S9.1.3 perfectly follow the trend of the obtained values from the adsorption measurements showing the increase in pore size from 4.05 nm for PP-TAB to 5.90 nm for dPP-TAPB and, thus, further support our interpretation of favored stacking motifs.

Overall, the structure refinements and the observed PSDs as well as the complementary calculations regarding the stacking interactions between the layers confirm the existence of significantly different stacking behaviors for the isoreticular, large-pore COF series. A clear trend between favorable interlayer interactions and increasing pore size due to specific stacking behavior of the COFs is evident. While PP based COFs with the least favorable stacking interactions prefer a staggered A$\overline{\text{B}}$-type stacking motif, resulting in reduced permanent pore size, the dPP based COFs, experiencing the most favorable stacking interactions through the methoxy "anchors", crystallize in a nearly eclipsed A$\overline{\text{A}}$-type layer stacking. The intermediate mPP based COF pair switches its stacking mode from eclipsed A$\overline{\text{A}}$-type for TAB towards staggered A$\overline{\text{B}}$-type for TAPB with increasing linker length, illustrating the tendency towards staggered conformations as a function of increasing node-to-node distance. While staggered, offset stacking conformations are usually designed by steric tuning,[58–61] the few large-pore COFs previously reported also show a tendency towards this.[18–23] Our results show that this stacking tendency of large-pore COFs is closely linked to the interlayer interactions. By prompting layer shifts and therefore reducing the effective pore size and layer overlap, targeted properties such as porosity and charge transfer can be negatively affected.[32] However, upon introducing additional interlayer interactions, the stacking behavior can be judiciously altered and effective pore sizes can be maximized.

Additionally, dPP-TAPB exhibits an adsorption behavior that so far has no precedence in COFs. It shows a very broad sorption hysteresis (Figure 4.2, d), which can be ascribed to a pore blocking phenomenon as typically found for ink-bottle shaped pores.[62,63] Compared to dPP-TAB, dPP-TAPB has a disparate PSD for the adsorption and desorption branch of the isotherm (Figure 4.5, a). While the adsorption branch shows the expected delayed pore condensation for the major pore size of 5.8 nm, in good agreement with the structural model, the desorption branch signals that evaporation of the capillary condensate is dominated by a neck size of 5.0 nm diameter. However, the complete lack of pores with 5.0 nm diameter in the PSD of the adsorption branch indicates a very thin neck size, which is not recognized as individual pores. The tendency of the other isoreticular COF systems with weaker interlayer interactions to form staggered structures with pore sizes of around 5 nm thus suggests a potential offset of just one or very few "labile" outer layers into a staggered arrangement, creating this smaller neck size (Figure 4.5, b).

Thermal stability and phase transition of large pore phenylphenanthridine COFs

Observing different stacking modes for otherwise isoreticular and chemically extremely similar COF systems, we further investigated how these different stacking modes and interlayer interactions influence the thermal behavior of large pore COFs. As previously shown by Evans et al.,[37,64] COFs can undergo structural change and loss of crystallinity well below the degradation temperature measured by thermogravimetric analysis (TGA). An increasing buckling of the COF layers at higher temperatures was found, leading to amorphization of the network. In addition, a trend of lower thermal stability with increasing pore size and pore functionalization was identified. It was postulated that larger and more mobile pendant groups, similar to the methoxy groups used here, can already cause significant disruption of interlayer interactions in 2D COF sheets as thermal energy is added, thus resulting in lower thermal stability. Taking into account that thermal stability can become a limiting factor in the application of COFs,[65,66] insights into this effect, especially at large pore sizes, is a key prerequisite.

Thermal Behavior

In TGA measurements, all COFs in our series show a typical, high thermal stability of up to 400 °C before any mass loss is detected (Figure S9.1.7). The XRPD patterns for the *in situ* heating experiments were consecutively collected at 30 °C, 80 °C, 100 °C, 120 °C, 140 °C, 160 °C, 180 °C, and 200 °C (Figure 4.6, a and b, and Figure S9.1.14-17), with a delay period of 4 h prior to each measurement in order to ensure equilibration. The final patterns at 200 °C for all COFs were further refined according to the models described above (Figure S9.1.7-12).

For the staggered A$\bar{\text{B}}$-type stacked COFs, PP-TAB, PP-TAPB, and mPP-TAPB, a minor reduction in crystallinity and peak broadening as well as a slight shift of the hk0 reflections was observed (Figure S9.1.14-16). These observations stem from additional layer buckling at higher temperatures as previously described by Evans *et al.*[37,38] This additional layer buckling is irreversible and remains upon cooling of the samples.

dPP-TAB COF shows almost no change in its reflections upon heating to 200 °C except for a slight shift of the 002 stacking reflection towards lower diffraction angles (Figure 4.5, a). This shift can be ascribed to a small thermal expansion between the layers of 0.08 Å, which was also found to be reversible upon cooling.

mPP-TAB and dPP-TAPB show the most significant changes upon heating (Figure 4.5, b and Figure S9.1.17). Up to a transition temperature of 140 °C for mPP-TAB and 120 °C for dPP-TAPB, both COFs still behave comparable to the temperature stable dPP-TAB. A slight shift of the 002 stacking reflection indicates thermal expansion, while no buckling of the layers is evident. At transition temperature, the basal 002 reflections show a substantial broadening and completely merges with the background at higher temperatures. Simultaneously, an initial shift of the hk0 reflections and their broadening takes place. Continuing stepwise further up to 200 °C, the final

60
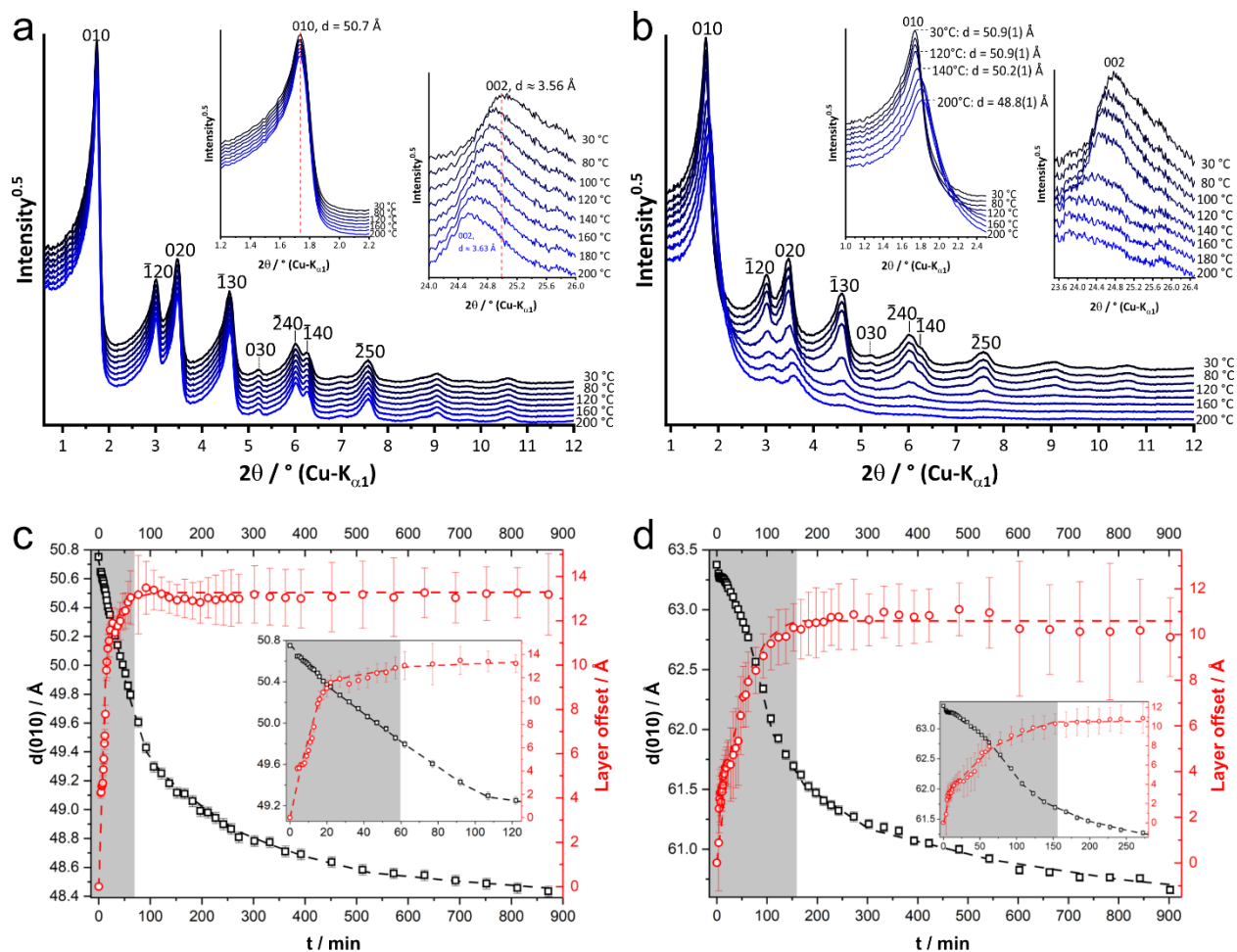
Figure 4.6. (a) Temperature dependent in situ XRPD patterns of dPP-TAB including selected reflection indices as close-up of the low 2θ region, close-up of the 010 reflections, and close-up of the 002 reflection. (b) Temperature dependent in situ XRPD patterns of mPP-TAB including selected reflection indices as close-up of the low 2θ region, close-up of the 010 reflections, and close-up of the 002 reflection. Evolution of the 010 lattice plane distance (black squares) and of the mean layer offset (red cycles) while holding (c) mPP-TAB at 140 °C and (d) dPP-TAPB at 120 °C. The insets show the initial evolution of the 010 lattice plane distance and the mean layer offset. The grey shaded areas indicate the period in which the mean layer offset significantly increases.

shift of the 010 reflection corresponds to a reduction of the a and b lattice parameters by 2.1 Å and 3.3 Å, respectively. As for PP-TAB, PP-TAPB and mPP-TAPB, this shift is a result of temperature induced layer buckling. However, the observed peak broadening that ultimately results in the disappearance of higher angle hk0 reflections, strongly resembles our simulations for the transition of a nearly eclipsed stacked $A\overline{A}$-type structure to an ordered, staggered $A\overline{B}$-type stacking (Figure 4.3, e). The results of the Rietveld refinement of the final ht-XRPD patterns at 200 °C are summarized in Table S9.1.2. They show for ht-mPP-TAB and ht-dPP-TAPB, which have visible similarity to the patterns of staggered PP-TAB and PP-TAPB, a staggered $A\overline{B}$-type stacking mode with satisfying agreement factors (R_{wp} = 4.39 % and 3.09 %, respectively).

To confirm this observation of a temperature-induced phase transition from an eclipsed towards a staggered type stacking for mPP-TAB and dPP-TAPB, corresponding sorption experiments

were performed. For this purpose, the samples were consecutively activated under vacuum at the given temperatures for 4 h before measurement. For mPP-TAPB no major changes below the transition temperature of 140 °C occur, in analogy to the XRPD heating experiments (Figure S9.1.29). Reaching the transition temperature, the previously steep uptake at around $P/P_0 = 0.5$ resembling the capillary condensation in 4.8 nm wide pores, begins to flatten out. With increasing temperature, the initially broad hysteresis then closes. During the step-wise transition, the S_{BET} almost halves from 1823 m^2 g^{-1} at room temperature to 930 m^2 g^{-1} after activation at 200 °C. The PSD shows a related, harsh drop in the cumulative pore volume of 4.8 nm and the appearance of a new pore size at 4.0 nm at 140 °C (Figure S9.1.29). With higher temperatures, all pores at 4.8 nm disappear after being transformed into the smaller pores correlating to a staggered A$\bar{\text{B}}$-type stacking of ht-mPP-TAB. Similar behavior is observed for dPP-TAPB, with a decrease of the S_{BET} to 920 m^2 g^{-1} and the disappearance of pores with 5.8 nm diameter accompanied by a rise of 4.8 nm pores at 120 °C and above (Figure S9.1.30). The S_{BET} and PSD of the ht-phases are in good accordance with the values found for isoreticular, already at room temperature staggered, PP-TAB and PP-TAPB COFs.

While the structural change is irreversible and permanent upon cooling, exposing the COFs to solvent followed by supercritical scCO$_2$ activation could recover the initial high crystallinity, S_{BET}, and PSD in both cases (Figure S9.1.31 and S9.1.32). As shown by Sick *et al.*,[67] this process can even at low temperatures sufficiently recover interlayer correlation, indicating the near-eclipsed stacking of mPP-TAB and dPP-TAPB is preferred in solution.

While phase changes by interlayer shifting under solvent influences[68,69] or by removal of structurally incorporated solvent[70] are known, our heating experiments show a remarkable, temperature induced phase transition for COFs due to layer mobility, which was to the best of our knowledge never observed before. The structural transition of mPP-TAB and dPP-TAPB from eclipsed into staggered already occurs at rather mild temperatures of 140 °C and 120 °C, respectively, and is reversible upon contact with solvent. The findings show again correlation between interlayer interactions and pore size, as for the room temperature isoreticular series. While the relatively smaller-sized pores of dPP-TAB with strong interlayer interactions are unaffected up to 200 °C, the isoreticular mPP-TAB only shows structural integrity up to 140 °C, when layer mobility gets sufficient to transform it into a staggered structure. With the increased pore size of dPP-TAPB, compared to dPP-TAB, the interlayer interactions are again not strong enough to prevent layer displacement above 120 °C. In our case, the increased interlayer interactions of pendant methoxy groups, anchoring the layers in nearly eclipsed stacking, does not follow the general negative influence on thermal stability of other pore functionalization found by Evans *et al.*[37,64] and therefore, offers new insights into the thermal stability of COFs.

Kinetic Study of Phase Transition

To monitor the development of the observed phase change over time, mPP-TAB and dPP-TAPB were heated above the transition temperature, to 140 °C and to 120 °C respectively, and the evolution of the diffraction patterns was monitored while holding the samples at constant temperatures. As an example, the XRPD patterns of mPP-TAB are shown in Figure S9.1.18. Several minutes after heating at the transition temperature, a decrease in intensity of the 010, $\bar{1}$20, 020 and $\bar{1}$30 reflections, indicating a shift of the layers towards a staggered A$\bar{B}$-type stacking, can be observed (Figure S9.1.18, a). In addition, the 010 reflections shift to higher 2θ angles (Figure S9.1.18, b), which is attributed to the development of a buckling of the COF layers. These processes continue, even after more than two hours.

In order to gain further insights into the mechanism of shifting and curving of the layers, the patterns were analyzed by fully weighted Rietveld refinements,[71] using the previously applied 2-layer unit cells with a planar COF conformation. The almost eclipsed A$\bar{A}$-type stacked structure was used for the patterns collected at 30 °C. For the refinement of the patterns collected at higher temperatures, the space group symmetry was lowered to P1 and the upper layer was allowed to shift freely within the ab-plane. The absolute value of the shifting vector of the upper lattice plane was used as a measure of transition from nearly eclipsed towards staggered A$\bar{B}$-type stacking. The a and b lattice parameters were constrained and refined as well in order to get a measure on the development of the COF-layer buckling. Symmetry adapted spherical harmonics were applied to the peak widths in order to compensate the peak broadening caused by intra- and interlayer disorder. All refinements were carried out in a serial way, which means that for the refinement of a pattern collected at a time t_i, the refined parameters of the preceding pattern collected at t_{i-1} were used. The parameters were released iteratively. At first, the lattice parameter was refined, and then the layer shift and finally the peak profile parameters were released. The resulting evolution of the mean layer offset and the curving of the COF-layers of mPP-TAB and dPP-TAPB are given in Figure 4.6, c and d.

For both mPP-TAB (Figure 4.6, c) and dPP-TAPB (d) the curving and the shifting of the COF layers start immediately. The absence of an induction period in the evolution of the layer offset and the shrinking of the a and b lattice parameters indicates that buckling of the layers does not require any initial shift and shifting of the layers does not require any initial buckling. The development of the layer offset (Figure 4.6, grey shaded areas) is always faster than curving of the layers. As a consequence, both processes seem to proceed independently of each other. However, the lack of temperature-induced layer curving in dPP-TAB even at 200 °C, which also does not show any signs of layer shifting, indicates that a slight initial layer shift might be necessary for the occurrence of layer buckling under thermal stress. In mPP-TAB the shifting and curving of the layers occurs faster than in dPP-TAPB, which is attributed to the higher transition temperature. During the development of the COF-layer offset in mPP-TAB, the layer shifts by 13 ± 2 Å, whereas
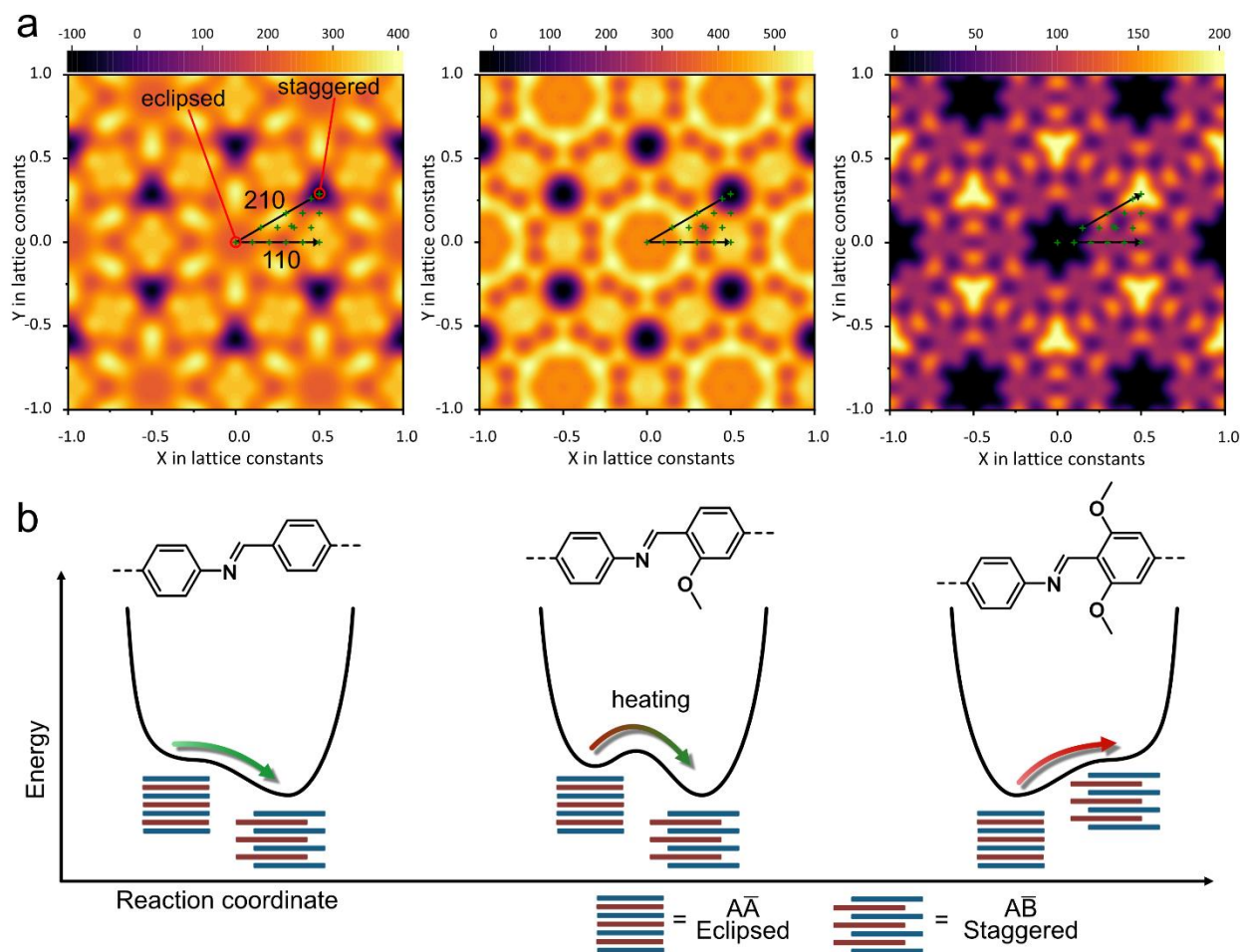
Figure 4.7. (a) Potential energy landscapes assuming a shift of the A̅-type layer in comparison to the A-type layer by a certain vector (Figure 4.3, c) of PP-TAB, mPP-TAB, and dPP-TAB (left to right); green crosses show surface data points used for interpolation, black arrows indicate the respective direction in space and total eclipsed and staggered positions are marked in the left graph. (b) Schematic potential energy changes as a function of the stacking mode of PP-TAB, mPP-TAB, and dPP-TAB.

in case of dPP-TAPB the layer shifts by 11 ± 2 Å. The layer shift found is in good agreement with the staggered structure model obtained for ht-mPP-TAB and ht-dPP-TAPB at 200 °C.

Computational investigations of stacking potential energy landscapes

To gain further insights into the origin of the phase transition, displacement potential energy landscapes for PP-TAB, mPP-TAB and dPP-TAB were calculated (Figure 4.7, a). Investigations were performed for the relative displacement of two layers per unit cell constructed by using the knowledge of the structural analysis, to resemble the most stable molecular arrangements for eclipsed stacking. We created the initial structure by arranging both layers with overlapping centers of mass as the displacement origin. Starting from this arrangement we displaced the upper layer along the marked points in Figure 4.7, a, sampling the asymmetric unit of a D6-symmetric 2D unit cell, i.e., one triangle necessary to create the full hexagonal unit cell as shown in (Figure S9.1.54). For every displacement we performed geometry and cell optimizations using GFN-

xTB[72] as implemented in CP2K, as it showed qualitatively similar behavior when compared with single-point energies for the optimized cells using GPW-DFT (Figure S9.1.52). The obtained energy values were then interpolated by a plane-wave expansion with D6 symmetry. The obtained potential energy landscapes show the distribution in the potential energy landscapes assuming a shift of the $\overline{A}$-type layer in comparison to the A-type layer by a certain vector as shown in Figure 4.3, c, with the totally eclipsed stacking as origin in the center of the landscapes at (0,0).

For dPP-TAB with the strongest interlayer interactions only a small, clearly favorable energy window corresponding to a nearly eclipsed stacking is found.[31] PP-TAB COF shows the energetic minima consistent with staggered stacking. The mPP-TAB displays a similar landscape as PP-TAB with the energetic minima predicting staggered configurations. However, in this case a small energy barrier between the nearly eclipsed and staggered configurations was found. These observations are rationalized in a simplified qualitative scheme (Figure 4.7, b). PP-TAB with the least pronounced interlayer interactions shows a single clear minimum for a staggered conformation, while dPP-TAB, with the strongest interlayer interactions, shows a minimum for the nearly eclipsed arrangement. The experimentally observed stacking arrangements match these findings. However, mPP-TAB displays two significant minima, a local one for the eclipsed structure and a global one for the staggered structure with a small, yet significant energy barrier dividing both. While mPP-TAB crystallizes with nearly eclipsed stacking when synthesized at a temperature of 120 °C, just below the transition temperature and in the presence of a solvent, heating can provide the necessary activation energy to transform it into the more stable staggered arrangement. Of note, the reversibility after exposure to solvent indicates that in the solvated form the nearly eclipsed configuration is favored and only becomes metastable after solvent removal.

4.3. Conclusion

We successfully developed six novel large-pore COFs with a maximum pore size of 5.8 nm, which is among the largest pore sizes reported for COFs to date. More importantly, methoxy groups in phenylphenanthridine building blocks were identified to act as anchors that eliminate the tendency toward slipped layer stacking in large-pore COFs, which typically leads to notoriously reduced effective pore sizes and surface areas. XRPD results together with theoretical modelling indicate mPP-TAB, dPP-TAB and dPP-TAPB to adopt a nearly eclipsed stacking mode with maximized pore sizes, attributed to enhanced interlayer interaction in these COFs, mediated by the methoxy groups. While increasing interlayer interactions positively influence the thermal stability of the COFs, we further demonstrate, for the first time, a temperature-induced phase transition to the staggered stacking polytype, enabled by high layer mobility even at temperatures as low as 120 °C. The slow transition could be readily followed by in situ XRPD measurements, shedding light on the two independent processes involved, layer shifting and buckling. Altered porosity and crystallinity for the high-temperature phases are persistent but were easily reversed by solvent exposure, suggesting solvent-induced changes of the stacking mode to be an additional degree

of freedom in influencing the layer stacking besides the observed thermally induced phase transitions. Considering the fact that the synthesis of large-pore COFs with > 5 nm pore size remains a challenging task in the COF chemistry, we anticipate that the findings presented herein will aid the rational design of COFs with targeted pore size, layer registry and thermal stability for specific applications.

4.4. Bibliography

[1]   C. S. Diercks, O. M. Yaghi, *Science* **2017**, *355*, 923.
[2]   H. Xu, X. Chen, J. Gao, J. Lin, M. Addicoat, S. Irle, D. Jiang, *Chem. Commun.* **2014**, *50*, 1292–1294.
[3]   C. S. Diercks, S. Lin, N. Kornienko, E. A. Kapustin, E. M. Nichols, C. Zhu, Y. Zhao, C. J. Chang, O. M. Yaghi, *J. Am. Chem. Soc.* **2018**, *140*, 1116–1122.
[4]   X. Wang, L. Chen, S. Y. Chong, M. A. Little, Y. Wu, W. H. Zhu, R. Clowes, Y. Yan, M. A. Zwijnenburg, R. S. Sprick, A. I. Cooper, *Nat. Chem.* **2018**, *10*, 1180–1189.
[5]   B. P. Biswal, H. A. Vignolo-González, T. Banerjee, L. Grunenberg, G. Savasci, K. Gottschling, J. Nuss, C. Ochsenfeld, B. V. Lotsch, *J. Am. Chem. Soc.* **2019**, *141*, 11082–11092.
[6]   H. Furukawa, O. M. Yaghi, *J. Am. Chem. Soc.* **2009**, *131*, 8875–8883.
[7]   Q. Gao, X. Li, G. H. Ning, H. Sen Xu, C. Liu, B. Tian, W. Tang, K. P. Loh, *Chem. Mater.* **2018**, *30*, 1762–1768.
[8]   L. Zhai, N. Huang, H. Xu, Q. Chen, D. Jiang, *Chem. Commun.* **2017**, *53*, 4242–4245.
[9]   H. L. Nguyen, N. Hanikel, S. J. Lyle, C. Zhu, D. M. Proserpio, O. M. Yaghi, *J. Am. Chem. Soc.* **2020**, *142*, 2218–2221.
[10]   L. Stegbauer, M. W. Hahn, A. Jentys, G. Savasci, C. Ochsenfeld, J. A. Lercher, B. V. Lotsch, *Chem. Mater.* **2015**, *27*, 7874–7881.
[11]   F. Xu, S. Yang, X. Chen, Q. Liu, H. Li, H. Wang, B. Wei, D. Jiang, *Chem. Sci.* **2019**, *10*, 6001–6006.
[12]   F. Xu, H. Xu, X. Chen, D. Wu, Y. Wu, H. Liu, C. Gu, R. Fu, D. Jiang, *Angew. Chemie Int. Ed.* **2015**, *54*, 6814–6818.
[13]   D. A. Vazquez-Molina, G. S. Mohammad-Pour, C. Lee, M. W. Logan, X. Duan, J. K. Harper, F. J. Uribe-Romo, *J. Am. Chem. Soc.* **2016**, *138*, 9767–9770.
[14]   Z. Zhou, W. Zhong, K. Cui, Z. Zhuang, L. Li, L. Li, J. Bi, Y. Yu, *Chem. Commun.* **2018**, *54*, 9977–9980.
[15]   Y. Peng, Y. Huang, Y. Zhu, B. Chen, L. Wang, Z. Lai, Z. Zhang, M. Zhao, C. Tan, N. Yang, F. Shao, Y. Han, H. Zhang, *J. Am. Chem. Soc.* **2017**, *139*, 8698–8704.
[16]   H. Singh, V. K. Tomer, N. Jena, I. Bala, N. Sharma, D. Nepak, A. De Sarkar, K. Kailasam, S. K. Pal, *J. Mater. Chem. A* **2017**, *5*, 21820–21827.
[17]   Y. Song, Q. Sun, B. Aguila, S. Ma, *Adv. Sci.* **2019**, *6*, 1801410.
[18]   S. Jin, K. Furukawa, M. Addicoat, L. Chen, S. Takahashi, S. Irle, T. Nakamura, D. Jiang, *Chem. Sci.* **2013**, *4*, 4505–4511.
[19]   F. Xu, S. Jin, H. Zhong, D. Wu, X. Yang, X. Chen, H. Wei, R. Fu, D. Jiang, *Sci. Rep.* **2015**, *5*, 1–6.
[20]   Q. Fang, Z. Zhuang, S. Gu, R. B. Kaspar, J. Zheng, J. Wang, S. Qiu, Y. Yan, *Nat. Commun.* **2014**, *5*, 4503.
[21]   S. B. Yu, H. Lyu, J. Tian, H. Wang, D. W. Zhang, Y. Liu, Z. T. Li, *Polym. Chem.* **2016**, *7*, 3392–3397.
[22]   T. Xu, S. An, C. Peng, J. Hu, H. Liu, *Ind. Eng. Chem. Res.* **2020**, *59*, 8315–8322.
[23]   C. Zhao, H. Lyu, Z. Ji, C. Zhu, O. M. Yaghi, *J. Am. Chem. Soc.* **2020**, *142*, 14450–14454.
[24]   V. S. Vyas, M. Vishwakarma, I. Moudrakovski, F. Haase, G. Savasci, C. Ochsenfeld, J. P. Spatz, B. V. Lotsch, *Adv. Mater.* **2016**, *28*, 8749–8754.
[25]   S. Liu, C. Hu, Y. Liu, X. Zhao, M. Pang, J. Lin, *Chem. – A Eur. J.* **2019**, *25*, 4315–4319.
[26]   G. Zhang, X. Li, Q. Liao, Y. Liu, K. Xi, W. Huang, X. Jia, *Nat. Commun.* **2018**, *9*, 1–11.
[27]   H. Deng, S. Grunder, K. E. Cordova, C. Valente, H. Furukawa, M. Hmadeh, F. Gándara, A. C. Whalley, Z. Liu, S. Asahina, H. Kazumori, M. O'Keeffe, O. Terasaki, J. F. Stoddart, O. M. Yaghi, *Science* **2012**, *336*, 1018–1023.
[28]   V. Muralidharan, C. Y. Hui, *Macromol. Rapid Commun.* **2004**, *25*, 1487–1490.
[29]   J. Weber, L. Bergström, *Langmuir* **2010**, *26*, 10158–10164.

[30] M. Calik, T. Sick, M. Dogru, M. Döblinger, S. Datz, H. Budde, A. Hartschuh, F. Auras, T. Bein, *J. Am. Chem. Soc.* **2016**, *138*, 1234–1239.

[31] F. Haase, K. Gottschling, L. Stegbauer, L. S. Germann, R. Gutzler, V. Duppel, V. S. Vyas, K. Kern, R. E. Dinnebier, B. V. Lotsch, *Mater. Chem. Front.* **2017**, *1*, 1354–1361.

[32] F. Haase, B. V. Lotsch, *Chem. Soc. Rev.* **2020**, *49*, 8469–8500.

[33] F. Haase, E. Troschke, G. Savasci, T. Banerjee, V. Duppel, S. Dörfler, M. M. J. Grundei, A. M. Burow, C. Ochsenfeld, S. Kaskel, B. V. Lotsch, *Nat. Commun.* **2018**, *9*, 1–10.

[34] X. Liu, D. Huang, C. Lai, G. Zeng, L. Qin, H. Wang, H. Yi, B. Li, S. Liu, M. Zhang, R. Deng, Y. Fu, L. Li, W. Xue, S. Chen, *Chem. Soc. Rev.* **2019**, *48*, 5266–5302.

[35] S. Bi, C. Yang, W. Zhang, J. Xu, L. Liu, D. Wu, X. Wang, Y. Han, Q. Liang, F. Zhang, *Nat. Commun.* **2019**, *10*, 1–10.

[36] J. Maschita, T. Banerjee, G. Savasci, F. Haase, C. Ochsenfeld, B. V. Lotsch, *Angew. Chemie Int. Ed.* **2020**, *59*, 15750–15758.

[37] A. M. Evans, M. R. Ryder, N. C. Flanders, E. Vitaku, L. X. Chen, W. R. Dichtel, *Ind. Eng. Chem. Res.* **2019**, *58*, 9883–9887.

[38] A. M. Evans, M. R. Ryder, W. Ji, M. J. Strauss, A. R. Corcos, E. Vitaku, N. C. Flanders, R. P. Bisbey, W. R. Dichtel, *Faraday Discuss.* **2021**, *225*, 226–240.

[39] H. Xu, J. Gao, D. Jiang, *Nat. Chem.* **2015**, *7*, 905–912.

[40] A. Halder, S. Karak, M. Addicoat, S. Bera, A. Chakraborty, S. H. Kunjattu, P. Pachfule, T. Heine, R. Banerjee, *Angew. Chemie Int. Ed.* **2018**, *57*, 5797–5802.

[41] A. M. Pütz, M. W. Terban, S. Bette, F. Haase, R. E. Dinnebier, B. V. Lotsch, *Chem. Sci.* **2020**, *11*, 12647–12654.

[42] A. A. Coelho, J. S. O. Evans, J. W. Lewis, *J. Appl. Crystallogr.* **2016**, *49*, 1740–1749.

[43] R. E. Dinnebier, A. Leineweber, J. S. O. Evans, in *Rietveld Refinement Pract. Pattern Anal. Using Topas 6.0*, De Gruyter, Berlin, **2018**, pp. 1–349.

[44] R. Ahlrichs, M. Bär, M. Häser, H. Horn, C. Kölmel, *Chem. Phys. Lett.* **1989**, *162*, 165–169.

[45] F. Weigend, R. Ahlrichs, *Phys. Chem. Chem. Phys.* **2005**, *7*, 3297–3305.

[46] J. P. Perdew, K. Burke, M. Ernzerhof, *Phys. Rev. Lett.* **1996**, *77*, 3865–3868.

[47] S. Grimme, J. Antony, S. Ehrlich, H. Krieg, *J. Chem. Phys.* **2010**, *132*, 24103.

[48] J. Kästner, J. M. Carr, T. W. Keal, W. Thiel, A. Wander, P. Sherwood, *J. Phys. Chem. A* **2009**, *113*, 11856–11865.

[49] P. Sherwood, A. H. De Vries, M. F. Guest, G. Schreckenbach, C. R. A. Catlow, S. A. French, A. A. Sokol, S. T. Bromley, W. Thiel, A. J. Turner, S. Billeter, F. Terstegen, S. Thiel, J. Kendrick, S. C. Rogers, J. Casci, M. Watson, F. King, E. Karlsen, M. Sjøvoll, A. Fahmi, A. Schäfer, C. Lennartz, *J. Mol. Struct. THEOCHEM* **2003**, *632*, 1–28.

[50] T. D. Kühne, M. Iannuzzi, M. Del Ben, V. V. Rybkin, P. Seewald, F. Stein, T. Laino, R. Z. Khaliullin, O. Schütt, F. Schiffmann, D. Golze, J. Wilhelm, S. Chulkov, M. H. Bani-Hashemian, V. Weber, U. Borštnik, M. Taillefumier, A. S. Jakobovits, A. Lazzaro, H. Pabst, T. Müller, R. Schade, M. Guidon, S. Andermatt, N. Holmberg, G. K. Schenter, A. Hehn, A. Bussy, F. Belleflamme, G. Tabacchi, A. Glöß, M. Lass, I. Bethune, C. J. Mundy, C. Plessl, M. Watkins, J. VandeVondele, M. Krack, J. Hutter, *J. Chem. Phys.* **2020**, *152*, 194103.

[51] M. Krack, *Theor. Chem. Acc.* **2005**, *114*, 145–152.

[52] J. VandeVondele, J. Hutter, *J. Chem. Phys.* **2007**, *127*, 114105.

[53] P. Chakrabarti, R. Bhattacharyya, *Prog. Biophys. Mol. Biol.* **2007**, *95*, 83–137.

[54] R. Chelli, F. L. Gervasio, P. Procacci, V. Schettino, *J. Am. Chem. Soc.* **2002**, *124*, 6133–6143.

[55] A. V. Neimark, Y. Lin, P. I. Ravikovitch, M. Thommes, *Carbon N. Y.* **2009**, *47*, 1617–1628.

[56] G. Y. Gor, M. Thommes, K. A. Cychosz, A. V. Neimark, *Carbon N. Y.* **2012**, *50*, 1583–1590.

[57] M. Thommes, K. Kaneko, A. V. Neimark, J. P. Olivier, F. Rodriguez-Reinoso, J. Rouquerol, K. S. W. Sing, *Pure Appl. Chem.* **2015**, *87*, 1051–1069.

[58] Y. Fan, Q. Wen, T.-G. Zhan, Q.-Y. Qi, J.-Q. Xu, X. Zhao, *Chem. - A Eur. J.* **2017**, *23*, 5668–5672.

[59] X. Wu, X. Han, Y. Liu, Y. Liu, Y. Cui, *J. Am. Chem. Soc.* **2018**, *140*, 16124–16133.

[60] F. Auras, L. Ascherl, A. H. Hakimioun, J. T. Margraf, F. C. Hanusch, S. Reuter, D. Bessinger, M. Döblinger, C. Hettstedt, K. Karaghiosoff, S. Herbert, P. Knochel, T. Clark, T. Bein, *J. Am. Chem. Soc.* **2016**, *138*, 16703–16710.

[61] C. M. Thompson, G. Occhialini, G. T. McCandless, S. B. Alahakoon, V. Cameron, S. O. Nielsen, R. A. Smaldone, *J. Am. Chem. Soc.* **2017**, *139*, 10506–10513.

[62] M. Thommes, B. Smarsly, M. Groenewolt, P. I. Ravikovitch, A. V. Neimark, *Langmuir* **2006**, *22*, 756–764.

[63] P. I. Ravikovitch, A. V. Neimark, *Langmuir* **2002**, *18*, 9830–9837.

[64] A. M. Evans, M. R. Ryder, W. Ji, M. J. Strauss, A. R. Corcos, E. Vitaku, N. C. Flanders, R. P. Bisbey, W. R. Dichtel, *Faraday Discuss.* **2021**, *225*, 226–240.

[65] H.-S. Xu, S.-Y. Ding, W.-K. An, H. Wu, W. Wang, *J. Am. Chem. Soc.* **2016**, *138*, 11489–11492.

[66] S. Chandra, T. Kundu, S. Kandambeth, R. Babarao, Y. Marathe, S. M. Kunjir, R. Banerjee, *J. Am. Chem. Soc.* **2014**, *136*, 6570–6573.

[67] T. Sick, J. M. Rotter, S. Reuter, S. Kandambeth, N. N. Bach, M. Döblinger, J. Merz, T. Clark, T. B. Marder, T. Bein, D. D. Medina, *J. Am. Chem. Soc.* **2019**, *141*, 12570–12581.

[68] C. Kang, Z. Zhang, V. Wee, A. K. Usadi, D. C. Calabro, L. S. Baugh, S. Wang, Y. Wang, D. Zhao, *J. Am. Chem. Soc.* **2020**, *142*, 12995–13002.

[69] S. Cai, B. Sun, X. Li, Y. Yan, A. Navarro, A. Garzón-Ruiz, H. Mao, R. Chatterjee, J. Yano, C. Zhu, J. A. Reimer, S. Zheng, J. Fan, W.-G. Zhang, Y. Liu, *ACS Appl. Mater. Interfaces* **2020**, *12*, 19054–19061.

[70] Y. Du, D. Calabro, B. Wooler, Q. Li, S. Cundy, P. Kamakoti, D. Colmyer, K. Mao, P. Ravikovitch, *J. Phys. Chem. C* **2014**, *118*, 399–407.

[71] H. M. Rietveld, *J. Appl. Crystallogr.* **1969**, *2*, 65–71.

[72] S. Grimme, C. Bannwarth, P. Shushkov, *J. Chem. Theory Comput.* **2017**, *13*, 1989–2009.

5. Olefin Metathesis in Confinement: Towards Covalent Organic Framework Scaffolds for Increased Macrocyclization Selectivity

The work in this chapter was published, reproduced, and adapted from:

Olefin Metathesis in Confinement: Towards Covalent Organic Framework Scaffolds for Increased Macrocyclization Selectivity

Sebastian T. Emmerling,* Felix Ziegler,* Felix R. Fischer, Roland Schoch, Matthias Bauer, Bernd Plietker, Michael R. Buchmeiser, and Bettina V. Lotsch

*equally contributed

Sebastian T. Emmerling and Bettina V. Lotsch conceived the project. Sebastian T. Emmerling wrote the manuscript with assistance of Felix Ziegler, Bettina V. Lotsch and with input from all other authors. Sebastian T. Emmerling and Felix Ziegler designed the experiments, synthesized the materials, and performed most of the analysis and evaluated the data. Sebastian T. Emmerling and Felix R. Fischer performed the XAFS experiments. Felix R. Fischer and Roland Schoch performed the XRPD analysis and simulations with supervision of Matthias Bauer and Bernd Plietker. All authors assisted the analysis of their respective experiments and the overall discussion. Bettina V. Lotsch supervised the work.

Supporting information can be found in Chapter 9.2.

Figure 5.1. Table of content figure for the increased macrocyclization selectivity of olefin metathesis by confinement in COF scaffolds.

Abstract

Covalent organic frameworks (COFs) offer vast structural and chemical diversity enabling a wide and growing range of applications. While COFs are well-established as heterogeneous catalysts, so far, their high and ordered porosity has scarcely been utilized to its full potential when it comes to spatially confined reactions in COF pores to alter the outcome of reactions. Here, we present a highly porous and crystalline, large-pore COF as catalytic support in α,ω-diene ring-closing metathesis reactions, leading to increased macrocyclization selectivity. COF pore-wall modification by

immobilization of a Grubbs-Hoveyda-type catalyst via a mild silylation reaction provides a molecularly precise heterogeneous metathesis catalyst. An increased macro(mono)cyclization (MMC) selectivity over oligomerization (O) for the heterogeneous COF-catalyst (MMC:O = 1.35) of up to 51% compared to the homogeneous catalyst (MMC:O = 0.90) was observed along with a substrate-size dependency in selectivity, pointing to diffusion limitations induced by the pore confinement.

5.1. Introduction

Covalent organic frameworks (COFs) are 2D or 3D extended structures, which are defined by their covalent connectivity, porosity, and crystallinity, while consisting exclusively of light elements.[1] The vast structural and chemical diversity of COFs and the possibility to tune their framework with atomic precision has put COFs in the spotlight for a variety of applications that benefit from precise framework design, including photocatalytic water splitting,[2,3] sensing,[4] batteries,[5] gas adsorption,[6] or heterogeneous catalysis.[7] With their ordered micro- and mesoporosity and large specific surface areas exposing a large number of functional or even active catalytic sites, COFs are among the most promising materials for molecular heterogeneous catalysis. Classical approaches to design COFs for heterogeneous catalysis utilizing this feature include incorporation of catalytic centers directly in the pore wall,[8] pore surface engineering by molecular catalysts via a post-synthetic reaction,[9] integration of monodisperse nanoparticles in the framework by pore templating, or embedding polymers into the pores to combine multiple catalytic centers.[10,11]

However, despite the promise of COFs as versatile scaffolds for catalysis, examples for the exploitation of reaction-specific pore confinement effects during catalysis, such as the substrate-
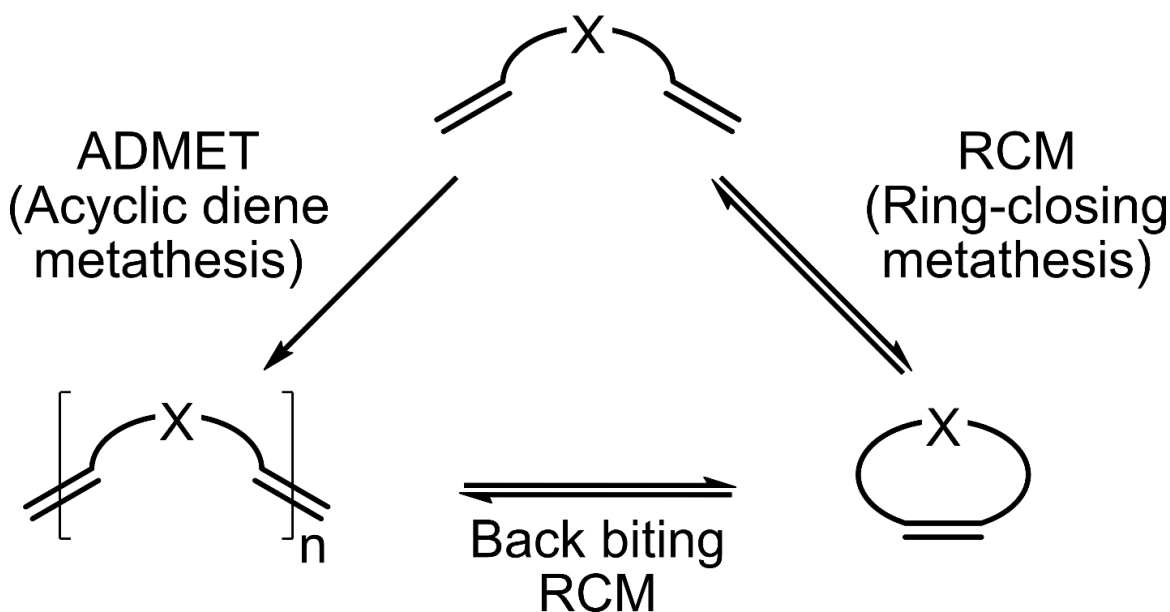
Scheme 5.1. Competing metathesis reactions of α,ω-dienes resulting in macro(mono)cycles and oligomerization products.
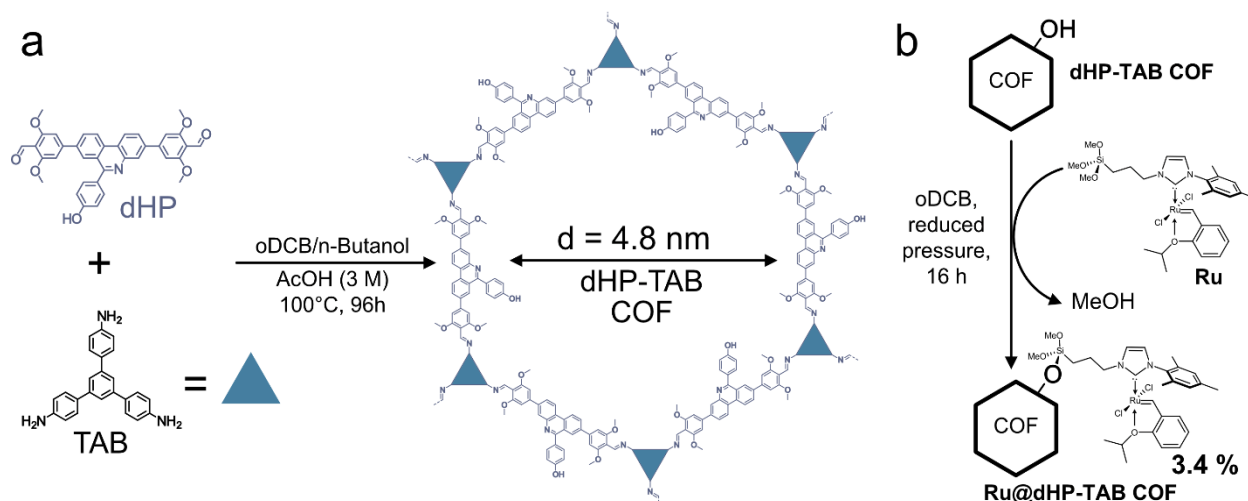
Figure 5.2. (a) Synthesis of **dHP-TAB** COF. (b) Immobilization of **Ru** catalyst on **dHP-TAB** by silylation to form **Ru@dHP-TAB**.

specific and size-selective Knoevenagel-reaction achieved for microporous COFs by Fang *et al.,*[12] are still rare. Altering selectivity and reactivity of the catalyzed reaction by spatial confinement is an immensely successful principle used in nature by enzymes and enzyme-inspired artificial catalysis. Taking full advantage of the ordered structural porosity of COFs thus bodes well for a biomimetic approach to catalysis where the precise spatial arrangement of catalytic centers and substrates, as well as pore confinement is utilized to direct product selectivity.[13]

In this work, we present a large-pore imine-COF as a molecular heterogeneous catalyst to study the effect of spatial confinement on product selectivity during olefin metathesis reactions; in particular macro(mono)cyclization (MMC) selectivity by ring-closing metathesis (RCM) and back-biting depolymerization vs. acyclic diene metathesis (ADMET) oligomerization (O, Scheme 5.1).

Olefin metathesis-based macrocyclization offers an important pathway to useful compounds for industrial or pharmaceutical chemistry,[14] however, still poses severe challenges. Oftentimes, only low MMC yields are achieved due to the competing oligomerization by ADMET, originating from a ring-chain equilibrium during catalysis and back-biting RCM.[15,16] The biomimetic approach by spatial confinement of metathesis reactions in pores for increased selectivity towards MMC products was already successfully shown for mesoporous silica by Jee *et al.* and Ziegler *et al.*[16,17] Applying this biomimetic approach to a COFs system not only diversifies the scope of possible confinement effects and framework-catalyst-reactant interactions, but at the same time offers new opportunities for precise, substrate- and product-specific catalyst-framework designs due the high structural and chemical diversity of COFs.

5.2. Results and Discussion

For the study of olefin metathesis reactions under spatial confinement in COFs, the model system, **dHP-TAB** COF, was synthesized by the condensation of 4,4'-(6-(4-hydroxyphenyl)phenanthridine-3,8-diyl)bis-(2,6-dimethoxybenzaldehyde) (**dHP**) and 5'-(4-aminophenyl)-[1,1':3',1''-terphenyl]-4,4''-diamine (**TAB**) in a solvent mixture of 1,2-dichlorbenzene (oDCB) and *n*-butanol (3 : 7) with 3 M acetic acid (AcOH) as catalyst for 96 h at 100°C (**Error! Reference source not found.**, a). After isolation by filtration, the solid was washed with methanol and subsequently activated by supercritical CO_2. The large-pore COF system was chosen to accommodate the bulky catalyst and substrates and prevent pore blocking during immobilization and catalysis. Methoxy groups incorporated in the COF act

Figure 5.3. Experimental XRPD pattern of **dHP-TAB** COF, Rietveld refinement,[19] difference curve and positions of the Bragg reflections. Inset: Structure of the respective AĀ stacked **dHP-TAB** along the *a* and *b* axis after refinement.

as non-covalent anchors to achieve better layer registry and thus high porosity and large, well-defined pore sizes for this framework.[18]

Imine formation during the initial COF synthesis was confirmed by FT-IR analysis (Figure S9.2.7). The spectrum shows the absence of the prominent aldehyde C=O stretching band at 1674 cm^{-1} and amine N-H stretching bands at 3355 cm^{-1} and 3431 cm^{-1}, corresponding to the starting materials, indicating full conversion into imine bonds. The new imine stretching band is mostly concealed as slight shoulder at around 1614 cm^{-1} of the strong aromatic C-C stretching bands at 1593 cm^{-1}. The solid-state ^{13}C resonance (CP-MAS ssNMR) spectrum confirms the successful condensation by showing the typical imine signal at 160.0 ppm and the absence of aldehyde signals (Figure S9.2.18).

Crystallinity of **dHP-TAB** COF was confirmed by X-ray powder diffraction (XRPD), with the pattern (Co-K$_{\alpha1}$) displaying several well-resolved diffraction peaks at 2 θ = 2.0°, 3.5°, 4.0°, 5.3°, 6.9°, 7.3°, 8.8°, 10.5° and a broadened stacking reflection centered around 28.5° (Figure 5.3). The structure was modeled in *P*31c symmetry with an alternating nearly-eclipsed AĀ stacking order of the layers. This assumed model is based on previous findings for phenylphenanthridine based COFs[18] and shows a good match when compared to the simulated patterns of an AĀ stacked model (Figure S9.2.10). Rietveld refinement[19] of the pattern with the assumed model yielded unit cell
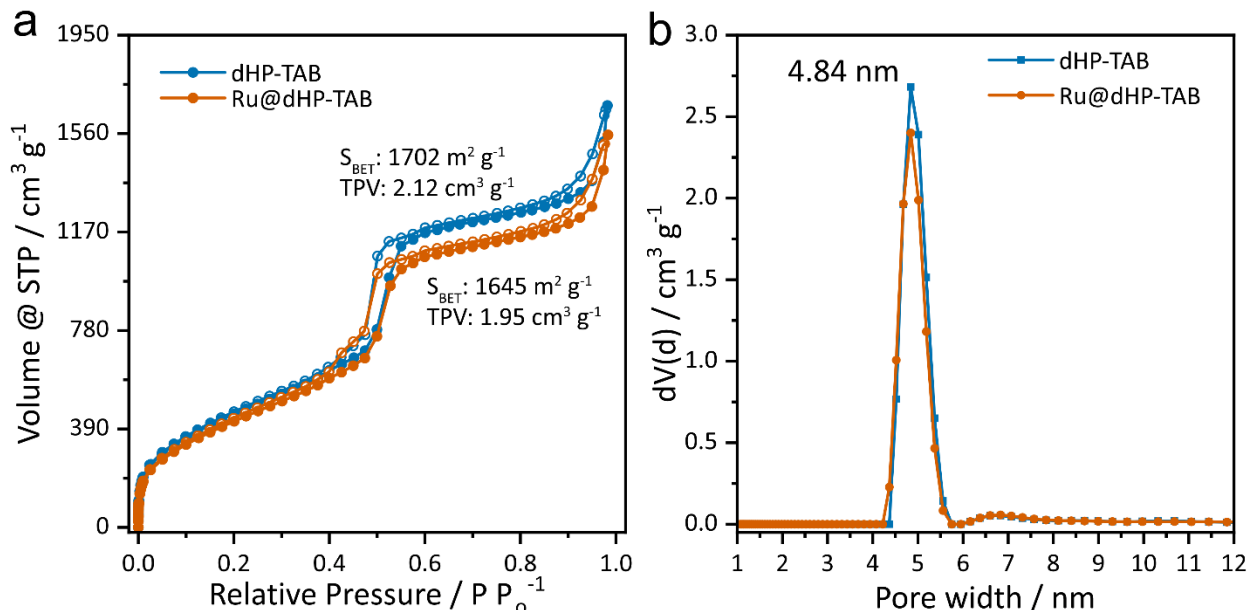
Figure 5.4. Comparison of (a) nitrogen isotherms at 77 K (filled circles for adsorption, empty circles for desorption) and (b) pore size distribution obtained from the adsorption branch of **dHP-TAB** and **Ru@dHP-TAB** after immobilization of the catalyst.

parameters ($a = b = 58.824$ Å and $c = 7.3$ Å) with a satisfying agreement factor ($R_{wp} = 7.10\%$, $R_p = 4.88\%$) (Figure 5.3).

Porosity of **dHP-TAB** COF was investigated by nitrogen physisorption measurements at 77 K, showing a type-IV isotherm, which is typical for mesoporous systems. The Brunauer-Emmett-Teller surface area (S_{BET}) was calculated to be 1702 m^2 g^{-1} with a total pore volume of 2.12 cm^3 g^{-1} at $P/P_0 = 0.95$. The pore size distribution (PSD) was determined from the adsorption branch by quenched solid density functional theory (QSDFT) based on the carbon model for cylindrical pores. It shows a narrow PSD around 4.8 nm, which is in good agreement with the structure model and closely related, isoreticular COFs.[18]

Next, the molecular catalyst $RuCl_2$(N-mesityl-N-(3-(trimethoxysilyl)prop-1-yl)-imidazol-2-yli-dene)(CH-2-(2-PrO-C_6H_4)) (**Ru**) was immobilized in the framework *via* silylation, utilizing the incorporated hydroxyl groups of the protruding phenols as anchor points (Figure 5.2, b). The immobilization was performed at room temperature in high-boiling oDCB as solvent under reduced pressure. Performing the reaction under reduced pressure significantly increases the catalyst loading by removing the accruing methanol from the reaction mixture and driving the reaction towards the desired outcome, yielding the catalyst-loaded **Ru@dHP-TAB** COF. Inductively-Coupled Plasma Optical Emission Spectroscopy (ICP-OES) of the washed and dried sample revealed a Ru-content of $c(Ru) = 42.3$ µmol/g for **Ru@dHP-TAB** COF. This corresponds to a successful silylation of approximately 3.4 % of the hydroxyl groups contained in the COF or roughly one catalyst per pore at every tenth layer. No changes in the FT-IR spectra of **Ru@dHP-TAB** compared to the pristine COF are visible, which can be attributed to the comparatively low amounts

of immobilized catalyst (Figure S9.2.8) and the XRPD pattern (Figure S9.2.9) as well as transmission electron microscopy (TEM) images show a retention of crystallinity (Figure S9.2.26). Nitrogen sorption measurements reveals only a minimal reduction in surface area (S_{BET} = 1645 m^2 g^{-1}) and total pore volume (1.95 cm^3 g^{-1} at P/P$_0$ = 0.95) compared to **dHP-TAB** with nearly identical pore size distribution (Figure 5.4). The largely retained porosity suggests that no substantial fraction of pores was fully blocked during the immobilization.
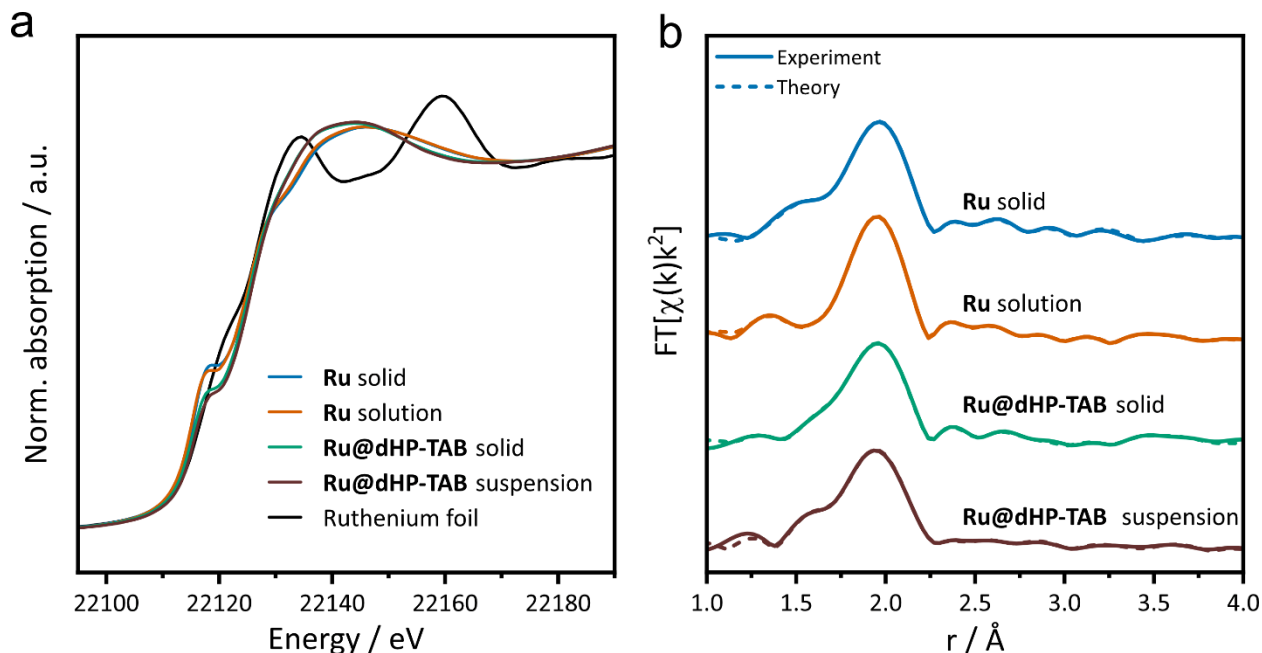
Figure 5.5. (a) XANES spectra of the homogeneous **Ru** complex in the solid state (red), solution (green), immobilized in the mesoporous COF in the solid state (yellow), as suspension in benzene (brown), as well as of the Ru(0) foil used for calibration (black). (b) Fourier-transformed EXAFS data of the four Ru complexes. Continuous line: experimental data, dotted line: fitted data.

To confirm the stability of the catalyst during immobilization and to gain knowledge of the catalyst's structure in the pore, X-ray absorption (XAS) measurements were performed. Spectra of **Ru** and **Ru@dHP-TAB** as solids and in solution/suspension (benzene), respectively, were recorded. The obtained X-ray absorption near edge structure (XANES) spectra (Figure 5.5, a and Figure S9.2.19), providing information about the oxidation state of the Ru-metal center,[20] shows no differences in the edge energy for all four samples measured. A change in the electronic structure or oxidation state by immobilization in the COF can thus be excluded

Results of extended X-ray absorption fine structure (EXAFS) analysis, probing the local geometric structure around an X-ray absorbing atom of the **Ru** catalyst under homogeneous and immobilized conditions are shown in Figure 5.5, b.[21] The corresponding first shell scattering paths combined with coordination numbers, bond distances and Debye-Waller factors, which describe the static and dynamic disorder in the coordination shell, are collected in Figure S9.2.21 and Table S9.2.7. The results of the structure analysis for all samples are in good agreement with the single-crystal structure of the **Ru** catalyst.[16] In the solid immobilized sample **Ru@dHP-TAB**, the second
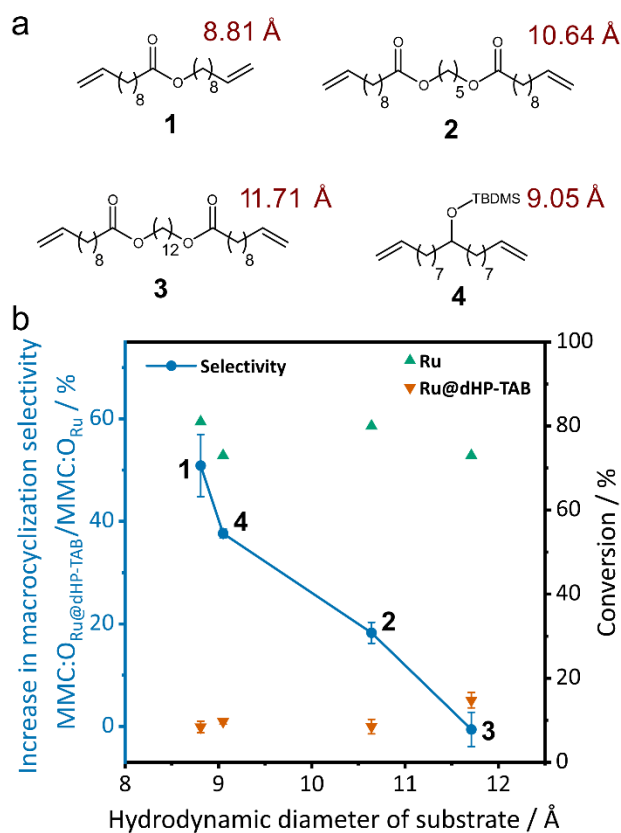
Figure 5.6. (a) Substrates **1-4** used in this study and their respective hydrodynamic radius (red) acc. to Ziegler *et al.*[16] (b) Correlation between the hydrodynamic radii of the substrates and increase in macrocyclization selectivity (blue) and conversion rate for the homogeneous (green) and heterogeneous catalyst (orange). The average of three reaction with **Ru@dHP-TAB** are displayed.

Ru-C distance is slighty elongated compared to the pure **Ru** complex, and the coordination number of this shell is increased. Since the changes cannot be explained by major structural modifications, they are assigned to the effect of the immobilization, such as pore wall interactions. This conclusion is backed by the results for **Ru@dHP-TAB** in benzene, where the structural alterations are reversed, as identified by structural parameters very similar to those of **Ru** in solution. Based on these observations, it can be concluded that neither the dissolution of the homogeneous complex in benzene nor the immobilization in a mesoporous COF led to significant changes of the complex structure, which stays intact after immobilization. Neither ligand dissociation nor an association can be observed.

After confirmation of the stability of the COF framework and its immobilized catalyst, metathesis reactions were carried out to determine the catalytic efficiency and the effect of the spatial confinement on MMC:O product selectivity. For this purpose metathesis reactions of four substrates (Figure 5.6, a), differing in their hydrodynamic radius[16] and polarity were performed with the homogeneous **Ru** complex (Figure 5.2, b) as well as with **Ru@dHP-TAB.** The reactions were carried out under identical conditions at 50 °C for 16 h in C_6D_6 using 0.5-mol% of catalyst and a substrate concentration of 25 mM; results are summarized in Table 5.1. Stability of the COF framework during catalysis conditions was confirmed by post-catalysis XRPD, nitrogen sorption, ICP-OES and TEM measurements of the isolated materials, showing the retention of crystallinity and porosity (Figure S9.2.11, S9.2.15, S9.2.28). While the framework remains intact, the formation of unstable Ru methylidene complexes occurring during the catalysis ultimately deactivates the immobilized catalyst and therefore prevents recyclability.

The immobilization significantly alters the productivity of the catalyst, reducing the overall conversion after 16 h reaction time from around 80% to around 10%. This reduction was consistent for all substrates, independent of their size. This drastically reduced productivity is attributed to diffusion limitations and catalyst decomposition occurring during the reaction. However, a size-dependent increase in selectivity MMC:O was found for the catalysis with **Ru@dHP-TAB** compared

to **Ru** (Figure 5.6, b). For the smallest substrate **1** (8.81 Å), an increase of 51% in the MMC:O ratio from 0.90 for **Ru** to 1.35 for **Ru@dHP-TAB** was found, corresponding to a 9 % increase in selectivity compared to the homogeneous catalyst system. Furthermore, a continuously reduced macro(mono)cyclization selectivity with increasing substrate size is observed. For substrate **4** (9.05 Å), with a very similar radius to **1**, the MMC:O ratio is increased by 38%. The very similar increase in selectivity for **1** and **4** with almost identical size but different polarity suggests that the polarity of the substrate has little influence on the reaction outcome. For the second largest substrate **2** (10.64 Å) only 18% are achieved and the largest substrate **3** (11.71 Å) shows the same selectivity when catalyzed by **Ru@dHP-TAB** compared to the homogeneous **Ru**. This considerable size effect is rationalized by the substrate diffusion limitation into the COF mesoporous pores with increasing hydrodynamic radius. In the case of larger substrates, the reaction is mostly catalyzed by catalyst bound on the outer surface and close to the pore openings, mimicking the homogeneous ring-chain equilibrium.[15] Smaller substrates can diffuse more easily and penetrate into the COF pores more deeply, where pore confinement effects can take place, favoring RCM for the ring-chain equilibrium products of the reaction by suppressing the formation of higher oligomers.[22,23]. This is likely due to the very large internal surface area of the highly porous COF material that offers enough "inner" pore surface area for this size selective confinement effect to take place and to alter the ring-chain equilibrium.

Table 5.1. Conversion, MMC:O ratio and selectivity for the RCM of substrate **1 - 4** by the action of **Ru** (0.5 mol-%) and **Ru@dHP-TAB** (0.5 mol-%) at 50 °C as determined by NMR (Figure S9.2.2-6).

Substrate	Conversion after 16h [%]		MMC:O		MMC Selectivity [%]	
	Ru	**Ru@ dHP-TAB**[a]	**Ru**	**Ru@ dHP-TAB**[a]	**Ru**	**Ru@ dHP-TAB**[a]
1	81	9	0.90	1.35	47	56
2	77	10	0.84	0.99	46	50
3	80	9	0.65	0.63	39	39
4	73	14	0.40	0.55	28	35

[a]Average over three performed reactions.

5.3. Conclusion

In summary, we have developed a phenylphenanthridine-based COF, containing accessible hydroxyl-groups on its protruding phenyl groups that allowed the successful immobilization of a Hoveyda-Grubbs-type catalyst in its pores to study possible pore confinement effects on the MMC selectivity during olefin metathesis reactions. The structure and ordered porosity of large-pore dHP-TAB COF with a pore size of 4.8 nm, suitable to accommodate both the bulky molecular catalyst and nm-sized substrates, was ascertained by XRPD analysis and nitrogen sorption experiments. The Ru-catalyst was effectively immobilized by simple silylation on hydroxyl-anchor groups integrated quantitatively in the framework and the retention of the catalyst's structure upon

immobilization was confirmed by XANES/EXAFS measurements. A set of four diene substrates for the metathesis reactions, differing in their hydrodynamic radius and polarity, were used to probe the pore confinement effect during the reaction. Our results reveal significant confinement effects, which significantly enhance the macrocyclization over oligomerization selectivity in the pores as compared to the homogeneous reaction. A clear trend between substrate size and MMC:O selectivity was found and can be attributed to a size-related, slower diffusion of the larger substrates into the pores, thus reducing the efficiency of confinement effects for the larger substrates while enhancing it for the smaller ones. Our results point to the possibility of tailoring the selectivity of metathesis and other size-sensitive catalytic reactions by adjusting the subtle interplay between the size and polarity of both the COF pores and the substrates used for catalysis.

5.4. Bibliography

[1]   M. S. Lohse, T. Bein, *Adv. Funct. Mater.* **2018**, *28*, 1705553.
[2]   X. Wang, L. Chen, S. Y. Chong, M. A. Little, Y. Wu, W. H. Zhu, R. Clowes, Y. Yan, M. A. Zwijnenburg, R. S. Sprick, A. I. Cooper, *Nat. Chem.* **2018**, *10*, 1180–1189.
[3]   B. P. Biswal, H. A. Vignolo-González, T. Banerjee, L. Grunenberg, G. Savasci, K. Gottschling, J. Nuss, C. Ochsenfeld, B. V. Lotsch, *J. Am. Chem. Soc.* **2019**, *141*, 11082–11092.
[4]   L. Ascherl, E. W. Evans, M. Hennemann, D. Di Nuzzo, A. G. Hufnagel, M. Beetz, R. H. Friend, T. Clark, T. Bein, F. Auras, *Nat. Commun.* **2018**, *9*, 3802.
[5]   S. Jhulki, J. Kim, I. C. Hwang, G. Haider, J. Park, J. Y. Park, Y. Lee, W. Hwang, A. A. Dar, B. Dhara, S. H. Lee, J. Kim, J. Y. Koo, M. H. Jo, C. C. Hwang, Y. H. Jung, Y. Park, M. Kataria, Y. F. Chen, S. H. Jhi, M. H. Baik, K. Baek, K. Kim, *J. Clean. Prod.* **2020**, *6*, 2035–2045.
[6]   Y. Ge, H. Zhou, Y. Ji, L. Ding, Y. Cheng, R. Wang, S. Yang, Y. Liu, X. Wu, Y. Li, *J. Phys. Chem. C* **2018**, *122*, 27495–27506.
[7]   Y. Zhi, Z. Wang, H. L. Zhang, Q. Zhang, *Small* **2020**, *16*, 2001070.
[8]   S.-Y. Ding, J. Gao, Q. Wang, Y. Zhang, W.-G. Song, C.-Y. Su, W. Wang, *J. Am. Chem. Soc.* **2011**, *133*, 19816–19822.
[9]   H. Xu, J. Gao, D. Jiang, *Nat. Chem.* **2015**, *7*, 905–912.
[10]   Q. Sun, Y. Tang, B. Aguila, S. Wang, F. Xiao, P. K. Thallapally, A. M. Al-Enizi, A. Nafady, S. Ma, *Angew. Chemie* **2019**, *131*, 8762–8767.
[11]   J. Guo, D. Jiang, *ACS Cent. Sci.* **2020**, *6*, 869–879.
[12]   Q. Fang, S. Gu, J. Zheng, Z. Zhuang, S. Qiu, Y. Yan, Q. Fang, S. Gu, J. Zheng, Z. Zhuang, Y. S. Yan, S. Qiu, *Angew. Chem. Int. Ed.* **2014**, *53*, 2878 –2882.
[13]   B. Mitschke, M. Turberg, B. List, *Chem* **2020**, *6*, 2515–2532.
[14]   C. Heinis, *Nat. Chem. Biol.* **2014**, *10*, 696–698.
[15]   S. Monfette, D. E. Fogg, *Chem. Rev.* **2009**, *109*, 3783–3816.
[16]   F. Ziegler, J. Teske, I. Elser, M. Dyballa, W. Frey, H. Kraus, N. Hansen, J. Rybka, U. Tallarek, M. R. Buchmeiser, *J. Am. Chem. Soc.* **2019**, *141*, 19014–19022.
[17]   J. E. Jee, J. L. Cheong, J. Lim, C. Chen, S. H. Hong, S. S. Lee, *J. Org. Chem.* **2013**, *78*, 3048–3056.
[18]   S. T. Emmerling, R. Schuldt, S. Bette, L. Yao, R. E. Dinnebier, J. Kästner, B. V. Lotsch, *J. Am. Chem. Soc.* **2021**, *143*, 38, 15711–15722.
[19]   H. M. Rietveld, *J. Appl. Crystallogr.* **1969**, *2*, 65–71.
[20]   M. A. Gotthardt, R. Schoch, S. Wolf, M. Bauer, W. Kleist, *Dalt. Trans.* **2015**, *44*, 2052–2056.
[21]   M. Benedikter, J. Musso, M. K. Kesharwani, K. Leonard Sterz, I. Elser, F. Ziegler, F. Fischer, B. Plietker, W. Frey, J. Kastner, M. Winkler, J. van Slageren, M. Nowakowski, M. Bauer, M. R. Buchmeiser, *ACS Catal.* **2020**, *10*, 14810–14823.
[22]   U. Tallarek, J. Hochstrasser, F. Ziegler, X. Huang, C. Kübel, M. R. Buchmeiser, *ChemCatChem* **2021**, *13*, 281–292.

[23]   F. Ziegler, T. Roider, M. Pyschik, C. P. Haas, D. Wang, U. Tallarek, M. R. Buchmeiser, *ChemCatChem* **2021**, *13*, 2234–2241.

6. *In Situ* Monitoring of Mechanochemical Covalent Organic Framework Formation Reveals Templating Effect of Liquid Additive

Sebastian T. Emmerling,* Luzia S. Germann,* Patrick A. Julien, Igor Moudrakovski, Martin Etter, Tomislav Friščić, Robert E. Dinnebier, and Bettina V. Lotsch

Sebastian T. Emmerling, Luzia S. Germann, and Bettina V. Lotsch conceived the project. Sebastian T. Emmerling wrote the manuscript with assistance of Luzia S. Germann, Bettina V. Lotsch and with input from all other authors. Sebastian T. Emmerling and Luzia S. Germann designed the experiments, synthesized the materials and performed the *in situ* XRPD experiments and most of the analysis and evaluated the data. Martin Etter supervised the experiments at the P02.1 beamline at DESY. Patrick A. Julien performed the *in situ* Raman experiments and analysis with supervision of Tomislav Friščić. Luzia S. Germann performed the XRPD analysis and simulations with supervision of Robert E. Dinnebier. Igor Moudrakovski performed the solid-state NMR experiments. All authors assisted the analysis of their respective experiments and the overall discussion. Bettina V. Lotsch supervised the work.

Supporting information can be found in Chapter 9.3.
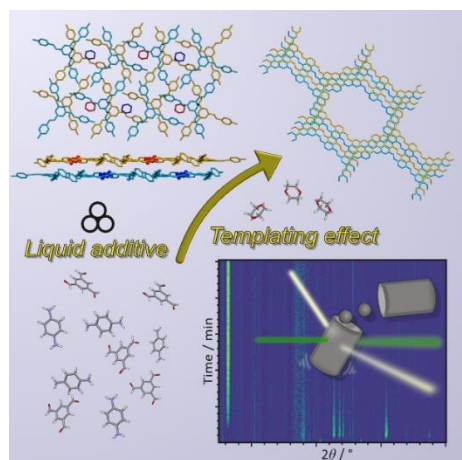
Figure 6.1. Table of content for the observation of key intermediates and liquid templating effect during mechanochemical COF formation.

Abstract

Covalent organic frameworks (COFs) have emerged as a new class of molecularly precise, porous functional materials characterized by broad structural and chemical versatility, with a diverse range of applications. Despite their increasing popularity, fundamental aspects of COF formation are poorly understood, lacking profound experimental insights into their assembly. Here, we use a combination of *in situ* X-ray powder diffraction and Raman spectroscopy to elucidate the reaction mechanism of mechanochemical synthesis of imine COFs, leading to the observation of key reaction intermediates that offer direct experimental evidence of framework templating through liquid additives. Moreover,

the solid-state catalyst scandium triflate is instrumental in directing the reaction kinetics and mechanism, yielding COFs with crystallinity and porosity on par with solvothermal products. This work provides the first experimental evidence of solvent-based COF templating and is a significant advance in mechanistic understanding of mechanochemistry as a green route for COF synthesis.

6.1. Introduction

Covalent organic frameworks (COFs) are an emergent class of organic solids whose advanced properties result from a tunable, molecularly precise backbone, paired with porosity and crystallinity.[1,2] The reticular assembly of molecular building blocks with inherently different sizes, shapes, and flexibility into two- (2D) or three-dimensional (3D) frameworks of increasingly complex structures and topologies allows for the tailored design of functional materials with targeted properties. The so far proposed applications of COFs are many, including gas storage and separation,[3–5] heterogeneous catalysis,[6–9] photocatalysis,[10–12] fuel cells,[13,14] and sensing.[15–17] COFs are typically synthesized by solution methods, *e.g.* solvothermally, sonochemically, by microwave irradiation or in continuous flow,[18] and more recently also by electron beam irradiation,[19] as well as by mechanochemistry.[20–23]

Mechanochemistry, *i.e.* the application of mechanical agitation to conduct and sustain chemical and materials transformations, has recently been established as a cornerstone of green, solvent-free chemistry.[24–26] Mechanochemical synthesis has successfully been applied to a wide range of reactions, including the formation of nanoparticles,[27] molecular cages,[28] small molecules,[29] cocrystals,[30,31] solid electrolytes,[32] coordination polymers,[33] as well as metal-organic frameworks (MOFs)[34] and COFs.[20–23] Synthesis by mechanochemistry is not only highly efficient for accessing new, metastable solid phases,[34] but is also a superior technique to screen for and explore the phase landscape of new polymorphs or organic and metal-organic solids.[35,36] Bulk mechanochemical reactions are usually performed by either direct grinding of reactants (neat grinding), or in the presence of minuscule amounts of grinding additives, as in liquid-assisted grinding (LAG).[37] Recently, mechanistic studies of mechanochemistry have been facilitated by the development of methods for *in situ* monitoring using synchrotron X-ray powder diffraction (XRPD),[38,39] Raman spectroscopy,[40,41] X-ray absorption spectroscopy,[42] solid-state nuclear magnetic resonance spectroscopy (ssNMR),[43] and/or thermal measurements.[44] This has enabled rapid progress in fundamental understanding of mechanochemical processes and the discovery of new materials.[45]

Although COFs are well established, mechanistic and time-resolved studies of their formation are rare. While previous work has mostly focused on characterization,[46–48] post-synthetic modifications and transformations of COFs,[49–51] only a handful of reports so far have investigated the underlying crosslinking, particle growth, and self-assembly processes.[52–57] Here we report the first real-time mechanistic study of mechanochemical COF formation using time-resolved *in situ*

Scheme 6.1. (a) Schematic representation of imine COF synthesis starting from an amine and aldehyde precursor. (b) Combinations of C_2 and C_3 as well as C_3 and C_3 linkers resulting in reticular 2D hexagonal COF structures. (c) Representation of the amine and aldehyde linkers used throughout this study. Symbol for mechanochemistry (three balls) adapted from Rightmire and Hanusa.[58]

synchrotron XRPD and Raman spectroscopy. A library of four different 2D hexagonal imine COFs based on C_2 and C_3 linkers were chosen as model systems (Scheme 6.1), with only one system (COF-LZU1) previously prepared mechanochemically.[20] The effects of liquid additive and catalyst on reaction kinetics and product formation were investigated, revealing pronounced effects on COF formation, regarding both the reaction kinetics and mechanism, as well as crystallinity of the products. The time-resolved *in situ* experiments led to the observation of crystalline reaction intermediates, which provided the first direct structural evidence of templating effects by the liquid additive, highlighting the role and critical importance of the presence of small solvent molecules during COF synthesis.

6.2. Results and Discussion

Real-time *in situ* XRPD measurements were performed using an X-ray energy of 60 keV (λ = 0.207 Å) at the Powder Diffraction and Total Scattering beamline P02.1 at the Deutsches Elektronen-Synchrotron (DESY),[58] using a modified Retsch MM400 ball mill operating at a frequency of 30 Hz.[38] The reactions were carried out in custom-made 5 mL volume X-ray transparent poly(me-

Figure 6.2. (a to d) Background subtracted 2D XRPD plots for the mechanochemical reaction of COF-LZU1 (a), TbBd-COF (b), IISERP-COF4 (c), and N-COF (d) using AcOH as catalyst. Calculated XRPD patterns of reactants, **1**, **2**, and COFs are shown below and above the 2D plots (λ = 0.207 Å). Diffraction of PMMA is visible by the broad signal around 1.7 °2θ, marked by an asterisk. Artefacts from background subtraction appear at ca. 1.1 and 2.6 °2θ in (a) due to background subtraction. (e) Normalized integrated peak intensities of COF-LZU1 and **1** (top) and TbBd-COF and **2** (bottom).

thyl methacrylate) (PMMA) milling jars, enabling direct, real-time monitoring of the mechanochemical COF formation with a time resolution of 10 or 20 s. We used a combination of different C_2 and C_3 amine and aldehyde linkers, forming four different hexagonal 2D imine COFs (Scheme 6.1). Reactions were performed with one 7 mm diameter stainless steel ball (1.38 grams weight), using a 1,4-dioxane/mesitylene mixture (1:1 v/v) as a liquid additive, with either aqueous acetic acid (AcOH) or scandium(III) triflate (Sc(OTf)$_3$) as a catalyst. The optimal reaction conditions were extensively screened prior to the beamtime by maximizing the measured diffraction intensities of the as-synthesized COFs in laboratory XRPD measurements. This step was crucial to improve the diffraction signal of the weakly scattering light-element based COFs sufficiently for real-time, *in situ* studies (Figure S9.3.6-11 in Supplemental Experimental Procedure, SEP).

In situ monitoring of COF formations

In situ monitoring of mechanochemical COF-LZU1[9] formation was performed by milling *p*-phenylenediamine (*p*PDA) with 1,3,5-triformylbenzene (Tb) in the presence of a 1,4-dioxane/mesitylene mixture (1:1 v/v) using AcOH as catalyst with the ratio of liquid additive volume to reactant weight (η-parameter)[37] of 0.60 µL/mg. Unexpectedly, the formation of COF-LZU1 proceeded via
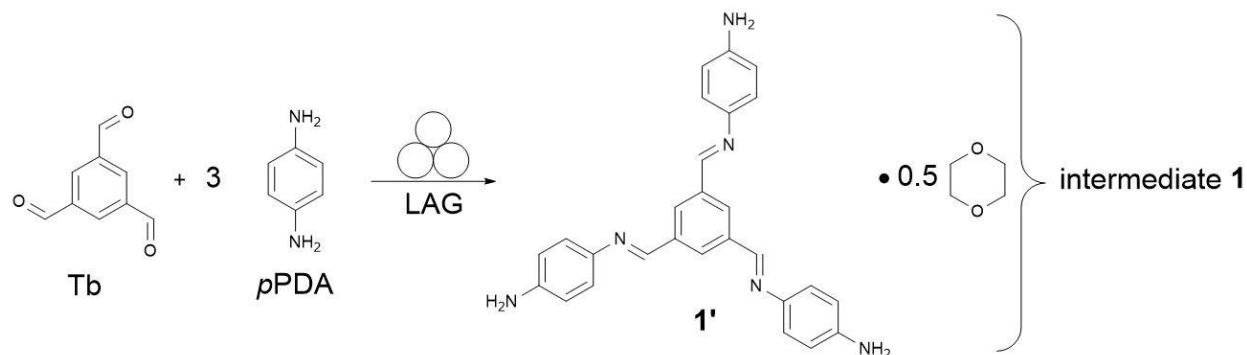
Scheme 6.2. Mechanochemical formation of intermediate **1** (a crystalline dioxane solvate of **1'**) by milling Tb with three eq. pPDA, requiring 1,4-dioxane as liquid additive.

a reaction intermediate (**1**), visible by the appearance of new Bragg reflections at 2.3, 2.4, 2.5, and 3.2 °2θ (Figure 6.2, a). This previously unknown phase was later identified and characterized by *ex situ* XRPD and spectroscopic techniques (Figures S9.3.1, S9.3.33-34, and S9.3.37-38). The COF formation was readily followed by integrating the most intense 100 reflection of the COF and the Bragg reflections of the intermediate. The intermediate formed immediately upon grinding, simultaneously with the loss of pPDA signal and only traces of Tb were observable after ca. 3 minutes. The 100 X-ray reflection of the COF appeared after ca. 3 mins with the intensity initially growing fast and slowing down after ca. 15 min of milling, to produce a sigmoidal reaction profile.[59] The reaction was found to be complete after ca. 25 min, coinciding with the disappearance of the diffraction signal of **1** (Figure 6.2, b). The XRPD pattern of the sample measured *ex situ* showed the formation of COF-LZU1 in accordance with previous reports (Figure S9.3.15).[9,60]

Next, the isoreticular TbBd-COF[61] was synthesized by milling benzidine (Bd), an extended linear diamine linker, with Tb. Mechanochemical formation of TbBd-COF was conducted using a 1,4-dioxane/mesitylene (1:1, v/v) mixture with 6 M AcOH as catalyst (η = 0.61 µL/mg). As for COF-LZU1, the COF formation proceeds via a reaction intermediate (**2**), with corresponding diffraction signals at 2.4, 2.6, 2.9, 3.0, 3.2, and 3.8 °2θ (Figure 6.2, b). The reaction was readily followed by integrating the most intense Bragg reflections of the intermediate and TbBd-COF. The diffraction signals of the reactants were barely visible after few minutes of milling, with signals of an intermediate appearing after ca. 4 min. The COF formation was found to be significantly slower in comparison to COF-LZU1, likely due to lower reactivity of the amine linker Tb compared to pPDA. The COF diffraction signals started to appear after an initial induction time of ca. 10 min, with those of the intermediate persisting for up to 60 min of milling (Figure 6.2, b, e). The measured *ex situ* XRPD pattern of the milled sample shows the successful formation of TbBd-COF, in accordance with previous reports (Figure S9.3.15).[61]

The third COF in the series of C_3-C_2 linkers, IISERP-COF4,[62] was obtained by milling 2,4,6-tris(4-aminophenyl)-1,3,5-triazine (TAT) with terephthaladehyde (BDA) in the presence of 1,4-dioxane/mesitylene (1:1 v/v) as a liquid additive, and using 6 M AcOH as a catalyst (η = 0.94 µL/mg) (Figure 6.2, c). No reaction intermediate was observed in this case and the reaction was readily

followed by integrating the most intense Bragg reflections of the reactants and the 100 X-ray reflection of the IISERP-COF4 product (Figure 6.2, c and S9.3.13, a). Notably, the second most intense 110 X-ray reflection was also observed during *in situ* monitoring (Figure 6.2, c and S9, a). The formation of the COF starts after an induction period of ca. 10 min, with an initially steep growth rate, and is complete after 40 minutes of milling time. Full consumption of the TAT reactant was only achieved after milling for around 60 minutes. Measured *ex situ* XRPD pattern shows the formation of IISERP-COF4, in accordance with literature reports (Figure S9.3.15).[62]

Next, we monitored the mechanochemical formation of N-COF[63] by milling the two C_3 components TAT and Tb together in a 1:1 ratio, in the presence of a 1,4-dioxane/mesitylene (1:1 v/v) mixture and 6 M AcOH as a catalyst (η = 0.73 µL/mg) (Figure 6.2, d). The reaction was readily followed by integrating the most intense Bragg reflections of the reactants and the 100 reflection of the N-COF product (Figure S9.3.14, b). There was no evidence for the appearance of a crystalline intermediate during the synthesis. The COF formation was first observed after an induction period of ca. 4 minutes, with an initial fast formation rate over the first 20 minutes and subsequently entering a continuous growth regime (Figure 6.2, d). The reaction did not reach completion within the measurement time frame of 80 minutes, as evident by the remaining diffraction peaks of the TAT solid reactant. The XRPD pattern measured *ex situ* confirms the formation of the N-COF product, in accordance with previous reports (Figure S9.3.15).[63]

Structure Elucidation of Reaction Intermediates

We attempted to separately synthesize and *ex situ* characterize the first reaction intermediate **1** using reaction conditions identical to those used during *in situ* monitoring of COF-LZU1 synthesis. Subsequent analysis of the reaction mixture after 3 min of milling failed due to poor XRPD data quality, with time-resolved XRPD measurements showing that the mixture further polymerized into a poorly crystalline COF-LZU1 over several hours (Figure S9.3.5). *In situ* Raman monitoring under similar reaction conditions indicated that the first reaction step constitutes an imine condensation reaction, visible by the appearance of a strong Raman band at 1623 cm^{-1}, assigned to the $\nu_{C=N}$ vibration (Figures S9.3.24-25). Further milling led to an increase in baseline of the Raman spectra, likely caused by fluorescence associated with the assembly of the COF-LZU1 conjugated π-system (Figure S9.3.23). Since the diffraction signal of the Tb linker coexisted with intermediate **1** during the time-resolved synchrotron XRPD experiments, we considered that **1** might be a condensation product of *p*PDA and Tb in a stoichiometric ratio greater than one. Indeed, milling of Tb and *p*PDA in the respective stoichiometric ratio 1 to 3 ratio produced a phase-pure sample of the intermediate **1** (Scheme 6.2). The crystal structure of **1** was successfully solved *ab initio* from *ex situ* XRPD data (Figure S9.3.1), revealing the formation of a triple imine condensation product of Tb (**1'**) as a solvate with 0.5 equivalents of 1,4-dioxane per molecular formula. This composition was further confirmed by liquid- and ssNMR, Fourier-transform infrared (FT-IR) and high-resolution mass spectroscopy, as well as by thermogravimetric analysis (TGA, see ESI). Intermediate **1** crystallizes in the triclinic space group $P\bar{1}$ with one molecule of **1'** and

a

b
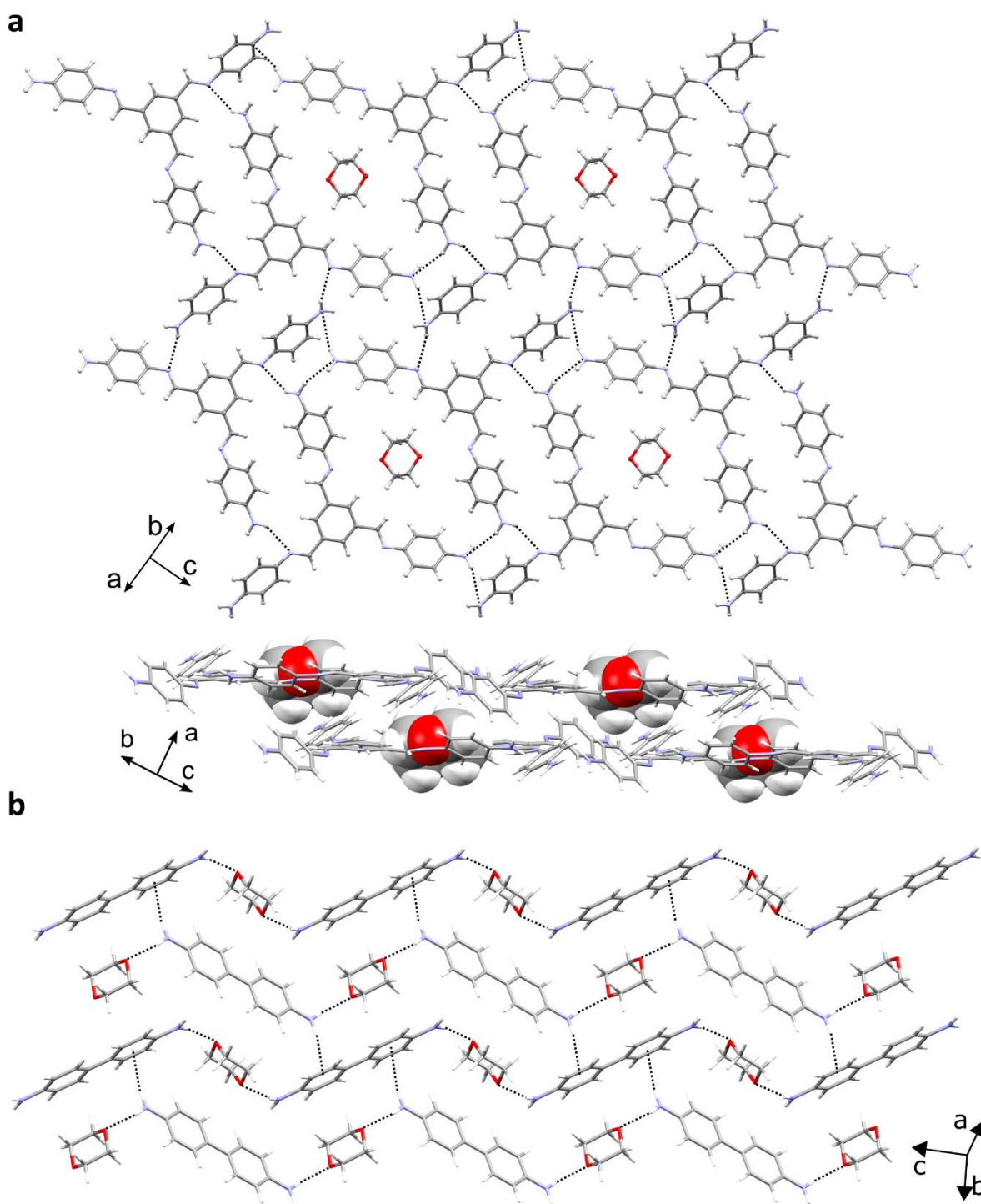
Figure 6.3. (a) Crystal structures of reaction intermediate **1** with view onto one hydrogen bonded layer (top) and perpendicular to it (bottom). (b) Crystal structures of reaction intermediate **2**. Hydrogen bonds and N-H⋯π interactions are represented by dashed lines.

half a 1,4-dioxane molecule in the asymmetric unit. The molecules of **1'** form a layered hydrogen-bonded network, in which two amine groups interact with adjacent imine functionalities, while the third amine forms a weak N-H⋯π hydrogen bond (Figure 6.3, a). This is in good agreement with

the ^{15}N ssNMR spectrum, where two signals for the three crystallographically inequivalent amine groups are observed (Figures S9.3.38-39). Adjacent hydrogen-bonded layers are mutually offset by ½ of the crystallographic repeat unit. Prominently, 1,4-dioxane molecules are embedded between two **1'** molecules forming rhombohedrally-shaped cavities (Figure 6.3, a). The described structure of **1** can conceptually be "transformed" into the final COF-LZU1 product by rotation and/or translation of **1'** units within the hydrogen-bonded layer, and cross-linking by additional Tb linkers (Figure 6.4 and S9.3.3). In this process, 1,4-dioxane acts as a template for the subsequent pore formation in the assembly of the COF-LZU1 framework.

The non-solvated **1'** was readily obtained by milling in the absence of any liquid or catalyst (Scheme S1), with the liquid and ssNMR spectra being essentially the same as for **1**, except for the absence of 1,4-dioxane signals (Figures S9.3.33-41 and S9.3.64). While the crystal structure of **1'** could not be determined due to poor crystallinity (Figure S9.3.4), physicochemical characterization suggests the presence of two polymorphic forms. The ^{13}C and ^{15}N ssNMR spectra indicate that two phases with identical chemical connectivity, but slightly different intermolecular arrangement are present (Figures S9.3.40-41). These differences with respect to the well-organized
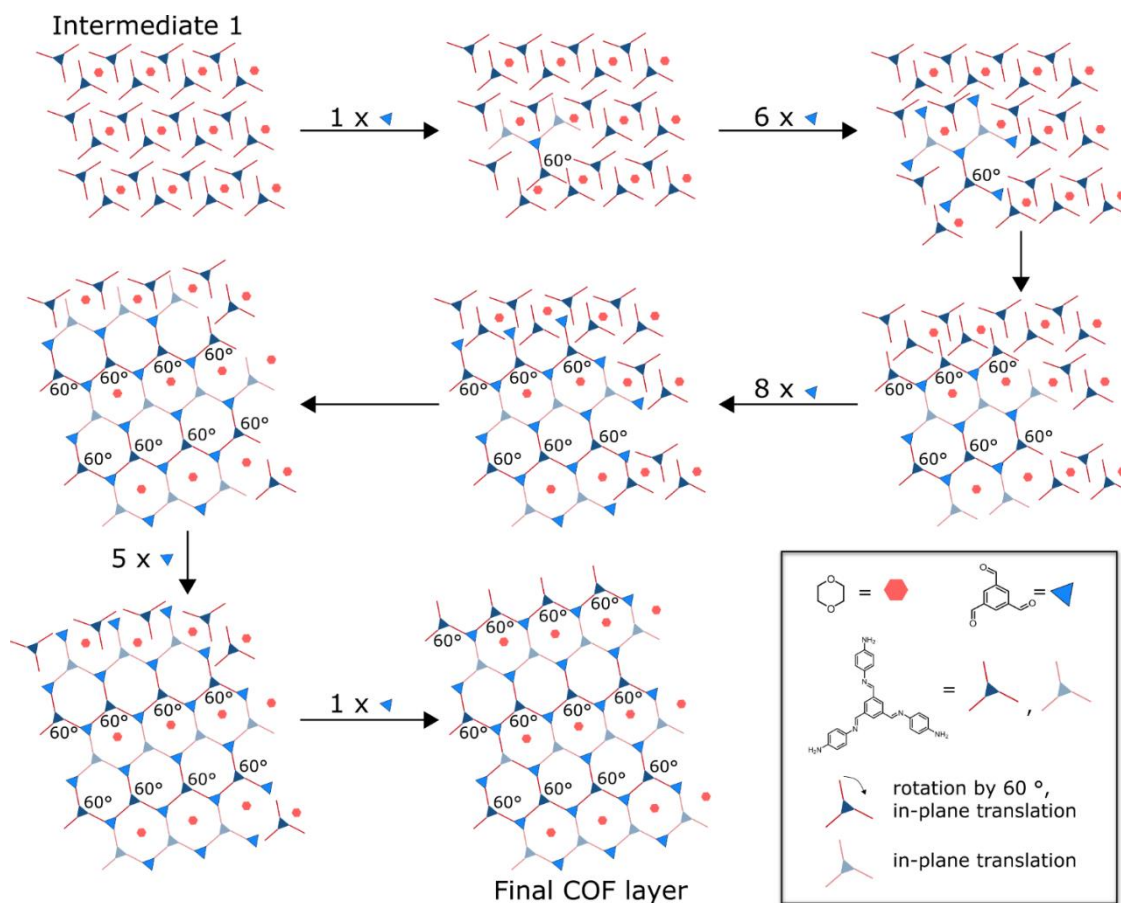
Figure 6.4. Schematic representation of the stepwise transformation from intermediate **1** into a layer of COF-LZU1 by molecular rearrangements and addition of remaining Tb linker. The **1'** units are of different color, depending on whether they were rotated by 60° and translated (dark blue), or solely translated (light blue).
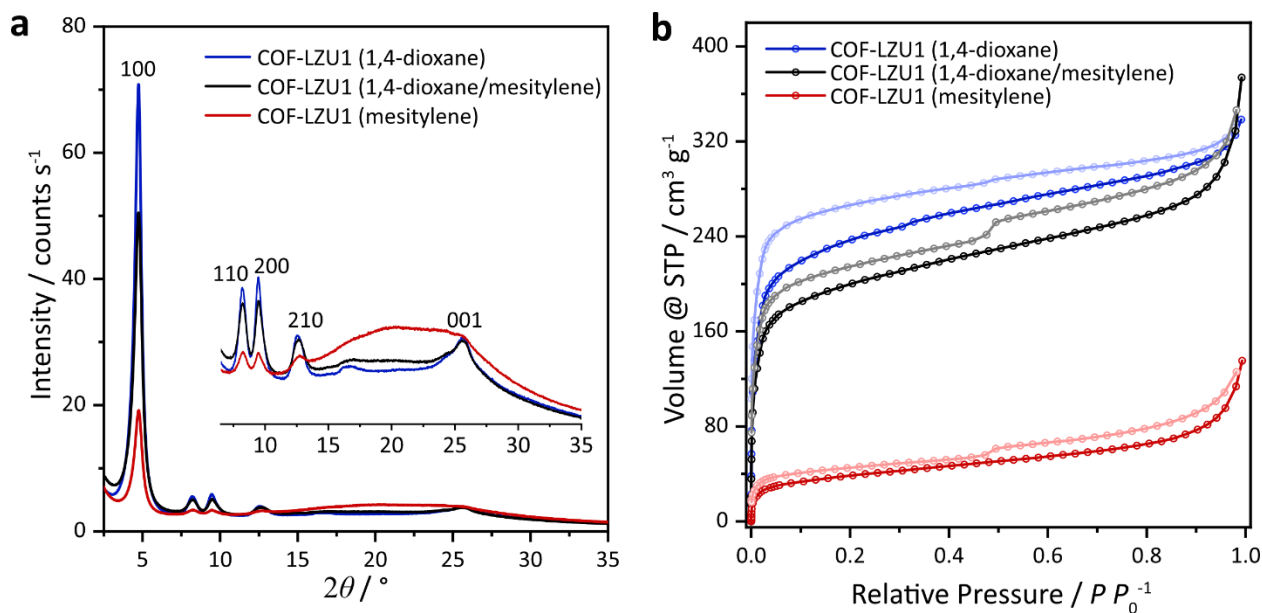
Figure 6.5. (a) Comparison of measured XRPD (λ = 1.54 Å) patterns using different solvent mixtures. (b) N_2 isotherms at 77 K using different solvent mixtures. COF-LZU1 synthesis using either pure 1,4-dioxane (blue curve), a 1,4-dioxane/mesitylene mixture (black curve), or pure mesitylene (red curve) as LAG additives.

structure of **1** further reinforce the view that 1,4-dioxane molecules act as structure-directing agents during milling with a profound influence on crystallinity and molecular arrangement.

Different experimental conditions were screened for the preparation of the compound **2**, which was first observed during *in situ* XRPD monitoring of the mechanochemical TbBd-COF synthesis. Compound **2** only formed as the main phase by milling solely Bd in the presence of 1,4-dioxane. Different grinding additives led to different phases: neat grinding or grinding with aqueous AcOH lead to a polymorphic transformation of Bd, and the additional appearance of a new phase in the case of AcOH, while reactions with 1,4-dioxane as the liquid additive produced **2** (Figure S9.3.22). The formation of different crystalline phases or polymorphs using different grinding additives is well-known in organic mechanochemistry.[35] The crystal structure of **2** was determined through *ab initio* XRPD structure solution and subsequently geometry optimized using periodic density functional theory (DFT) calculations (Figure S9.3.2). Compound **2** was characterized using liquid- and ssNMR, as well as FT-IR spectroscopy (Figure S9.3.29, S9.3.42-S43). It was found to be a 1,4-dioxane solvate of benzidine, crystallizing in the monoclinic space group $P2_1/c$ with both Bd and 1,4-dioxane molecules lying on a crystallographic center of inversion (Table S9.3.1). The crystal structure is composed of hydrogen-bonded zig-zag chains along the *c*-axis with alternating molecules of Bd and 1,4-dioxane, forming amine – ether N-H$\cdots$O hydrogen bonds ($d_{N\cdots O}$ = 3.02 Å). All adjacent supramolecular chains have a slight offset to each other, described by glide planes, which enables a weak N-H$\cdots\pi$ interaction between neighboring chains (Figure 6.3, b).

Influence of Liquid Additives

To further investigate the influence of liquid additives on mechanochemical COF formation and potentially templating, additional *ex situ* milling studies were performed by changing the liquid additive. Specifically, either pure mesitylene, 1,4-dioxane, or their mixture were used as an additive while keeping the volume of liquid to reactant mass constant (η = 0.6 μL/mg). Notably, the LAG experiments with either mesitylene or 1,4-dioxane as a liquid additive led to the formation of COF-LZU1, as confirmed by laboratory XRPD measurements using CuKα_1 radiation (Figure 6.5, a and S9.3.20-21). However, COF-LZU1 prepared with pure mesitylene exhibited significantly lower crystallinity compared to the materials obtained with 1,4-dioxane, lacking the 001 reflection at ca. 26° 2θ (Figure 6.5, a), associated with COF layer stacking. This indicates the loss of structural coherence perpendicular to the stacking planes. Moreover, the sample exhibited a very broad diffraction signal around 21° 2θ, typical for materials with amorphous content. These trends in crystallinity are in good agreement with porosity measurements, where the Brunauer–Emmett–Teller (BET) surface areas (S_{BET}) for the materials synthesized with pure 1,4-dioxane (S_{BET} = 880 $m^2 g^{-1}$) or a 1,4-dioxane/mesitylene mixture (S_{BET} = 757 $m^2 g^{-1}$) are significantly higher compared to that for the product obtained using pure mesitylene (S_{BET} = 138 $m^2 g^{-1}$) (Figure 6.5, b). The increased crystallinity and surface area in samples prepared in the presence of 1,4-dioxane are attributed to the formation of intermediate **1**, where the 1,4-dioxane embedded in rhombohedrally-shaped cavities acts as a template for the COF pore formation. The pre-orientation of the layered hydrogen-bonded units of **1** facilitates the final condensation step and layer assembly through templating, which consequently improves the overall crystallinity of the COF product. Moreover, the displacement of layers in **1** is expected to prohibit strong π-π interactions between molecular building blocks, which were previously found to prohibit high crystallinity due to creation and locking-in of defects.[56,64] While templating effects in COF formation have been proposed in previous theoretical work,[56] our results represent, to the best of our knowledge, the first experimental evidence of solvent templating during COF formation. Notably, our results also suggest that the liquid additive mixture could even be simplified to pure 1,4-dioxane, meaning that complex mixtures involving high-boiling solvents are not always necessary for COF synthesis, at least when using mechanochemistry.

Influence of Catalyst

We further explored the influence of the catalyst on the mechanism and kinetics of COF synthesis. Matsumoto *et al.* previously reported the use of metal triflates "*as superior catalysts for imine-linked COF formation*" and high activity for transamination in solution, leading to a significant reduction in reaction time. While different metal triflates have been used, the highest crystallinity and surface areas have been reported with the strong Lewis acid Sc(OTf)$_3$.[65] Therefore, all *in situ* monitoring experiments were repeated by replacing aqueous AcOH with solid Sc(OTf)$_3$ as a catalyst. In all *in situ* monitored reactions, 0.06 equivalents of Sc(OTf)$_3$ were used with respect to the corresponding amine components. While the overall reaction pathway was mostly unaffected
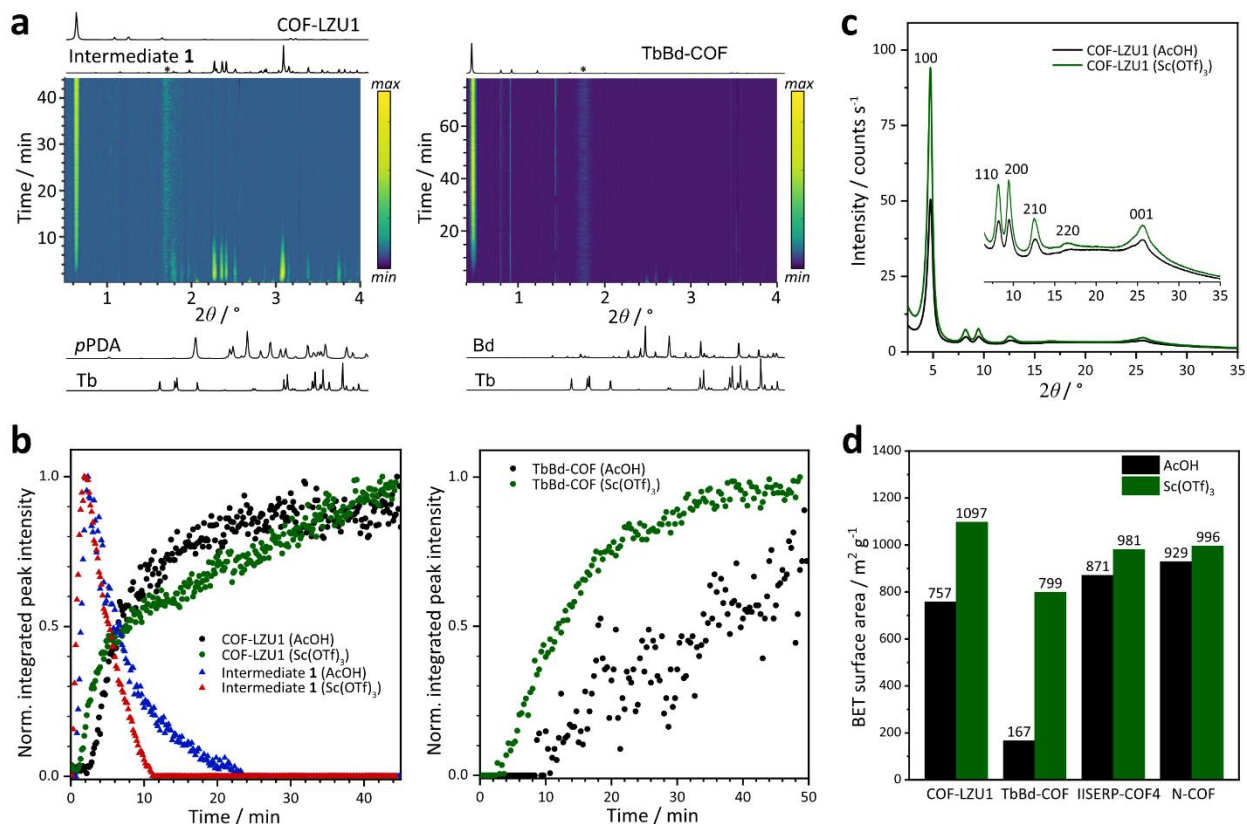
Figure 6.6. (a) Background subtracted 2D XRPD plots for the mechanochemical reaction of COF-LZU1 (left) and TbBd-COF (right) using Sc(OTf)$_3$ as catalyst. Diffraction of PMMA is visible by the broad peak around 1.7° 2θ, marked by an asterisk. Artefacts from background subtraction appear at ca. 0.8, 0.9, and 1.4 °2θ due to background subtraction. (b) Comparison of the normalized integrated peak intensities of **1** and COF-LZU1 (left) derived from the *in situ* monitoring using AcOH (black and blue) and Sc(OTf)$_3$ (green and red) as catalyst and of TbBd-COF (right) using AcOH (black) and Sc(OTf)$_3$ (green) as catalyst. (c) Measured *ex situ* XRPD patterns (λ = 1.54 Å) of COF-LZU1 using different catalysts. (d) Comparison of BET surface areas of COF samples prepared with either AcOH or Sc(OTf)$_3$ as catalyst determined by N$_2$ sorption experiments at 77 K.

by the choice of catalyst, the reaction kinetics, as well as crystallinity of the final COFs, were improved.

The appearance of intermediate **1** was observed in the synthesis of COF-LZU1 also when using the catalyst Sc(OTf)$_3$: **1** formed immediately upon milling, with the diffraction signal of COF-LZU1 appearing after ca. one min (Figure 6.6, a). The diffraction signal of **1** completely vanished within 12 min, *i.e.* in approximately half of the time compared to the reaction catalyzed by AcOH (ca. 25 min). The intensity of the 100 Bragg reflection of COF-LZU1 increased throughout the entire experiment, even after the consumption of **1** (Figure 6.6, b). The continuous increase in diffracted intensity might arise from a continued error correction mechanism in which Sc(OTf)$_3$ acts as a transimination catalyst to improve overall framework crystallinity (Figure 6.6, c).[66]

The induction times for the synthesis of most other COF systems were reduced significantly, by a factor of two or more, when using Sc(OTf)$_3$ as a catalyst (Figure 6.6, b and S9.3.12-14). The synthesis of TbBd-COF was most significantly affected by the change in catalyst, both through a

reduction in the induction time, as well as an increase in the rate of product formation. The TbBd-COF formation started after an induction period of only ca. 3 min without proceeding *via* intermediate **2** and was found to reach completion after ca. 30 minutes using $Sc(OTf)_3$. This is a significant change compared to the process in the presence of AcOH, in which the diffraction signal of the COF appeared only after ca. 30 min, still exhibited only a weak scattering signal after 60 min, and with **2** observable throughout the entire experiment.

The absence of **2** in the reaction based on $Sc(OTf)_3$ is explained by the increased efficiency of imine formation and thus consumption of Bd before solvate **2** can form. These findings illustrate that different reaction pathways may open up as a function of liquid and catalyst choice. We further explored the influence of using $Sc(OTf)_3$ catalyst on the properties of the mechanochemically synthesized COFs. The replacement of AcOH with $Sc(OTf)_3$ as catalyst led to materials with not only improved crystallinity (Figure 6.6, c and S9.3.16-19), but also generally higher S_{BET} values (Figure 6.6, d and S9.3.44-63). This was most evident for TbBd-COF, which exhibited an increase in S_{BET} of 475 %. These results are in good agreement with our *in situ* studies, which showed an increased rate of COF formation. Interestingly, while previous purely mechanochemical COF syntheses reported a qualitatively lower crystallinity and significantly lower porosity ($S_{BET} < 300$ m^2 g^{-1}) compared to the respective solvothermal syntheses,[20–22] the herein presented results show that the opposite is also possible (Table 6.1). Most notably, the surface area of mechanochemically made IISERP-COF4 exceeds that reported for the solvothermally obtained product by almost 40 %, independent of the catalyst choice. Also, the surface area of COF-LZU1 made with $Sc(OTf)_3$ was found to be almost 2.7 times higher ($S_{BET} = 1097$ m^2 g^{-1}) than most literature values for solvothermally made material ($S_{BET} = 410$ m^2 g^{-1}),[9] but is still somewhat lower compared to products from other synthetic strategies, where S_{BET} values of 1523 m^2 g^{-1} have been reported (Table 6.1).[60,67] It is noteworthy, however, that the latter materials required much longer synthesis times, between 48-120 h, whereas the milling reaction was found to be complete within an hour. The increase in S_{BET} in comparison to previously reported cases of mechanochemical COF synthesis are attributed to a milder activation process. Activation under harsher conditions, *e.g.* solvent exchange and heating under vacuum, are known to lead to a collapse of the framework pore structure through the action of capillary forces, and consequently to a reduction or loss of porosity.[68] This strongly depends on the polarity of the used solvent, as well as on the framework stability.[69] In contrast, the use of supercritical CO_2 ($scCO_2$) is considered a mild activation strategy, which due to very low capillary forces, enables the retention of framework structural integrity during activation.[68]

Overall, the use of $Sc(OTf)_3$ as a catalyst for imine formation exhibits clear advantages in terms of reaction times and measured surface areas, offering a valuable alternative to AcOH for COF mechanosynthesis. Fine-tuning of reaction conditions, followed by activation with $scCO_2$, enabled

the mechanochemical preparation of COFs that are on an equal footing with solvothermally synthesized materials, while introducing the benefits of significantly reduced reaction times, milder reaction conditions, and improvement in scale.

Table 6.1. Pore sizes and comparison of surface areas of mechanochemically synthesized COFs with literature values of solvothermally synthesized pendants.

COF	Pore size[a] / nm	Mechanochemical synthesis with AcOH S_{BET}(AcOH) / $m^2 g^{-1}$	Mechanochemical synthesis with Sc(OTf)$_3$ S_{BET}(Sc(OTf)$_3$) / $m^2 g^{-1}$	Reported values S_{BET} / $m^2 g^{-1}$
COF-LZU1	1.9	757	1097	410[9], 1523[60]
TbBd-COF	2.2	167	799	1948[61]
IISERP-COF4	3.2	871	981	716[62]
N-COF	1.5	929	996	1163[63]

[a]calculated by DFT derived from N$_2$ sorption isotherms. See also Figure S9.3.39-58.

6.3. Conclusion

In conclusion, we reported the first *in situ* studies of mechanochemical COF formation, providing the first direct experimental evidence of solvent-based templating effects during framework assembly. Specifically, using 1,4-dioxane as a component of the liquid additive in a mechanochemical reaction led to the observation of crystalline solvate reaction intermediates in the syntheses of both COF-LZU1 and TbBd-COF frameworks. The intermediate in TbBd-COF synthesis is the result of a competing reaction, which can occur due to slow imine bond formation and is suppressed by using Sc(OTf)$_3$ as a catalyst. In contrast, the intermediate in the formation of the COF-LZU1 framework is a solvated form of a triple imine condensation product, organized in the solid state around 1,4-dioxane molecules that act as templates for subsequent pore formation. The layered molecular arrangement in the solvate does not only inhibit initial π-π stacking during the early stages of the self-assembly, an effect that is known to lower the overall crystallite size,[64] but also promotes the formation of 2D COF sheets. The herein observed formation of a triple imine condensation product offers potential new opportunities for rational design of mixed-linker COFs, as recently seen for mixed-metal MOFs.[70] Finally, our study reveals pronounced effects of the catalyst choice – AcOH vs Sc(OTf)$_3$ – on COF formation, both regarding reaction kinetics, mechanism and product crystallinity, due to the high activity of mediating imine formation and

transimination.[65] Notably, a combination of Sc(OTf)$_3$ as a catalyst and mild activation with super-critical CO$_2$ results in COFs with surface areas that can match and even exceed those reported for solvothermally made frameworks, which generally require higher reaction temperatures, longer times, and the use of bulk solvents.

Our results highlight the potential of mechanochemical synthesis not only as a materials-efficient, green and potentially scalable synthetic route, but reveal the subtle interplay between liquid additives, catalyst choice, and activation procedure in the synthesis of COFs, which often follows standardized procedures owing to the lack of mechanistic insights. Utilizing the power of templated COF synthesis through the targeted formation of intermediates thus enables a more rational design of COFs by utilizing a toolbox of non-covalent interactions and directed self-assembly.

6.4. Bibliography

[1]   M. S. Lohse, T. Bein, *Adv. Funct. Mater.* **2018**, *28*, 1705553.
[2]   O. M. Yaghi, *ACS Cent. Sci.* **2019**, *5*, 1295–1300.
[3]   K. Gottschling, L. Stegbauer, G. Savasci, N. A. Prisco, Z. J. Berkson, C. Ochsenfeld, B. F. Chmelka, B. V. Lotsch, *Chem. Mater.* **2019**, *31*, 1946–1955.
[4]   H. Furukawa, O. M. Yaghi, *J. Am. Chem. Soc.* **2009**, *131*, 8875–8883.
[5]   J. T. Yu, Z. Chen, J. Sun, Z. T. Huang, Q. Y. Zheng, *J. Mater. Chem.* **2012**, *22*, 5369–5373.
[6]   H. Xu, J. Gao, D. Jiang, *Nat. Chem.* **2015**, *7*, 905–912.
[7]   M. Mu, Y. Wang, Y. Qin, X. Yan, L. Li, L. Chen, *ACS Appl. Mater. Interfaces* **2017**, *9*, 22856–22863.
[8]   H. Xu, X. Chen, J. Gao, J. Lin, M. Addicoat, S. Irle, D. Jiang, *Chem. Commun.* **2014**, *50*, 1292–1294.
[9]   S.-Y. Ding, J. Gao, Q. Wang, Y. Zhang, W.-G. Song, C.-Y. Su, W. Wang, *J. Am. Chem. Soc.* **2011**, *133*, 19816–19822.
[10]   T. Banerjee, F. Haase, G. Savasci, K. Gottschling, C. Ochsenfeld, B. V. Lotsch, *J. Am. Chem. Soc.* **2017**, *139*, 16228–16234.
[11]   X. Wang, L. Chen, S. Y. Chong, M. A. Little, Y. Wu, W. H. Zhu, R. Clowes, Y. Yan, M. A. Zwijnenburg, R. S. Sprick, A. I. Cooper, *Nat. Chem.* **2018**, *10*, 1180–1189.
[12]   B. P. Biswal, H. A. Vignolo-González, T. Banerjee, L. Grunenberg, G. Savasci, K. Gottschling, J. Nuss, C. Ochsenfeld, B. V. Lotsch, *J. Am. Chem. Soc.* **2019**, *141*, 11082–11092.
[13]   H. B. Aiyappa, J. Thote, D. B. Shinde, R. Banerjee, S. Kurungot, *Chem. Mater.* **2016**, *28*, 4375–4379.
[14]   C.-Y. Lin, L. Zhang, Z. Zhao, Z. Xia, *Adv. Mater.* **2017**, *29*, 1606635.
[15]   H. Singh, V. K. Tomer, N. Jena, I. Bala, N. Sharma, D. Nepak, A. De Sarkar, K. Kailasam, S. K. Pal, *J. Mater. Chem. A* **2017**, *5*, 21820–21827.
[16]   W. Li, C. X. Yang, X. P. Yan, *Chem. Commun.* **2017**, *53*, 11469–11471.
[17]   Z. Zhou, W. Zhong, K. Cui, Z. Zhuang, L. Li, L. Li, J. Bi, Y. Yu, *Chem. Commun.* **2018**, *54*, 9977–9980.
[18]   Y. Peng, W. K. Wong, Z. Hu, Y. Cheng, D. Yuan, S. A. Khan, D. Zhao, *Chem. Mater.* **2016**, *28*, 5095–5101.
[19]   M. Zhang, M. Zhang, M. Zhang, J. Chen, S. Zhang, X. Zhou, L. He, M. V. Sheridan, M. Yuan, M. Zhang, L. Chen, X. Dai, F. Ma, J. Wang, J. Hu, G. Wu, X. Kong, R. Zhou, T. E. Albrecht-Schmitt, Z. Chai, S. Wang, *J. Am. Chem. Soc.* **2020**, *142*, 9169–9174.
[20]   B. P. Biswal, S. Chandra, S. Kandambeth, B. Lukose, T. Heine, R. Banerjee, *J. Am. Chem. Soc.* **2013**, *135*, 5328–5331.
[21]   G. Das, D. Balaji Shinde, S. Kandambeth, B. P. Biswal, R. Banerjee, *Chem. Commun.* **2014**, *50*, 12615–12618.
[22]   D. B. Shinde, H. B. Aiyappa, M. Bhadra, B. P. Biswal, P. Wadge, S. Kandambeth, B. Garai, T. Kundu, S. Kurungot, R. Banerjee, *J. Mater. Chem. A* **2016**, *4*, 2682–2690.

[23]   S. Karak, S. Kandambeth, B. P. Biswal, H. S. Sasmal, S. Kumar, P. Pachfule, R. Banerjee, *J. Am. Chem. Soc.* **2017**, *139*, 1856–1862.

[24]   T. Friščić, C. Mottillo, H. M. Titi, *Angew. Chemie Int. Ed.* **2020**, *59*, 1018–1029.

[25]   S. L. James, C. J. Adams, C. Bolm, D. Braga, P. Collier, T. Friščic, F. Grepioni, K. D. M. Harris, G. Hyett, W. Jones, A. Krebs, J. Mack, L. Maini, A. G. Orpen, I. P. Parkin, W. C. Shearouse, J. W. Steed, D. C. Waddell, *Chem. Soc. Rev.* **2012**, *41*, 413–447.

[26]   D. DeSantis, J. A. Mason, B. D. James, C. Houchins, J. R. Long, M. Veenstra, *Energy and Fuels* **2017**, *31*, 2024–2032.

[27]   P. Baláž, M. Achimovicová, M. Baláž, P. Billik, C. Z. Zara, J. M. Criado, F. Delogu, E. Dutková, E. Gaffet, F. J. Gotor, R. Kumar, I. Mitov, T. Rojac, M. Senna, A. Streletskii, W. C. Krystyna, *Chem. Soc. Rev.* **2013**, *42*, 7571–7637.

[28]   M. Leonardi, M. Villacampa, J. C. Menéndez, *Chem. Sci.* **2018**, *9*, 2042–2064.

[29]   A. Bruckmann, A. Krebs, C. Bolm, *Green Chem.* **2008**, *10*, 1131–1141.

[30]   T. Friščič, W. Jones, *Cryst. Growth Des.* **2009**, *9*, 1621–1637.

[31]   D. Hasa, W. Jones, *Adv. Drug Deliv. Rev.* **2017**, *117*, 147–161.

[32]   N. V. Kosova, N. F. Uvarov, E. T. Devyatkina, E. G. Avvakumov, *Solid State Ionics* **2000**, *135*, 107–114.

[33]   C. Cappuccino, F. Farinella, D. Braga, L. Maini, *Cryst. Growth Des.* **2019**, *19*, 4395–4403.

[34]   A. D. Katsenis, A. Puškarić, V. Štrukil, C. Mottillo, P. A. Julien, K. Užarević, M. H. Pham, T. O. Do, S. A. J. Kimber, P. Lazić, O. Magdysyuk, R. E. Dinnebier, I. Halasz, T. Friščić, *Nat. Commun.* **2015**, *6*, 1–8.

[35]   D. Hasa, E. Miniussi, W. Jones, *Cryst. Growth Des.* **2016**, *16*, 4582–4588.

[36]   L. S. Germann, M. Arhangelskis, M. Etter, R. E. Dinnebier, T. Friščić, *Chem. Sci.* **2020**, 10092–10100.

[37]   T. Friščić, S. L. Childs, S. A. A. Rizvi, W. Jones, *CrystEngComm* **2009**, *11*, 418–426.

[38]   T. Friščić, I. Halasz, P. J. Beldon, A. M. Belenguer, F. Adams, S. A. J. Kimber, V. Honkimäki, R. E. Dinnebier, *Nat. Chem.* **2013**, *5*, 66–73.

[39]   I. Halasz, S. A. J. Kimber, P. J. Beldon, A. M. Belenguer, F. Adams, V. Honkimäki, R. C. Nightingale, R. E. Dinnebier, T. Friščić, *Nat. Protoc.* **2013**, *8*, 1718–1729.

[40]   D. Gracin, V. Štrukil, T. Friščić, I. Halasz, K. Užarević, *Angew. Chemie Int. Ed.* **2014**, *53*, 6193–6197.

[41]   L. Batzdorf, F. Fischer, M. Wilke, K.-J. Wenzel, F. Emmerling, *Angew. Chemie Int. Ed.* **2015**, *54*, 1799–1802.

[42]   P. F. M. de Oliveira, A. A. L. Michalchuk, A. G. Buzanich, R. Bienert, R. M. Torresi, P. H. C. Camargo, F. Emmerling, *Chem. Commun.* **2020**, *56*, 10329–10332.

[43]   J. G. Schiffmann, F. Emmerling, I. C. B. Martins, L. Van Wüllen, *Solid State Nucl. Magn. Reson.* **2020**, 101687.

[44]   K. Užarević, V. Štrukil, C. Mottillo, P. A. Julien, A. Puškarić, T. Friščić, I. Halasz, *Cryst. Growth Des.* **2016**, *16*, 2342–2347.

[45]   K. Užarević, I. Halasz, T. Friščić, *J. Phys. Chem. Lett.* **2015**, *6*, 4129–4140.

[46]   F. Haase, K. Gottschling, L. Stegbauer, L. S. Germann, R. Gutzler, V. Duppel, V. S. Vyas, K. Kern, R. E. Dinnebier, B. V. Lotsch, *Mater. Chem. Front.* **2017**, *1*, 1354–1361.

[47]   L. Ascherl, T. Sick, J. T. Margraf, S. H. Lapidus, M. Calik, C. Hettstedt, K. Karaghiosoff, M. Döblinger, T. Clark, K. W. Chapman, F. Auras, T. Bein, *Nat. Chem.* **2016**, *8*, 310–316.

[48]   Y. B. Zhang, J. Su, H. Furukawa, Y. Yun, F. Gándara, A. Duong, X. Zou, O. M. Yaghi, *J. Am. Chem. Soc.* **2013**, *135*, 16336–16339.

[49]   F. Haase, E. Troschke, G. Savasci, T. Banerjee, V. Duppel, S. Dörfler, M. M. J. Grundei, A. M. Burow, C. Ochsenfeld, S. Kaskel, B. V. Lotsch, *Nat. Commun.* **2018**, *9*, 1–10.

[50]   T. Jadhav, Y. Fang, C.-H. Liu, A. Dadvand, E. Hamzehpoor, W. Patterson, A. Jonderian, R. S. Stein, D. F. Perepichka, *J. Am. Chem. Soc.* **2020**, *142*, 8862–8870.

[51]   Y. Du, D. Calabro, B. Wooler, Q. Li, S. Cundy, P. Kamakoti, D. Colmyer, K. Mao, P. Ravikovitch, *J. Phys. Chem. C* **2014**, *118*, 399–407.

[52]   H. Li, A. D. Chavez, H. Li, H. Li, W. R. Dichtel, J. L. Bredas, *J. Am. Chem. Soc.* **2017**, *139*, 16310–16318.

[53]   I. Castano, A. M. Evans, H. Li, E. Vitaku, M. J. Strauss, J. L. Brédas, N. C. Gianneschi, W. R. Dichtel, *ACS Cent. Sci.* **2019**, *5*, 1892–1899.

[54]   B. J. Smith, N. Hwang, A. D. Chavez, J. L. Novotney, W. R. Dichtel, *Chem. Commun.* **2015**, *51*, 7532–7535.
[55]   R. L. Li, N. C. Flanders, A. M. Evans, W. Ji, I. Castano, L. X. Chen, N. C. Gianneschi, W. R. Dichtel, *Chem. Sci.* **2019**, *10*, 3796–3801.
[56]   B. T. Koo, R. F. Heden, P. Clancy, *Phys. Chem. Chem. Phys.* **2017**, *19*, 9745–9754.
[57]   C. Feriante, A. M. Evans, S. Jhulki, I. Castano, M. J. Strauss, S. Barlow, W. R. Dichtel, S. R. Marder, *J. Am. Chem. Soc.* **2020**, *142*, 18637–18644.
[58]   A. C. Dippel, H. P. Liermann, J. T. Delitz, P. Walter, H. Schulte-Schrepping, O. H. Seeck, H. Franz, *J. Synchrotron Radiat.* **2015**, *22*, 675–687.
[59]   E. Colacino, M. Carta, G. Pia, A. Porcheddu, P. C. Ricci, F. Delogu, *ACS Omega* **2018**, *3*, 9196–9209.
[60]   T. Shiraki, G. Kim, N. Nakashima, *Chem. Lett.* **2015**, *44*, 1488–1490.
[61]   M. C. Daugherty, E. Vitaku, R. L. Li, A. M. Evans, A. D. Chavez, W. R. Dichtel, *Chem. Commun.* **2019**, *55*, 2680–2683.
[62]   R. Gomes, P. Bhanja, A. Bhaumik, *Chem. Commun.* **2015**, *51*, 10050–10053.
[63]   P. Wang, Q. Xu, Z. Li, W. Jiang, Q. Jiang, D. Jiang, *Adv. Mater.* **2018**, *30*, 1801991.
[64]   V. Nguyen, M. Grünwald, *J. Am. Chem. Soc.* **2018**, *140*, 3306–3311.
[65]   M. Matsumoto, R. R. Dasari, W. Ji, C. H. Feriante, T. C. Parker, S. R. Marder, W. R. Dichtel, *J. Am. Chem. Soc.* **2017**, *139*, 4999–5002.
[66]   N. Giuseppone, J. L. Schmitt, E. Schwartz, J. M. Lehn, *J. Am. Chem. Soc.* **2005**, *127*, 5528–5539.
[67]   Y. Liao, J. Li, A. Thomas, *ACS Macro Lett.* **2017**, *6*, 1444–1450.
[68]   C. H. Feriante, S. Jhulki, A. M. Evans, R. R. Dasari, K. Slicker, W. R. Dichtel, S. R. Marder, *Adv. Mater.* **2020**, *32*, 1905776.
[69]   G. Ayoub, T. Islamoglu, S. Goswami, T. Friščić, O. K. Farha, *ACS Appl. Mater. Interfaces* **2019**, *11*, 15788–15794.
[70]   G. Ayoub, B. Karadeniz, A. J. Howarth, O. K. Farha, I. Lilović, L. S. Germann, R. E. Dinnebier, K. Užarević, T. Friščić, *Chem. Mater.* **2019**, *31*, 5494–5501.

7. NO as a Reagent for Topochemical Framework Transformation and Con-trolled Nitric Oxide Release in Covalent Organic Frameworks

The work in this chapter was published, reproduced, and adapted from:

NO as a Reagent for Topochemical Framework Transformation and Con-trolled Nitric Oxide Release in Covalent Organic Frameworks

Sebastian T. Emmerling,* Johannes Maschita,* Bettina V. Lotsch

*equally contributed

Sebastian T. Emmerling, Johannes Maschita and Bettina V. Lotsch conceived the project. Sebastian T. Emmerling wrote the manuscript with assistance of Johannes Maschita and Bettina V. Lotsch. Sebastian T. Emmerling and Johannes Maschita designed the experiments, synthesized the materials and performed the analysis and evaluated the data. All authors assisted the analysis of their respective experiments and the overall discussion. Bettina V. Lotsch supervised the work.

Supporting information can be found in Chapter 9.4.

Abstract

Covalent organic frameworks (COFs) have emerged as versatile platforms for the separation and storage of hazardous gases. Simultaneously, the synthetic toolbox to tackle the "COF trilemma" has been diversified to include topochemical linkage transformations and post-synthetic stabilization strategies. Herein, we converge these themes and reveal the unique potential of NO as a new reagent for the scalable gas-phase transformation of COFs. Using physisorption and solid-state nuclear magnetic resonance spectroscopy on ^{15}N-enriched COFs, we study the gas uptake capacity and selectivity of NO adsorption and unravel the interactions of NO with COFs. Our study reveals the clean deamination of terminal amine groups on the particle surfaces by NO, exemplifying a unique surface passivation strategy for COFs. We further describe the formation of a

Figure 7.1. Table of content figure for NO adsorption in COFs and its usage as reagent for surface passivation and topochemical framework transformation for controlled nitric oxide release in COFs

NONOate-linkage by the reaction of NO with an amine-linked COF, which shows controlled release of NO under physiological conditions. NONOate-COFs thus show promise as tunable NO delivery platforms for bioregulatory NO release in biomedical applications.

7.1. Introduction

Beginning in the late 1980s, nitric oxide (NO) gained increasing interest in biological research after its key role as signal molecule in various physiological processes in the human body was discovered.[1] While NO plays a significant role for human health by regulating blood pressure, wound healing, and neurotransmission,[2–5] it is more widely known as a (problematic) component of NO_x found in exhaust gases of combustion engines.[6] With increasing road traffic, agriculture productivity, or electricity generation, artificial NO pollution became almost omnipresent in the environment around us.[7–9] However, in contrast to the essential NO needed for physiological processes, in which NO rarely exceeds an internal concentration of 5 nM, the artificial presence of NO in our external environment can have adverse effects on human health.[10–12] The combustion-based NO_x emissions count as major air pollutants and as gaseous precursor of fine particulate matter ($PM_{2.5}$), which is considered a leading environmental health risk factor, associated with 3 to 4 million premature deaths each year and a significantly reduced life expectancy.[13] Environmental and healthcare organizations like the World Health Organization (WHO) repeatedly appeal for a reduction of air pollution and readjust their guidelines for $PM_{2.5}$ to lower levels.[14] Current strategies to reduce NO emissions are based on rare earth metal three-way catalysts, as found in automobiles, which reduce NO to nitrogen while simultaneously oxidizing noxious CO and hydrocarbons to CO_2.[15] Other strategies focus on capture and release systems, "washing" the exhaust gas by binding NO onto functional groups by forming nitrosamines, N-diazeniumdiolates (NONOates), and nitroso-metal-complexes.[16,17] The reversible formation of these species allows the subsequent controlled release and recycling of NO and can also be the basis of various pharmaceuticals.[18,19]

Recent advances in heterogeneous systems for NO release were made including surface-crafted polymers and silica particles with exposed NO-binding functional groups.[20–22] Lately, highly porous materials were discovered as candidates for NO removal *via* adsorption and chemisorption or as catalyst/catalyst support materials for NO decomposition.[23] Metal organic frameworks (MOF) have been developed as NO release materials utilizing either unsaturated and open metal sites or implemented amino functionalities to adsorb NO in their pores.[1,24,25]

Covalent organic frameworks (COFs) are recent additions to the class of highly porous framework materials.[26] Due to their high specific surface area, defined structure, high modularity and low density COFs could be promising candidates for NO adsorption/separation applications or as heterogeneous catalyst/catalyst support materials for NO decomposition.[27–29] Conductive COFs

have already been successfully used in chemiresistive sensor devices to detect NO and other harmful gases in the ppb range.[30,31]

Despite the possible applicability of COFs as functional materials for such applications, there remain concerns regarding their stability. Assembled into frameworks by reversible covalent bond formation, their stability against the reactive NO gas might be limited at these crucial points of connection. Especially early introduced and well-established linkages like boronic esters or imine bonds suffer from instability against harsher chemical conditions.[32] However, in recent years numerous novel linkages, post-synthetic-modifications and other stabilization strategies for COFs have been developed, broadening our tool-box to design materials that can be suitable for NO adsorption.[33–37]

In this work we determine the stability of four different COF linkages – imine, amine, thiazole, and imide – against NO exposure and examine their suitability for NO separation applications by calculating their specific selectivity against N_2 and CO_2. By targeted ^{15}N enrichment at the crucial COF-linkages, we investigate and identify chemical modifications in the COFs' frameworks induced by NO. These chemical modifications, including a novel type of linkage, are evaluated for their potential applications in COF chemistry and biomedical research.

7.2. Results and Discussion

To study the effect of NO on COFs, we synthesized four ^{15}N-enriched frameworks, namely TTI-COF, rTTI-COF, TTT-COF, and TT-Imide-COF (Figure 7.2),[33,37–39] which are all based on an enriched 4,4',4"-(1,3,5-triazine-2,4,6-triyl)trianiline-^{15}N linker (TT-$^{15}NH_2$, Figure 7.2). The isotope enrichment of the COFs enhances the sensitivity in ^{15}N CP-MAS solid-state nuclear magnetic resonance (ssNMR) spectroscopy and thus allows a detailed analysis of the respective linkages. This is essential since we expect these nitrogen sites to be the most reactive groups towards NO and therefore to constitute the most interesting moieties in the COFs during this study.
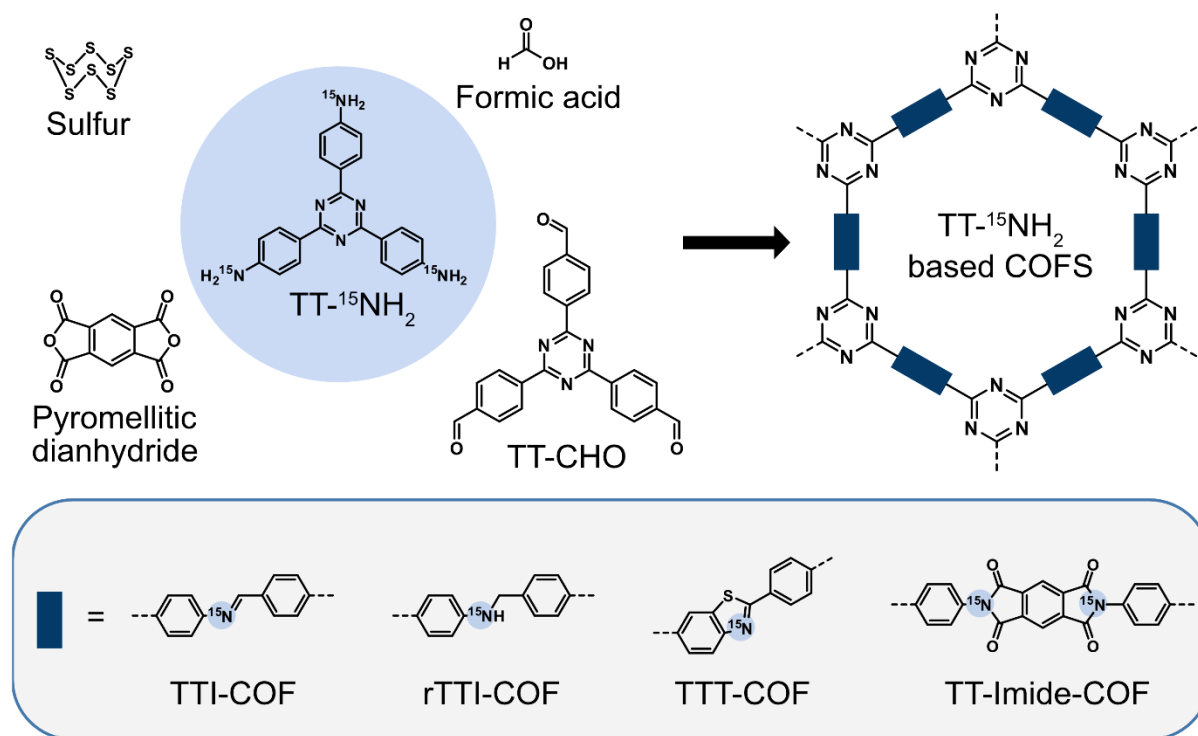
Figure 7.2. Synthesis of the four ^{15}N-enriched COFs TTI-COF, rTTI-COF, TTT-COF and TT-Imide-COF bearing imine, amine, thiazole, and imide linkages, respectively. All COFs are based on an enriched 4,4',4''-(1,3,5-triazine-2,4,6-triyl)trianiline-^{15}N linker, TT-^{15}NH$_2$, which was synthesized starting from 4-cyanobenzoyl chloride and ^{15}NH$_4$Cl (Scheme S1) in a three-step procedure with a good overall yield of 12.6 %.

NO Uptake

NO sorption measurements on ^{15}N-enriched COFs were performed starting at 298 K. In all cases, an initial high but only partially reversible adsorption capacity was found within the first adsorption cycle. In this first measurement COF-dependent uptakes between 1.5 and 6 mmol g^{-1} NO were observed. In addition, a steep adsorption slope below 2 kPa for TT-Imide-COF and TTI-COF (Figure 7.3, a and Figure S9.4.28), around 30 kPa for TTT-COF (Figure S9.4.32) and around 90 kPa for rTTI-COF was found (Figure S9.4.30). The steep uptake within the first cycle at different pressure points for each COF indicates differing mechanisms for the irreversible chemisorption of NO. Thus, in each case the hysteresis does not close to the initial point during the first measurement. Multiple adsorption and desorption cycles at 298 K show a strong decrease in NO uptake after the first cycle towards a fraction of the initial uptake. This trend of an initial high and irreversible NO uptake and its strong decline in further cycles indicates a chemisorption process of NO on the frameworks, consistent with a progressive quenching of the reactive sites.

For all frameworks, the decline in irreversible uptake of NO towards the second cycle is most prominent, while the following sorption cycles show only a small decrease which stabilizes after approximately three cycles (Figure S29, S31, S33, S34). To ensure reproducible NO physisorption data at different temperatures, all COFs were cycled seven times to ensure stabilization of
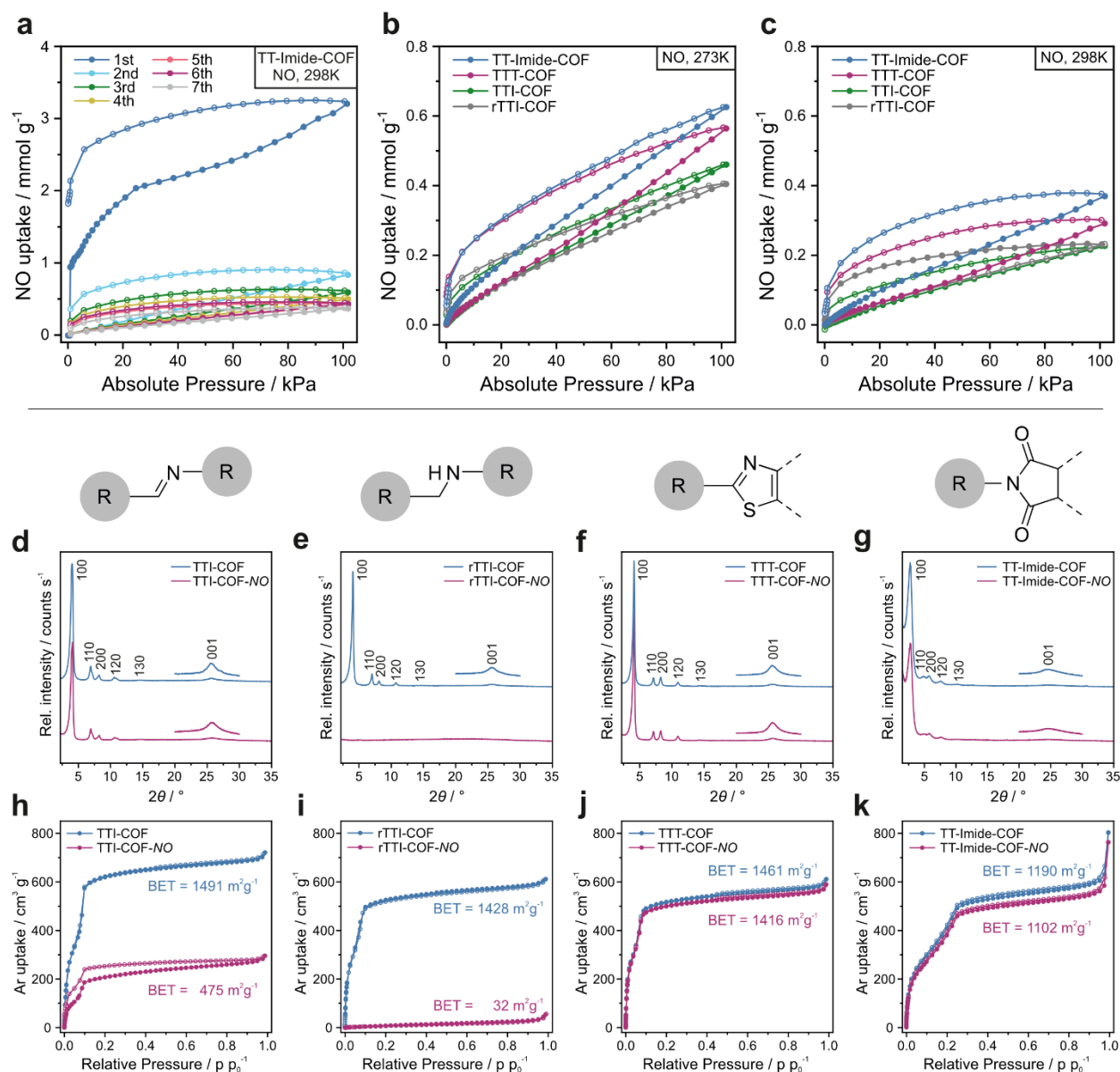
Figure 7.3. (a) NO-adsorption cycles of TT-Imide-COF. Comparison of stabilized NO-adsorption of TTI-COF, rTTI-COF, TTT-COF, and TT-Imide-COF at (b) 273 K and (c) 298 K after completing the 7th run. PXRD and argon sorption measurement at 87 K of TTI-COF (d,h), rTTI-COF (e,i), TTT-COF (f,j), and TT-Imide-COF (g,k) before (blue) and after (red) NO exposure. Filled circles represent the adsorption, empty circles the desorption.

the systems before measurements at 273 K, 288 K, and 298 K were performed (Figure 7.3, b, c and S9.4.35). In contrast to the initial NO sorption cycles, subsequent measurements show fully reversible isotherms for all four COFs indicating a saturation of the systems. Further, they reveal an unusual hysteresis due to delayed NO desorption visible for all temperatures and COFs.

The measured NO physisorption capacities at 298 K - ranging between 0.2 mmol g^{-1} and 0.4 mmol g^{-1} as compared to 1.5-6 mmol g^{-1} during initial uptake - are in good agreement with the values found for simulated NO adsorption isotherms for boronate ester-based COF-105 and COF-

108 by Wang *et al.*[40] Note that experimental values on NO sorption in COFs have not yet been reported.

Since the NO sorption measurements suggest a reaction of NO with the frameworks, we investigated the reactions occurring during contact with the highly reactive gas. At first, the stability of the COFs towards NO was evaluated by examining the materials after exposure. These will be labeled with -*NO* further on.

Powder X-ray diffraction (PXRD) analysis of the samples reveals that TTI-COF-*NO* becomes slightly less crystalline after NO exposure and rTTI-COF-*NO* turns amorphous (Figure 7.3, d, e). The Brunauer–Emmett–Teller specific surface area (S_{BET}) and specific pore volume (V_P) decreases for the imine-COF (Figure 7.3, h) from $S_{BET} = 1491$ m^2 g^{-1} ($V_P = 0.917$) to less than a third for the post-NO imine-COF with $S_{BET} = 475$ m^2 g^{-1} ($V_P = 0.376$). The amine-COF rTTI-COF (Figure 7.3, i) with initially $S_{BET} = 1428$ m^2 g^{-1} ($V_P = 0.778$) becomes non-porous after NO exposure with $S_{BET} = 32$ m^2 g^{-1} ($V_P = 0.071$ cm^3 g^{-1}). For TTT-COF and TT-Imide-COF (Figure 7.3, j, k) no changes in crystallinity after exposure are noticeable and the S_{BET} and pore volume of the samples decrease just by small amounts from 1461 m^2 g^{-1} ($V_P = 0.778$ cm^3 g^{-1}) to 1416 m^2 g^{-1} ($V_P = 0.750$ cm^3 g^{-1}) and from 1190 m^2 g^{-1} ($V_P = 0.802$ cm^3 g^{-1}) to 1102 m^2 g^{-1} ($V_P = 0.744$ cm^3 g^{-1}), respectively. For the latter, the Fourier-transform infrared (FT-IR) spectra before and after NO exposure show no difference (Figure S9.4.8-9). However, TTI-COF-*NO* displays a new band at 1699 cm^{-1}, a typical range for an aldehyde HC=O vibration, while otherwise remaining unchanged (Figure S9.4.6). The spectrum of rTTI-COF-*NO* shows significant changes compared to pristine rTTI-COF; most prominent is the appearance of three distinct bands at 1700 cm^{-1}, 1084 cm^{-1}, and 916 cm^{-1} (Figure S9.4.7). We also observed a color change of the sample after NO exposure. UV-Vis measurements reveal slightly altered absorption spectra for the post-NO COFs (Figure S9.4.19-22). The most obvious color changes were perceived for TTI-COF and rTTI-COF– both changing from yellow to brownish color. This analysis reveals that the thiazole and imide linkages are largely inert against NO exposure since the structural integrity and porosity of the respective COFs remains unaffected. In contrast, the imine and amine linkages seem to react to a varying degree with the gas, indicated by changes in the FT-IR spectra, resulting in a loss of structural integrity and porosity.

Narrowing down suitable COF linkages for NO adsorption and separation applications to thiazole and imide functionalities, we further investigated the physisorption performance and calculated the selectivity for NO compared to carbon dioxide by applying the ideal adsorption solution theory (IAST). Using the post-NO CO_2 adsorption isotherms as a reference, we calculated the initial heats of adsorption, Q_{st}, adsorption capacities, and IAST selectivities over nitrogen for CO_2 and NO (Table S9.4.1). For the selectivity calculations we chose a 15/85 gas mixture for CO_2/N_2 as commonly found in the literature,[41] and a 3/97 gas mixture for NO/N_2, due to the low abundance of NO in exhaust gas mixtures.[42] We calculated the IAST selectivity of CO_2 over nitrogen for TT-Imide-COF-*NO* and TTT-COF-*NO* as 9.22 and 6.44, respectively. The IAST selectivities of NO

over nitrogen were calculated to be 5.55 for the TT-Imide-COF-*NO* and 3.95 for TTT-COF-*NO*. Furthermore, the pressure dependent selectivties of a binary CO_2/NO (50/50) gas mixture were calculated (Figure S9.4.36, c). Overall, our results show that imide- and thiazole-linked COFs exhibit remarkable resistance to NO gas and are promising platforms for NO gas capture or separation. Moreover, these systems show significant IAST selectivity of NO uptake over N_2.

Solid-State NMR Analysis

Next, we turn our attention to the imine and amine linkages which are more susceptible to NO exposure. To deconvolute the irreversible chemisorption phenomenon during the first NO adsorption cycles and to gain insights into possible reactions involved, we performed ^{13}C and ^{15}N CP-MAS ssNMR experiments. Utilizing the high sensitivity of our ^{15}N-enriched COFs we were able to capture even less-sensitive species like the thiazole nitrogen and minor framework defects as will be discussed in the following.
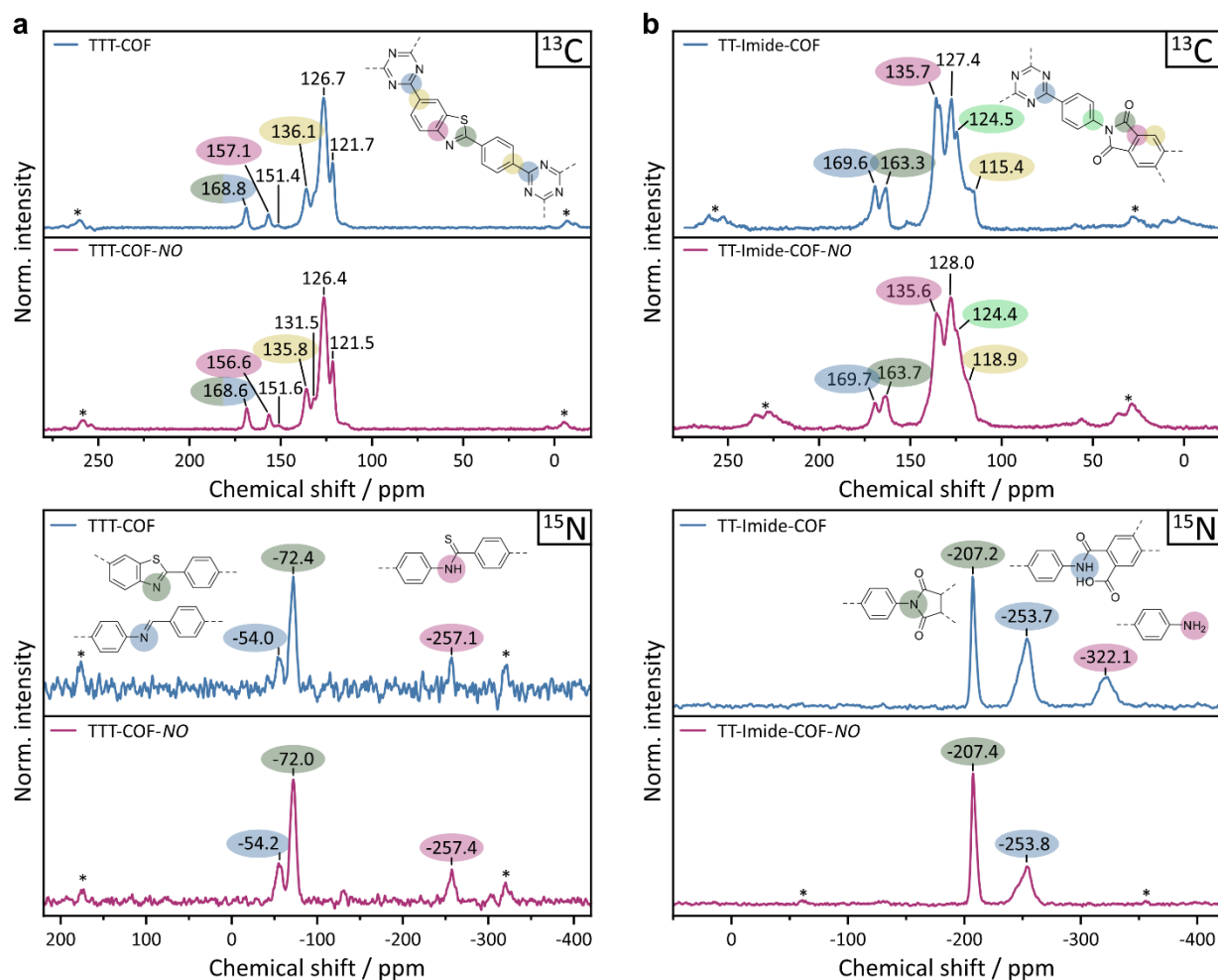
Figure 7.4. [13]C CP-MAS (top row) and ^{15}N CP-MAS ssNMR (bottom row) of (a) TTT-COF (blue) and TTT-COF-NO (red) and (b) TT-Imide-COF (blue) and TT-Imide-COF-NO (red).

a

b
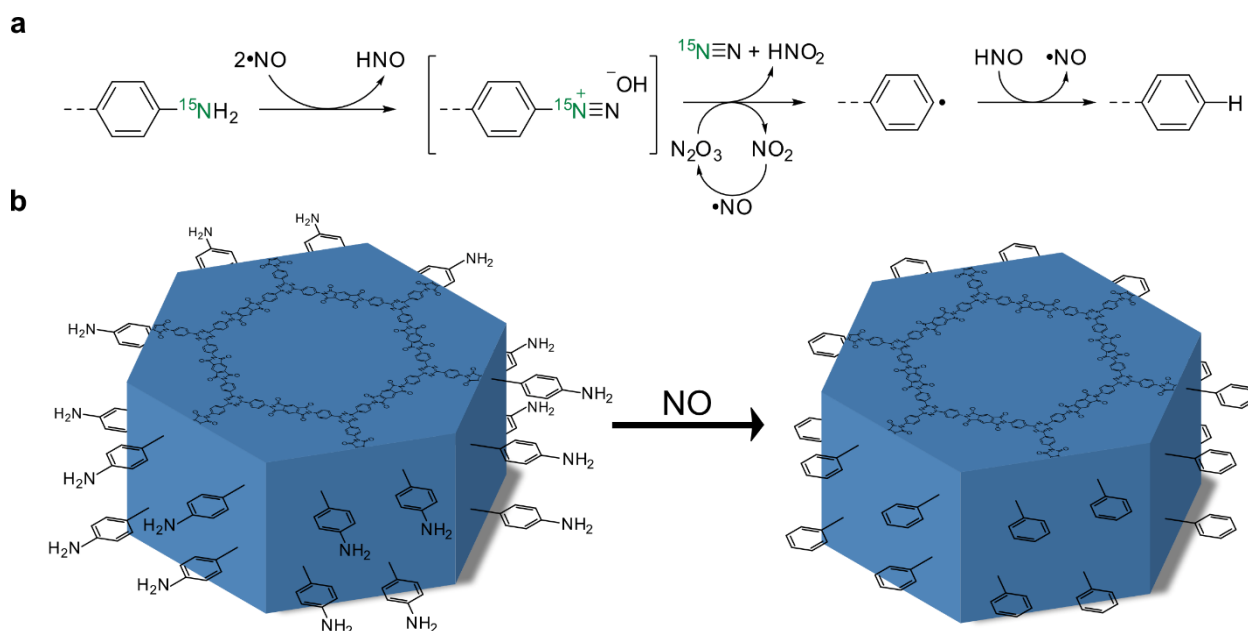
Figure 7.5. Proposed mechanism for deamination of arylamines upon NO exposure. First, a diazonium salt is formed in the reaction of the free amine with NO. This salt further reacts with catalytic amounts of N_2O_3 impurities in the NO gas, cleaving the diazonium moiety as dinitrogen and nitrous acid. The resulting phenyl radical is subsequently quenched by exposure to the nitroxyl released in the first step or any other proton-bearing volatile compound, like H_2O.[43] (b) Schematic representation of crystal surface passivation of terminal amines by NO-induced deamination.

As one of the NO resistant frameworks, TTT-COF-*NO* shows no visible changes in its ^{13}C and ^{15}N spectra compared to the pristine TTT-COF (Figure 7.4, a). Interestingly, the high sensitivity of our 15N measurements reveals small amounts of imine residuals at -54 ppm (Figure 7.4, a, bottom) that were not transformed into thiazole during the topochemical conversion. Another unexpected peak was found at -257 ppm, which we assign to a thioamide, the proposed intermediate of the topochemical conversion.[33] It should be noted that the intensities of both moieties are more pronounced in the CP-MAS experiments compared to thiazole due to polarization transfer from neighboring protons. The related signal for the imine bond in 13C CP-MAS ssNMR, expected at 151 ppm,[33] is barely visible. No obvious signs of the increased initial NO uptake are visible. Considering the relatively minor irreversible NO uptake of 1.5 mmol g-1 compared to the other COFs (3-6 mmol g-1), reactions of NO with remaining oligomer impurities, sulfur and/or remaining imine bonds, as observed for TTI-COF (infra vide), are plausible.

The 13C spectrum of TT-Imide-COF-NO resembles the spectrum of the pristine COF (Figure 7.4, b, top). A minor peak broadening is observed which might be a result of slightly increased structural disorder of the framework. The 15N-CP-MAS spectrum of TT-Imide-COF reveals three signals at -207 ppm, -254 ppm, and -322 ppm, assigned to the imide, the intermediate amic acid, and the remaining terminal amine nitrogen at the crystallite edges, respectively (Figure 7.4, b, bottom). However, only the imide signal is observed in a (quantitative) direct excitation experiment, suggesting that the proton-bearing species constitute a minor side phase and are overemphasized due to their sensitivity in CP-MAS experiments (Figure S9.4.11). Upon exposure to NO, the signal at -322 ppm, assigned to terminal amine groups, vanished completely, giving the first

direct indication for a chemical reaction of the framework with the adsorbate. Furthermore, the relative intensity of the amide at -254 ppm is lowered compared to the imide at 207 ppm after NO treatment. Lacking any new signals, we suspect a clean conversion of the amines by NO, passivating the crystallite surface edges, according to a proposed denitrogenation radical reaction mechanism depicted in Figure 7.5 based on findings of Itoh *et al.* on the deamination of aniline.[43]

First, a diazonium salt is formed in the reaction of the free amine with NO. This salt further reacts with catalytic amounts of N_2O_3 impurities in the NO gas, cleaving the diazonium moiety as dinitrogen and nitrous acid. The resulting phenyl radical is subsequently quenched by exposure to the nitroxyl released in the first step or any other proton-bearing volatile compound, like H_2O. Due to the deamination of the enriched ^{15}N the amine peak disappears and no new signal is visible. We envision that this interaction between the free amine groups and the NO gas could be used as a rational surface passivation strategy to purposefully remove the remaining and potentially reactive amine sites. Clearing the COF's surface from terminal amines could be of particular interest when their chemical reactivity or electronic properties hinder or alter the targeted properties of the framework (e.g., in catalysis), especially when exposed at the crystal surface.
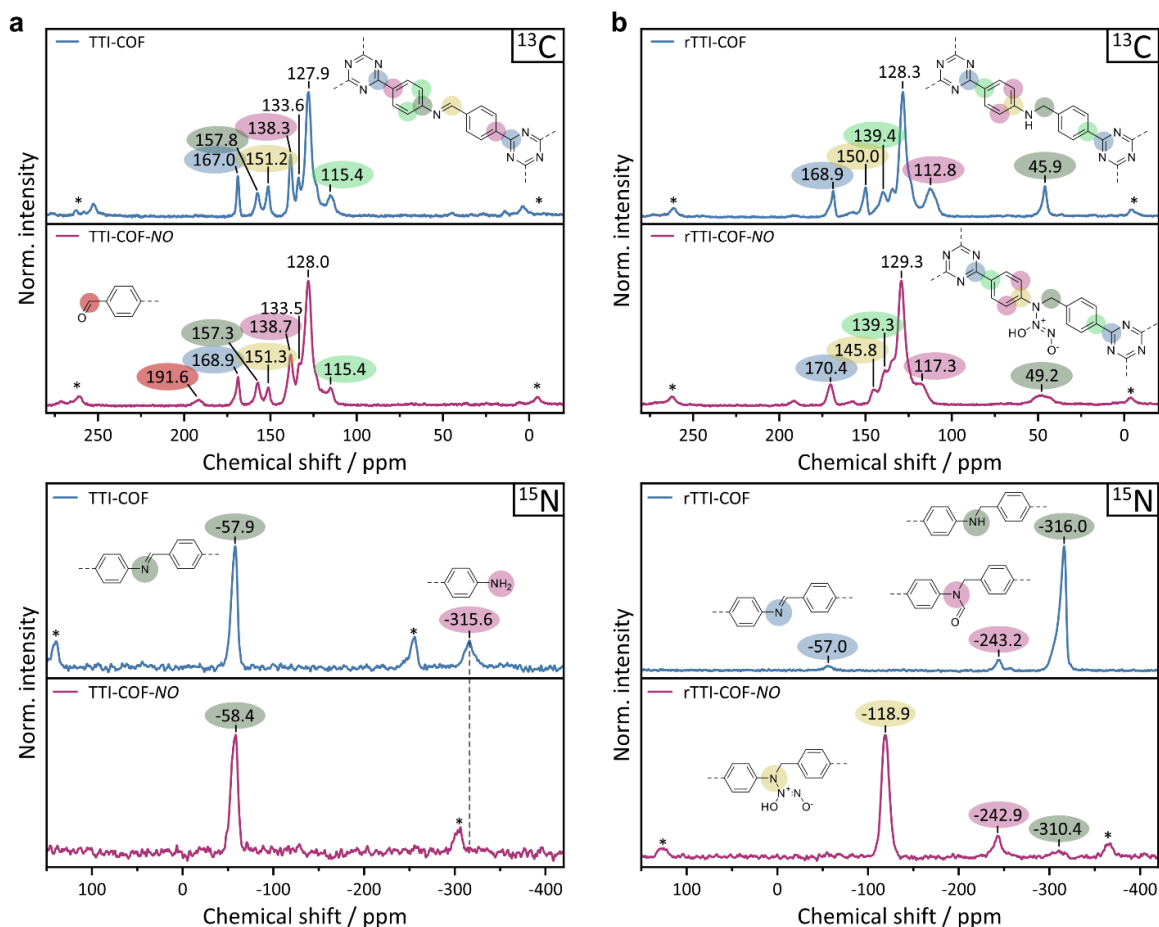
Figure 7.6. ^{13}C (top row) and ^{15}N CP-MAS (bottom row) ssNMR of (a) TTI-COF (blue) and TTI-COF-NO (red) and (b) rTTI-COF (blue) and rTTI-COF-NO (red).
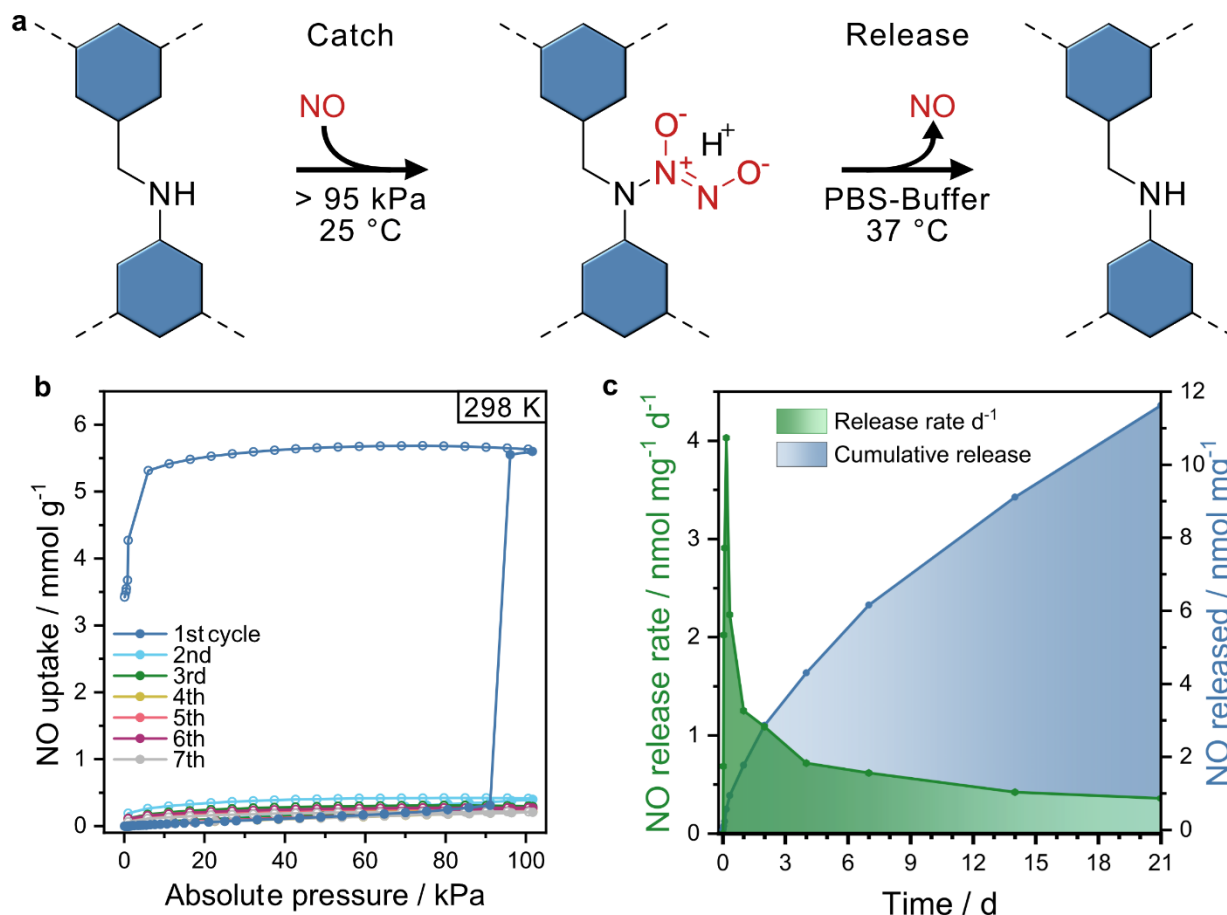
Figure 7.7. Catch and release steps of the secondary amine-COF-linkage. (b) NO adsorption cycles of rTTI-COF. (c) NO release and estimated release rate of rTTI-COF-NO in a pH 7.4 PBS-buffer solution monitored by the Griess assay.

A reaction with the remaining amic acid intermediates remains uncertain. While a slight decline in the relative intensity compared to the imide signal is observed, only a single case of a reaction of NO with primary amides (under strongly basic conditions) has been reported in the literature, making at least a quantitative reaction unlikely in this case.[44]

Judging from the diffraction and sorption results, we expect more significant changes in the ssNMR spectra of TTI-COF and rTTI-COF. Indeed, TTI-COF shows a slight broadening of the peaks in the 13C CP-MAS NMR after NO exposure and a new signal at 191 ppm appears (Figure 7.6, a, top). This peak corresponds to the proposed aldehyde, visible in the FT-IR spectra as a new band at 1699 cm-1. In parallel, a reduction of the imine signal intensity at 151 ppm compared to the remaining signals is observed, which is especially visible when comparing to the neighboring signal at 157 ppm. These findings indicate a partial cleavage of imine bonds, resulting in exposed aldehyde groups. The 15N CP-MAS NMR of TTI-COF-NO exhibits the same removal of terminal amine groups (Figure 7.6, a, bottom), visible at 316 ppm, by deamination after contact with NO as found for TT-Imide-COF (Figure 7.5). The imine signal at 58 ppm remains with minor peak broadening, as do the 13C signals.

We rationalize these observations with an incipient decomposition according to a reaction mechanism upon NO contact shown in Scheme S2: By a [2+2] cycloaddition of NO to the imine bond, as described by Hrabie *et al.* for Schiff-bases,[45] the adduct is cleaved into the free aldehyde as observed by the ^{13}C signal at 191 ppm, and a diazo radical. Subsequently, an aryl radical is formed by elemination of nitrogen, which is ultimately quenched.

rTTI-COF-*NO* shows a strong broadening of all signals in the ^{13}C spectrum (Figure 7.6, a, top). Especially the benzylic quaternary carbon at 49 ppm broadens and almost disappears into the background. This observation reflects the disorder introduced into the framework and is in good agreement with the amorphization and loss of long-distance order seen in the PXRD pattern (Figure 7.3, e). The ^{15}N spectrum reveals a significant shift of the ^{15}N signal of the linkage (Figure 7.6, b, bottom). The secondary amine-related peak of rTTI-COF at 316 ppm shifts to 119 ppm for rTTI-COF-*NO*, indicating a complete transformation of the bond. This novel linkage is identified as *N*-diazeniumdiolate (NONOate), a species that is also observed during NO adsorption in amine functionalized MOFs and is formed by the addition of two equivalents of NO to the amine linkage of rTTI-COF at 95 kPa NO pressure (Figure 7.7, a, b).[1,24] The post-synthetic linkage modification is mirrored in the FT-IR spectrum by the appearance of three new, distinct bands at 1700 cm^{-1}, 1084 cm^{-1}, and 916 cm^{-1} as mentioned above (Figure S9.4.7). The complete disappearance of the ^{15}N-amine indicates full conversion of the amine into the NONOate linkage. Introducing such polar, bulky NONOate groups adds both steric and electrostatic repulsion between the layers, thus forcing the layers to distort and shift, resulting in the observed loss of long-range order, layer integrity and porosity. Besides this drawback, the described simple gas phase modification of amine-linked COFs by NO introducing NONOate groups displays exciting new possibilities for the design of polymers and COFs bearing novel linkages and functionalities.

NO release

Along these lines, implementing NONOate functional groups holds great promise towards COFs as nitric oxide releasing delivery platforms for bioregulatory NO release in therapeutic or medicinal chemistry applications (Figure 7.7, a).[5,46,47] Nitric oxide release under physiological conditions was tested by suspending rTTI-COF-*NO* in a pH 7.4 PBS-buffer solution at 37 °C and monitoring the NO release using a Griess assay.[48] The NO release profile of rTTI-COF-*NO* shows an exponential release behavior with an overall very slow but steady release of the chemisorbed NO over several days (Figure 7.7, c). An initial faster release over the first 24 h of around 1.8 nmol NO is observed, followed by a long period of 3 weeks in which another 9.9 nmol NO is released. After NO release, crystallinity and specific surface area are partially recovered (Figure S9.4.5, S9.4.39), evidencing the successful rearrangement of the regenerated amine-linked domains into an ordered structure. While the total amount of NO delivered by the COF is significantly lower than the NO physiosorbed in recently published MOFs or polymers,[23,46,49] they are well in the concentration range of physiological processes.[10,50] In addition, the controlled release of NO over such long periods (i.e. multiple days to weeks) sets rTTI-COF-*NO* apart from the typical rapid release over

seconds to hours observed for other NONOate derivatives and suggests that NONOate-COFs could be promising candidates for wound healing or related applications where a slow NO release is key.[18,50] Unlike MOFs, COFs also do not contain heavy metals that can prevent their use in pharmaceuticals. Further, we presume that the origin of this moderate but gradual release is due to the limited diffusion of water into and NO out of the disordered and non-porous, but flexible framework. The diffusion of water into the framework is crucial to protonate the NONOate functional groups and trigger the NO release. Hence, control over the crystallinity during linkage transformation may be used to control the rate and amount of NO released by NONOate-COFs. Crystallinity and therefore enhanced accessibility of the NONOate functional groups in the COF pores could be achieved by implementing readily available strategies to direct and lock the layer stacking, or by using 3D COFs.[51–54]

Taken together, our NMR analysis explains the different linkage stabilities and transformations, and rationalizes the observed initial irreversible adsorption behavior, which is largely due to the chemical reaction of NO with terminal amine groups or linkages of the frameworks.

7.3. Conclusion

We have identified NO as a synthetically flexible reagent for the rational topochemical framework modification in COFs. We have developed a straightforward synthesis of a ^{15}N enriched version of the commonly used TT-amine linker, which was successfully used to prepare multiple COFs with varying linkage chemistries – imine, amine, thiazole, and imide. The ^{15}N-enriched linkage-archetypes were then used as chemical probes to verify the existence of previously postulated terminal groups and reaction intermediates during linkage formation and modification. We demonstrated that all frameworks with unreacted terminal amine sites can be quantitatively passivated with NO by a denitrogenation reaction, leading to a clean surface defunctionalization of the frameworks. In addition, we could show that the reactivity of the different linkages towards NO is distinctly different: While imide and thiazole-linked COFs were found to be largely unreactive towards NO, imine and amine-linked COFs undergo local (imine) and global (amine) linkage conversions leading to significant changes in the surface area and framework crystallinity. We have further demonstrated a topochemical modification of amine-linked COFs by NO, forming the novel NONOate COF linkage by a solid-gas phase reaction at room temperature. Controlled and extended NO release by this NONOate linkage was observed under physiological conditions, which opens the door to the use of amine-linked COFs as potential platforms for "NO catch and release" scenarios in biomedical applications. We have thus demonstrated that besides being toxic and highly reactive, NO is a versatile reagent for crystal surface and linkage modification, thus greatly expanding the synthetic toolbox of COF chemistry.

7.4. Bibliography

[1] K. Peikert, L. J. McCormick, D. Cattaneo, M. J. Duncan, F. Hoffmann, A. H. Khan, M. Bertmer, R. E. Morris, M. Fröba, *Microporous Mesoporous Mater.* **2015**, *216*, 118–126.
[2] M. Shabani, S. K. Pulfer, J. P. Bulgrin, D. J. Smith, *Wound Repair Regen.* **1996**, *4*, 353–362.
[3] M. T. Gladwin, J. H. Crawford, R. P. Patel, *Free Radic. Biol. Med.* **2004**, *36*, 707–717.
[4] A. W. Carpenter, M. H. Schoenfisch, *Chem. Soc. Rev.* **2012**, *41*, 3742–3752.
[5] S. Paul, S. Pan, A. Mukherjee, P. De, *Mol. Pharm.* **2021**, *18*, 3181–3205.
[6] *Handbook of Air Pollution From Internal Combustion Engines*, Elsevier, **1998**.
[7] F. Klingstedt, K. Arve, K. Eränen, D. Y. Murzin, *Acc. Chem. Res.* **2006**, *39*, 273–282.
[8] S. Roy, A. Baiker, *Chem. Rev.* **2009**, *109*, 4054–4091.
[9] W. Song, X. Y. Liu, C. C. Hu, G. Y. Chen, X. J. Liu, W. W. Walters, G. Michalski, C. Q. Liu, *Nat. Commun.* **2021**, *12*, 243.
[10] C. N. Hall, J. Garthwaite, *Nitric Oxide - Biol. Chem.* **2009**, *21*, 92–103.
[11] G. B. Hamra, F. Laden, A. J. Cohen, O. Raaschou-Nielsen, M. Brauer, D. Loomis, *Environ. Health Perspect.* **2015**, *123*, 1107–1112.
[12] O. K. Kurt, J. Zhang, K. E. Pinkerton, *Curr. Opin. Pulm. Med.* **2016**, *22*, 138.
[13] V. A. Southerland, M. Brauer, A. Mohegh, M. S. Hammer, A. van Donkelaar, R. V Martin, J. S. Apte, S. C. Anenberg, *Lancet Planet. Heal.* **2022**, *6*, e139–e146.
[14] WHO Regional Office for Europe, *Health Risks of Particulate Matter from Long-Range Transboundary Air Pollution*, **2006**.
[15] P. Granger, V. I. Parvulescu, *Chem. Rev.* **2011**, *111*, 3155–3207.
[16] J. F. Quinn, M. R. Whittaker, T. P. Davis, *J. Control. Release* **2015**, *205*, 190–205.
[17] J. Cheng, K. He, Z. Shen, G. Zhang, Y. Yu, J. Hu, *Front. Chem.* **2019**, *7*, 530.
[18] M. R. Miller, I. L. Megson, *Br. J. Pharmacol.* **2007**, *151*, 305–321.
[19] S. P. Nichols, W. L. Storm, A. Koh, M. H. Schoenfisch, *Adv. Drug Deliv. Rev.* **2012**, *64*, 1177–1188.
[20] M. M. Reynolds, J. A. Hrabie, B. K. Oh, J. K. Politis, M. L. Citro, L. K. Keefer, M. E. Meyerhoff, *Biomacromolecules* **2006**, *7*, 987–994.
[21] J. H. Shin, S. K. Metzger, M. H. Schoenfisch, *J. Am. Chem. Soc.* **2007**, *129*, 4612–4619.
[22] J. Kim, Y. Lee, K. Singha, H. W. Kim, J. H. Shin, S. Jo, D. K. Han, W. J. Kim, *Bioconjug. Chem.* **2011**, *22*, 1031–1038.
[23] A. C. McKinlay, B. Xiao, D. S. Wragg, P. S. Wheatley, I. L. Megson, R. E. Morris, *J. Am. Chem. Soc.* **2008**, *130*, 10440–10444.
[24] A. H. Khan, K. Peikert, F. Hoffmann, M. Fröba, M. Bertmer, *J. Phys. Chem. C* **2019**, *123*, 4299–4307.
[25] A. M. Wright, C. Sun, M. Dincă, *J. Am. Chem. Soc.* **2021**, *143*, 681–686.
[26] C. Diercks, M. Kalmutzki, O. Yaghi, *Molecules* **2017**, *22*, 1575.
[27] Y. Ge, H. Zhou, Y. Ji, L. Ding, Y. Cheng, R. Wang, S. Yang, Y. Liu, X. Wu, Y. Li, *J. Phys. Chem. C* **2018**, *122*, 27495–27506.
[28] X. Cao, Z. Wang, Z. Qiao, S. Zhao, J. Wang, *ACS Appl. Mater. Interfaces* **2019**, *11*, 5306–5315.
[29] Y. Huang, X. Hao, S. Ma, R. Wang, Y. Wang, *Chemosphere* **2022**, *291*, 132795.
[30] Z. Meng, R. M. Stolz, K. A. Mirica, *J. Am. Chem. Soc.* **2019**, *141*, 11929–11937.
[31] M. Yar, K. Ayub, *Microporous Mesoporous Mater.* **2020**, *300*, 110146.
[32] S. Kandambeth, A. Mallick, B. Lukose, M. V. Mane, T. Heine, R. Banerjee, *J. Am. Chem. Soc.* **2012**, *134*, 19524–19527.
[33] F. Haase, E. Troschke, G. Savasci, T. Banerjee, V. Duppel, S. Dörfler, M. M. J. Grundei, A. M. Burow, C. Ochsenfeld, S. Kaskel, B. V. Lotsch, *Nat. Commun.* **2018**, *9*, 1–10.
[34] A. Halder, M. Ghosh, A. Khayum M, S. Bera, M. Addicoat, H. S. Sasmal, S. Karak, S. Kurungot, R. Banerjee, *J. Am. Chem. Soc.* **2018**, *140*, 10941–10945.
[35] C. Zhao, C. S. Diercks, C. Zhu, N. Hanikel, X. Pei, O. M. Yaghi, *J. Am. Chem. Soc.* **2018**, *140*, 16438–16441.
[36] H. Lyu, C. S. Diercks, C. Zhu, O. M. Yaghi, *J. Am. Chem. Soc.* **2019**, *141*, 6848–6852.
[37] L. Grunenberg, G. Savasci, M. W. Terban, V. Duppel, I. Moudrakovski, M. Etter, R. E. Dinnebier, C. Ochsenfeld, B. V. Lotsch, *J. Am. Chem. Soc.* **2021**, *143*, 3430–3438.
[38] F. Haase, K. Gottschling, L. Stegbauer, L. S. Germann, R. Gutzler, V. Duppel, V. S. Vyas, K. Kern, R. E. Dinnebier, B. V. Lotsch, *Mater. Chem. Front.* **2017**, *1*, 1354–1361.

[39]   X. Zhu, S. An, Y. Liu, J. Hu, H. Liu, C. Tian, S. Dai, X. Yang, H. Wang, C. W. Abney, S. Dai, *AIChE J.* **2017**, *63*, 3470–3478.

[40]   L. Wang, L. Wang, J. Zhao, T. Yan, *J. Appl. Phys.* **2012**, *111*, 112628.

[41]   S. Bin Baek, D. Moon, R. Graf, W. J. Cho, S. W. Park, T. U. Yoon, S. J. Cho, I. C. Hwang, Y. S. Bae, H. W. Spiess, H. C. Lee, K. S. Kim, *Proc. Natl. Acad. Sci. U. S. A.* **2015**, *112*, 14156–14161.

[42]   S. Eckert, S. Rakowski, *Grundlagen Verbrennungsmotoren*, Springer Fachmedien Wiesbaden, Wiesbaden, **2014**.

[43]   T. Itoh, K. Nagata, Y. Matsuya, M. Miyazaki, A. Ohsawa, *J. Org. Chem.* **1997**, *62*, 3582–3585.

[44]   R. J. Holland, J. R. Klose, J. R. Deschamps, Z. Cao, L. K. Keefer, J. E. Saavedra, *J. Org. Chem.* **2014**, *79*, 9389–9393.

[45]   J. A. Hrabie, A. Srinivasan, C. George, L. K. Keefer, *Tetrahedron Lett.* **1998**, *39*, 5933–5936.

[46]   N. A. Stasko, M. H. Schoenfisch, *J. Am. Chem. Soc.* **2006**, *128*, 8265–8271.

[47]   Y. L. Zhao, S. L. Garrison, C. Gonzalez, W. D. Thweatt, M. Marquez, *J. Phys. Chem. A* **2007**, *111*, 2200–2205.

[48]   J. Sun, X. Zhang, M. Broderick, H. Fein, *Sensors* **2003**, *3*, 276–284.

[49]   H. T. T. Duong, K. Jung, S. K. Kutty, S. Agustina, N. N. M. Adnan, J. S. Basuki, N. Kumar, T. P. Davis, N. Barraud, C. Boyer, *Biomacromolecules* **2014**, *15*, 2583–2589.

[50]   Y. Kang, J. Kim, Y. M. Lee, S. Im, H. Park, W. J. Kim, *J. Control. Release* **2015**, *220*, 624–630.

[51]   Y. B. Zhang, J. Su, H. Furukawa, Y. Yun, F. Gándara, A. Duong, X. Zou, O. M. Yaghi, *J. Am. Chem. Soc.* **2013**, *135*, 16336–16339.

[52]   Y. Liu, Y. Ma, J. Yang, C. S. Diercks, N. Tamura, F. Jin, O. M. Yaghi, *J. Am. Chem. Soc.* **2018**, *140*, 16015–16019.

[53]   S. B. Alahakoon, K. Tan, H. Pandey, S. D. Diwakara, G. T. McCandless, D. I. Grinffiel, A. Durand-Silva, T. Thonhauser, R. A. Smaldone, *J. Am. Chem. Soc.* **2020**, *142*, 12987–12994.

[54]   S. T. Emmerling, R. Schuldt, S. Bette, L. Yao, R. E. Dinnebier, J. Kästner, B. V. Lotsch, *J. Am. Chem. Soc.* **2021**, *143*, 15711–15722.

8. Conclusion

Covalent organic frameworks have emerged in recent years as incredibly variable and useful frameworks for numerous applications such as optoelectronics,[1,2] energy storage,[3,4] gas storage and separation,[5,6] photosensitizers,[7,8] and heterogeneous catalysis.[9–11] In this work, a series of comprehensive studies was carried out to understand the effect of modulating COF structure and synthesis protocol on COF crystallinity and porosity. In particular, a new aspect for COFs as heterogeneous catalyst platform has been explored and demonstrated by confining homogeneous catalysts and reactions in COF pores, thus tailoring them to specific reaction outcomes. The work demonstrates several facets related to developing COFs as a new platforms for heterogeneous catalysis under confinement: (i) the influence of non-covalent interlayer interactions on the design and stability of large COF systems, (ii) the interactions between scaffold, catalyst and reactant during confinement that affect product selectivity, (iii) insights into reaction pathways of green synthesis alternatives, and (iv) development of post-synthetic COF modifications altering surface properties and introduction of noel COF applications.

Large-pore COF platforms

COFs with large pores are still a rarity, despite their potential for heterogeneous catalysis and adsorption of larger biomolecules. While many aspects of general COF formation are being studied, the problems associated with large pore COF systems have not yet been specifically addressed.

In this work, the influence of non-covalent interlayer interactions on the structure and stability of COFs with large pore aperture was investigated while creating a modifiable, isoreticular COF series. The platforms were based on extended C2-phenylphenanthridine-aldehyde units combined with C3-, 1,3-5-triphenylbenzene- (TAB), or 1,3,5-tri(4-biphenyl)benzene-based amine (TAPB) building blocks to form isoreticular 2D COFs with hexagonal structure and two pore sizes. For the proposed different interlayer interactions, the phenylphenanthridine units were modified stepwise with o-methoxy groups in respect to the aldehyde (PP, mPP, dPP), which has already been shown in the literature to improve layer correlation. Therefore, the interlayer interactions could be tuned in three levels, from low, without methoxy groups (PP-TAB, PP-TAPB), to medium (mPP-TAB, mPP-TAPB) or to high (dPP-TAB, dPP-TAPB), with two or four methoxy groups per building block. A total matrix of six COFs was created to investigate the effects of pore size and interlayer interactions by (*in situ* heating) XRPD, TEM, ssNMR, TGA, gas sorption analysis, computational DFT structural studies, and computational stacking potential energy landscapes.

PP-TAB and PP-TAPB with weak interlayer interactions deviated from the normally expected AA-eclipsed layer stacking, and a shift of the layers with respect to each other was evident, resulting in an overall AB-staggered layer confirmation. This AB staggered conformation resulted in a significant deviation of the observable pore size of 0.6 nm for the smaller and 1.0 nm for the larger

variant from the expected values. This observation of stacking structure and reduction in pore size is consistent with previous findings in the literature for wide aperture COFs.[12,13] In contrast, dPP-TAB and dPP-TAPB with the highest interlayer interactions both exhibited well-defined AA stacking, resulting in the expected pore sizes of 4.8 nm and 5.8 nm. This obvious contrast of stacking behavior demonstrates the great influence of noncovalent interlayer interactions on the structure of large pore size COFs. Moreover, mPP-TAB with intermediate interlayer interactions shows a well-defined AA eclipsed layer stacking, but the AB staggered conformation for mPP-TAPB, leading to almost identical effective pore sizes for both COFs despite the different linker size of and TPB and TAPB. This represents an edge case where the interlayer interactions are sufficient to allow AA stacking for medium sized COFs but insufficient for larger variants, illustrating the effect of increasing pore size on COF stacking. Furthermore, it shows that simply increasing the size of the building blocks does not necessarily increase the effective size of the pores, which prevents the formation of isoreticular series with large apertures without considering the interlayer interactions as a design tool.

In addition to the influence of structure, the thermal stability of the scaffolds was investigated. As recently shown, TGA analysis can be deceptive about the true structural integrity of COF scaffolds, which is evident in amorphization at lower temperatures than expected.[14,15] *In situ* XRPD heating experiments up to 200 °C and corresponding *ex situ* gas sorption experiments showed that the AB-stacked COFs, PP-TAB, PP-TAPB, and mPP-TAPB, of our series exhibit only a slightly increased stacking disorder and their structure does not change significantly throughout the temperature change. For the AA-stacked COFs, the smaller variant with high interlayer interactions (dPP-TAB) exhibits a small and fully reversible thermal expansion of the layer spacing, while otherwise maintaining its structural integrity. However, the smaller COF with intermediate interactions (mPP-TAB) and the larger COF with high interactions (dPP-TAPB) both exhibit a novel phase transition from AA eclipsed to AB staggered layer stacking at 140 °C and 120 °C, respectively. The resulting structure types correspond to the respective AB staggered variants of the weakly interacting COFs. These phase transitions are irreversible upon cooling, but can be reversed by simple contact with solvent. In conjunction with the calculated DFT energy landscapes of the stacking potential, this reversibility behavior reveals the AA-shifted stacking type for these COFs as a metastable phase once the solvent is removed from the pores.

This work highlights the importance of interlayer interactions for layer stacking of COFs and their usefulness as a design tool for large pore COF systems. The interplay of pore aperture, interlayer interactions, and stacking has been demonstrated, as well as the effects on structural integrity at elevated temperatures. This work can provide helpful guidance for rational design of large COF systems that are tailored to specific material applications in terms of structure and stability.

Molecular heterogeneous catalysis under confinement

Heterogeneous catalysis practiced with COFs is of increasing interest due to their chemical flexibility, as they can be adapted and tailored to the specific needs of their application reaction. Due to their large surface area and composition of light elements, they are generally used as efficient catalysts for various purposes.[16,17] To compete with other cheaper mesoporous materials, such as silica, the still high cost of COFs would require highly specialized unique properties and efficient uses for them. Utilizing not only the large surface area provided by COF porosity, but also the highly modifiable and well-defined pores for confinement can therefore open a new pathway for COFs toward highly specialized biomimetic catalyst supports and differentiate them from other support materials.

In this work, the specific use of COFs and their pore confinement to modify the reaction outcome of molecular heterogeneous catalysis is investigated. To achieve this, the previously identified design principles for large pore size COFs were used to build the framework, as the pore size for the expected effect is in the range of 4 to 6 nm. Building on the previous work, the highly stable and robust methoxy-containing phenylphenanthridine-based COF was further modified with hydroxyl groups on the phenylphenanthridine building block as anchoring sites for molecular catalyst immobilization. The hydroxyl functionalization was introduced into the protruding phenyl group, which is well suited to place the molecular catalyst in the pore. XRPD, NMR and gas sorption experiments confirmed the formation of the functionalized scaffold, and a well-defined layer correlation with highly ordered and uniform pores was found. The confinement effect itself was tested for the selectivity of macro(mono)cyclization (MMC) over oligomerization (O) in α,ω-diene ring closure metathesis reactions compared to homogeneous reaction with a non-immobilized catalyst. The Ru-Grubbs-Hoveyda type catalyst in question was modified with tri-methoxy(alkyl)silane and immobilized on the framework by a silylation reaction. Ru-ICP analysis confirmed the successful loading of the catalyst to about 3.4% of all hydroxyl groups present in the framework. EXAFS analysis also confirmed that the structure of the catalyst remained intact after immobilization. MMO/O selectivity was investigated using four α,ω-diene substrates that differed in size and polarity. A strong correlation was found between substrate size and increased MMO/O selectivity compared to heterogeneous catalysis, as well as an overall decrease in activity of the immobilized catalyst. While no difference was apparent for the largest substrate, selectivity increased with decreasing substrate size. This can be explained by the fact that the smaller substrates diffuse more easily into the pores and therefore these have a stronger influence on the ring chain equilibrium during catalysis.[18,19] For larger substrates that do not diffuse into the pores, the reaction is limited to the outer surface of the material, which does not offer a changed ring chain equilibrium . No differences were observed with respect to the polarity of the substrate, indicating little interaction between the scaffold and reactant for this COF. The scaffold remained fully intact after catalysis, but unfortunately, due to the nature and fragility of the catalyst used, catalyst cycling could not be performed.

Despite the reduced catalyst activity affecting the overall effectiveness of the catalyst system, a successful confinement effect was demonstrated to modify the reaction outcome. Design principles for large-pore COF systems were successfully applied to create a suitable framework demonstrating the viability of a substrate- and product-specific catalyst framework utilizing COF pore confinement. These results represent a first step towards novel biomimetic catalyst supports rationally designed for specific reactions.

Green and scalable COF mechanosynthesis

COFs for academic research purposes are often synthesized by solvothermal reactions in small amounts, which still requires relatively large amounts of often toxic solvents, high temperatures, and long reaction times. Successful COF synthesis by mechanochemistry, which has re-established itself as a green synthesis alternative in recent years, has introduced a new tool for COF formation. Despite the great advantages - short reaction time, low solvent consumption and easy scalability to industrial scales - the lower quality of the obtained COFs compared to the classical synthesis strategies inhibits their diffusion in the field of COFs. Also, compared to the conventional synthesis strategies, there are no studies on the mechanism of COF formation that could facilitate improving the product quality.

In this work, the formation of COF during mechanochemical liquid-assisted grinding (LAG) synthesis using a classical AcOH catalyst or the highly active solid $Sc(OTf)_3$ catalyst is investigated. Using *in situ* XRPD and Raman spectroscopy, the first direct experimental evidence of intermediates and solvent-based templating effects during framework formation was obtained. Of the four COF systems studied, two exhibited a crystalline solvate reaction intermediate. This is either a competitive side reaction or a triple imine condensation product that provides important insight into the formation mechanism and can rationally lead to improved synthesis of higher quality products. The intermediate in the synthesis of TbBd-COF, a solvate of 1,4-dioxane with diamine educt formed by a competitive reaction, was formed due to a slow imine formation. By switching from the classical AcOH catalyst to the more active $Sc(OTf)_3$ catalyst, the formation of the intermediate solvate was suppressed, the quality of the COFs was significantly improved, and the specific surface area was almost quintupled. In contrast, the intermediate in the formation of the COF-LZU1 framework is a solvated form of a triple imine condensation product organized in the solid state around 1,4-dioxane molecules that serve as templates for subsequent pore formation. The layered molecular arrangement in the solvate not only prevents the initial π-π stacking in the early stages of self-assembly, an effect known to reduce the overall crystallite size, but also promotes the formation of 2D COF layers.[20] Furthermore, it has been shown that replacing the originally used 1,4-dioxane/mesitylene LAG mixture with pure 1,4-dioxane can further improve the COF surface area. By the use of these adjustments, active $Sc(OTf)_3$, and/or activation by supercritical CO_2 we were able to improve the crystallinity and surface area of all the COF systems mechanochemically synthesized in this study to bring within reach or exceed those of classically synthesized systems

Alternative applications for COFs

The variable structural and chemical properties of COFs make them suitable materials for various applications beyond heterogeneous catalysis. High surface area materials such as COFs are excellent for gas storage and separation applications, and several studies are available on CO_2, H_2, and even SO_2 adsorption.[5,21] However, the adsorption of nitrogen oxide, a reactive and toxic component in exhaust gas of combustion processes, on COFs has not yet been studied.

In this work, the adsorption of nitrogen oxide on different COF scaffolds is investigated as a novel application of these materials. The stability of the materials and the different linkages, imines, amines, thiazoles and imides, towards the reactive gas was investigated. The ^{15}N enrichment on the bonds to increase the sensitivity in ssNMR was used to observe the effect of NO on the scaffold and to dissect the reactions involved.

The study showed high stability of thiazole and imide linkages to NO exposure, as well as chemical and structural stability of these frameworks. Although stable under these conditions, the initial adsorption was found to involve an irreversible chemisorption step. The amounts of NO adsorbed by this process were far greater than the amounts physically adsorbed in subsequent cycles. The origin of this high irreversible chemisorption was identified in the reaction of terminal amines in the materials. These reactive terminal amines, which inevitably remain after framework formation, can alter the surface properties of the crystallites, or even undergo undesirable reactions in further applications. By reacting with NO, we were able to reveal a novel passivation strategy for these terminal groups on the outer surface of COFs.

In comparison, the imine and amine linkages reacted directly with NO, resulting in partial bond breakage and conversion to a novel NONOate linkage, respectively. The imine bonds partially split into aldehyde groups, which were visible in FT-IR and ^{13}C NMR spectroscopy measurements, and amine groups, which were further passivated as with the terminal amine functions. The loss of the crystallinity and surface area of the material indicates the instability of this type of bonding and renders it useless for NO sorption applications. The newly formed NONOate due to the addition of two NO molecules to the secondary amine-COF bond led to a structural deformation of the COF, which was also visible by its amorphization and loss of porosity. The effective chemisorption of NO at these linkages with complete conversion to form stable NONOates showed potential utility for gas purification. Moreover, this novel COF linkage showed promise for drug delivery by slowly releasing bound NO, an important signaling molecule in cellular chemistry, under physiological conditions in PBS buffer at 37 °C. The unusually slow release compared to other NO-releasing MOFs or polymers could prove valuable for wound healing or similar applications.

In this work, progress towards COFs as platforms for heterogeneous catalysis under confinement has been demonstrated in several aspects. Design principles for large pore COFs were developed that link non-covalent interlayer interactions with COF stacking and thermal stability. An α,ω-diene

ring-closure metathesis reaction with a Ru-Grubbs-Hoveyda catalyst was introduced to investigate and successfully demonstrate a confinement effect on the selectivity of macro(mono)cyclization (MMC) over oligomerization (O) in COF pores. Insights were gained into the mechanism of mechanochemical formation of COFs, a promising synthetic strategy for the future of the growing COF field. In addition, advances towards new applications in NO adsorption and drug delivery were achieved. This work sheds light on the complexity of COF design and applications and provides important insights, tools for fabrication and better understanding of the nature of COFs. Various applications have successfully demonstrated the great versatility of COFs and can provided new stimulus for further work in this area.

Bibliography

[1]   N. Keller, T. Bein, *Chem. Soc. Rev.* **2021**, *50*, 1813–1845.
[2]   A. Yi-feng Xiong, Q. Liao, Z. Huang, X. Huang, C. Ke, H. Zhu, C. Dong, H. Wang, K. Xi, P. Zhan, F. Xu, Y. Lu, *Advanced Mat.* **2020**, *32*, 1907242.
[3]   F. Xu, S. Yang, X. Chen, Q. Liu, H. Li, H. Wang, B. Wei, D. Jiang, *Chem. Sci.* **2019**, *10*, 6001–6006.
[4]   Y. An, S. Tan, Y. Liu, K. Zhu, L. Hu, Y. Rong, Q. An, *Energy Storage Mater.* **2021**, *41*, 354–379.
[5]   C. J. Doonan, D. J. Tranchemontagne, T. G. Glover, J. R. Hunt, O. M. Yaghi, *Nat. Chem. 2010 23* **2010**, *2*, 235–238.
[6]   X. Guan, H. Li, Y. Ma, M. Xue, Q. Fang, Y. Yan, V. Valtchev, S. Qiu, *Nat. Chem. 2019 116* **2019**, *11*, 587–594.
[7]   Y. Zhi, Z. Li, X. Feng, H. Xia, Y. Zhang, Z. Shi, Y. Mu, X. Liu, *J. Mater. Chem. A* **2017**, *5*, 22933–22938.
[8]   B. P. Biswal, H. A. Vignolo-González, T. Banerjee, L. Grunenberg, G. Savasci, K. Gottschling, J. Nuss, C. Ochsenfeld, B. V. Lotsch, *J. Am. Chem. Soc.* **2019**, *141*, 11082–11092.
[9]   X. Han, Q. Xia, J. Huang, Y. Liu, C. Tan, Y. Cui, *J. Am. Chem. Soc.* **2017**, *139*, 8693–8697.
[10]   J. Guo, D. Jiang, *ACS Cent. Sci.* **2020**, *6*, 869–879.
[11]   H. B. Aiyappa, J. Thote, D. B. Shinde, R. Banerjee, S. Kurungot, *Chem. Mater.* **2016**, *28*, 4375–4379.
[12]   Q. Fang, Z. Zhuang, S. Gu, R. B. Kaspar, J. Zheng, J. Wang, S. Qiu, Y. Yan, *Nat. Commun.* **2014**, *5*, 4503.
[13]   C. Zhao, H. Lyu, Z. Ji, C. Zhu, O. M. Yaghi, *J. Am. Chem. Soc.* **2020**, *142*, 14450–14454.
[14]   A. M. Evans, M. R. Ryder, N. C. Flanders, E. Vitaku, L. X. Chen, W. R. Dichtel, *Ind. Eng. Chem. Res.* **2019**, *58*, 9883–9887.
[15]   A. M. Evans, M. R. Ryder, W. Ji, M. J. Strauss, A. R. Corcos, E. Vitaku, N. C. Flanders, R. P. Bisbey, W. R. Dichtel, *Faraday Discuss.* **2021**, *225*, 226–240.
[16]   R. Freund, O. Zaremba, G. Arnauts, R. Ameloot, G. Skorupskii, M. Dincă, A. Bavykina, J. Gascon, A. Ejsmont, J. Goscianska, M. Kalmutzki, U. Lächelt, E. Ploetz, C. S. Diercks, S. Wuttke, *Angew. Chemie Int. Ed.* **2021**, *60*, 23975–24001.
[17]   H. R. Abuzeid, A. F. M. EL-Mahdy, S. W. Kuo, *Giant* **2021**, *6*, 100054.
[18]   S. Monfette, D. E. Fogg, *Chem. Rev.* **2009**, *109*, 3783–3816.
[19]   F. Ziegler, J. Teske, I. Elser, M. Dyballa, W. Frey, H. Kraus, N. Hansen, J. Rybka, U. Tallarek, M. R. Buchmeiser, *J. Am. Chem. Soc.* **2019**, *141*, 19014–19022.
[20]   V. Nguyen, M. Grünwald, *J. Am. Chem. Soc.* **2018**, *140*, 3306–3311.
[21]   H. Furukawa, O. M. Yaghi, *J. Am. Chem. Soc.* **2009**, *131*, 8875–8883.

9. Appendix

9.1. Supporting Information of Chapter 4 - "Interlayer Interactions as Design Tool for Large-Pore COFs"

9.1.1. Experimental Procedures

Chemicals. All starting materials and reagents were obtained from commercial suppliers and used without further purification. All solvents, unless otherwise specified, were obtained from Acros Organics, and used without further purification. 1,3,5-Tris[4-amino(1,1-biphenyl-4-yl)]benzene was prepared according to a literature procedure.[1]

X-Ray Powder Diffraction. XRPD patterns were collected at 30 °C, 80 C, 100 °C, 120 °C, 140 °C, 160 °C, 180 °C, and 200 °C on a laboratory powder diffractometer in Debye-Scherrer geometry (Stadi P-diffractometer (Stoe), Cu-K$_{\alpha 1}$ radiation from primary Ge(111)-Johann-type monochromator, triple array of Mythen 1 K detectors (Dectris)). The sample was sealed in a 1.0 mm diameter borosilicate glass capillary (Hilgenberg glass no. 0140), which were spun during the measurements. Heating was performed using a capillary heater Oxford Cryostream 700 (Oxford Cryosystems), applying a delay period of 4 h prior to each measurement in order to ensure equilibration. Each powder pattern was collected in a 2θ range from 0 ° to 110 ° with a total scan time of 3 hours. The program TOPAS 6.0 was used for the data analyses. All details on the refinements are described below. The XRPD measurements of the heating kinetics were performed at constant temperatures using the same device. After reaching a constant temperature, powder patterns were collected in a 2θ range from 0 ° to 110 ° with a total scan time of one minute. During the first 10 minutes, powder patterns were collected every minute, during the subsequent 10 minutes every two minutes, during the subsequent 40 minutes every 5 minutes, during the subsequent 210 minutes every 15 minutes, during the subsequent 120 minutes every 30 minutes, and during the subsequent 600 minutes every 60 minutes.

FT-IR Spectroscopy. Infrared spectra were measured in attenuated total reflection (ATR) geometry on a PerkinElmer UATR Two equipped with a diamond crystal. All spectra were background corrected.

Liquid State Nuclear Magnetic Resonance. All liquid state nuclear magnetic resonance (NMR) measurements were performed on a JEOL ECZ 400S 400 MHz spectrometer (magnetic field 9.4 T). ^{1}H, ^{13}C and ^{15}N measurements were performed in 5 mm NMR tubes using deuterium field lock. NMR spectra were internally calibrated to the corresponding solvent signal.[2] Abbreviations for multiplicities: s (singlet), bs (broad singlet), d (dublet), t (triplet), q (quartet), hept (heptet), m (multiplet).

Solid State Nuclear Magnetic Resonance. Solid-state NMR (ssNMR) was recorded on a Bruker Avance III 400 MHz spectrometer (magnetic field 9.4 T). Samples were packed in 4 mm ZrO_2 rotors, which were spun at 12-14 kHz in a Bruker WVT BL4 double resonance MAS probe. Chemical shift was referenced relative to tetramethylsilane (^{13}C). A standard cross-polarization sequence with a 2 ms ramped contact pulse was used for ^{13}C and a total of 4096-8192 scans were routinely accumulated. All spectra were background corrected.

Sorption Measurements. Sorption measurements were performed on a Quantachrome Instruments Autosorb iQ 3 with nitrogen at 77 K. The pore size distribution (PSD) was determined from nitrogen adsorption isotherms using the QSDFT (cylindrical pores, adsorption branch) or QSDFT (cylindrical pores, equilibrium) kernel in carbon for nitrogen at 77 K implemented in the ASiQwin software v 3.01. Samples were activated under high vacuum at room temperature for 12 h before measurement unless stated otherwise.

Mass Spectrometry. Electrospray ionization (ESI) mass spectrometry was performed on a Thermo Finnigan LTQ FT in the positive and negative mode. Samples were dissolved in an acetonitrile/water mixture.

Thermal Analysis. Thermogravimetric analysis was performed on a *NETZSCH STA 449 F3 Jupiter*. Measurements were carried out with 5 mg of sample in an Al_2O_3 crucibles under Helium protective gas flow in a temperature range between 40 to 1000 °C and a heating rate of 10 K/min.

Scanning Electron Microscopy. SEM SE (secondaryelectron) detector images were obtained on a Zeiss Merlin.

Transmission Electron Microscopy. TEM was performed with a Philips CM30 ST at 300kV (LaB6cathode). Samples were prepared dry onto a holey carbon/copper grid.

9.1.2. Experimental Section
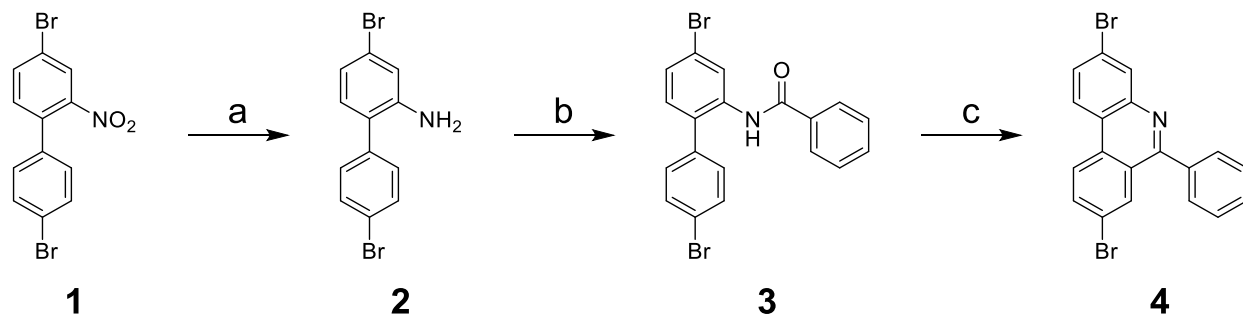
Scheme S9.1.1. Synthesis route to the phenylphenanthridine precurser for the COF building block.

Synthesis of 4,4'-dibromo-[1,1'-biphenyl]-2-amine (2). 4,4'-dibromo-[1,1'-biphenyl]-2-amine (**2**) was synthesized according to a modified literature procedure.[3] Aqueous HCl (25 mL, 37%) was added to a solution of **1** (5.28 g, 14.8 mmol) in 50 mL ethanol. Tin powder (3.52 g, 29.6 mmol) was added to the stirring solution portionwise and the mixture was heated to reflux overnight. After cooling, the mixture was poured into ice water (300 mL) under stirring, the precipitate was collected by filtration and washed with water. The washed precipitate was dried under vacuum to give the product **2** that was used for the next step without further purification (4.50 g, 13.8 mmol, 93%). ^{1}H NMR (400 MHz, DMSO-d_6) δ 7.62 (d, J = 8.2 Hz, 2H), 7.34 (d, J = 8.2 Hz, 2H), 6.95 (d, J = 1.6 Hz, 2H), 6.89 (d, J = 8.1 Hz, 1H), 6.75 (dd, J = 8.1, 2.0 Hz, 1H), 5.15 (s, 2H). ^{13}C NMR (101 MHz, DMSO-d_6) δ 147.0, 137.7, 131.7, 131.7, 130.8, 123.5, 121.5, 120.3, 118.9, 117.1. HRMS (ESI) exact mass calculated for [M+H]+ ($C_{12}H_9Br_2N$) requires m/z 326.90813, found m/z 326.9069.

Synthesis of *N*-(4,4'-dibromo-[1,1'-biphenyl]-2-yl)benzamide (3). *N*-(4,4'-dibromo-[1,1'-bi-phenyl]-2-yl)benzamide (**3**) was synthesized according to a modified literature procedure.[3] Under argon **2** (2.00 g, 6.14 mmol) and triethylamine (1.00 mL, 7.37 mml) were dissolved in dry CH_2Cl_2 (30 mL) and benzoyl chloride (0.79 mL, 6.75 mmol) was added dropwise. The reaction mixture was stirred at room temperature overnight, then ethanol (5 mL) was added. After 1 h, the solution was poured into water (50 mL) and extracted with CH_2Cl_2. The combined organic layers were dried over anhydrous Na_2SO_4 and evaporated under reduced pressure. The resulting crude product was purified by recrystallization from CH_2Cl_2/*n*-hexane to obtain **3** (2.26 g, 5.24 mmol, 85%). ^{1}H NMR (400 MHz, DMSO-d_6) δ 10.01 (s, 1H), 7.79 (s, 1H), 7.75 (dd, J = 8.2, 1.5 Hz, 2H), 7.62 – 7.52 (m, 4H), 7.48 (t, J = 7.4 Hz, 2H), 7.38 (d, J = 8.5 Hz, 2H), 7.35 (d, J = 8.3 Hz, 1H). ^{13}C NMR (101 MHz, DMSO-d_6) δ 165.8, 137.4, 136.5, 136.0, 134.1, 131.9, 131.7, 131.3, 130.6, 130.5, 129.5, 128.4, 127.5, 121.0, 120.4. HRMS (ESI) exact mass calculated for [M+H]+ ($C_{19}H_{13}Br_2NO$) requires m/z 430.93434, found m/z 430.9318.

Synthesis of 3,8-dibromo-6-phenylphenanthridine (4). 3,8-dibromo-6-phenylphen-anthridine (**4**) was synthesized according to a modified literature method.[4] Under argon a Biotage micro-wave vial was charged with **3** (1.00 g, 2.34 mmol), 2-chloropyridine (0.27 mL, 2.81 mmol) and dry CH_2Cl_2 (10 mL). Trifluormethansulfonic anhydride (0.43 mL, 2.57 mmol) was added dropwise at 0°C. After 5 minutes, the solution was warmed to room temperature, the vial was capped and under microwave irradiation, the solution was heated to 140 °C for 30 minutes. After the solution was cooled to room temperature, triethylamine (0.65 mL, 4.68 mmol) was added dropwise to neu-tralize the trifluormethanesulfonate salts. All volatiles were removed under reduced pressure and the residue was purified by flash column chromatography (SiO_2, n-hexane/ CH_2Cl_2) to obtain **4** (0.90 g, 2.17 mmol, 93%). ^1H NMR (400 MHz, $CDCl_3$) δ 8.47 (d, J = 8.9 Hz, 1H), 8.40 (d, J = 2.1 Hz, 1H), 8.38 (d, J = 8.8 Hz, 1H), 8.24 (d, J = 2.1 Hz, 1H), 7.93 (dd, J = 8.8, 2.0 Hz, 1H), 7.76 (dd, J = 8.8, 2.1 Hz, 1H), 7.70 (dd, J = 7.3, 2.1 Hz, 1H), 7.63 – 7.52 (m, 3H). ^{13}C NMR (101 MHz, $CDCl_3$) δ 161.3, 144.7, 138.8, 134.4, 133.0, 132.0, 131.4, 130.7, 129.8, 129.4, 128.9, 126.6, 124.1, 123.4, 123.1, 122.1, 121.8. HRMS (ESI) exact mass calculated for [M+H]+ ($C_{19}H_{11}Br_2N$) requires m/z 412.92378, found m/z 412.9230.
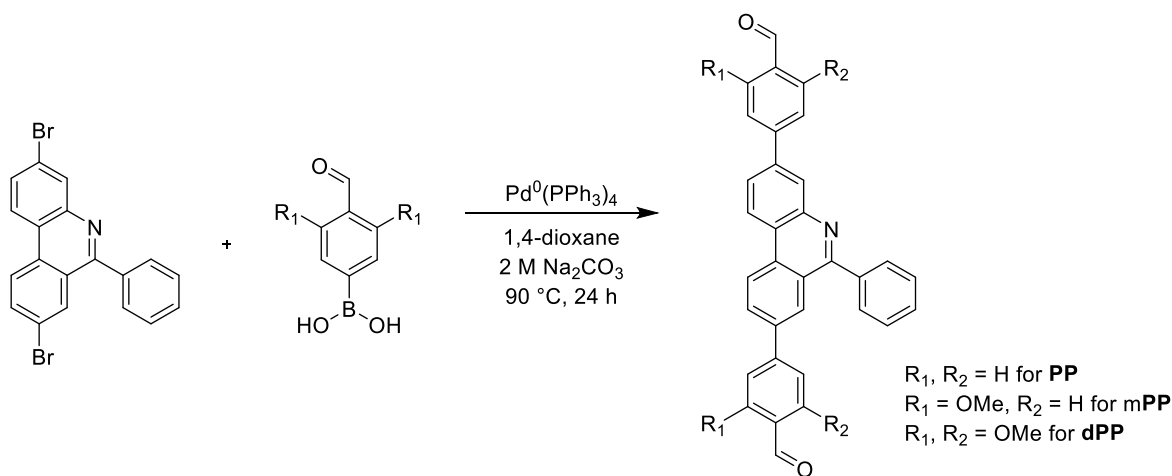
Scheme S9.1.2. Synthesis of phenylphenanthridine based COF building blocks **PP**, **mPP**, and **dPP** starting from precurser **4**.

Synthesis of 4,4'-(6-phenylphenanthridine-3,8-diyl)dibenzaldehyde (PP). Under argon, **4** (0.50 g, 1.21 mmol), 4-formylphenylboronic acid (0.73 g, 4.84 mmol) and Tetrakis(tri-phenylphosphin)palladium(0) (0.07 g, 0.06 mmol) were dissolved in 1,4-dioxane (15 mL) and 2 M aqueous Na_2CO_3 (3.6 mL) was added. After degassing the solution with argon for 30 minutes the mixture was stirred for 24 h at 90 °C. After cooling to room temperature, water was added and the mixture extracted with $CHCl_3$. The combined organic layers were dried over anhydrous Na_2SO_4 and evaporated under reduced pressure. The solid residue was purified by flash column chromatography (SiO_2, n-hexane/$CHCl_3$) to obtain **PP** (0.42 g, 0.90 mmol, 74%).

^1H NMR (400 MHz, $CDCl_3$) δ 10.09 (d, J = 9.8 Hz, 2H), 8.84 (d, J = 8.6 Hz, 1H), 8.74 (d, J = 8.6 Hz, 1H), 8.59 (s, 1H), 8.41 (d, J = 1.8 Hz, 1H), 8.18 (dd, J = 8.6, 1.8 Hz, 1H), 8.06 – 7.96 (m, 7H),

7.81 (t, J = 7.7 Hz, 4H), 7.66 – 7.55 (m, 3H). ^{13}C NMR (101 MHz, CDCl$_3$) δ 192.0, 191.8, 162.2, 146.1, 146.0, 140.5, 139.0, 135.8, 135.8, 133.2, 130.6, 130.2, 129.9, 129.5, 128.9, 128.1, 128.0, 127.8, 126.4, 125.8, 123.5, 123.4, 123.2. IR v_{max}/cm^{-1} 3062, 2818, 2730, 1698, 1602, 1554, 1474, 1367, 1309, 1212, 1171, 966, 807, 703, 517. HRMS (ESI) exact mass calculated for [M+H]+ (C$_{33}$H$_{21}$NO$_2$) requires m/z 464.16058, found m/z 463.1568.

Synthesis of 4,4'-(6-phenylphenanthridine-3,8-diyl)bis(2-methoxybenzaldehyde) (mPP).
Under argon, **4** (0.50 g, 1.21 mmol), 4-formyl-3-methoxyphenylboronic acid (0.76 g, 4.24 mmol) and Tetrakis(triphenylphosphin)palladium(0) (0.10 g, 0.09 mmol) were dissolved in 1,4-dioxane (15 mL) and 2 M aqueous Na$_2$CO$_3$ (3.6 mL) was added. After degassing the solution with argon for 30 minutes the mixture was stirred for 24 h at 90 °C. After cooling to room temperature, water was added and the mixture extracted with CHCl$_3$. The combined organic layers were dried over anhydrous Na$_2$SO$_4$ and evaporated under reduced pressure. The solid residue was purified by flash column chromatography (SiO$_2$, *n*-hexane/CHCl$_3$) to obtain **mPP** (0.40 g, 0.79 mmol, 63%). ^{1}H NMR (400 MHz, CDCl$_3$) δ 10.51 (s, 1H), 10.50 (s, 1H), 8.83 (d, J = 8.6 Hz, 1H), 8.73 (d, J = 8.5 Hz, 1H), 8.39 (s, 1H), 8.19 (d, J = 8.4 Hz, 1H), 8.04 (d, J = 8.2 Hz, 1H), 7.96 (d, J = 8.0 Hz, 1H), 7.93 (d, J = 8.0 Hz, 1H), 7.87 – 7.82 (m, 2H), 7.70 – 7.61 (m, 3H), 7.54 (d, J = 7.7 Hz, 1H), 7.50 – 7.42 (m, 2H), 7.28 (d, J = 8.1 Hz, 1H), 7.20 (s, 1H), 4.05 (s, 3H), 4.00 (s, 3H) ppm. ^{13}C NMR (101 MHz, CDCl$_3$) δ 189.6, 189.4, 162.4, 162.3, 147.6, 133.2, 132.3, 132.2, 132.1, 132.1, 129.5, 129.4, 128.9, 128.7, 128.6, 128.0, 128.0, 126.7, 125.6, 124.3, 123.5, 123.1, 120.1, 119.9, 110.7, 56.0, 55.9 ppm. IR v_{max}/cm^{-1} 3363, 3060, 2874, 1676, 1601, 1571, 1470, 1404, 1185, 1116, 1029, 854, 796, 697, 539. HRMS (ESI) exact mass calculated for [M+H]+ (C$_{35}$H$_{25}$NO$_4$) requires m/z 523.17836, found m/z 523.1772.

Synthesis of 4,4'-(6-phenylphenanthridine-3,8-diyl)bis(2,6-dimethoxybenzaldeyde) (dPP).
Under argon, **4** (0.50 g, 1.21 mmol), 4-formyl-3,5-dimethoxyphenylboronic acid (0.89 g, 4.24 mmol) and Tetrakis(triphenylphosphin)palladium(0) (0.14 g, 0.12 mmol) were dissolved in 1,4-dioxane (15 mL) and 2 M aqueous Na$_2$CO$_3$ (6 mL) was added. After degassing the solution with argon for 30 minutes the mixture was stirred for 24 h at 90 °C. After cooling to room temperature, water was added and the mixture extracted with CHCl$_3$. The combined organic layers were dried over anhydrous Na$_2$SO$_4$ and evaporated under reduced pressure. The solid residue was purified by flash column chromatography (SiO$_2$, *n*-hexane/CHCl$_3$) to obtain **dPP** (0.46 g, 0.79 mmol, 66%). ^{1}H NMR (400 MHz, CDCl$_3$) δ 10.55 (s, 1H), 10.53 (s, 1H), 8.82 (d, J = 8.7 Hz, 1H), 8.73 (d, J = 8.6 Hz, 1H), 8.59 (s, 1H), 8.36 (d, J = 1.7 Hz, 1H), 8.14 (dd, J = 8.5, 1.7 Hz, 1H), 8.00 (dd, J = 8.5, 1.8 Hz, 1H), 7.83 (dd, J = 7.5, 1.6 Hz, 1H), 7.60 (d, J = 7.3 Hz, 3H), 7.00 (s, 2H), 6.79 (s, 2H), 4.01 (s, 6H), 3.96 (s, 6H) ppm. ^{13}C NMR (101 MHz, CDCl$_3$) δ 189.1, 189.0, 162.7, 162.7, 162.3, 147.9, 147.8, 141.0, 139.7, 133.3, 132.3, 132.2, 132.1, 132.0, 130.0, 129.9, 129.5, 128.8, 128.7, 128.6, 127.8, 126.2, 125.7, 123.6, 123.4, 123.1, 113.6, 103.3, 103.2, 56.4, 56.3 ppm. IR v_{max}/cm^{-1} 3356, 3066, 2941, 2848, 2783, 1674, 1599, 1568, 1455, 1399, 1242, 1178, 1125, 927,

807, 707, 576, 509. HRMS (ESI) exact mass calculated for [M+H]+ ($C_{37}H_{29}NO_6$) requires m/z 583.19949, found m/z 583.1984.
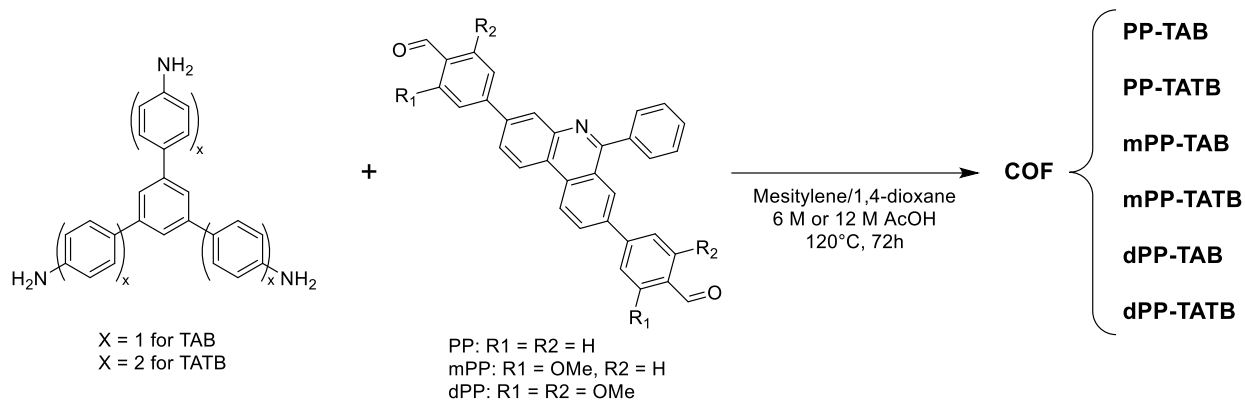
Scheme S9.1.3. Synthesis of phenylphenanthridine COFs.

General synthesis of phenylphenanthridine COFs

Into a 5 mL *Biotage* microwave vial, the amine (1.0 eq) and aldehyde (1.5 eq) were placed. A mesitlyene/1,4-dioxane mixture was added, followed by 6M or 12M AcOH. The vial was capped and placed in an aluminum heating block that was preheated to 120°C. Under stirring at 500 rpm the mixture was kept at 120°C for 72h, then it was allowed to cool to room temperature. The solid was filtered off, washed with MeOH and then subjected to Soxhlet extraction with MeOH for 16h. The MeOH soaked solid was then activated by scCO2 drying and further under high vacuum for 24h to obtain the COF.

Table S9.1.1. Synthesis of phenylphenanthridine COFs.

COF	Aldehyde	Amine	Mesity-lene/1,4-di-oxane, (v/v) / ml	Catalyst	Yield
PP-TAB	PP (20.0 mg, 0.045 mmol)	TAB (10.8 mg, 0.030 mmol)	1/1	6M AcOH (50 µl)	21.1 mg (75 %)
PP-TAPB	PP (30.0 mg, 0.065 mmol)	TAPB (25.0 mg, 0.043 mmol)	1.5/1.5	6M AcOH (75 µl)	32.0 mg (60 %)
mPP-TAB	mPP (23.6 mg, 0.045 mmol)	TAB (10.8 mg, 0.030 mmol)	1.4/0.6	6M AcOH (50 µl)	22.9 mg (71 %)
mPP-TAPB	mPP (23.6 mg, 0.045 mmol)	TAPB (18.7 mg, 0.030 mmol)	1/1	6M AcOH (50 µl)	27.3 mg (69 %)
dPP-TAB	dPP (26.3 mg, 0.045 mmol)	TAB (10.8 mg, 0.030 mmol)	0.7/0.3	12M AcOH (15 µl)	26.6 mg (76 %)
dPP-TAPB	dPP (40.1 mg, 0.069 mmol)	TAPB (26.6 mg, 0.046 mmol)	1.5/0.5	6M AcOH (50 µl)	43.3 mg (67 %)

9.1.3. FT-IR Spectroscopy
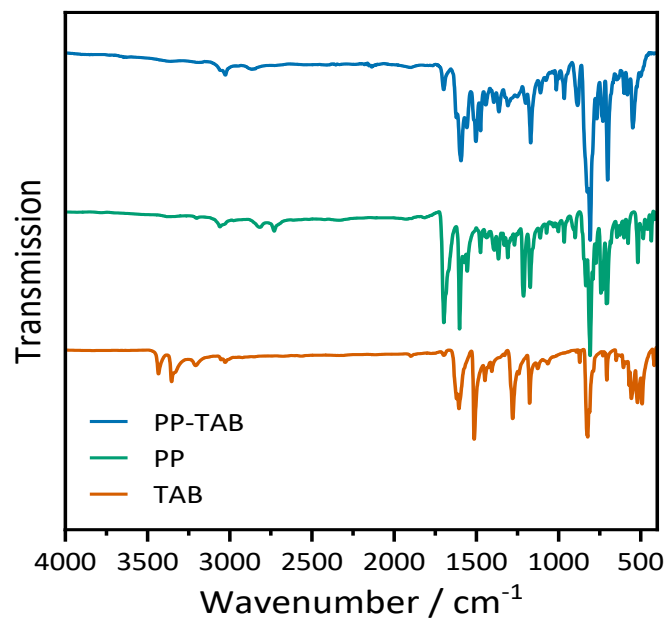
Figure S9.1.1. FT-IR comparison of **PP-TAB** and the starting materials **PP** and **TAB**.
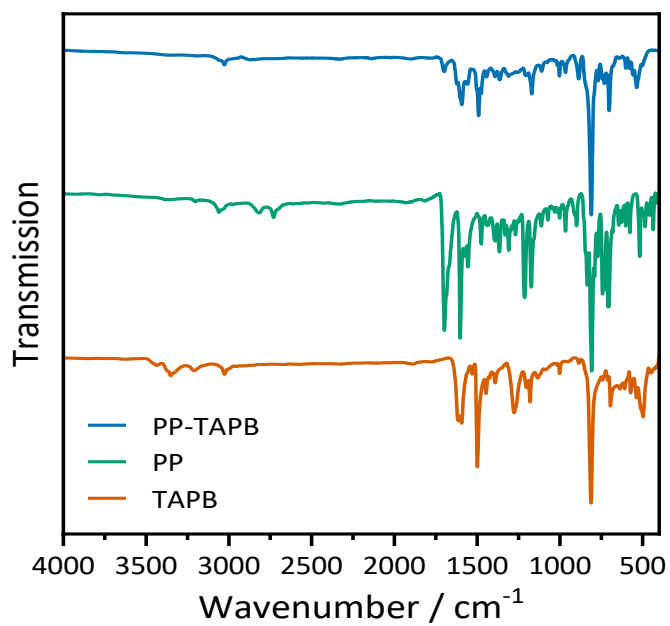
Figure S9.1.2. FT-IR comparison of **PP-TAPB** and the starting materials **PP** and **TAPB**.
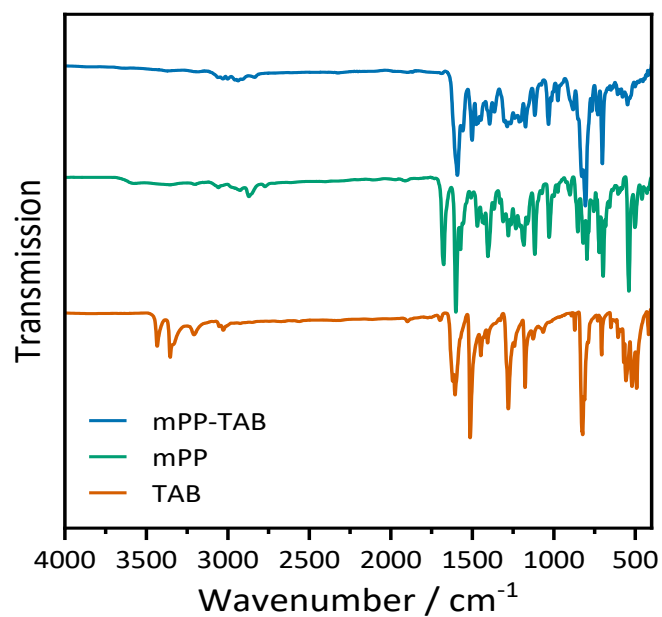
Figure S9.1.3. FT-IR comparison of **mPP-TAB** and the starting materials **mPP** and **TAB**.
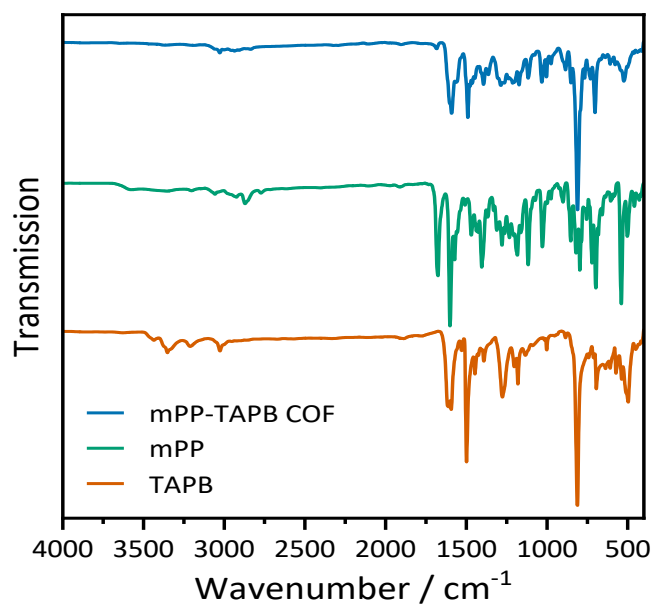
Figure S9.1.4. FT-IR comparison of **mPP-TAPB** and the starting materials **mPP** and **TAPB**.
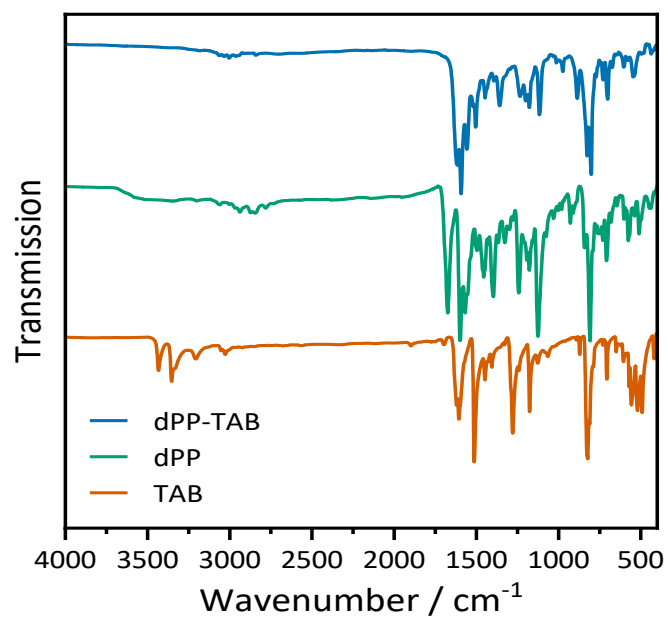
Figure S9.1.5. FT-IR comparison of **dPP-TAB** and the starting materials **dPP** and **TAB**.
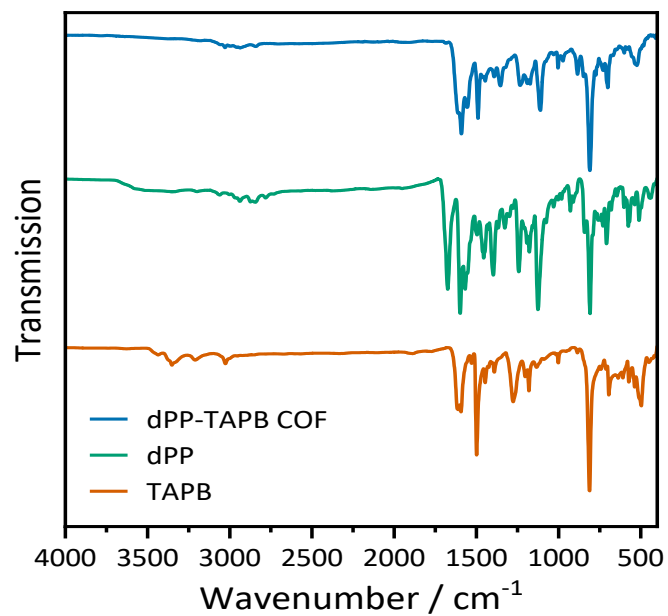
Figure S9.1.6. FT-IR comparison of **dPP-TAB** and the starting materials **dPP** and **TAPB**.

9.1.4.   XRPD Measurements and Refinements
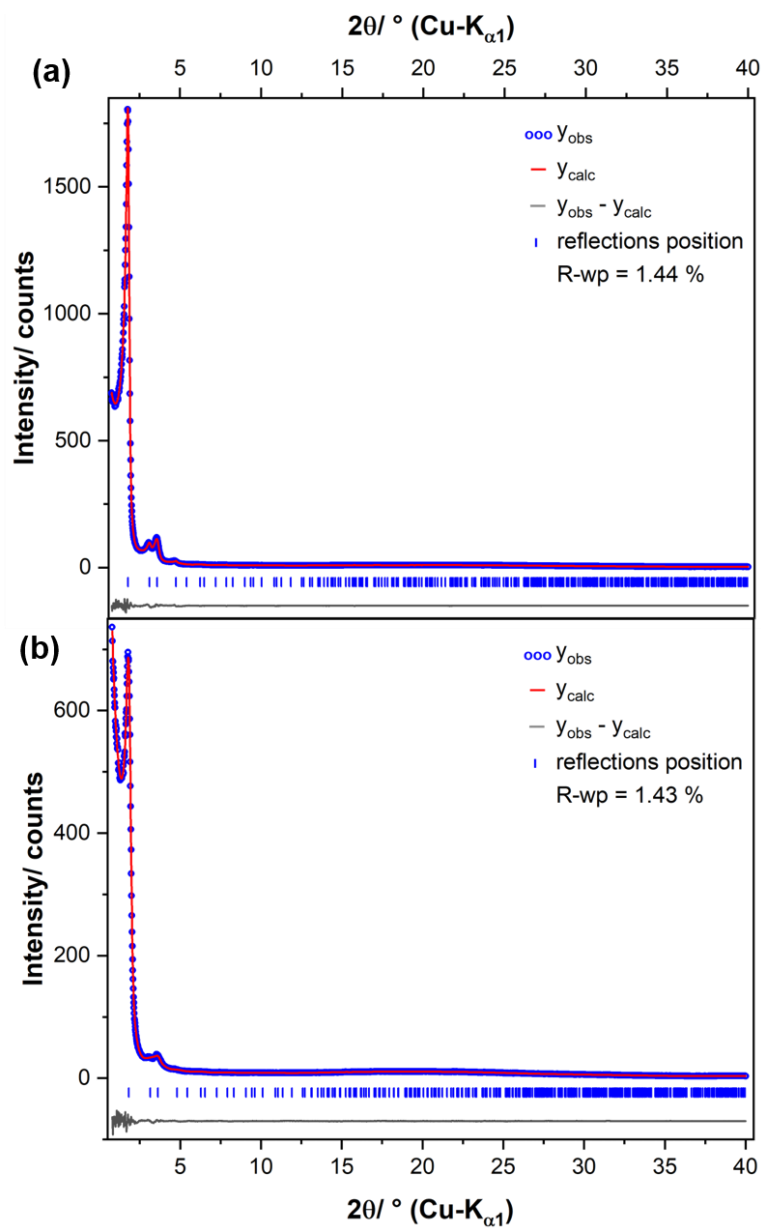
Figure S9.1.7. Graphical results of the final Rietveld refinements of the patterns of **PP-TAB.**(a) at 30 °C using a 12 layer supercell model with a disordered A$\overline{\text{B}}$-type staggered stacking and (b) at 200 °C using a 12 layer supercell model with a disordered A$\overline{\text{B}}$-type staggered stacking with a considerably larger layer offset.
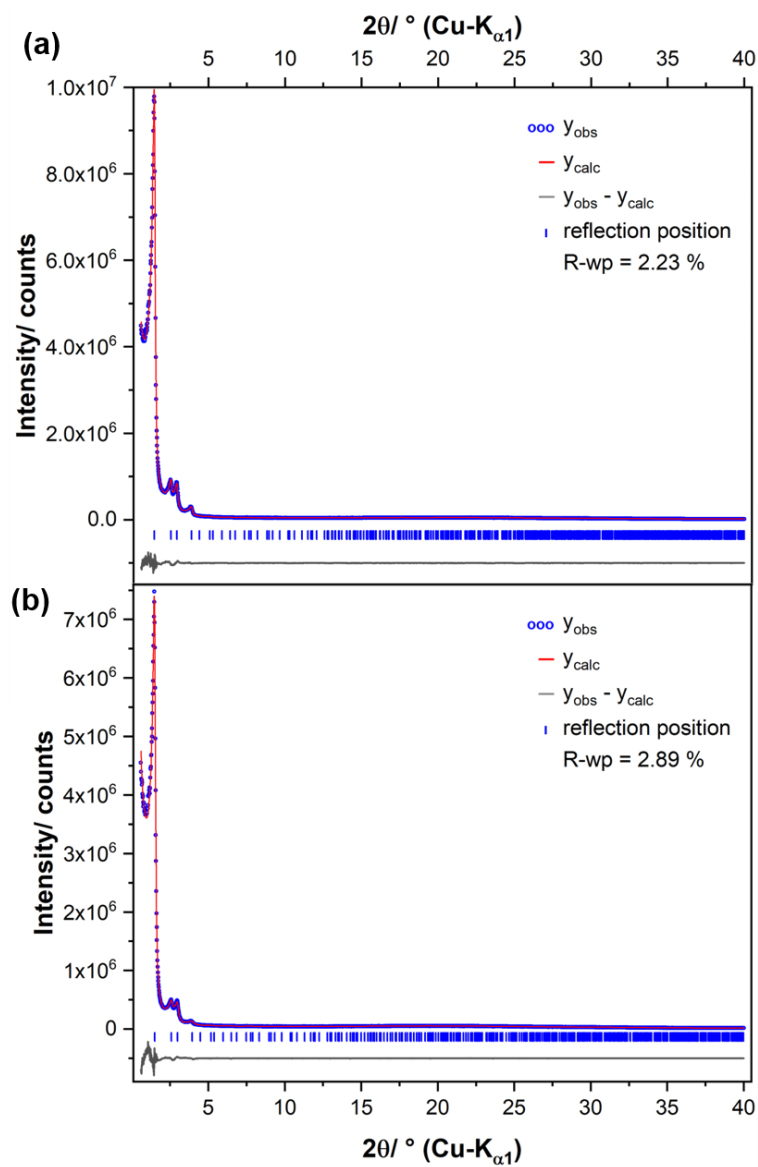
Figure S9.1.8. Graphical results of the final Rietveld refinements of the patterns of **PP-TATB** (a) at 30 °C using a 12 layer supercell model with a disordered A$\overline{\text{B}}$-type staggered and (b) at 200 °C using a 12 layer supercell model with a disordered A$\overline{\text{B}}$-type staggered stacking with a considerably larger layer offset.
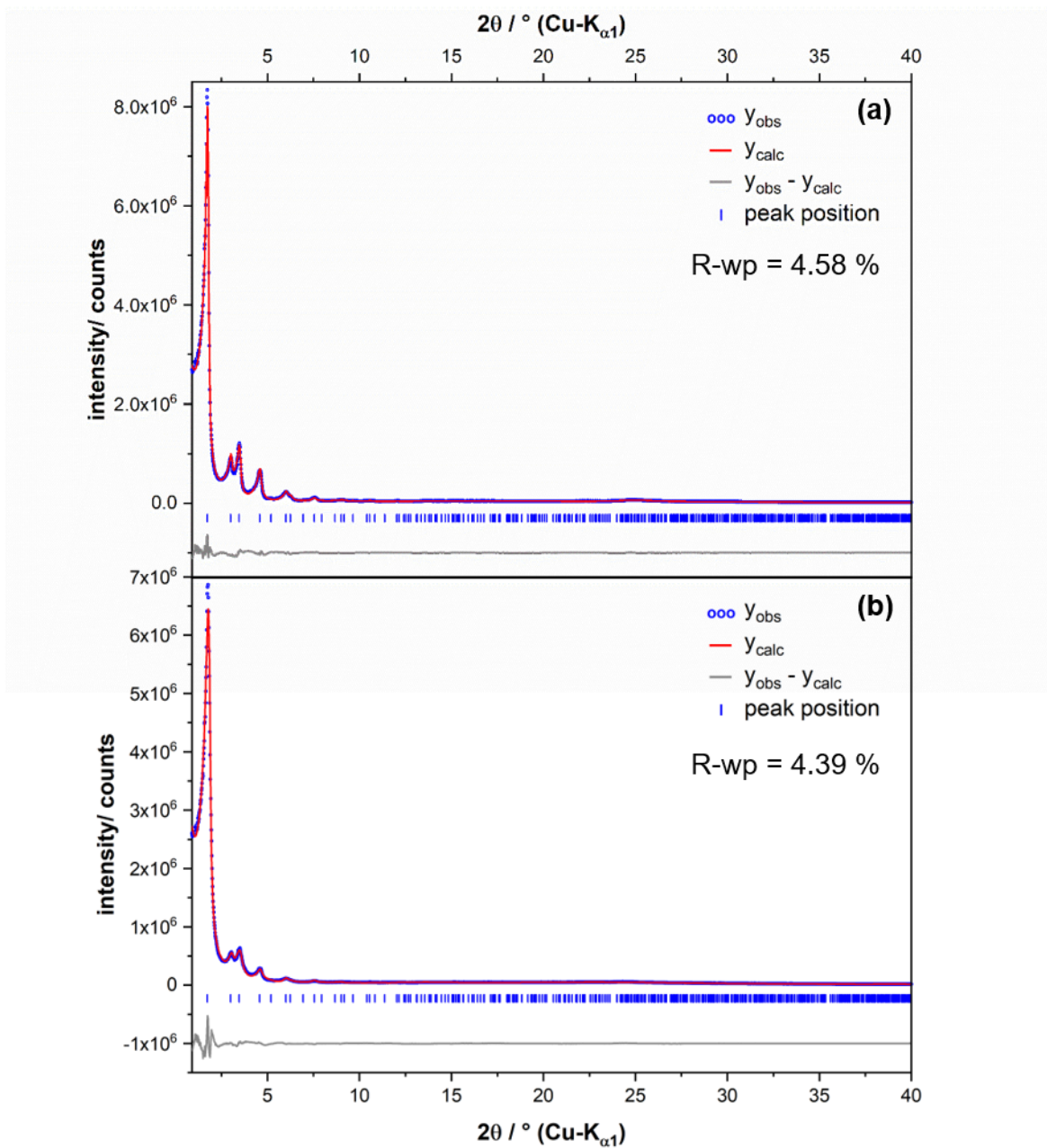
Figure S9.1.9. Graphical results of the final Rietveld refinements of the patterns of **mPP-TAB** (a) at 30 °C using an ordered A$\overline{\text{A}}$-type eclipsed stacking and (b) at 140 °C using a 4 layer supercell and a slightly disordered A$\overline{\text{B}}$-type staggered stacking.
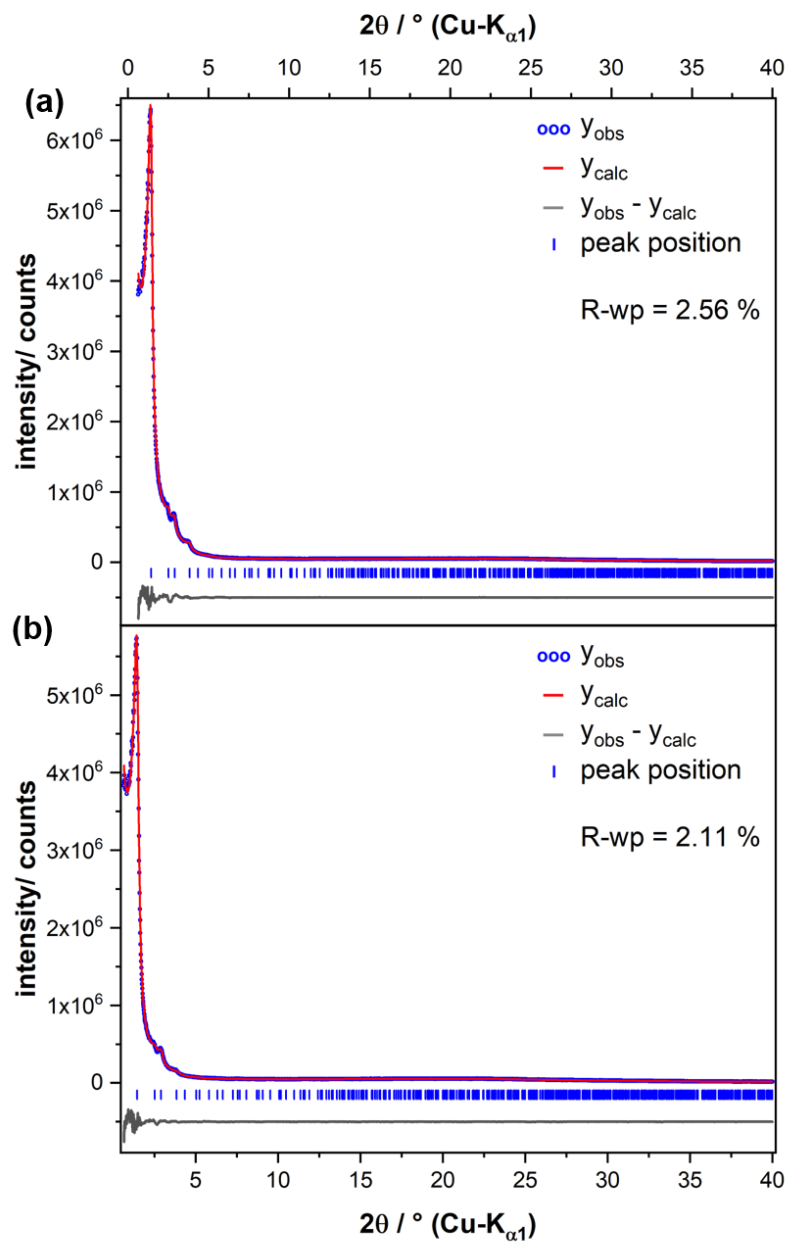
Figure S9.1.10. Graphical results of the final Rietveld refinements of the patterns of **mPP-TATB** (a) at 30 °C using a 12 layer supercell model with a disordered A$\overline{\text{B}}$-type staggered stacking and (b) at 200 °C using a 12 layer supercell model with a disordered A$\overline{\text{B}}$-type staggered stacking larger layer offset.
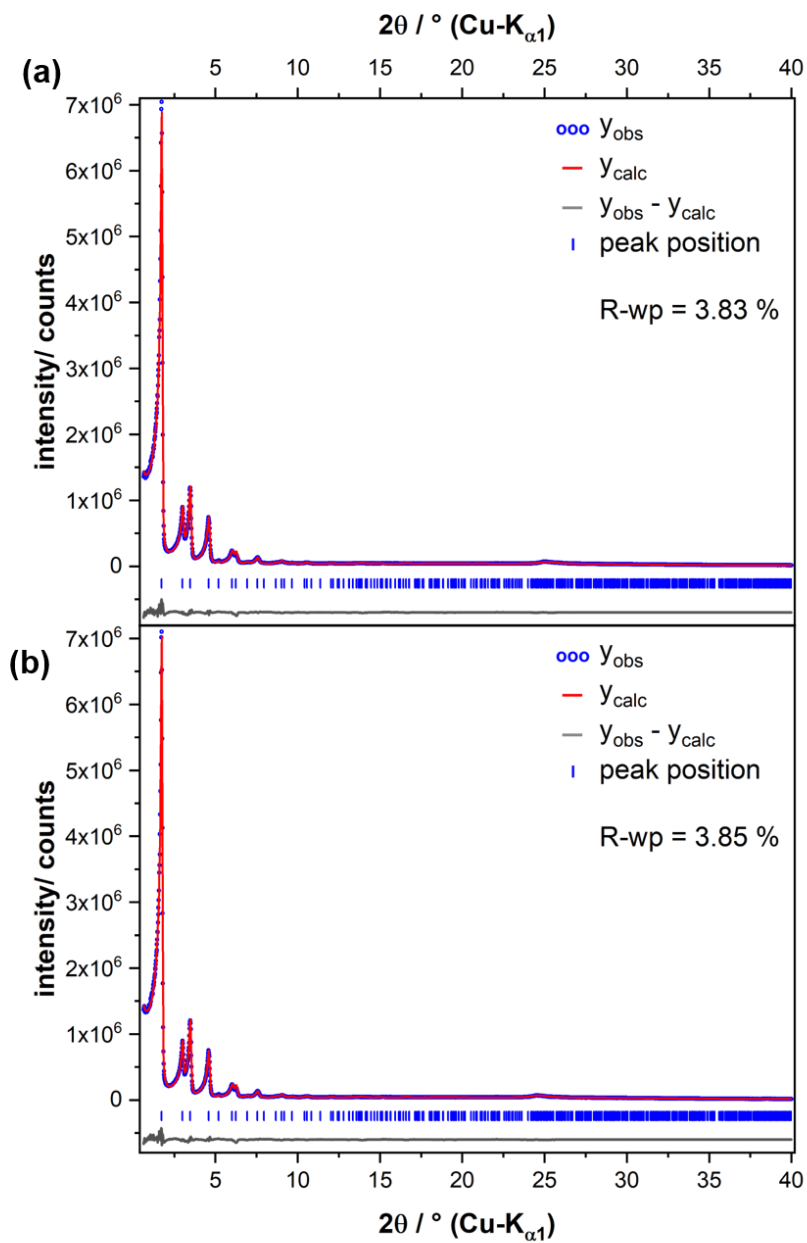
Figure S9.1.11. Graphical results of the final Rietveld refinements of the patterns of **dPP-TAB** (a) at 30 °C using a 2-layer model with an ordered A$\overline{\text{A}}$-type nearly eclipsed stacking and (b) at 200 °C using a 2-layer model with an ordered A$\overline{\text{A}}$-type nearly eclipsed stacking.
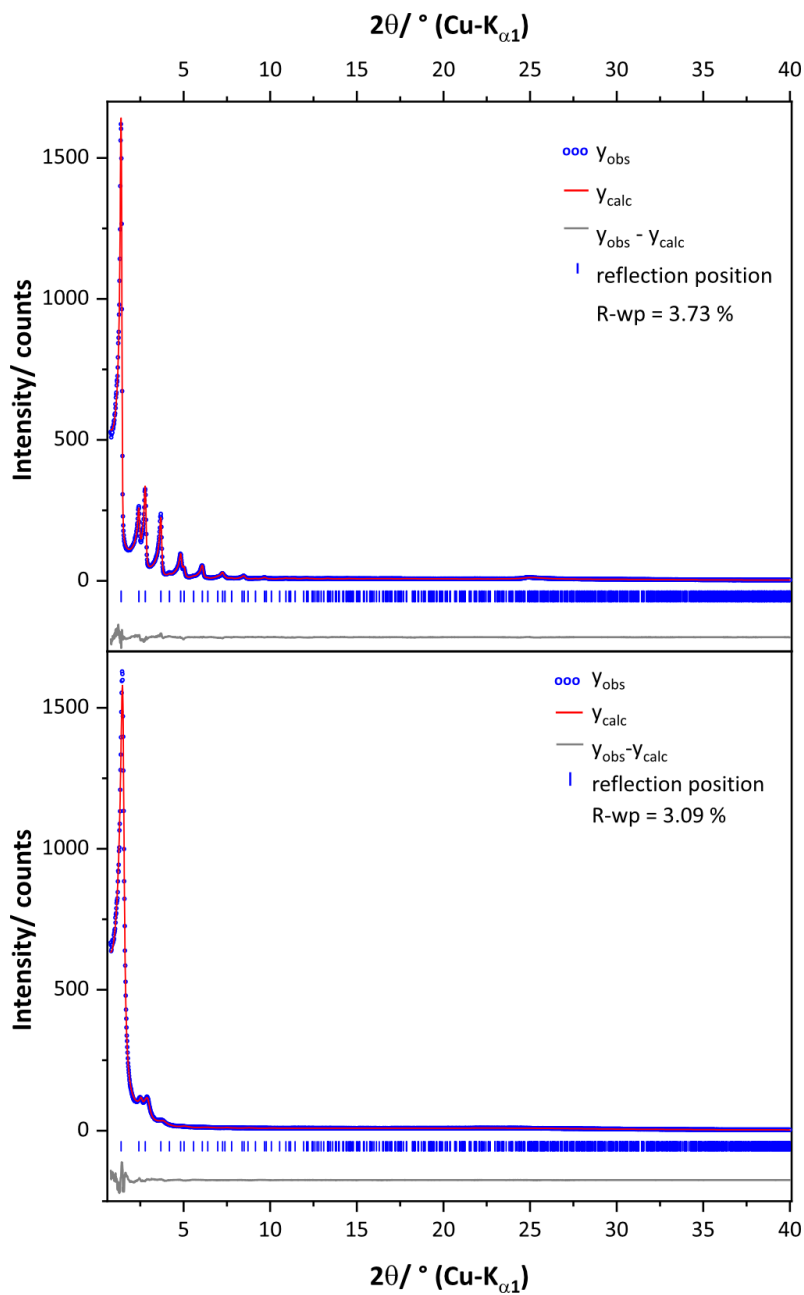
Figure S9.1.12. Graphical results of the final Rietveld refinements of the patterns of **dPP-TAPB** (a) at 30 °C using an ordered A$\overline{\text{A}}$-type eclipsed stacking and (b) at 140 °C using a 4 layer supercell and a slightly disordered A$\overline{\text{B}}$-type staggered stacking.
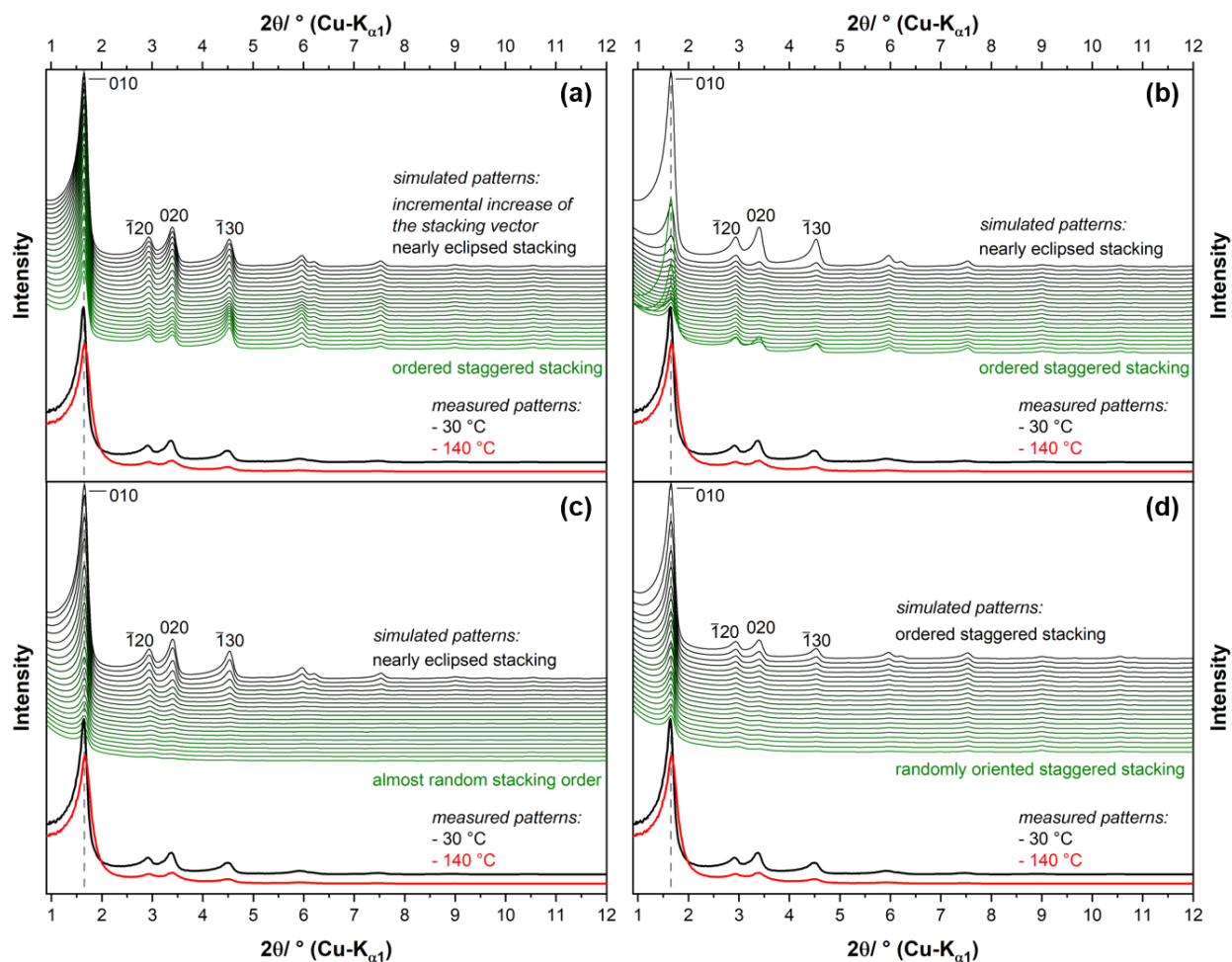
Figure S9.1.13. Comparison of simulated and measured diffraction patterns of **mPP-TAB**. (a) incrementally increasing the lengths of the stacking vector starting at 0 Å, i.e. A$\overline{\text{A}}$-type eclipsed stacking (b) using a faulting scenario describing the transition from ordered A$\overline{\text{A}}$-type eclipsed stacking to ordered staggered stacking via randomly ordered mixed states, (c) using a faulting scenario describing the transition from ordered A$\overline{\text{A}}$-type eclipsed stacking to a random stacking order and (d) using a faulting scenario describing the transition from ordered A$\overline{\text{B}}$-type staggered stacking to a randomly oriented staggered stacking order.
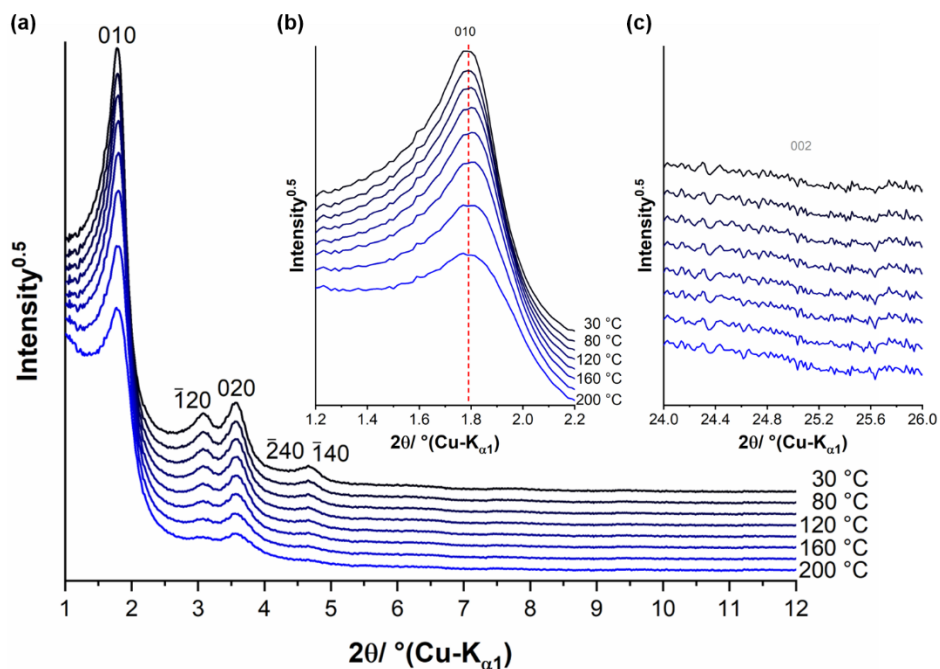
Figure S9.1.14. Temperature dependent in situ XRPD patterns of **PP-TAB** including selected reflection indices, (a) close-up of the low 2θ region, (b) close-up of the 010 reflections, (c) close-up of the 002 reflection.
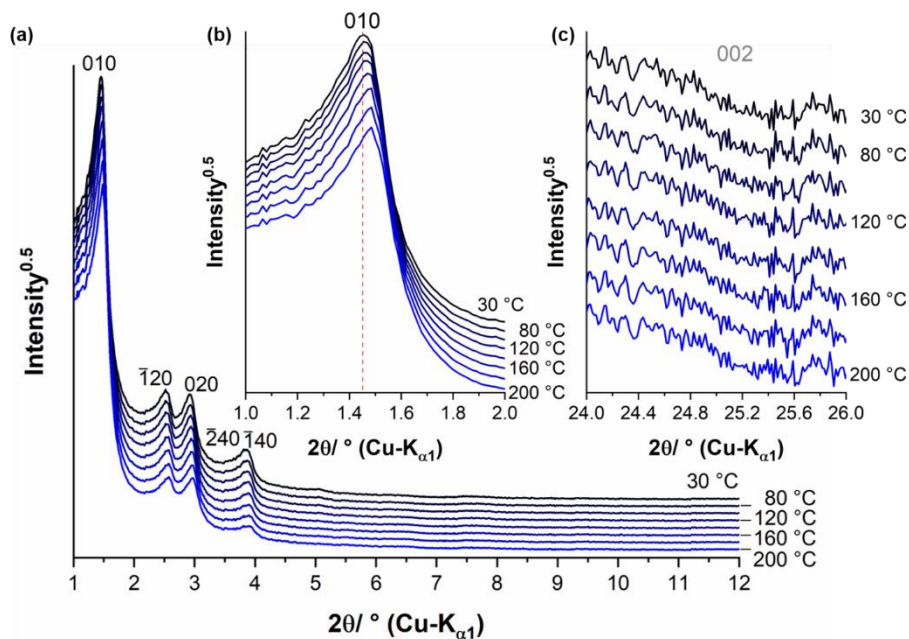
Figure S9.1.15. Temperature dependent in situ XRPD patterns of **PP-TATB** including selected reflection indices, (a) close-up of the low 2θ region, (b) close-up of the 010 reflections, (c) close-up of the 002 reflection.
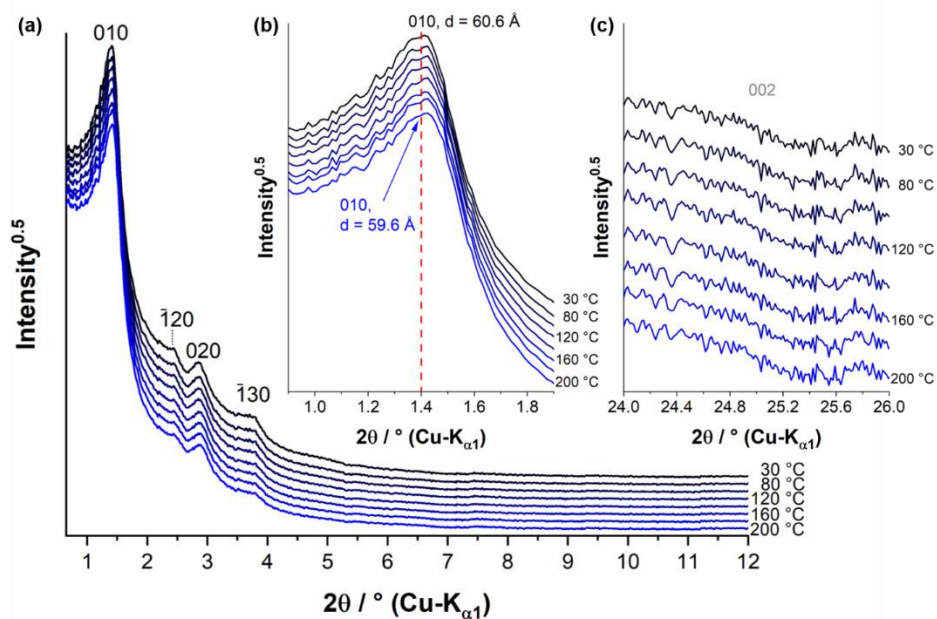
Figure S9.1.16. Temperature dependent in situ XRPD patterns of **mPP-TATB** including selected reflection indices, (a) close-up of the low 2θ region, (b) close-up of the 010 reflections, (c) close-up of the 002 reflection.
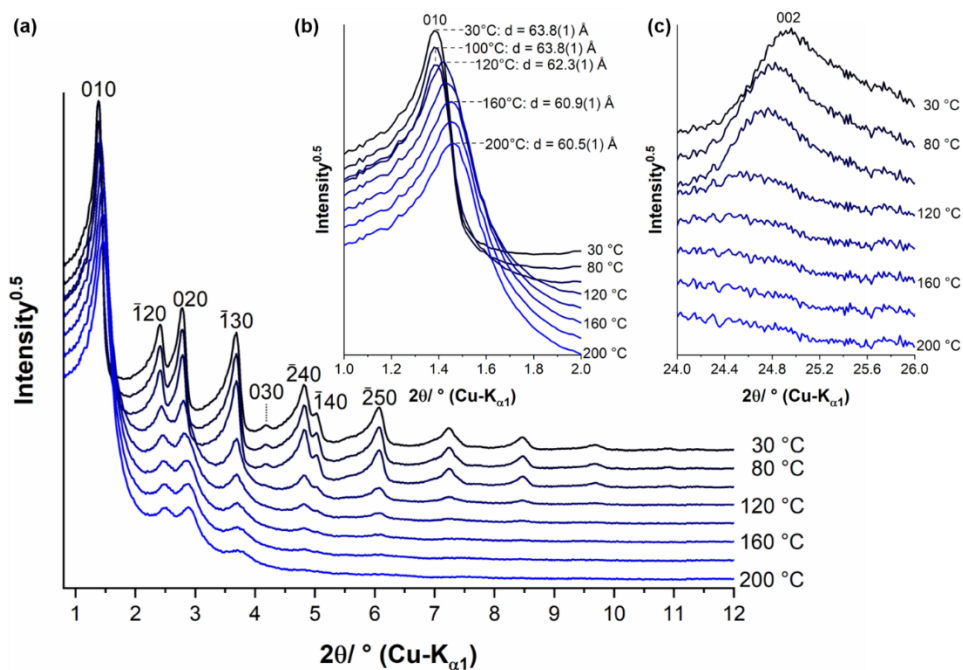
Figure S9.1.17. Temperature dependent in situ XRPD patterns of **dPP-TATB** including selected reflection indices, (a) close-up of the low 2θ region, (b) close-up of the 010 reflections, (c) close-up of the 002 reflection.
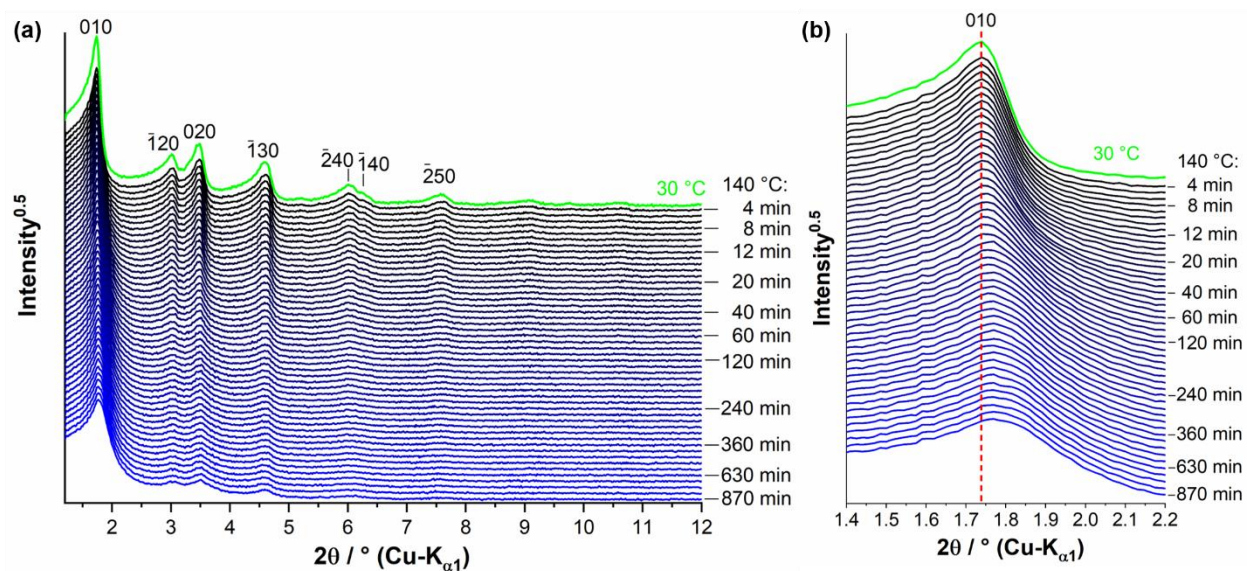
Figure S9.1.18. XRPD patterns of **mPP-TAB** collected at 30 °C (green pattern) and collected while holding the sample at 140 °C (black and blue patterns) for ca. 900 min (≡ 15 h), (a) excerpt of the low 2θ region, (b) excerpt showing the 010 reflection.

Table S9.1.2**.** Comparison of crystal structure features at room temperature and heating-induced structural changes of a series of investigated COFs.

COF	*a* and *b* / Å		thermal behavior		
	RT	200 °C	layer shifting	transition temperature	layer curving
PP-TAB	56.62(9)	56.17(9)	slight	-	slight increase
mPP-TAB	58.46(4)	55.03(3)	strong	(120–140) °C	strong increase
dPP-TAB	58.49(7)	58.53(5)	no	-	no
PP-TAPB	69.29(6)	68.20(0)	slight	-	medium increase
mPP-TAPB	69.97(4)	68.81(2)	slight	-	medium increase
dPP-TAPB	73.17(6)	70.04(8)	strong	(100–120) °C	strong increase

9.1.5. Gas Sorption Experiments
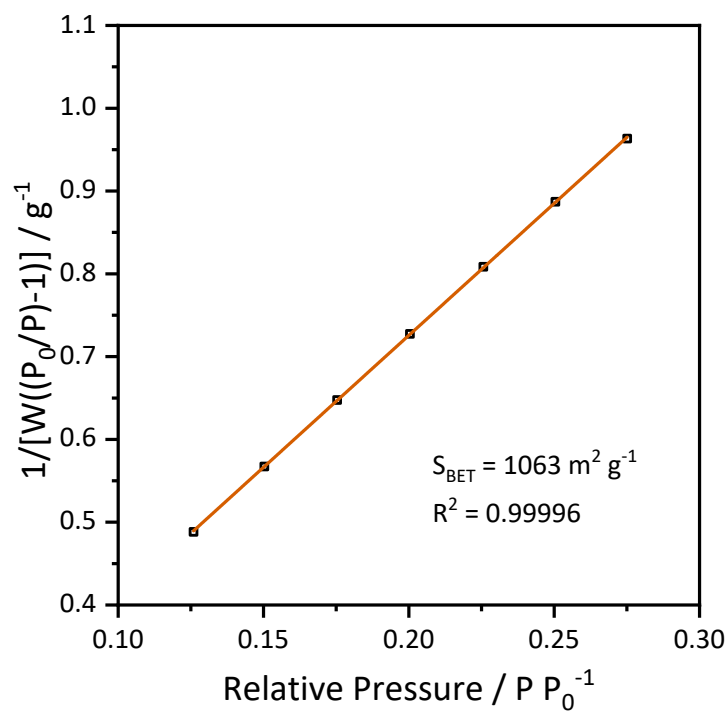
Figure S9.1.19. Multi-point BET surface area fit of **PP-TAB** derived from N_2 sorption isotherm.
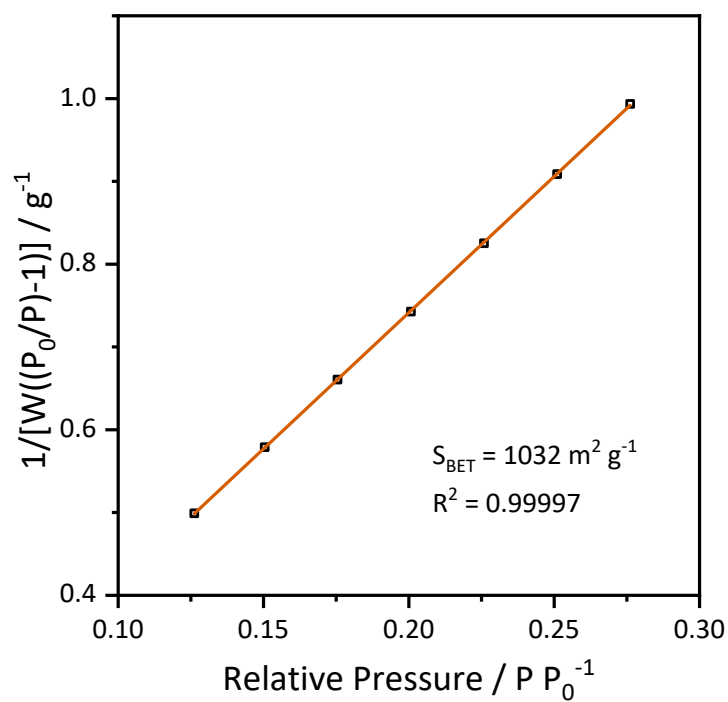
Figure S9.1.20. Multi-point BET surface area fit of **PP-TAPB** derived from N_2 sorption isotherm.
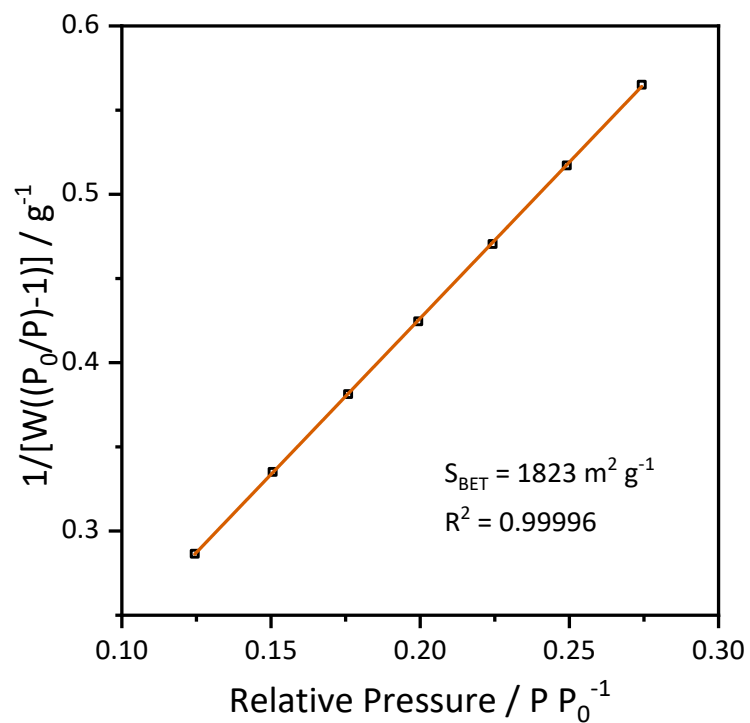
Figure S9.1.21. Multi-point BET surface area fit of **mPP-TAB** derived from N_2 sorption isotherm.
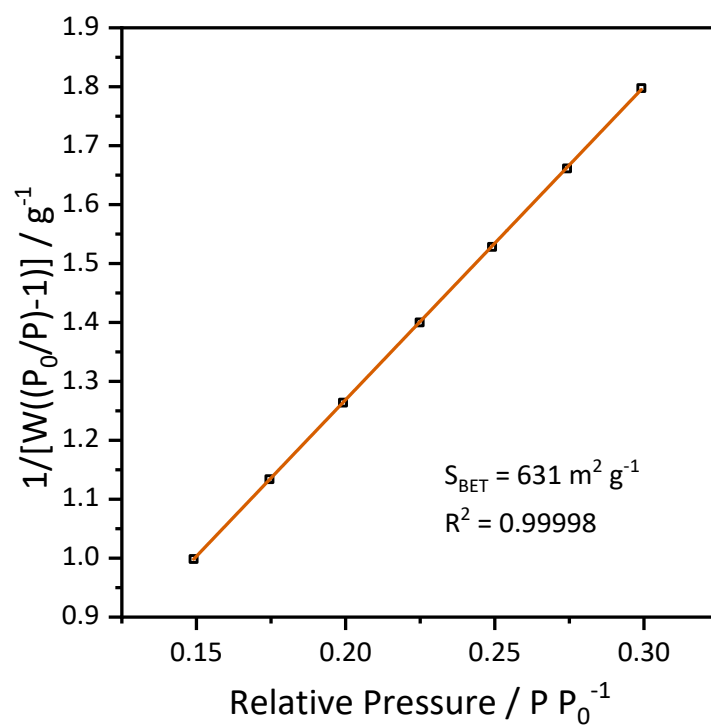
Figure S9.1.22. Multi-point BET surface area fit of **mPP-TAPB** derived from N_2 sorption isotherm.
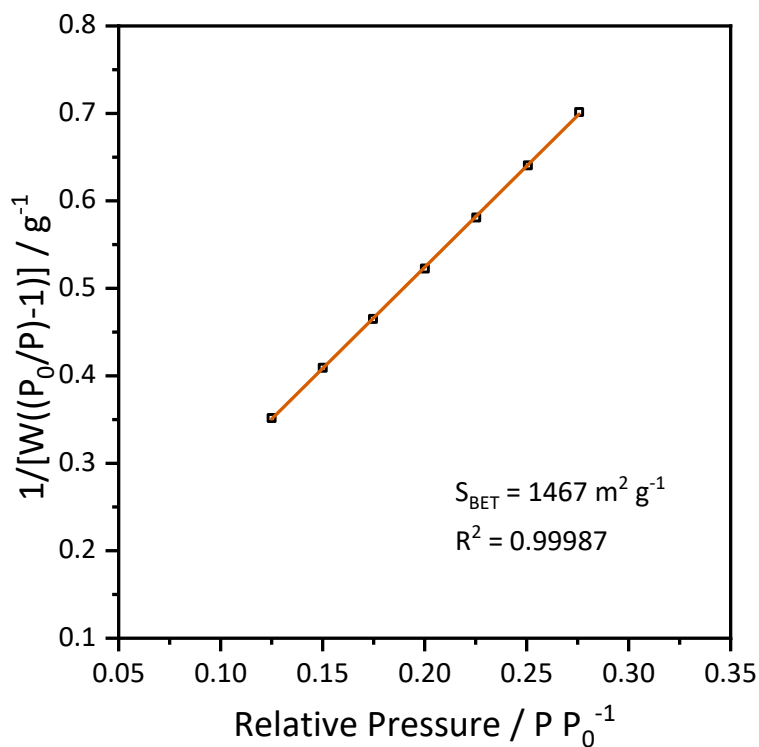
Figure S9.1.23. Multi-point BET surface area fit of **dPP-TAB** derived from N_2 sorption isotherm.
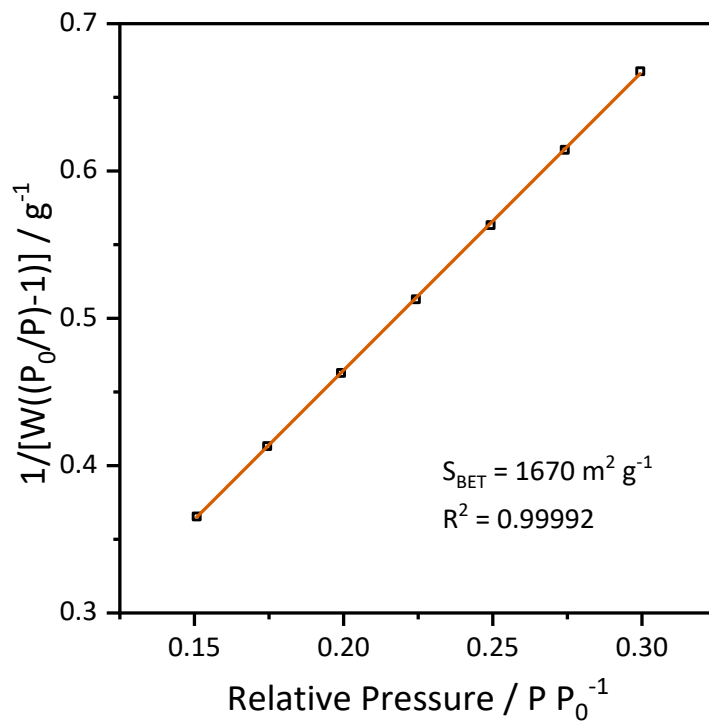
Figure S9.1.24. Multi-point BET surface area fit of **dPP-TAPB** derived from N_2 sorption isotherm.
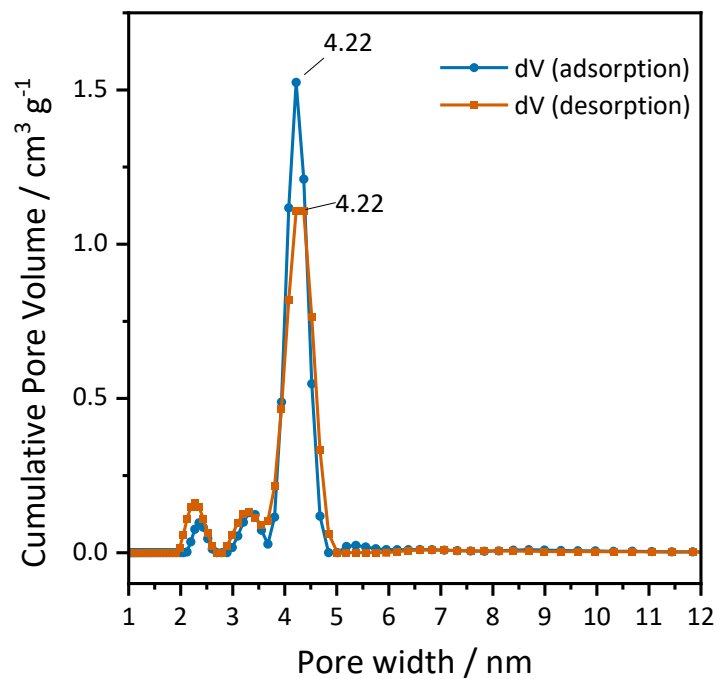
Figure S9.1.25. Comparison of PSD derived from the adsorption branch (blue) and the desorption branch (orange) for **PP-TAB**.
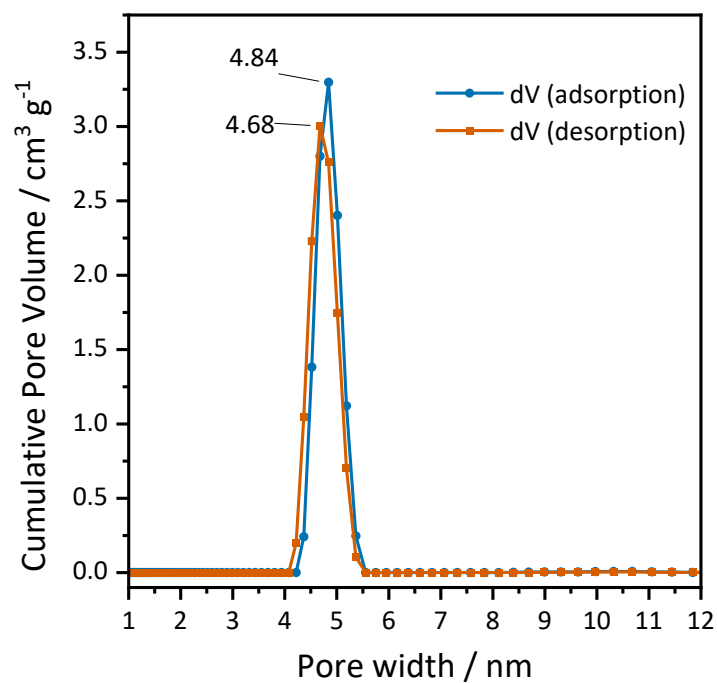
Figure S9.1.26. Comparison of PSD derived from the adsorption branch (blue) and the desorption branch (orange) for **PP-TAPB**.
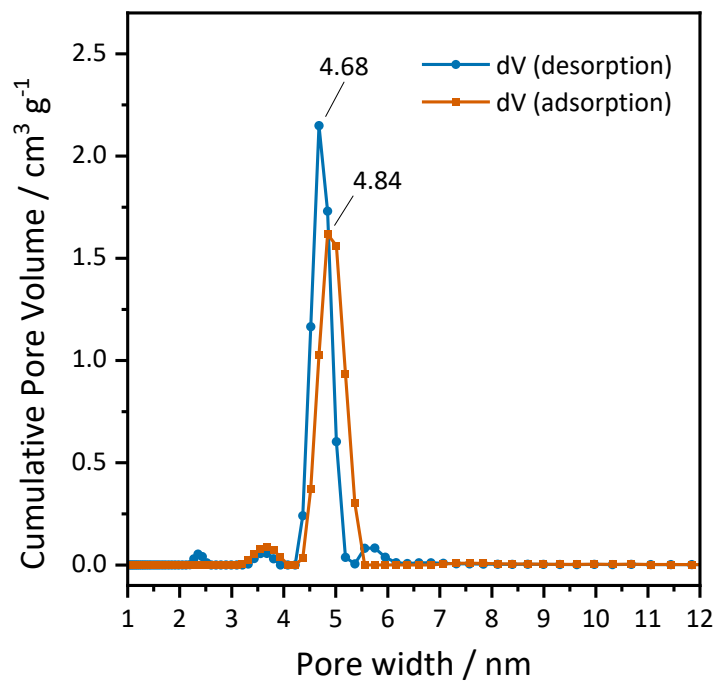
Figure S9.1.27. Comparison of PSD derived from the adsorption branch (blue) and the desorption branch (orange) for **mPP-TAB**.
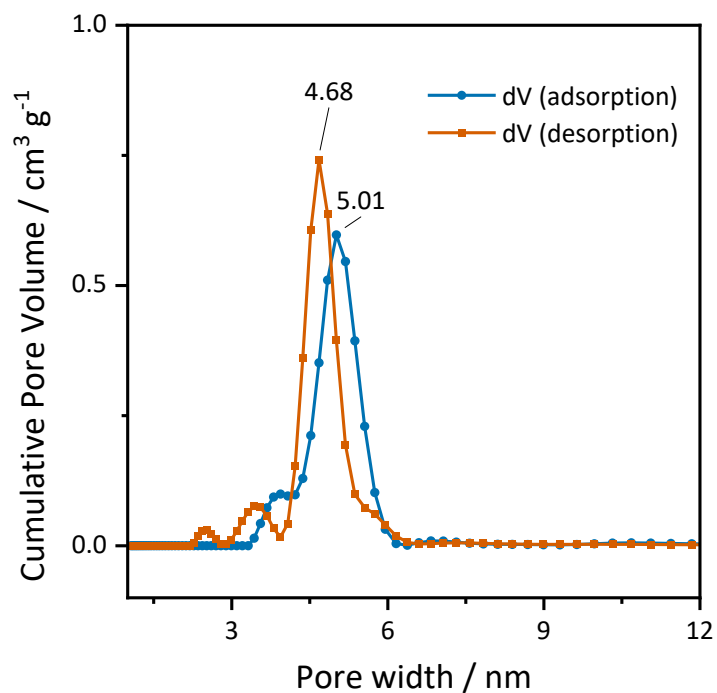
Figure S9.1.28. Comparison of PSD derived from the adsorption branch (blue) and the desorption branch (orange) for **mPP-TAPB**.
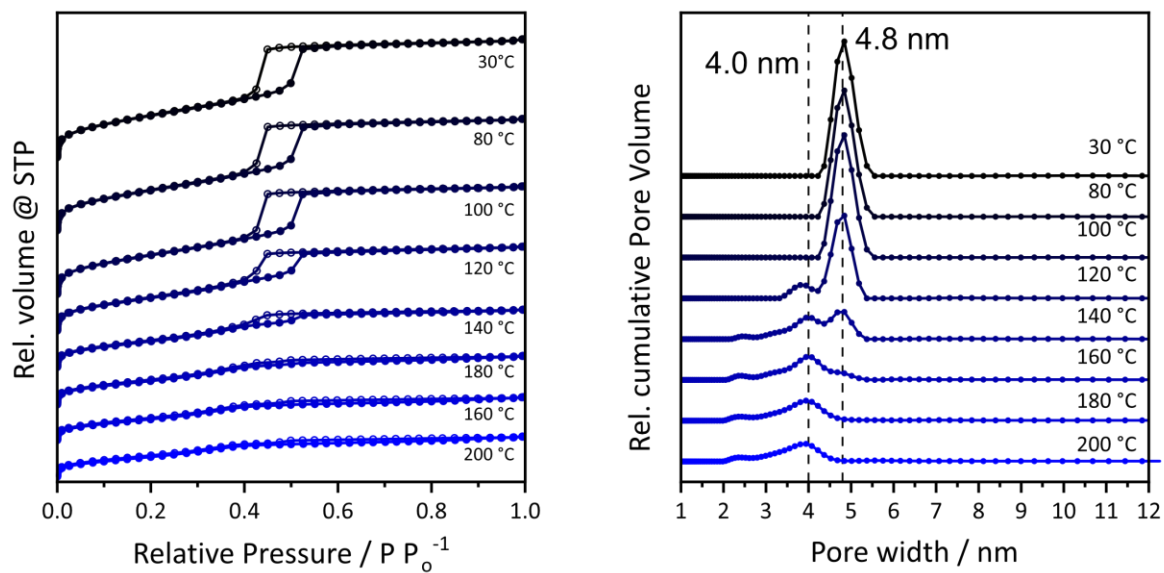
Figure S9.1.29. Evolution of isotherms (left) and pore size distribution (right) of mPP-TAB.
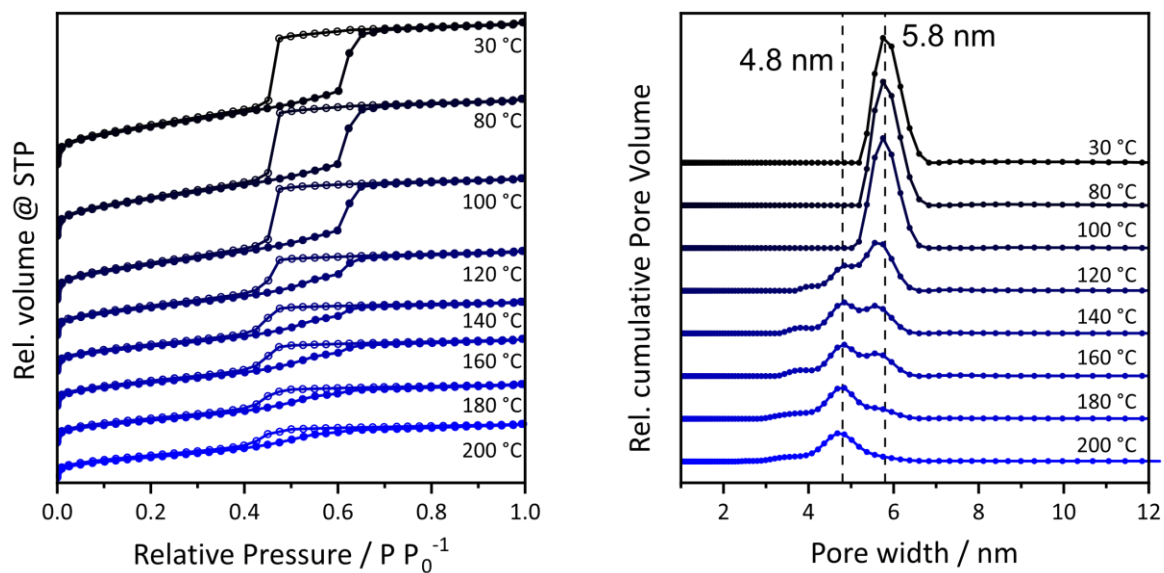
Figure S9.1.30. Evolution of isotherms (left) and pore size distribution (right) of dPP-TAPB.
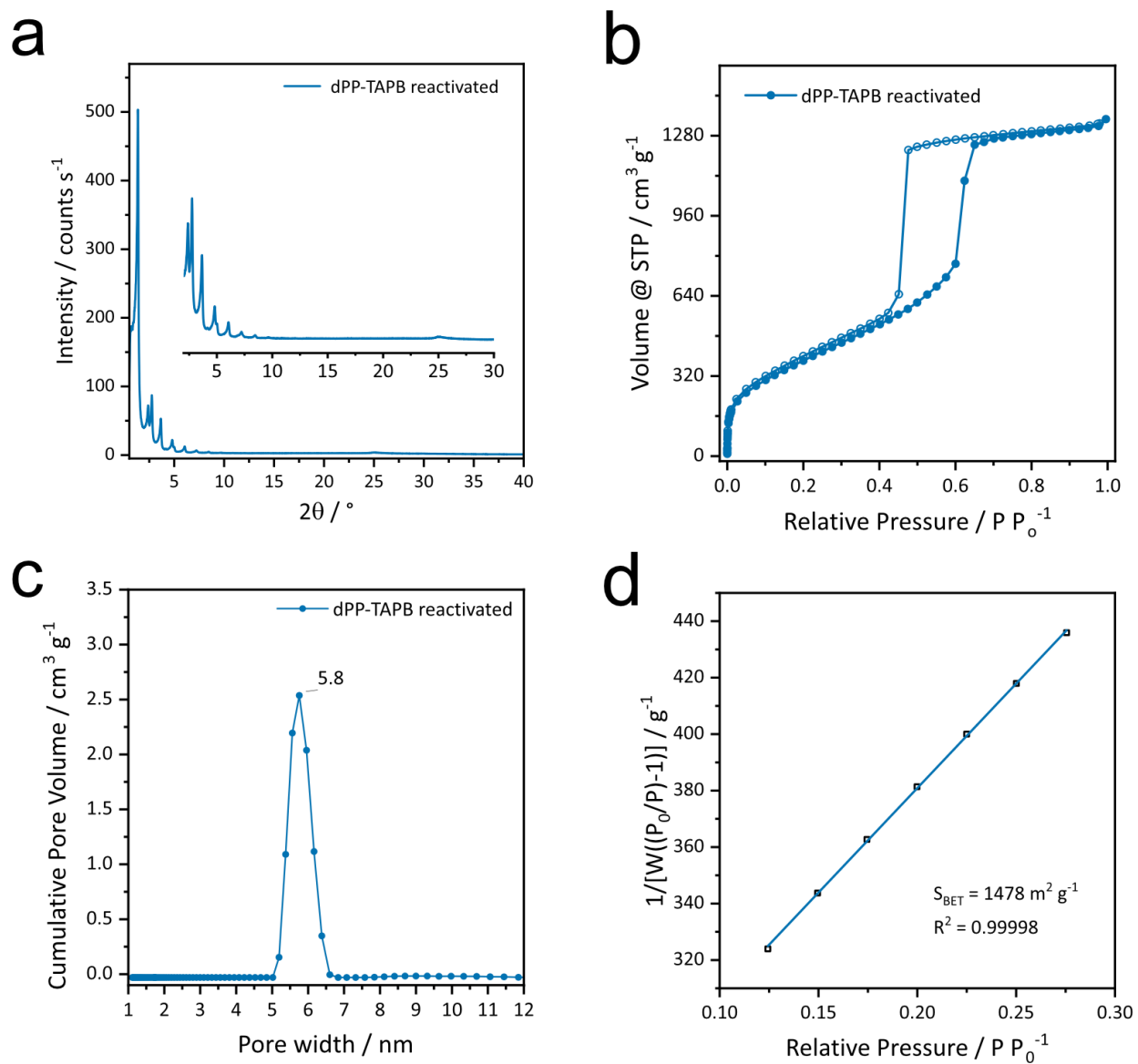
Figure S9.1.31. XRPD (Cu-K$_{\alpha1}$) (**a**), N$_2$ Isotherms at 77 K (**b**), PSD derived from the adsorption branch (**c**), and multi-point BET surface area fit (**d**) of reactivated samples after heat treatment of **dPP-TAPB.**
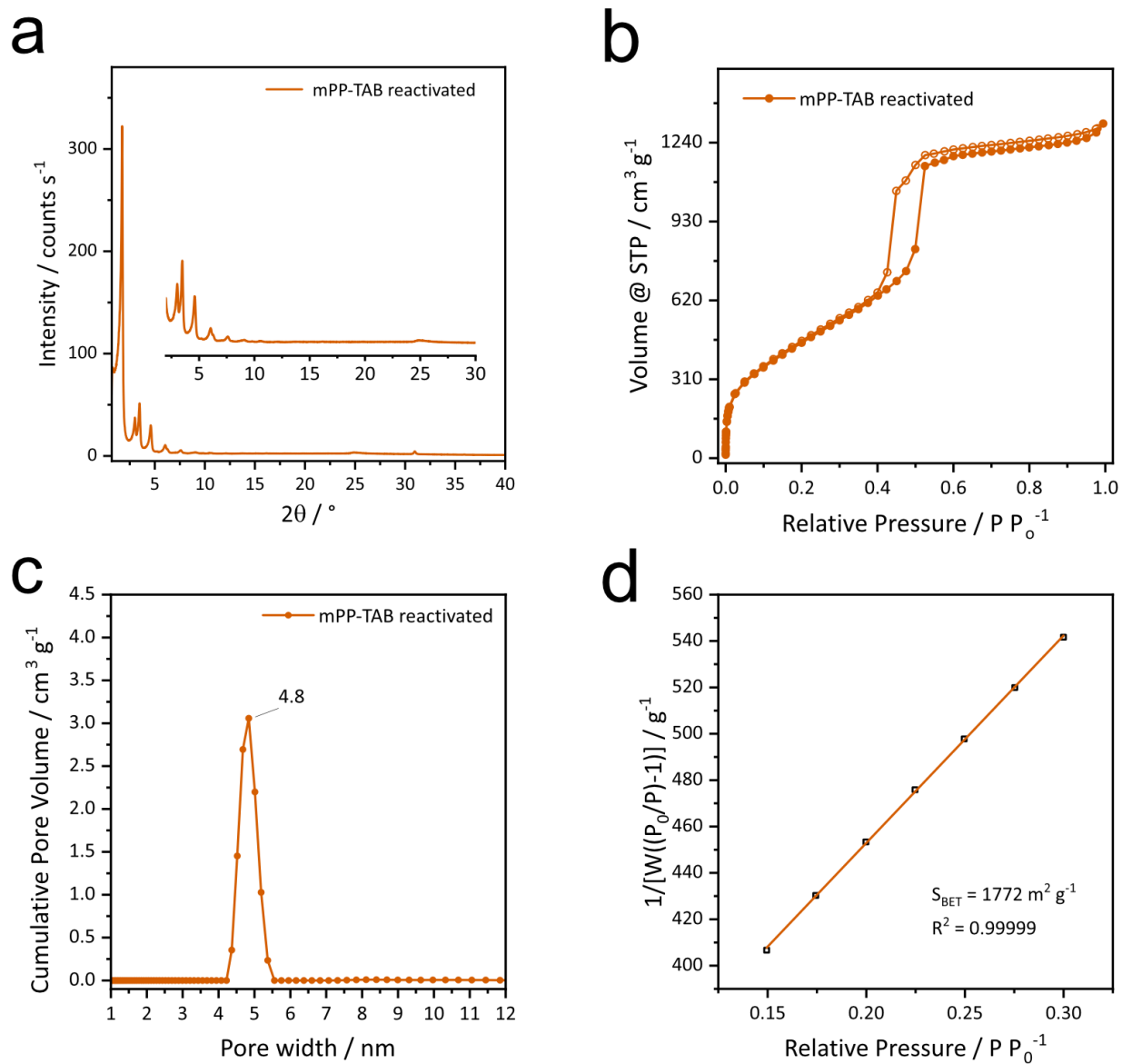
Figure S9.1.32. XRPD (Cu-K$_{\alpha1}$) (**a**), N$_2$ Isotherms at 77 K (**b**), PSD derived from the adsorption branch (**c**), and multi-point BET surface area fit (**d**) of reactivated samples after heat treatment of **mPP-TAB**.

9.1.6. Solid State NMR
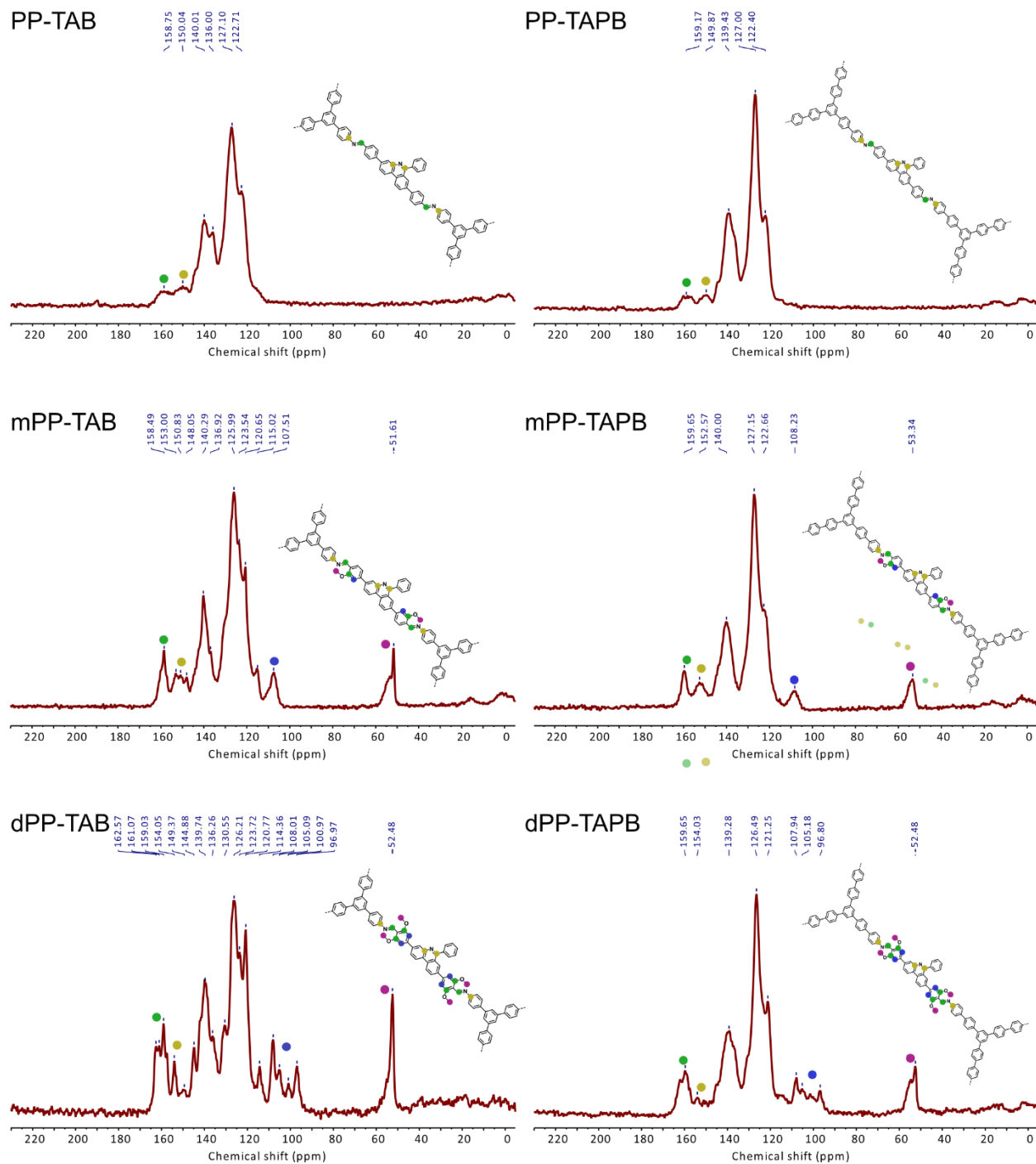
Figure S9.1.33. ^{13}C MAS ssNMR of **PP-TAB**, **PP-TAPB**, **mPP-TAB**, **mPP-TAPB**, **dPP-TAB** and **dPP-TAPB**.

9.1.7. Thermogravimetric Analysis
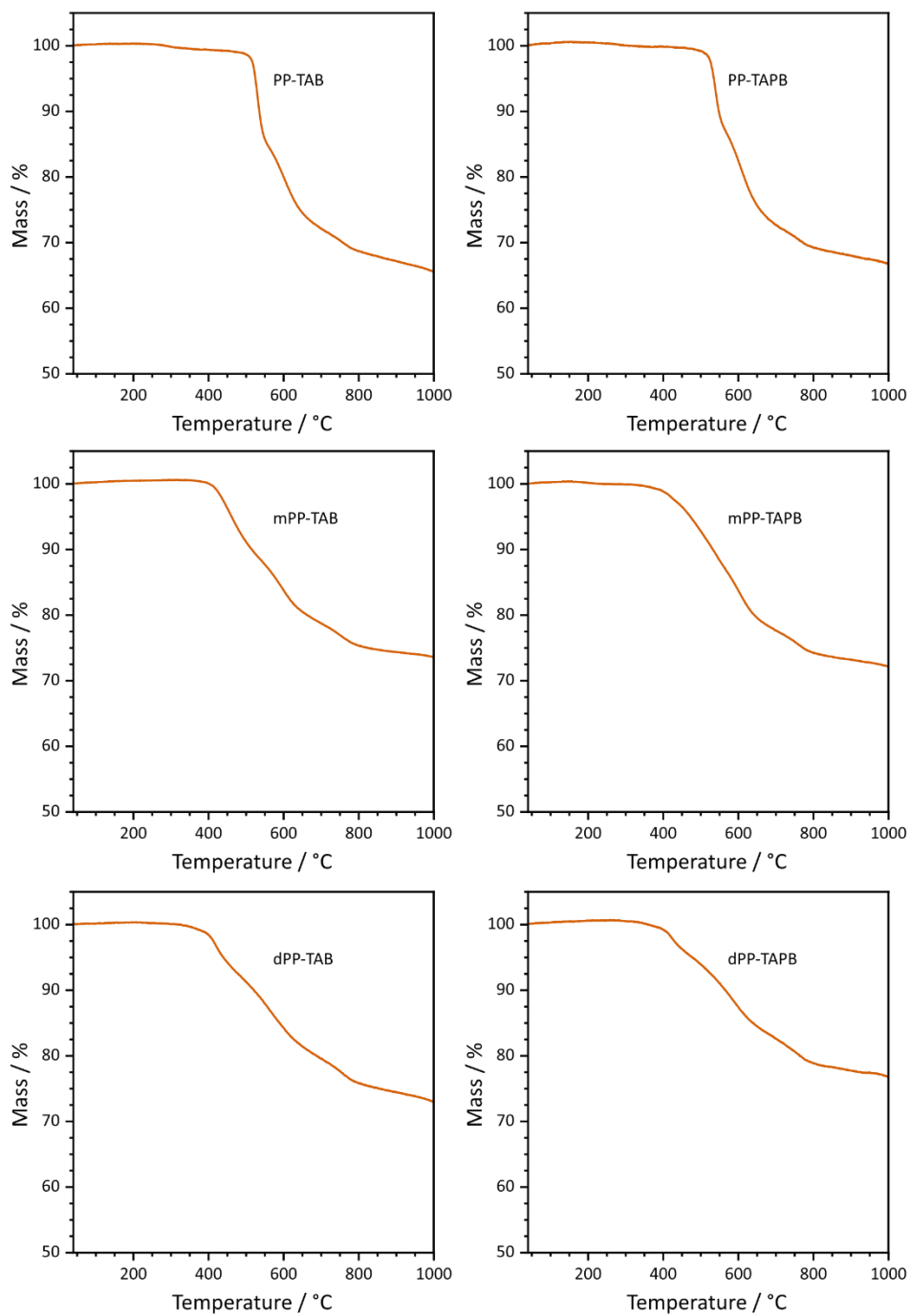
Figure S9.1.34. Thermogravietric analysis of **PP-TAB**, **PP-TAPB**, **mPP-TAB**, **mPP-TAPB**, **dPP-TAB** and **dPP-TAPB**.

9.1.8. Liquid State NMR
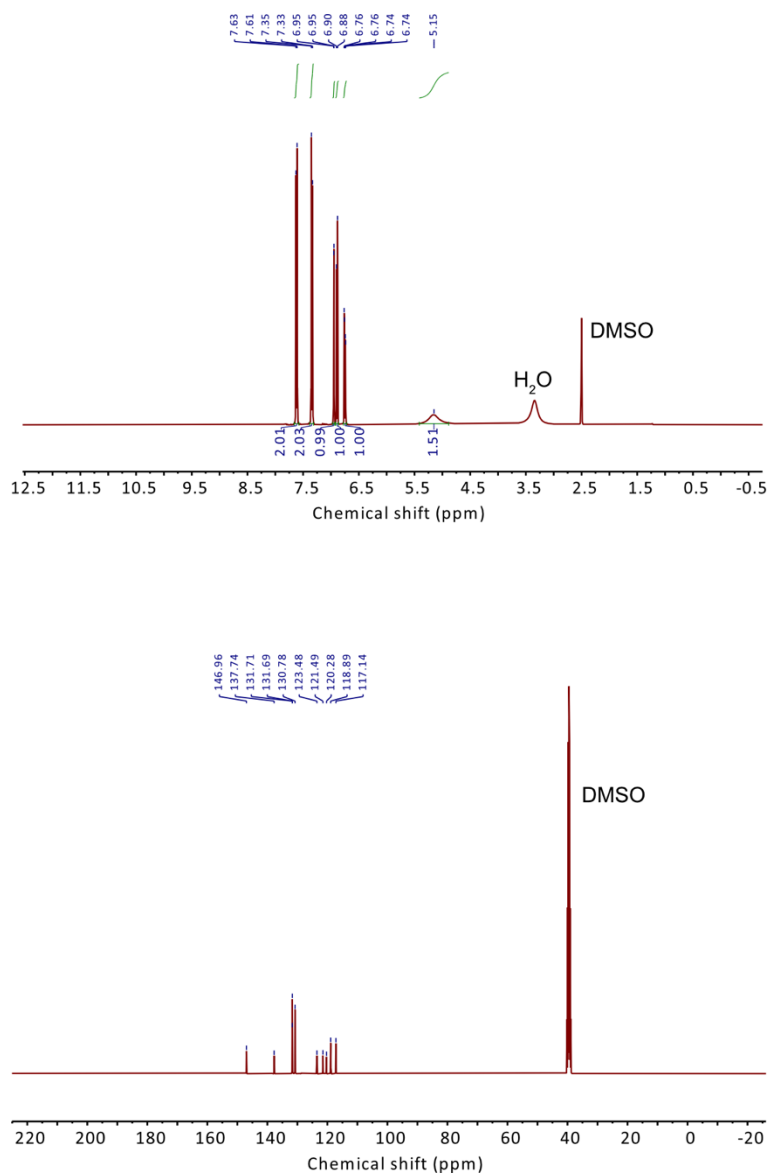
Figure S9.1.35. ^{1}H NMR (top) and ^{13}C NMR (bottom) of **4,4'-dibromo-[1,1'-biphenyl]-2-amine (2).**
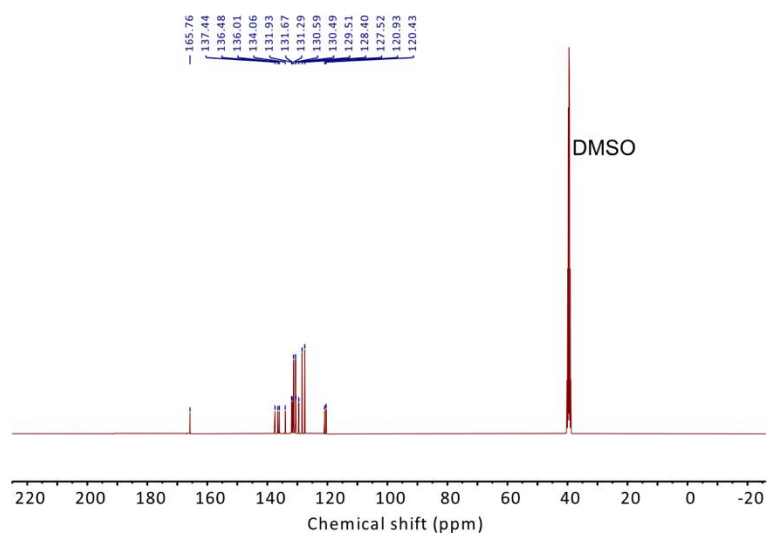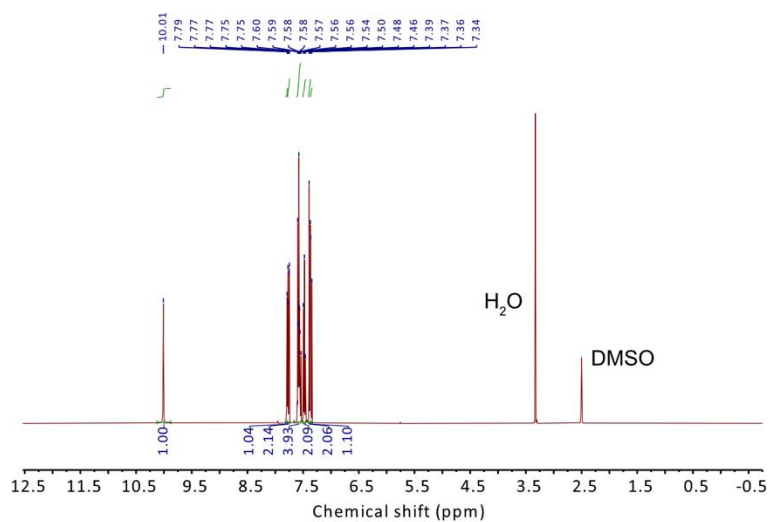
Figure S9.1.36. ^{1}H NMR (top) and ^{13}C NMR (bottom) of **N-(4,4'-dibromo-[1,1'-biphenyl]-2-yl)benzamide (3).**
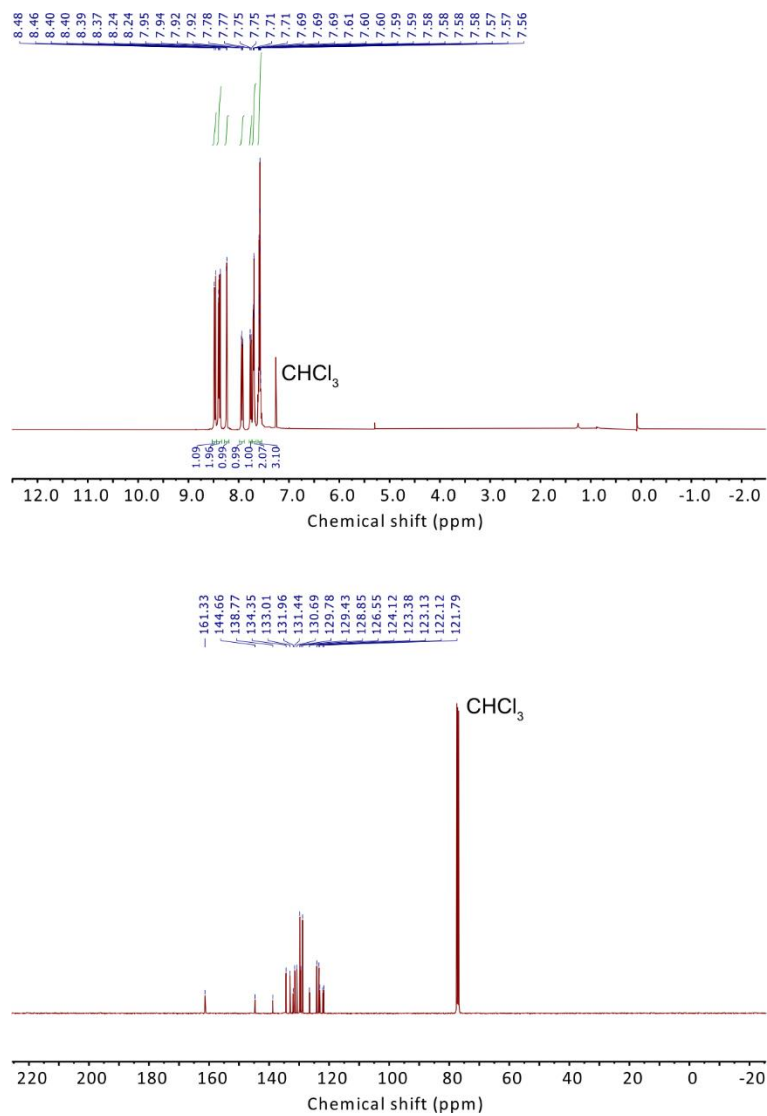
Figure S9.1.37. ^{1}H NMR (top) and ^{13}C NMR (bottom) of **3,8-dibromo-6-phenylphenanthridine (4).**
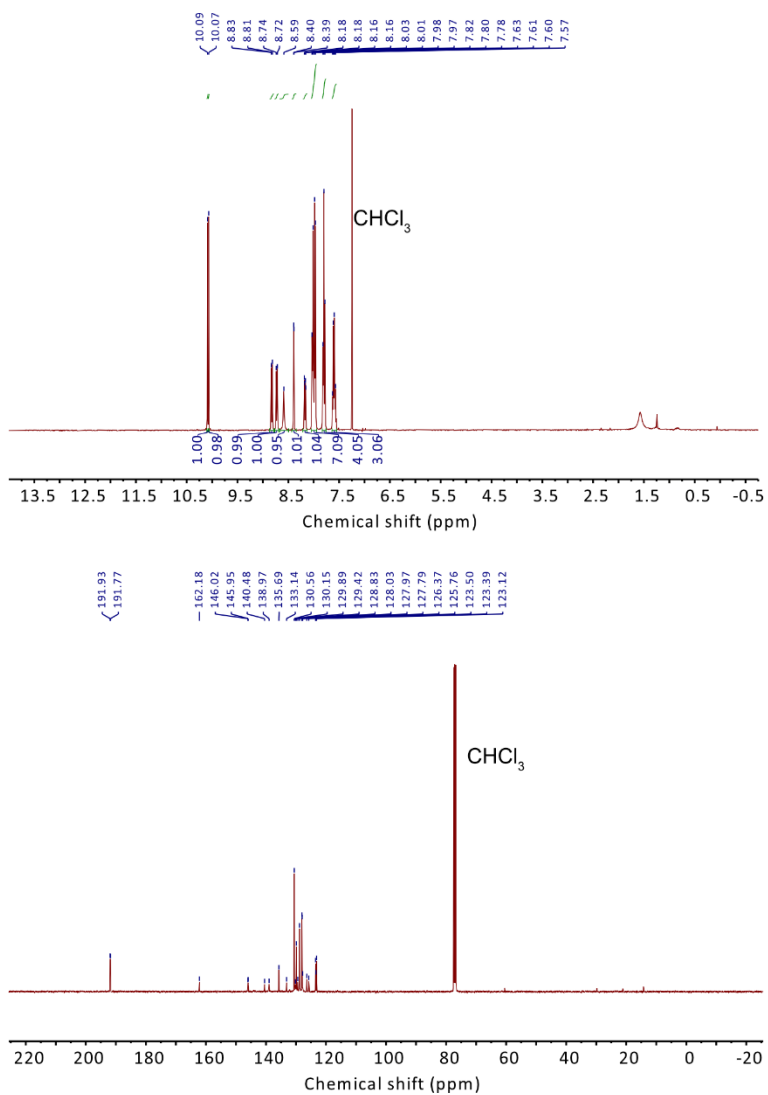
Figure S9.1.38. ^{1}H NMR (top) and ^{13}C NMR (bottom) of **4,4'-(6-phenylphenanthridine-3,8-diyl)dibenzaldehyde (PP).**
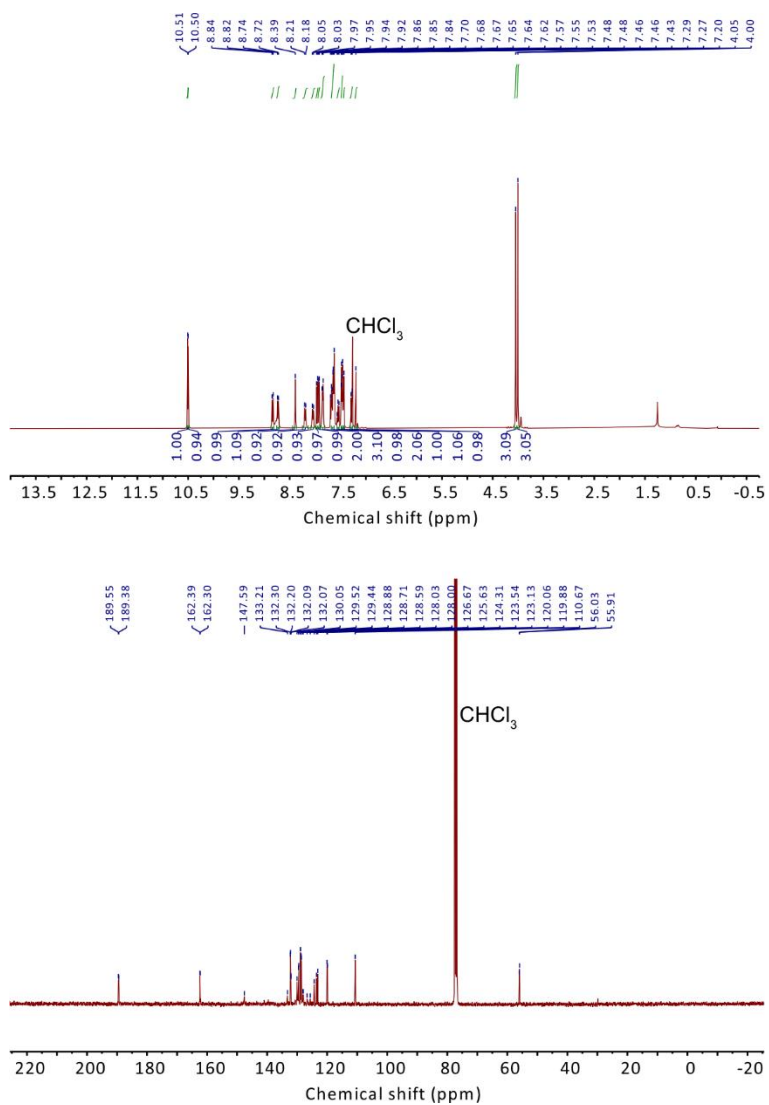
Figure S9.1.39. ¹H NMR (top) and ¹³C NMR (bottom) of **4,4'-(6-phenylphenanthridine-3,8-diyl)bis(2-methoxybenzaldehyde) (mPP).**
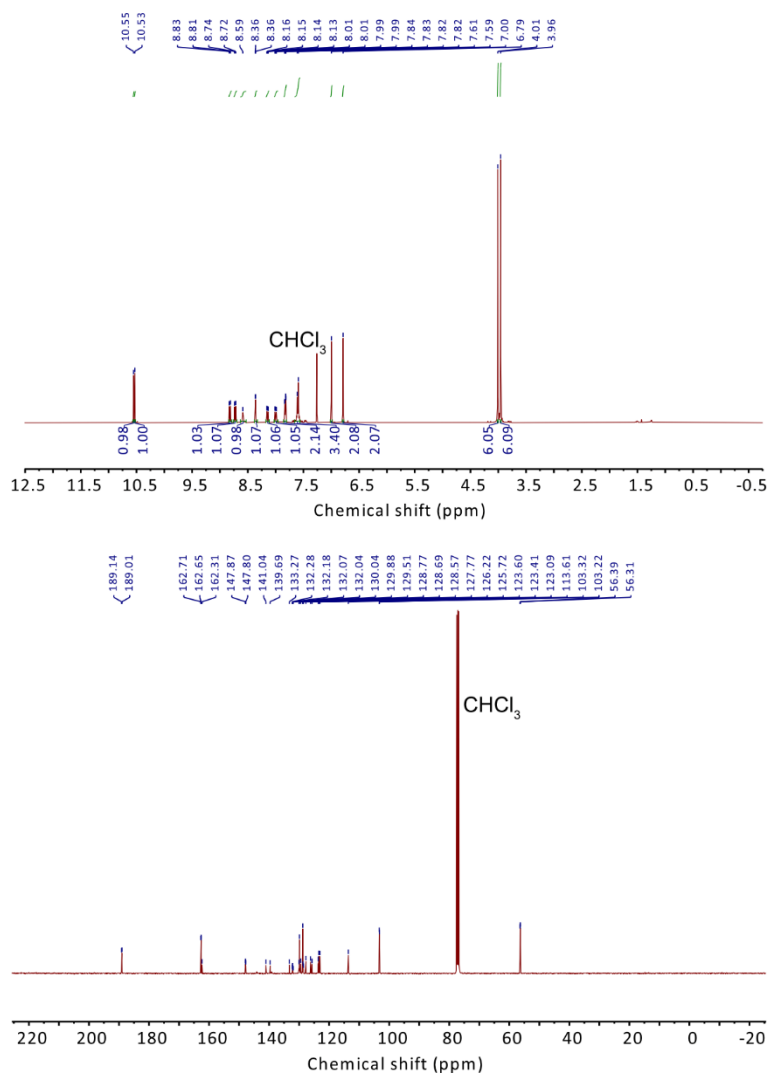
Figure S9.1.40. ^{1}H NMR (top) and ^{13}C NMR (bottom) of 4,4'-(6-phenylphenanthridine-3,8-diyl)bis(2,6-dimethoxybenzaldeyde) (dPP).

9.1.9. Geometry-Based Pore Size Calculation

For the experimentally obtained structures we performed a geometry-based pore size calculation. We constructed extended systems based on the obtained unit cells. This was done by in-plane displacement of layers, adjacent in stacking direction, of r_{disp} = 1.55 Å in a random direction. As the narrowest points are located in the plane of the investigated layers, we determined the maximum sphere radius from these planes for each layer as schematically shown in Figure S41, including up to 5 adjacent layers for taking care of the 3D nature of the resulting sphere. In order to obtain a geometric estimate of the pore sizes, we calculated the minimum distances of atoms r_{min} from the estimated pore center K_0. To account for the 3D nature of the problem, we then calculated these distances on a grid of points K_{shift} located around the estimated pore center. Afterwards we took the largest obtained value for the minimum distances η_{max} as representative for the maximum pore size corresponding to the investigated layer (L_2 in the picture). Additionally, we assumed the closest approachable distance as the van-der-Waals radius of the edge molecules. To determine the total pore size of our constructed arrangements, we averaged over the biggest spheres corresponding to each used layer L_i.
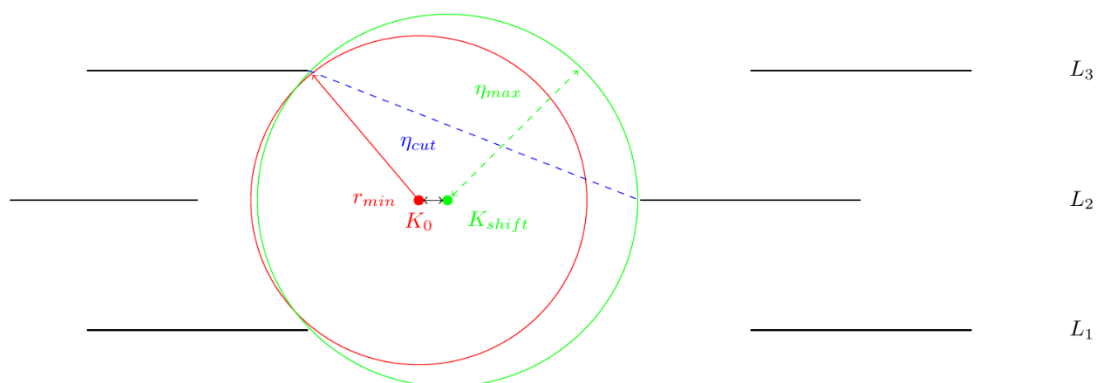
Scheme S9.1.4. Schematic drawing for geometry-based pore size calculation.
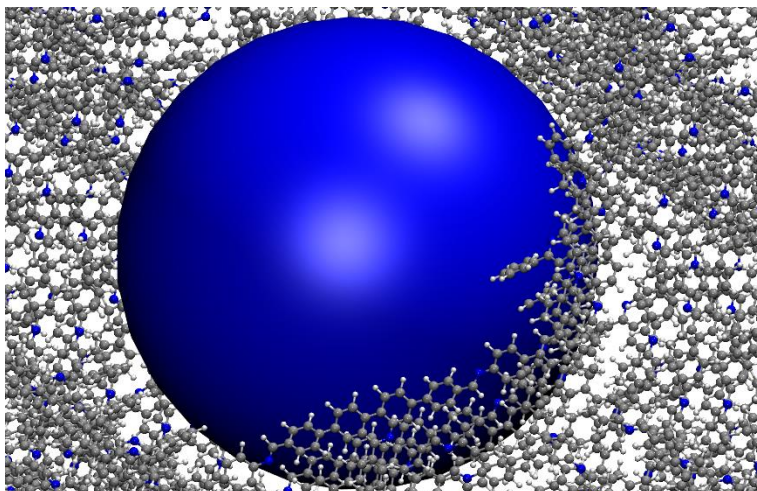
Figure S9.1.41. Sphere for layer 5 in a PP-TAB arrangement illustrating the utilized method.
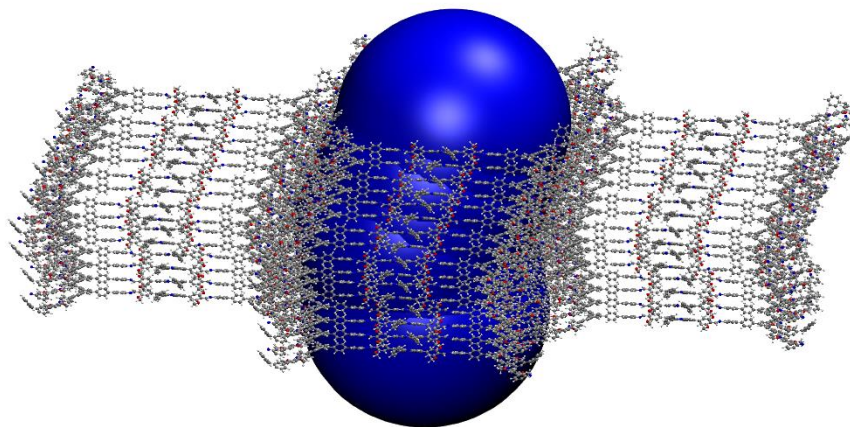
Figure S9.1.42. Distribution of spheres for 16 layers in a dPP-TAB arrangement with a small random offset between each layer to simulate the nearly eclipsed stacking.

Table S9.1.3: predicted values for geometry-based pore size calculation

	Sphere Radius / Å	Pore Diameter / nm
PP-TAB (staggered)	20.3A	4.05 nm
dPP-TAB (nearly eclipsed)	23.1A	4.62 nm
PP-TAPB (staggered)	22.8A	4.56 nm
dPP-TAPB (nearly eclipsed)	29.6A	5.92 m

9.1.10. Technical Details for the Theoretical Investigations

In the following we present the utilized setups for the computational investigations. Gas phase DFT geometry optimizations were performed using the TURBOMOLE program package for energy calculations and DL-find interfaced via CHEMSHELL for the geometry optimization.

Periodic DFT calculations were performed using the GPW approach as implemented in the CP2K program package. If not stated otherwise, total electronic energy calculations in the periodic case were performed using a PW cutoff of 300 Rydberg, GTH-PBE pseudo-potentials for the 2 1s core electrons, the PBE exchange and correlation functional as well as the TZV2P-GTH basis set.

All cell optimizations were performed using the conjugated gradient (CG) method as implemented in CP2K until the total forces acting on the molecules were below 4.5×10^{-4} Hartree/Bohr with the relative change in geometry being below 3.0×10^{-3} Bohr and a pressure tolerance of below 100 bar with respect to the environment was reached. If not stated otherwise, we used the default values for the convergence criteria.

Analysis of possible component orientations

For the component analysis of isolated molecular fragments building up the investigated COF system, geometry optimizations using TURBOMOLE were performed using the PBE functional with Grimme's D3 dispersion correction and Ahlrich's def2-TZVPP basis-set. We choose the PBE functional for comparison with periodic calculations described below using the Gaussian and plane waves approach as implemented in CP2K.
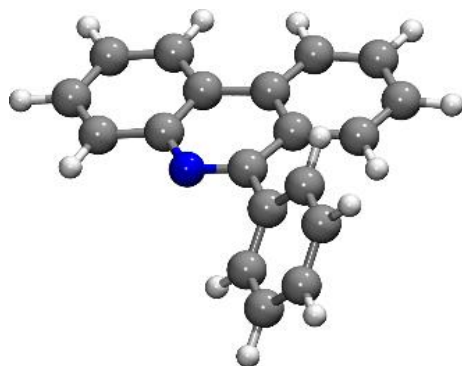
Figure S9.1.43. Phenylphenatridine component.

To determine the interaction energies, combinations of two fragments were optimized and compared to the total electronic energies of the optimized isolated molecules. Interaction energies for molecules a, b were calculated as:

$$E_{int} = E_{combination} - E_a - E_b$$

Initially, two molecules were placed close to each other, approximately 3.5 Å apart, for initializing the optimization procedure. For the orientations of two condensed triphenyl groups with respect to each other, the nomenclature follows the Scheme S4.
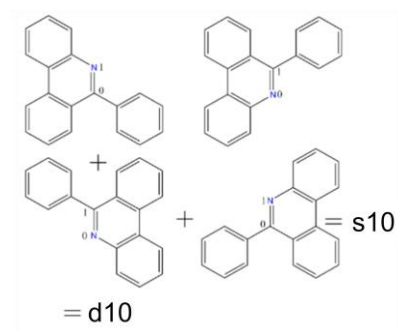
Scheme S9.1.5. Nomenclature scheme for phenylphenanthridine stacking options. The letters S and D indicate the side of the linker's attachment with respect to each other, whereas the numbers refer to the linker's attachment position at the middle ring. Additionally, we investigated the possibilities of T-shaped phenyl linker's arrangement as shown in Figure S40. T-shaped phenyls are indicated with the addition –T in the nomenclature.

Table S9.1.4. Energies of component's orientations as displayed is Scheme S4.

Orientation	E_{int} in (kcal/mol)
s10-T	-13.304
s11-T	-13.590
d10	-12.198
d11	-12.482
s10	-14.826
s11	-14.079
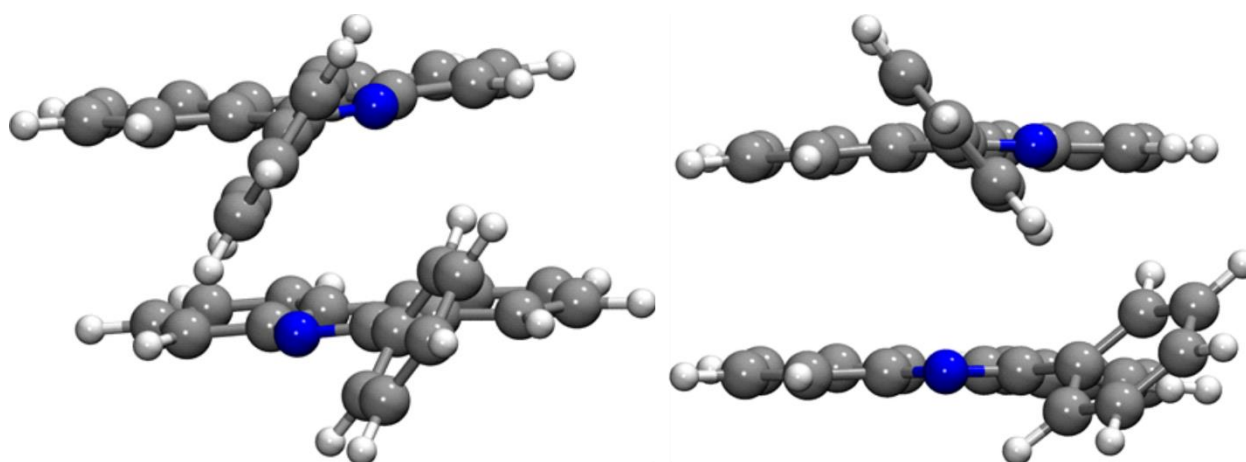
Figure S9.1.44. Exemplary structures for the S10 (left) and S10-T (right) orientations after the optimization.

Investigation of possible imine-linker orientations

The possible arrangements of the imine linkers with and without methoxy groups were investigated using the same procedure as for the phenyl linkers. The nomenclature was chosen to reflect the relative arrangement of the imine linker group, where the abbreviations alt and para refer to alternating and parallel oriented imines, respectively.
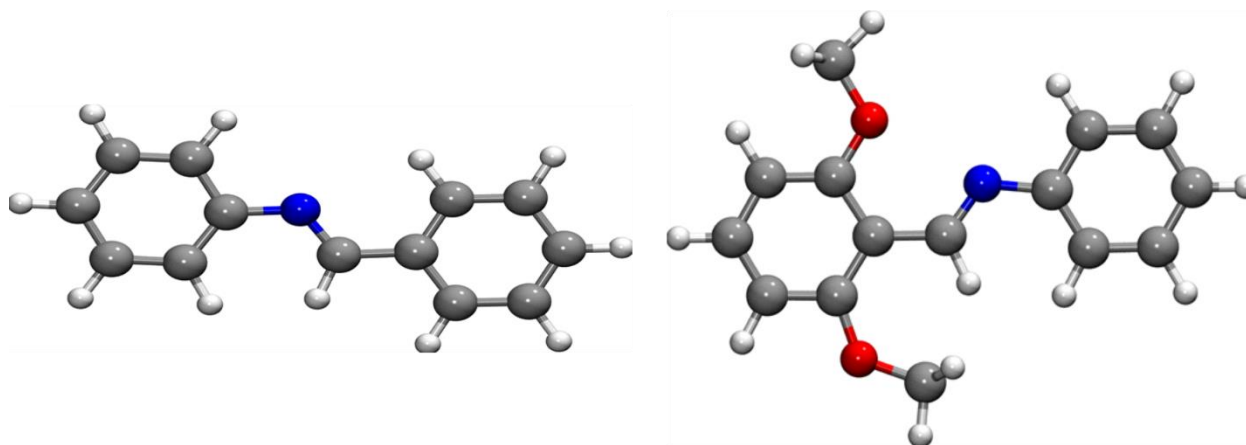
Figure S9.1.45. Components used to investigate possible imine linker orientations.

Table S9.1.5. Energies of component orientations as displayed is Figure S45.

Orientation	E_{int} in (kcal/mol)
Para	-7.68
Alt	-11.20
Methoxy-para	-9.24
Methoxy-alt	-11.94
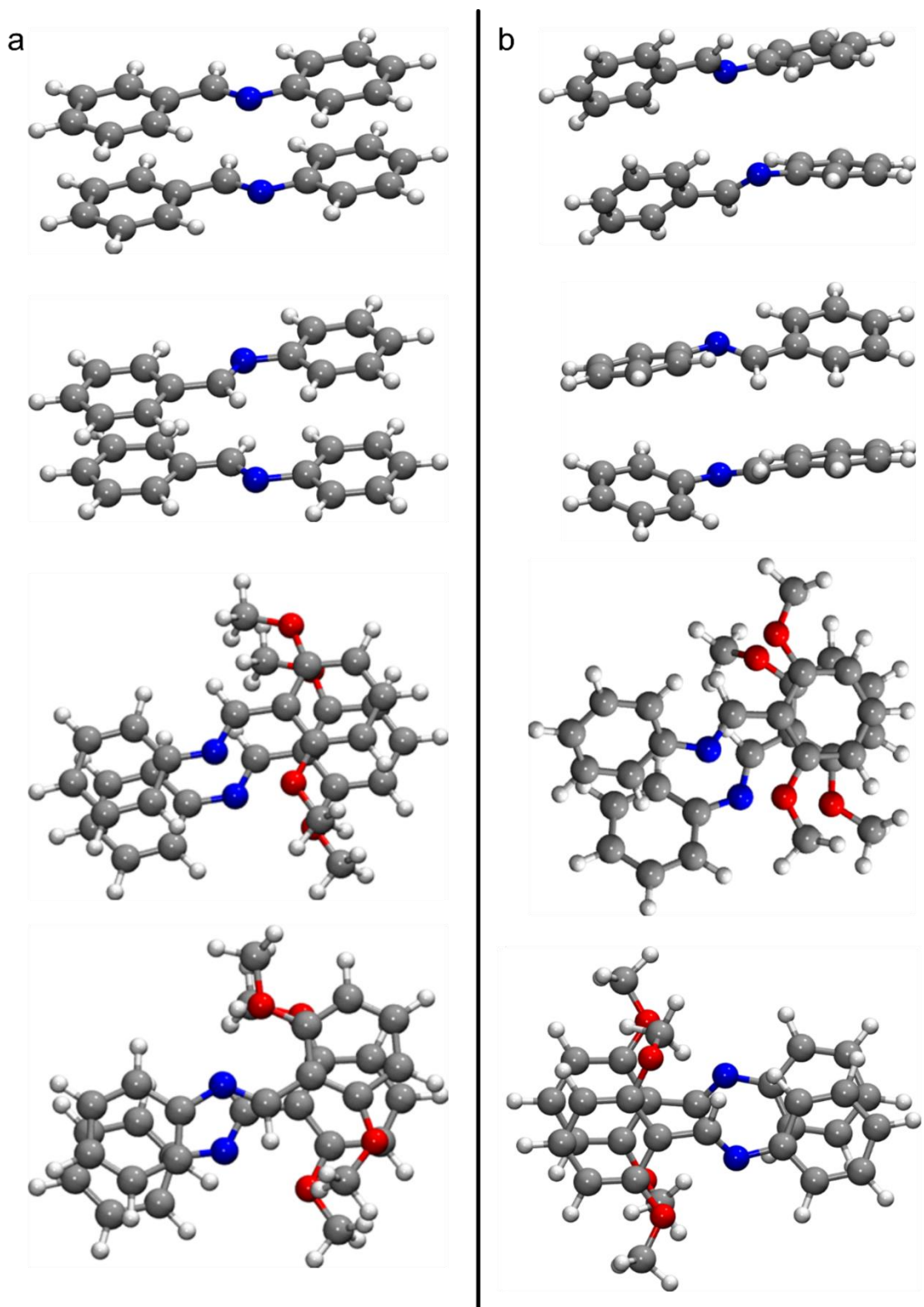
Figure S9.1.46. Figure S9.1.47. Initial arrangements before (**a**) and after (**b**) optimization of Para, Alt, Methoxy-para, and Methoxy-alt (from top to bottom), displaying the resulting arrangements after the optimization, showing that the molecules are rotated with respect to each other and, thus, not aligned as would be expected in the crystal structure.

From the obtained interaction energies, it can be seen that alternatingly oriented imine groups are energetically favorable. The methoxy versions of the linkers seem to be generally more stable and show smaller energy differences between alternatingly and parallel-oriented imine groups. It was observed that the obtained optimized structures were rotated strongly from the initial plane, indicating that the underlying effects might not occur at the same level of magnitude in the crystalline structures as rotation is restricted there.

Calculation of electrostatic potential maps

For isolated components, electrostatic potential maps were calculated using the Gaussian08[5] program package. Geometries were optimized by means of DFT on the DGTZVP-PBE-D3 level of theory. For the optimized geometries reference densities and electrostatic potentials were visualized using Gauss-view the graphical interface to Gaussian. In the presented pictures, the electrostatic potential is mapped onto the isosurface of the density at an iso-value of 0.04 e/Bohr^3 with iso-values for the potential ranging from -0.02 to 0.4. The colors of the electrostatic potential maps indicate the energy of a positive probe charge with tones from blue to red indicating the transition from repulsion to attraction. Additional in-plane potential lines with normal vector (0,0,1) were included to show the influence of the electrostatic potential in close vicinity to the highlighted surface, yellow-colored regions correspond to repulsive red to attractive forces.
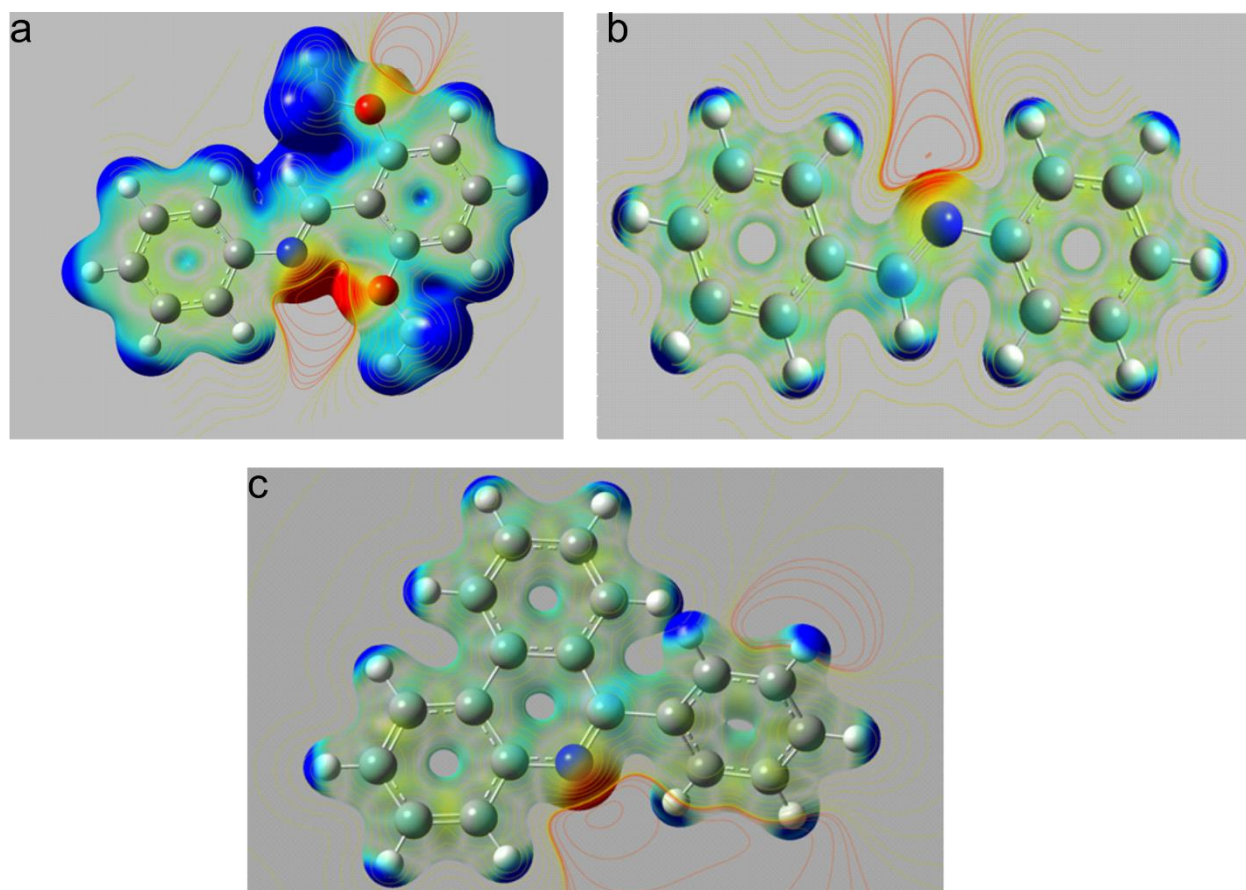
Figure S9.1.48. Electrostatic potential maps of methoxy-imine-linker-group (**a**), imine-linker-group (**b**), and phenylphenanthridine group (**c**).

Computation of periodic components (DFT/PBE-TZV2P-GTH)

In order to minimize in-plane rotational movement and allow for an estimation of stabilizing effects due to inter-layer interactions, we restrained the components by introducing PBCs and connecting the sides of the imine-linkers by additional phenyl groups to mimic the effects of the adjacent components in the full COF-system. We performed GPW-DFT cell optimizations on the TZV2P-GTH/PBE-D3 level of theory. The nomenclature in this section and the following is extended by referring to the components without methoxy groups as "simple".

Energy differences are calculated as:

$$\Delta E = E_{alt} - E_{para}$$

Simple: ΔE = 12.74 kcal/mol

Methoxy: ΔE = -1.13 kcal/mol

The arrangement for alternatingly oriented imines is favorable for the simple blocks by a rather large amount 12.7 kcal/mol, however it becomes obvious that with additional methoxy groups, the difference between the two imine orientations is with $\Delta E = -1.13$ kcal/mol rather small.
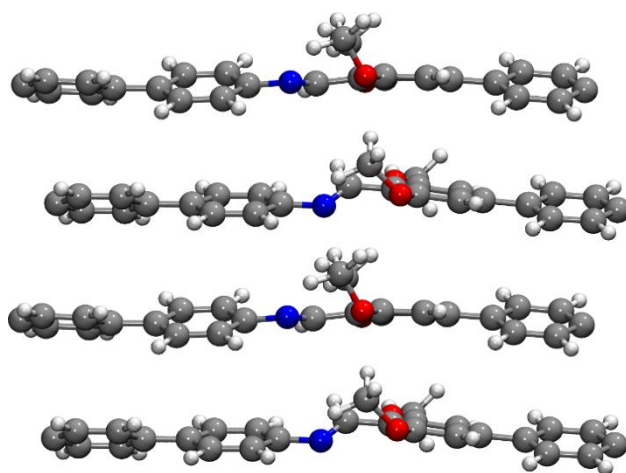
Figure S9.1.49. Exemplary periodic component of methoxy-imine-linker mimicking the effects of the adjacent components in the full COF-system.

Computation of periodic combinations of blocks (DFT/PBE-TZV2P-GTH)

In order to gain an overview on the influence of possible orientations of a whole wall of the COF pores we constructed combinations of blocks considering imine arrangements as well as phenyl linker orientations. Blocks were constructed for the simple-PP structure as well as the modified versions with one and two additional methoxy groups at the imine linkers. In order to consider the additional possibilities of methoxy group attachments to the imine sites we further distinguished in this case between parallel and anti-parallel arranged methoxy groups as can be seen in Fig.1-methoxy-cases. Calculations were performed using periodic boundary conditions with an ortho-rhombic unit cell. The initial cell vectors were chosen to be a=33, b=25.5, c=7.5 Angstroms, where b was chosen ad-hoc as a large value to minimize interactions between the arrangements in this direction (the dispersion cutoff was chosen to be 12 Angstrom). In order to guarantee the maximum flexibility for the components, the structure was connected via a C-C triple bond over the periodic extension. By doing so the rotation of components along the axis of alignment is possible while the in-plane rotation out of alignment is still suppressed, as can be expected for the full pore system. For every arrangement we performed cell-optimizations with simultaneous geometry optimization utilizing the BFGS method as implemented in CP2K. The total electronic energies were obtained by using the GPW scheme for the SCF calculations on the TZV2P-GTH/PBE-D3 level using the corresponding GTH-PBE pseudo-potentials. The obtained energies are always compared to the reference value that was lowest in energy and ,thus, are given in relative differences ΔE.
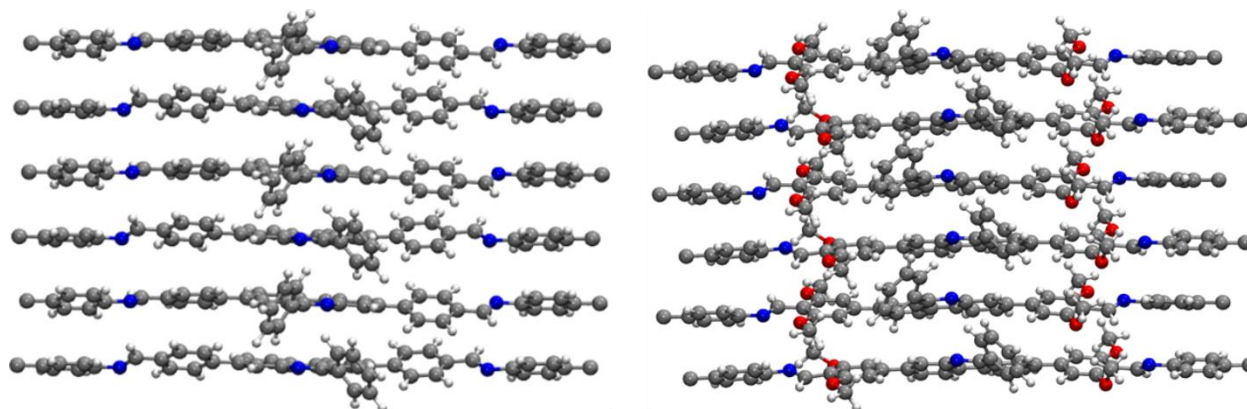
Figure S9.1.50. Exemplary segments of periodic combination of building blocks used for investigating imine arrangements as well as phenyl linker orientations for **PP-TAB** (left) and **dPP-TAB** (right).

Table S9.1.6. Results of cell-optimizations with simultaneous geometry optimization using DFT/PBE-TZV2P-GTH for **PP-TAB** mimicking periodic segments.

Component-arrangement	ΔE in kcal/mol
simple-alt-s10	0
simple-alt-s11	0.03
simple-mixed-s10	5.48
simple-mixed-s11	5.68
simple-para-s11	0.6
simple-para-s10	4.71
simple-alt-d10	1.94
simple-alt-d11	2.03
simple-mixed-d10	0.51
simple-mixed-d11	0.57
simple-para-d11	3.37
simple-para-d10	2.18

Table S9.1.7. Results of cell-optimizations with simultaneous geometry optimization using DFT/PBE-TZV2P-GTH for **dPP-TAB** mimicking periodic segments

Component-arrangement	ΔE in kcal/mol
methoxy-alt-s10	0
methoxy-alt-s11	21.71
methoxy-mixed-s10	1.04

methoxy-mixed-s11	1.83
methoxy-para-s11	4.42
methoxy-para-s10	0.5
methoxy-para-d11	18.04
methoxy-para-d10	17.16
methoxy-alt-d10	13.01
methoxy-alt-d11	34.83
methoxy-mixed-d10	15.3
methoxy-mixed-d11	17.55

For the additional analysis for component arrangements with one methoxy group additional distinguishing para and anti methoxy group arrangements. The nomenclature is thus further extended by an abbreviation -para and -anti after the identifier for the phenyl linker arrangement. In Figure S48, the additional differentiation is shown at the example of the para-S10 orientation.
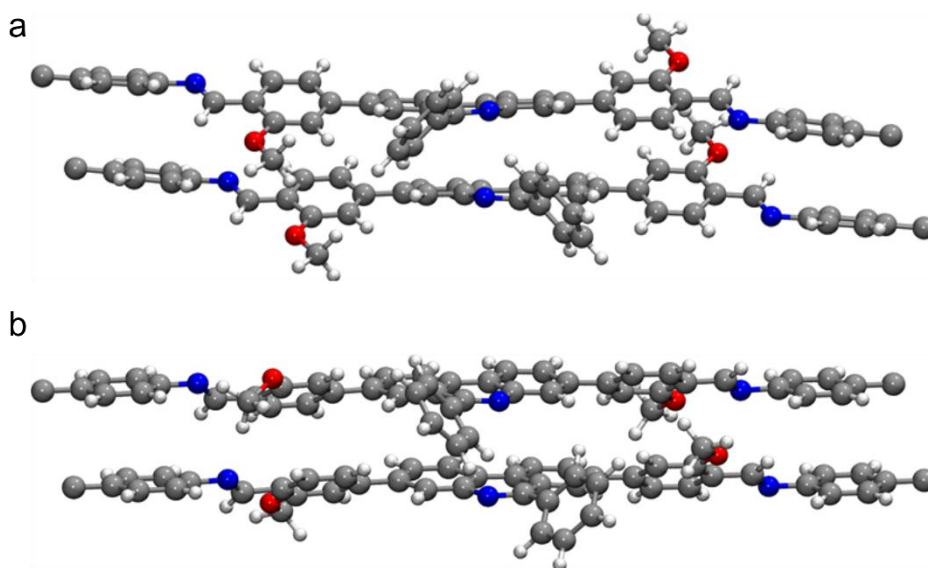
Figure S9.1.51. Component arrangements para-S10-para (**a**) and 1-methoxy-para-S10-anti (**b**) of **mPP-TAB**.

Table S9.1.8. Results of cell-optimizations with simultaneous geometry optimization using DFT/PBE-TZV2P-GTH for **dPP-TAB** mimicking periodic segments.

Component-arrangement	ΔE in kcal/mol

1-methoxy-para-s10-para	0
1-methoxy-para-d11-anti	12.98
1-methoxy-alt-d11-para	13.51
1-methoxy-alt-d11-anti	25.6
1-methoxy-alt-s10-anti	23.24
1-methoxy-alt-s10-para	10.26
1-methoxy-alt-s11-anti	24.58
1-methoxy-alt-s11-para	8.78
1-methoxy-para-s11-anti	14.47
1-methoxy-para-s11-para	3.17
1-methoxy-para-s10-anti	19.09
1-methoxy-para-d11-para	13.17
1-methoxy-alt-d10-anti	24.00
1-methoxy-alt-d10-para	11.80
1-methoxy-para-d10-anti	10.02
1-methoxy-para-d10-para	14.12

The results for the differentiation between para- and anti-arrangement for the methoxy groups show, that the para arrangement is overall more stable by a significant amount leading to the conclusion that this arrangement is the more probable of the two, regardless of the other components orientation. Furthermore it suggests that interactions between two methoxy groups are stabilizing.

Comparison of relative energies of isolated components (GFN-xTB)

Relative stability of components were analyzed by means of GFN-xTB after comparing the total electronic energies obtained by in vacuo geometry optimizations. The enumeration follows the scheme presented in Scheme S4. The relative interaction energies were compared to the isolated molecules and are given in Kcal/mol in relation to the isolated molecules.

Table S9.1.9. Relative energies of isolated phenylphenanthridine components.

Component-arrangement	ΔE in kcal/mol
d10-displaced	-14.684

d11-displaced	-13.425
s10-90grad	-13.667
s11-90grad	-14.156
d10	-12.093
d11	-12.905
s10	-17.600
s11	-15.636

Investigation of periodic combinations of blocks (GFN-xTB)

In order to investigate the influence of the adjacent components on the possible stacking behavior, we performed cell optimization with simultaneous geometry optimization using GFN-xTB as implemented in the CP2K program package. As we wanted to minimize the possibility of the components to shift and rotate out of plane as it was observed to happen in the gas phase calculations, we utilized periodic boundary conditions. The initial cell was chosen to be an orthorhombic lattice with cell vectors of length a=33, b=25.5, c=7.5 Angstrom, where b was chosen ad-hoc as a large value to minimize interactions between the arrangements in this direction (the dispersion cutoff was chosen to be 12 Angstrom). The enumeration used for the orientations of the phenyl linkers is the same as in section S12. To judge the influence of methoxy groups upon the organization, components were constructed with one methoxy group and 2 groups per imine-linker alongside the bare structures. The energies were then calculated and the different arrangements of units were compared concerning their total energies, where relative energies to the structure lowest in energy are given in Table S9. It has to be noted here, that the unit cells belonging to each structure after optimization can be found along the obtained geometries in the attached PDB-files, but are left out as we were mainly interested in the stability of the overall components.

Table S9.1.10. Results of cell-optimizations with simultaneous geometry optimization using GFN-xTB for **PP-TAB** mimicking periodic segments.

Component-arrangement	Relative Energy shift (kcal/mol)
simple-para-s10	1.14
simple-alt-s10	3.26
simple-alt-s11	6.49
simple-mixed-s10	5.09
simple-mixed-s11	8.21
simple-para-s11	1.14

simple-alt-d10	7.89
simple-alt-d11	0.91
simple-mixed-d10	0.55
simple-mixed-d11	2.83
simple-para-d11	2.42
simple-para-d10	0.00

Table S9.1.11. Results of cell-optimizations with simultaneous geometry optimization using GFN-xTB for **mPP-TAB** mimicking periodic segments.

Component-arrangement	Relative Energy shift (kcal/mol)
1-methoxy-para-s10-para	0.00
1-methoxy-alt-d10-anti	17.07
1-methoxy-alt-d10-para	10.26
1-methoxy-para-d10-anti	14.11
1-methoxy-para-d10-para	9.78
1-methoxy-para-d11-para	1.66
1-methoxy-para-d11-anti	8.57
1-methoxy-alt-d11-para	7.89
1-methoxy-alt-d11-anti	18.30
1-methoxy-alt-s10-anti	11.06
1-methoxy-alt-s10-para	7.82
1-methoxy-alt-s11-anti	14.15
1-methoxy-alt-s11-para	10.44
1-methoxy-para-s11-anti	9.61
1-methoxy-para-s11-para	2.87
1-methoxy-para-s10-anti	7.19

Table S9.1.12. Results of cell-optimizations with simultaneous geometry optimization using GFN-xTB for **dPP-TAB** mimicking periodic segments.

Component-arrangement	Relative Energy shift (kcal/mol)
methoxy-para-s11	0.00

methoxy-alt-s10	1.85
methoxy-alt-s11	9.77
methoxy-mixed-s10	1.03
methoxy-mixed-s11	6.91
methoxy-para-s10	3.80
methoxy-alt-d10	6.51
methoxy-alt-d11	69.46
methoxy-mixed-d10	10.49
methoxy-mixed-d11	6.07
methoxy-para-d11	1.94
methoxy-para-d10	8.05

Calculation of a reference pathway from $A\overline{A} \rightarrow A\overline{B}$ for comparing (GPW-DFT) and (GFN-xTB)

In order to justify the use of GFN-xTB as a tool to analyze the potential energy surface of COFs under displacements a pathway from AA' stacking to AB stacking was calculated with equidistant shifting vectors along the direct line of displacement with cell optimization and simultaneous geometry optimization performed at every of the 20 reference structures. The resulting path consisting of total energy values was then re-investigated using GPW-DFT single-point calculations using CP2K on the TZV2P-GTH/PBE-D3-level for comparison. The relative energies in reference to the initial structure, shown in Figure S9.1.52, are showing that DFT and GFN-xTB energy calculations show qualitatively similar tendencies for relative energy shifts, thus, we used GFN-xTB for the further analysis as it is by far the computationally cheaper method. The displacement from $A\overline{A}$ to $A\overline{B}$ stacking was split into 20 steps, with the fraction of the displacement vector acting as x coordinate.
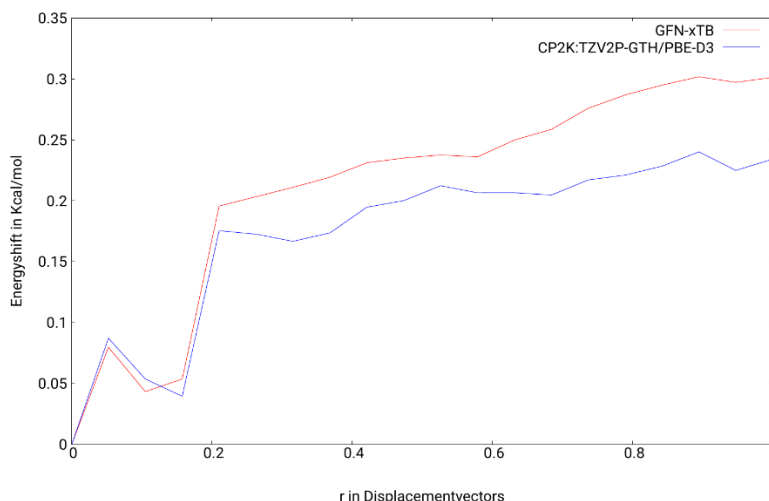
Figure S9.1.52. Reference pathway from A$\overline{\text{A}}$ → A$\overline{\text{B}}$ for comparing (GPW-DFT) and (GFN-xTB).

Calculation of cell-parameters for the full COF Systems (GFN-xTB)

Cell parameters for different components arrangements determined by cell optimization with simultaneous geometry optimization using GFN-xTB as implemented in CP2K are shown in Table. S12. The optimizations were performed using the conjugated gradients (CG) method and conducted until the total forces acting on the molecules were below $4.5*10^{-4}$ Hartree/Bohr with the relative change in geometry being below $3.0*10^{-3}$ Bohr and a pressure tolerance of below 100 bar with respect to the environment was reached. All optimizations were performed with fixed hexagonal-symmetry.

Table S9.1.13. Results cell parameter calculations determined by cell optimization with simultaneous geometry optimization using GFN-xTB for **PP-TAB** and **dPP-TAB**.

COF arrangement	$a = b$ / Å	c / Å
PP-TAB-para-s10	58.524	7.26
PP-TAB-para-s11	58.577	7.31
PP-TAB-alt-s10	58.233	7.13
PP-TAB-alt-s11	58.145	7.21
dPP-TAB-alt-s10	58.198	7.25
dPP-TAB-alt-s11	58.242	7.32
dPP-TAB-para-s10	58.779	7.47
dPP-TAB-para-s11	58.608	7.37

Calculation of stacking types for the phenylphenanthridine-COFs and investigation of the role of methoxy Groups for total arrangements using various DFT-functionals

The influence of ordered and disordered methoxy-groups was investigated along with cell parameters. Relative energy differences between the structures were compared for the PBE and BP86[6,7] DFT functionals respectively, using Grimmes DFT-D2 and DFT-D3 dispersion corrections. Further we compared to the semi empirical tight binding method GFN-xTB as implemented in CP2K. The energies were obtained after performing a cell optimization with simultaneous geometry optimization utilizing the method of conjugated gradients (CG) with constrained hexagonal symmetry.
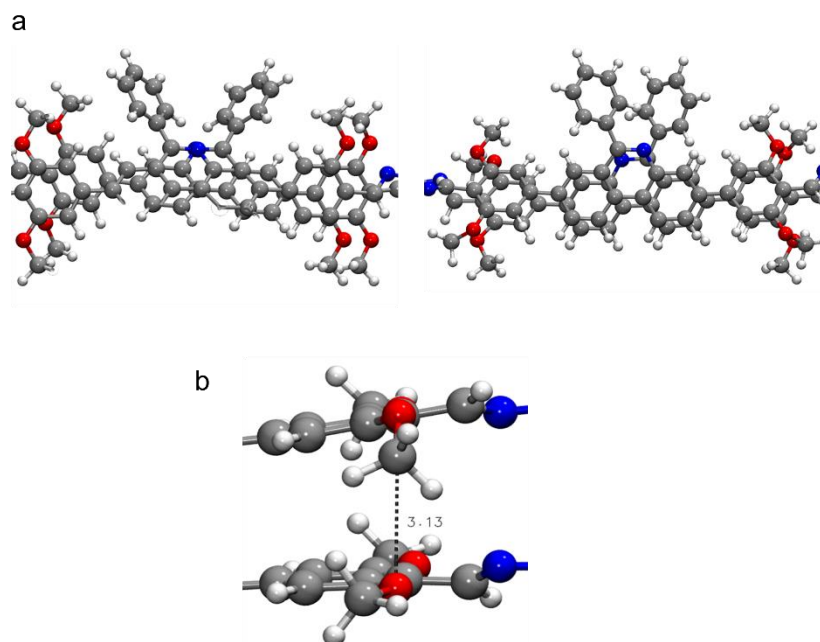
Figure S9.1.53. Influence of ordered and disordered methoxy-groups. (**a**) Excerpts of ordered (left) and disordered methoxy groups (right). (**b**) Approach of CH_3 group towards methoxy group of next layer observed after structure optimization.

We calculated the relative energy difference between unordered E_u and ordered E_o structures as:

$$\Delta E = E_o - E_u$$

The results are shown in Table S13. Cell parameters for ordered initial structures are shown in Table S13.

Cell parameters for disordered initial structures are shown in Table S14.

Table S9.1.14. Relative difference between the obtained energies of the optimized structures for the different methods.

Utilized level of theory	Energy difference ΔE (Kcal/mol)
TZV2P-GTH/PBE-D2	28.24
TZV2P-GTH/PBE-D3	31.38
TZV2P-GTH/BP-D2	11.90
TZV2P-GTH/GFN-xTB	3.14

Table S9.1.15. Cell parameters for ordered initial structures obtained after optimizing structures for the different methods.

Utilized level of theory	$a = b$ / Å	c / Å
TZV2P-GTH/PBE-D2	58.125	7.720
TZV2P-GTH/PBE-D3	58.211	8.002
TZV2P-GTH/BP-D2	57.974	7.446
TZV2P-GTH/GFN-xTB	57.817	7.343

Table S9.1.16. Cell parameters for disordered initial structures obtained after optimizing structures for the different methods.

Utilized level of theory	$a = b$ / Å	c / Å
TZV2P-GTH/PBE-D2	58.370	7.795
TZV2P-GTH/PBE-D3	58.460	8.034
TZV2P-GTH/BP-D2	58.252	7.503
TZV2P-GTH/GFN-xTB	58.222	7.232

Calculation of displacement maps using a plane-wave expansion (GFN-xTB)

To gain insight in the overall stability properties of the investigated COFs, we displaced two layers against each other and performed geometry optimizations with simultaneous cell optimization at each point. For the energy calculations we used GFN-xTB as implemented in CP2K. The cell optimizations were performed under the constraint of fixed hexagonal symmetry. For the starting point for the displacement, the centers of mass of both layers were placed at the origin of the elementary unit cell. We then displaced the layers in multiples of the cell vectors with the data points chosen as can be seen in the corresponding tables. The choice of sample points was motivated by assuming the COF-structures to be of D_6-symmetry (full hexagonal) in two dimensions and sample the lower triangle of the unit cell, the asymmetric unit, as shown in Figure S49, using a total of up to 16 data points. We then expanded the obtained energy surface in a plane-wave basis set, optimizing the coefficients c_n in a least square manner utilizing the singular value decomposition.

$$E(x,y) = \sum_n c_n \phi_n(x,y)$$

With plane wave basis functions corresponding to the assumed hexagonal symmetry as shown previously, where n is the index of the basis function and x, y are the spatial positions. As we used a polar representation, **r** is the two-dimensional position vector and φ is the angle between the components of the wave vector $\mathbf{k}_n = n_1 \mathbf{b}_1 + n_2 \mathbf{b}_2$ with $n_1 + n_2 < n$.

$$\phi_n(\phi) = \sum_i^6 \cos\left(\mathbf{k}_{n,i}\mathbf{r}\right)$$

The wave vectors $k_{n,i}$ build the parts for the PW-basis function *n* with hexagonal symmetry, and are given in terms of the wave vectors absolute value $k_n = |\mathbf{k}_n|$ as:

$$\mathbf{k}_{n,i} = k_n \cdot \begin{pmatrix} \cos(\alpha \cdot (\phi + \frac{\pi}{3}(i-1))) \\ \sin(\alpha \cdot (\phi + \frac{\pi}{3}(i-1))) \end{pmatrix}$$
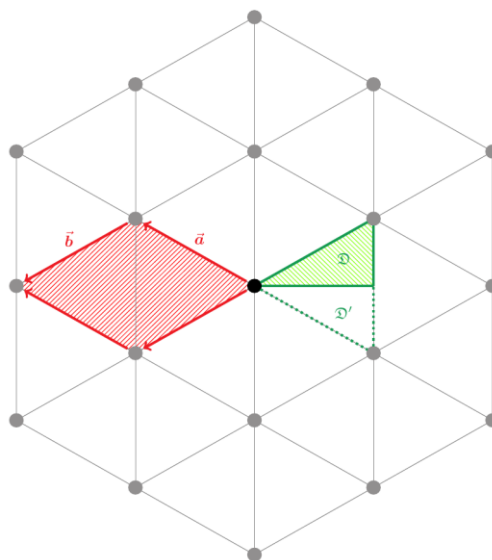
Figure S9.1.54. Schematic representation of the utilized symmetry assumptions entering in the plane wave fit for the potential energy surface. The treatment of the hexagonal unit cell shown in red with cell vectors a and b was further simplified by using the properties of the D6 symmetry, which leaves only the green triangle which spans a quarter of the original area of the unit cell as sampling area. The remaining part of the unit cell that is constructed by mirroring the interpolated triangle D is indicated by D' which then spans the half of the utilized unit cell indicated in red, and thus leads to sufficient information to construct the full unit cell.

In the following the grid points used for the interpolations are listed with their respective in plane positions given in multiples of the cell vectors **a** and **b** as well as the calculated total electronic energy in kcal/mol.

Table S9.1.17. Grid points for the basis set expansion (**PP-TAB**).

a	*b*	Total Energy (kcal/mol)

0	0	-779.247
0.1	0.1	-779.109
0.1	0	-779.226
0.2	0.2	-779.031
0.2	0	-779.194
0.277	0.111	-779.164
0.3	0.1	-779.186
0.3	0.2	-779.285
0.3	0	-779.267
0.4	0.1	-779.094
0.4	0.2	-779.209
0.4	0	-779.093
0.5	0	-779.076
0.3	0.3	-779.597
0.333	0.333	-779.375

Table S9.1.18. Grid points for the basis set expansion (**mPP-TAB**).

a	*b*	**Total Energy (kcal/mol)**
0	0	-874.051
0.1	0.1	-873.948
0.1	0	-874.040
0.2	0.1	-873.893
0.2	0.2	-873.962
0.2	0	-873.928
0.277	0.111	-873.907
0.3	0.1	-874.379
0.3	0.2	-873.997
0.3	0.3	-874.618
0.3	0	-874.040
0.333	0.333	-874.683
0.4	0.1	-873.911

0.4	0.2	-874.204
0.4	0	-873.896
0.5	0	-873.896

Table S9.1.19. Grid points for the basis set expansion (**dPP-TAB**).

a	*b*	**Total Energy (kcal/mol)**
0	0	-968.840
0.1	0.1	-968.818
0.1	0	-968.837
0.2	0.1	-968.681
0.2	0.2	-968.667
0.2	0	-968.707
0.277	0.111	-968.678
0.3	0.1	-968.781
0.3	0.2	-968.689
0.3	0.3	-968.534
0.3	0	-968.705
0.333	0.333	-968.507
0.4	0.1	-968.647
0.4	0.2	-968.674
0.4	0	-968.693
0.5	0	-968.735

Investigations of arrangements for the full unit cells (Layer Curving)

For COF arrangements with layers shifted from the initial A$\overline{\text{A}}$ stacking, we could observe an increase of layer curving depending on the distance from the eclipsed mode. The curving is visible in the cell parameters a, b by a shortening of their respective length after optimization. An exemplary structure with the upper layer shifted by 0.2*a and 0.1*b for the Methoxy-1-COF is shown in Figure S9.1.55, where the curving leads to an in-plane cell vector length of 56.709 Angstrom compared to 58.872 Angstrom in the eclipsed case, which is observed to be almost planar.
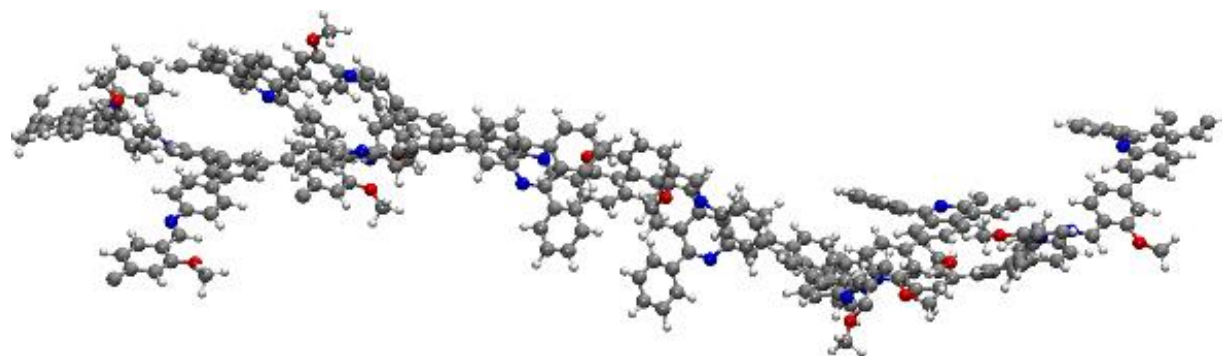
Figure S9.1.55. Curving in the arrangement for an optimized structure with initial upper layer displacement of (0.2,0.1).

9.1.11. SEM and TEM
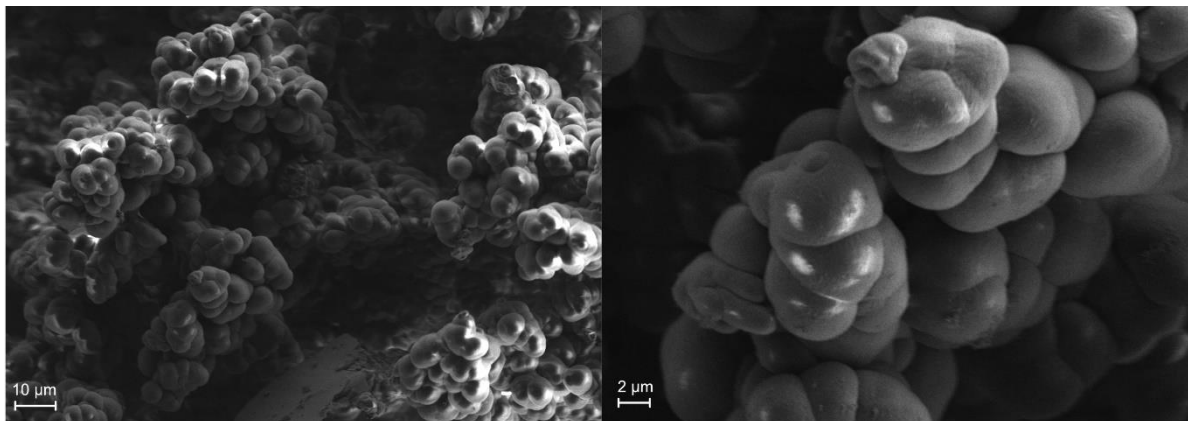
Figure S9.1.56. SEM imagess of **PP-TAB**.
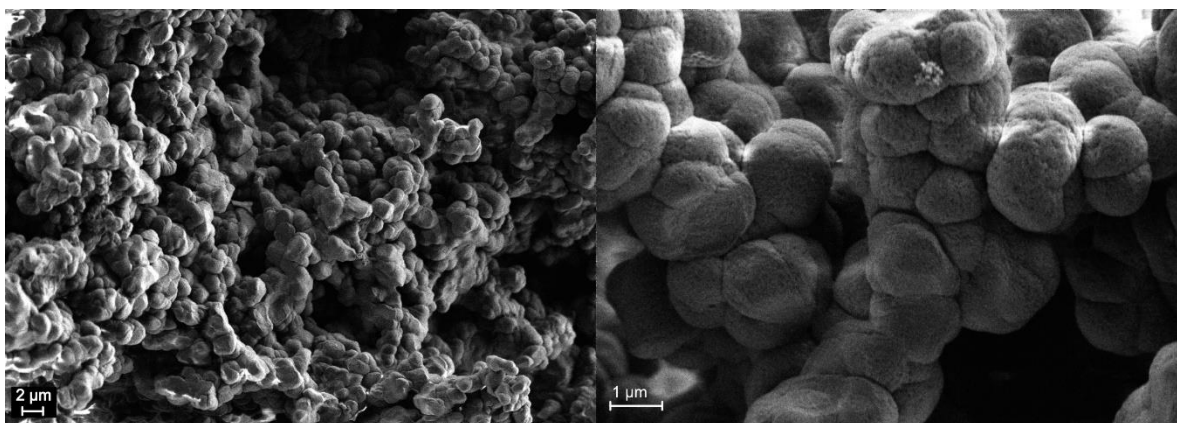
Figure S9.1.57. SEM images of **PP-TAPB**.
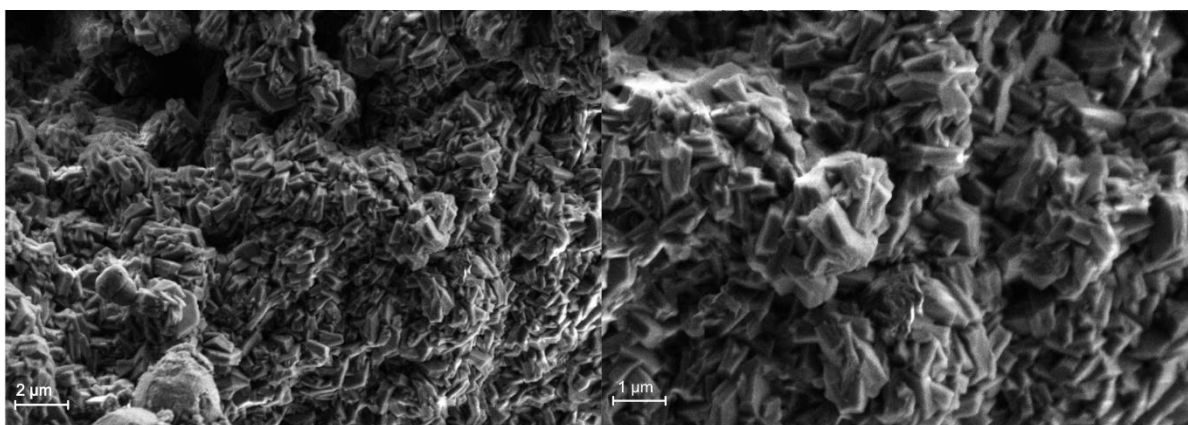
Figure S9.1.58. SEM images of **mPP-TAB**.
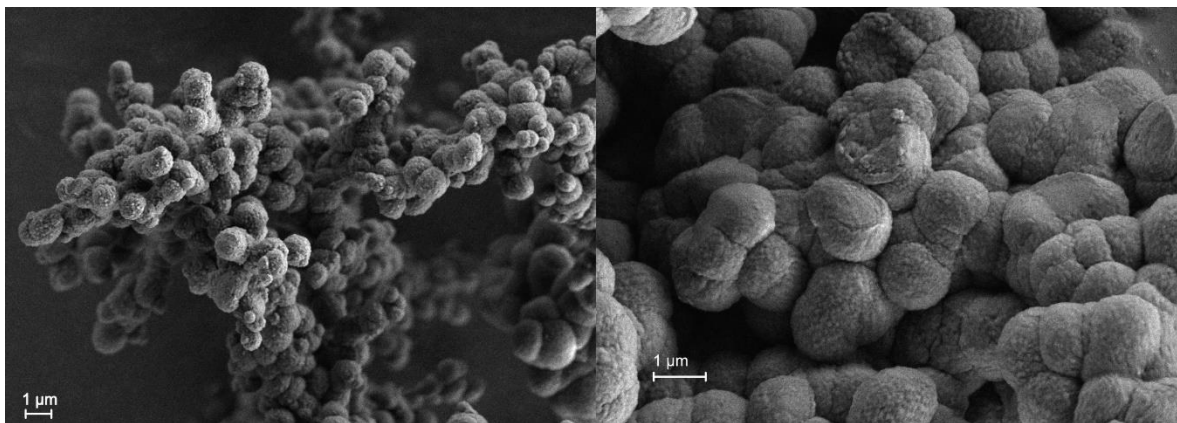
Figure S9.1.59. SEM images of **mPP-TAPB**.
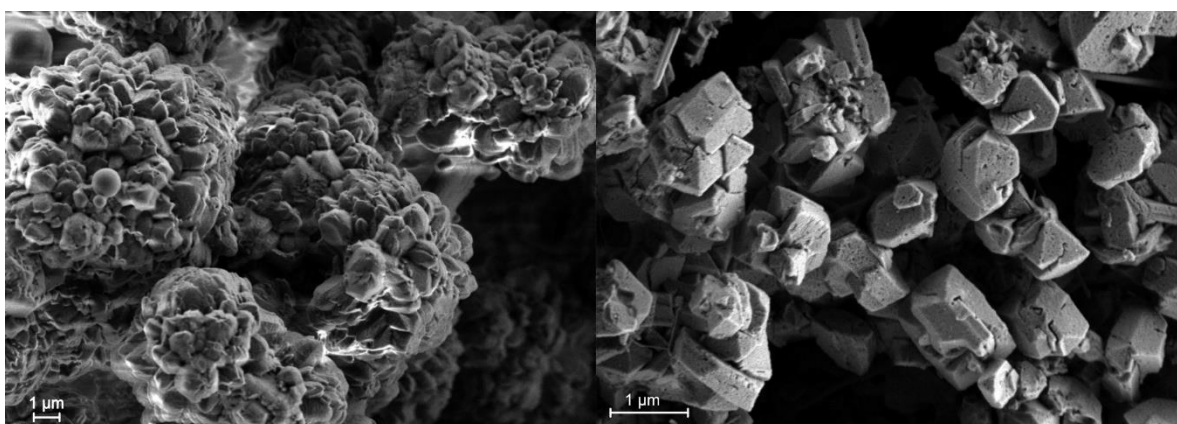
Figure S9.1.60. SEM images of **dPP-TAB**.
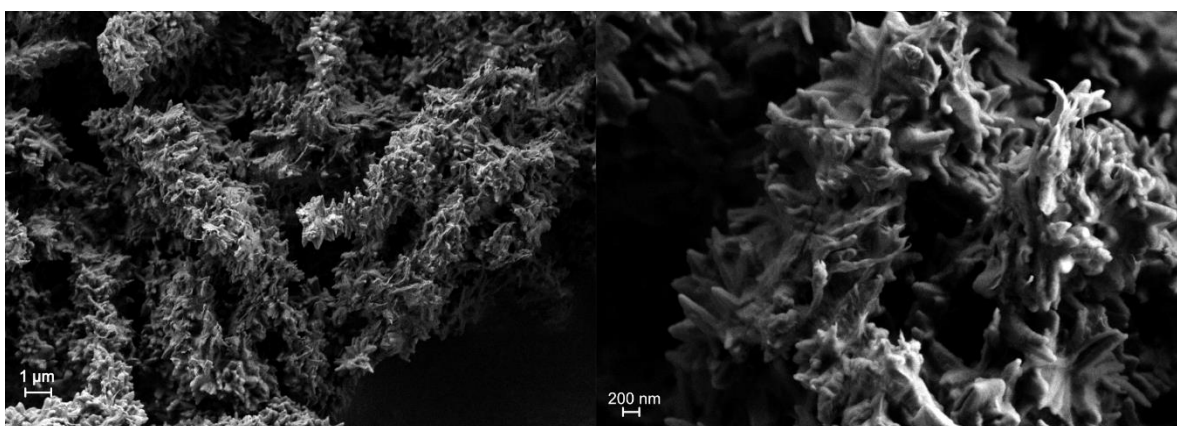
Figure S9.1.61. SEM images of **dPP-TAPB**.
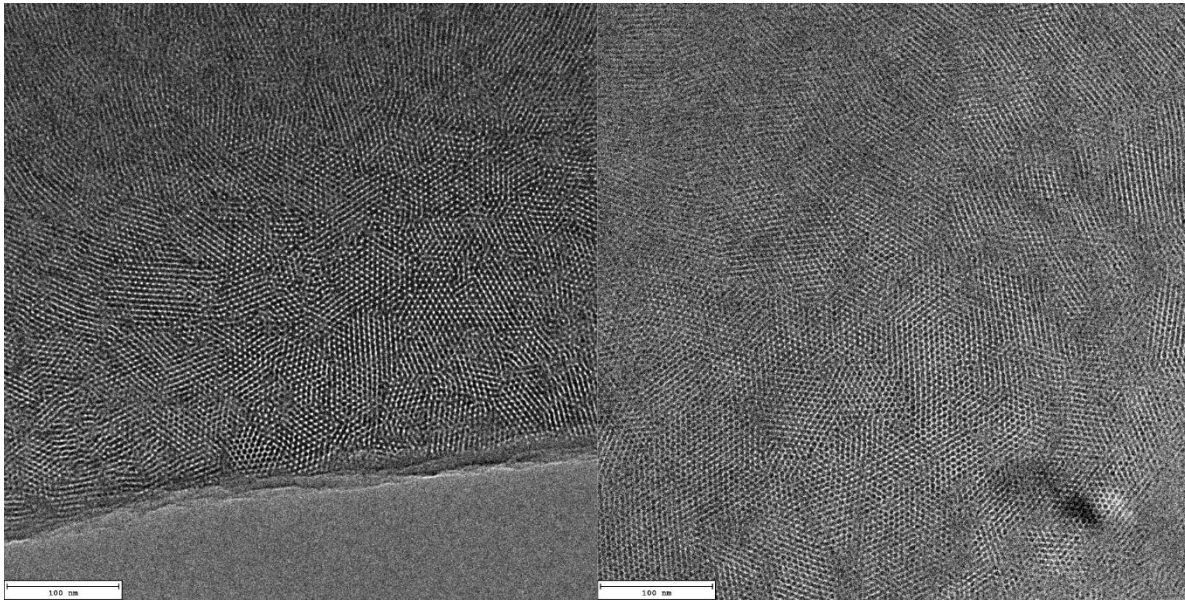
Figure S9.1.62. TEM images of **PP-TAB**.
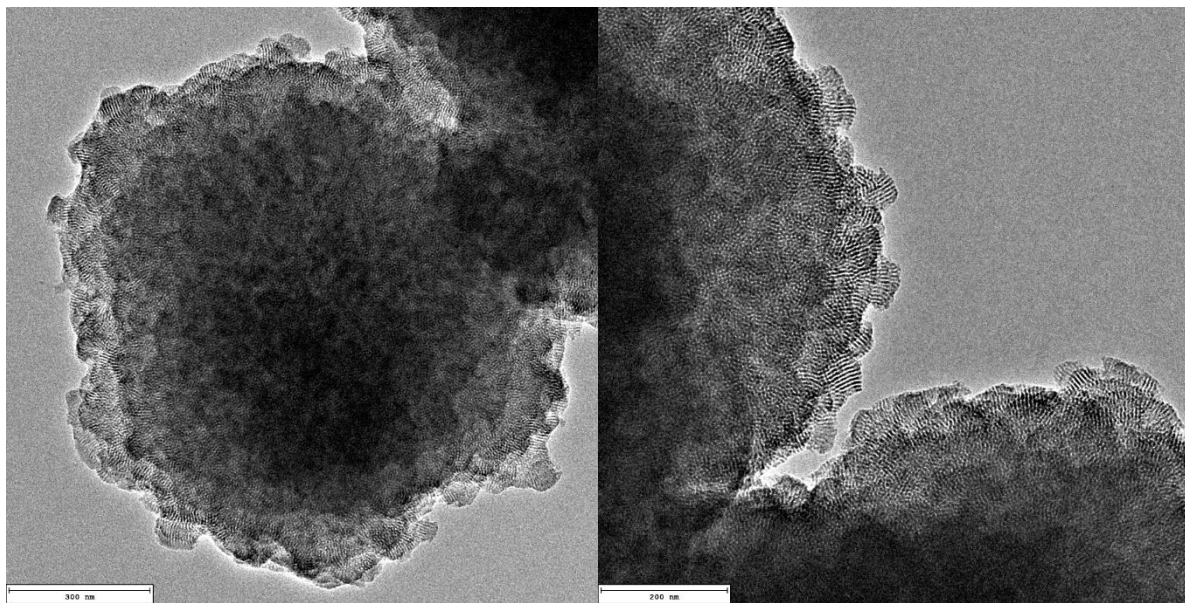
Figure S9.1.63. TEM images of **PP-TAPB**.
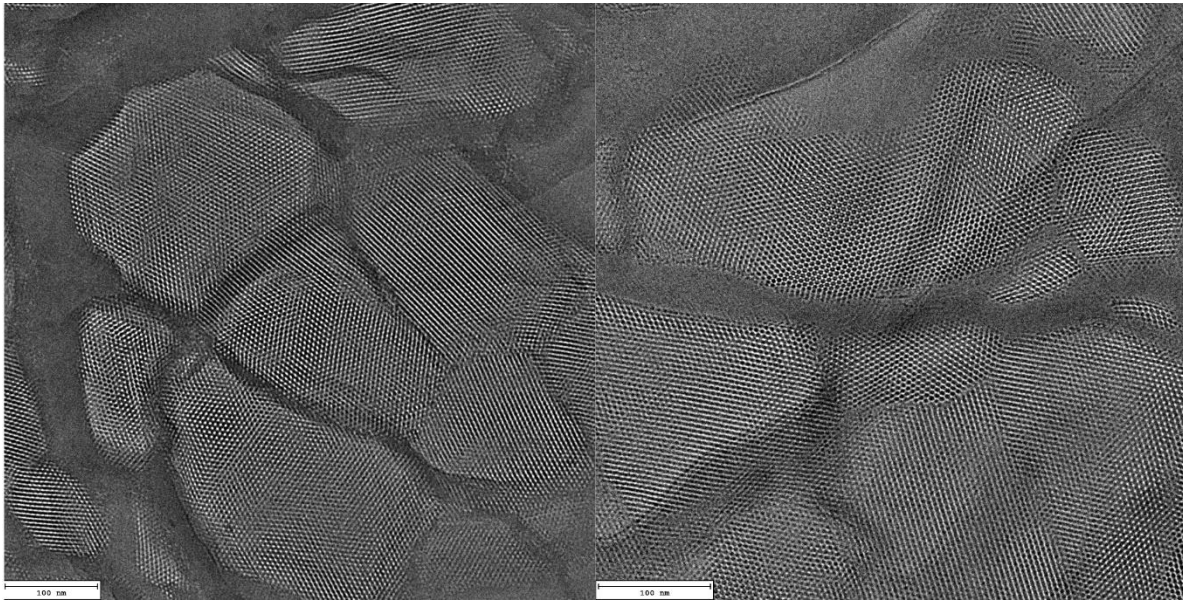
Figure S9.1.64. TEM images of **mPP-TAB**.
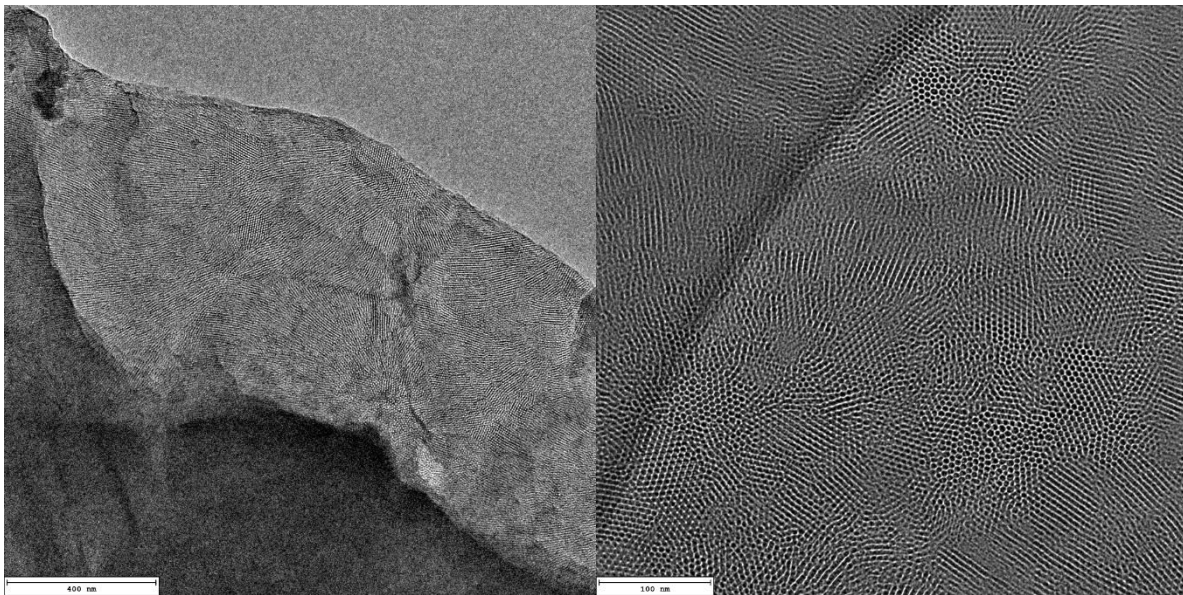
Figure S9.1.65. TEM images of **mPP-TAPB**.
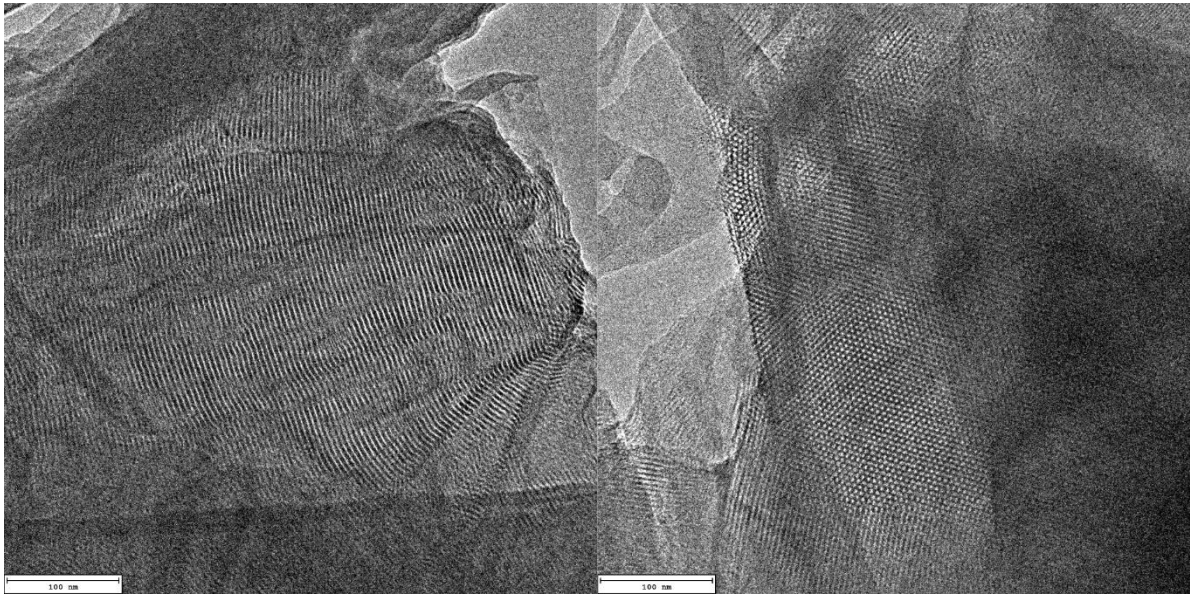
Figure S9.1.66. TEM images of **dPP-TAB**.
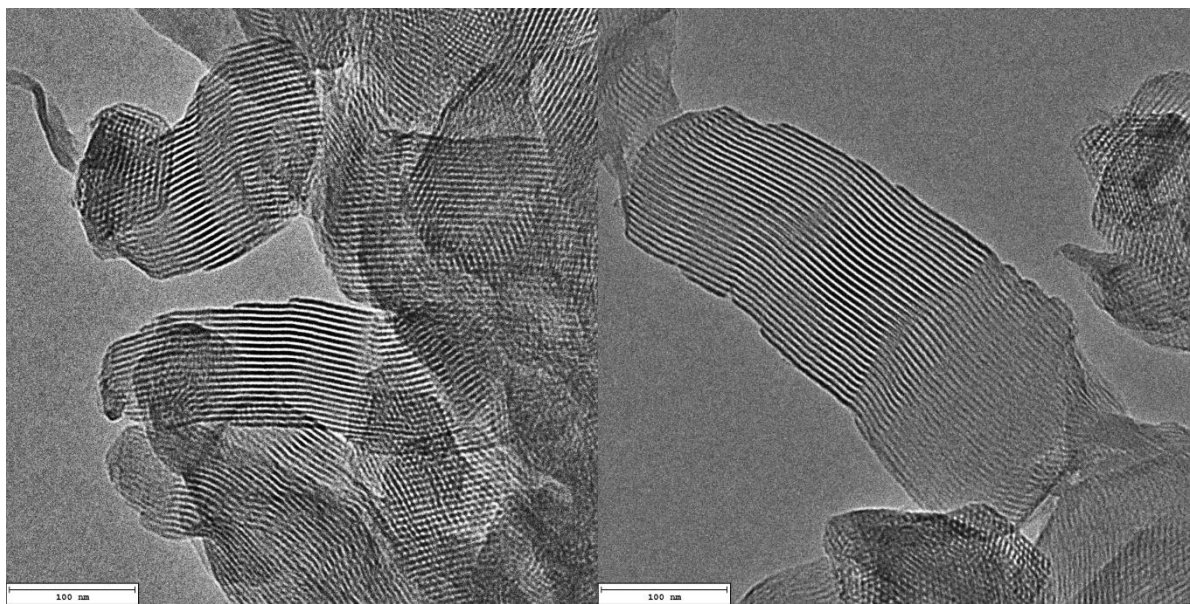
Figure S9.1.67. TEM images of **dPP-TAPB**.

9.1.12. Bibliography

[1]   Q. Fang, Z. Zhuang, S. Gu, R. B. Kaspar, J. Zheng, J. Wang, S. Qiu, Y. Yan, *Nat. Commun.* **2014**, *5*, 4503.

[2]   G. R. Fulmer, A. J. M. Miller, N. H. Sherden, H. E. Gottlieb, A. Nudelman, B. M. Stoltz, J. E. Bercaw, K. I. Goldberg, *Organometallics* **2010**, *29*, 2176–2179.

[3]   Y. Chen, F. Li, Z. Bo, *Macromolecules* **2010**, *43*, 1349–1355.

[4]   M. Movassaghi, M. D. Hill, *Org. Lett.* **2008**, *10*, 3485–3488.

[5]   D. J. F. M. J. Frisch, G. W. Trucks, H. B. Schlegel, G. E. Scuseria, M. A. Robb, J. R. Cheeseman, G. Scalmani, V. Barone, G. A. Petersson, H. Nakatsuji, X. Li, M. Caricato, A. V. Marenich, J. Bloino, B. G. Janesko, R. Gomperts, B. Mennucci, H. P. Hratchian, J. V., **2016**, Gaussian 16, Revision C.01.

[6]   A. D. Becke, *Phys. Rev. A* **1988**, *38*, 3098–3100.

[7]   J. P. Perdew, A. Zunger, *Phys. Rev. B* **1981**, *23*, 5048–5079.

9.2. Supporting Information of Chapter 5 - "Olefin Metathesis in Confinement: Towards Covalent Organic Frameworks Scaffolds for Increased Macrocyclization Selectivity"

9.2.1. Experimental Procedures

Chemicals. All catalytic reactions were performed under the exclusion of air and moisture in a N$_2$-filled glove box (MBraun Labmaster) unless noted otherwise; all COF building block reactions were carried out under Ar *via* Schlenk technique unless noted otherwise. Chemicals were purchased from *ABCR*, *Acros Organics*, *Alfa Aesar*, *Sigma Aldrich, Fluka* and *TCI*. 1,2-Dichlorobenzene (anhydrous) was purchased from Sigma Aldrich. *n*-Pentane was dried using an MBraun SPS-800 solvent purification system and stored over 4 Å molecular sieves. Deuterated solvents were stored over activated alumina and 4 Å molecular sieves for a minimum of 24 h prior to use. All other solvents, unless otherwise specified, were obtained from Acros Organics, and used without further purification. 4,4'-Dibromo-[1,1'-biphenyl]-2-amine (**6**) was synthesized according to a literature procedure.[1]

X-Ray Powder Diffraction. XRPD patterns were collected on a laboratory powder diffractometer in Debye-Scherrer geometry (Stadi P-diffractometer (Stoe), using Co-K$_{\alpha 1}$ radiation from a primary Ge(111)-Johann-type monochromator and a Mythen 1 K detector (Dectris)). The sample was sealed in a 1.0 mm diameter borosilicate glass capillary, which was spun during measurements. Each powder pattern was collected in a 2θ range from 0 ° to 40 ° with a total scan time of 5 hours. The program TOPAS 6.0 was used for the data analyses. The initially model for refinement was build and geometrically optimized in BIOVIA Materials Studio 2017 (17.1.0.48). Single atom positins were not refined. The LP factor was adjusted for the device and fixed at 31.787, in a Double-Voigt approach crystallite size and strain was accounted for and a stephens model (hexagonal) was used.

FT-IR Spectroscopy. Infrared spectra were measured in attenuated total reflection (ATR) geometry on a PerkinElmer UATR Two equipped with a diamond crystal. All spectra were background corrected.

Liquid State Nuclear Magnetic Resonance. Liquid state nuclear magnetic resonance (NMR) measurements for the COF building blocks were performed on a JEOL ECZ 400S 400 MHz spectrometer (magnetic field 9.4 T). ^{1}H, ^{13}C and ^{15}N measurements were performed in 5 mm NMR tubes using deuterium field lock. NMR spectra for the Ru-catalysis reactions were recorded on a Bruker Avance III 400 spectrometer. NMR spectra were internally calibrated to the corresponding solvent signal.[2] Abbreviations for multiplicities: s (singlet), bs (broad singlet), d (dublet), t (triplet), q (quartet), hept (heptet), m (multiplet).

Solid State Nuclear Magnetic Resonance. Solid-state NMR (ssNMR) was recorded on a Bruker Avance III 400 MHz spectrometer (magnetic field 9.4 T). Samples were packed in 4 mm ZrO_2 rotors, which were spun at 12-14 kHz in a Bruker WVT BL4 double resonance MAS probe. Chemical shift was referenced relative to tetramethylsilane (^{13}C). A standard cross-polarization sequence with a 2 ms ramped contact pulse was used for ^{13}C and a total of 4096-8192 scans were routinely accumulated. All spectra were background corrected.

Sorption Measurements. Sorption measurements were performed on a Quantachrome Instruments Autosorb iQ 3 with nitrogen at 77 K. The pore size distribution (PSD) was determined from nitrogen adsorption or desorption isotherms using the QSDFT (cylindrical pores, adsorption branch) kernel in carbon for nitrogen at 77 K implemented in the ASiQwin software v 3.01. Samples were activated under high vacuum at room temperature for 12 h before measurement.

Mass Spectrometry. Electrospray ionization (ESI) mass spectrometry was performed on a Thermo Finnigan LTQ FT in the positive and negative mode. Samples were dissolved in an acetonitrile/water mixture.

Inductively-Coupled Plasma Optical Emission Spectroscopy (ICP-OES) was performed on a VARIA VISTA RL simultaneous spectrometer (Agilent Technologies, Santa Clara, California, USA) with a CCD-detector. Samples were dissolved in conc. nitric acid (65%) at 185 °C for 25 min using a Discover-SP-D microwave by CEM.

Scanning Electron Microscopy. SEM SE (secondaryelectron) detector images were obtained on a Zeiss Merlin.

Transmission Electron Microscopy. TEM was performed with a Philips CM30 ST at 300kV (LaB$_6$cathode). Samples were prepared dry onto a holey carbon/copper grid.

Thermal Analysis. Thermogravimetric analysis was performed on a *NETZSCH STA 449 F3 Jupiter*. Measurement was carried out with 5 mg of sample in an Al_2O_3 crucibles under Helium protective gas flow in a temperature range between 40 to 1000 °C and a heating rate of 10 K/min.

9.2.2. Experimental Section

COF Synthesis
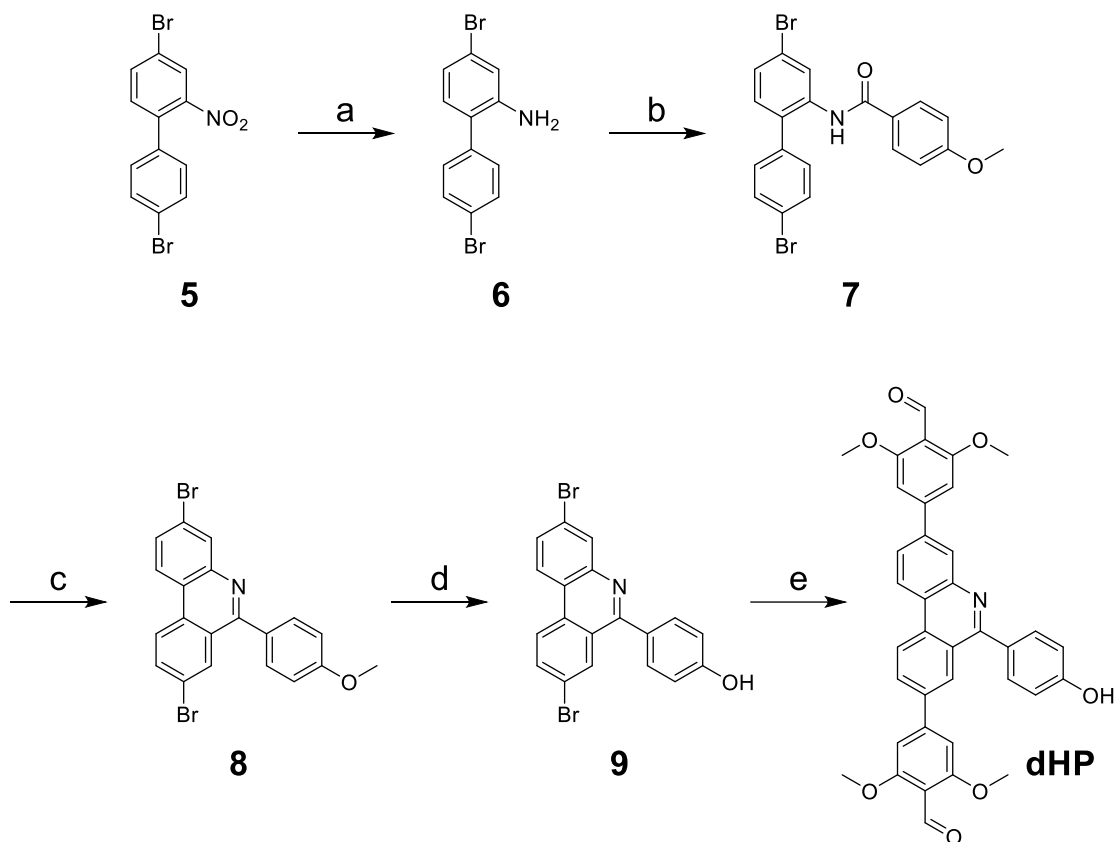
Scheme S9.2.1. Synthesis route to the phenylphenanthridine precurser. (a) Sn, HCl (conc), ethanol, reflux, 5h; (b) 4-methoxybenzoyl chloride, Et₃N, CH₂Cl₂, rt, 1h; (c) 2-chloropyridine, trifluormethansulfonic anhydride, CH₂Cl₂, 0 °C to 140 °C, 0.5 h; (d) BF₃•Me₂S, CH₂Cl₂, rt, 16 h; (e) 4-formyl-3,5-dimethoxyphenylboronic acid, tetrakis(triphenylphosphin)palladium(0), Na₂CO₃, 1,4-dioxane, 90 °C, 72 h.

Synthesis of *N*-(4,4'-dibromo-[1,1'-biphenyl]-2-yl)-4-methoxybenzamide (7). *N*-(4,4'-di-bromo-[1,1'-biphenyl]-2-yl)-4-methoxybenzamide (**7**) was synthesized according to a modified lit-erature procedure.[3] Under argon **6** (1.00 g, 3.06 mmol) and triethylamine (1.28 mL, 9.18 mml) were dissolved in dry CH₂Cl₂ (35 mL) and 4-methoxybenzoyl chloride (0.62 mL, 4.59 mmol) was added dropwise. The reaction mixture was stirred at room temperature overnight for 16 h, then ethanol (5 mL) was added. After 1 h, the solution was poured into water (50 mL) and extracted with CH₂Cl₂. The combined organic layers were dried over anhydrous Na₂SO₄ and evaporated under reduced pressure. The resulting crude product was purified by recrystallization from CH₂Cl₂ /*n*-hexane to obtain **7** (1.25 g, 2.71 mmol, 88%). ¹H NMR (400 MHz, CDCl₃) δ 8.70 (d, J = 2.0 Hz, 1H), 7.78 (s, 1H), 7.67 – 7.61 (m, 2H), 7.58 – 7.53 (m, 2H), 7.32 (dd, J = 8.2, 2.0 Hz, 1H), 7.30 – 7.26 (m, 2H), 7.10 (d, J = 8.1 Hz, 1H), 6.92 – 6.88 (m, 2H), 3.84 (s, 3H) ppm. ¹³C NMR (101 MHz, CDCl₃) δ 164.7, 162.8, 136.3, 136.2, 132.7, 131.2, 130.9, 129.9, 128.9, 127.5, 126.4, 124.5, 122.9, 122.8, 114.8, 55.6 ppm. FT-IR vmax/cm⁻¹ 3434, 2839, 1669, 1574, 1503, 1412, 1252, 1179,

1031, 845, 808, 754, 542. HRMS (ESI) exact mass calculated for [M+H]+ ($C_{20}H_{15}Br_2NO_2$) requires m/z 461.9449, found m/z 461.95227.

Synthesis of 3,8-dibromo-6-(4-methoxyphenyl)phenanthridine (8). 3,8-dibromo-6-(4-methoxyphenyl)phenanthridine (**8**) was synthesized according to a modified literature method.[4] Under argon a *Biotage* microwave vial was charged with **7** (1.20 g, 2.6 mmol), 2-chloropyridine (0.29 mL, 3.12 mmol) and dry CH_2Cl_2 (13 mL). Trifluormethansulfonic anhydride (0.48 mL, 2.86 mmol) was added dropwise at 0°C. After 5 minutes, the solution was warmed to room temperature, the vial was capped and under microwave irradiation, the solution was heated to 140 °C for 30 minutes. After the solution was cooled to room temperature, triethylamine (0.73 mL, 5.2 mmol) was added dropwise to neutralize the trifluormethanesulfonate salts. All volatiles were removed under reduced pressure and the residue was purified by flash column chromatography (SiO$_2$, *n*-hexane/ CH_2Cl_2) to obtain **4** (1.06 g, 2.39 mmol, 92%). ^{1}H NMR (400 MHz, CDCl$_3$) δ 8.46 (d, J = 8.8 Hz, 1H), 8.41 – 8.33 (m, 2H), 8.30 (d, J = 2.0 Hz, 1H), 7.92 (dd, J = 8.8, 2.1 Hz, 1H), 7.74 (dd, J = 8.7, 2.1 Hz, 1H), 7.70 – 7.64 (m, 2H), 7.15 – 7.08 (m, 2H), 3.93 (s, 3H) ppm. ^{13}C NMR (101 MHz, CDCl$_3$) δ 160.9, 160.7, 144.8, 134.2, 132.9, 132.0, 131.5, 131.3, 130.4, 126.7, 124.1, 123.4, 123.1, 121.9, 121.7, 114.3, 55.6 ppm. FT-IR v_{max}/cm^{-1} 2958, 2839, 1593, 1557, 1511, 1463, 1357, 1303, 1249, 1176, 1034, 964, 828, 799, 596, 518. HRMS (ESI) exact mass calculated for [M+H]+ ($C_{20}H_{13}Br_2NO$) requires m/z 443.9343, found m/z 443.94166.

Synthesis of 4-(3,8-dibromophenanthridin-6-yl)phenol (9). Under argon a flask was charged with **3** (0.50 g, 1.13 mmol), and dry CH_2Cl_2 (30 mL). A boron trifluoride-dimethyl sulfide complex (1.42 mL, 13.6 mmol) was added dropwise at room temperature. The solution was stirred at room temperature for 16 h, then cooled to 0 °C and methanol was added dropwise to quench the reaction. All volatiles were removed under reduced pressure and the residue was purified by flash column chromatography (SiO$_2$, CH_2Cl_2/MeOH) to obtain **9** (0.42 g, 0.98 mmol, 87%). ^{1}H NMR (400 MHz, DMSO-D6) δ 8.86 (d, J = 9.6 Hz, 1H), 8.76 (d, J = 9.0 Hz, 1H), 8.27 (d, J = 2.0 Hz, 1H), 8.19 (d, J = 7.9 Hz, 2H), 7.92 (dd, J = 8.8, 2.1 Hz, 1H), 7.67 – 7.59 (m, 2H), 7.10 – 7.00 (m, 2H), 5.74 (s, 1H) ppm. ^{13}C NMR (101 MHz, DMSO-D6) δ 160.4, 159.7, 135.8, 132.2, 131.9, 131.3, 130.9, 129.0, 125.7, 125.6, 125.2, 123.1, 121.9, 115.6 ppm. FT-IR v_{max}/cm^{-1} 3368 (br), 3182, 3093, 1636, 1582, 1468, 1360, 1225, 1184, 1084, 1068, 994, 818, 661, 520. HRMS (ESI) exact mass calculated for [M+H]+ ($C_{19}H_{11}Br_2NO$) requires m/z 429.9187, found m/z 429.92596.

Synthesis of 4,4'-(6-phenylphenanthridine-3,8-diyl)bis(2,6-dimethoxybenzaldeyde) (dHP). Under argon in a 20 mL *Biotage* microwave vial, **9** (0.25 g, 0.58 mmol), 4-formyl-3,5-dimethoxyphenylboronic acid (0.49 g, 2.34 mmol) and tetrakis(triphenylphosphin)palladium(0) (0.068 g, 0.06 mmol) were dissolved in 1,4-dioxane (15 mL) and 2 M aqueous Na$_2$CO$_3$ (2.6 mL) was added. After degassing the solution with argon for 30 minutes the vial was capped and the mixture was stirred for 72 h at 90 °C. After cooling to room temperature, all solvents were removed and the residual solid was extracted with CHCl$_3$ (3 x 50 mL). The combined organic extracts were

evaporated under reduced pressure. The solid residue was purified by flash column chromatography (SiO$_2$, n-hexane/CHCl$_3$ with 1% Et$_3$N) to obtain **dHP** (0.21 g, 0.35 mmol, 61%). ^{1}H NMR (400 MHz, CHLOROFORM-D) δ 10.53 (s, 1H), 10.45 (s, 1H), 8.84 (d, J = 8.7 Hz, 1H), 8.73 (d, J = 8.7 Hz, 1H), 8.40 (s, 1H), 8.22 (d, J = 8.3 Hz, 1H), 8.08 (d, J = 8.6 Hz, 1H), 7.90 (d, J = 4.9 Hz, 2H), 7.66 – 7.61 (m, 3H), 6.98 (s, 2H), 6.79 (s, 2H), 3.99 (s, 6H), 3.96 (s, 6H) ppm. ^{13}C NMR (101 MHz, CHLOROFORM-D) δ 188.96, 162.63, 130.27, 130.24, 130.21, 130.17, 128.83, 123.62, 123.47, 123.09, 113.68, 113.57, 103.32, 103.18, 56.40, 56.30 ppm. FT-IR v_{max}/cm^{-1} 3423 (br), 2936, 2876, 1676, 1597, 1567, 1455, 1393, 1241, 1123, 809, 705, 576. HRMS (ESI) exact mass calculated for [M+H]+ (C$_{37}$H$_{29}$NO$_7$) requires m/z 600.1944, found m/z 600.20211.
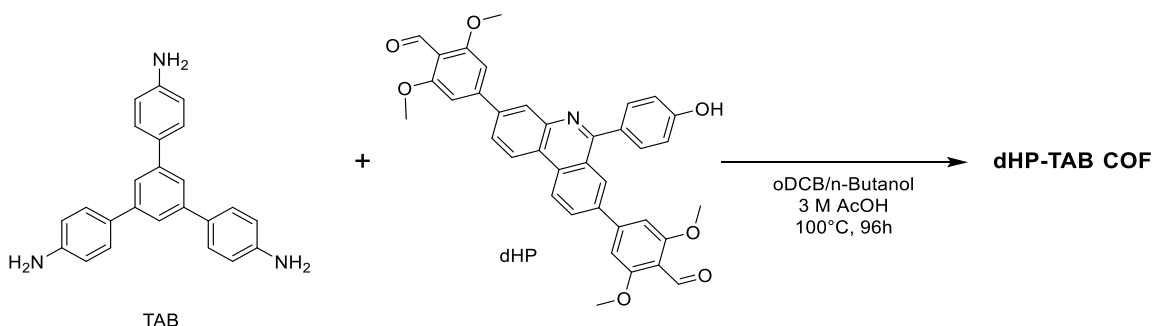
Scheme S9.2.2. Synthesis of dHP-COF.

Synthesis of dHP-TAB COF. 1,3,5-Tris(4-aminophenyl)benzene (**TAB)** (0.1 mmol, 35.1 mg) and **dHP** (0.15 mmol, 90.0 mg) were placed into a 5 mL *Biotage* microwave vial. 4 mL of a 1,2-dichlorobenzene/n-butanol (1:4) mixture were added, followed by 80 µL 3M AcOH. The vial was capped and placed in an aluminum heating block that was preheated to 100°C. Under stirring at 500 rpm the mixture was kept at 100°C for 96 h, then it was allowed to cool to room temperature. The solid was filtered off, washed with MeOH and then subjected to Soxhlet extraction with MeOH for 16 h. The MeOH soaked solid was then activated by scCO2 drying and further under high vacuum for 24 h to obtain 93.1 mg **dHP-TAB** COF (78 %).

Substrates and Ru-catalyst
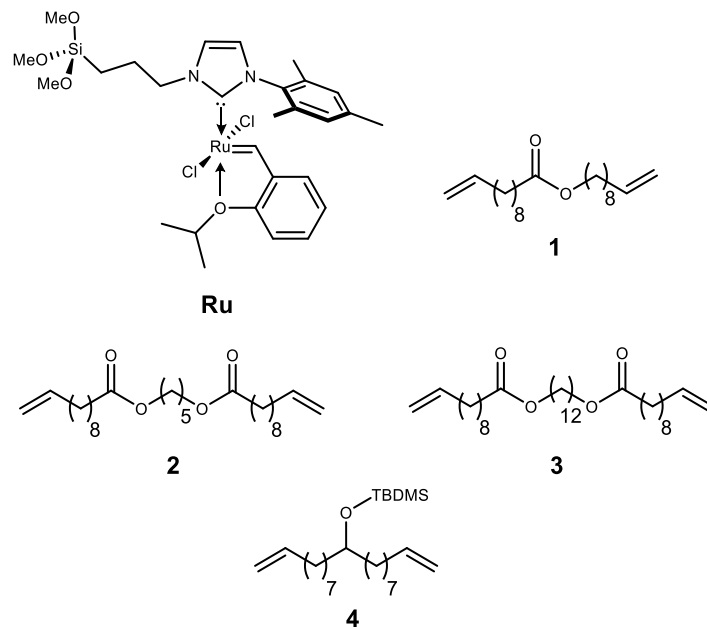
Scheme S9.2.3. Ru-catalyst and substrated used in macrocyclization reactions.

RuCl$_2$(N-mesityl-N-(3-(trimethoxysilyl)prop-1-yl)-imidazol-2-ylidene)(CH-2-(2-PrO-C$_6$H$_4$)) Ru,[5] dec-9-en-1-yl undec-10-enoate 1,[5] pentane-1,5-diyl bis(undec-10-enoate) 2,[5,6] dodecane-1,12-diyl bis(undec-10-enoate) 3,[5] tert-butyldimethyl(nonadeca-1,18-dien-10-yloxy)silane 4,[5,6] (E)+(Z)-oxacycloicos-11-en-2-one,[6] (E)+(Z)-1,7-dioxacycloheptacos-17-ene-8,27-dione,[7] (E)+(Z)-1,14-di-oxacyclotetratriacont-24-ene-15,34-dione[5] and (E)+(Z)-tert-butyl(cycloheptadec-9-en-1-yloxy)di-methylsilane[6] were synthesized according to the literature.

Immobilization of Ru and Ru@dHP-TAB loading

A solution of **Ru** (10 mg) in 1,2-dichlorobenzene was added to the **dHP-TAB COF** (~100 mg). For the removal of nitrogen in the pores, vacuum was applied. The suspension was stirred for 16 hours at room temperature. Then, the suspension was filtered, and the resulting **Ru@dHP-TAB COF** containing the immobilized catalyst was washed with 1,2-dichlorobenzene (200 mL), n-pentane (200 mL), dried in vacuo at room temperature for 3 h, and stored under an inert atmosphere at −35 °C.

Table S9.2.1. Ru-content of COF as determined by ICP-OES.

Material	c(Ru) on COF [µmol Ru/g COF]
Ru@dHP-TAB	42.3

Leak test of Ru@dHP-TAB

Ru@dHP-TAB (30 mg) was stirred in 4 mL benzene at 50 °C for 16 h. The solid was filtered off, the solvent removed and the residue was dired under vacuum at elevated temperature. The remaining oil-like residue was tested by ICP-OES for its ruthenium content. No ruthenium was detected.

Additionally, **Ru@dHP-TAB** was tested by ICP-OES after performing the general procedure for the RCM of α,ω-dienes with substrate 1. The recovered material showed a concentration c(Ru) of 51.74 µmol Ru/g COF, even slighty higher than the pristine material. We attribute the increase to slight sample inhomegeneities in the batch used.

Macrocyclization Reactions

General procedure for the RCM of α,ω-dienes (GP-1). The substrate was dissolved in C_6D_6 (1000 µL) and the catalyst (stock solution) was added. After 16 hours, ^1H NMR spectra were acquired. Conversion and macro(mono)cyclization:oligomer (MMC:O) ratios were determined by integration of the corresponding signals.

***Example reaction with 0.5 mol% catalyst, MMC with* Ru: 1** (8.1 mg, 0.025 mmol, 1 eq.) was dissolved in C_6D_6 (995.8 µL, 25.1 mM) and a stock solution of catalyst **Ru** (4.2 µL, 2.9 mM; 0.5 mol-%) was added. The resulting mixture (substrate concentration 25 mM) was stirred for 16 hours at 50 °C and subjected to ^1H NMR spectroscopy. Overall conversion: 81%. MMC:O = 0.9 (selectivity = 47%).

For the correct determination of the conversion by NMR, the deconvolution function of MestReNova (Version 12.0.0) was used. This was necessary because part of the oligomer signals of the terminal double bonds were covered by the signals of the starting material (see Figure S1).
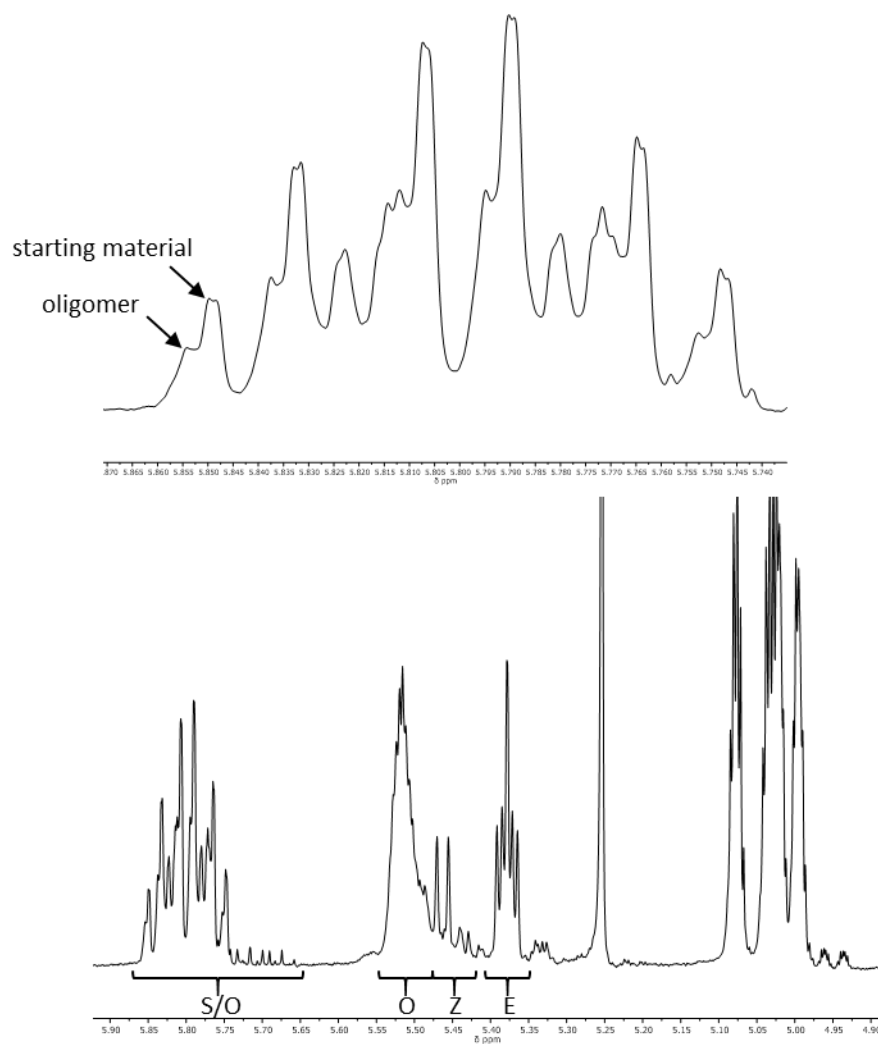
Figure S9.2.1: ^{1}H NMR spectrum of the reaction mixture of the MMC of **1** with the homogeneous catalyst **Ru** in C$_6$D$_6$. MMC:O = 0.9 (selectivity = 47%) and an enlarged area where deconvolution was applied.

Table S9.2.2. Conversion, MMC:O ratio and selectivity for the RCM of substrate **1 - 4** by the action of **Ru** (0.5 mol-%) as determined by NMR.

Substrate	Conversion [%]	MMC:O	Selectivity [%]
1	81	0.90	47
2	77	0.84	46
3	80	0.65	39
4	73	0.40	28

General procedure for the RCM of α,ω-dienes with Ru@dHP-TAB (GP-2). The substrate was dissolved in C_6D_6 (1.0 mL) and the corresponding COF material containing the Ru-catalyst (3-6 mg, depending on the Ru content and the catalyst:substrate ratio) was added. After 16 hours, ^{1}H NMR data were acquired. Conversion, the MMC:O ratio and the selectivity were determined by integration of the corresponding signals.

MMC with **Ru@dHP-TAB: 1** (8.1 mg, 0.025 mmol, 1 eq.) was dissolved in C_6D_6 (1.00 mL, 25 mM) and **Ru@dHP-TAB** (2.9 mg, 0.5 mol-%) was added. The resulting mixture was stirred at 50 °C for 16 hours and subjected to ^{1}H NMR spectroscopy. Overall conversion: 11%. MMC:O = 1.3 (selectivity = 56%).
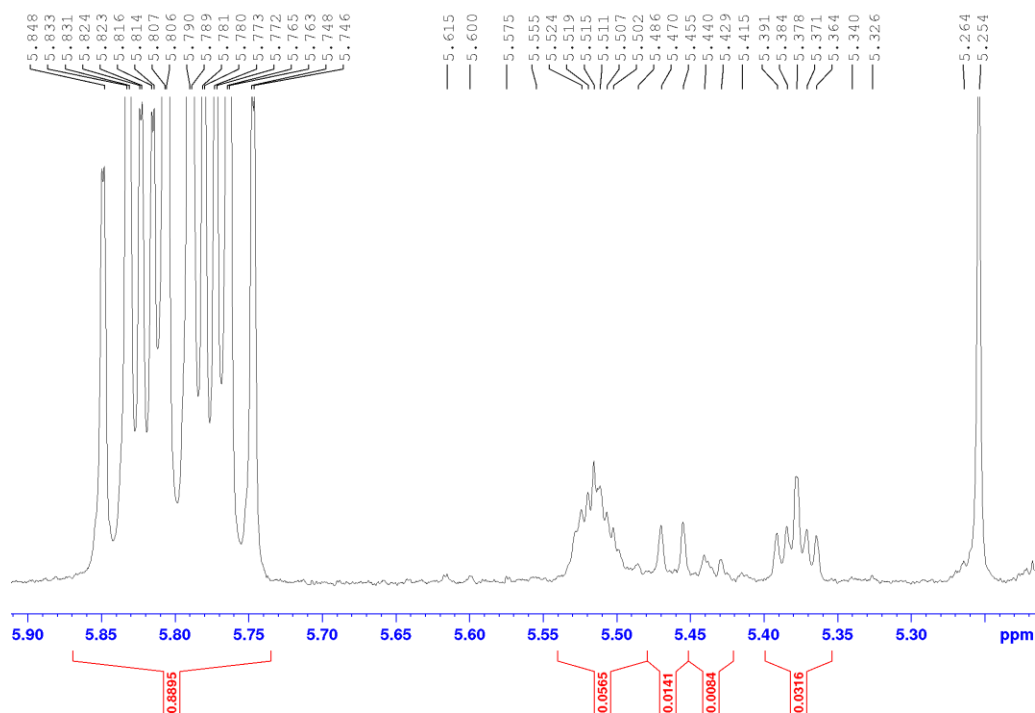
Figure S9.2.2: ^{1}H NMR spectrum of the MMC reaction mixture of **1** with the homogeneous catalyst **Ru@dHP-TAB** in C_6D_6. MMC:O = 1.3 (selectivity = 56%).

MMC with **Ru@dHP-TAB: 1** (8.1 mg, 0.025 mmol, 1 eq.) was dissolved in C_6D_6 (1.00 mL, 25 mM) and **Ru@dHP-TAB** (5.8 mg, 1.0 mol-%) was added. The resulting mixture was stirred at 50 °C for 16 hours and subjected to ^{1}H NMR spectroscopy. Overall conversion: 15%. MMC:O = 1.3 (selectivity = 56%).
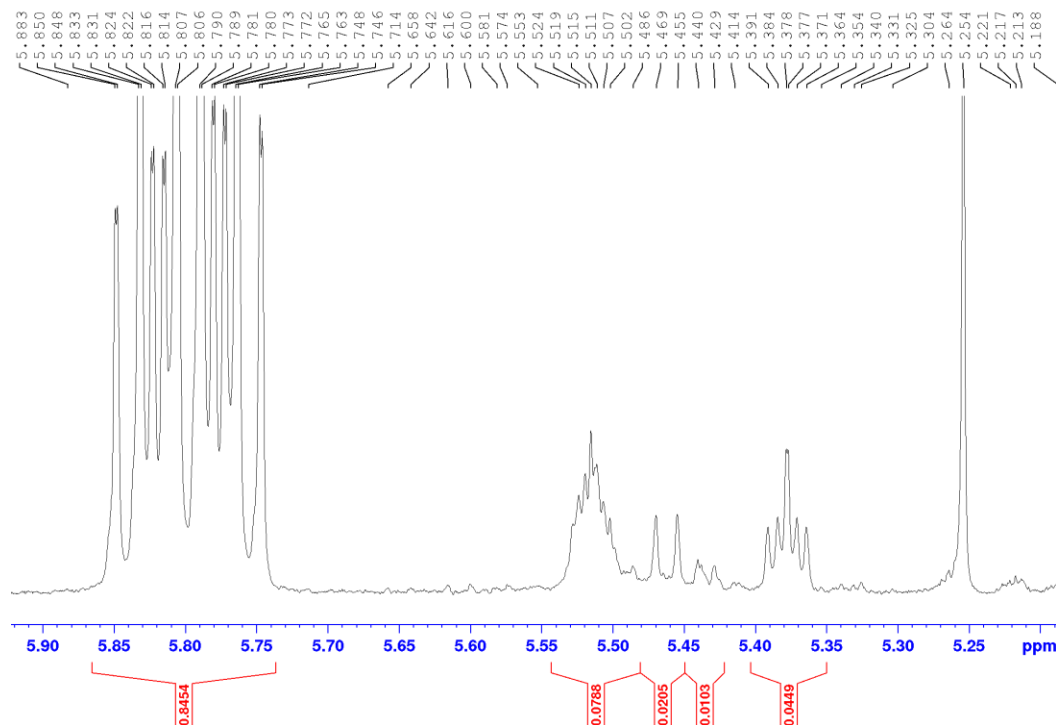
Figure S9.2.3: ^{1}H NMR spectrum of the MMC reaction mixture of **1** with the homogeneous catalyst **Ru@dHP-TAB** in C_6D_6. MMC:O = 1.3 (selectivity = 56%).

MMC with **Ru@dHP-TAB: 2** (10.3 mg, 0.025 mmol, 1 eq.) was dissolved in C_6D_6 (1.00 mL, 25 mM) and **Ru@dHP-TAB** (2.9 mg, 0.5 mol-%) was added. The resulting mixture was stirred at 50 °C for 16 hours and subjected to ^{1}H NMR spectroscopy. Overall conversion: 11%. MMC:O = 1.0 (selectivity = 49%).
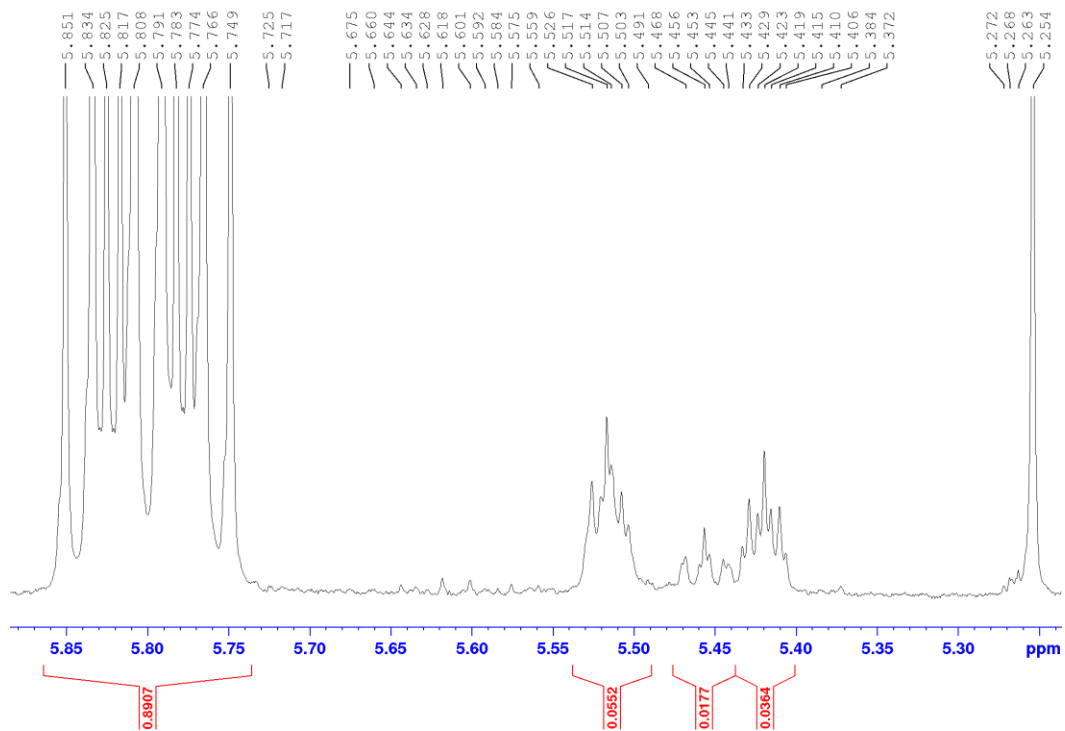
Figure S9.2.4: ^{1}H NMR spectrum of the MMC reaction mixture of **2** with the homogeneous catalyst **Ru@dHP-TAB** in C_6D_6. MMC:O = 1.0 (selectivity = 49%).

***MMC with* Ru@dHP-TAB: 3** (13.4 mg, 0.025 mmol, 1 eq.) was dissolved in C_6D_6 (1.00 mL, 25 mM) and **Ru@dHP-TAB** (2.9 mg, 0.5 mol-%) was added. The resulting mixture was stirred at 50 °C for 16 hours and subjected to ^{1}H NMR spectroscopy. Overall conversion: 11%. MMC:O = 0.6 (selectivity = 39%).
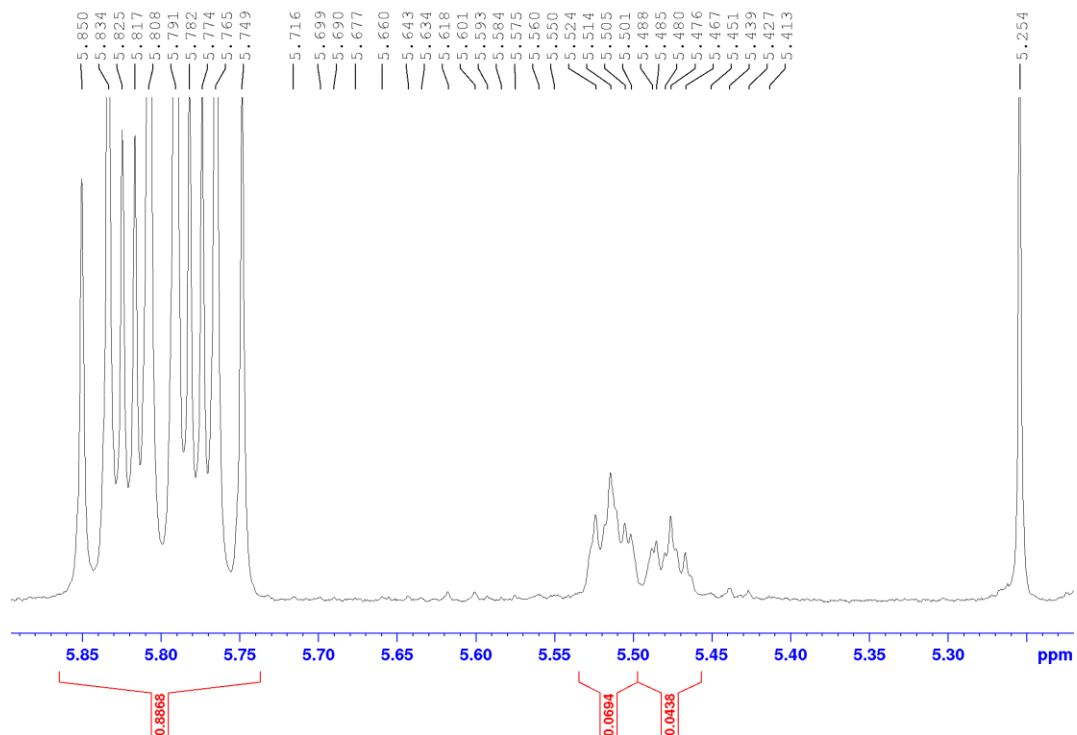
Figure S9.2.5: ^{1}H NMR spectrum of the MMC reaction mixture of **3** with the homogeneous catalyst **Ru@dHP-TAB** in C_6D_6. MMC:O = 0.6 (selectivity = 39%).

***MMC with* Ru@dHP-TAB: 4** (9.9 mg, 0.025 mmol, 1 eq.) was dissolved in C_6D_6 (1.00 mL, 25 mM) and **Ru@dHP-TAB** (2.9 mg, 0.5 mol-%) was added. The resulting mixture was stirred at 50 °C for 16 hours and subjected to ^{1}H NMR spectroscopy. Overall conversion: 12%. MMC:O = 0.5 (selectivity = 35%).
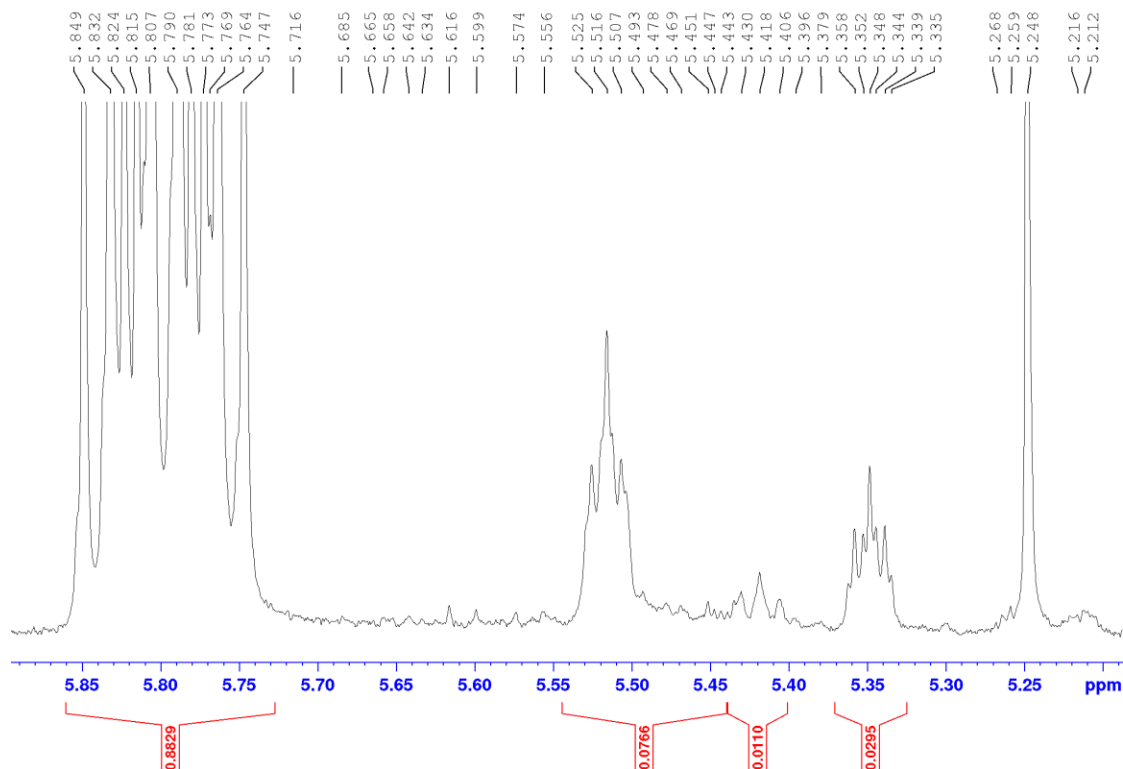
Figure S9.2.6: ^{1}H NMR spectrum of the MMC reaction mixture of **4** with the homogeneous catalyst **Ru@dHP-TAB** in C$_6$D$_6$. MMC:O = 0.5 (selectivity = 35%).

Kinetics

Each table entry is an independent reaction which was hot filtered at the time mentioned in Table S3. The NMR solution shows no change over time.

Table S9.2.3. Conversion, MMC:O ratio and selectivity for the RCM of substrate **1** by the action of **Ru@dHP-TAB** terminated at a different time.

Time [min]	Conversion [%]	MMC:O	Selectivity [%]
30	3	1.1	52
60	4	1.1	52
180	7	1.3	57
360	9	1.2	55
960	11	1.3	56

9.2.3. FT-IR Spectroscopy
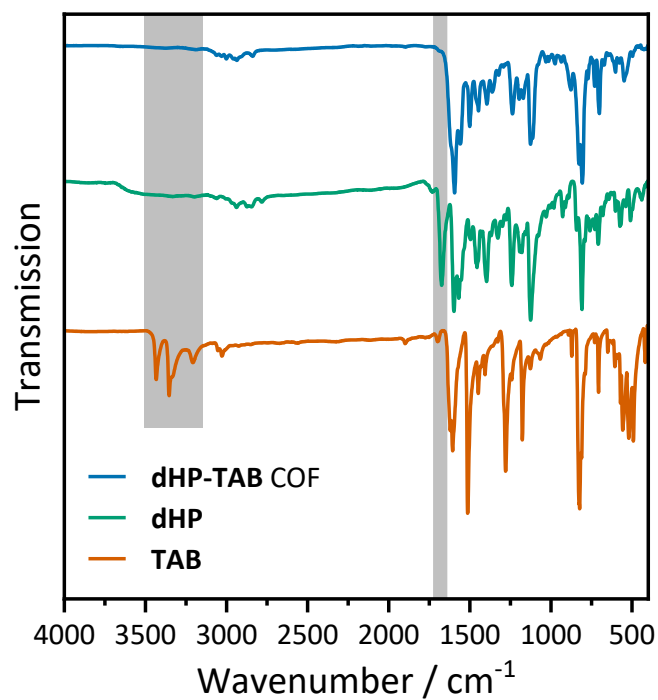
Figure S9.2.7. FT-IR comparison of **dHP-TAB COF** and the starting materials **dHP** and **TAB**.
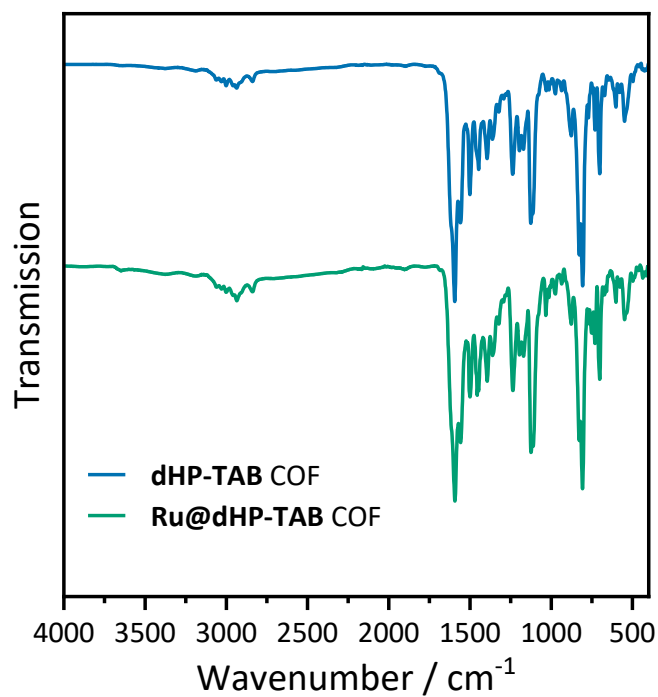
Figure S9.2.8. FT-IR comparison of **dHP-TAB COF** and **Ru@dHP-TAB COF.**

9.2.4.   XRPD Measurements and Refinements
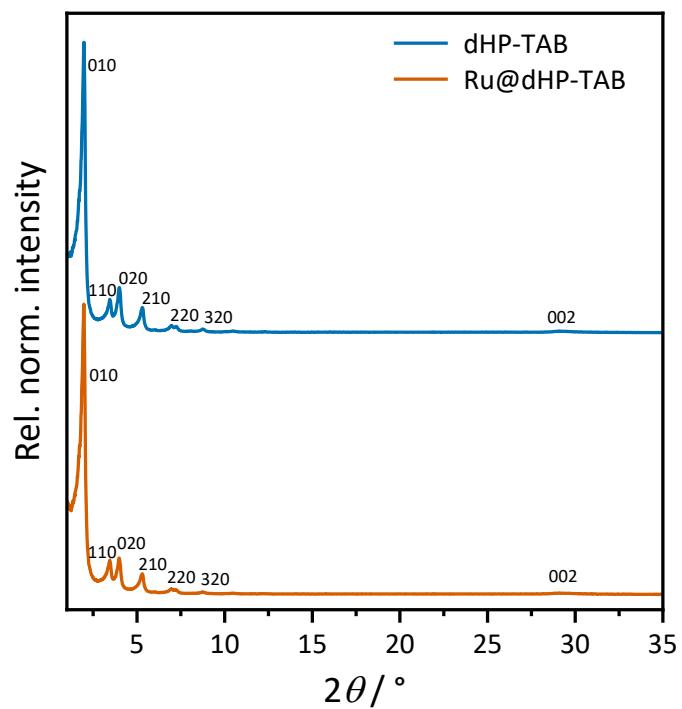
Figure S9.2.9. XRPD comparison (λ = 1.789 Å) of **dHP-TAB** COF and **Ru@dHP-TAB** COF**.**
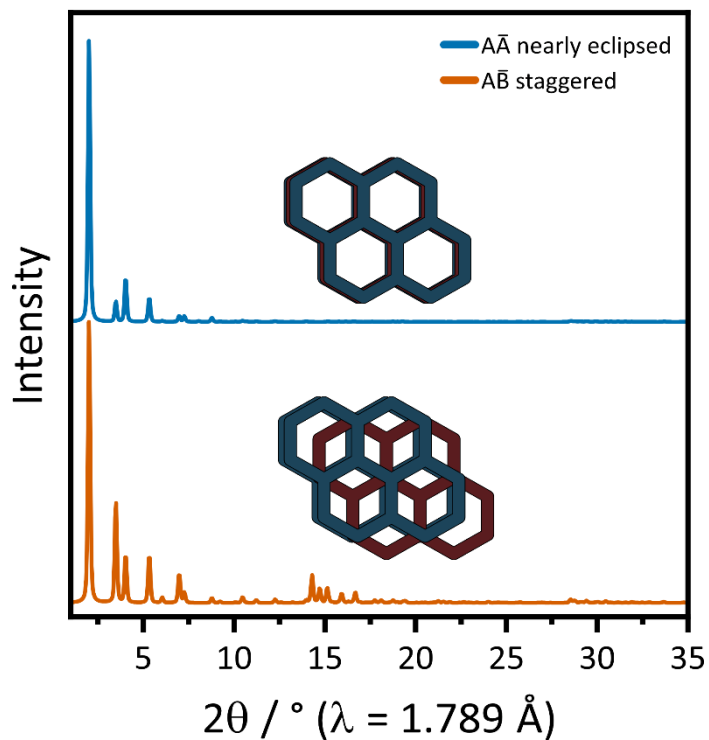
Figure S9.2.10. Simulated patterns of AĀ (top) and AB̄ (bottom) stacking for **dHP-TAB**.

Table S9.2.4. Results of Rietveld refinement, atom site positions of **dHP-TAB COF**. Atom position were not refined.

	*P*31*c*			*a* = *b* = 58.824(10) Å and *c* = 7.3(0) Å	
atom_site_label	_atom_site_fract_x	atom_site_fract_y	atom_site_fract_z	atom_site_type _symbol	atom_site_ occu-pancy
C1	0.05439	0.49425	-0.18419	C	1
C2	0.02761	0.48209	-0.18561	C	1
C3	0.01474	0.49505	-0.12657	C	1
C4	0.02962	0.52109	-0.07024	C	1
C5	0.05657	0.53248	-0.0601	C	1
C6	0.06914	0.51943	-0.11904	C	1
C7	0.98596	0.48225	-0.12263	C	1
C8	0.9747	0.49666	-0.06227	C	1
N9	0.98959	0.52152	-0.01218	N	1
C10	0.0171	0.53487	-0.02117	C	1
C11	0.96958	0.45645	-0.17515	C	1
C12	0.94287	0.44573	-0.17248	C	1
C13	0.93175	0.46035	-0.1168	C	1
C14	0.94797	0.48574	-0.05847	C	1
C15	0.09765	0.53216	-0.10987	C	1
C16	0.10959	0.51828	-0.05672	C	1
C17	0.13661	0.53012	-0.04681	C	1
C18	0.15182	0.55663	-0.08696	C	1
C19	0.13991	0.57098	-0.1388	C	1
C20	0.11286	0.55832	-0.1517	C	1
C21	0.18029	0.56889	-0.07376	C	1
O22	0.15566	0.59758	-0.17398	O	1
C23	0.14391	0.6125	-0.21847	C	1
O24	0.14929	0.51641	-2.40E-04	O	1
C25	0.135	0.48893	-0.00352	C	1
C26	0.03083	0.56315	0.0099	C	1
C27	0.05034	0.58021	-0.10877	C	1

C28	0.06306	0.60672	-0.07743	C	1
C29	0.05603	0.61669	0.06939	C	1
C30	0.03572	0.59989	0.18299	C	1
C31	0.02302	0.57338	0.15161	C	1
C32	0.54621	0.09658	-0.12705	C	1
C33	0.57181	0.10651	-0.1814	C	1
C34	0.58897	0.13322	-0.19012	C	1
C35	0.57995	0.15036	-0.14882	C	1
C36	0.55393	0.14053	-0.09562	C	1
C37	0.53745	0.11363	-0.08449	C	1
C38	0.59839	0.17857	-0.16036	C	1
O39	0.61511	0.14365	-0.23909	O	1
C40	0.62609	0.1273	-0.2345	C	1
O41	0.5456	0.15814	-0.05175	O	1
C42	0.51904	0.14867	-0.01409	C	1
N43	0.8047	0.39561	-0.13729	N	1
C44	0.68131	0.36016	-0.15619	C	1
C45	0.6518	0.30609	-0.15604	C	1
C46	0.72271	0.35881	-0.15447	C	1
C47	0.7355	0.3468	-0.07659	C	1
C48	0.76233	0.35904	-0.07557	C	1
C49	0.77718	0.38382	-0.14637	C	1
C50	0.76469	0.39596	-0.22564	C	1
C51	0.73782	0.3835	-0.23087	C	1
N52	0.40883	0.60416	-0.14723	N	1
C53	0.36013	0.6816	-0.15351	C	1
C54	0.30613	0.6515	-0.15331	C	1
C55	0.36451	0.6419	-0.1515	C	1
C56	0.35526	0.61729	-0.22809	C	1
C57	0.37004	0.60526	-0.22317	C	1
C58	0.39461	0.61758	-0.14594	C	1
C59	0.40423	0.64231	-0.07146	C	1

C60	0.38923	0.65413	-0.07242	C	1
H61	0.06359	0.48387	-0.23435	H	1
H62	0.01743	0.4626	-0.23532	H	1
H63	0.06798	0.55127	3.90E-04	H	1
H64	0.97686	0.44428	-0.22165	H	1
H65	0.93098	0.42619	-0.22051	H	1
H66	0.9399	0.49734	-0.01242	H	1
H67	0.09758	0.49827	-0.02074	H	1
H68	0.10333	0.5686	-0.19602	H	1
H69	0.18827	0.55879	-0.00209	H	1
H70	0.05576	0.57307	-0.22564	H	1
H71	0.07837	0.61955	-0.16794	H	1
H72	0.02966	0.60731	0.2951	H	1
H73	1.00708	0.5609	0.23803	H	1
H74	0.57811	0.09318	-0.21968	H	1
H75	0.51781	0.10566	-0.03919	H	1
H76	0.61843	0.18506	-0.18605	H	1
H77	0.69262	0.38087	-0.15611	H	1
H78	0.72499	0.32825	-0.01087	H	1
H79	0.77167	0.34944	-0.01402	H	1
H80	0.77539	0.41464	-0.289	H	1
H81	0.72907	0.3931	-0.29997	H	1
H82	0.38083	0.69314	-0.15324	H	1
H83	0.33688	0.60739	-0.29663	H	1
H84	0.36248	0.58635	-0.28312	H	1
H85	0.42303	0.6526	-0.00959	H	1
H86	0.39694	0.6726	-0.00598	H	1
H87	0.13127	0.61185	-0.10643	H	1
H88	0.13278	0.60556	-0.34629	H	1
H89	0.1592	0.63279	-0.23879	H	1
H90	0.14836	0.48158	0.0235	H	1
H91	0.12613	0.48184	-0.13927	H	1

H92	0.12007	0.48131	0.10438	H	1
H93	0.61763	0.11229	-0.34155	H	1
H94	0.62352	0.11834	-0.09818	H	1
H95	0.64701	0.13911	-0.262	H	1
H96	0.51296	0.13641	0.10899	H	1
H97	0.50703	0.13775	-0.13185	H	1
H98	0.51611	0.16524	0.01161	H	1
O99	0.35676	0.42591	1.09848	O	1
H100	0.35137	0.41405	1.20787	H	1
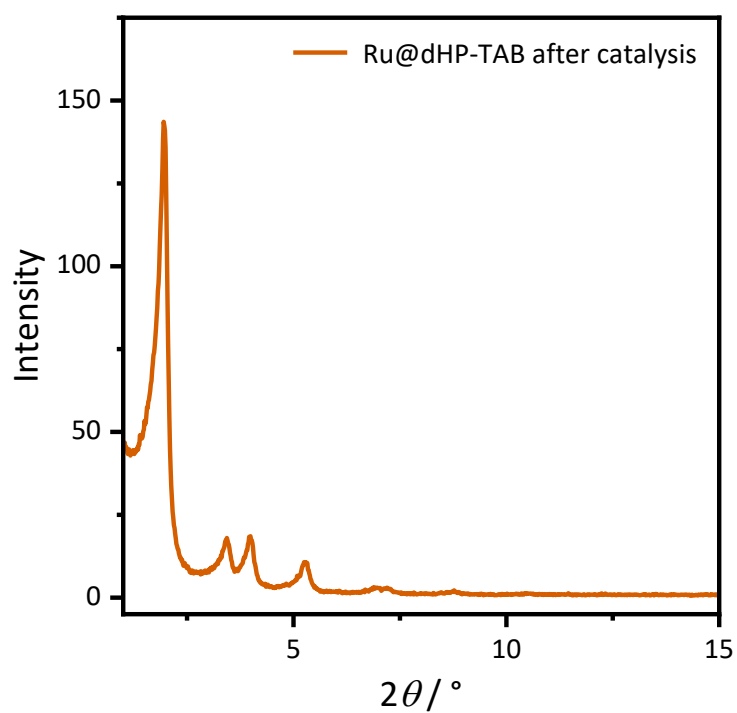
Figure S9.2.11. XRPD (λ = 1.789 Å) of **Ru@dHP-TAB** after catalysis.

9.2.5. Gas Sorption Experiments
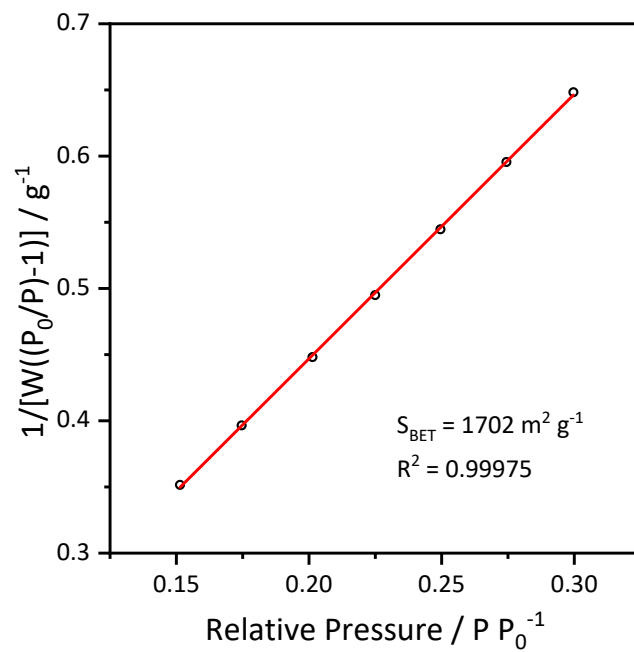
Figure S9.2.12. Multi-point BET surface area fit of **dHP-TAB COF** derived from N_2 sorption isotherm.
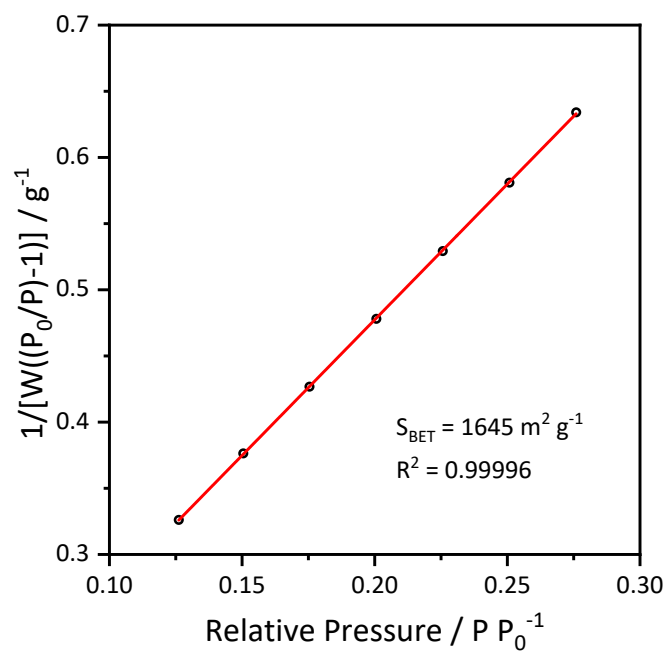
Figure S9.2.13. Multi-point BET surface area fit of **Ru@dHP-TAB COF** derived from N_2 sorption isotherm.
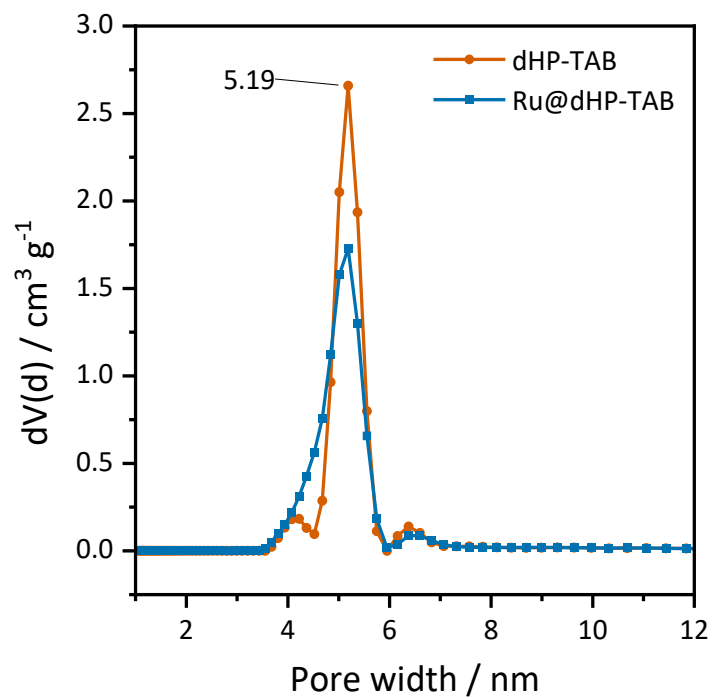
Figure S9.2.14. Pore size distribution obtained from the desorption branch of **dHP-TAB** and **Ru@dHP-TAB** after immobilization of the catalyst.
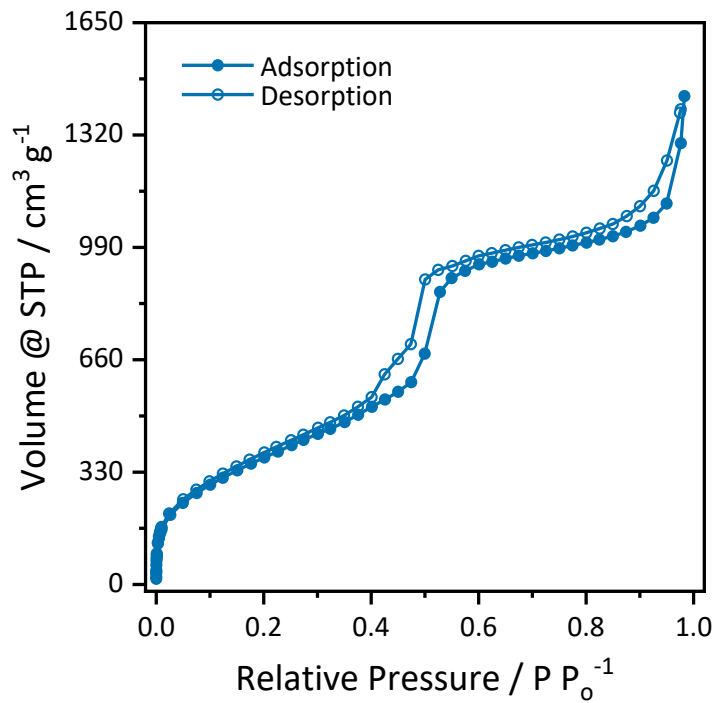
Figure S9.2.15. Nitrogen sorption isotherm at 77 K of **Ru@dHP-TAB** after catalysis.
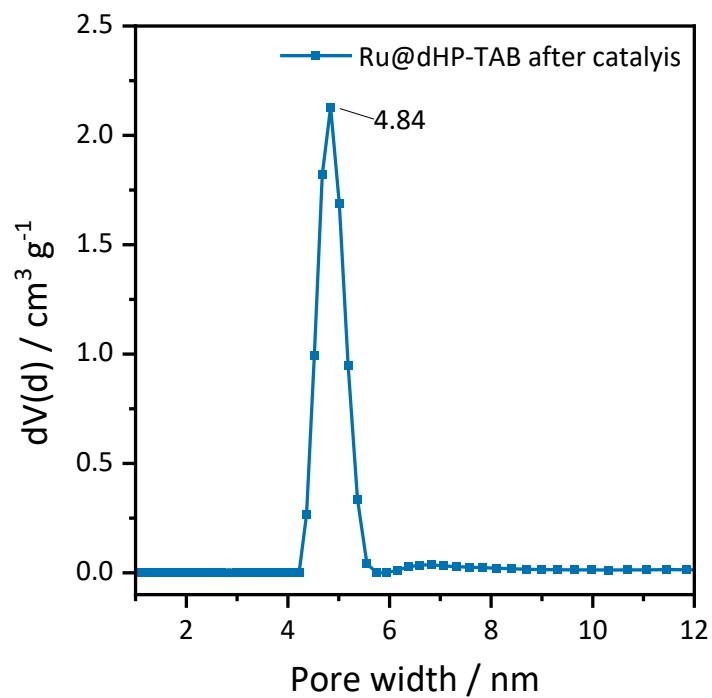
Figure S9.2.16. Pore size distribution obtained from the adsorption branch of **Ru@dHP-TAB** after catalysis.
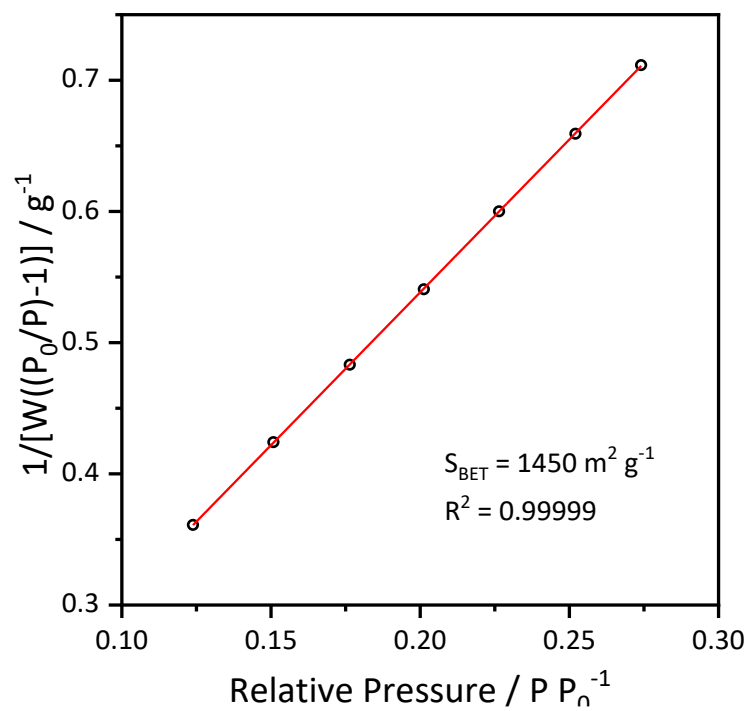
Figure S9.2.17. Multi-point BET surface area fit of **Ru@dHP-TAB COF** after catalysis derived from N_2 sorption isotherm.

9.2.6. Solid State NMR
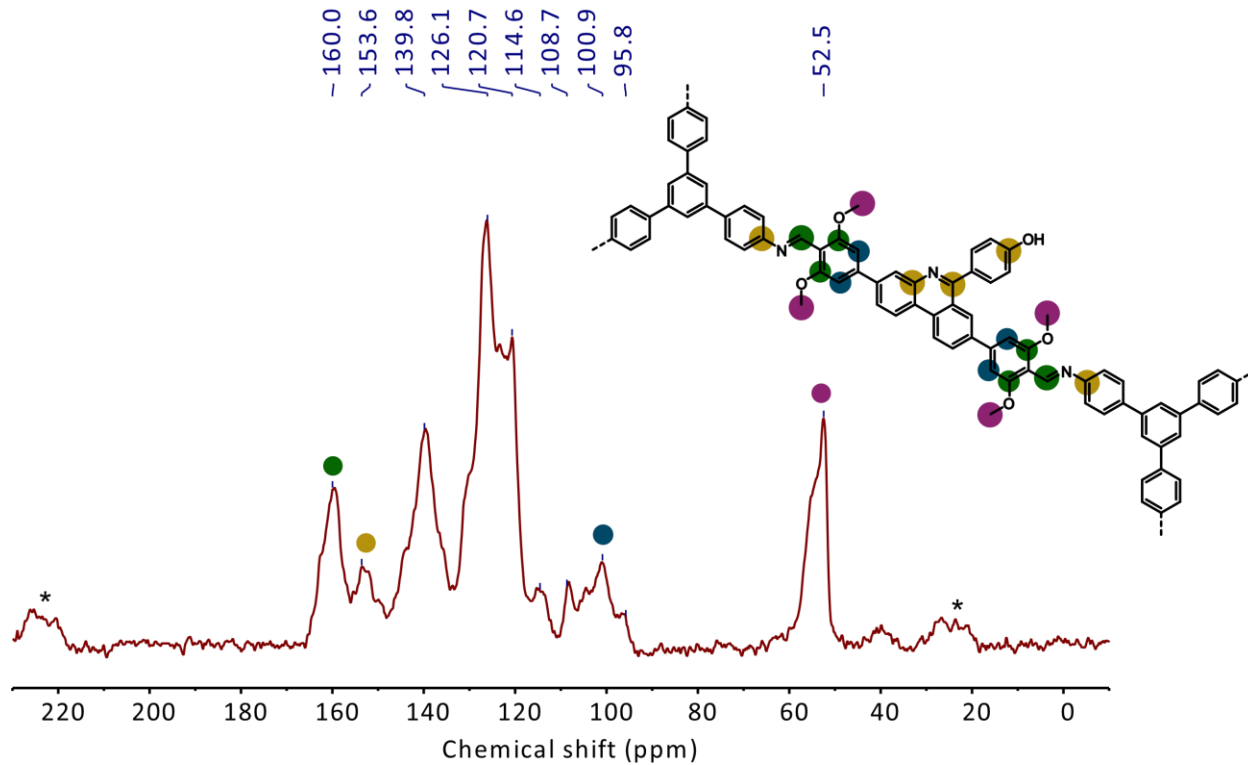
Figure S9.2.18. ^{13}C MAS ssNMR of **dHP-TAB COF**.

9.2.7. XAS

Experimental details

All XAS experiments were carried out at PETRA III beamline P65 at Deutsches Elektronensynchrotron (DESY) in Hamburg, Germany. The measurements at the Ruthenium K-edge (22117 eV) were performed in transmission using a Si(111) double-crystal monochromator and a maximum synchrotron beam current of 100 mA. **Ru** in solid state (**Ru** solid) was studied as self-supporting wafer using boron nitride (BN) as binder. Spectra of **Ru** in solution (**Ru** solution) of benzene (50 mM) were recorded using a specially designed measurement cell allowing for protection gas atmosphere. The sample containing the immobilized complex on the COF (**Ru@dHP-TAB** solid) was measured without binder as powder sealed between Kapton foil. This sample was also measured as stirred suspension in benzene (**Ru@dHP-TAB** suspension). Sample preparation was carried out under inert atmosphere in a glove box. For energy calibration, a Ruthenium foil was used. Calibration was performed using the first inflection point in Ru K-edge XANES spectrum. The data acquisition was performed in continuous scan mode and rebinning with a window of 0.5 eV was applied. All measurements were carried out at room temperature.

Data analysis

In the first step of data analysis the background of the spectrum was removed by subtracting a Victoreen-type polynomial.[8–11] Due to the very differing shapes of the absorption edges of the samples and the used references, the first inflection point of the first derivative of the corresponding spectrum was defined as energy E_0. Afterwards a piecewise polynomial was used to determine the smooth part of the spectrum and was adjusted in a way that the low-R components of the resulting Fourier transform were minimal. The background-subtracted spectrum was divided by its smoothed part and the photon energy was converted to photoelectron wave number k. For evaluation of the EXAFS spectra the resulting functions were weighted with k^2 and calculated with *ARTEMIS* program. Curve fitting was performed using ab-initio-calculated phases and amplitudes from the FEFF8 program from the University of Washington. *ARTEMIS* works based on the EXAFS function and according to a formulation in terms of radial distribution functions:[8,12]

$$\chi(k) = \sum_j S_0^2(k) F_j(k) \int P_j(r_j) \frac{e^{\frac{-2r_j}{\lambda}}}{kr_j^2} \sin\left[2kr_j + \delta_j(k)\right] dr_j$$

The number of independent points N_{ind} was calculated according to information theory to determine the degree of overdeterminacy:[8]

$$N_{ind} = \frac{2\Delta k \Delta R}{\pi}$$

Here, Δk describes the range in k-space used for data analysis and ΔR corresponds to the distance range in the Fourier filtering process. The values used for the analysis are shown in Table S6. The quality of a fit was determined using two methods. The reduced χ^2_{red} considers the degree of overdeterminacy of the system and the number of fitted parameters p. It therefore allows a direct comparison of different models:[13]

$$\chi^2_{red} = \frac{(N_{ind}/N)}{N_{ind} - p} \sum_i \left(\frac{k_i^n}{\sum_j k_j^n \left| \chi_j^{exp}(k_j) \right|} \right)^2 (\chi^{exp}(k_i) - \chi^{theo}(k_i))^2$$

The R-factor, which represents the percental disagreement between experiment and adjusted function and takes into account both systematic and random errors according to the equation:[13]

$$R = \sum_i \frac{k_i^n}{\sum_j k_j^n \left| \chi_j^{exp}(k_j) \right|} |\chi^{exp}(k_i) - \chi^{theo}(k_i)| \cdot 100\%$$

The accuracy of the determined distances is 1 %, of the Debye-Waller-like factor 10 %[14] and of the coordination numbers depending of the distance 5-15 %. Initial values for coordination numbers and distances were adopted from Rietveld-analysis and afterwards iterated free in every fit as well as the Debye-Waller-like factor and the amplitude reducing factor.

XANES analysis details
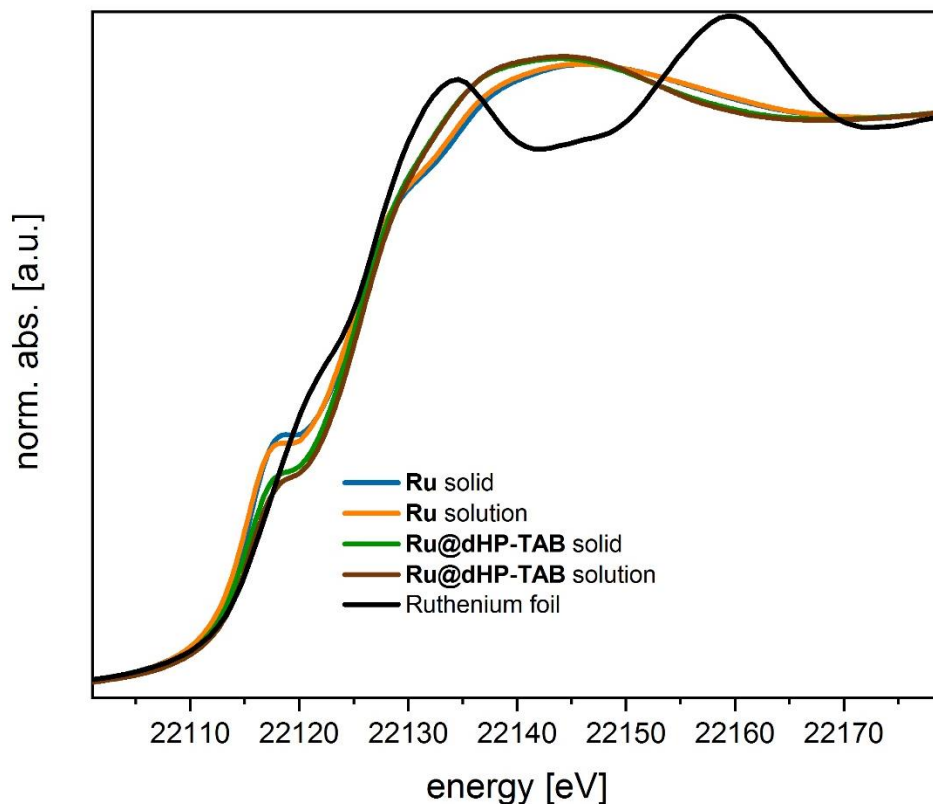
Figure S9.2.19. XANES spectra of **Ru** in the solid state (**Ru** solid, blue), solution (**Ru** solution, orange), **Ru** immobilized in a mesoporous COF in the solid state (**Ru@dHP-TAB** solid, green), as suspension in benzene **Ru@dHP-TAB** solution, brown) as well as of the Ru(0) foil used for calibration (black).

The edge energy in a XANES spectrum gives information about the oxidation state of the analyzed complex. Metal centers with a higher oxidation number typically show a higher edge energy. The XANES spectra in Figure S14 reveal no edge energy shift compared to each other. This indicates that no changes in the oxidation state during the dissolution and immobilization of the homogeneous complex occur. The XANES spectra of Ru complexes (Figure S14) have the same edge energy of around 22115.4 eV. The absorption energy for the 1s electrons is in all cases around 1.6 eV lower than for the Ru(0)-foil (22117 eV, black line) that was used for the calibration of the spectra. Despite the lower edge energy, the XANES spectra of the Ru complex show nearly no edge shift compared to the Ru(0) foil, which is explained by ligand effects, since the formal ruthenium oxidation state in the complexes is +II. However, the two carbene ligands act as strong electron donors and increase the electronic density at the Ru center significantly, which could be responsible for the rather low absorption edge energy of the present compounds. In addition, the presence of an intense feature within the edge step overlaps with the edge step function, interfering with the edge step determination.

Table S9.2.5. Edge energies of the four Ru samples.

Sample	Edge Energy E_0 [eV]
Ru solid	22115.5
Ru solution	22115.4
Ru@dHP-TAB solid	22115.4
Ru@dHP-TAB solution	22115.8
Ru(0) foil	22117.0

EXAFS analysis details:

The k- and R-ranges applied in the analysis of the Ru complexes together with the corresponding fit parameters are summarized in Table S6. Figure S15 shows the Fourier-transformed EXAFS spectra of the four Ru complexes together with corresponding first shell scattering paths. Figure S16 illustrates the fitted function, experimental data, residual plot as well as first shell contributions for the Ru samples in k-space. The corresponding first shell scattering paths including coordination numbers, bond distances and Debye-Waller factors are collected in Table S7.

Table S9.2.6. k- and R ranges as well as corresponding fit parameters of the analysis of the four Ru samples.

sample	k-range [Å^{-1}]	R-range [Å]	R-factor	Reduced Chi-square	SO2 value
Ru solid	2.80 - 15.20	1.15 - 4.50	0.0025	59	1.0
Ru solution	2.60 - 14.70	1.15 - 4.50	0.0009	8	1.0
Ru@dHP-TAB solid	2.60 - 14.30	1.15 - 4.50	0.0047	7	1.0
Ru@dHP-TAB solution	2.78 - 14.70	1.15 - 4.50	0.0039	63	1.0
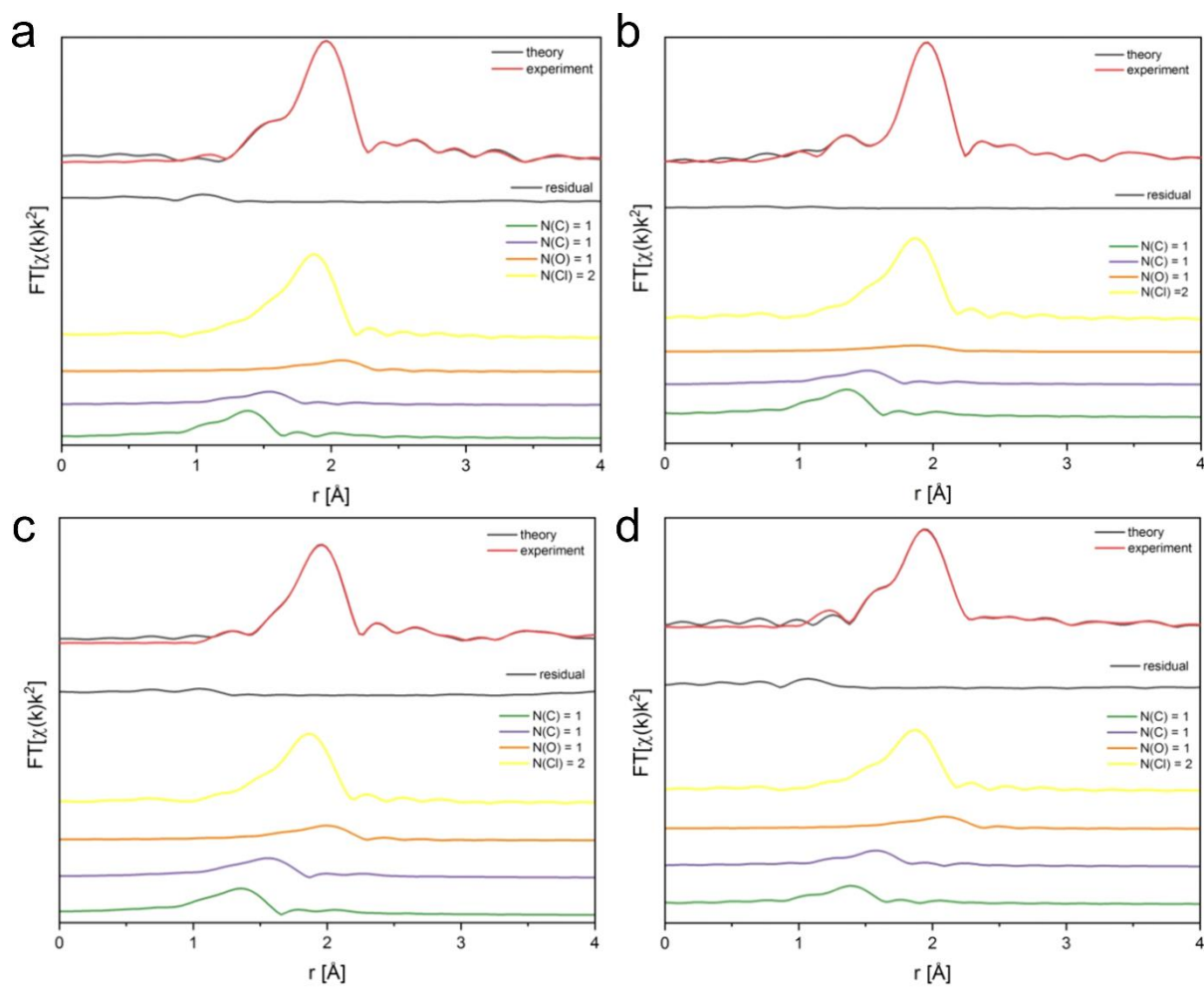
Figure S9.2.20. Fourier-transformed EXAFS spectra of the **Ru** in solid state and solution (benzene) as well as immobilized in a mesoporous COF. a) **Ru** solid, b) **Ru** solution, c) **Ru@dHP-TAB** solid, d) **Ru@dHP-TAB** solution.
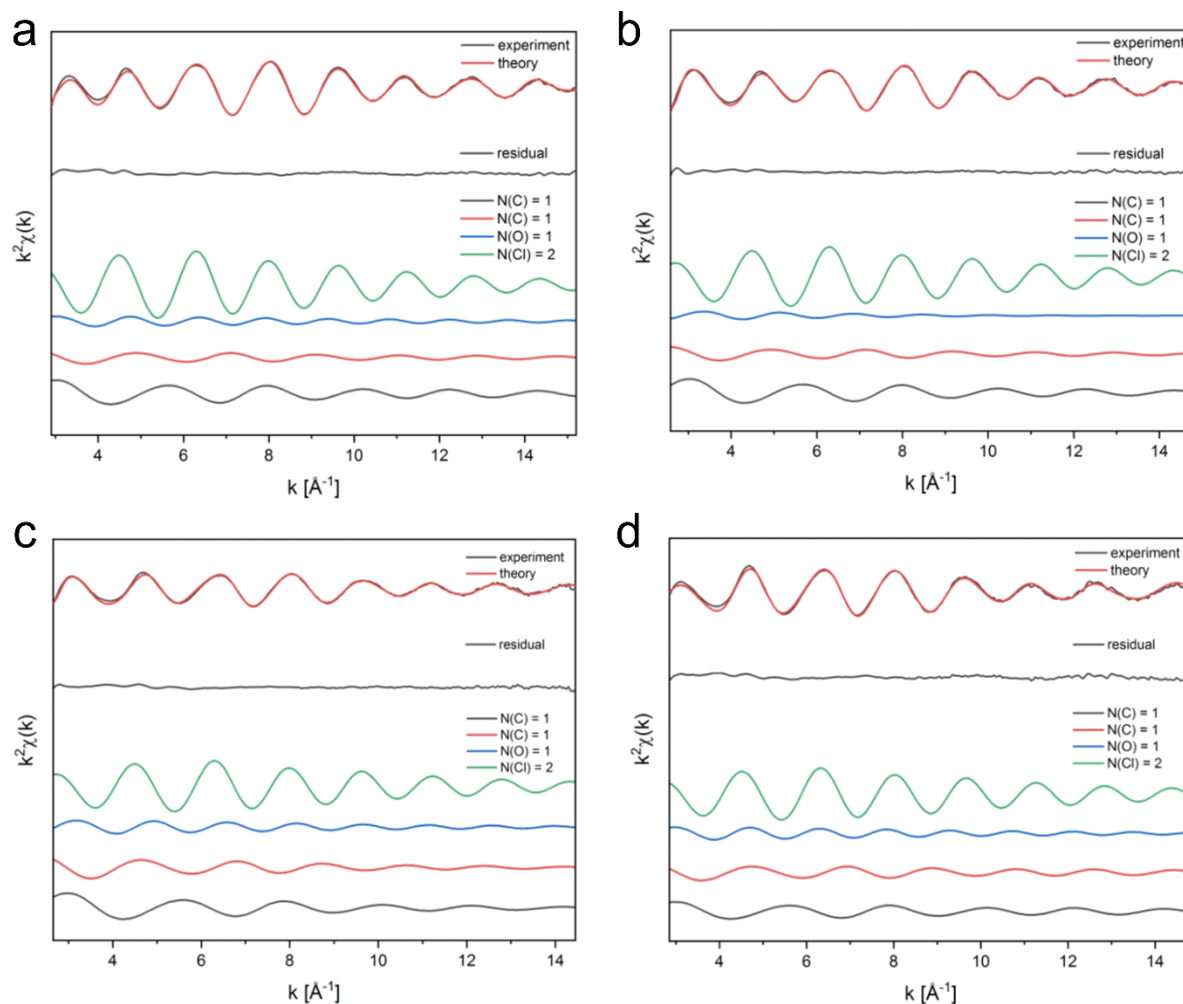
Figure S9.2.21. Fitted function compared with experimental data, residual plot and first coordination shell paths for the four Ru samples in k-space. a) **Ru** solid, b) **Ru** solution, c) **Ru@dHP-TAB** solid, d) **Ru@dHP-TAB** solution.

Table S9.2.7. First shell coordination Numbers (N), bond lengths (R + ΔR) and Debye-Waller factors of the measured samples.

Scattering paths	solid			solution/ suspension			Difference of bond lengths
	N	$R + \Delta R$ [Å]	σ^2 [Å^2]	N	N	$R + \Delta R$ [Å]	σ^2 [Å^2]
Ru				**Ru**			
Ru-C	1.0(1)	1.819(4)	0.0012(3)	Ru-C	1.0(1)	1.819(4)	0.0012(3)
Ru-C	0.7(1)	1.983(9)	0.0013(3)	Ru-C	0.7(1)	1.983(9)	0.0013(3)
Ru-O	0.8(1)	2.549(20)	0.0018(15)	Ru-O	0.8(1)	2.549(20)	0.0018(15)
Ru-Cl	2.4(0)	2.323(4)	0.0032(1)	Ru-Cl	2.4(0)	2.323(4)	0.0032(1)

Ru@dHP-TAB				**Ru@dHP-TAB**			
Ru-C	1.2(1)	1.836(6)	0.0036(3)	Ru-C	1.2(1)	1.836(6)	0.0036(3)
Ru-C	1.3(2)	2.051(11)	0.0040(4)	Ru-C	1.3(2)	2.051(11)	0.0040(4)
Ru-O	1.0(2)	2.491(17)	0.0028(9)	Ru-O	1.0(2)	2.491(17)	0.0028(9)
Ru-Cl	1.7(1)	2.326(4)	0.0031(2)	Ru-Cl	1.7(1)	2.326(4)	0.0031(2)

9.2.8. Liquid State NMR
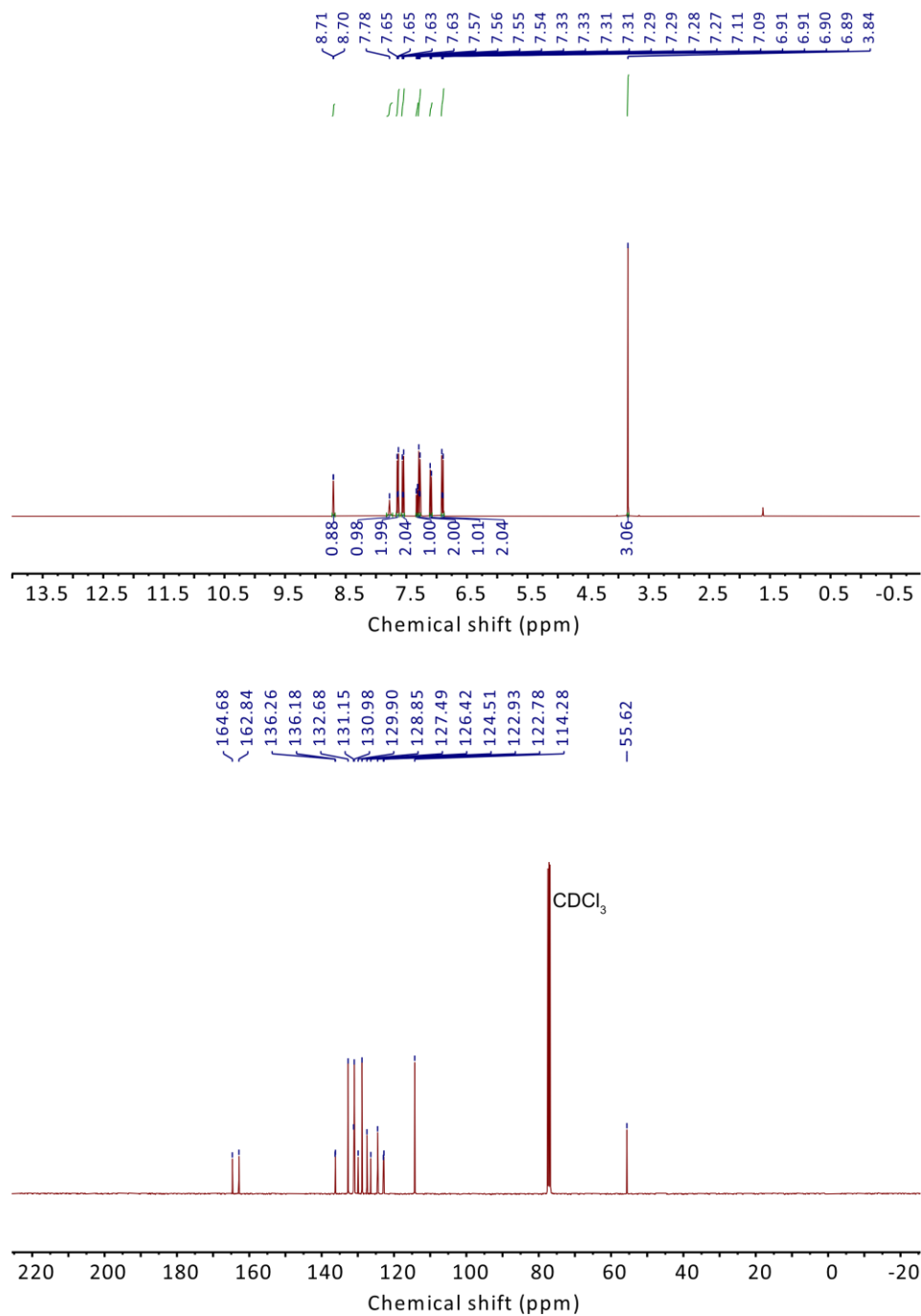
Figure S9.2.22. ¹H NMR (top) and ¹³C NMR (bottom) of **N-(4,4'-dibromo-[1,1'-biphenyl]-2-yl)-4-methoxybenzamide (7)** in CDCl₃.
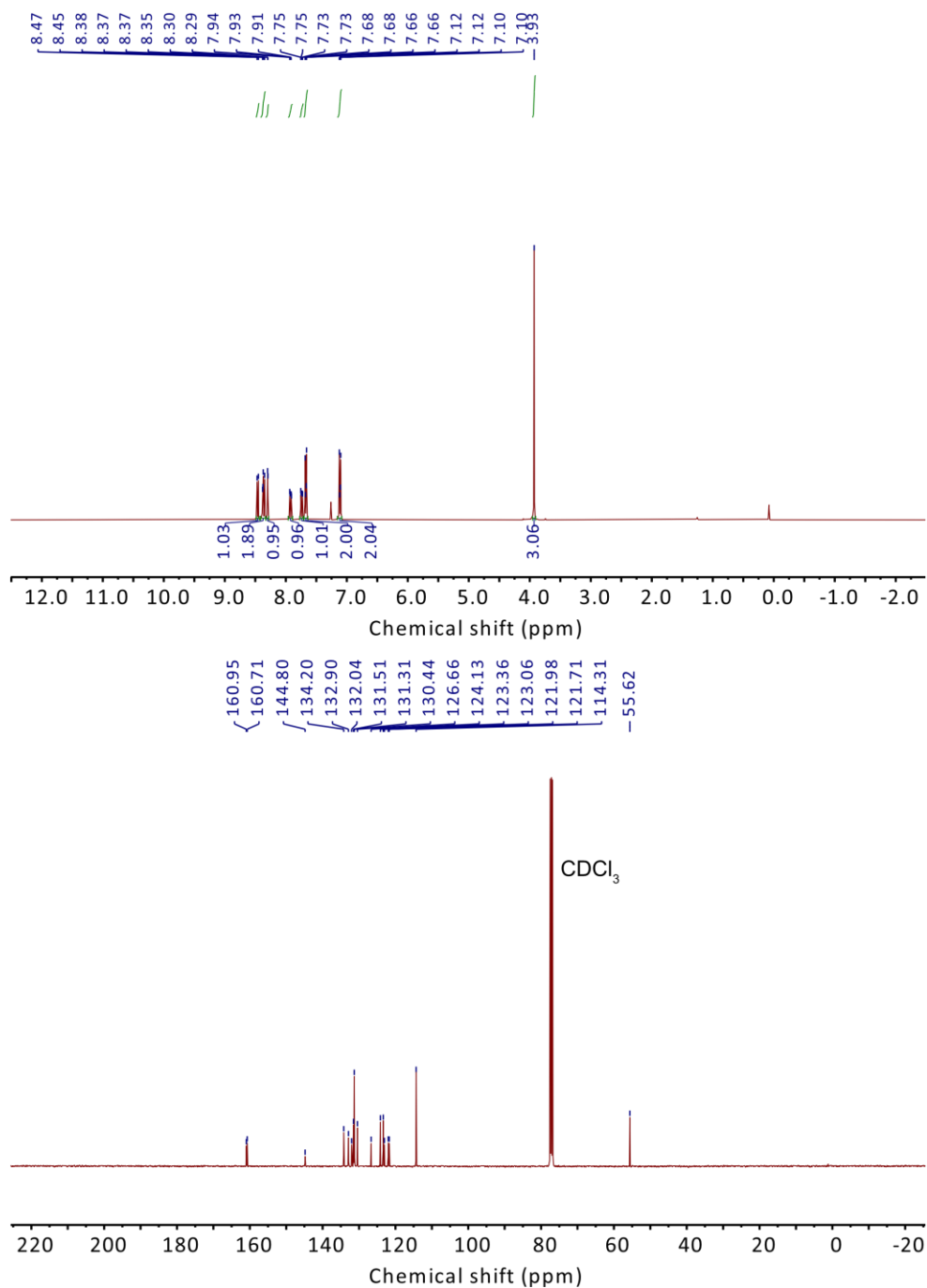
Figure S9.2.23. ¹H NMR (top) and ¹³C NMR (bottom) of **3,8-dibromo-6-(4-methoxyphenyl)phenanthridine (8)** in CDCl₃.
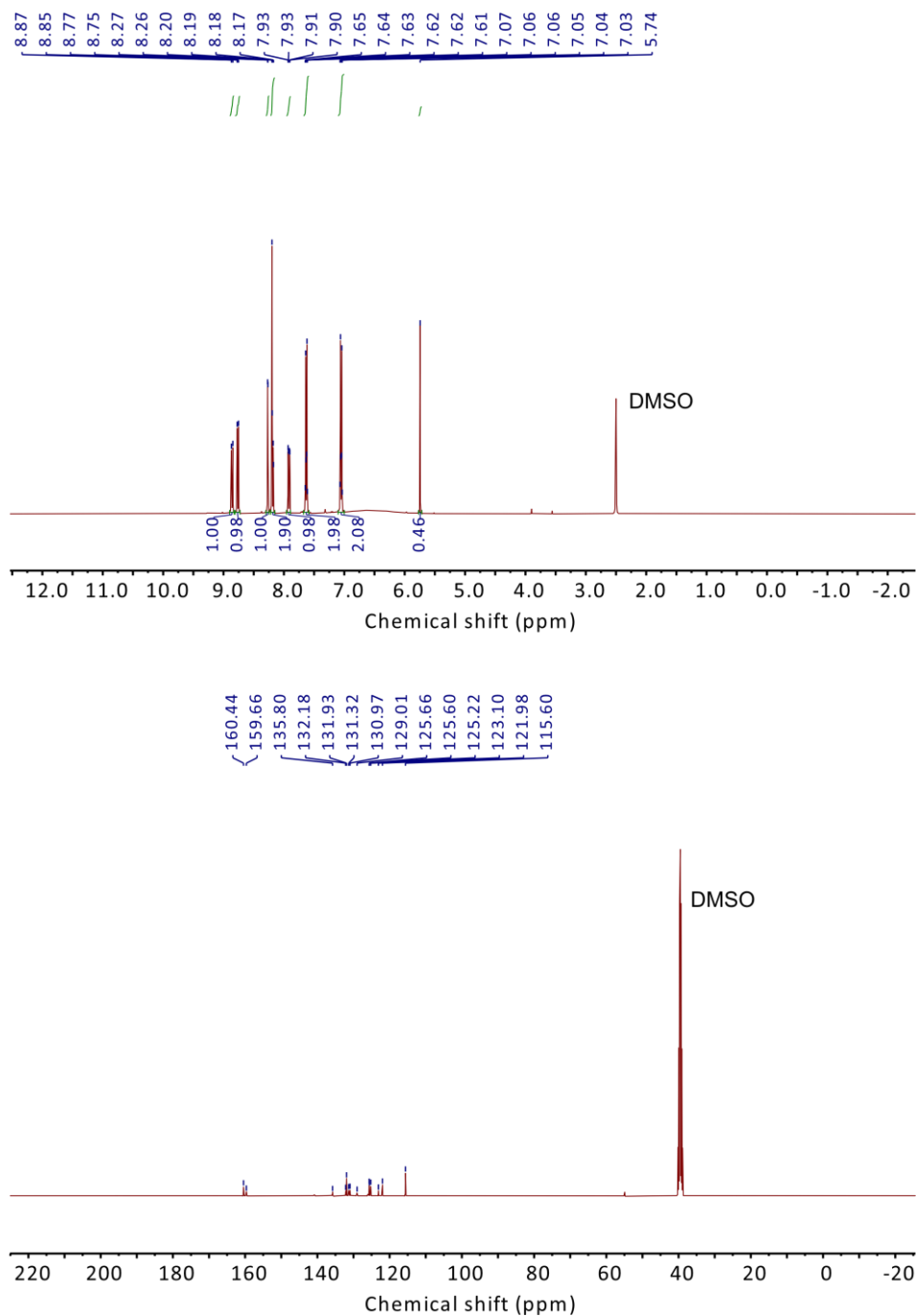
Figure S9.2.24. ^{1}H NMR (top) and ^{13}C NMR (bottom) of **4-(3,8-dibromophenanthridin-6-yl)phenol (9)** in DMSO.
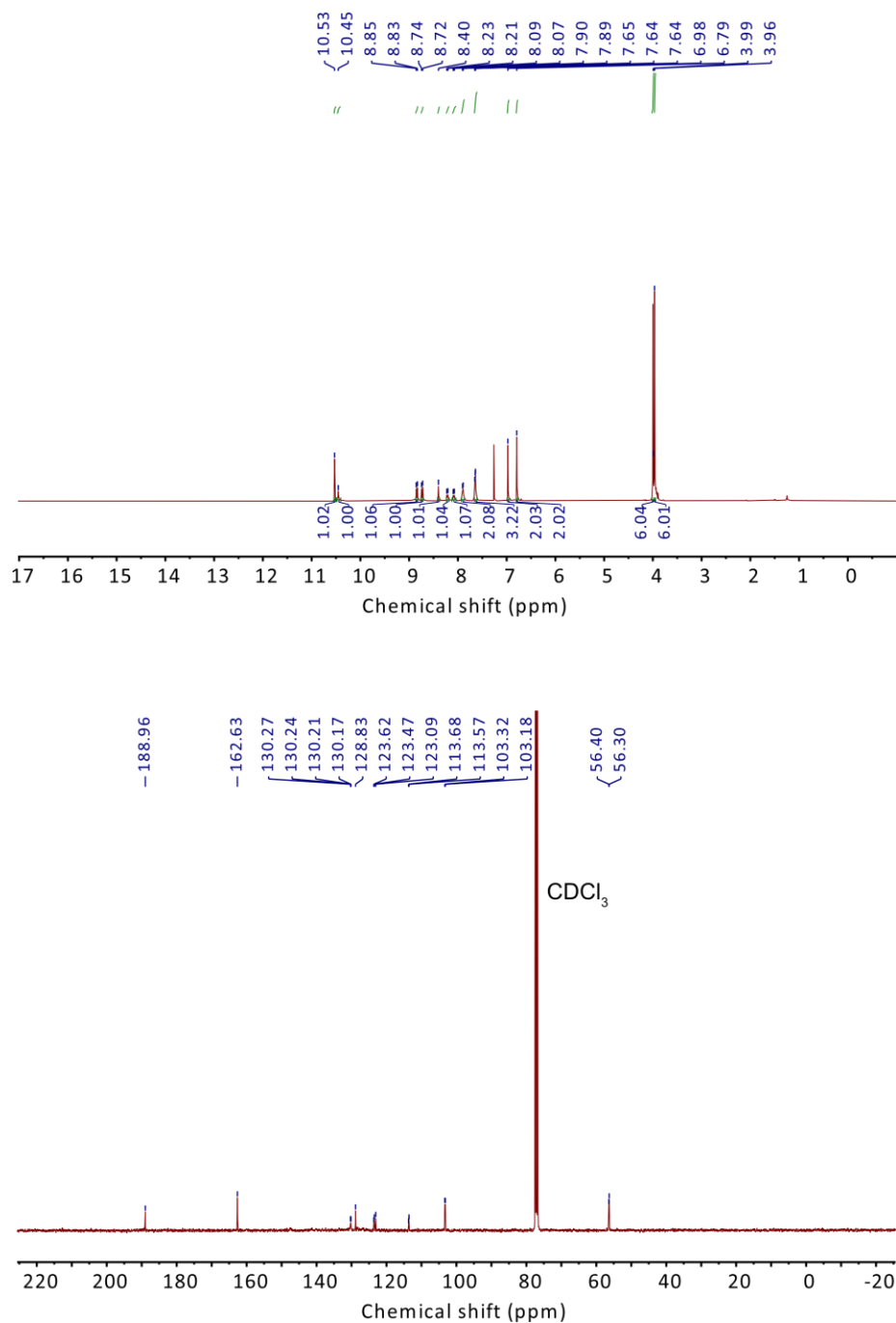
Figure S9.2.25. ^{1}H NMR (top) and ^{13}C NMR (bottom) of **4,4'-(6-phenylphenanthridine-3,8-diyl)bis(2,6-dimethoxybenzaldeyde) (dHP)** in CDCl3.

9.2.9. SEM/TEM and EDX analysis
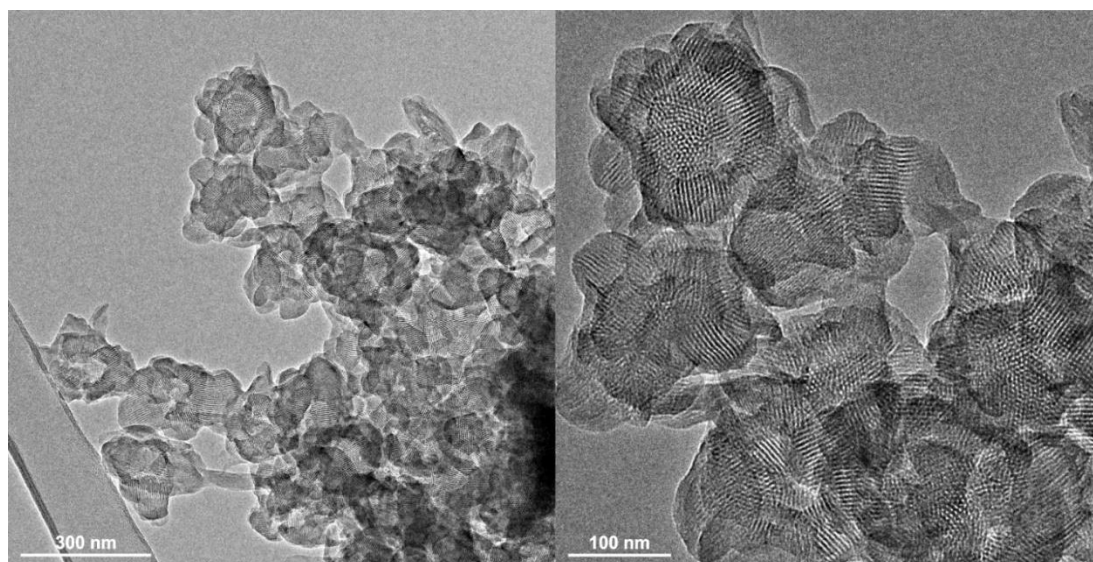
Figure S9.2.26. TEM images of **Ru@dHP-TAB COF**.
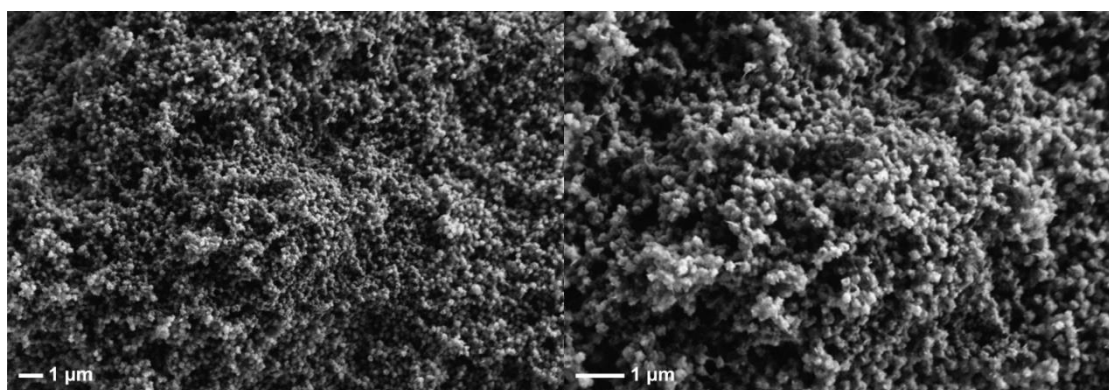
Figure S9.2.27. SEM images of **Ru@dHP-TAB COF**.
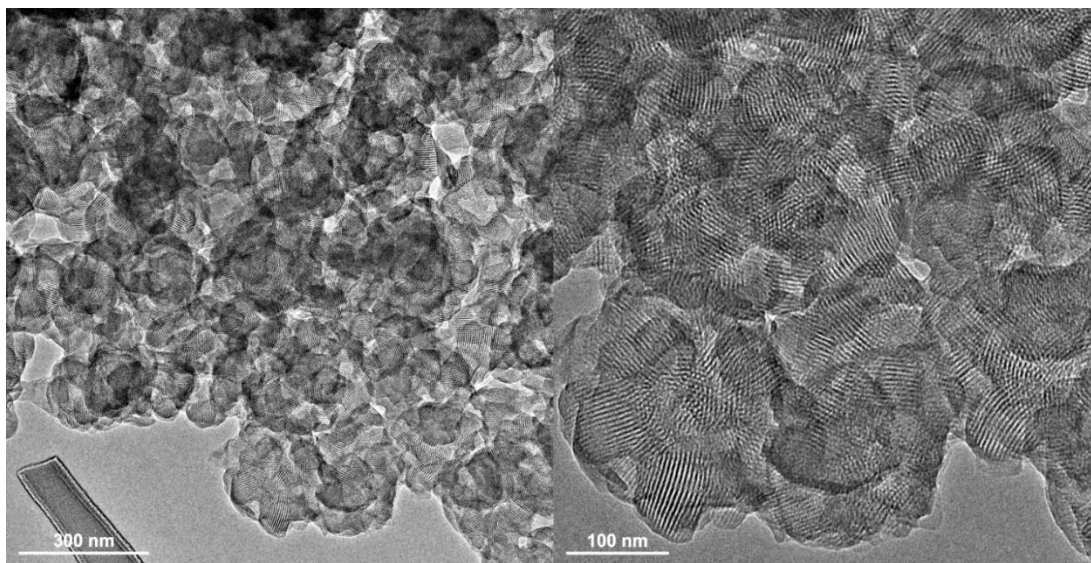
Figure S9.2.28. TEM images of **Ru@dHP-TAB COF** after catalysis.
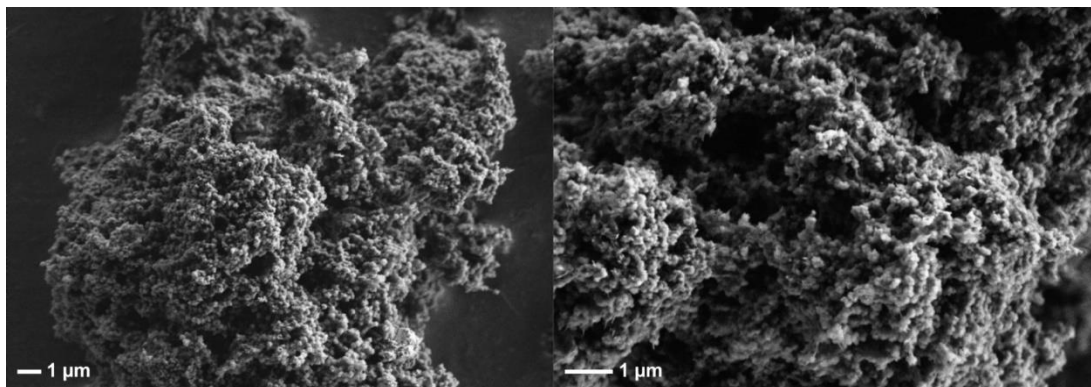
Figure S9.2.29. SEM images of **Ru@dHP-TAB COF** after catalysis.

9.2.10. TGA analysis
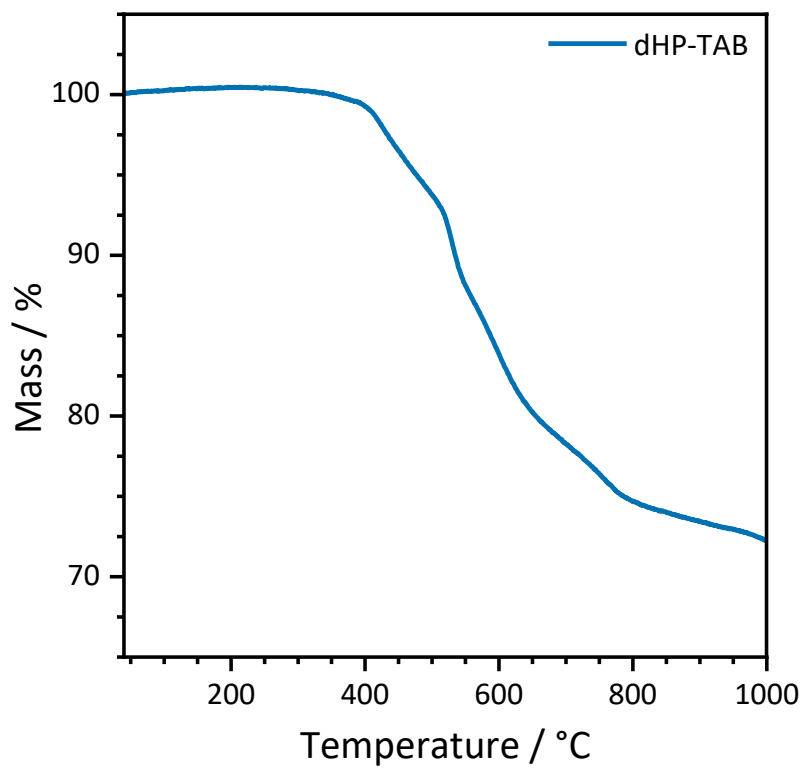
Figure S9.2.30. TGA measurement of **dHP-TAB** COF.

9.2.11. Bibliography

[1]   S. T. Emmerling, R. Schuldt, S. Bette, L. Yao, R. E. Dinnebier, J. Kästner, B. V. Lotsch, *J. Am. Chem. Soc.* **2021**, *143*, (38), 15711–15722.
[2]   G. R. Fulmer, A. J. M. Miller, N. H. Sherden, H. E. Gottlieb, A. Nudelman, B. M. Stoltz, J. E. Bercaw, K. I. Goldberg, *Organometallics* **2010**, *29*, 2176–2179.
[3]   Y. Chen, F. Li, Z. Bo, *Macromolecules* **2010**, *43*, 1349–1355.
[4]   M. Movassaghi, M. D. Hill, *Org. Lett.* **2008**, *10*, 3485–3488.
[5]   F. Ziegler, J. Teske, I. Elser, M. Dyballa, W. Frey, H. Kraus, N. Hansen, J. Rybka, U. Tallarek, M. R. Buchmeiser, *J. Am. Chem. Soc.* **2019**, *141*, 19014–19022.
[6]   V. M. Marx, M. B. Herbert, B. K. Keitz, R. H. Grubbs, *J. Am. Chem. Soc.* **2013**, *135*, 94–97.
[7]   J. E. Jee, J. L. Cheong, J. Lim, C. Chen, S. H. Hong, S. S. Lee, *J. Org. Chem.* **2013**, *78*, 3048–3056.
[8]   B. Ravel, M. Newville, *J. Synchrotron Radiat.* **2005**, *12*, 537–541.
[9]   M. Newville, P. Liviņ, Y. Yacoby, J. J. Rehr, E. A. Stern, *Phys. Rev. B* **1993**, *47*, 14126–14131.
[10]   M. Newville, *J. Synchrotron Radiat.* **2001**, *8*, 322–324.
[11]   T. S. Ertel, H. Bertagnolli, S. Hückmann, U. Kolb, D. Peter, *Appl. Spectrosc.* **1992**, *46*, 690–698.
[12]   N. Binsted, S. S. Hasnain, *J. Synchrotron Radiat.* **1996**, *3*, 185–196.
[13]   M. Bauer, H. Bertagnolli, *J. Phys. Chem. B* **2007**, *111*, 13756–13764.
[14]   D. C. Koningsberger, B. L. Mojet, G. E. Van Dorssen, D. E. Ramaker, *Top. Catal.* **2000**, *10*, 143–155.

9.3. Supporting Information of Chapter 6 - "*In Situ* Monitoring of Mechanochemical Covalent Organic Framework Formation Reveals Templating Effect of Liquid Additive"

9.3.1. Experimental Procedures

Chemicals. All starting materials, unless otherwise specified, were obtained from Sigma-Aldrich Chemicals, and used without further purification. All solvents, unless otherwise specified, were obtained from Acros Organics, and used without further purification. *p*-Phenylenediamine was obtained from TCI Europe N.V. and purified by sublimation before use. 2,4,6-Tris(4-aminophenyl)-1,3,5-triazine was prepared according to a literature procedure.[1]

Since the *in situ* synthesized COFs could not be washed and dried on site at the beamline, selected analytical measurements (*e. g.* sorption measurements) were performed on separately synthesized materials under identical condition as *in situ* synthesized materials with a fixed milling time of 60 min. This enables the comparison of analytical measurements and properties of the mechanochemically synthesized COFs that are potentially compromised by storing wetted samples for multiple days.

Ex situ **milling.** All laboratory, *ex situ* mechanochemical syntheses were performed in custom made 5 mL poly-(methylmethacrylate) (PMMA) milling jars using a MM400 Retsch shaker mill operating at 30 Hz.

Ex situ **X-ray powder diffraction.** *Ex situ* X-ray powder diffraction (XRPD) measurements for phase analysis and crystal structure determinations were performed on a Stoe Transmission Powder Diffractometer (STADI-P, STOE & CIE) with Cu Kα$_1$ radiation, equipped with an array of three MYTHEN 1K detectors (Dectris Ltd.), and a Ge(111) Johann-type monochromator (STOE & CIE). XRPD measurement used for indexing of **1** was performed on a STOE STADI-P with Co Kα$_1$ radiation, equipped with a MYTHEN 1K detector (Dectris Ltd.), and a Ge(111) Johann-type monochromator (STOE & CIE). For consistency samples were separately synthesized using the experimental descriptions below with an identical milling time of 60 min. For better particle statistics all samples were spun during data collection.

FT-IR Spectroscopy. Infrared spectra were measured in attenuated total reflection (ATR) geometry on a PerkinElmer UATR Two equipped with a diamond crystal. The spectra were background corrected.

Liquid State Nuclear Magnetic Resonance. All liquid state nuclear magnetic resonance (NMR) measurements were performed on a JEOL ECZ 400S 400 MHz spectrometer (magnetic field 9.4 T). ^{1}H, ^{13}C and ^{15}N measurements were performed in 5 mm NMR tubes using deuterium field lock.

Solid-State Nuclear Magnetic Resonance. Solid-state NMR (ssNMR) spectra were recorded on a Bruker Avance III 400 MHz spectrometer (magnetic field 9.4 T). For ssNMR spectroscopy, the samples were packed in 4 mm ZrO_2 rotors, which were spun in a Bruker WVT BL4 double resonance MAS probe. Chemical shift was referenced relative to tetramethylsilane (^{13}C), and CH_3NO_2 (^{15}N). The spinning rate was 12-14 kHz for ^{13}C and 8 kHz for ^{15}N measurements. A standard cross-polarization sequence with a 2 ms ramped contact pulse was used for ^{13}C and a total of 4096-8192 scans were routinely accumulated. ^{15}N ssNMR spectra were obtained with ramped cross-polarization and contact pulses of 3-8 ms optimized for the best signal. Both ^{13}C and ^{15}N measurements were performed in conditions of high-power broadband proton decoupling (SPINAL 64) with the spectral conditions being optimized for the shortest relaxation delay by measuring ^{1}H T1 relaxation time.

Sorption Measurements. Sorption measurements were performed on a Quantachrome Instruments Autosorb iQ 3 with nitrogen at 77 K. The pore size distribution was determined from nitrogen adsorption isotherms using the QSDFT (cylindrical pores, adsorption branch) kernel in carbon for nitrogen at 77 K implemented in the ASiQwin software v 3.01. Samples were activated in high vacuum at 120 °C for 12 h before measurement.

Elemental Microanalyses (EA). The elemental analyses were performed on a UNICUBE - Micro Combustion Analyzer.

Mass Spectrometry. Electrospray ionization (ESI) mass spectrometry was performed on a Thermo Finnigan LTQ FT in positive and negative mode. Samples were dissolved in an acetonitrile/water mixture.

Thermogravimetric analysis. Thermogravimetric analysis (TGA) measurements were performed on a STA 409 CD machine (Netzsch Co., Germany). Intermediates **1,** and **1´** were filled into Al_2O_3 crucibles. The experiments were conducted from 40 – 450 °C with a heating rate of 5 °C/min under a protective Ar flow.

In situ **X-ray powder diffraction.** All 2D XRPD patterns were collected at the P02.1 Powder Diffraction and Total Scattering beamline at the Deutsches Elektronen-Synchrotron (DESY) in Hamburg, Germany. The beamline is equipped with a modified MM400 Retsch shaker mill[2] and a PerkinElmer 2D area detector. The wavelength was determined with the NIST NSR 660a (LaB_6) standard, using two different detector positions to be 0.20736 Å (59.78 keV) and 0.20747 Å (59.78 keV). All 2D XRPD patterns were integrated using either Fit2D or Dioptas.[3,4] A custom made Matlab script was used to subtract background and plot the time-resolved XRPD patterns in a 2D plot. Background subtraction was only performed for visual presentation.

In situ **Raman spectroscopy.** All Raman spectra were collected on RamanRxn1™ analyzer equipped with a 785 nm laser by Kaiser Optical Systems Inc. Real-time Raman monitoring was

conducted in an approximately 8 mL sapphire milling jar with spectra acquired at 10 second intervals as a sum of 7 spectra with 10 ms acquisition time. A Retsch MM400 mill was operated at 30 Hz and a single 7 mm stainless steel ball. The Holograms® software package Spectra was used to dark and intensity correct the data. Subsequent baseline correction was performed using the Sonneveld and Visser algorithm[5] and vector normalization (L2 Norm).

Density Function Theory calculation. Density function theory (DFT) calculations with periodic boundary conditions were performed for intermediate **1** and **2** using the plane wave DFT code CASTEP 19.11.[6] Both crystal structures of **1** and **2** were geometry-optimized and **1** subsequently used for ssNMR calculations.

The CASTEP input file was prepared from the corresponding crystallographic information file (CIF) using the program cif2cell.[7] Geometry optimization was performed using the PBE[8] functional combined with the Grimme-D2 dispersion correction.[9] The plane wave basis set was truncated at 700 eV cutoff and norm-conserving pseudopotentials were used to describe the core regions of electron density. The electronic Brillouin zone was sampled with a 0.07 Å^{-1} Monkhorst-Pack k-point grid. Geometry optimization involved full relaxation of atom coordinates and unit cell parameters, subject to symmetry constraints of the corresponding space groups. Calculation were deemed finished after the following convergence criteria had been satisfied: ΔE/atom < 2·10^{-5} eV, maximum atom displacement < 0.001 Å, maximum force on atom < 0.05 eV Å^{-1} and maximum residual stress < 0.1 GPa.

The optimized crystal structure of **1** was used for NMR calculations with Gauge Including Projector Augmented Waves (GIPAW) method.[10] Calculations were performed with a PBE functional, the plane-wave cutoff was increased to 900 eV, and on-the-fly generated ultrasoft pseudopotentials were used for modelling the core part of the Coulomb potential. The NMR calculation provided isotropic chemical shieldings (σ_{iso}) for ^{15}N nuclei, which were converted to isotropic chemical shifts (δ_{iso}) using the equation:

$$\delta_{iso} = -\sigma_{iso} - \delta_{ref}$$

where δ_{ref} value was fitted as a single to find the best match between calculated and experimental spectra. Calculated ssNMR spectrum was plotted using MagresView 1.6.2.[11]

9.3.2. Experimental Section

In situ syntheses

COF LZU-1. 1,3,5-Triformylbenzene (Tb, 100 mg, 0.598 mmol) and *p*-phenylenediamine (*p*PDA, 100 mg, 0.897 mmol) were placed into a 5 mL PMMA reaction jar and a 7 mm steel ball (1.38 g weight) was added. Either 1,4-dioxane (40 μL), mesitylene (40 μL) and 6 M acetic acid (40 μL, $\eta = 0.60$ μL/mg) or 1,4-dioxane (80 μL), mesitylene (20 μL) with Sc(OTf)$_3$ (17.7 mg, 0.036 mmol, $\eta = 0.50$ μL/mg) were added, respectively. The mixture was milled at 30 Hz until no further change in the *in situ* XPRD data was visible. The resulting solid was washed with acetone, DMF, dichloromethane, methanol, and a 12 h Soxhlet extraction with MeOH. The wet sample was then activated by supercritical CO_2 drying and further drying under high vacuum for 24 h. Yield: 150.7 mg (93%) for AcOH as catalyst and 151.1 mg (93%) for Sc(OTf)$_3$ as catalyst. Elemental Analysis, calc.: C, 79.98; H, 4.47; N, 15.55; found for AcOH: C, 76.92; H, 4.97; N, 14.46; found for Sc(OTf)$_3$: C, 75.84; H, 4.97; N, 13.69.

TbBd-COF. 1,3,5-Triformylbenzene (Tb, 76.2 mg, 0.47 mmol) and benzidine (Bd, 130 mg, 0.706 mmol) were placed into a 5 mL PMMA reaction jar and a 7 mm steel ball (1.38 g weight) was added. 1,4-Dioxane (62.5 μL), mesitylene (62.5 μL) and as catalyst 6 M acetic acid (25 μL, $\eta = 0.73$ μL/mg) or Sc(OTf)$_3$ (13.9 mg, 0.028 mmol, $\eta = 0.61$ μL/mg) were added, respectively. The mixture was milled at 30 Hz until no further change in the *in situ* XRPD data was visible. The resulting solid was washed with acetone, DMF, dichloromethane, methanol, and a 12 h Soxhlet extraction with MeOH. The wet sample was then activated by supercritical CO_2 drying and further drying under high vacuum for 24 h. Yield: 156 mg (86%) for AcOH as catalyst and 161 mg (89%) for Sc(OTf)$_3$ as catalyst. Elemental Analysis, calc.: C, 84.35; H, 4.72; N, 10.93; found for AcOH: C, 81.46; H, 4.98; N, 10.35; found for Sc(OTf)$_3$: C, 81.64; H, 5.01; N, 10.16.

IISERP-COF4. 2,4,6-Tris(4-aminophenyl)-1,3,5-triazine (TAT, 126 mg, 0.356 mmol) and terephthalaldehyde (BDA, 73.1 mg, 0.534 mmol) were placed into a 5 mL PMMA reaction jar and a 7 mm steel ball (1.38 g weight) was added. 1,4-Dioxane (75 μL), mesitylene (75 μL) and as catalyst 6 M acetic acid (37.5 μL, $\eta = 0.94$ μL/mg) or Sc(OTf)$_3$ (10.5 mg, 0.021 mmol, $\eta = 0.75$ μL/mg) were added, respectively. The mixture was milled at 30 Hz until no further change in the *in situ* XRPD data was visible. The resulting solid was washed with acetone, DMF, dichloromethane, methanol, and a 12 h Soxhlet extraction with MeOH. The wet sample was then activated by supercritical CO_2 drying and further drying under high vacuum for 24 h. Yield: 149.2 mg (84%) for AcOH as catalyst and 153.0 mg (86%) for Sc(OTf)$_3$ as catalyst. Elemental Analysis, calc.: C, 79.02; H, 4.22; N, 16.76; found for AcOH: C, 76.95; H, 4.44; N, 15.87; found for Sc(OTf)$_3$: C, 77.42; H, 4.45; N, 15.80.

N-COF. 1,3,5-Triformylbenzene (Tb, 60 mg, 0.37 mmol) and 2,4,6-tris(4-aminophenyl)-1,3,5-triazine (TAT, 131 mg, 0.37 mmol) were placed into a 5 mL PMMA reaction jar and a 7 mm steel ball

(1.38 g weight) was added. 1,4-Dioxane (50 μL), mesitylene (50 μL) and as catalyst 6 M acetic acid (40 μL, $\eta = 0.73$ μL/mg) or Sc(OTf)$_3$ (10.9 mg, 0.022 mmol, $\eta = 0.52$ μL/mg) were added, respectively. The mixture was milled at 30 Hz until no further change in the *in situ* XRPD data was visible. The resulting solid was washed with acetone, DMF, dichloromethane, methanol, and a 12 h Soxhlet extraction with MeOH. The wet sample was then activated by supercritical CO_2 drying and further drying under high vacuum for 24 h. Yield: 152.0 mg (89%) for AcOH as catalyst and 159.4 mg (93%) for Sc(OTf)$_3$ as catalyst. Elemental Analysis, calc.: C, 77.91; H, 3.92; N, 18.17; found for AcOH: C, 74.83; H, 4.28; N, 16.84; found for Sc(OTf)$_3$: C, 74.54; H, 4.30; N, 16.82.

In situ Raman spectroscopy synthesis

Tb (100 mg, 0.598 mmol) were milled with *p*PDA (100 mg, 0.897 mmol), along with 62 μL of 1,4-dioxane, 62 μL mesitylene, and 25 μL of 6 M AcOH ($\eta = 0.745$ μL/mg) in a ca. 8 mL sapphire milling jar using a single 7 mm stainless steel ball (1.38 g weight) at a milling frequency of 30 Hz.

Ex situ Syntheses
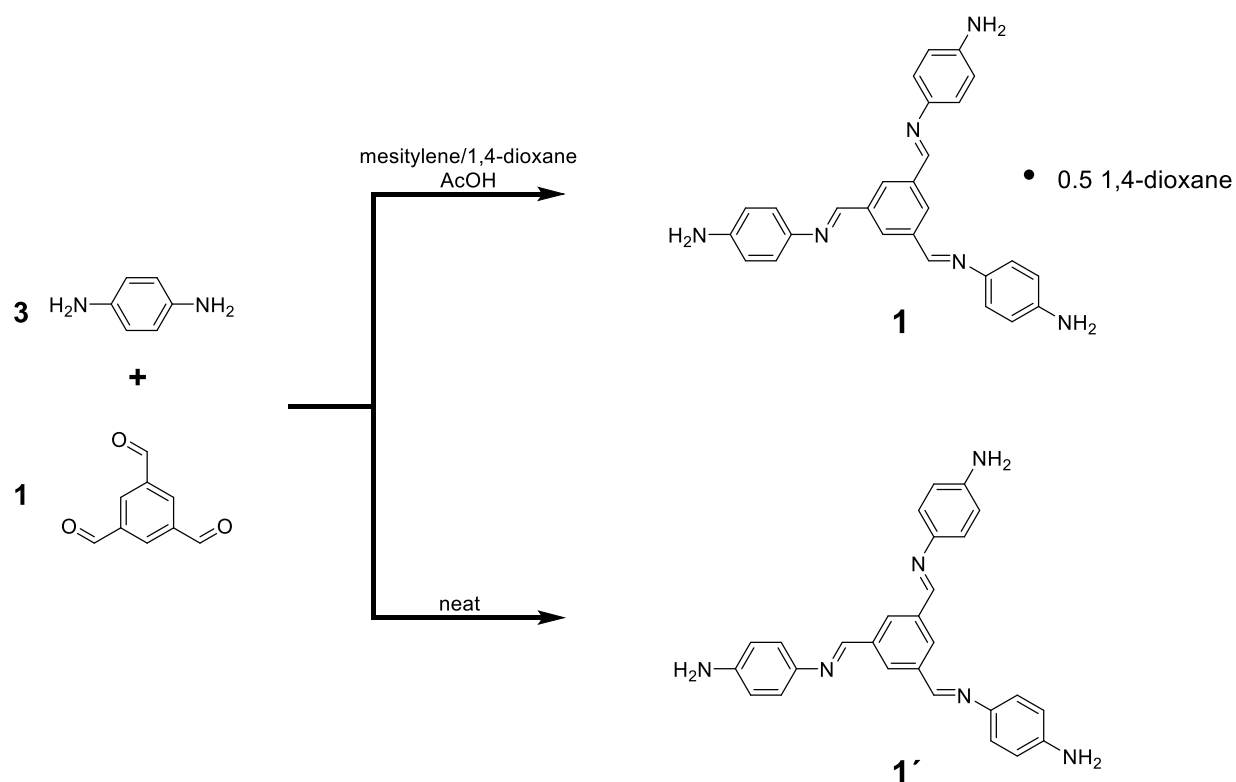
Scheme S9.3.1. Reaction scheme for the synthesis of the solvated intermediate **1** trimer and its non-solvated form **1'**.

4,4',4''-(((1E,1'E,1''E)-benzene-1,3,5-triyltris(methaneylylidene))tris(azaneyl-ylidene))triani-line•0.5 1,4-dioxane (1). 1,3,5-Triformylbenzene (Tb, 50 mg, 0.299 mmol) and *p*-phenylenedia-mine (*p*PDA, 100 mg, 0.897 mmol) were placed into a 5 mL PMMA reaction jar and a 7 mm steel ball was added. 1,4-Dioxane (31.5 µL), mesitylene (31.5 µL) and as catalyst 6 M acetic acid (12.5 µL, η = 0.50 µL/mg) was added. The mixture was milled at 30 Hz for 30 min. The resulting solid was dried under high vacuum for 24 h to remove remaining solvents and analyzed without further purification. IR v_{max}/cm^{-1} 3455, 3434, 3407, 3352, 3326, 3219, 3032, 2908, 2882, 2853, 1628, 1602, 1584, 1507, 1284, 1255, 1171, 1141, 1117, 1082, 964, 872, 830, 682, 562, 522, 494, 470, 418; ^{1}H NMR (400 MHz, DMSO-d_6) δ 8.76 (s, 3H), 8.40 (s, 3H), 7.22 (d, J = 7.4 Hz, 6H), 6.63 (d, J = 7.4 Hz, 6H), 5.30 (s, 6H), 3.57 (s, 4H); ^{13}C NMR (101 MHz, DMSO-d_6) δ 153.27, 148.33, 139.08, 137.80, 128.60, 122.75, 114.09, 66.34; HRMS (ESI) exact mass calculated for [M+H]+ (C27H26N6) requires m/z 433.21352, found m/z 433.21385.

4,4',4''-(((1E,1'E,1''E)-benzene-1,3,5-triyltris(methaneylylidene))tris(azaneyl-ylidene))triani-line (1'·). 1,3,5-Triformylbenzene (TB, 50 mg, 0.299 mmol) and *p*-phenylenediamine (*p*PDA, 100 mg, 0.897 mmol) were placed into a 5 mL PMMA reaction jar and a 7 mm steel ball was added (η = 0 µL/mg). The mixture was milled at 30 Hz for 30min. The resulting solid was dried

under high vacuum for 24 h to remove remaining solvents and analyzed without further purification. IR v_{max}/cm^{-1} 3435, 3337, 3208, 3032, 3002, 2882, 2856, 1622, 1599, 1578, 1505, 1282, 1167, 1137, 1083, 970, 873, 828, 681, 643, 583, 523, 493, 474, 410; ^{1}H NMR (400 MHz, DMSO-d_6) δ 8.76 (s, 3H), 8.40 (s, 3H), 7.22 (d, J = 7.4 Hz, 6H), 6.63 (d, J = 7.4 Hz, 6H), 5.30 (s, 6H), 3.57 (s, 4H); ^{13}C NMR (101 MHz, DMSO- d_6) δ 153.27, 148.33, 139.08, 137.80, 128.60, 122.75, 114.09, 66.34; HRMS (ESI) exact mass calculated for [M+H]$^+$ ($C_{27}H26N_6$) requires m/z 433.21352, found m/z 433.21385.

Benzidine•1,4-dioxane (2). Benzidine (Bd, 100 mg, 0.543 mmol) and 1,4-dioxane (46.5 µL) were placed into a 5 mL PMMA reaction jar and a 7 mm steel ball was added (η = 0.47 µL/mg). The mixture was milled at 30 Hz for 10 min. The resulting solid was immediately analyzed without further purification. IR v_{max}/cm^{-1} 3450, 3403, 3356, 3328, 3207, 3025, 2953, 2859, 1632, 1607, 1498, 1289, 1264, 1175, 1112, 1079, 868, 817, 748, 702, 615, 526, 506; ^{1}H NMR (400 MHz, Chloroform-d) δ 7.34 (d, J = 7.9 Hz, 4H), 6.72 (d, J = 7.9 Hz, 4H), 3.70 (s, 8H), 3.65 (s, 4H); ^{13}C NMR (101 MHz, Chloroform-d) δ 145.07, 131.92, 127.39, 115.54, 67.19; HRMS (ESI) exact mass calculated for [M+H]$^+$ ($C_{27}H_{26}N_6$) requires m/z 184.10005, found m/z.

Solvent study

Mechanosynthesis of COF LZU-1 using pure mesitylene as a liquid additive. 1,3,5-Tri-formylbenzene (TB, 100 mg, 0.598 mmol) and p-phenylenediamine (pPDA, 100 mg, 0.897 mmol) were placed into a 10 mL steel reaction jar with the addition of 80 µL of mesitylene and 6 M acetic acid (40 µL, η = 0.60 µL/mg) as catalyst, and a 7 mm steel ball was added. The mixture was milled at 30 Hz for 1 h. The resulting solid was washed with acetone, DMF, dichloromethane, methanol, and a 12 h Soxhlet extraction with MeOH. The wet sample was activated by supercritical CO_2 drying and further drying under high vacuum for 24 h. Yield: 146.6 mg (91%). Elemental Analysis, calc.: C, 79.98; H, 4.47; N, 15.55; found C, 76.36; H, 4.91; N, 14.76.

Mechanosynthesis of COF LZU-1 using pure 1,4-dioxane as a liquid additive. 1,3,5-Tri-formylbenzene (TB, 100 mg, 0.598 mmol) and p-phenylenediamine (pPDA, 100 mg, 0.897 mmol) were placed into a 10 mL steel reaction jar with 80 µL 1,4-dioxane, 6 M acetic acid (40 µL, η = 0.60 µL/mg) as catalyst, and a 7 mm steel ball was added. The mixture was milled at 30 Hz for 1 h. The resulting solid was washed with acetone, DMF, dichloromethane, methanol, and a 12 h Soxhlet extraction with MeOH. The wet sample was then activated by supercritical CO_2 drying and further drying under high vacuum for 24 h. Yield: 151.0 mg (93%). Elemental Analysis, calc.: C, 79.98; H, 4.47; N, 15.55; C, 77.56; H, 4.76; N, 14.92.

9.3.3. XRPD measurements and refinements

Crystal structure determination of intermediate **1**

Indexing of the intermediate (**1**) was carried out by an iterative use of singular value decomposition leading to a triclinic space group ($P\bar{1}$) with the lattice parameters listed in Table S1. The peak profile was determined by a Pawley refinement using the fundamental parameter approach (FPA) as implemented in TOPAS. The background was modeled by a Chebychev polynomial of 13th order. The crystal structure of the intermediate was determined using the global optimization method of simulated annealing (SA). The intermediate was decomposed into four different rigid bodies during the *ab initio* structure solution process and for the consequent Rietveld refinement. The central part of the molecule (1,3,5-trimethylbenzene) and three 1,4-diamine molecules were described using rigid bodies in z-matrix notation with idealized bond lengths and bond angles, taken from related COF structures. The three imine bond distances (N11 – C11, N21 – C21, N31 – C31) were restraint to be 1.28 Å. 1,4-Dioxane was described by a rigid body in z-matrix notation including a dummy atom in the center of the ring, which was placed on a center of inversion (0, 0, 0). For the final Rietveld refinement, the background, lattice parameters, microstructure in form of microstrain (Gaussian and Lorentzian component), most translations and rotations of the rigid bodies were refined without any constraint for the final refinement. Only the translational components of 1,4-dioxane were constraint, so that a center of inversion is in the center of the molecule.

Crystal structure determination of benzidine solvate intermediate (**2**)

Indexing of the benzidine dioxane solvate intermediate (**2**) was performed by an iterative use of singular value decomposition using a XRPD pattern collected with Co-radiation. Indexing lead to a monoclinic space group ($P2_1/c$) with the lattice parameters listed in Table S1. The peak profile was determined by a Pawley refinement using FPA in TOPAS V6. The background was modeled by a Chebychev polynomial of 13th order. The crystal structure of **2** was determined using the global optimization method of SA. 1,4-Dioxane and benzidine were described using rigid bodies in z-matrix notation, with only half of each molecule in the rigid bodies, as they are both doubled by a center of inversion. A dummy atom was used to place both rigid bodies on the center of inversion, Wyckoff site *2a* (0, 0, 0) for benzidine and *2d* (0.5, 0, 0.5) for 1,4-dioxane. Initial bond lengths and angles were taken from related crystal structures found in the Cambridge Structural Database (CSD) and subsequently modified according to the bond lengths and angles obtained after DFT structure optimization. An overall isotropic thermal displacement parameter for each molecular moiety was refined using an U_{iso} = 1.2 with respect to parent atoms for all hydrogen atoms. For the final Rietveld refinement background, lattice parameters, microstructure in the form of microstrain and crystallite size (Gaussian and Lorentzian component), and rotations of both rigid bodies were freely refined.

Table S9.3.1. *Crystallographic information of the Rietveld refinements of the intermediate solvate (**1**) and benzidine dioxane solvate (**2**) with selected refinement information.*

Name	1	Benzidine dioxane solvate (2)
CCDC Number	2033639	2033638
Formula	$C_{29}H_{28}N_6O_1$	$C_{16}H_{20}N_2O_2$
MW / g mol-1	476.57	272.34
Crystal system	Triclinic	Monoclinic
Space group	$P\bar{1}$	$P2_1/c$
a / Å	8.6884(3)	5.94994(13)
b / Å	10.4970(4)	8.61502(17)
c / Å	14.2634(6)	14.1939(4)
α / °	93.855(3)	90
β / °	101.0341(19)	92.0849(14)
γ / °	96.487(3)	90
V / Å³	1263.36(9)	727.08(3)
T / K	295	295
λ / Å	1.540596	1.540596
Z	2	2
D_{calc} / mg cm⁻³	1.253	1.244
μ / mm⁻¹	0.6271	0.6612
R_{wp} /%[a]	5.23	4.50
R_p/%[a]	4.07	3.35
R_{exp}/%[a]	1.81	0.83
R_{Bragg}[a]	1.91	3.50
Starting angle / ° 2θ	5	7.6
Final angle / ° 2θ	85	89.9
Step width / ° 2θ	0.0075	0.0075

| Time per scan / h | 8 | 8 |
| No. of variables | 52 | 38 |

[a] R_{wp}, R_p, R_{exp}, R_{Bragg} as defined in TOPAS.
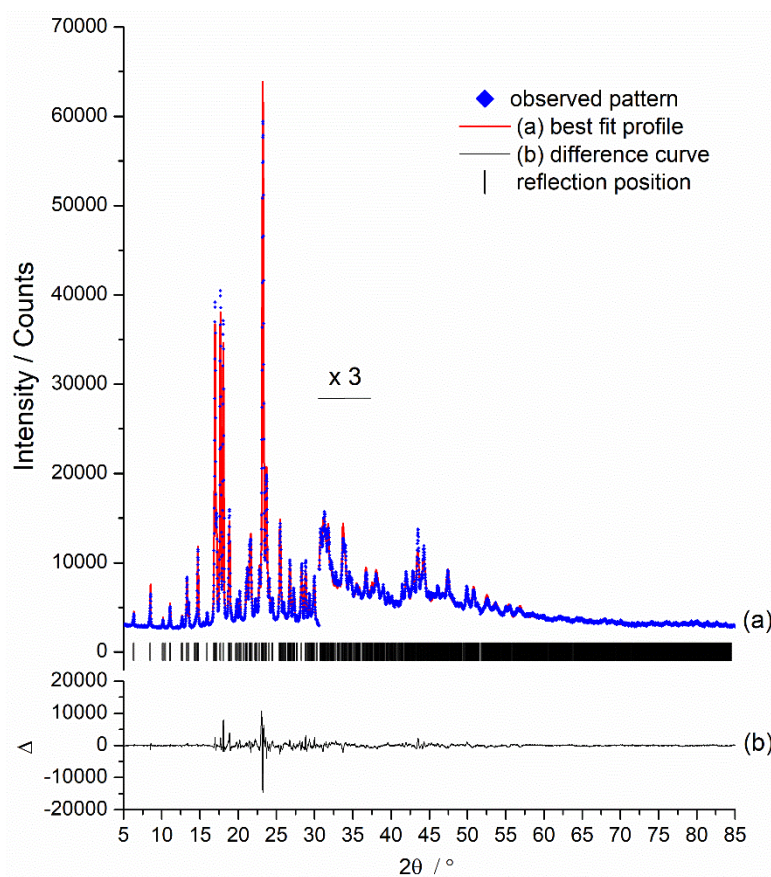
Figure S9.1. Rietveld refinement plot of **1** (λ = Cu Kα_1) with the observed pattern (blue diamonds), calculated pattern (red line), calculated peak positions (dashes), and the difference curve (black line). The higher scattering region (2θ > 30.5 °) was enlarged by a factor of 3 for better visualization.
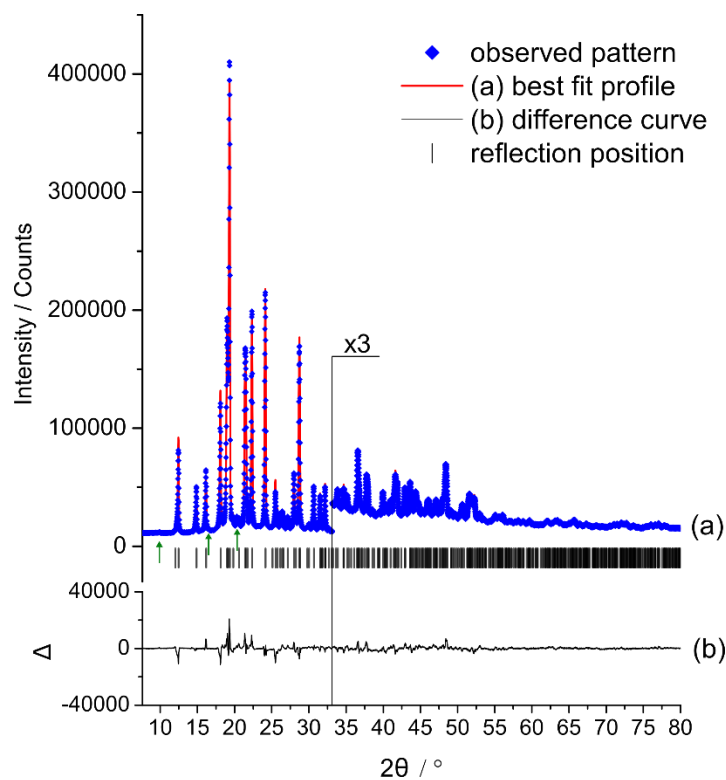
Figure S9.2. Rietveld refinement plot of **2** (λ = Cu Kα_1) with the observed pattern (blue diamonds), calculated pattern (red line), calculated peak positions (dashes), and the difference curve (black line). The higher scattering region ($2\theta >$ 33 °) was enlarged by a factor of 3 for better visualization. The sample contains a benzidine polymorph as minor side phase (CSD refcode BENZIE04), relevant weak diffraction peaks are marked with green arrows at 9.8, 16.5, and 20.3 ° 2θ.
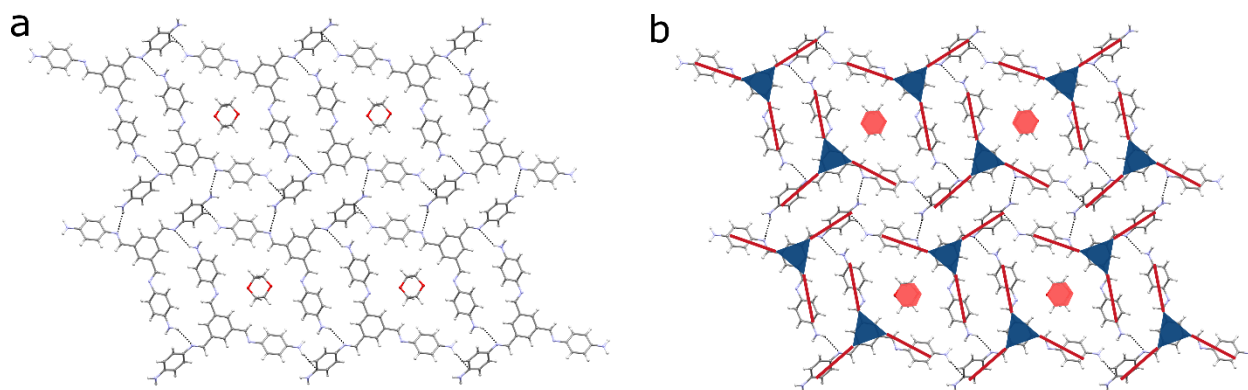
Figure S9.3. Crystal structure of intermediate **1**.
(**a**) Excerpt of the crystal structure of intermediate **1** with view on top of the layer.
(**b**) Schematic representation of trimer and 1,4-dioxane orientation, used for Figure 3 in the main text.
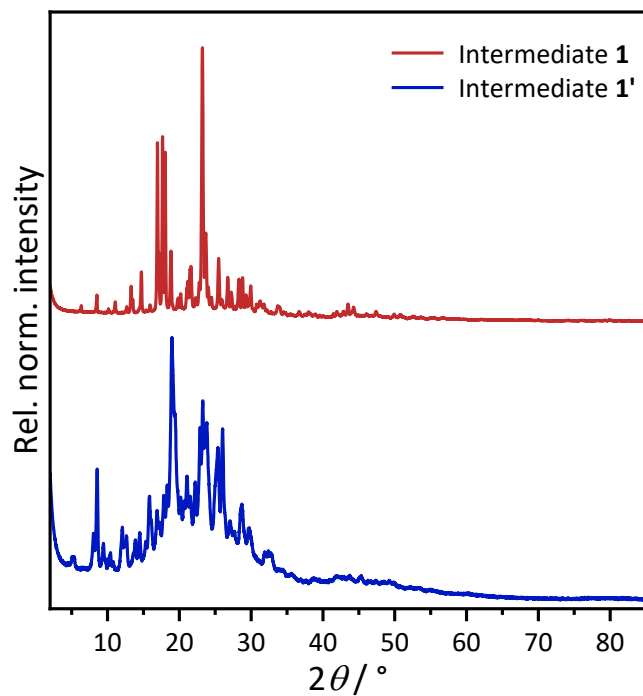
Figure S9.4. Comparison of measured *ex situ* XRPD patterns (λ = 1.54056 Å) of intermediate solvate **1** and **1´**.
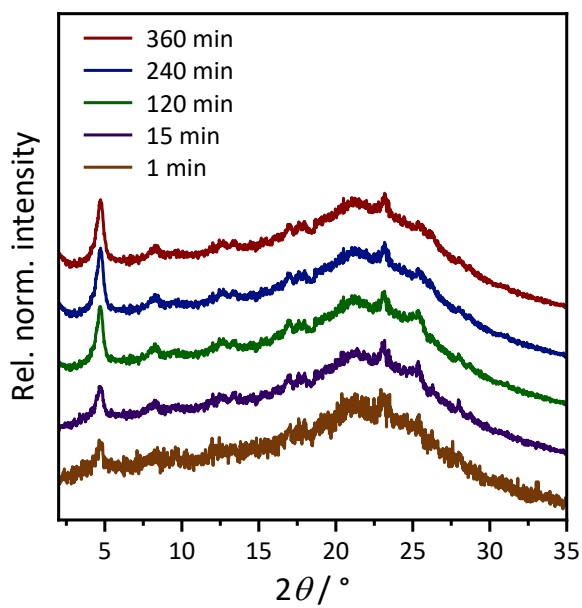
Figure S9.5. XRPD patterns of the reaction mixture during synthesis of **COF-LZU1**, stopped after 3 min of milling, with the attempt to capture the intermediate **1**, showing the continuation of the polymerization and self-assembly of **COF-LZU1** over time.

In situ XRPD measurements and sequential refinement

Sequential Rietveld refinements were performed using TOPAS V5. A LaB$_6$ standard measurement was used to describe the instrumental profile function (IPF) by applying equivalent conditions (same milling frequency and exposure time). The IPF was described using a modified Thompson-Cox-Hasting pseudo-Voight function as implemented in TOPAS. The diffraction signals of the COFs and the reaction intermediate (**1**) were modelled by single peak phases with fixed peak positions and peak widths. Reactants were modelled as single peaks except for those whose crystal structures were known from the CSD database, which were modelled by sequential Rietveld refinements
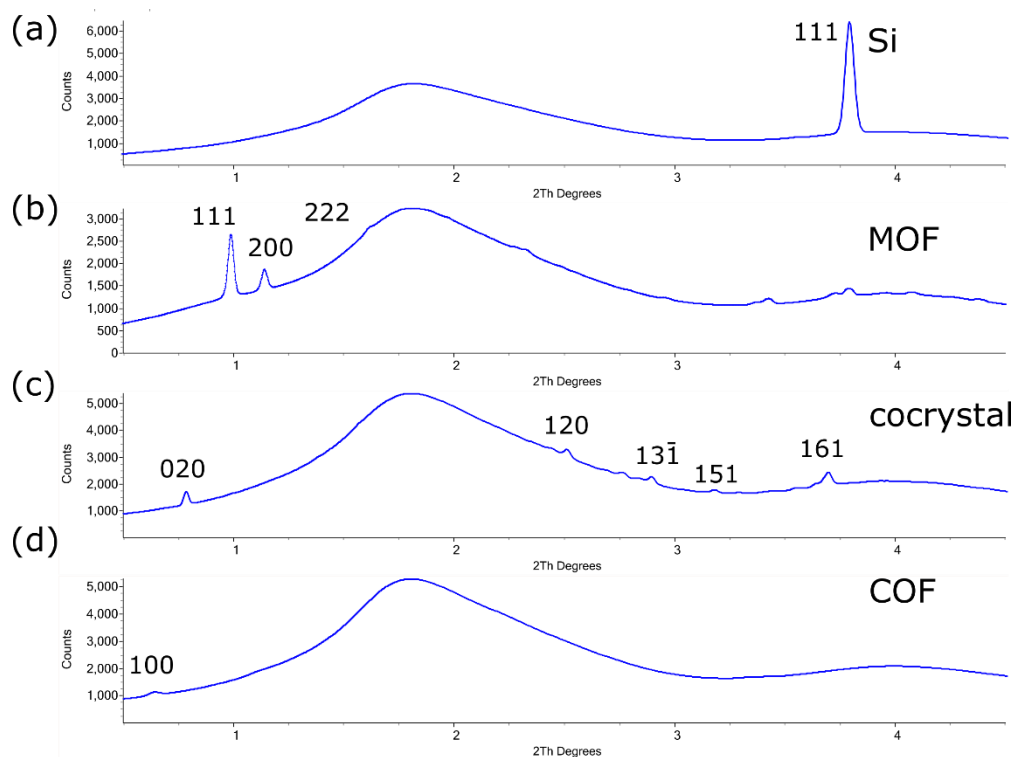
Figure S9.6. Comparison of measured *in situ* XRPD patterns of different material classes in PMMA jars during their mechanochemical synthesis at P02.1 Powder Diffraction and Total Scattering beamline with **(a)** a silicon standard (15 mL PMMA jar), (**b**) mechanosynthesis of UiO-66 (15 mL PMMA jars),[12] (**c**) **(nic)·(adi)** cocrystals (15 mL PMMA jars),[13] and (**d**) **COF-LZU1** system in 5 mL PMMA jars from this study. Diffraction signal of the most intense (100) COF reflection is visible at 0.64 °2θ. Wavelength in all cases approx. 0.207 Å (X-ray energy of 60 keV).

Differences between observed and calculated peak position in Figures S7-S10 are due to thermal effects (difference between sample temperature in milling jar during grinding and temperature at which the crystal structures were collected), instrumental aberrations (zero error), and potential microstructural effects (mechanically induced defects). While the intensity of calculated diffraction patterns is plotted on a linear scale, the intensities of measured XRPD patterns are plotted on a natural logarithmic scale for better visuality in Figure S7-S10. Selected peak positions are marked with dashed lines for better visualization.
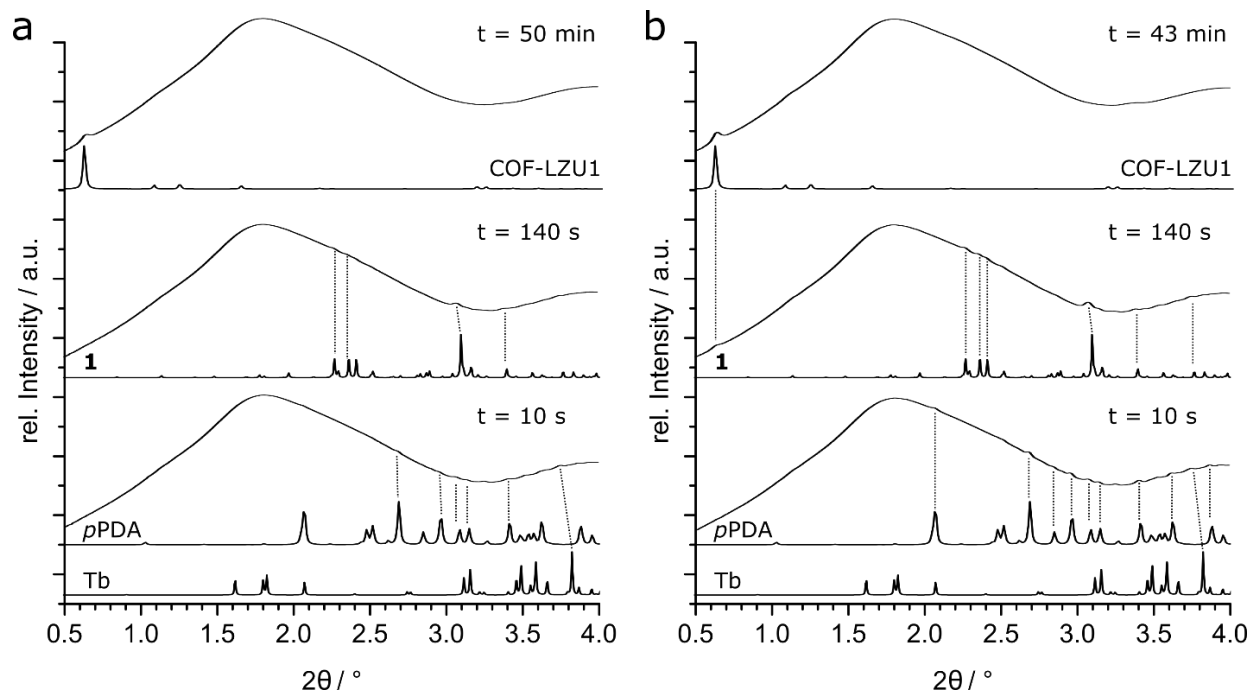
Figure S9.7. Comparison of measured XRPD patterns at different stages of the reaction during mechanosynthesis of **COF-LZU1** using (**a**) AcOH and (**b**) Sc(OTf)$_3$ as catalyst with calculated XRPD patterns of reactants, intermediate **1** as well as the final **COF-LZU1**, λ = 0.20736 Å.
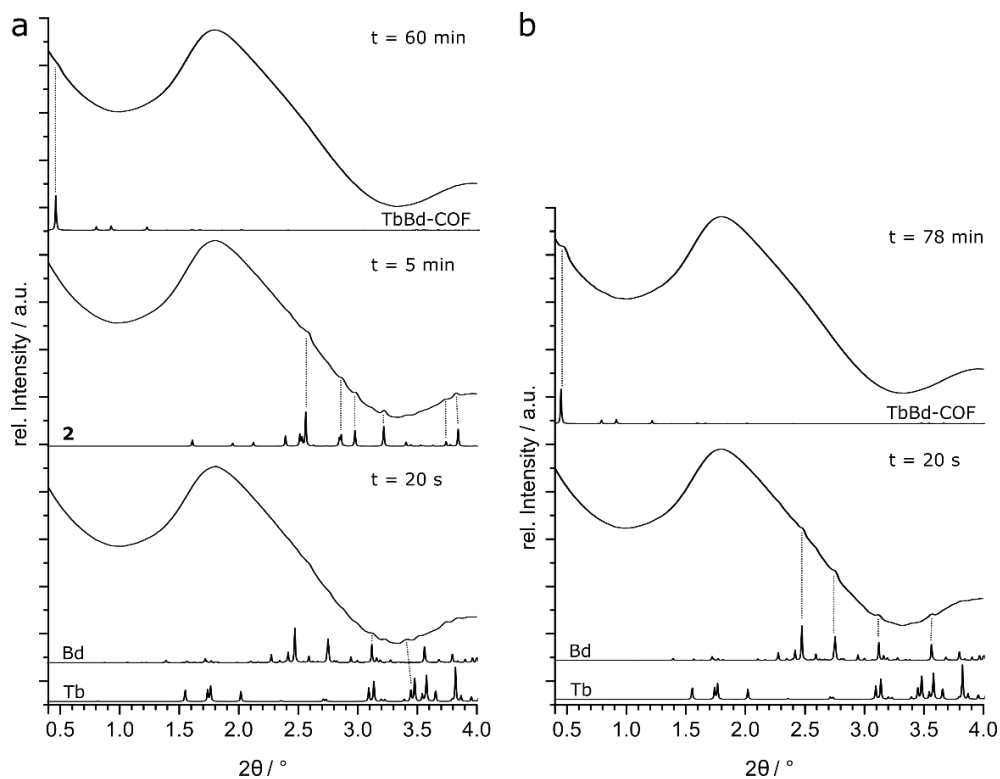
Figure S9.8. Comparison of measured XRPD patterns at different stages of the reaction during mechanosynthesis of **TbBd-COF** using (**a**) AcOH and (**b**) Sc(OTf)$_3$ as catalyst with calculated XRPD patterns of reactants, intermediate **2** as well as the final **TbBd-COF**, λ = 0.20747 Å.
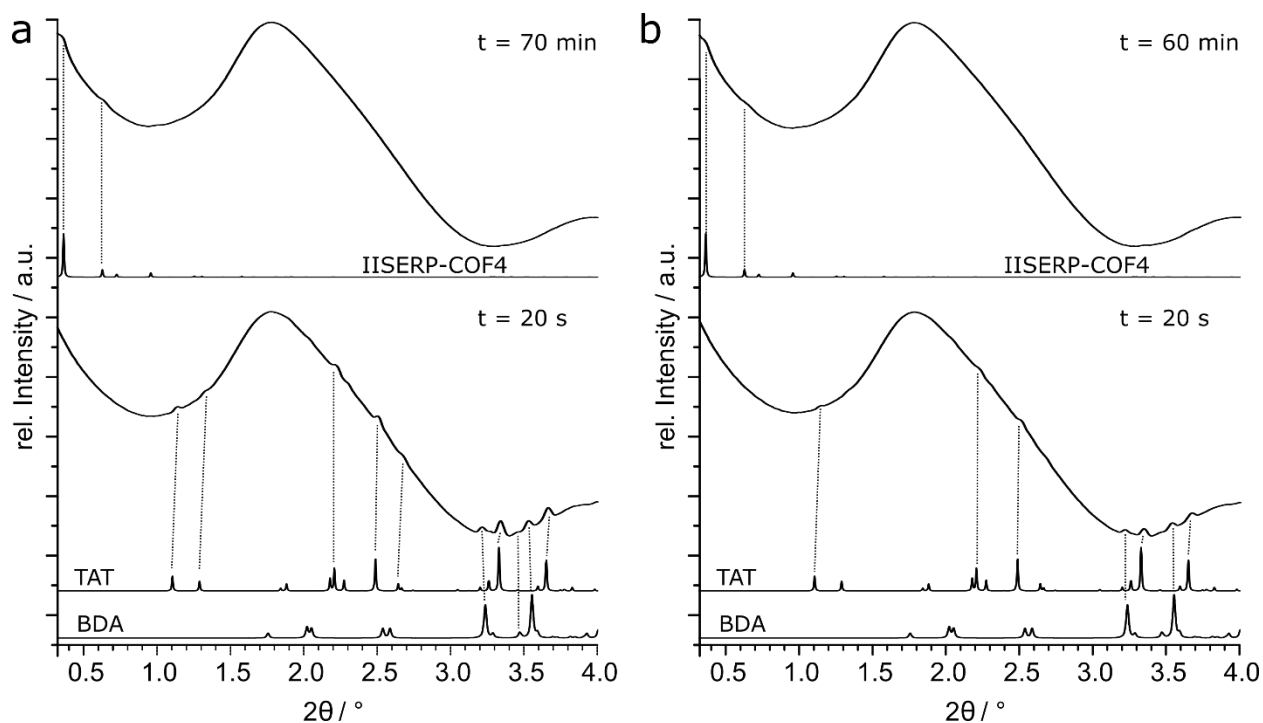
Figure S9.9. Comparison of measured XRPD patterns at different stages of the reaction during mechanosynthesis of **IISERP-COF4** using (**a**) AcOH and (**b**) Sc(OTf)$_3$ as catalyst with calculated XRPD patterns of reactants and the final **IISERP-COF4**, $\lambda = 0.20747$ Å.
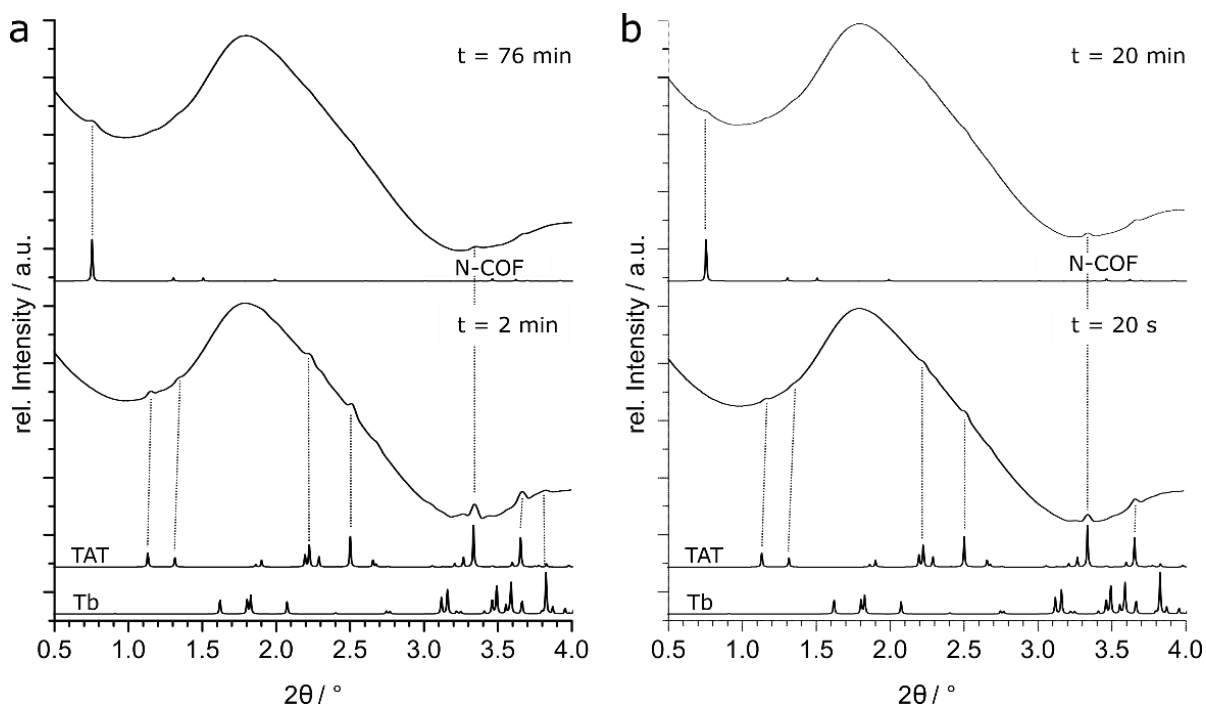
Figure S9.10. Comparison of measured XRPD patterns at different stages of the reaction during mechanosynthesis of **N-COF** using (**a**) AcOH and (**b**) Sc(OTf)$_3$ as catalyst with calculated XRPD patterns of reactants and the final **N-COF**, $\lambda = 0.20747$ Å.
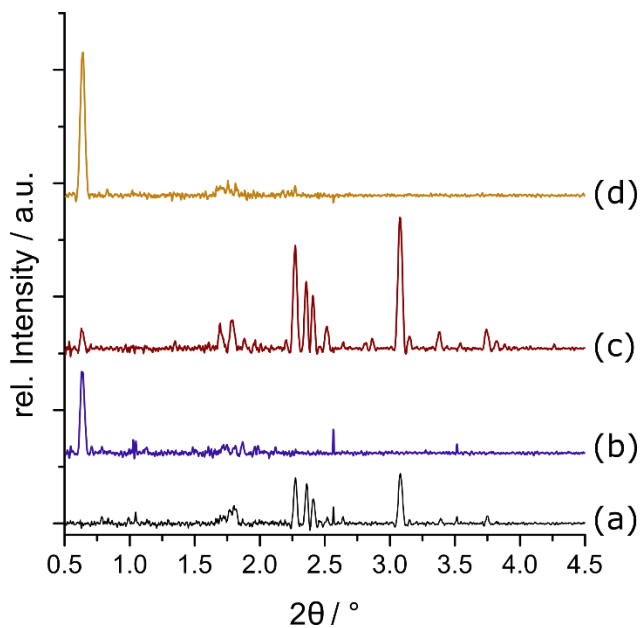
Figure S9.11. Comparison of measured, background subtracted *in situ* XRPD patterns during the mechanochemical synthesis of **COF-LZU1** using either (**a, b**) AcOH after (**a**) 3.3 min and (**b**) ca. 50 min of milling, and (**c,d**) Sc(OTf)$_3$ as catalyst, after (**c**) 3.3 min and (**d**) ca. 45 min of milling.
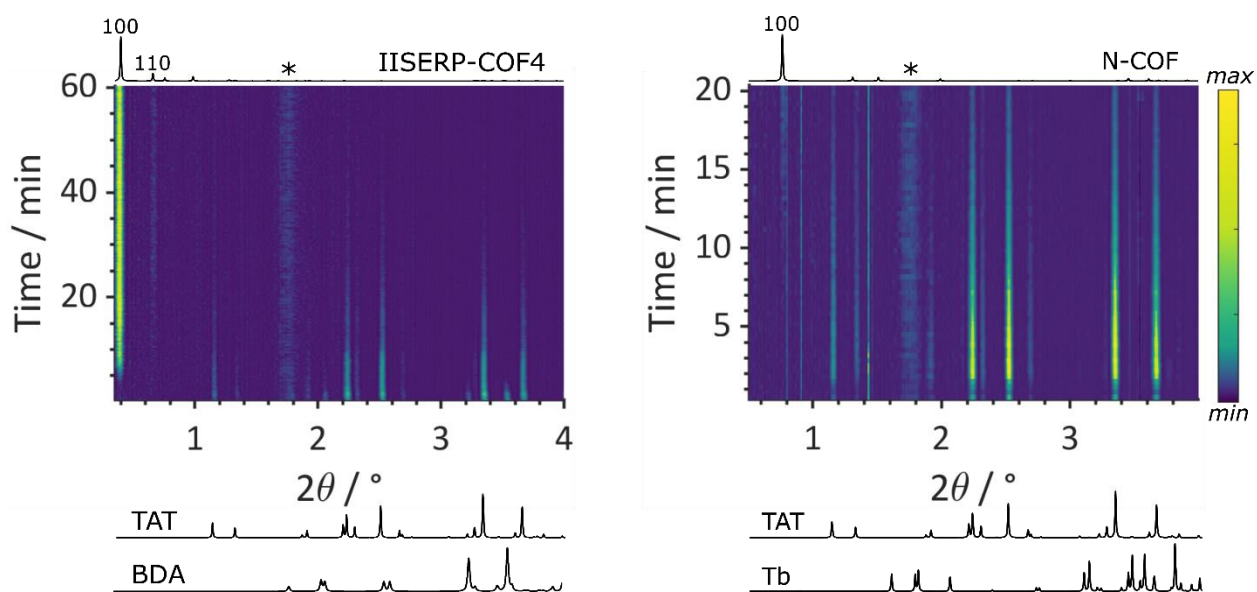
Figure S9.12. Background subtracted 2D XRPD plots of the mechanochemical synthesis of **IISERP-COF** (left) and **N-COF** (right) using Sc(OTf)$_3$ as catalyst. Calculated XRPD patterns of reactants and COFs are shown below and above the 2D plot, respectively, λ = 0.207 Å.
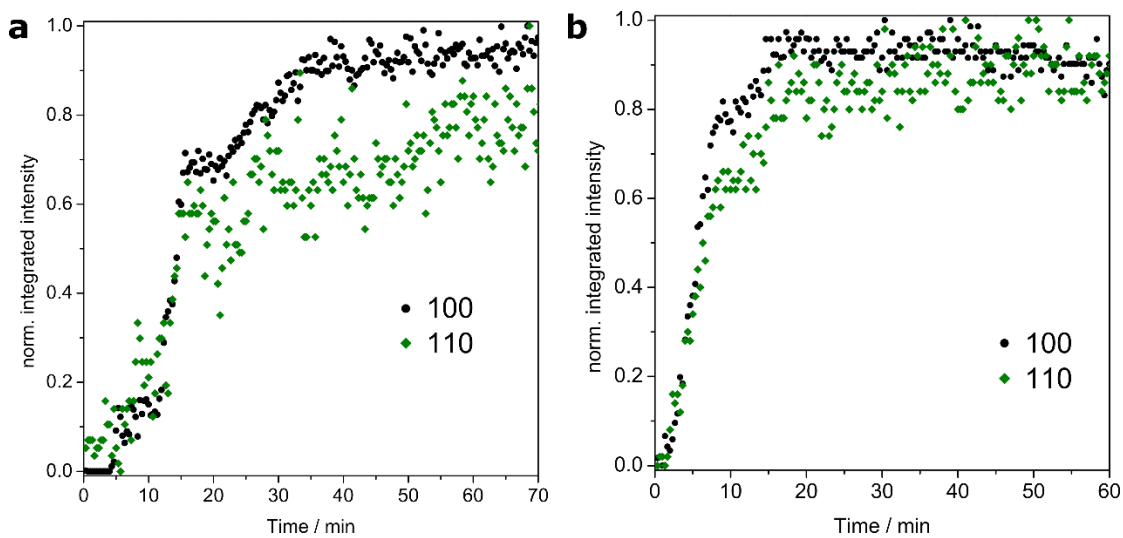
Figure S9.13. Comparison of the 100 and 110 reflection formation kinetics of **IISERP-COF4** using AcOH (**a**) and Sc(OTf)$_3$ (**b**) as catalyst**.**
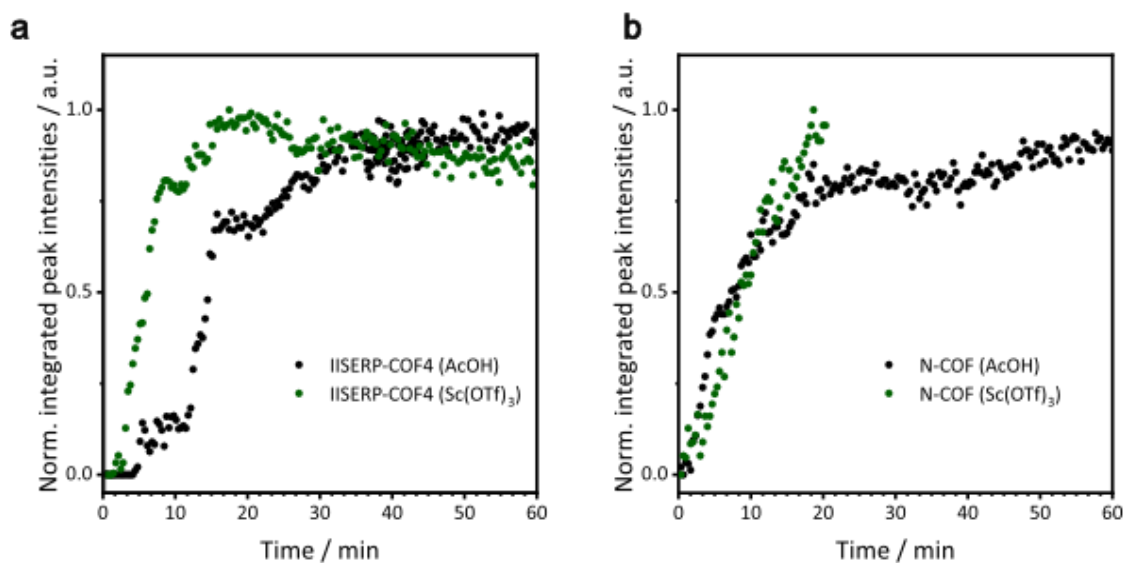
Figure S9.14. Comparison of the formation kinetics of **IISERP-COF4** (**a**) and **N-COF** (**b**) using AcOH or Sc(OTf)$_3$ as catalyst. Data collection of **N-COF** (Sc(OTf)$_3$) ends after 20 min due to beam dump.
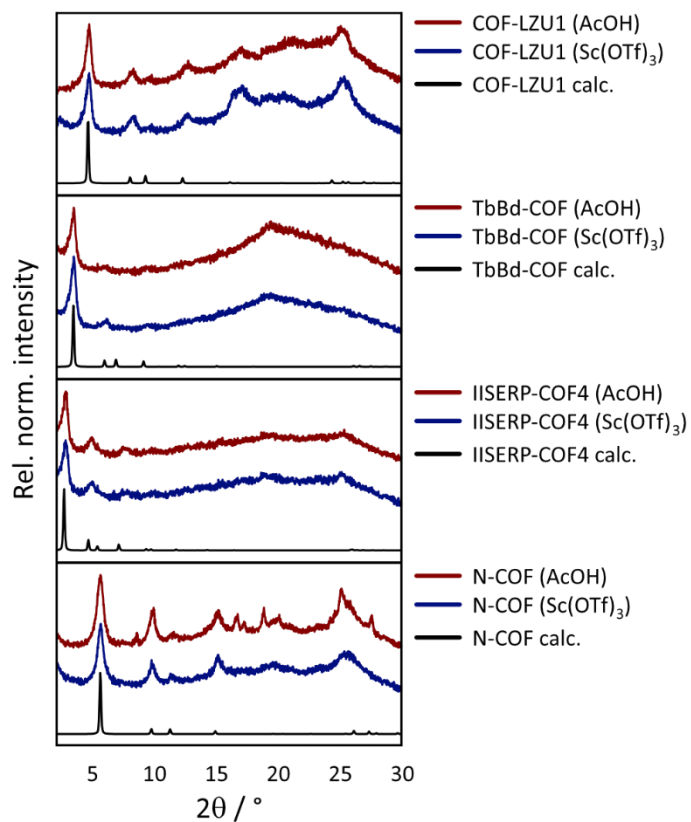
Figure S9.15. *Ex situ* XRPD patterns (λ = 1.54 Å) of as-synthesized COF samples obtained during *in situ* monitoring. From top to bottom: **COF-LZU1**, **TbBD-COF**, **IISERP-COF4**, and **N-COF** with AcOH and Sc(OTf)$_3$ as catalysts, as well as calculated XRPD patterns of the respective COF system.

Ex situ X-ray powder diffraction
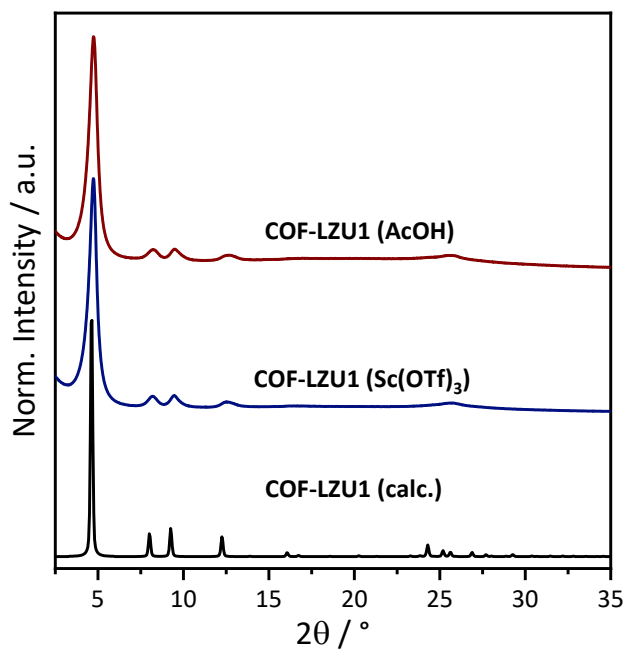
Figure S9.16. Comparison of measured *ex situ* XRPD patterns (λ = 1.54 Å): **COF**-**LZU1** (AcOH), **COF-LZU1** (Sc(OTf)$_3$) and the calculated pattern of **COF-LZU1**.
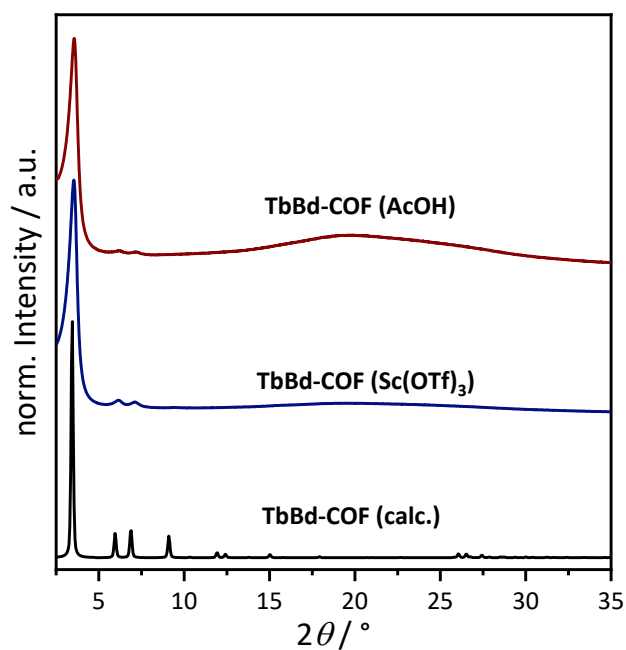
Figure S9.17. Comparison of measured *ex situ* XRPD patterns (λ = 1.54 Å): **TbBd-COF** (AcOH), **TbBd-COF** (Sc(OTf)$_3$) and the calculated pattern of **TbBd-COF**.
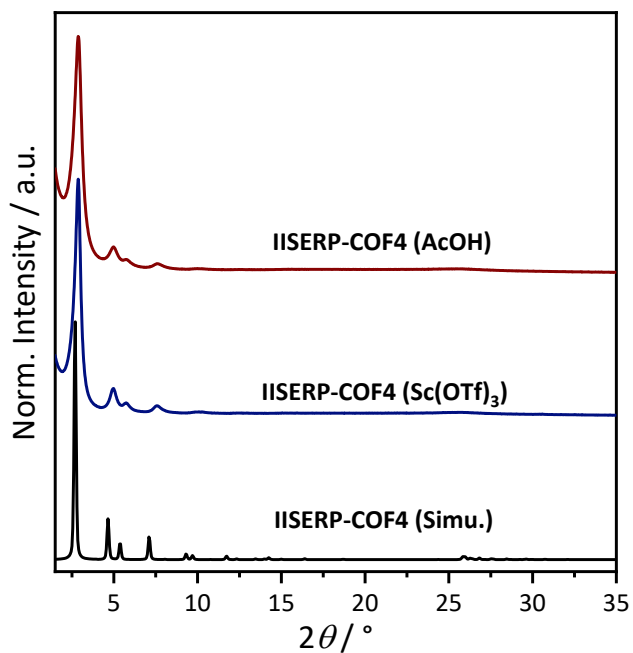
Figure S9.18. Comparison of measured *ex situ* XRPD patterns (λ = 1.54 Å) of washed and ssCO$_2$ activated **IISERP-COF4** (AcOH), **IISERP-COF4** (Sc(OTf)$_3$) and the calculated pattern of **IISERP-COF4**.
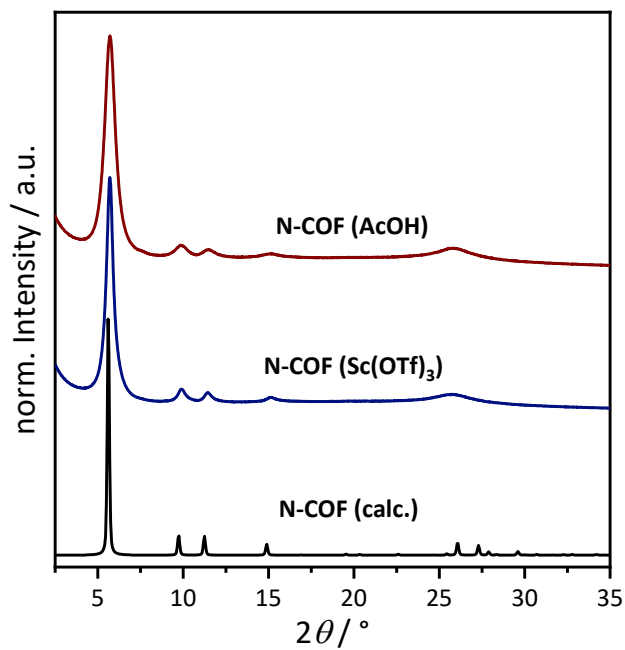
Figure S9.19. Comparison of measured *ex situ* XRPD patterns (λ = 1.54 Å) of washed and ssCO$_2$ activated **N-COF** (AcOH), **N-COF** (Sc(OTf)$_3$) and the calculated pattern of **N-COF**.
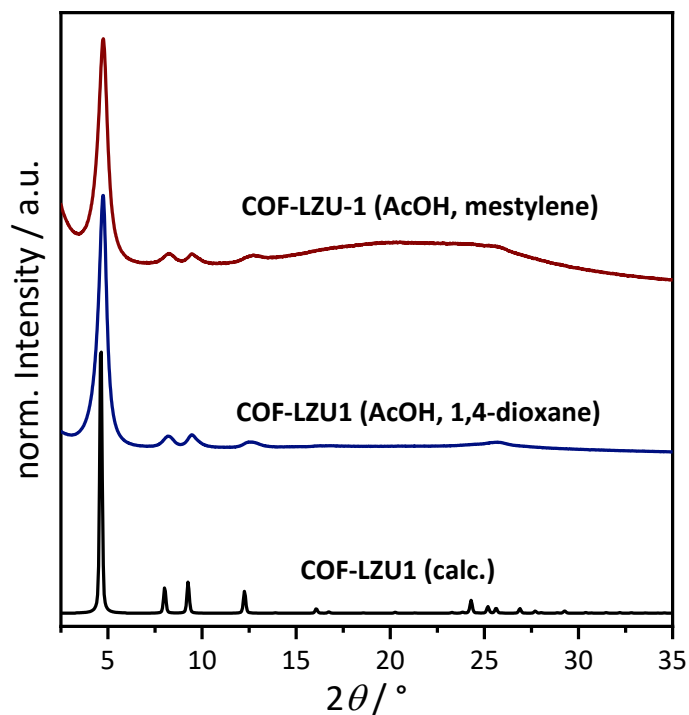
Figure S9.20. Comparison of *ex situ* XRPD patterns (λ = 1.54 Å) of washed and ssCO$_2$ activated **COF-LZU1** (AcOH, mesitylene), **COF-LZU1** (AcOH, 1,4 dioxane) and the calculated pattern of **COF-LZU1**.
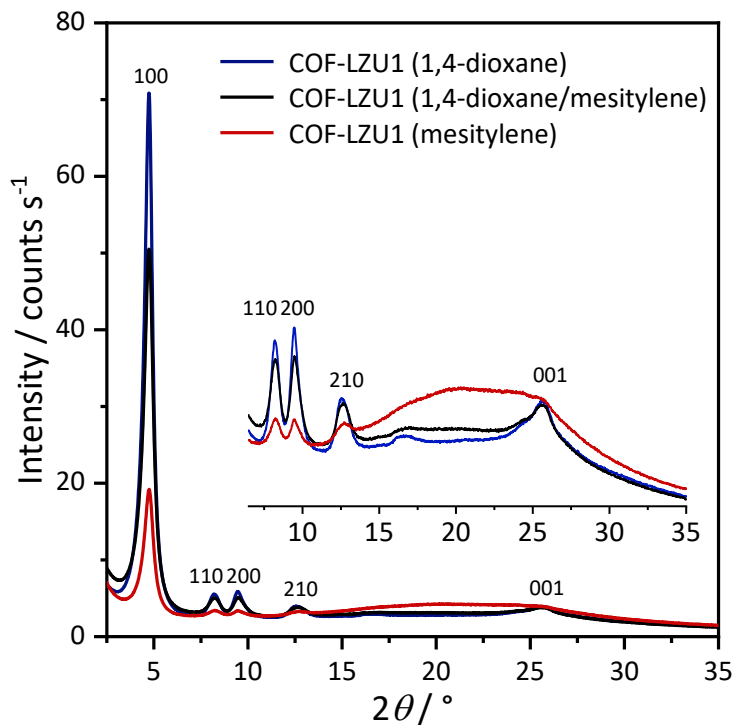
Figure S9.21. Direct comparison of *ex situ* XRPD patterns (λ = 1.54 Å) of washed and ssCO$_2$ activated **COF-LZU1** (red: AcOH, mesitylene), **COF-LZU1** (black: AcOH, mesitylene:1,4-dioxane) and **COF-LZU1** (blue: AcOH, 1,4-dioxane).
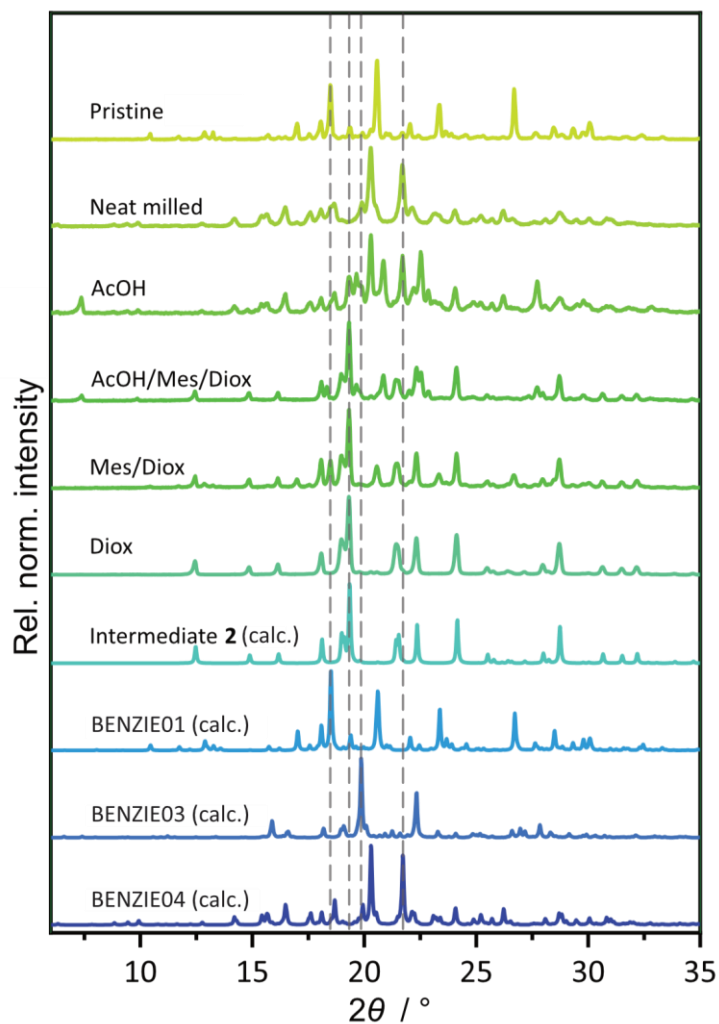
Figure S9.22. Comparison of XRPD-patterns for milling benzidine with different grinding additives. From top to bottom: pristine benzidine, neat grinding of benzidine, grinding benzidine in presence of AcOH, AcOH/mes/diox, mes/diox, and diox as liquid additives, calculated XRPD patterns of intermediate **2**, and different benzidine polymorphs with CCDC refcodes BENZIE01, BENZIE03, and BENZIE04.

9.3.4. *In Situ* Raman Spectroscopy

Real-time Raman monitoring of the reaction between 1,3,5-triformylbenzene and *p*-phenylenedi-amine revealed fluorescence along with a strong Raman signal of the condensation product under excitation of the 785 nm laser (Figure S23).
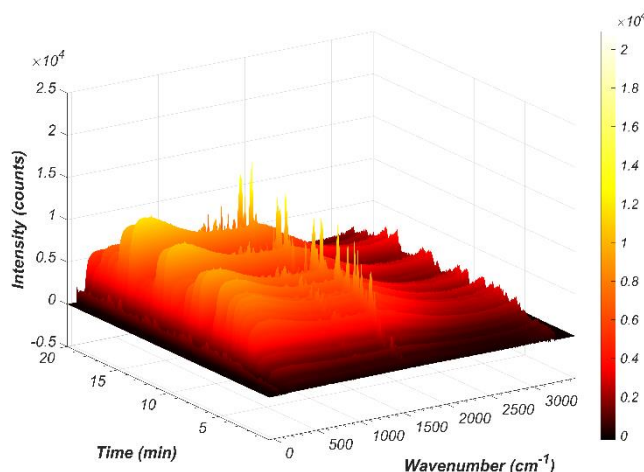
Figure S9.23. Raw signal of **COF-LZU1** formation, monitored *in situ* by real-time Raman spectroscopy. The appearance of the fluorescence caused by the assembly of **COF-LZU1** and consequently the formation of the conjugated π-system is visible after approx. 5 minutes.

Removal of the fluorescence signal via baseline subtraction and vector normalization reveals only a single set of Raman peaks with a minor component of the Raman signal from the sapphire milling jar (Figures S24 and S25). The Raman spectra of the trialdehyde and diamine starting materials were not observed in the reaction (Figure S9.25) and the characteristic peaks observed at 1574 cm^{-1} and 1625 cm^{-1} correspond well with $\nu_{C=N}$ and ν_{C-N} stretching bands of imines suggesting that imine formation is extremely rapid.[14]
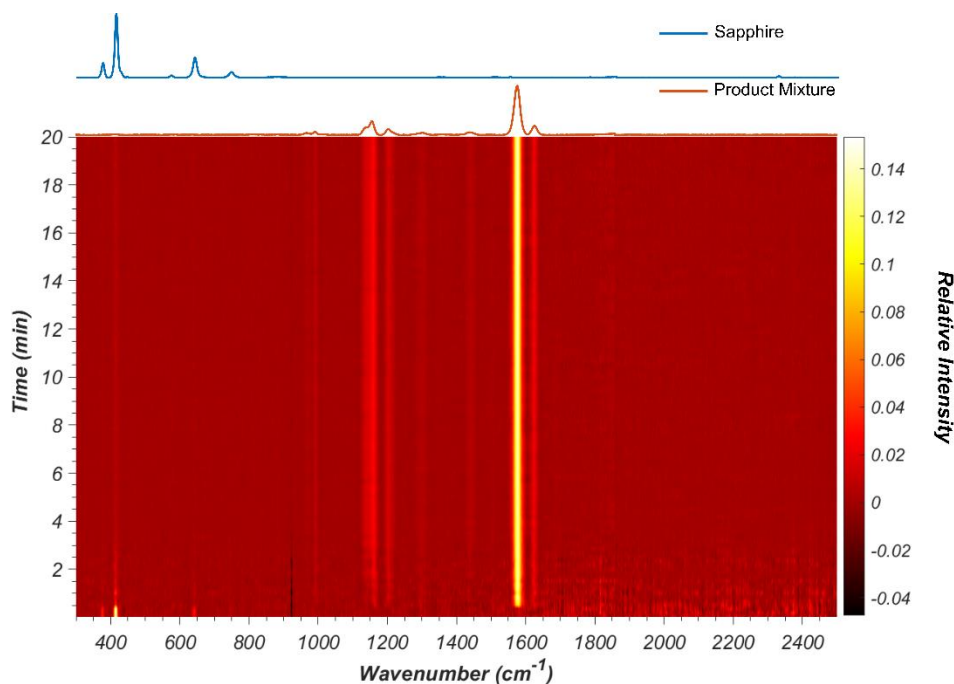
Figure S9.24. Real-time Raman monitoring of the **COF-LZU1** formation with the vector normalized, background subtracted Raman signal over time with the signal of the product mixture shown above the 2D plot.
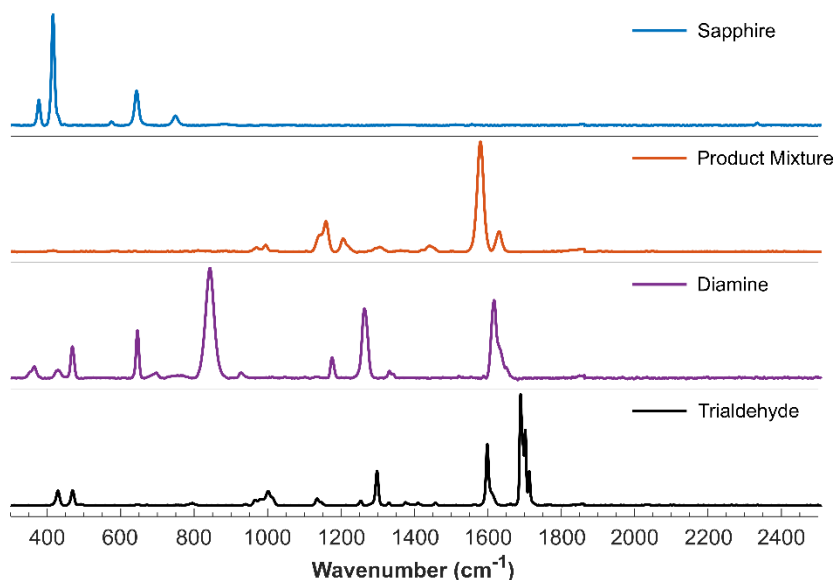
Figure S9.25. Baseline subtracted Raman spectra of the sapphire jar (blue), the reaction product mixture (red), pure *p*-phenylenediamine (purple), and 1,3,5-triformylbenzene (black).

The product of the reaction after *in situ* Raman monitoring was characterized using XRPD revealing a mixture of intermediate **1** and COF-LZU1 (Figure S26). This is most likely due to the lower catalyst loading (25 µL vs. 40 µL AcOH), and increased η value, which were selected trying to slow the reaction in order to better observe the fast imine formation, although differences in jar geometry (*i. e.* PMMA *vs* sapphire jars) affecting both, mixing and impact may also play a role.
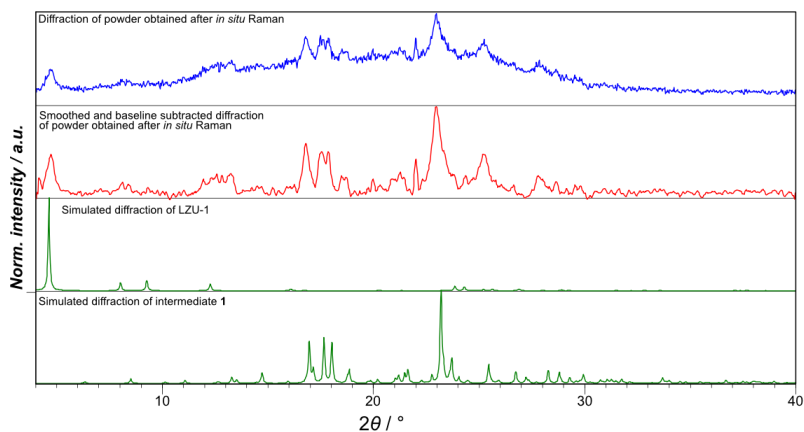
Figure S9.26. XRPD patterns (λ = 1.54 Å) of product after real time Raman monitoring (blue) was processed for visual clarity using baseline subtraction and cubic polynomial smoothing with a convolution range of 9 data points (red). The diffraction of the product is consistent with a mixture of intermediate **1** and **COF-LZU1** as evidenced by the powder diffraction patterns of these phases as simulated from their respective crystal structures.

Neither starting materials were observed in Raman monitoring, and no distinct Raman peaks differentiate intermediate **1** from COF-LZU1, however a notable increase in baseline was observed between samples containing only COF-LZU1 and a mixture of COF-LZU1 and intermediate **1** as determined by XRPD (Figure S26).
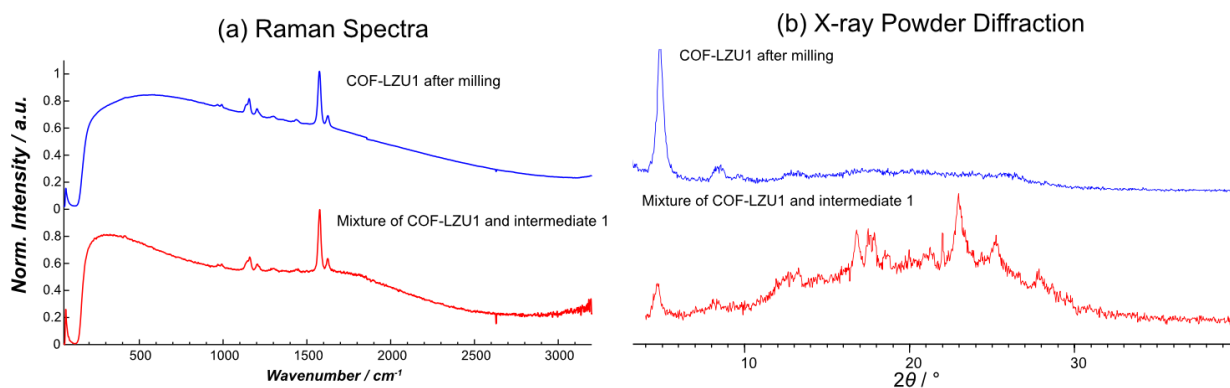
Figure S9.27. Comparisons of (a) Raman spectra and (b) X-ray powder diffraction patterns (λ = 1.54 Å) of reaction product mixtures containing either only **COF-LZU1** after milling or a mixture of **COF-LZU1** and intermediate **1** as identified by XRPD. The Raman spectra of both samples contain the same Raman peaks, however the presence of **COF-LZU1** appears to increase the fluorescence baseline.

9.3.5. FT-IR Spectroscopy
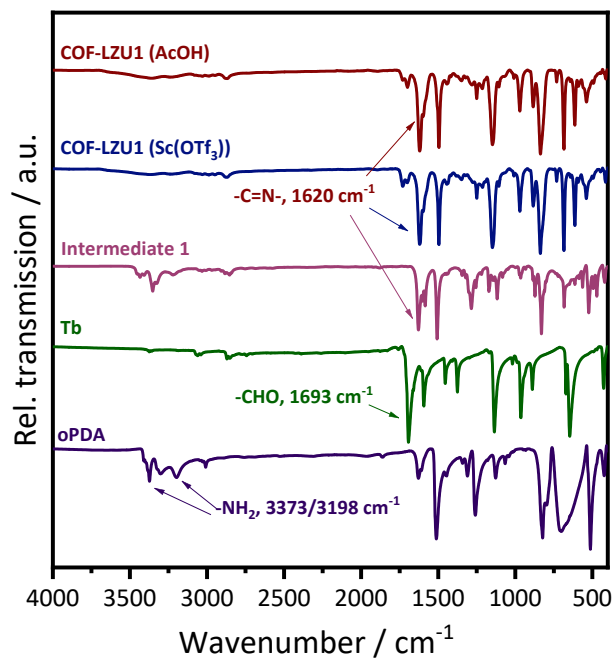
Figure S9.28. FT-IR comparison of **COF-LZU1** (AcOH), **COF-LZU1** (Sc(OTf)$_3$), Intermediate **1** and the starting materials **Tb** and **pPDA**.
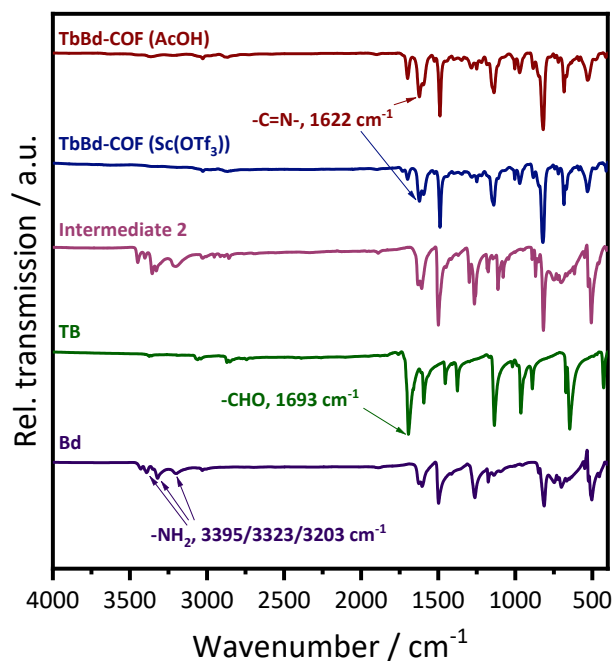
Figure S9.29. FT-IR comparison of **TbBd-COF** (AcOH), **TbBd-COF** (Sc(OTf)$_3$), Intermediate **2** and the starting materials **TB** and **Bd**.
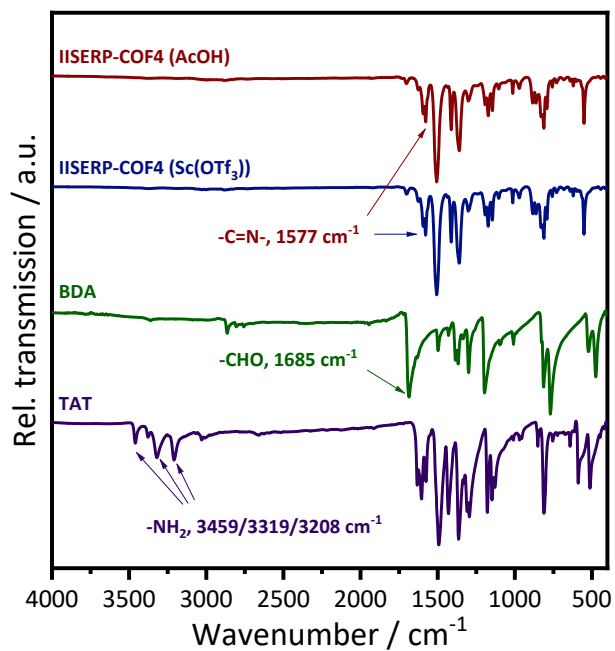
Figure S9.30. FT-IR comparison of **ISERP-COF4** (AcOH), **IISERP-COF4** (Sc(OTf)₃) and the starting materials **BDA** and **TAT**.
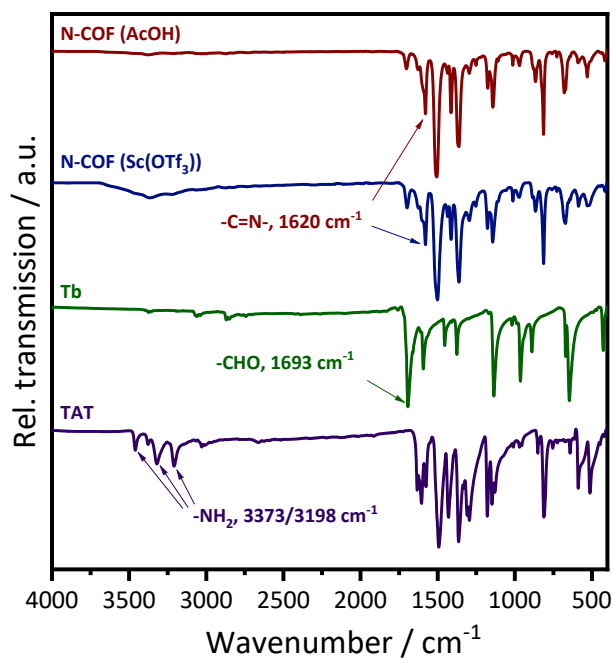
Figure S9.31. FT-IR comparison of **N-COF** (AcOH), **N-COF** (Sc(OTf)₃) and the starting materials **Tb** and **TAT**.
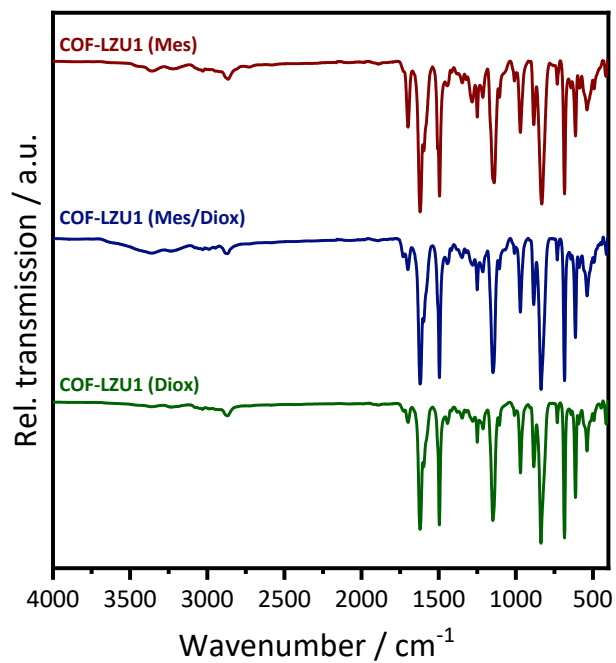
Figure S9.32. FT-IR comparison of **COF-LZU1** (mesitylene), **COF-LZU1** (mesitylene/1,4-dioxane) and **COF-LZU1** (1,4-dioxane).

9.3.6. Liquid State NMR
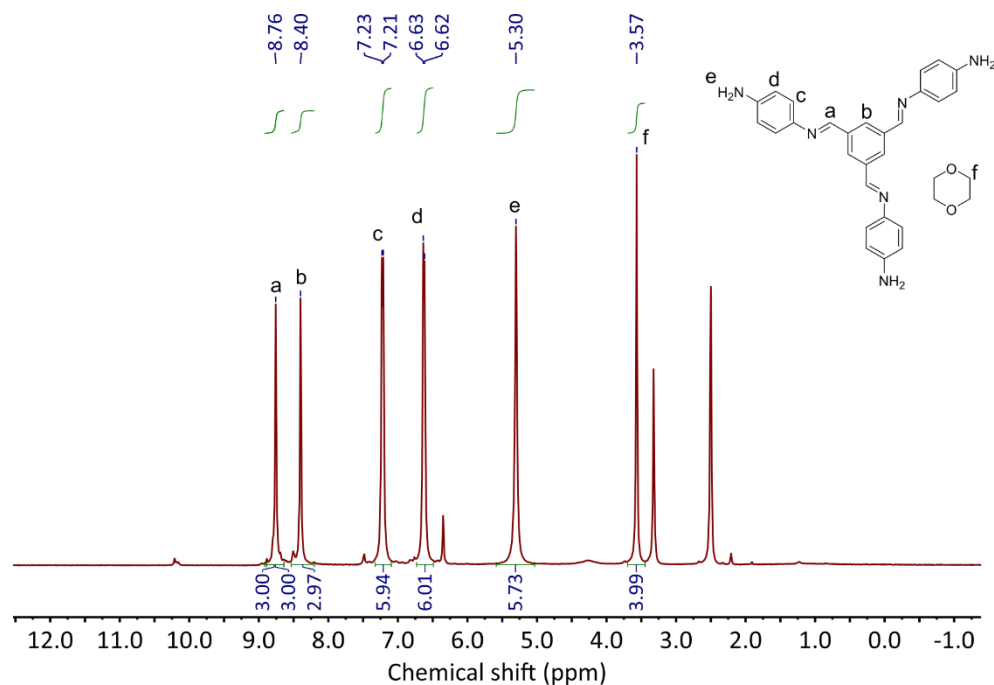
Figure S9.33. Measured liquid ^{1}H NMR spectrum of **1**.
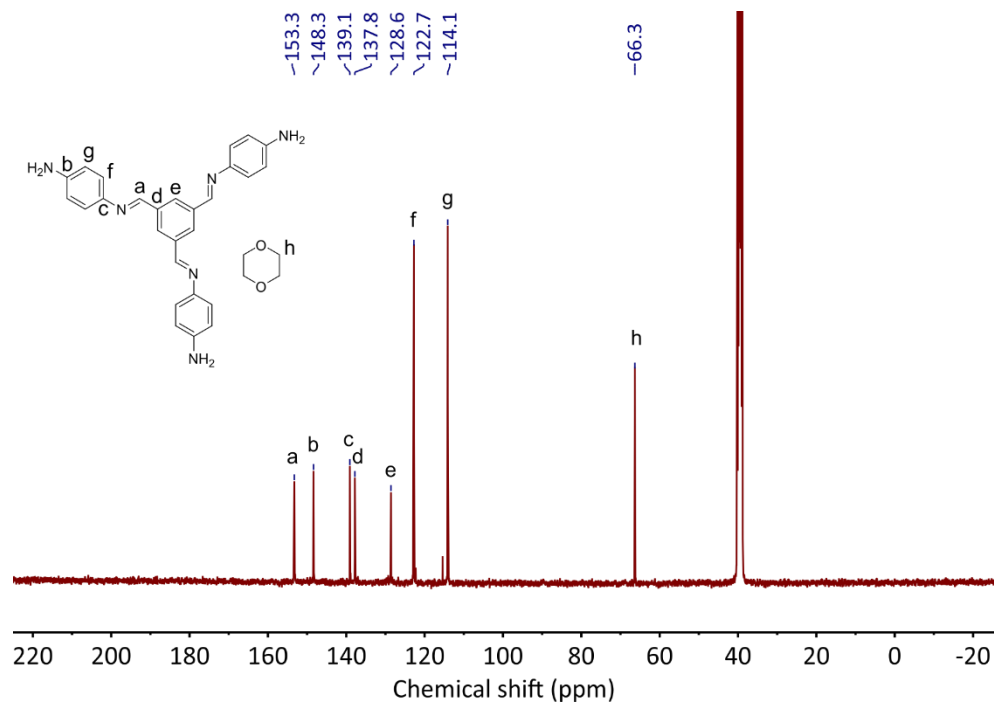
Figure S9.34**.** Measured liquid ^{13}C NMR spectrum of **1**.
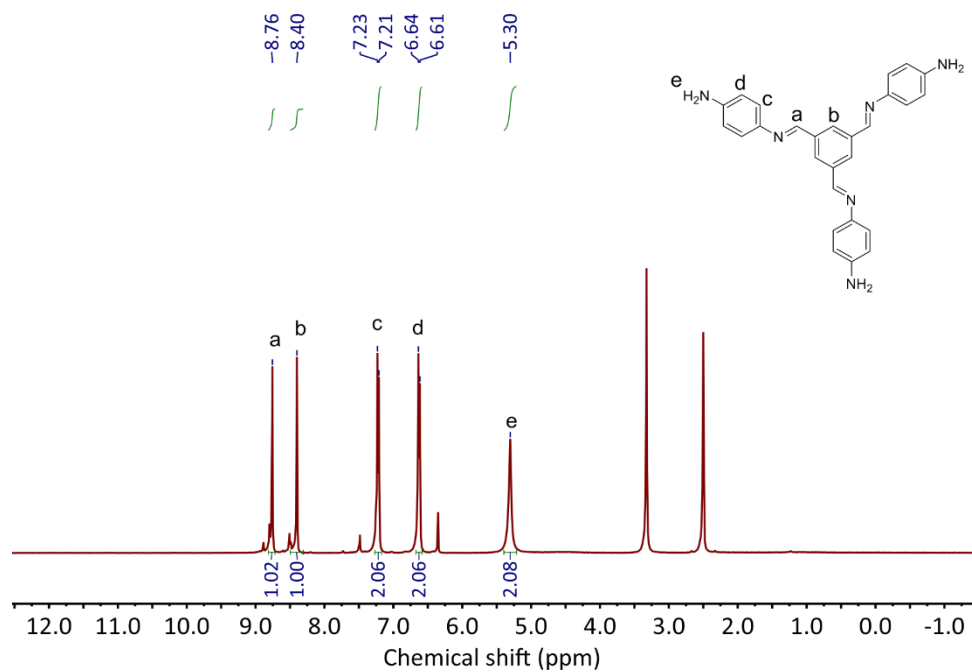
Figure S9.35. Measured liquid ^{1}H NMR spectrum of **1'**.
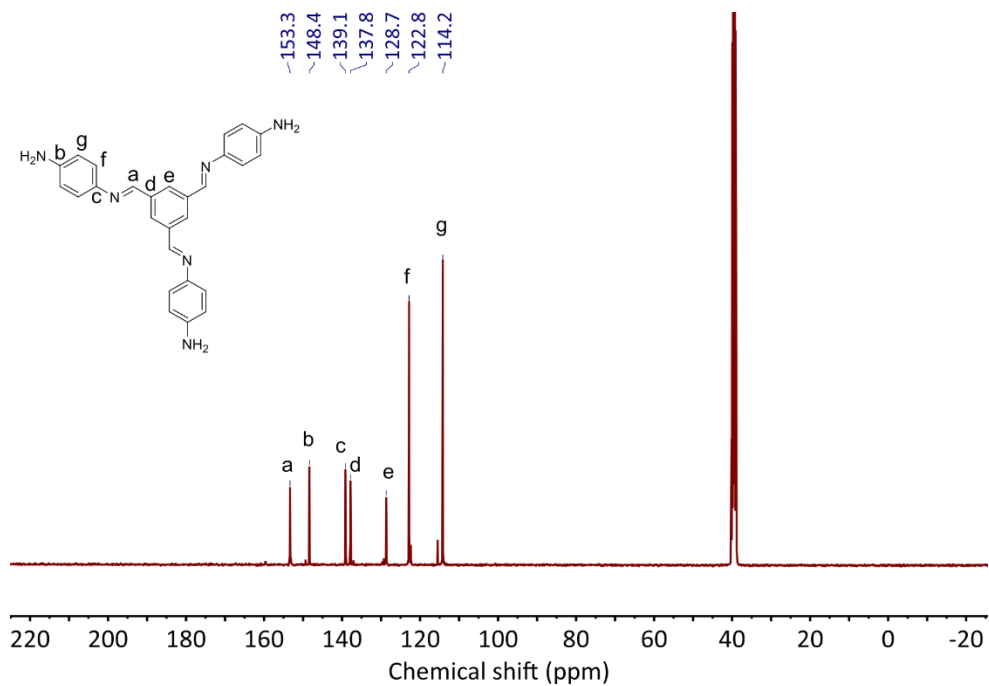
Figure S9.36. Measured liquid ^{13}C NMR spectrum of **1'**.

9.3.7. Solid State NMR
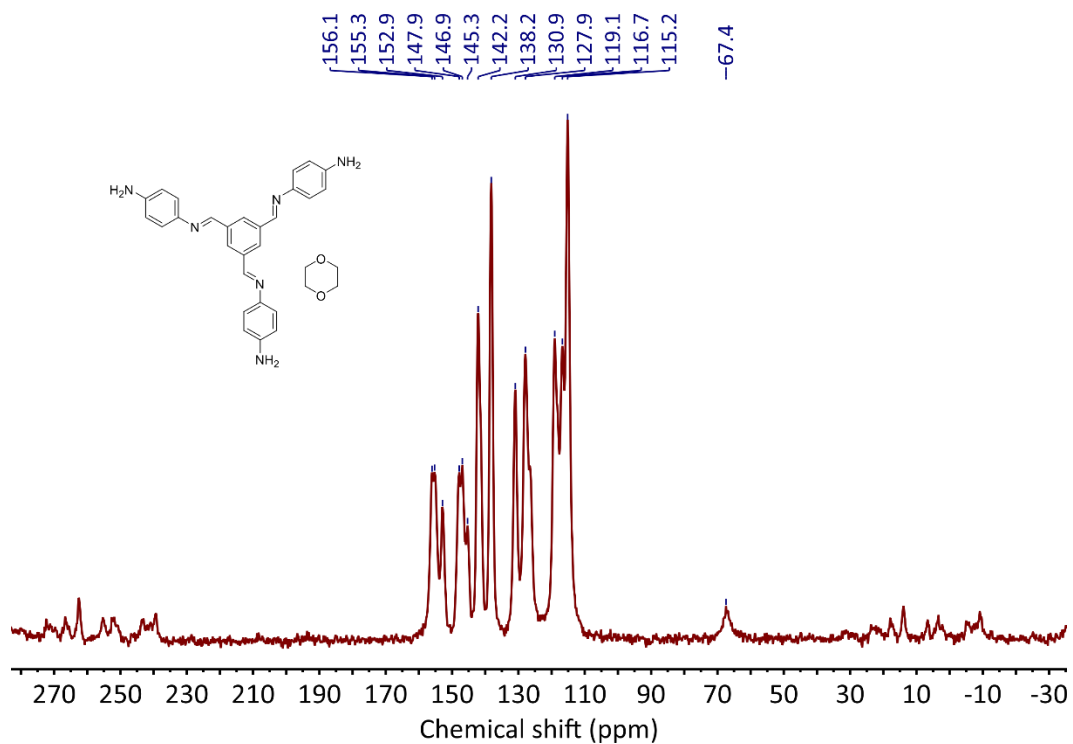
Figure S9.37. Measured ^{13}C ssNMR spectrum of **1**.
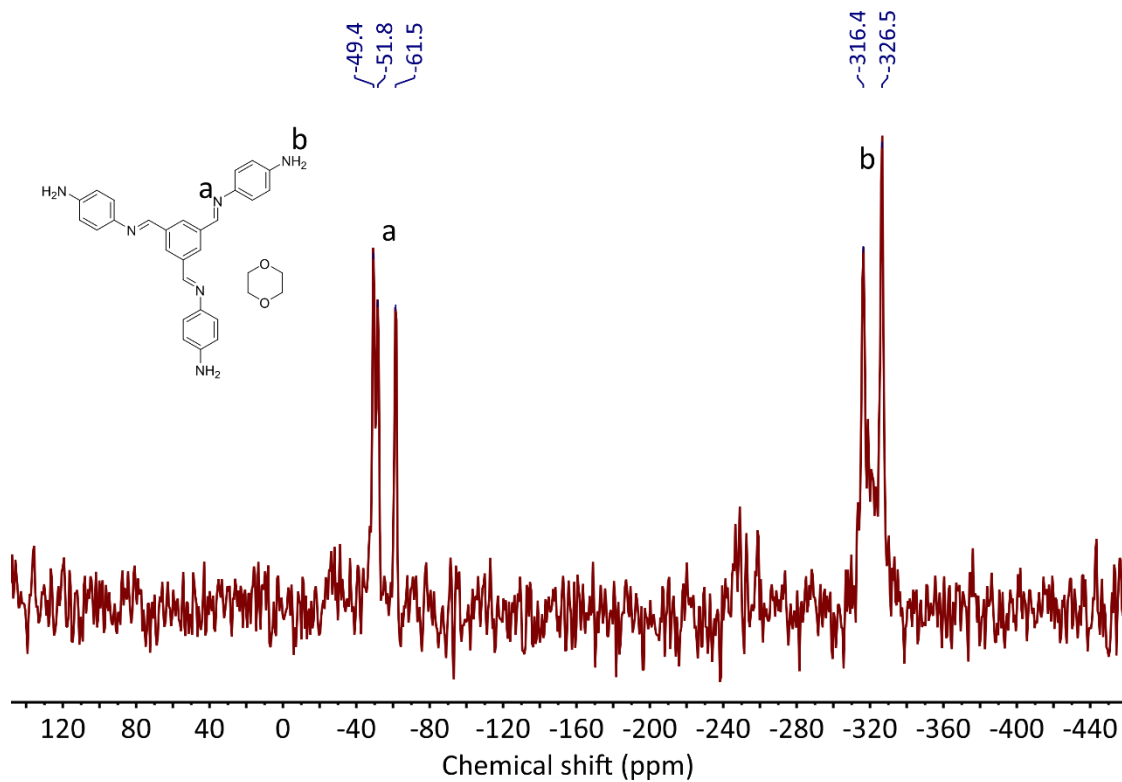
Figure S9.38. Measured ^{15}N ssNMR spectrum of **1**.
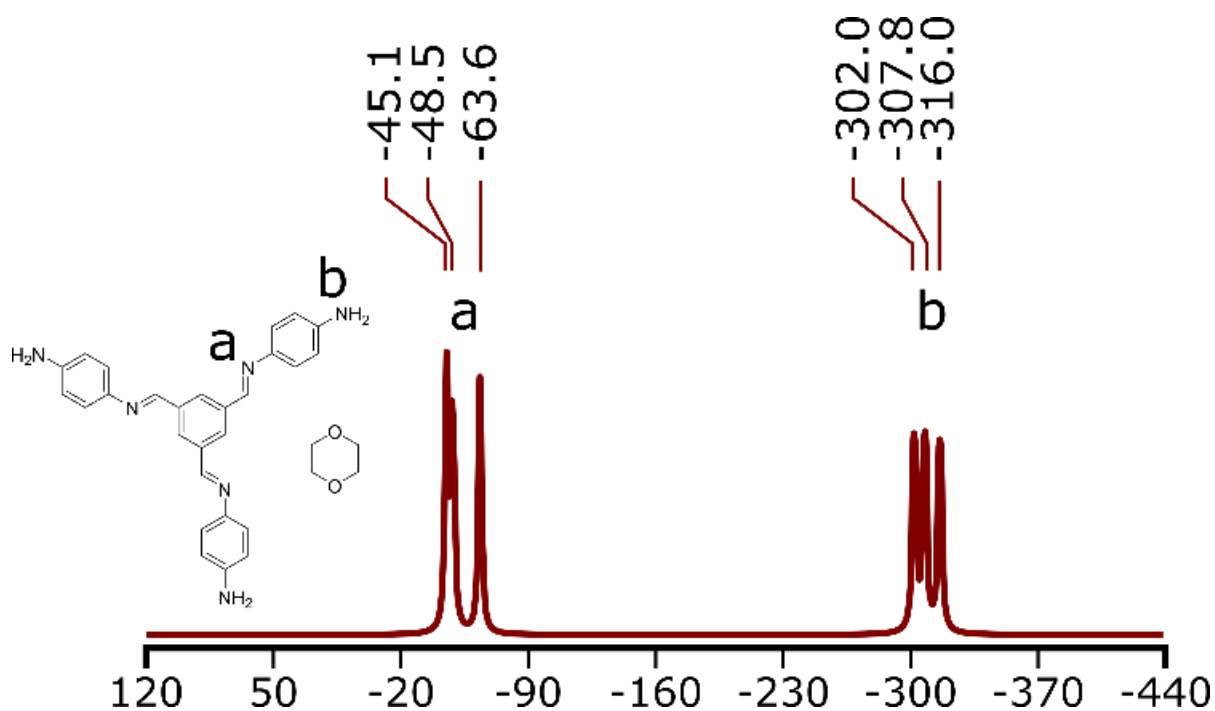
Figure S9.39. Calculated ^{15}N ssNMR spectrum of **1**.
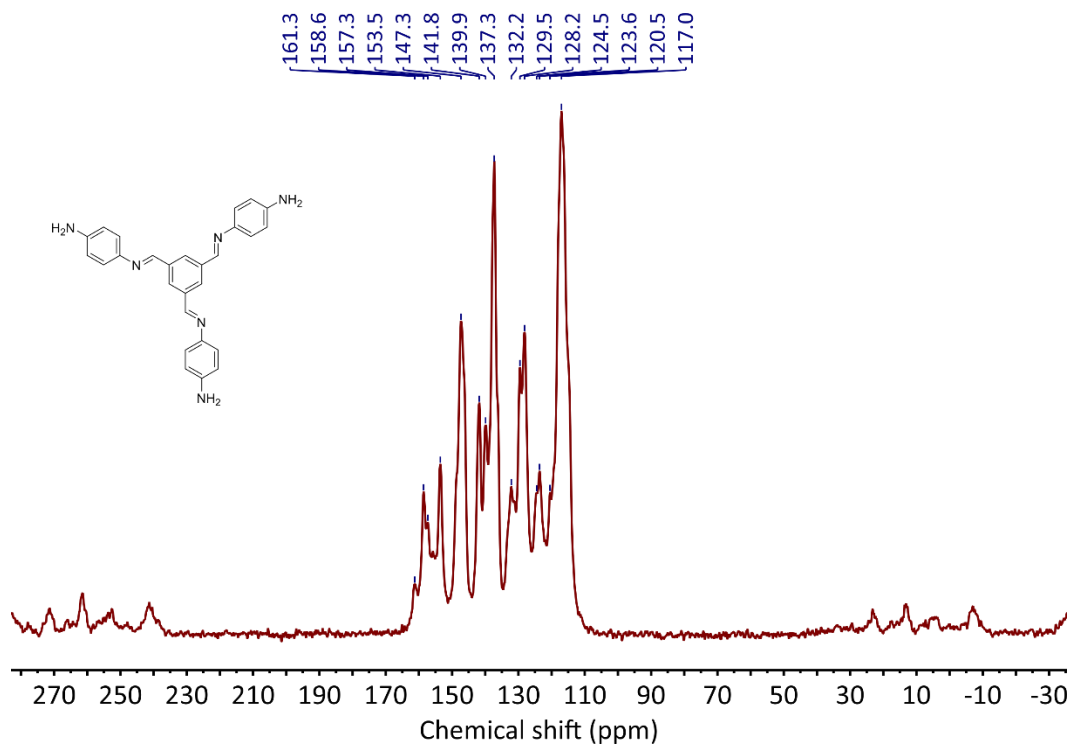
Figure S9.40. Measured ^{13}C ssNMR of the non-solvated **1'.**
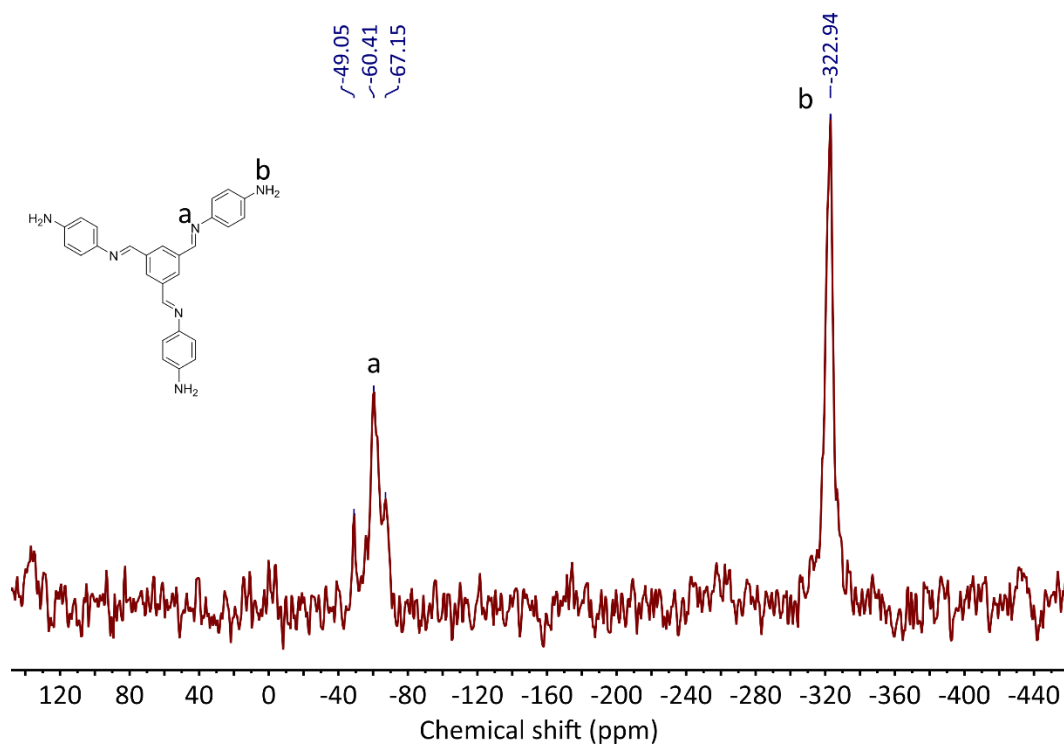
Figure S9.41. Measured ^{15}N ssNMR spectrum of the non-solvated **1'**.
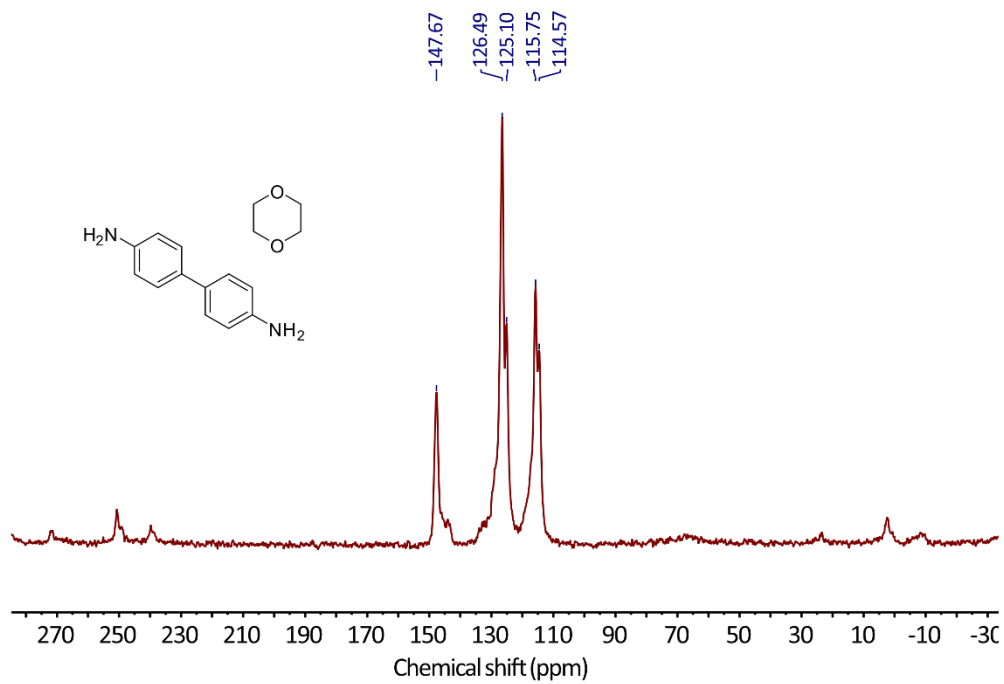
Figure S9.42. Measured ^{13}C ssNMR of intermediate **2**.
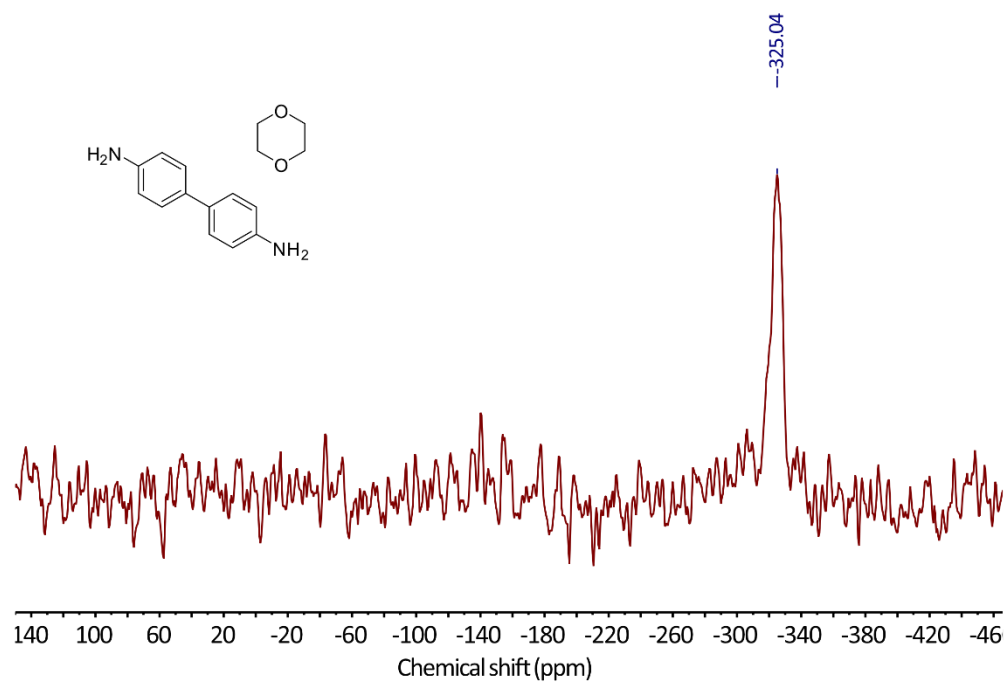
Figure S9.43. Measured ^{15}N ssNMR of intermediate 2.

9.3.8. Gas Sorption Experiments
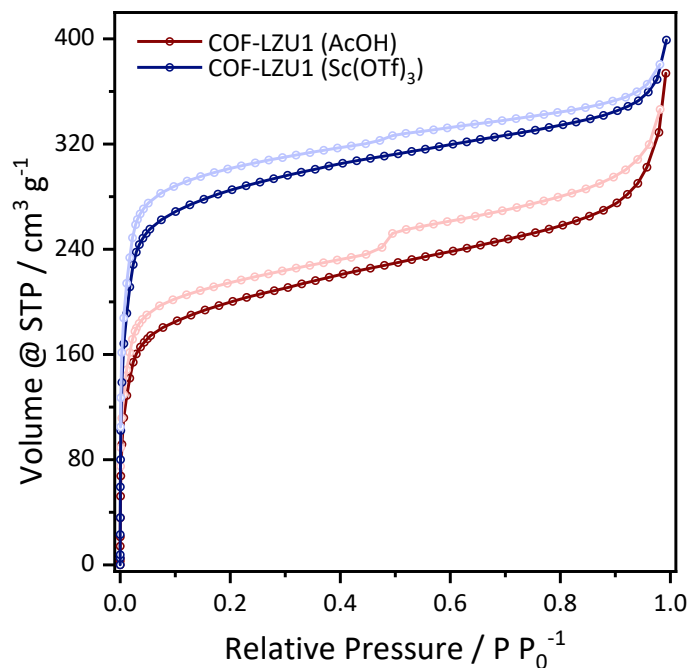
Figure S9.44. N_2-isotherms of **COF-LZU1** (AcOH, red curve), **COF-LZU1** (Sc(OTf)$_3$, blue curve), measured at 77 K. Darker colors represent adsorption, while lighter colors represent desorption.
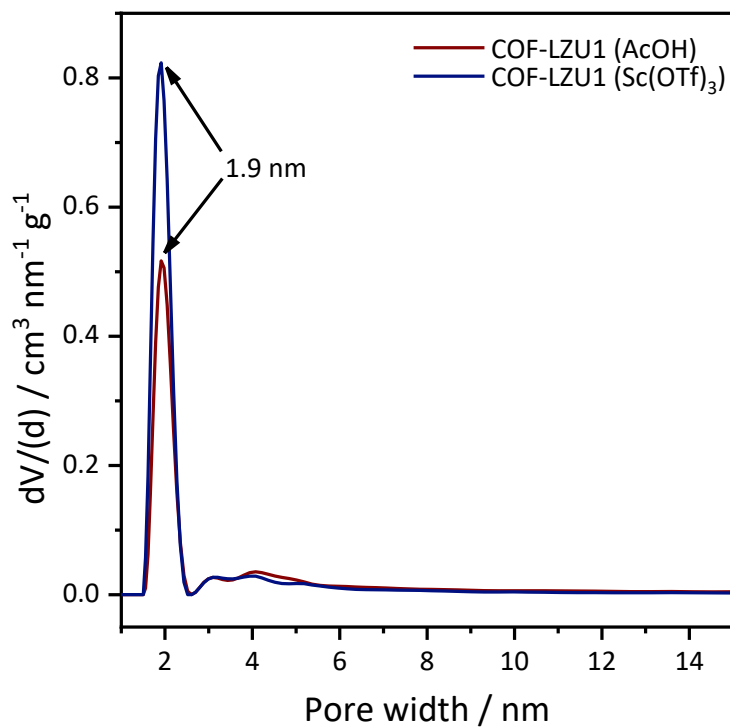
Figure S9.45. Pore size distributions of **COF-LZU1** (AcOH), **COF-LZU1** (Sc(OTf)$_3$) derived from N_2 sorption isotherms.
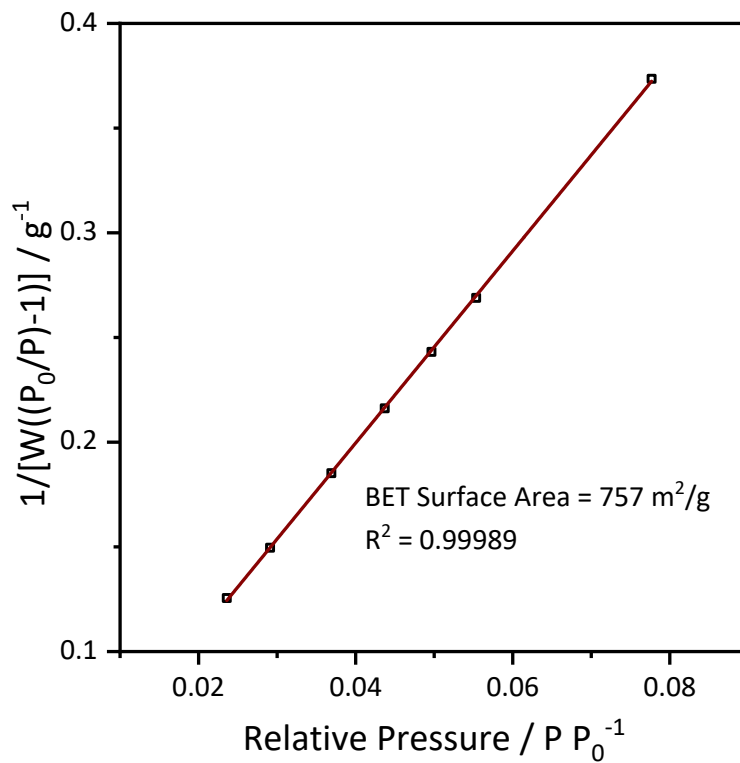
Figure S9.46. Multi-point S_{BET} surface area fit of **COF-LZU1** (AcOH) derived from N_2 sorption isotherm.
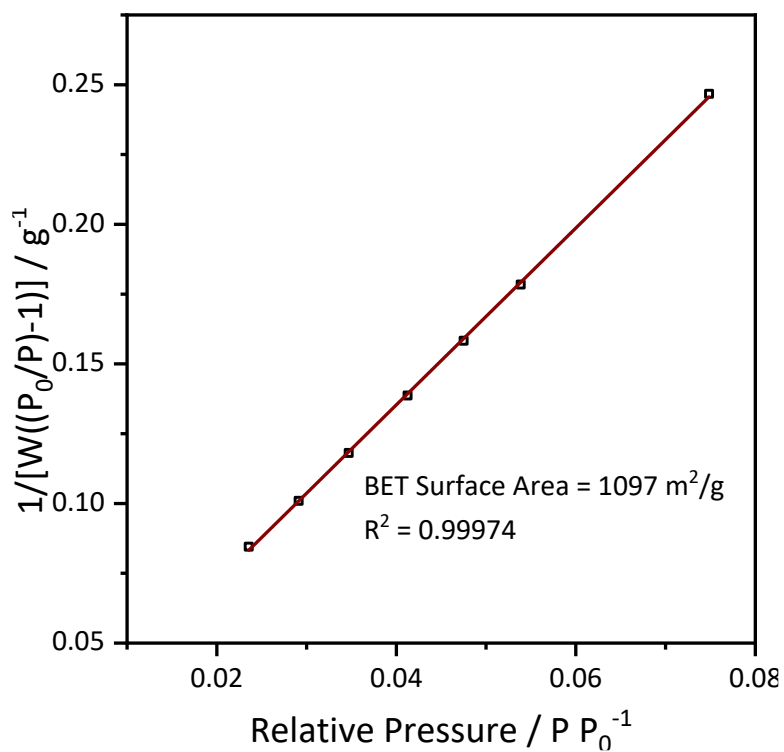
Figure S9.47. Multi-point S_{BET} surface area fit of **COF-LZU1** (Sc(OTf)$_3$) derived from N_2 sorption isotherm.
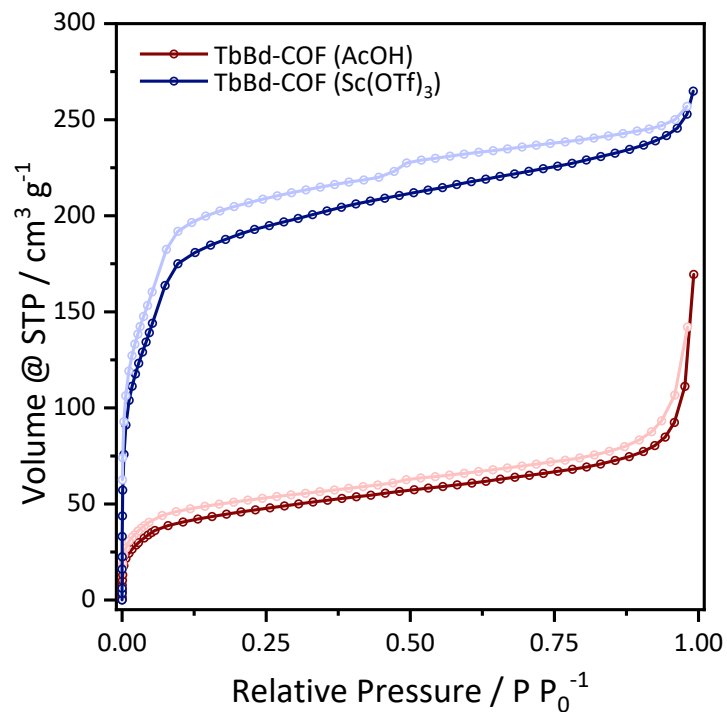
Figure S9.48. N$_2$-Isotherms of **TbBd-COF** (AcOH), **TbBd-COF** (Sc(OTf)$_3$), measured at 77 K. Darker colors represent adsorption, while lighter colors represent desorption.
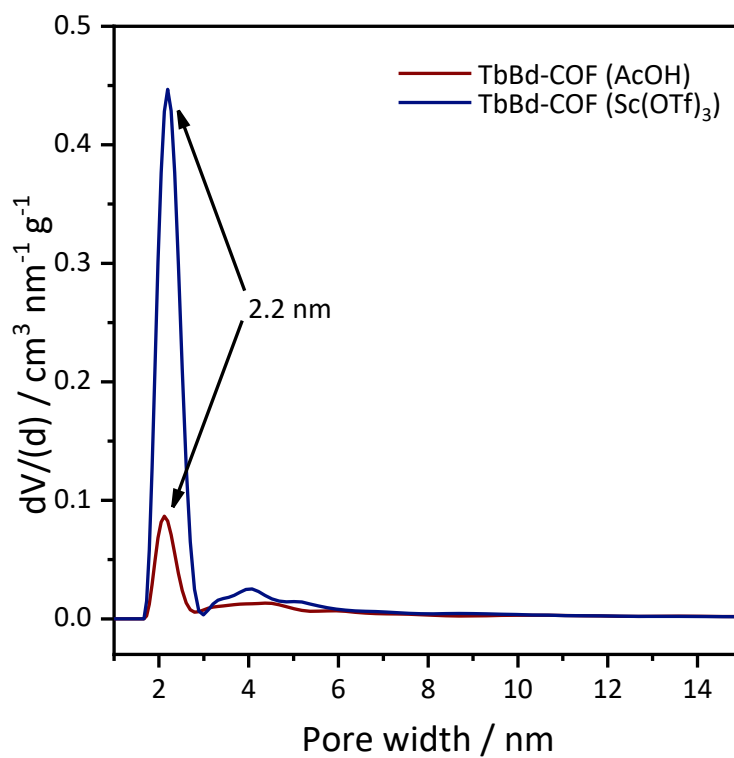
Figure S9.49. Pore size distributions of **TbBd-COF** (AcOH), **TbBd-COF** (Sc(OTf)$_3$) derived from N$_2$ sorption isotherms.
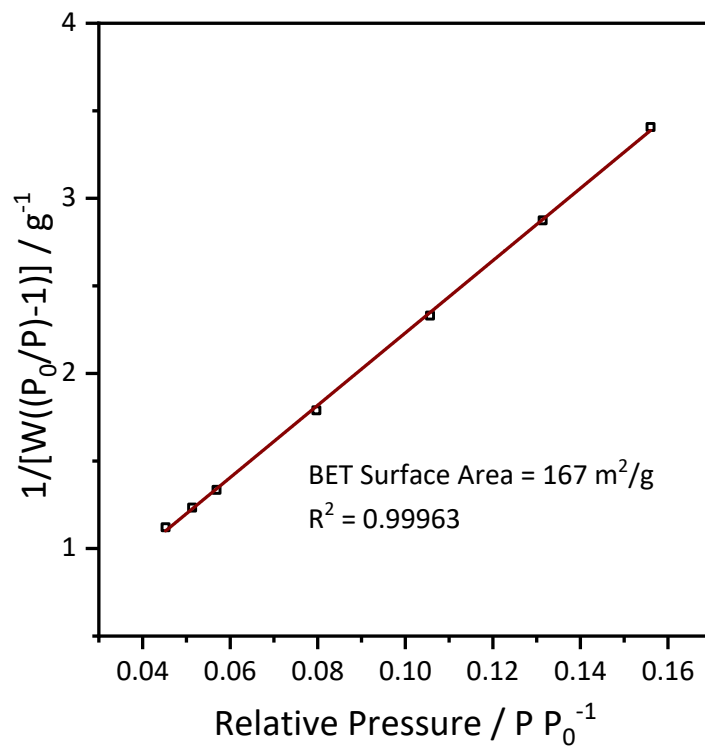
Figure S9.50. Multi-point S_{BET} surface area fit of **TbBd-COF** (AcOH) derived from N_2 sorption isotherm.
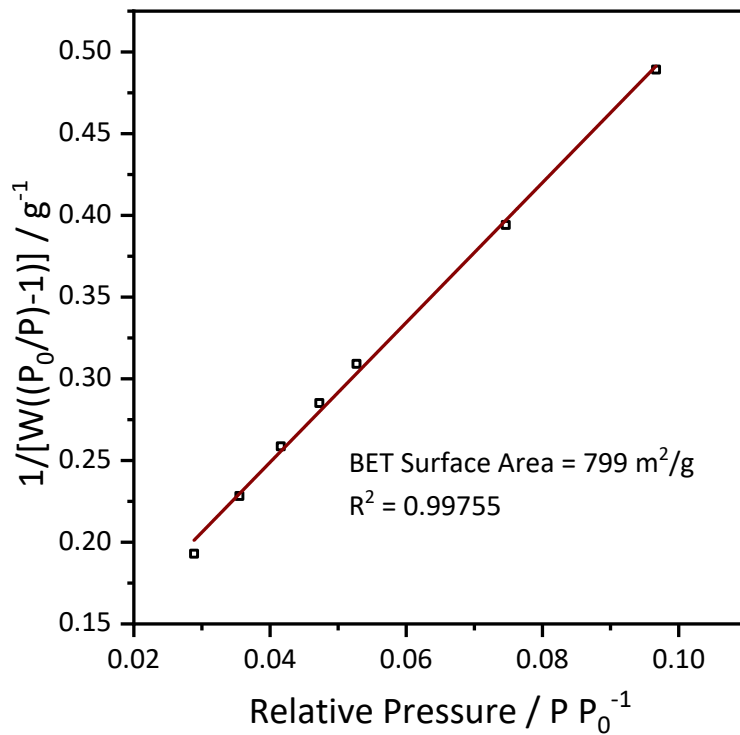
Figure S9.51. Multi-point S_{BET} surface area fit of **TbBd-COF** (Sc(OTf)$_3$) derived from N_2 sorption isotherm.
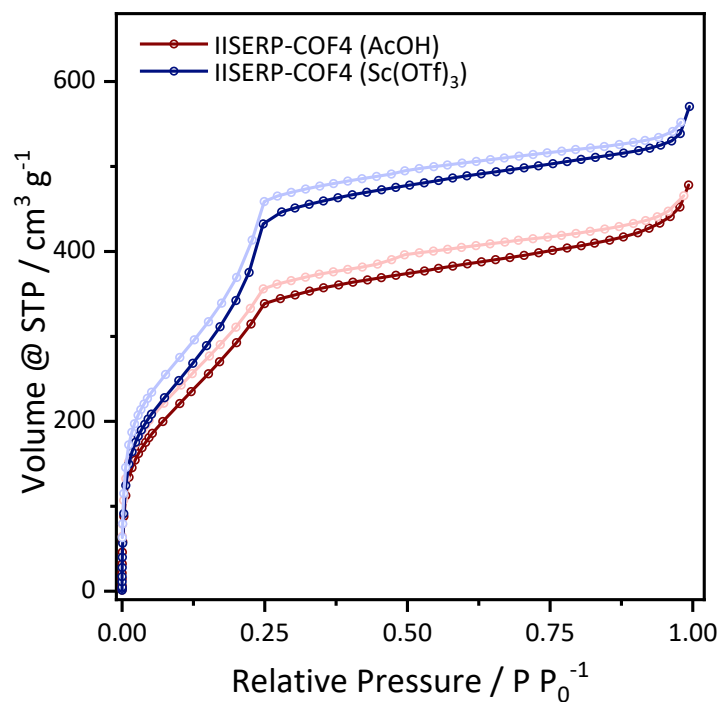
Figure S9.52. N_2-Isotherms of **IISERP-COF4** (red: AcOH), IISERP-COF4 (blue: Sc(OTf)$_3$), measured at 77 K. Darker colors represent adsorption, while lighter colors represent desorption.
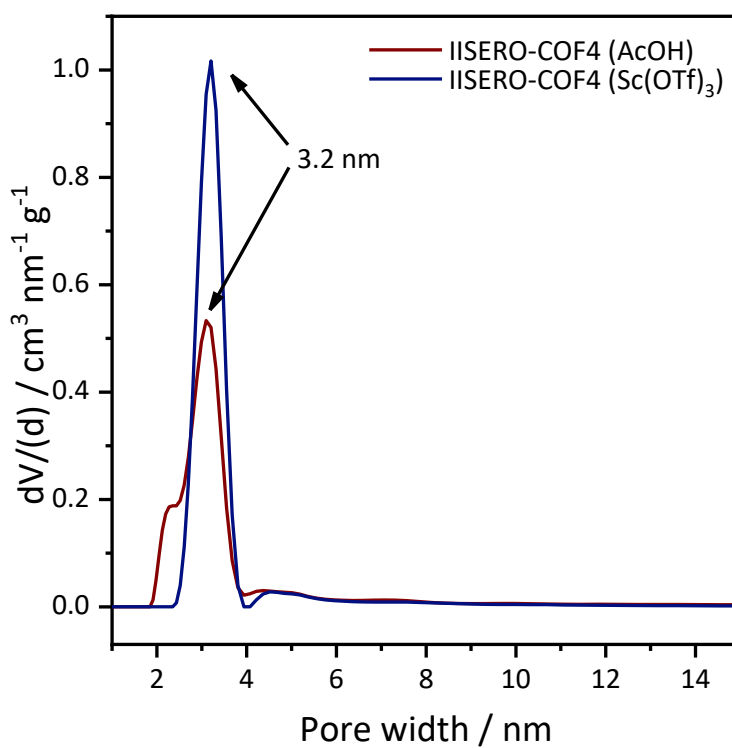
Figure S9.53**.** Pore size distributions of **IISERP-COF4** (AcOH), **IISERP-COF4** (Sc(OTf)$_3$) derived from N_2 sorption isotherms.
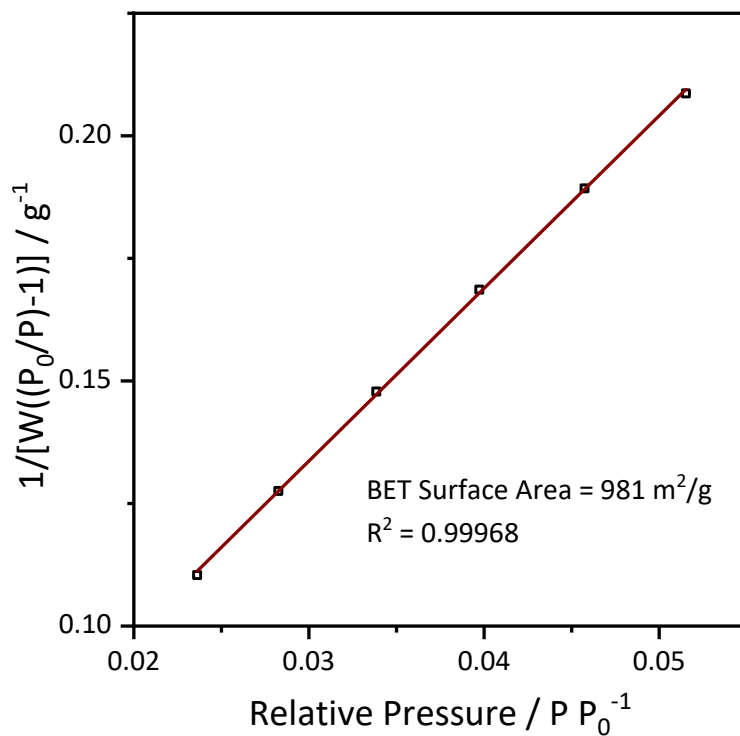
Figure S9.54. Multi-point S_{BET} surface area fit of **IISERP-COF4** (AcOH) derived from N_2 sorption isotherm.
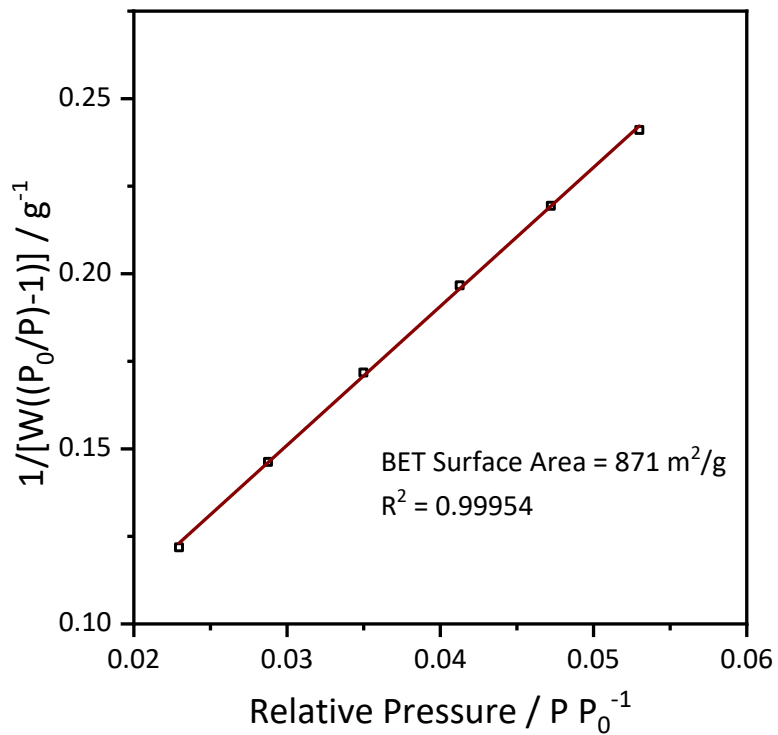
Figure S9.55. Multi-point S_{BET} surface area fit of **IISERP-COF4** (Sc(OTf)$_3$) derived from N_2 sorption isotherm.
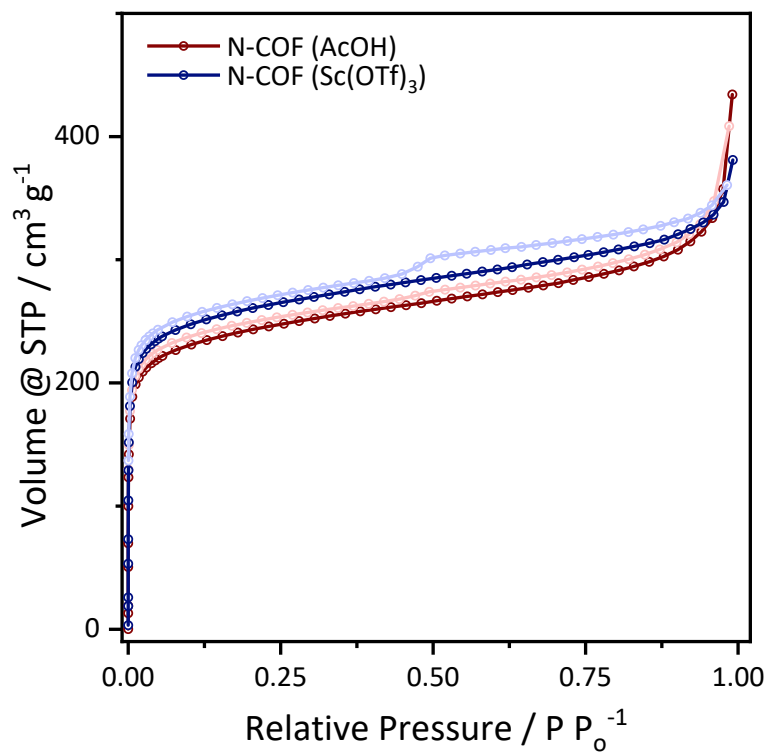
Figure S9.56. N_2-Isotherms of **N-COF** (AcOH), **N-COF** (Sc(OTf)$_3$), measured at 77 K. Darker colors represent adsorption, while lighter colors represent desorption.
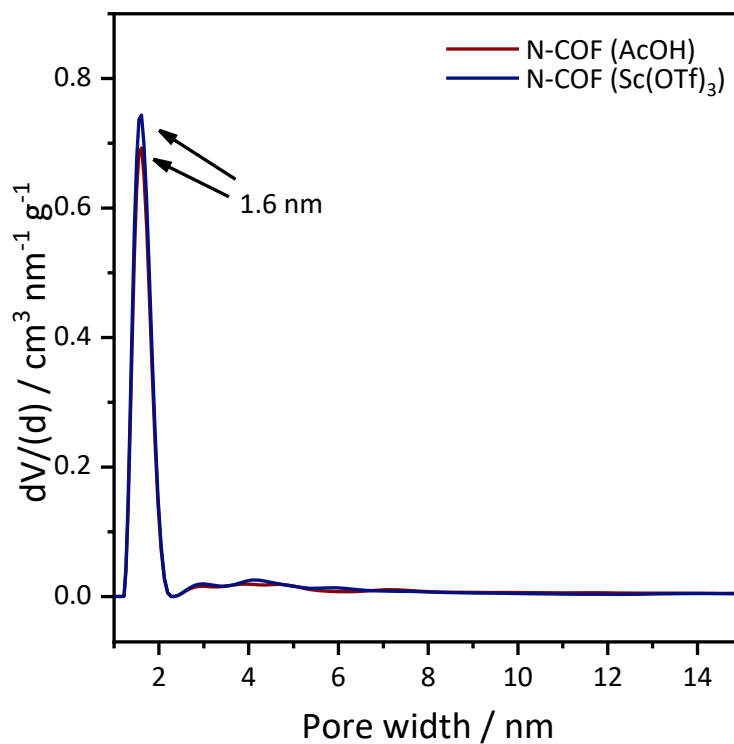
Figure S9.57. Pore size distributions of **N-COF** (AcOH), **N-COF** (Sc(OTf)$_3$) derived from N_2 sorption isotherms.
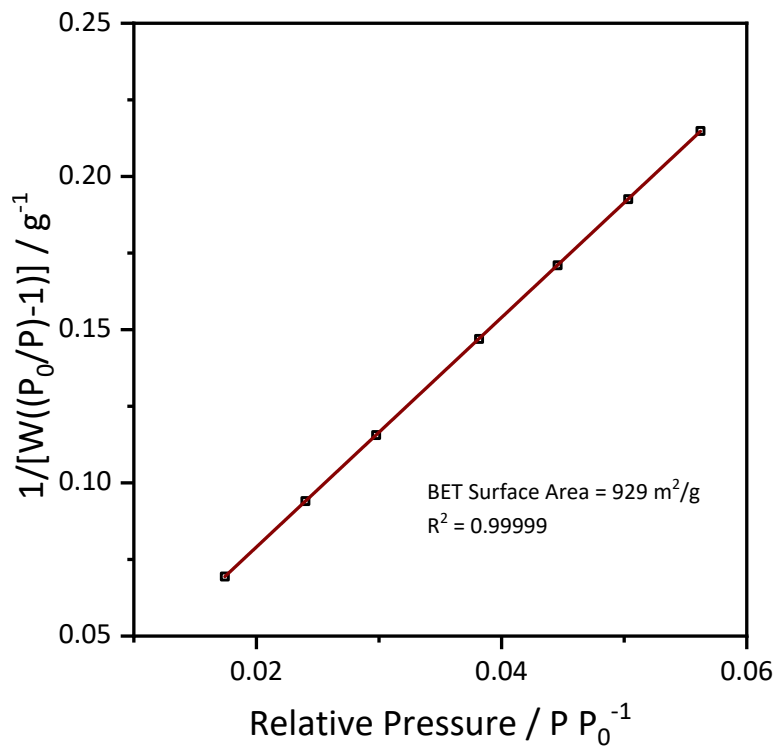
Figure S9.58. Multi-point S_{BET} surface area fit of **N-COF** (AcOH) derived from N_2 sorption isotherm.
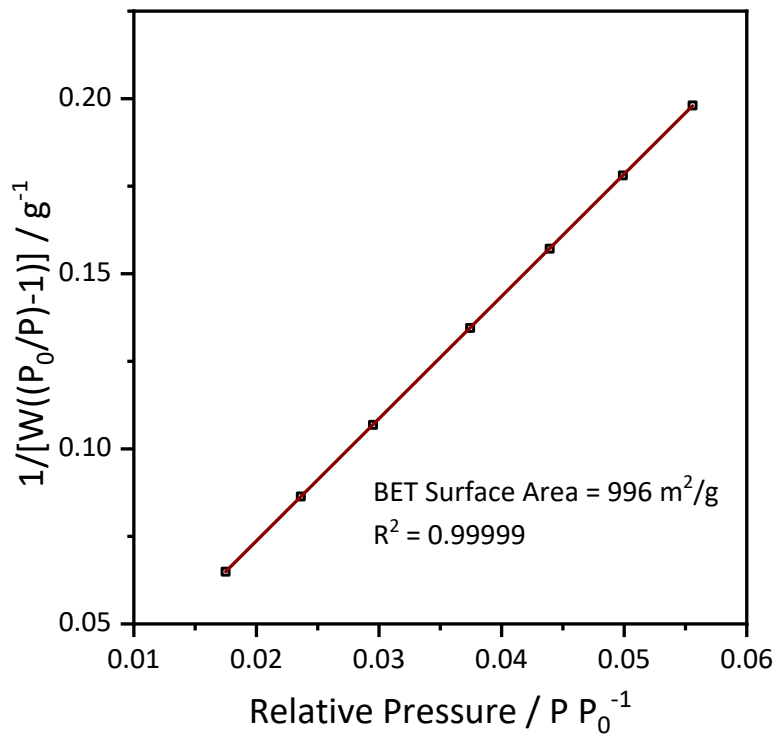
Figure S9.59. Multi-point S_{BET} surface area fit of **N-COF** (Sc(OTf)$_3$) derived from N_2 sorption isotherm.
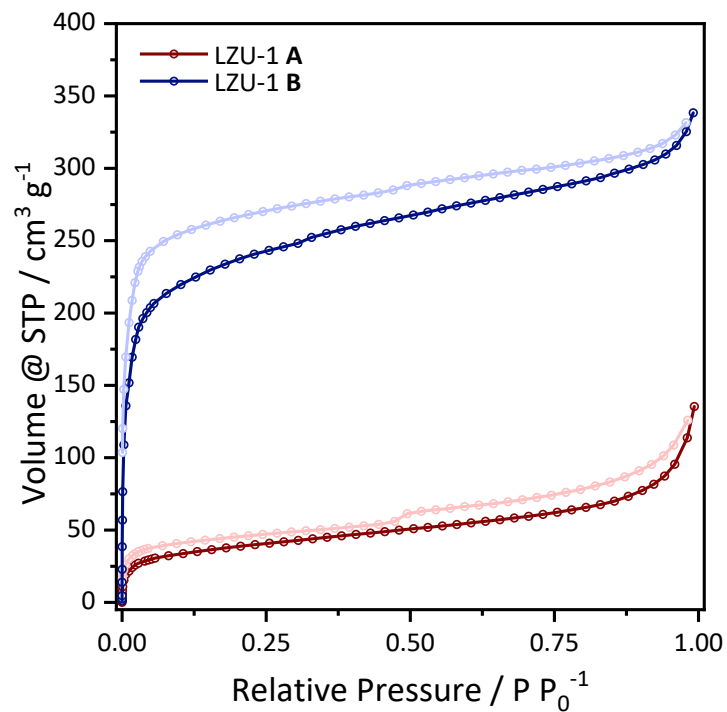
Figure S9.60. N_2-Isotherms of **COF-LZU1** with (**A**) mesitylene and (**B**) 1,4-dioxane as a liquid additive, measured at 77 K. Darker colors represent adsorption, while lighter colors represent desorption.
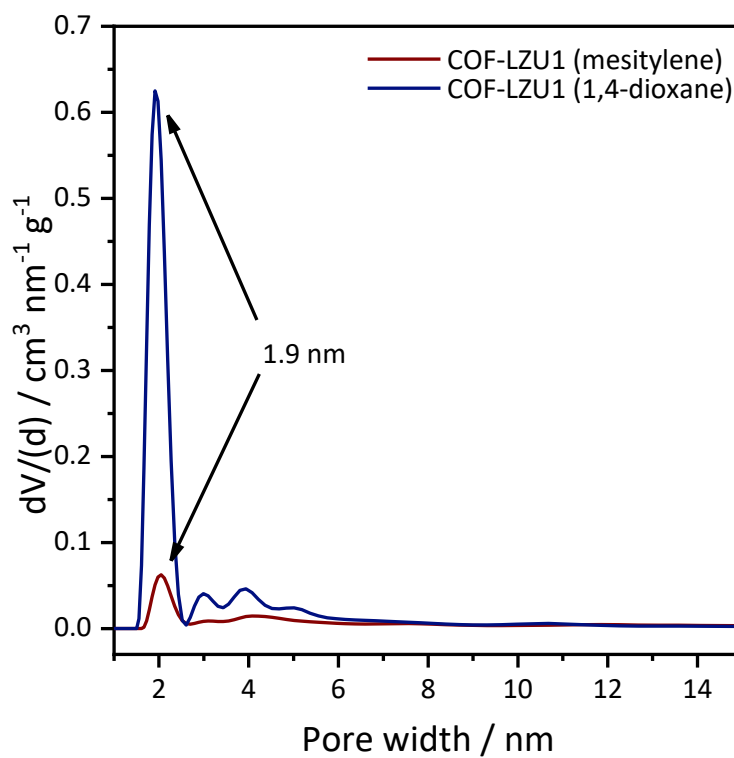
Figure S9.61. Pore size distribution of **COF-LZU1** with mesitylene (red) and 1,4-dioxane (blue) derived from N_2 sorption isotherms.
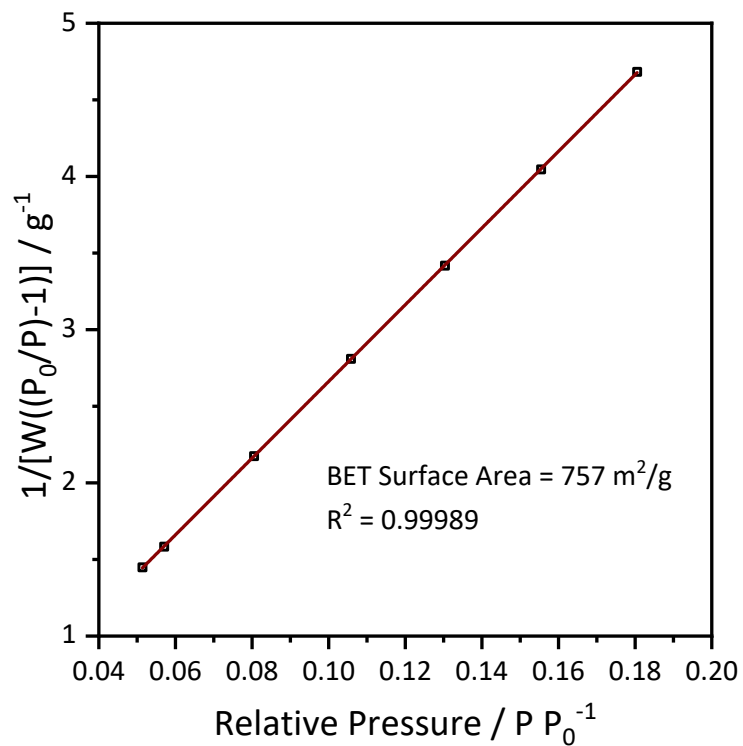
Figure S9.62. Multi-point S_{BET} surface area fit of **COF-LZU1** (mesitylene) derived from N_2 sorption isotherm.
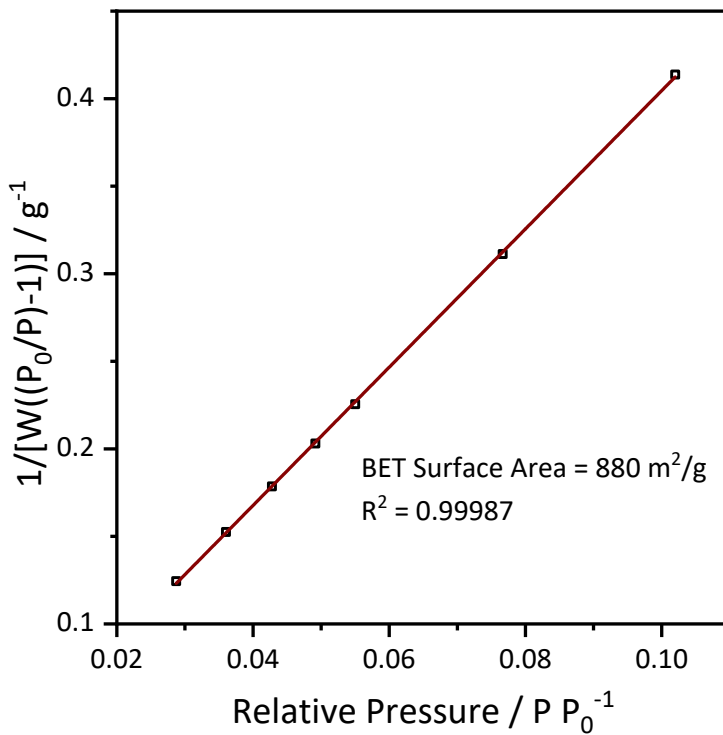
Figure S9.63. Multi-point S_{BET} surface area fit of **COF-LZU1** (1,4-dioxane) derived from N_2 sorption isotherm.

9.3.9. TGA Analysis
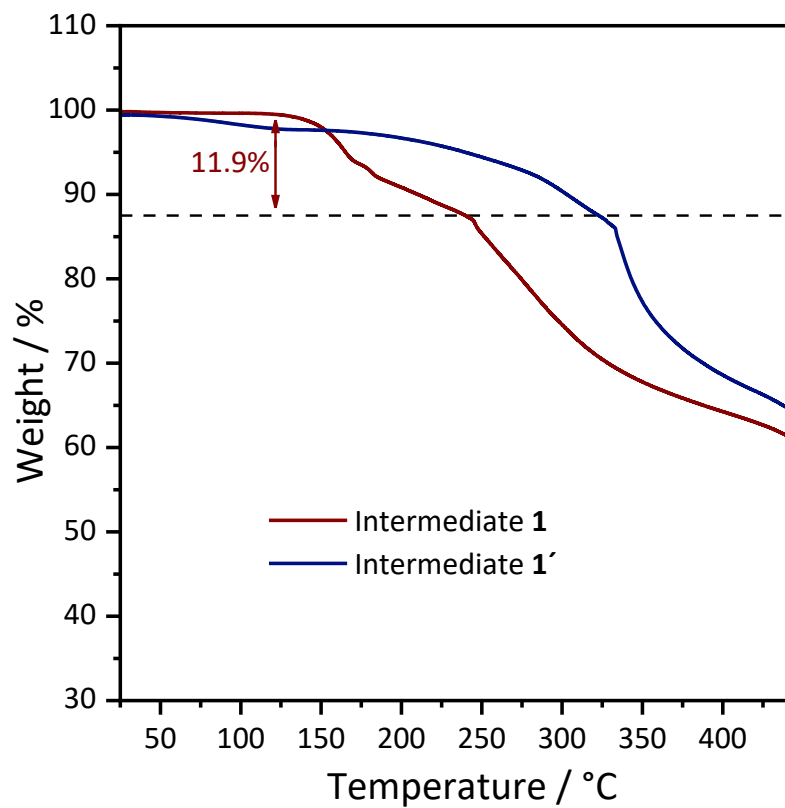
Figure S9.64. TGA curves for intermediate **1** and its non-solvated form **1´**. Measured mass loss of 11.9 % starting at ca. 150 °C corresponds to desolvation process and release of 1,4-dioxane (Δm_{calc} = 17 %).

9.3.10 Bibliography

[1]   V. S. Vyas, F. Haase, L. Stegbauer, G. Savasci, F. Podjaski, C. Ochsenfeld, B. V. Lotsch, *Nat. Commun.* **2015**, *6*, 8508.
[2]   I. Halasz, S. A. J. Kimber, P. J. Beldon, A. M. Belenguer, F. Adams, V. Honkimäki, R. C. Nightingale, R. E. Dinnebier, T. Friščić, *Nat. Protoc.* **2013**, *8*, 1718–1729.
[3]   C. Prescher, V. B. Prakapenka, *High Press. Res.* **2015**, *35*, 223–230.
[4]   A. P. Hammersley, *ESRF Intern. Rep.* **1998**, *ESRF98HA01*, FIT2D V9.129 Reference Manual V3.1 (1998).
[5]   E. J. Sonneveld, J. W. Visser, *J. Appl. Crystallogr.* **1975**, *8*, 1–7.
[6]   S. J. Clark, M. D. Segall, C. J. Pickard, P. J. Hasnip, M. I. J. Probert, K. Refson, M. C. Payne, *Zeitschrift fur Krist.* **2005**, *220*, 567–570.
[7]   T. Björkman, *Comput. Phys. Commun.* **2011**, *182*, 1183–1186.
[8]   J. P. Perdew, K. Burke, M. Ernzerhof, *Phys. Rev. Lett.* **1996**, *77*, 13865–3868.
[9]   S. Grimme, *J. Comput. Chem.* **2006**, *27*, 1787–1799.
[10]   C. J. Pickard, F. Mauri, *Phys. Rev. B - Condens. Matter Mater. Phys.* **2001**, *63*, 2451011–2451013.
[11]   S. Sturniolo, T. F. G. Green, R. M. Hanson, M. Zilka, K. Refson, P. Hodgkinson, S. P. Brown, J. R. Yates, *Solid State Nucl. Magn. Reson.* **2016**, *78*, 64–70.
[12]   L. S. Germann, A. D. Katsenis, I. Huskić, P. A. Julien, K. Užarević, M. Etter, O. K. Farha, T. Friščić, R. E. Dinnebier, *Cryst. Growth Des.* **2020**, *20*, 49–54.
[13]   L. S. Germann, M. Arhangelskis, M. Etter, R. E. Dinnebier, T. Friščić, *Chem. Sci.* **2020**, DOI 10.1039/D0SC03629C.
[14]   M. Lee, H. Kim, H. Rhee, J. Choo, *Bull. Korean Chem. Soc.* **2003**, *24*, 205–208.

9.4. Supporting Information of Chapter 7 - "NO as a Reagent for Topochemical Framework Transformation and Controlled Nitric Oxide Release in Covalent Organic Frameworks"

9.4.1. Experimental Procedures

Chemicals. All starting materials, unless otherwise specified, were obtained from Sigma-Aldrich Chemicals, and used without further purification. All solvents, unless otherwise specified, were obtained from Acros Organics, and used without further purification. ^{15}N-Ammonium Chloride was purchased from Sigma Aldrich. 2,4,6-Tris(4-aminophenyl)-1,3,5-triazine and 4,4',4''-(1,3,5-tria-zine-2,4,6-triyl)tribenzaldehyde were prepared according to a literature procedure.[3]

Fourier-Transform Infrared Spectroscopy. Fourier-transform infrared (FT-IR) spectra were recorded on a PerkinElmer UATR Two in attenuated total reflection (ATR) geometry equipped with a diamond crystal.

Transmission Electron Microscopy. Transmission electron microscopy (TEM) was performed with a Philips CM30 ST (300kV, LaB$_6$ cathode). The samples were prepared dry onto a copper lacey carbon grid (Plano). Images were recorded with a TVIPS TemCam-F216 CMOS camera. The program EM-Menu 4.0 Extended was used for analysis.

X-ray Powder Diffraction. X-ray powder diffraction (PXRD) measurements were performed on a Stoe Stadi-P diffractometer in Debye-Scherrer geometry with Cu-K$_{\alpha1}$ radiation equipped with a Ge(111) primary monochromator. The glass capillaries (1 mm in diameter) were spun during data collection for an improved particle statistics. Pawley refinements of the different COF structures were performed using TOPAS V6. Model structures created by Material Studio were used for the Pawley refinements with fixed atomic coordinates. The peak profile of the XRPD patterns was described by applying the fundamental parameter approach as implemented in TOPAS. The background was modeled by Chebychev polynomials. The microstructure of the different COFs was modeled using microstrain (Lorentzian and Gaussian components).

Nuclear Magnetic Resonance Spectroscopy. Solid state nuclear magnetic resonance spectra (ssNMR) were recorded on a Bruker Avance III 400 MHz spectrometer (magnetic field 9.4 T). For ssNMR spectroscopy, the samples were packed in ZrO$_2$ rotors, and spun in a Bruker WVT BL4 double resonance MAS probe. The spinning rate was 12-14 kHz in ^{13}C measurements, and 6 kHz in ^{15}N experiments. A standard cross-polarization sequence with a ramped contact pulse was used for both nuclei. The duration of contact pulse was 2 ms for ^{13}C and 4 ms for ^{15}N. A total of 4096-8192 scans were routinely accumulated in ^{13}C experiments, and 80000 scans in the experiments with ^{15}N. All the measurements were performed under conditions of high-power broadband proton decoupling (SPINAL 64) with the spectral conditions being optimized for the shortest relaxation delay by measuring ^{1}H T_1 relaxation time. Chemical shifts were referenced relative to

tetramethylsilane in ^{13}C (δ_{iso} = 0.0 ppm) and relative to nitromethane in ^{15}N (δ_{iso} = 0.0 ppm), with solid glycine as the secondary reference (δ_{iso} [^{15}N] = -347.54 ppm).

UV/VIS Spectroscopy. Diffuse reflectance UV-Vis spectra were collected on a Cary 5000 spectrometer referenced to barium sulfate as reference.

Sorption. Sorption measurements were performed on a Quantachrome Instruments Autosorb iQ MP. BET suface areas and pore size distributions were calculated from argon isotherms recorded at 87 K using the quenched solid-state density functional theory (QSDFT) for cylindrical pores in carbon model for argon at 87 K. CO_2 and NO isotherms were measured at 273, 288 and 298 K.[1]

Explanation of fittings and selectivity calculations based on ideal adsorption solution theory (IAST). The NO and CO_2 isotherms were fitted with a dual-site Langmuir-Freundlich model (Figure S36 and S37). n is the adsorbed gas amount (mmol g^{-1}), p is the pressure in the bulk gas phase (bar), q_{sat} is the saturation amount (mmol g^{-1}), b is the Langmuir-Freundlich parameter (bar), α is the Langmuir-Freundlich exponent (dimensionless) for two adsorption sites A and B.[2]

$$n = \frac{q_{sat,A} b_A p^{\alpha_A}}{1 + b_A p^{\alpha_A}} + \frac{q_{sat,B} b_B p^{\alpha_B}}{1 + b_B p^{\alpha_B}}$$

The IAST selectivities S_{IAST} were calculated with the IAST equation. SIAST is the selectivity (dimensionless), q is the adsorbed amount (mmol g^{-1}), and p is the partial pressure (bar). [2]

$$S_{IAST} = \frac{q_1/q_2}{p_1/p_2}$$

9.4.2. Experimental Section

Synthesis of 4,4',4''-(1,3,5-triazine-2,4,6-triyl)trianiline-^{15}N.
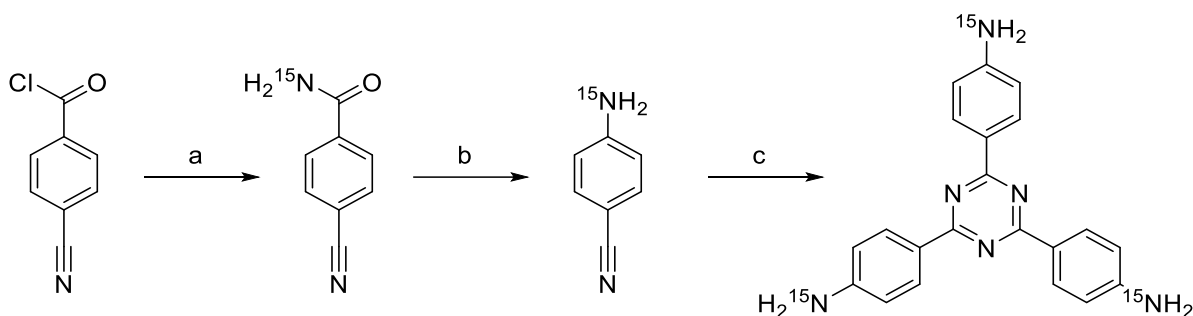
Scheme S9.4.1. Synthesis of ^{15}N-4,4',4''-(1,3,5-triazine-2,4,6-triyl)trianiline linker.

4-Cyanobenzamide-^{15}N. Ammonium chloride-^{15}N (1.81 g, 33.2 mmol) was dissolved in 12.5 mL water and the solution cooled to 0 °C. 20 mL diethyl ether was added followed by 4-cyanobenzoyl chloride (5.0 g, 20.2 mmol). After 5 minutes 5 mL aqueous sodium hydroxide (10 M) was added and the mixture stirred for 30 minutes. The white precipitate was collected by filtrations and washed with small amounts of ice cooled water. After drying the solid under air and *in vacuo*, 3.75 g (30.2 mmol, 85 %) of 4-cyanobenzamide-^{15}N was obtained.

^{1}H NMR (400 MHz, DMSO-*D*6) *δ* 8.04 – 7.99 (m, 2H), 7.97 – 7.91 (m, 2H), 7.56 (s, 2H). ^{13}C NMR (101 MHz, DMSO-*D*6) *δ* 166.57, 166.40, 138.36, 138.28, 132.41, 128.29, 118.41, 113.67. ^{15}N NMR (41 MHz, DMSO-*D*6) *δ* -273.21.

4-(Amino-^{15}N)benzonitrile. Bromine (1.58 mL, 30.9 mmol) was added dropwise to 125 mL aqueous sodium hydroxide solution (1 M) at 0 °C. 4-cyanobenzamide-^{15}N (3.0 g, 20.6 mmol) was added and the mixture stirred until fully dissolved. The solution was quickly heated to 70 °C with a pre-heated oil bath and stirred for 15 minutes before cooling to room temperature. The aqueous solution was extracted three times with dichloromethane, the combined organic phases washed with brine, dried with sodium sulfate and the solvent removed under reduced pressure. The resulting residue of 0.726 g (6.15 mmol, 30 %) 4-(amino-^{15}N)benzonitrile was used without further purification.

^{1}H NMR (400 MHz, CHLOROFORM-*D*) *δ* 7.50 – 7.36 (m, 2H), 6.76 – 6.61 (m, 2H), 4.18 (d, J = 56.0 Hz, 2H). ^{13}C NMR (101 MHz, CHLOROFORM-*D*) *δ* 150.60, 150.46, 133.92, 120.26, 114.56, 114.53, 100.28. ^{15}N NMR (41 MHz, CHLOROFORM-*D*) *δ* -315.30.

4,4',4''-(1,3,5-Triazine-2,4,6-triyl)trianiline-^{15}N. Under argon 4-(amino-^{15}N)benzonitrile (0.57 g, 4.82 mmol) was dissolved in 2 mL chloroform and trifluoromethanesulfonic acid (1.69 mL, 19.3 mmol) was added. The reaction mixture was stirred for 16 h at room temperature before 10 mL of water was carefully added and the mixture was neutralized with sodium hydroxide (1 M) to pH = 7. The precipitate was filtered off and washed with water, isopropanol, and dichloromethane.

The solid was dried *in vacuo* to obtain 0.28 g (1.59 mmol, 49 %) 4,4',4''-(1,3,5-triazine-2,4,6-triyl)trianiline-^{15}N.

^{1}H NMR (400 MHz, DMSO-*D*6) *δ* 8.35 (d, J = 8.6 Hz, 2H), 6.69 (dd, J = 8.7, 1.7 Hz, 2H), 5.90 (d, J = 85.8 Hz, 2H). ^{13}C NMR (101 MHz, DMSO-*D*6) *δ* 169.57, 153.03, 152.90, 130.14, 122.91, 113.09, 39.52. ^{15}N NMR (41 MHz, DMSO-*D*6) *δ* -308.66.

COF Synthesis

Synthesis of ^{15}N Enriched TTI-COF

TTI-COF was synthesized following a literature procedure.[3] Into a 10 mL *Biotage* microwave vial, 4,4',4''-(1,3,5-triazine-2,4,6-triyl)trianiline-^{15}N (9 mg, 0.025 mmol), 4,4',4''-(1,3,5-triazine-2,4,6-triyl)trianiline (36 mg, 0.102 mmol) and 4,4',4''-(1,3,5-triazine-2,4,6-triyl)tribenzaldehyde (50 mg, 0.127) were placed. Mesitlyene (2.5 mL), 1,4-dioxane (2.5 mL), and 6M AcOH (0.125 mL) was added. The vial was capped and placed in an aluminum heating block that was preheated to 120°C. Under stirring at 500 rpm the mixture was kept at 120°C for 72h. After cooling to room temperature the solid was isolated by filtration, washed with acetone, isopropanol, and methanol before subjecting it to a Soxhlet extraction with MeOH for 24h. The MeOH soaked solid was then activated by scCO2 drying to obtain TTI-COF (67.6 mg, 77 %).

Synthesis of ^{15}N Enriched rTTI-COF

rTTI-COF was synthesized following a literature procedure.[4] ^{15}N enriched TTI-COF (90 mg, 0.203 mmol) was suspended in mesitylene (6 mL) and 1,4-dioxane (3 mL). Formic acid (97%, 59.0 µL) was added and the suspension was heated at 120°C for 48 h. The solid was isolated by filtration, washed with methanol and subjected to a Soxhlet extraction with MeOH for 24h. The MeOH soaked solid was then activated by scCO2 drying to obtain TTI-COF (84 mg, 93 %).

Synthesis of ^{15}N Enriched TTT-COF

TTT-COF was synthesized following a literature procedure.[5] ^{15}N enriched TTI-COF (80 mg, 0.203 mmol) was thoroughly mixed with sulfur (1.2 g, 37.4 mmol) in a mortar and the homogeneous mixture was transferred to an aluminum oxide boat in a horizontal tubular furnace. Under constant argon flow, the tube was purged at 60 °C for 1 h followed by a temperature increase to 155 °C (1 K min^{-1} heating rate) for 3 h and a further increase to 350 °C (1.5 K min^{-1} heating rate) for another 3 h. After cooling to room temperature, the solid was subjected to Soxhlet extractions with CS$_2$ and methanol (24 h each). The MeOH soaked solid was then activated by scCO2 drying to obtain TTT-COF (72.2 mg, 80 %).

Synthesis of ^{15}N Enriched TT-Imide-COF

TT-Imide-COF was synthesized following a literature procedure.[6] A Schlenk tube was charged with the precursor molecules pyromellitic dianhydride (PMDA, 32.7 mg, 0.15 mmol) and ^{15}N enriched 2,4,6-tris(4-aminophenyl)-1,3,5-triazine (TT, 35.4 mg, 0.1 mmol) together with a mixture of 0.5 ml N-methyl-2-pyrrolidone, 0.5 ml mesitylene and 0.05 ml isoquinoline. The reaction mixture was degassed by four freeze-pump-thaw cycles and subsequently heated to 180 °C for 5 days. A yellow precipitate was formed, isolated by filtration and subjecting it to Soxhlet extractions with THF and methanol (24 h each). The MeOH soaked solid was then activated by scCO2 drying to obtain TT-Imide-COF (40.8 mg, 65 %).

Exposure of COFs to NO

The COFs were exposed to nitric oxide via the NO adsorption measurements on the Quantachrom Autosorb IQ3 system. All analytics on the post-NO materials were performed after the performance of all NO sorption experiments, including seven succeeding NO adsorption/desorption isotherms at 298 K and three isotherms at 298 K, 288 K and 273 K, respectively, to ensure full reaction of the frameworks with the gas.

NO release experiments

The NO release experiment was conducted by suspending 10 mg rTTI-COF-*NO* in 5 ml 0.1 M PBS buffer solution. The temperature was kept constant at 37 °C during the observation period and the mixture was shaken permanently to avoid precipitation of the COF. To determine the concentration of NO in the mixture, a Griess reagent kit for nitrite determination (G-7921) produced by *Probes* has been used. The conversion of the released nitric oxide to nitrite appears *in situ* by atmospheric oxygen:

$$2\,NO \;+\; O_2 \longrightarrow 2\,NO_2$$

$$2\,NO \;+\; 2\,NO_2 \longrightarrow 2\,N_2O_3$$

$$2\,N_2O_3 \;+\; 2\,H_2O \longrightarrow 4\,NO_2^- \;+\; 4\,H^+$$
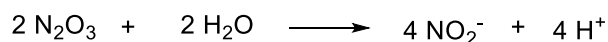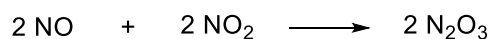
The formed nitrite is detected by using the Griess reagent through the formation of an azo-dye following the reaction:

Reagent A   Diazonium salt   Reagent B

azo dye
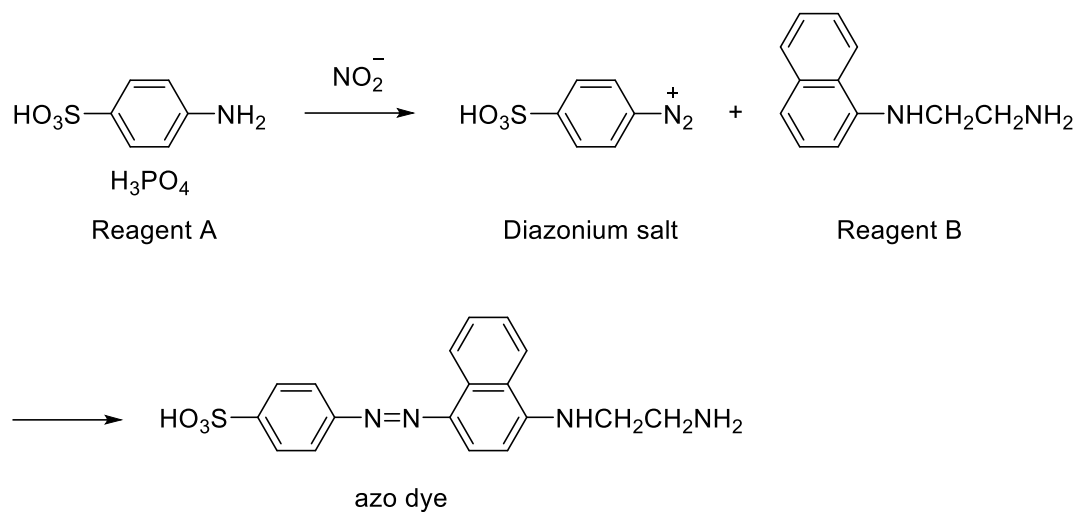
For each measurement, 500 µl sample were taken and centrifuged. 300 µl of the supernatant were mixed with 100 µl Griess reagent and diluted with 2.6 ml water. After 30 min dwelling time, the nitrite concentration was measured by UV/VIS spectroscopy using a serial dilution as reference. The remaining 200 µl supernatant together with the centrifuged COF were subsequently combined with the initial NO-release mixture again. Unavoidable volume changes through the sample withdrawal during the long-term experiment (300 µl) have been considered in the NO release calculations.

9.4.3. XRPD Measurements and Refinements

Symmetry	P1
Rwp (%)	3.147
Cell Volume	3997
alpha = beta	81.1(1)
gamma	120°
a = b	25.8(4)
c	7.2(7)
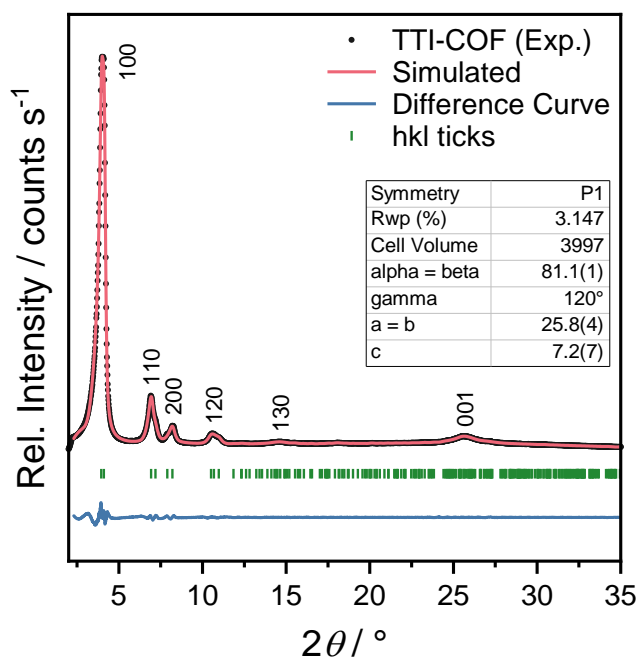
Figure S9.4.1. Experimental PXRD pattern of TTI-COF (black) together with the Pawley fit (red), calculated reflection positions, (green) and difference curves (blue).

Symmetry	P63/m
Rwp (%)	3.291
Cell Volume	3859
alpha = beta	90°
gamma	120°
a = b	25.09(2)
c	7.07(9)
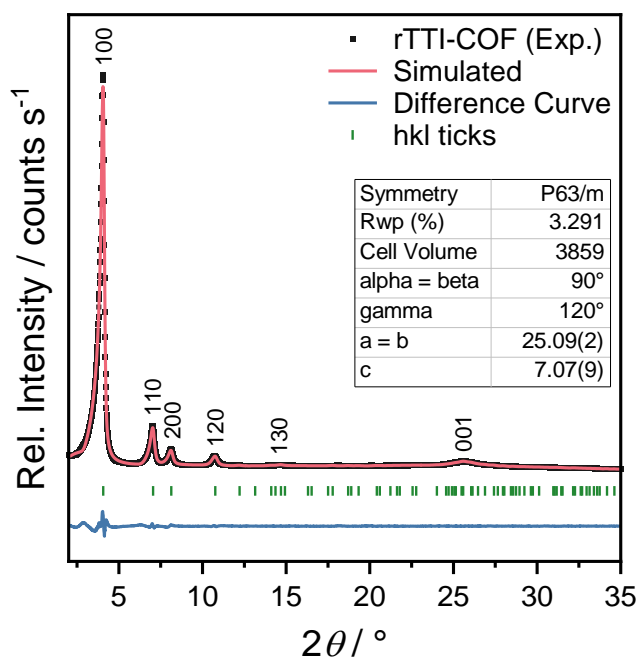
Figure S9.4.2. Experimental PXRD pattern of rTTI-COF (black) together with the Pawley fit (red), calculated reflection positions, (green) and difference curves (blue).
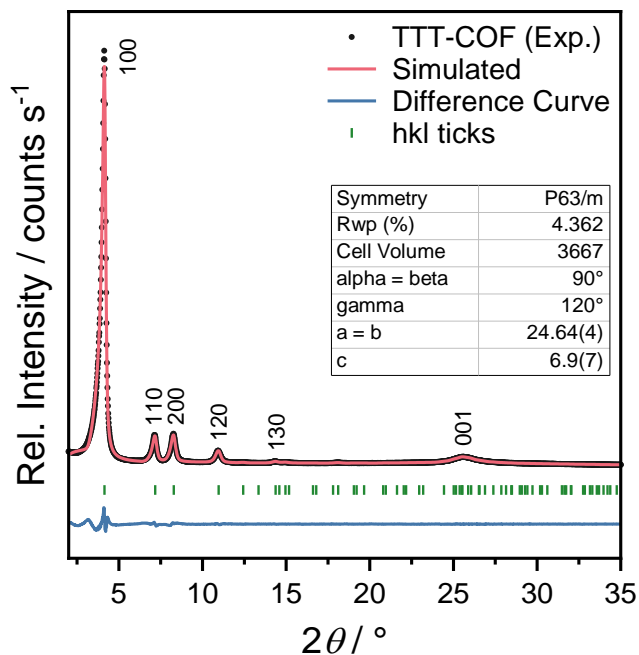
Figure S9.4.3. Experimental PXRD pattern of TTT-COF (black) together with the Pawley fit (red), calculated reflection positions, (green) and difference curves (blue).
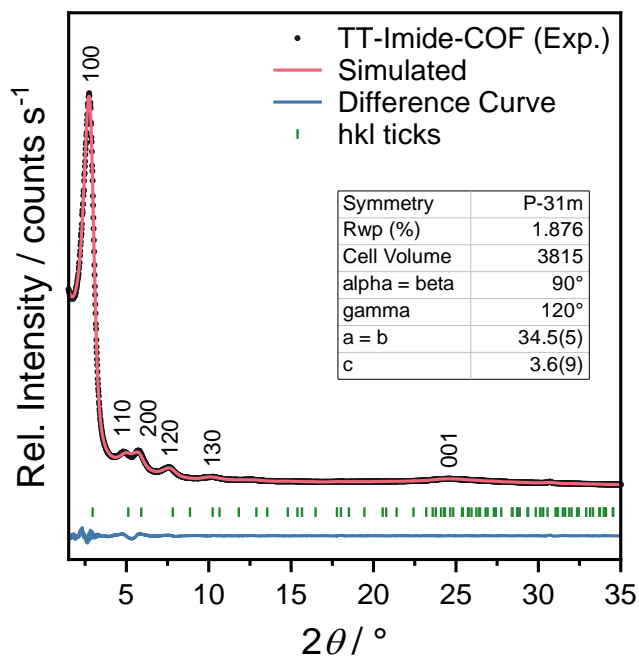
Figure S9.4.4. Experimental PXRD pattern of TT-Imide-COF (black) together with the Pawley fit (red), calculated reflection positions (green), and difference curves (blue).
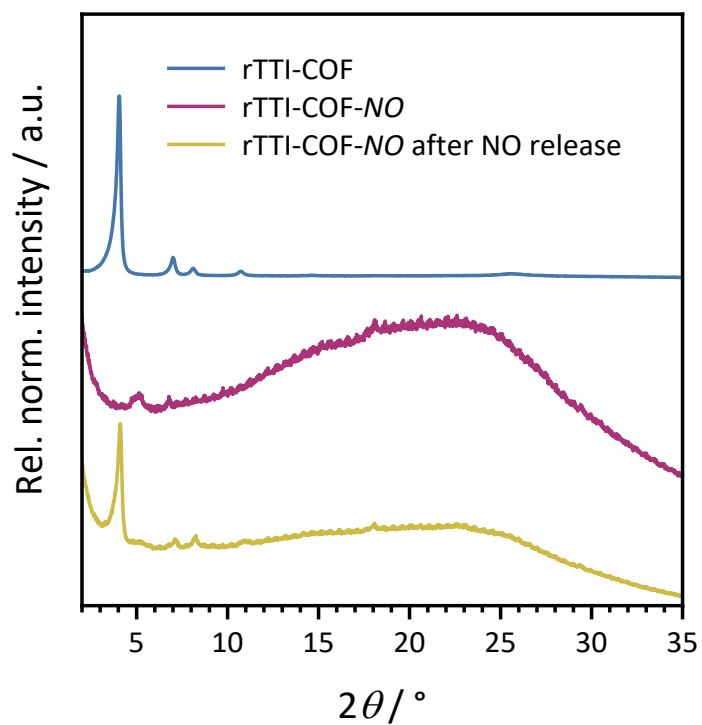
Figure S9.4.5. Comparison of experimental PXRD patterns of rTTI-COF (blue), rTTI-COF-NO, and rTTI-COF-NO after NO release.

9.4.4. FT-IR Spectroscopy
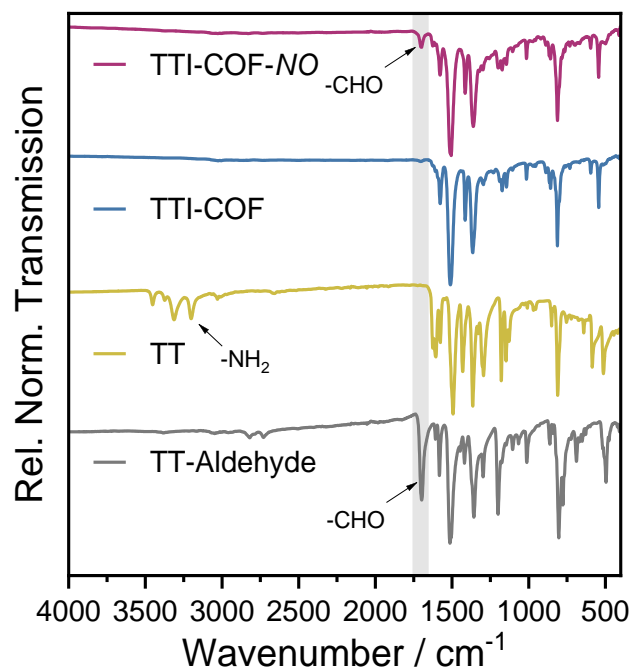
Figure S9.4.6. FT-IR spectra of TTI-COF before (blue) and after NO sorption experiments (red) together with FT-IR spectra of the precursor molecules TT-Aldehyde (black) and TT (yellow). The absence of amine vibrational bands at 3367 cm^{-1} and aldehyde vibrational bands at 1698 cm^{-1} in the COF spectrum indicate complete imine formation. After NO treatment the aldehyde vibrational band at 1698 cm^{-1} of the precursor TT-Aldehyde appears again, indicating imine bond breaking.
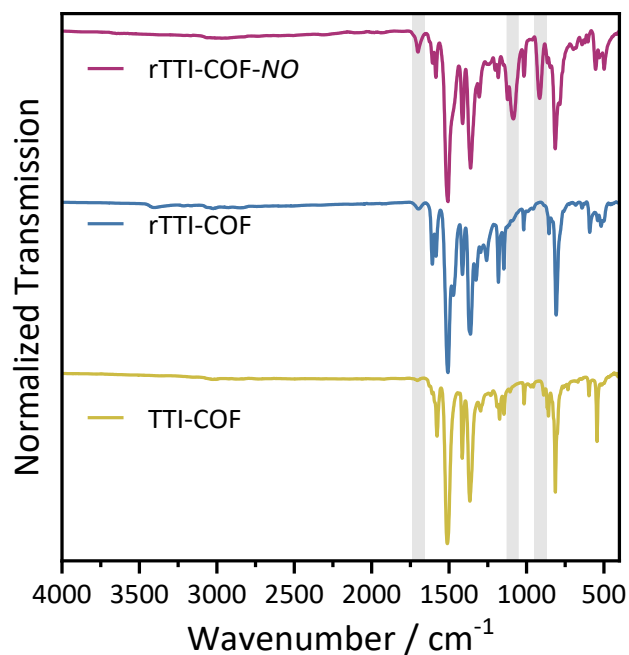
Figure S9.4.7. FT-IR spectra of rTTI-COF before (blue) and after NO adsorption experiments (red) together with the FT-IR spectrum of the precursor TTI-COF (yellow). After NO treatment three additional vibrational bands at 1700 cm^{-1}, 1084 cm^{-1}, and 916 cm^{-1} appear, indicating the formation of the NONOate.
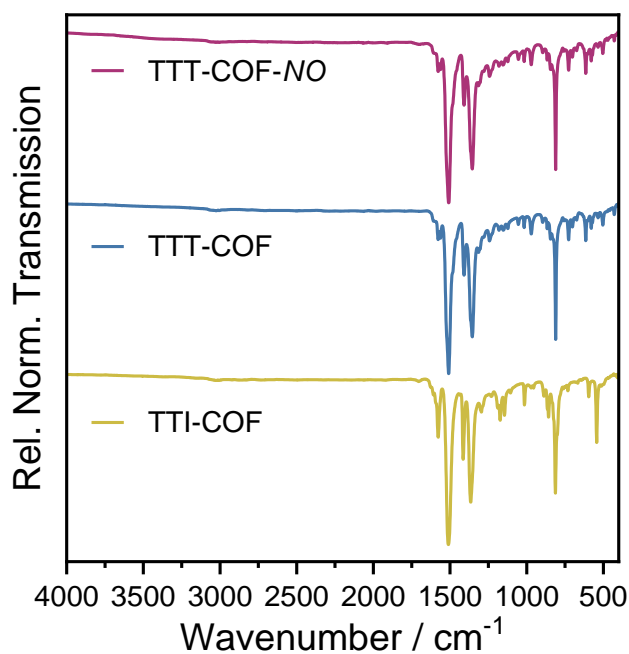
Figure S9.4.8. FT-IR spectra of TTT-COF before (blue) and after NO adsorption experiments (red) together with the FT-IR spectrum of the precursor TTI-COF (yellow). No changes can be observed in the spectrum of TTT-COF after NO treatment, indicating inertness of the system against NO.
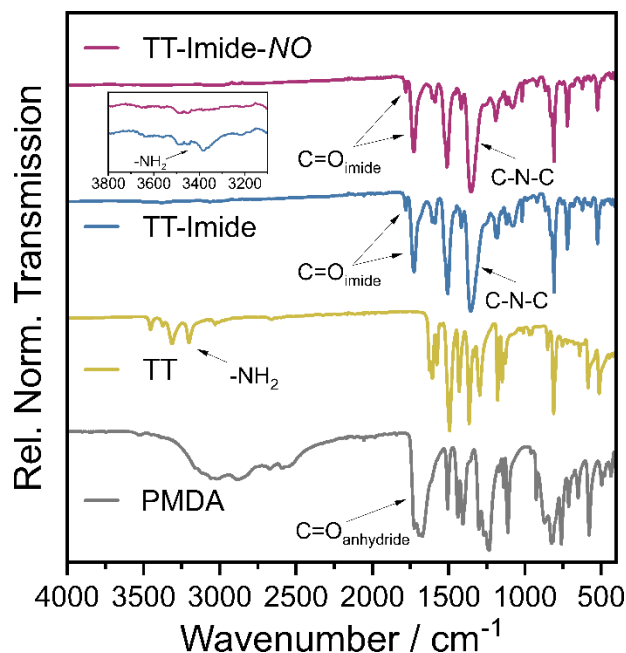
Figure S9.4.9. FT-IR spectra of TT-Imide-COF before (blue) and after NO adsorption experiments (red) together with FT-IR spectra of the precursor molecules PMDA (black) and TT (yellow). The absence of amine vibrational bands at 3367 cm^{-1} and anhydride vibrational bands at 1700 cm^{-1} in the COFs spectrum indicate complete imide formation. No strong changes can be observed in the spectrum after NO treatment, indicating strong inertness of the system towards NO. Inset shows the disappearance of faint amine vibrational bands at 3367 cm^{-1} after the NO-treatment, which are in good agreement to the findings of by ^{15}N CP-MAS ssNMR.
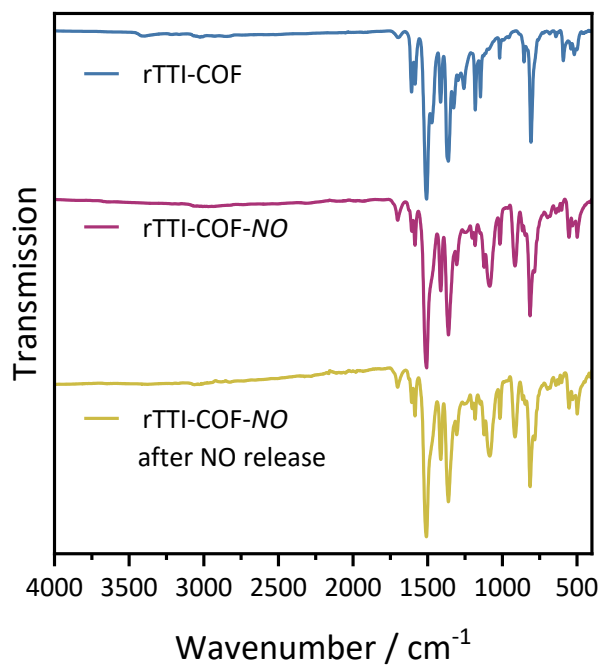
Figure S9.4.10. FT-IR spectra of rTTI-COF before (blue) and after NO adsorption experiments (red) as well as after the NO release (yellow), which show no significant changes.

9.4.5. Liquid and Solid State NMR
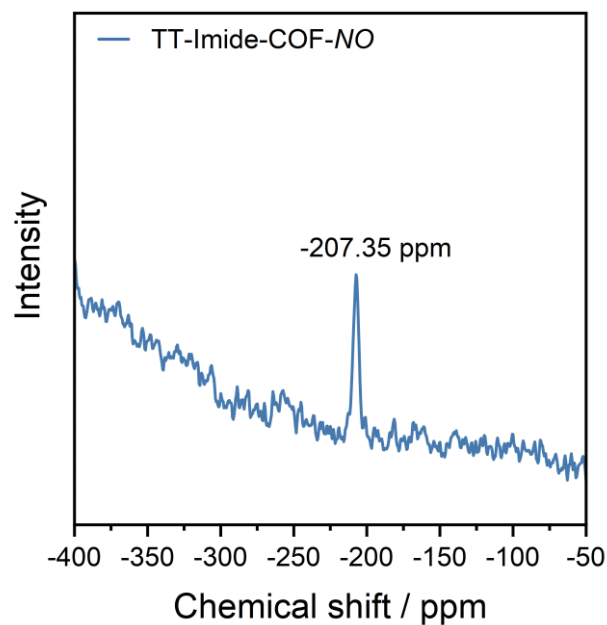
Figure S9.4.11. ^{15}N direct excitation NMR spectrum of TT-Imide COF showing one signal corresponding to the imide nitrogen at -207.35 ppm.
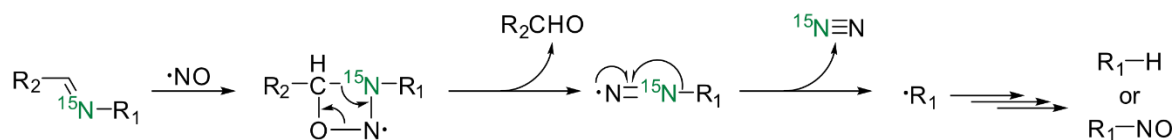
Scheme S9.4.2. Mechanism of imine linkage degradation by a [2+2] cycloaddition of NO to the imine bond, proposed by Hrabie et al.[7]

−273.21
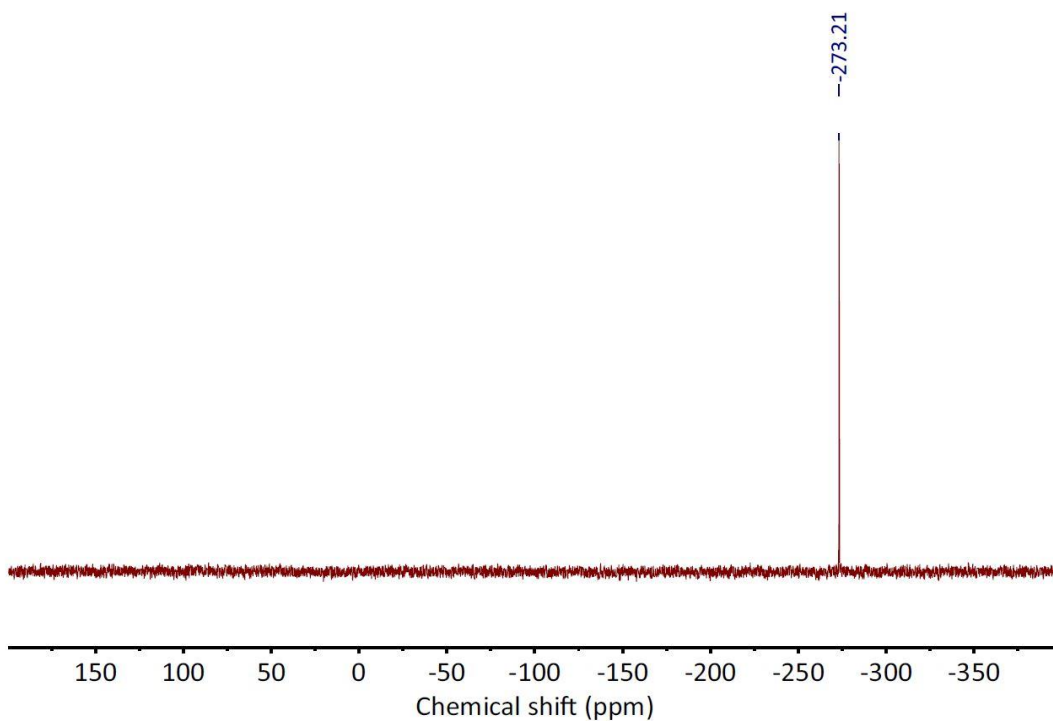
Figure S9.4.12. ^{15}N NMR of **4-cyanobenzamide-^{15}N** in DMSO-*D*6.

−315.30
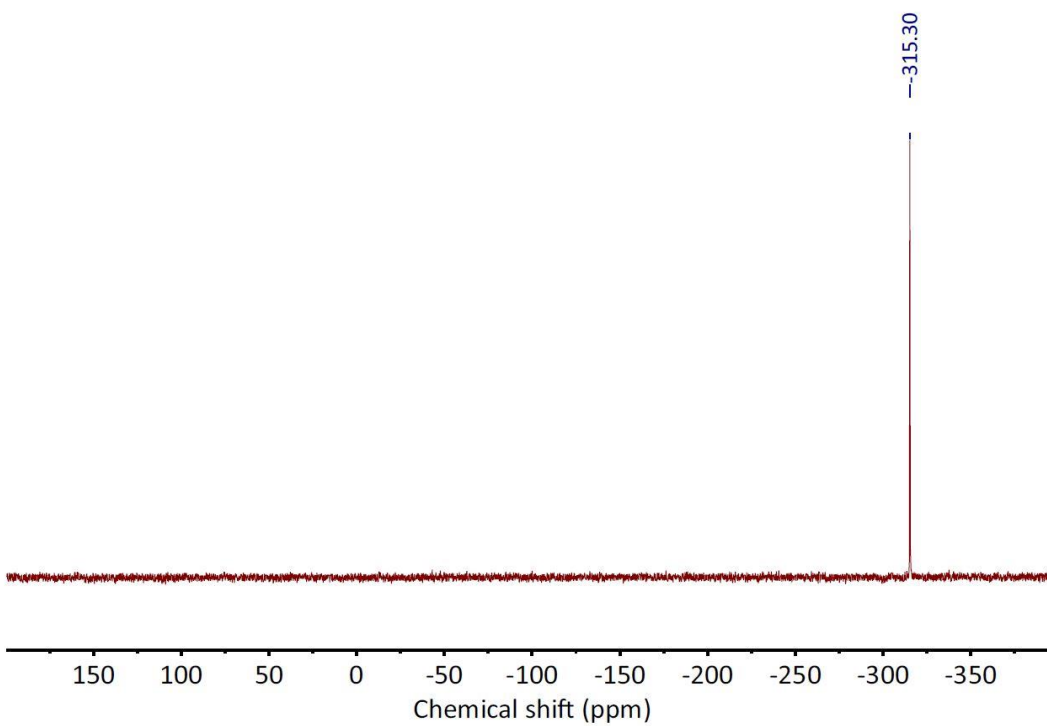
Figure S9.4.13. ^{15}N NMR of **4-(amino-^{15}N)benzonitrile** in CDCl₃.

−308.66
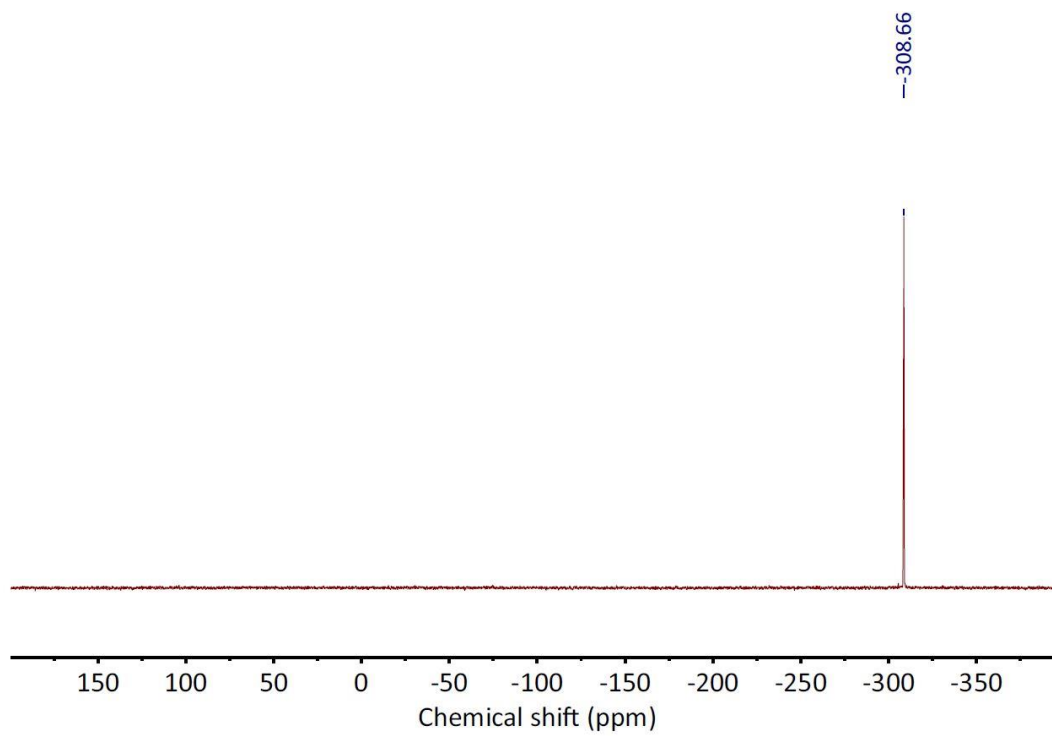
Figure S9.4.14. ^{15}N NMR of **4,4',4''-(1,3,5-triazine-2,4,6-triyl)trianiline-^{15}N** in DMSO-*D*6.

9.4.6. TEM analysis
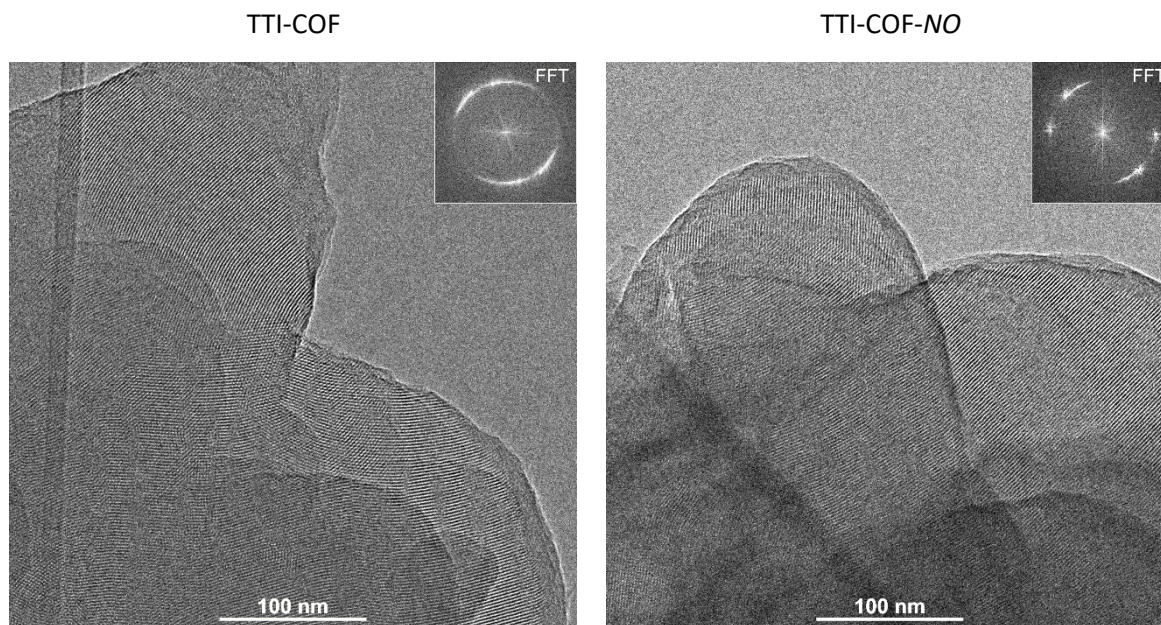
TTI-COF

TTI-COF-*NO*

Figure S9.4.15. TEM images of TTI-COF before (left) and after NO sorption measurements (right) showing retention of the crystalline structure.
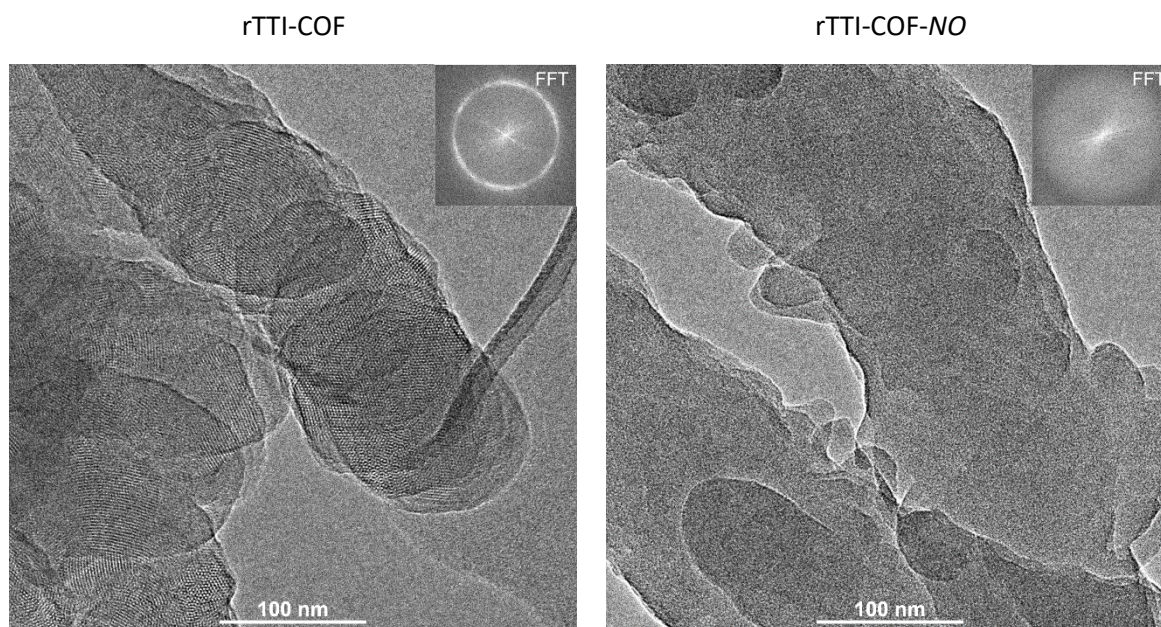
rTTI-COF

rTTI-COF-*NO*

Figure S9.4.16**.** TEM images of rTTI-COF before (left) and after NO sorption measurements (right) revealing a collapse of the crystalline structure.
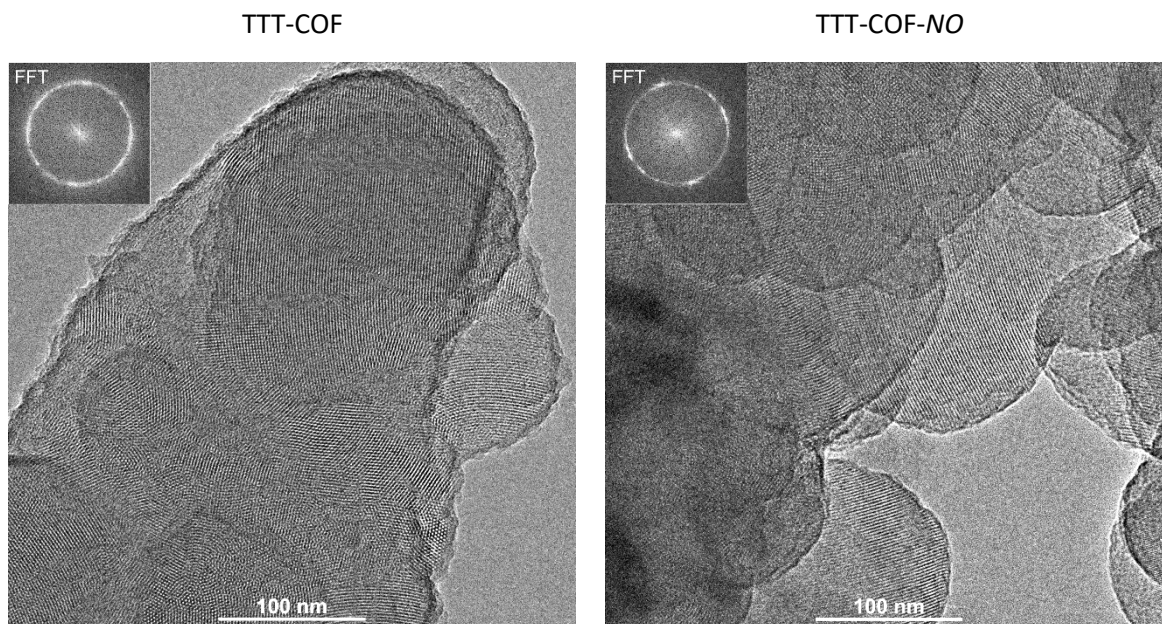
TTT-COF

TTT-COF-*NO*

Figure S9.4.17. TEM images of TTT-COF before (left) and after NO sorption measurements (right) showing retention of the crystalline structure.

TT-Imide-COF
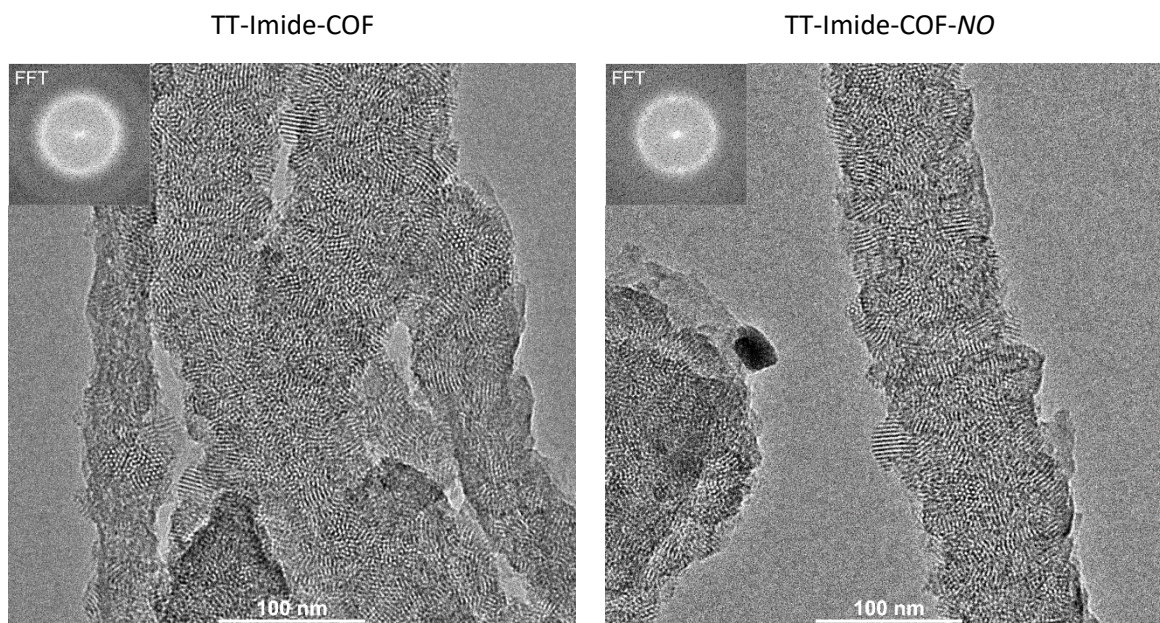
TT-Imide-COF-*NO*

Figure S9.4.18. TEM images of TT-Imide-COF before (left) and after NO sorption measurements (right) showing retention of the crystalline structure.

9.4.7. UV/VIS Spectra
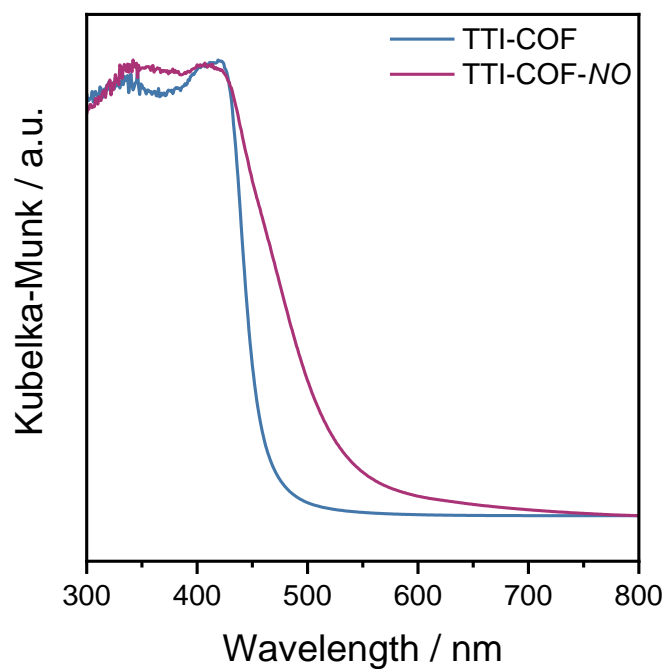
Figure S9.4.19. Diffuse reflectance spectra of TTI-COF before (blue) and after NO sorption experiments (red) revealing a shift of the absorption towards higher wavelengths, along with broadening/tailing of the absorption edge.
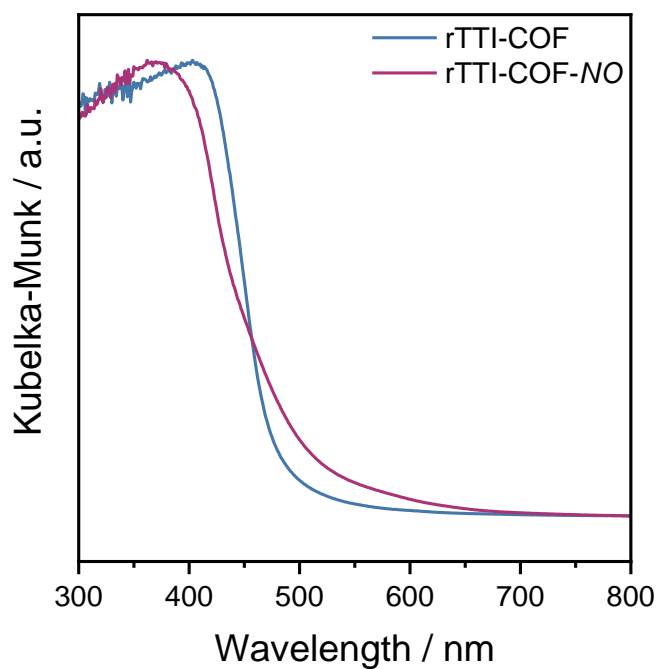
Figure S9.4.20. Diffuse reflectance spectra of rTTI-COF before (blue) and after NO sorption experiments (red) revealing a slight blueshift in the absorption edge, along with broadening/tailing.
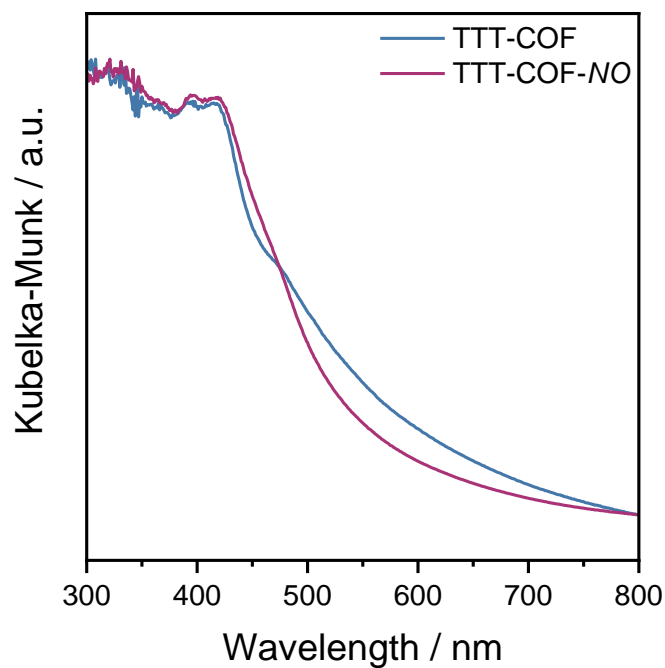
Figure S9.4.21. Diffuse reflectance spectra of TTT-COF before (blue) and after NO sorption experiments (red) showing slight changes in the structure of the absorption edge.
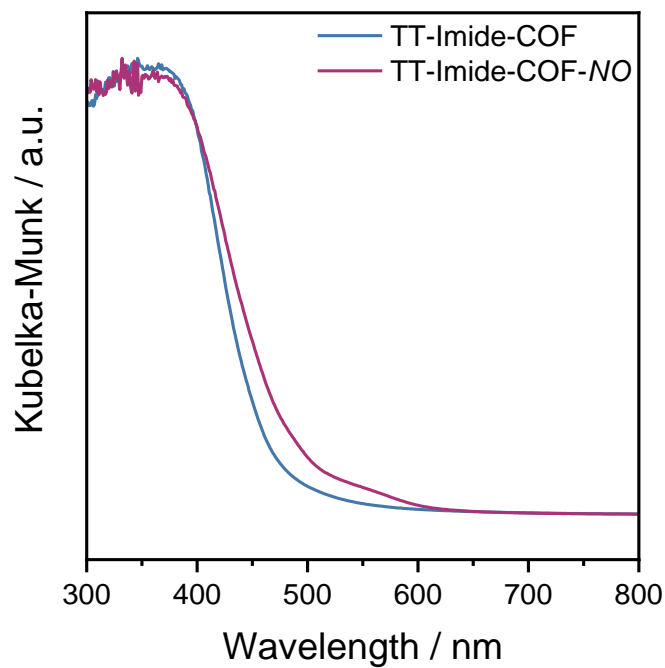
Figure S9.4.22. Diffuse reflectance spectra of TT-Imide-COF before (blue) and after NO sorption experiments (red), suggesting that the optical properties are largely retained.

9.4.8. Gas Sorption Experiments
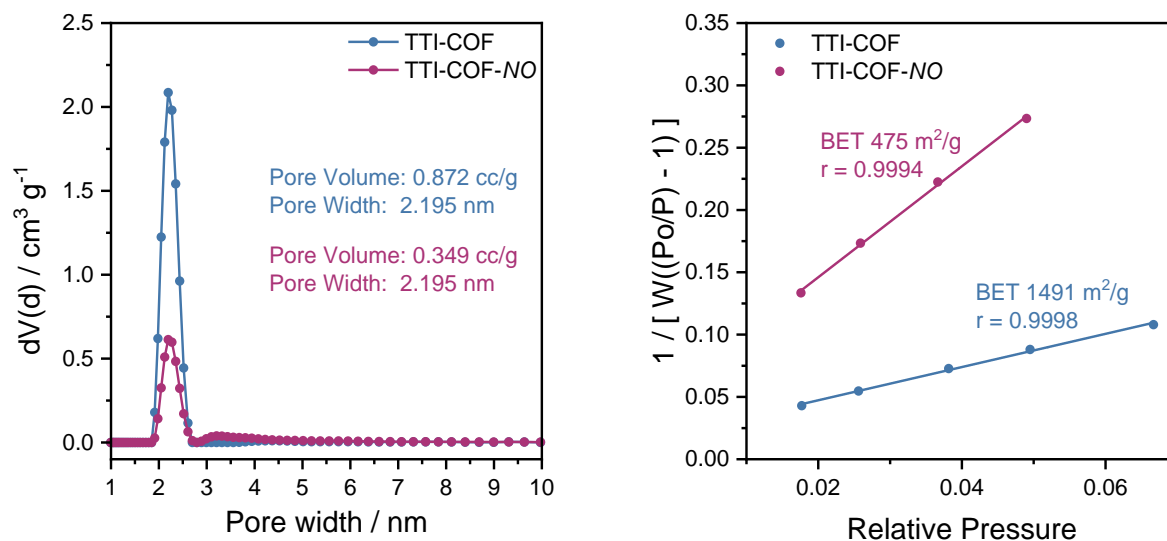
Figure S9.4.23. Calculated pore size distributions (left) and BET plots (right) of TTI-COF before (blue) and after NO sorption experiments (red), revealing a significant decrease in the surface area and pore volume after NO treatment.
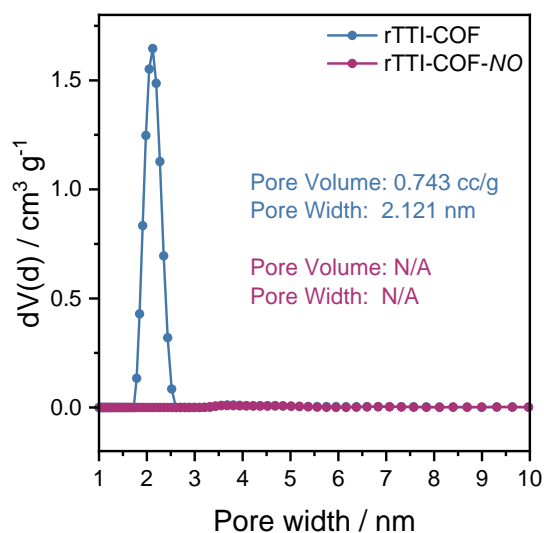
Figure S9.4.24. Calculated pore size distributions of rTTI-COF before (blue) and after NO sorption experiments (red), revealing a complete loss of structural porosity after NO treatment.
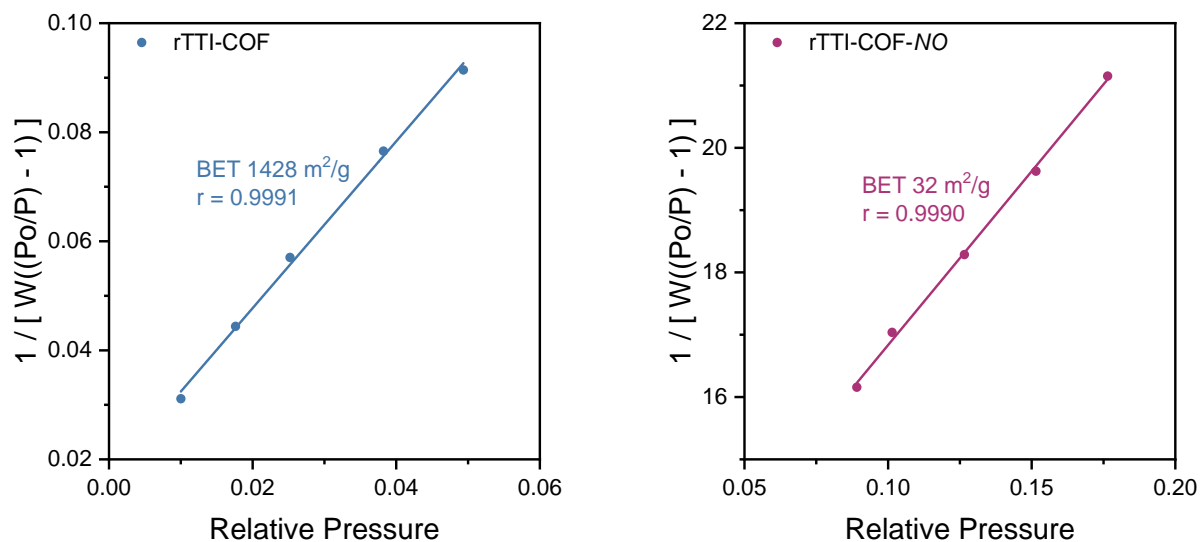
Figure S9.4.25. BET plots of rTTI-COF before (blue) and after NO sorption experiments (red), revealing an essentially complete loss of surface area after NO treatment.
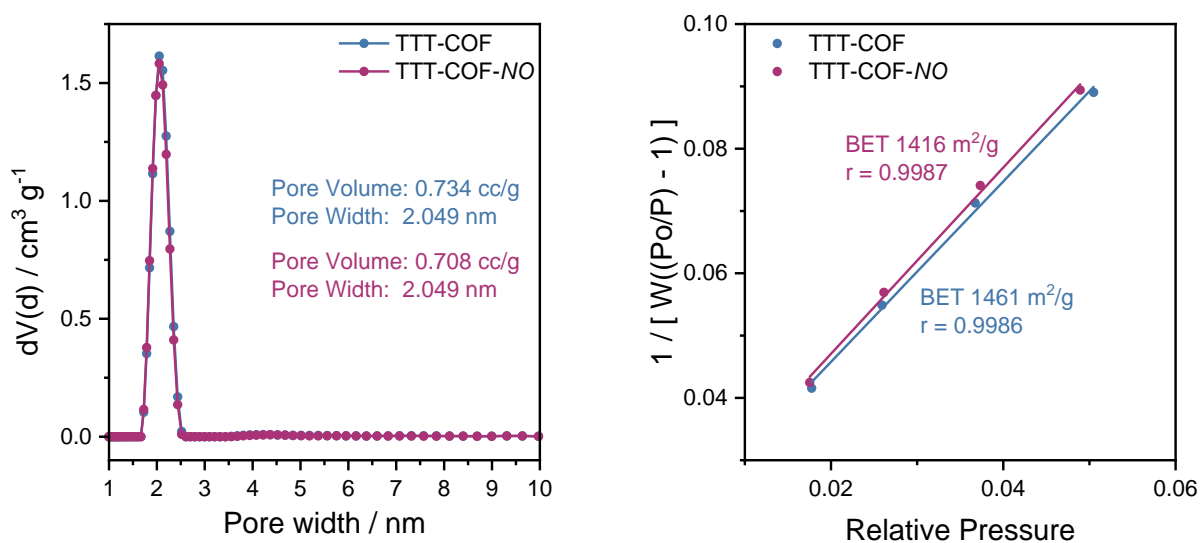
Figure S9.4.26. Calculated pore size distributions (left) and BET plots (right) of TTT-COF before (blue) and after NO sorption experiments (red), showing retention of its surface area and pore volume upon NO treatment indicating a strong robustness of the framework against NO.
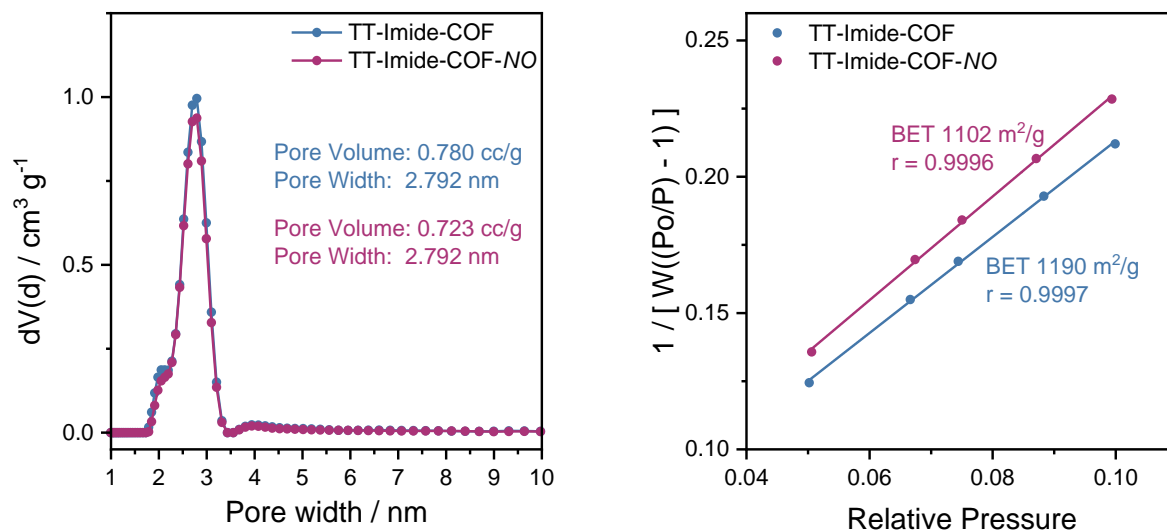
Figure S9.4.27. Calculated pore size distributions (left) and BET plots (right) of TT-Imide-COF before (blue) and after NO sorption experiments (red), showing retention of its surface area and pore volume upon NO treatment, indicating that the framework is robust against NO.
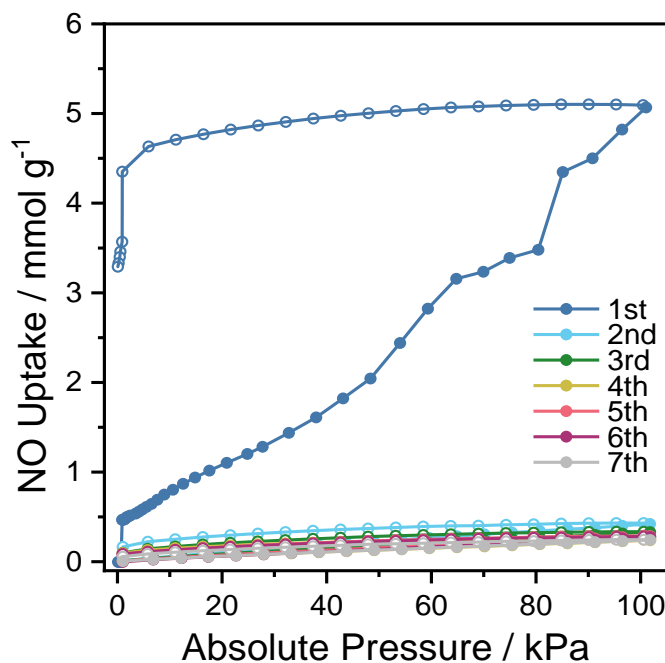
Figure S9.4.28. First seven NO adsorption and desorption isotherms of TTI-COF showing an unusual increased NO uptake within the first cycle. After the first cycle, the total uptake decreases until it stabilizes after three cycles.
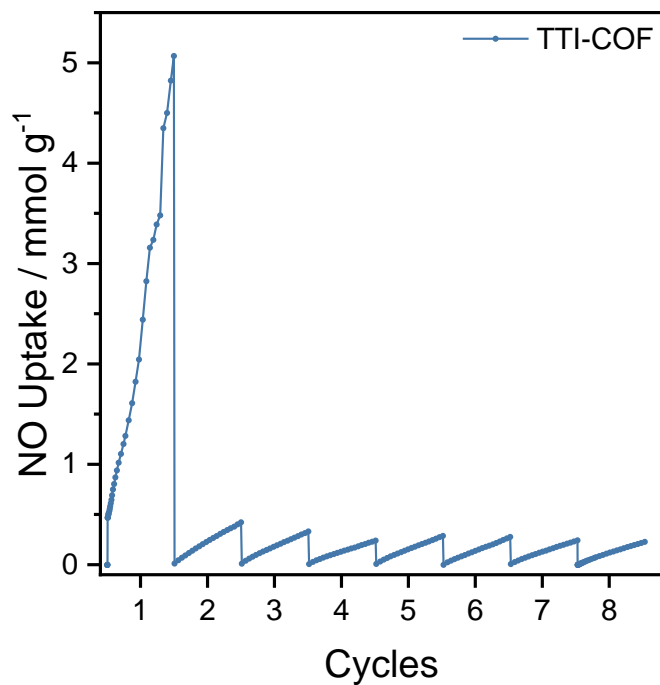
Figure S9.4.29. NO adsorption isotherms of TTI-COF plotted in a row, demonstrating the stabilization in NO uptake behavior after two to three cycles.
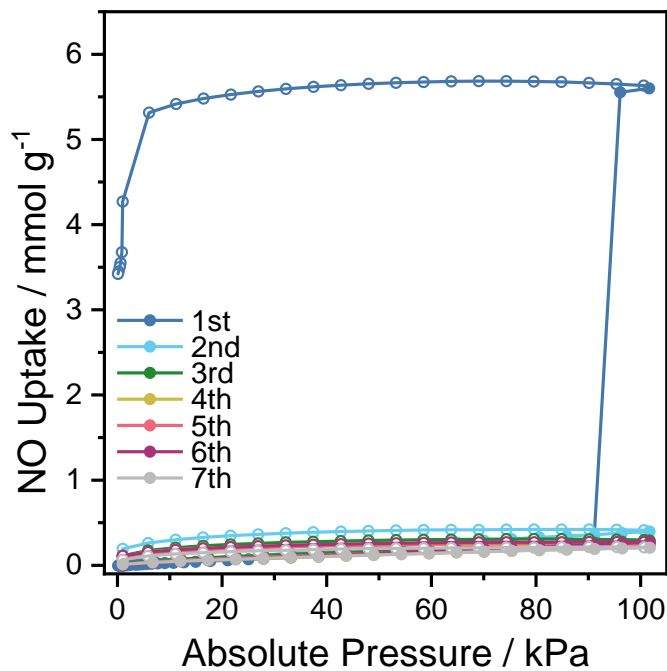
Figure S9.4.30. First seven NO adsorption and desorption isotherms of rTTI-COF showing an unusual increased NO uptake within the first cycle. After the first cycle, the total uptake decreases until it stabilizes after three cycles.
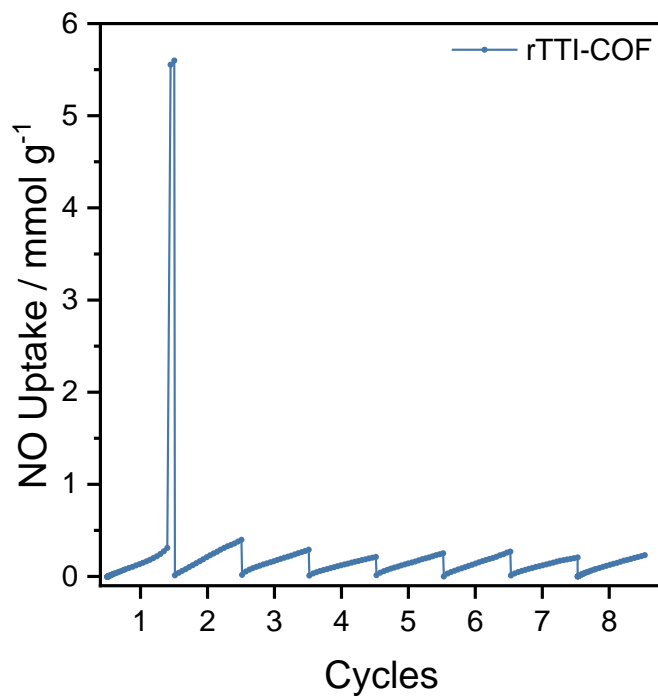
Figure S9.4.31. NO adsorption isotherms of rTTI-COF plotted in a row demonstrating the stabilization of NO uptake behavior after two to three cycles.
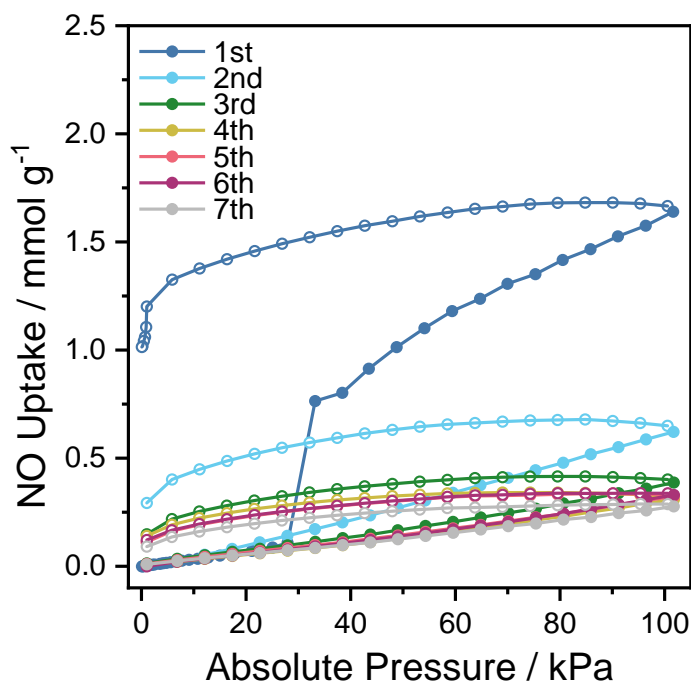
Figure S9.4.32. First seven NO adsorption and desorption isotherms of TTT-COF showing an unusual increased NO uptake within the first two cycles. Over the first and second cycle, the total uptake decreases until it stabilizes after three cycles.
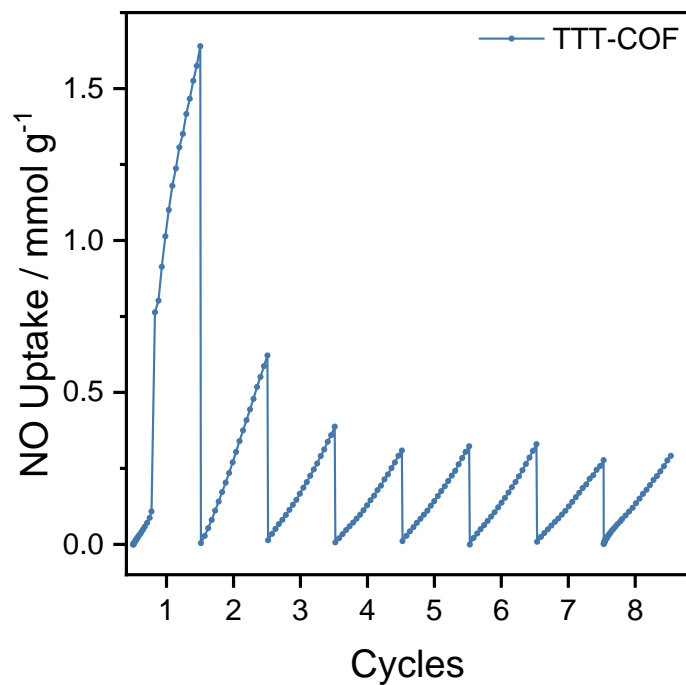
Figure S9.4.33. NO adsorption isotherms of TTT-COF plotted in a row demonstrating stabilization of the NO uptake behavior after three cycles.
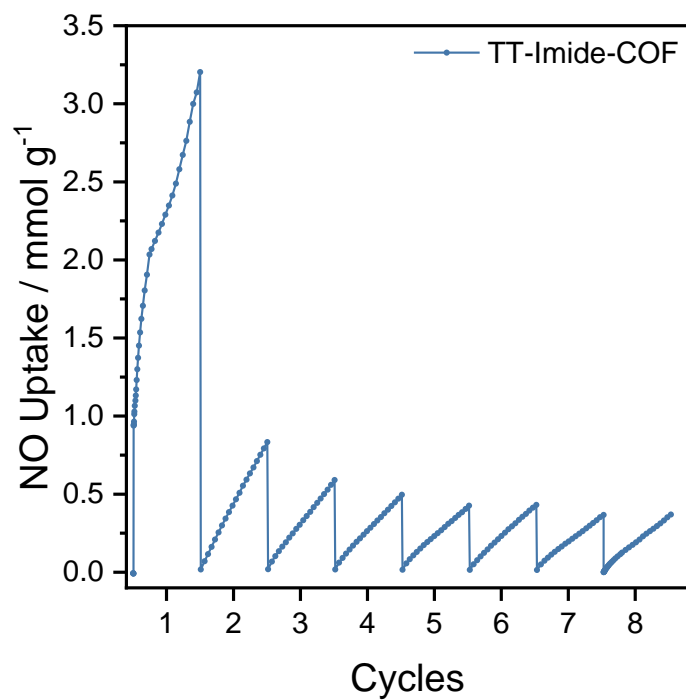
Figure S9.4.34. NO adsorption isotherms of TT-Imide-COF plotted in a row, demonstrating stabilization of the NO uptake behavior after two to four cycles.
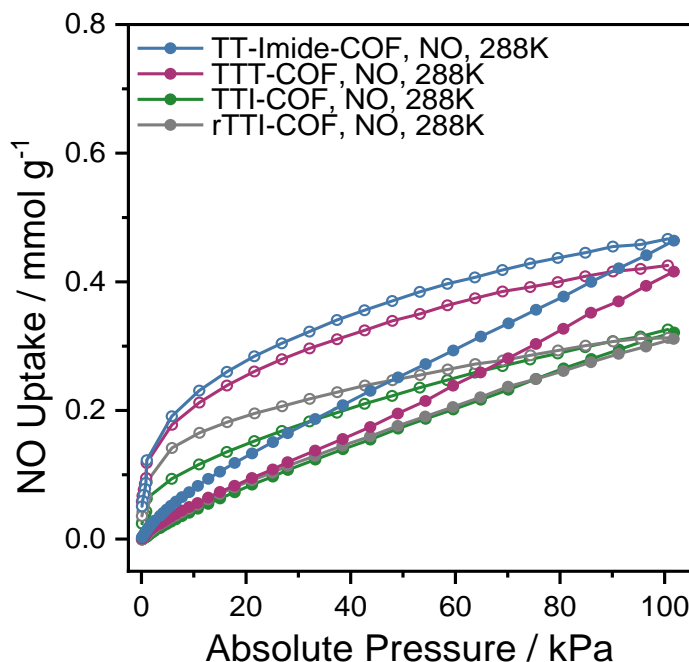
Figure S9.4.35. NO adsorption and desorption isotherms of TTI-, rTTI-, TTT-, and TT-Imide-COF at 288 K, after the cycling experiments. The reversibility of the isotherms indicates a process that can be described by physisorption.
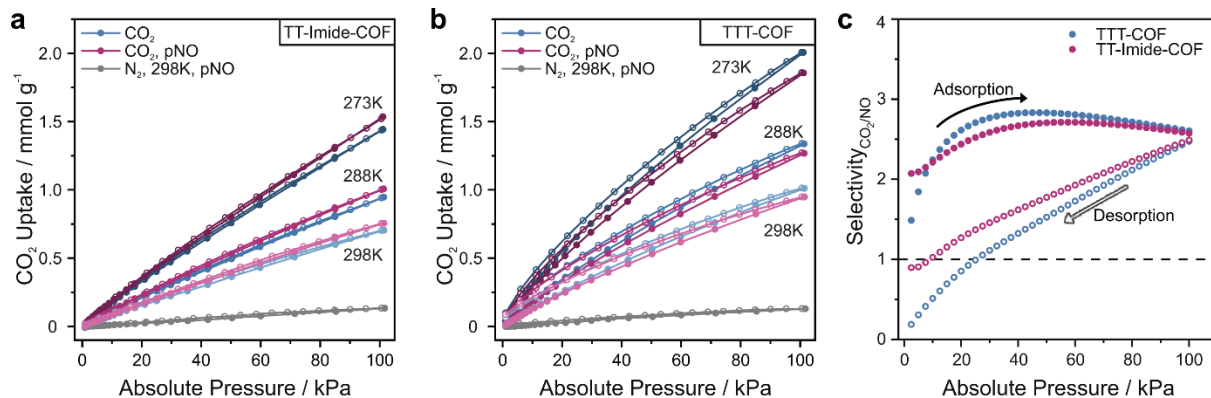
Figure S9.4.36. CO_2 isotherms of (a) TT-Imide-COF and (b) TTT-COF before (blue) and after NO exposure (red). Filled circles represent adsorption and empty circles desorption isotherms. (c) IAST selectivity of TTT-COF-NO and TT-Imide-COF-NO for a binary CO_2/NO (50/50) gas mixture during adsorption (filled circles) and desorption (empty circles). For a binary CO_2/NO (50/50) gas mixture, we found a selectivity towards CO_2 over the whole pressure range during adsorption up to 100 kPa for both COFs. The selectivities first increase until around 50 kPa before slightly declining to an almost identical value of 2.5 at 100 kPa. However, applying IAST to the desorption instead of the adsorption branch, in both COFs, the selectivity changes in favor of NO for low pressures below 30 kPa. In our opinion, this practice is a better representation of the thermodynamic equilibrium state due to the unusual and broad hysteresis of the pure NO isotherm.

Table S9.4.1. Calculated heats of adsorption, CO_2 and NO adsorption capacities and IAST selectivities for TT-Imide-COF-NO and TTT-COF-NO.

	Initial Q_{st} CO_2 (kJ mol^{-1})	CO_2 capacity (mmol g^{-1})		Selectivity[a] CO_2/N_2 (IAST)	Initial Q_{st} NO (kJ mol^{-1})	NO capacity (mmol g^{-1})		Selectivity[b] NO/N_2 (IAST)
		273K	298K			273K	298K	
TT-Imide-COF-*NO*	26.6-20.5	1.86	0.944	9.22	35.7-16.9	0.623	0.367	5.55
TTT-COF-*NO*	23.8-20.8	1.54	0.755	6.44	21.6-17.0	0.562	0.290	3.95

[a] Selectivity was calculated for 15/85 gas mixtures at 1 bar and 298 K for CO_2/N_2
[b] Selectivity was calculated for 3/97 gas mixtures at 1 bar and 298 K for NO/N_2
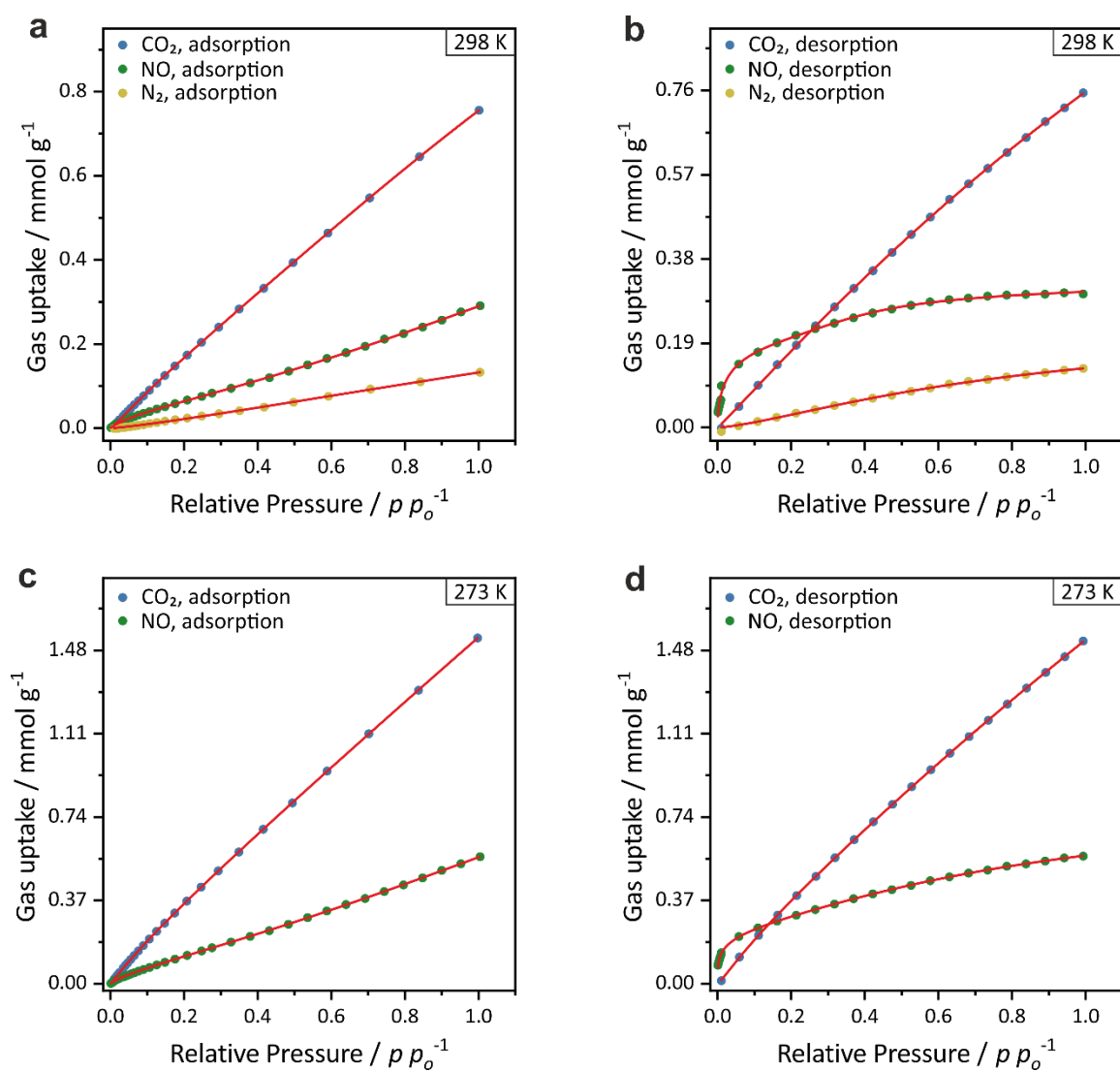
Figure S9.4.37. Fitting curves of **a** the adsorption isotherms at 298 K, **b** the desorption isotherms at 298 K, **c** the adsorption isotherms at 273 K and **d** the desorption isotherms at 273 K of TTT-COF.
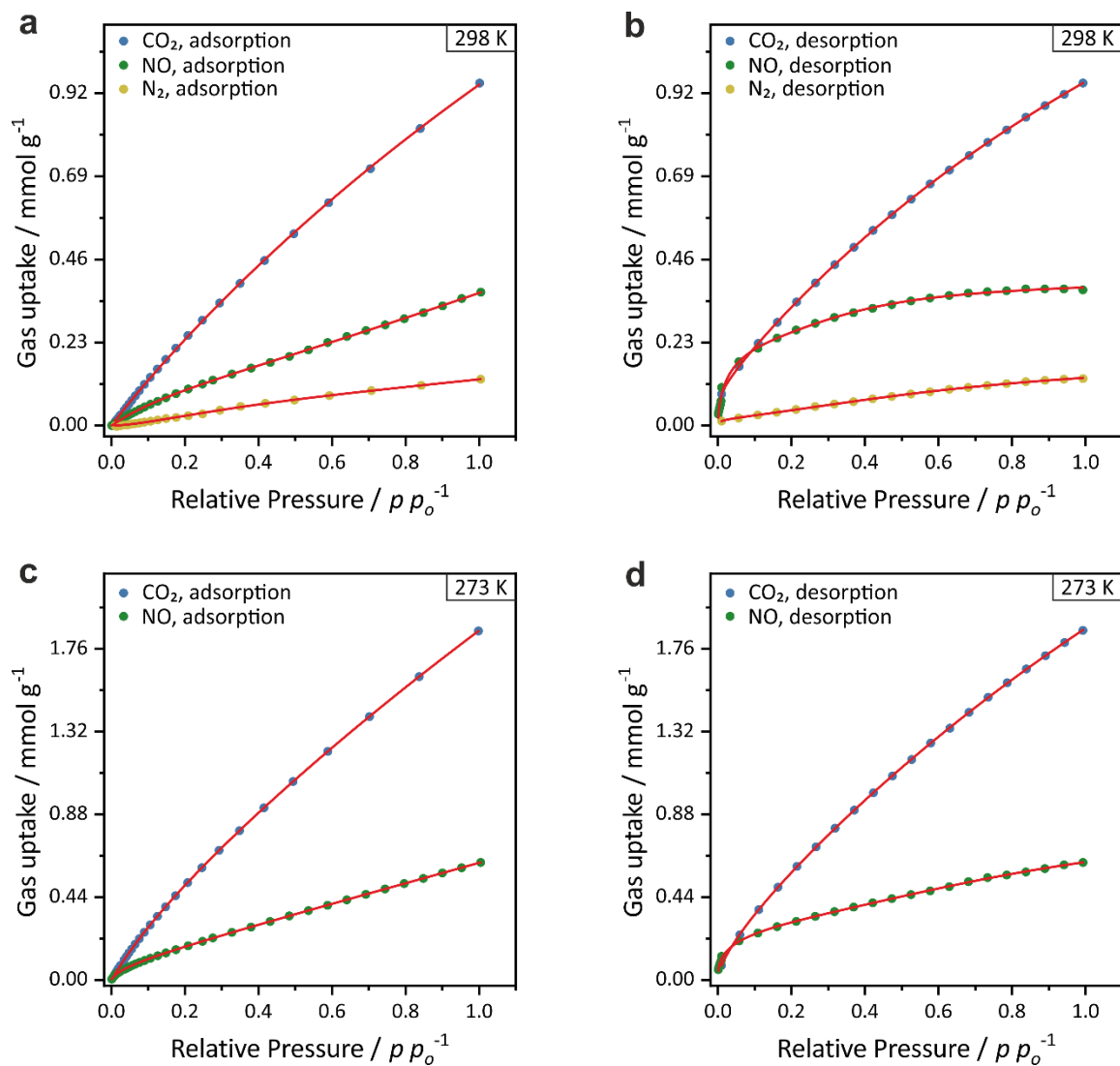
Figure S9.4.38. Fitting curves of **a** the adsorption isotherms at 298 K, **b** the desorption isotherms at 298 K, **c** the adsorption isotherms at 273 K and **d** the desorption isotherms at 273 K of TT-Imide-COF.
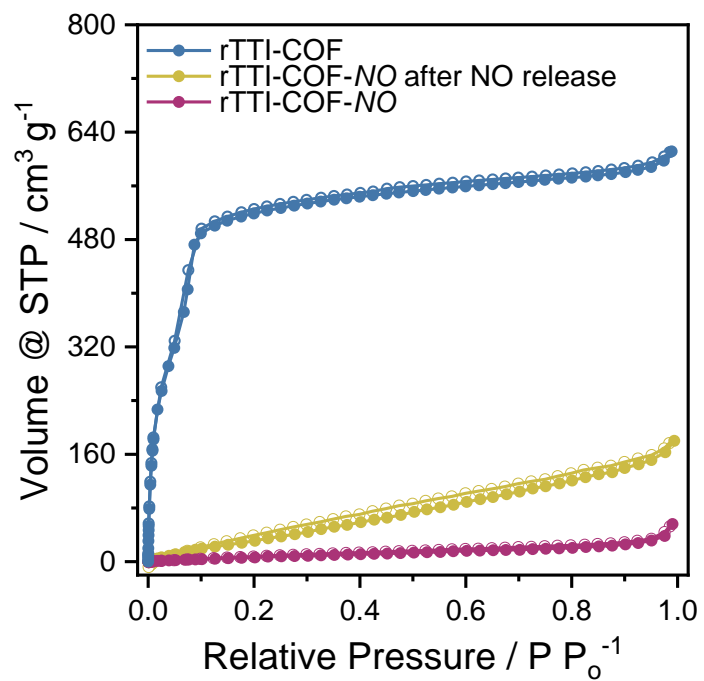
Figure S9.4.39. Argon adsorption isotherms at 87 K of rTTI-COF-*NO* (red) and rTTI-COF-*NO* after NO release (blue).

9.4.9. Bibliography

[1]   J. W. M. Osterrieth, D. Fairen-Jimenez *et al. Adv. Mater.* **2022**, 2201502.

[2]   J. Dong, Y. Wang, G. Liu, Y. Cheng, D. Zhao, *CrystEngComm* **2017**, 1*9*, 4899–4904.

[3]   F. Haase, K. Gottschling, L. Stegbauer, L. S. Germann, R. Gutzler, V. Duppel, V. S. Vyas, K. Kern, R. E. Dinnebier, B. V. Lotsch, *Mater. Chem. Front.* **2017**, *1*, 1354–1361.

[4]   L. Grunenberg, G. Savasci, M. W. Terban, V. Duppel, I. Moudrakovski, M. Etter, R. E. Dinnebier, C. Ochsenfeld, B. V. Lotsch, *J. Am. Chem. Soc.* **2021**, *143*, 3430–3438.

[5]   F. Haase, E. Troschke, G. Savasci, T. Banerjee, V. Duppel, S. Dörfler, M. M. J. Grundei, A. M. Burow, C. Ochsenfeld, S. Kaskel, B. V. Lotsch, *Nat. Commun.* **2018**, *9*, 1–10.

[6]   X. Zhu, S. An, Y. Liu, J. Hu, H. Liu, C. Tian, S. Dai, X. Yang, H. Wang, C. W. Abney, S. Dai, *AIChE J.* **2017**, *63*, 3470–3478.

[7]   J. A. Hrabie, A. Srinivasan, C. George, L. K. Keefer, *Tetrahedron Lett.* **1998**, *39*, 5933–5936.

9.5. List of Abbreviations

2D	Two-dimensional
3D	Three-dimensional
AcOH	Acetic acid
ADMET	Acyclic diene metathesis
Bd	Benzidine
BDA	Terephthaladehyde
BET	Brunauer-Emmet-Teller
CG	Conjugated gradient
COF	Covalent organic framework
DFT	Density functional theory
DI	Deionized water
dPP	4,4'-(6-phenylphenanthridine-3,8-diyl)bis(2,6-dimethoxybenzaldeyde)
ED	Electron diffraction
ESI	Electrospray ionization
EXAFS	Extended X-ray absorption fine structure
FFT	Fast Fourier transformed
FT-IR	Fourier-transformed infrared spectroscopy
FWHM	Full width half maximum
GC	Gas chromatograph
HER	Hydrogen evolution reaction
HETCOR	Heteronuclear correlation
HOMO	Highest occupied molecular orbital
HR	High resolution
HSQC	Heteronuclear single quantum coherence
INEPT	Insensitive nuclei enhanced polarization transfer
ICP-OES	Inductively-coupled plasma optical emission spectroscopy
lsNMR	liquid state nuclear magnetic resonance
LUMO	Lowest unoccupied molecular orbital
MAS	Magic-angle-spinning
MeOH	Methanol
MMC	Macro(mono)cyclization
MOF	metal-organic framework
mPP	4,4'-(6-phenylphenanthridine-3,8-diyl)bis(2-methoxybenzaldehyde)
O	Oligomerization
OER	Oxygen evolution reaction
PDF	Pair distribution function
PMMA	poly(methyl methacrylate)

PP	4,4'-(6-phenylphenanthridine-3,8-diyl)dibenzaldehyde
*p*PDA	*p*-phenylenediamine
PSD	Pore size distribution
PXRD/XRPD	Powder X-ray diffraction
QSDFT	Quenched solid density functional theory
SBA	Santa Barbara Amorphous
RCM	Ring-closing metathesis
scCO$_2$	Supercritical carbon dioxide
Sc(OTf)$_3$	Scandium(III) triflate
SE	Secondary electron
SEM	Scanning electron microscopy
S$_{BET}$	Brunauer-Emmet-Teller surface area
ssNMR	Solid state nuclear magnetic resonance
TAB	5'-(4-aminophenyl)-[1,1':3',1''-terphenyl]-4,4''-diamine
TAPB	1,3,5-tris[4-amino(1,1-biphenyl-4-yl)]benzene
TAT	2,4,6-tris(4-aminophenyl)-1,3,5-triazine
Tb	1,3,5-triformylbenzene
TEM	Transmission electron microscopy
TGA	Thermogravimetric analysis
UV-Vis	UV and visible light spectroscopy
XANES	X-ray absorption near edge structure
XAS	X-ray absorption
XPS	X-ray photoelectron spectroscopy

9.6. List of Publications

Publications that are part of this thesis

NO as a Reagent for Topochemical Framework Transformation and Controlled Nitric Oxide Release in Covalent Organic Frameworks

<u>Sebastian T. Emmerling</u>, Johannes Maschita, and Bettina V. Lotsch

submitted (ChemRxiv **2022**, DOI: 10.26434/chemrxiv-2022-czptr)

Olefin Metathesis in Confinement: Towards Covalent Organic Framework Scaffolds for Increased Macrocyclization Selectivity

<u>Sebastian T. Emmerling</u>, Felix Ziegler, Felix R. Fischer, Roland Schoch, Matthias Bauer, Bernd Plietker, Michael R. Buchmeiser, and Bettina V. Lotsch

Chem. Eur. J. **2022**, *28*, e202104108. DOI: 10.1002/chem.202104108

Interlayer Interactions as Design Tool for Large-Pore COFs

<u>Sebastian T. Emmerling</u>, Robin Schuldt, Sebastian Bette, Liang Yao, Robert E. Dinnebier, Johannes Kästner, and Bettina V. Lotsch

J. Am. Chem. Soc. **2021**, *143*, (38), 15711–15722. DOI: 10.1021/jacs.1c06518

In situ monitoring of mechanochemical covalent organic framework formation reveals templating effect of liquid additive

<u>Sebastian T. Emmerling</u>, Luzia S. Germann, Patrick A.Julien, Igor Moudrakovski, Martin Etter, Tomislav Friščić, Robert E. Dinnebier, and Bettina V. Lotsch

Chem **2021**, *7*, 1639–1652. DOI: 10.1016/j.chempr.2021.04.012

Publications that are not part of this thesis

Guest-responsive thermal expansion in the Zr-porphyrin metal-organic framework PCN-222

Hanna L. B. Boström, Sebastian Bette, <u>Sebastian T. Emmerling</u>, Maxwell W. Terban, and Bettina V. Lotsch

APL Materials **2022**, *10*, 071106. DOI: 10.1063/5.0091091

Covalent Organic Framework Nanoplates Enable Solution-Processed Crystalline Nanofilms for Photoelectrochemical Hydrogen Evolution

Liang Yao, Andrés Rodríguez-Camargo, Meng Xia, David Mücke, Roman Guntermann, Yongpeng Liu, Lars Grunenberg, Alberto Jiménez-Solano, <u>Sebastian T. Emmerling</u>, Viola Duppel, Kevin Sivula, Thomas Bein, Haoyuan Qi, Ute Kaiser, Michael Grätzel, and Bettina V. Lotsch

J. Am. Chem. Soc. **2022**, *144*, (23), 10291–10300. DOI 10.1021/jacs.2c01433

How Reproducible Are Surface Areas Calculated from the BET Equation?

Johannes W. M. Osterrieth, James Rampersad, David Madden, Nakul Rampal, Luka Skoric, Bethany Connolly, Mark D. Allendorf, Vitalie Stavila, Jonathan L. Snider, Rob Ameloot, João Marreiros, Conchi Ania, Diana Azevedo, Enrique Vilarrasa-Garcia, Bianca F. Santos, Xian-He Bu, Ze Chang, Hana Bunzen, Neil R. Champness, Sarah L. Griffin, Banglin Chen, Rui-Biao Lin, Benoit Coasne, Seth Cohen, Jessica C. Moreton, Yamil J. Colón, Linjiang Chen, Rob Clowes, François-Xavier Coudert, Yong Cui, Bang Hou, Deanna M. D'Alessandro, Patrick W. Doheny, Mircea Dincă, Chenyue Sun, Christian Doonan, Michael Thomas Huxley, Jack D. Evans, Paolo Falcaro, Raffaele Ricco, Omar Farha, Karam B. Idrees, Timur Islamoglu, Pingyun Feng, Huajun Yang, Ross S. Forgan, Dominic Bara, Shuhei Furukawa, Eli Sanchez, Jorge Gascon, Selvedin Telalović, Sujit K. Ghosh, Soumya Mukherjee, Matthew R. Hill, Muhammed Munir Sadiq, Patricia Horcajada, Pablo Salcedo-Abraira, Katsumi Kaneko, Radovan Kukobat, Jeff Kenvin, Seda Keskin, Susumu Kitagawa, Ken-ichi Otake, Ryan P. Lively, Stephen J. A. DeWitt, Phillip Llewellyn, Bettina V. Lotsch, <u>Sebastian T. Emmerling</u>, Alexander M. Pütz, Carlos Martí-Gastaldo, Natalia M. Padial, Javier García-Martínez, Noemi Linares, Daniel Maspoch, Jose A. Suárez del Pino, Peyman Moghadam, Rama Oktavian, Russel E. Morris, Paul S. Wheatley, Jorge Navarro, Camille Petit, David Danaci, Matthew J. Rosseinsky, Alexandros P. Katsoulidis, Martin Schröder, Xue Han, Sihai Yang, Christian Serre, Georges Mouchaham, David S. Sholl, Raghuram Thyagarajan, Daniel Siderius, Randall Q. Snurr, Rebecca B. Goncalves, Shane Telfer, Seok J. Lee, Valeska P. Ting, Jemma L. Rowlandson, Takashi Uemura, Tomoya Iiyuka, Monique A. van der Veen, Davide

Rega, Veronique Van Speybroeck, Sven M. J. Rogge, Aran Lamaire, Krista S. Walton, Lukas W. Bingel, Stefan Wuttke, Jacopo Andreo, Omar Yaghi, Bing Zhang, Cafer T. Yavuz, Thien S. Nguyen, Felix Zamora, Carmen Montoro, Hongcai Zhou, Angelo Kirchon, and David Fairen-Jimenez

Adv. Mater. **2022**, 2201502. DOI: 10.1002/adma.202201502

Influence of layer slipping on adsorption of light gases in covalent organic frameworks: A combined experimental and computational study

Christopher Kessler, Robin Schuldt, <u>Sebastian T. Emmerling</u>, Bettina V. Lotsch, Johannes Kästner, Joachim Gross, and Niels Hansen

Microporous and Mesoporous Materials **2022**, *336*, 111796. DOI: 10.1016/j.micromeso.2022.111796

Crystal Structure, Polymorphism, and Anisotropic Thermal Expansion of α-Ca(CH3COO)2

Sebastian Bette, Gerhard Eggert, <u>Sebastian T. Emmerling</u>, Martin Etter, Thomas Schleid, and Robert E. Dinnebier

Cryst. Growth Des. **2020**, *20*, (8), 5346–5355. DOI: 10.1021/acs.cgd.0c00563

Monitoring polymer-assisted mechanochemical cocrystallisation through in situ X-ray powder diffraction

Luzia S. Germann, <u>Sebastian T. Emmerling</u>, Manuel Wilke, Robert E. Dinnebier, Mariarosa Moneghini, and Dritan Hasa

Chem. Commun., **2020**, *56*, 8743-8746. DOI: 10.1039/D0CC03460F

Unsaturated Four-Membered Rings: Efficient Strategies for the Construction of Cyclobutenes and Alkylidenecyclobutanes

Michael Eisold, Andreas N. Baumann, Gabriel M. Kiefl, <u>Sebastian T. Emmerling</u>, and Dorian Didier

Chem. Eur. J. **2017**, *23*, 1634 –1644. DOI: 10.1002/chem.201604585